ABSTRACT

Title of dissertation: PREDICTING THE TRANSPORT PROPERTIES OF AEROSOL PARTICLES IN CREEPING FLOW FROM THE CONTINUUM TO THE FREE MOLECULE REGIME

James Corson, Doctor of Philosophy, 2018

Dissertation directed by: Professor Michael R. Zachariah
Department of Chemical
and Biomolecular Engineering

The transport of nanoscale aerosol particles plays an important role in many natural and industrial processes. Despite its importance, the transport behavior of aerosol aggregates is poorly understood, largely due its complex dependence on particle size, shape, and orientation. Often, these particles are in the transition regime, where neither the continuum approximation for large particles nor the free molecule approximation for small particles is valid.

At present, methods for calculating the aerodynamic force on and diffusive behavior of fractal aggregates in the transition regime either rely upon scaling laws fitted to experimental data or computationally-intensive direct simulation Monte Carlo or molecular dynamics approaches. Thus, there is a pressing need for a new method for determining aerosol transport properties.

This dissertation introduces such a method for calculating the drag and torque on an aerosol aggregate as a function of the primary sphere size and the aggregate

size and shape. This method is an extension of Kirkwood-Riseman theory to the transition regime, using an appropriate model for interactions between the individual spheres in an aggregate.

This dissertation also describes the application of this extended Kirkwood-Riseman (EKR) method to a number of problems related to aerosol transport, including computation of the scalar translational and rotational friction coefficients of aggregates formed by diffusion-limited processes, analysis of the effects of alignment on particle migration in an electric field, and the strength of interactions between particles due to their effects on the surrounding fluid flow field.

In each of these applications, results from the EKR method are in good agreement with published experimental data and computational results. EKR results also demonstrate that particle translational and rotational behavior becomes more continuum-like as both primary particle size and the number of spheres in the aggregate increase.

Using these results, new correlations have been developed for the translational and rotational friction coefficients of aggregates formed by diffusion-limited processes (e.g. soot); these correlations are more accurate than the empirical models currently available in the literature.

PREDICTING THE TRANSPORT PROPERTIES OF AEROSOL PARTICLES IN CREEPING FLOW FROM THE CONTINUUM TO THE FREE MOLECULE REGIME

by

James Corson

Dissertation submitted to the Faculty of the Graduate School of the
University of Maryland, College Park in partial fulfillment
of the requirements for the degree of
Doctor of Philosophy
2018

Advisory Committee:
Professor Michael R. Zachariah, Chair
Dr. George W. Mulholland
Professor Richard V. Calabrese
Professor Panagiotis Dimitrakopoulos
Professor Elaine S. Oran

Dedication

To my wife, Holly, who convinced me to go back to school to earn my Ph.D. Were it not for her encouragement, I would still be *Mr.* Corson.

Acknowledgments

First and foremost, I would like to thank my adviser, Prof. Michael Zachariah, as well as Dr. George Mulholland. They provided me with valuable guidance throughout my time at the University of Maryland, from suggesting that I take on a more focused and manageable project than the mess I had in my mind when I started at Maryland, to introducing me to the Kirkwood-Riseman method that plays such a prominent role in this dissertation, to mentioning ways to improve my papers and presentations. I could not ask for two better advisers.

I would also like to thank Prof. Howard Baum in the Department of Fire Protection Engineering at the University of Maryland for introducing me to the BGK model and explaining how one might go about solving the Boltzmann transport equation for flow around a sphere in the transition regime.

Thank you to Dr. Walid Keyrouz and Dr. Derek Juba at the National Institute of Standards and Technology, who provided me with the ZENO code. I have used the Deepthought2 cluster at Maryland to run Zeno and some of my own codes; thank you to the Division of Information Technology for maintaining the cluster and to Prof. Jeffery Klauda in the Department of Chemical and Biomolecular Engineering for helping me get an initial allocation to the cluster.

Finally, thank you to my wonderful family and friends, especially my parents and my wife. My parents always encouraged me to challenge myself and instilled in me the work ethic needed to complete all 21 years (!) of my formal education. My

wife encouraged me to go back to school for my Ph.D. and supported me throughout my time at Maryland, for which I am forever grateful.

This research was performed while under appointment to the U.S. Nuclear Regulatory Commission Graduate Fellowship Program.

Table of Contents

List of Tables

List of Figures

List of Abbreviations

APM	Aerosol Particle Mass [analyzer]
ASM	Adjusted Sphere Method
BGK	Bhatnagar-Gross-Krook [model]
DLCA	Diffusion-Limited Cluster Aggregation
DMA	Differential Mobility Analyzer
DSMC	Direct-Simulation Monte Carlo
EKR	Extended Kirkwood-Riseman [method]
GDE	General Dynamic Equation
KR	Kirkwood-Riseman [theory]
MC	Monte Carlo
NGDE	Nodal General Dynamic Equation [solver]
ODE	Ordinary Differential Equation
PA	Projected Area
PFDMA	Pulsed Field Differential Mobility Analyzer
PSD	Particle Size Distribution
RPY	Rotne-Prager-Yamakawa [tensor]
SPD	Self-Preserving Distribution
TDMA	Tandem Differential Mobility Analyzer

Chapter 1: Introduction

Nanoscale aerosol particles formed at high temperature are found in many natural and engineered environments [1–3]. A particle's size and shape significantly affect its transport properties, most notably the aerodynamic force it experiences as it moves through an external force field [4–6]. Research on this topic is motivated by the widespread use of aerosol reactors for the manufacturing of carbon black, ceramics (e.g. SiO_2 and TiO_2), catalysts, and optical fibers present in numerous consumer products [2, 7–10]; the impacts of aerosols generated in the combustion of fossil fuels or from volcanic eruptions on climate, both through direct absorption or scattering of incident solar radiation and through its influence on cloud formation [11–16]; and the adverse human health effects of particle uptake by the body [17–20] and exposure to radioactive particles from nuclear reactor accidents [21–25].

In many practical situations, these aerosol particles move very slowly with respect to the surrounding gas. As a result, one can neglect inertial effects in the fluid and treat the particle as if it is in the creeping flow regime. This significantly simplifies the fluid dynamics and makes problems of aerosol transport more tractible.

A further simplification is to treat particles as if they are spherical. The equivalent sphere size may be based on the particle mass – as if often done in aerosol

dynamics codes [26, 27] – or on its aerodynamic behavior, such as its experimentally-measured mobility. Using this equivalent sphere size, one can estimate any number of transport properties (e.g. diffusion and friction coefficients, coagulation rates, phoretic velocities, etc.) using various theoretical or experimental relations that have been developed for spheres [2].

Unfortunately, particles are often non-spherical. In fact, particles formed by random processes are often fractal aggregates of N spheres (or monomers) with radius a. The number of primary spheres in a fractal aggregate is related to the radius of gyration R_g of the particle by

$$N = k_0 \left(\frac{R_g}{a} \right)^{d_f} \tag{1.1}$$

Here, d_f and k_0 are the fractal dimension and prefactor. One important class of particles, those formed by diffusion-limited cluster-to-cluster aggregation (DLCA), have a fractal dimension of approximately 1.78 and a prefactor around 1.3 [4].

Treating a fractal aggregate as a sphere with an equivalent mass or equivalent mobility leads to an erroneous estimate of particle migration, coagulation, and deposition rates. There are existing methods for calculating the drag on a non-spherical particle, but most of these methods are only applicable in the continuum [28–31] or free molecule [32–36] regimes corresponding to particles much larger or much smaller than the mean free path of gas molecules. However, nano-scale aerosols typically have characteristic sizes that place them in the transition regime between the continuum and free molecule limits. There is also some ambiguity as to how one

should approach a situation where the aerosol is an aggregate of very many small spheres ($a \ll \lambda$, where a is the sphere diameter and λ the mean free path) while the characteristic size of the aggregate (such as R_g) is comparable to or larger than λ. Methods for calculating the drag on a particle in the transition regime are largely based on fits to empirical data [37–39], or rely on expensive computational methods such as the direct simulation Monte Carlo (DSMC) method [40, 41].

This dissertation describes a new method for calculating the drag and torque on an aggregate in creeping flow when continuum approaches are invalid. Before describing my method and presenting my results, I will first provide brief introductions to concepts in aerosol physics that are relevant to my dissertation. This introduction includes basic definitions on topics such as aerosol particle size distributions, an overview of creeping flow and its characteristics, review of the existing literature on drag and torque on particles in creeping flow, and a discussion of pertinent experimental equipment and methods used in aerosol transport studies that play some role in validating my theoretical methods. To conclude the introduction, I will outline the remaining scope of my dissertation.

1.1 Aerosol Basics

Aerosols are two-phase systems consisting of a dispersed phase of solid particles or liquid droplets in a continuous gas phase [1–3]. The particles may form from gas-phase processes (such as condensation of super-saturated vapor) or from breakup of solids or liquids. Gas-phase processes typically produce smaller particles (i.e. less

than 1 μm in diameter), while disintegration processes yield larger particles [2]. Particle size is often described in terms of the non-dimensional Knudsen number, which is defined as the ratio of the mean free path of molecules in the gas to the characteristic size of the particle, $\mathrm{Kn} = \lambda/L$. The mean free path is the average distance gas molecules travel between collisions, which is a function of the size of the gas molecules and their number density and is equal to approximately 65 nm for air at standard temperature and pressure [2]. The mean free path can be related to the gas viscosity through relations that depend on the choice of molecular model (e.g. hard sphere, Lennard-Jones) for the gas [40]. The characteristic size of a particle depends on its shape; for spheres, the radius is the characteristic size, while for more general shapes one can use the mobility radius or radius of gyration. The radius of gyration is a purely geometric quantity, while the mobility radius depends on the interaction between the particle and the fluid [2]. This topic will be discussed later in this introduction.

As mentioned previously, many aerosol particles are fractal-like aggregates of many smaller, primary spheres, that form when the primary spheres coagulate and stick together. Generally speaking, aggregates contain spheres with a distribution of sizes; however, the standard deviation in the primary sphere diameter is often small when compared to the mean diameter [38, 42–44]. As a result, most studies of aerosol fractal aggregate transport assume that the primary spheres are all the same size [2, 4]. Primary sphere sizes range from a few nanometers up to about 0.1 μm [2], while aggregates may include tens, hundreds or even thousands of primary spheres [2, 4, 7, 42–44].

Aerosol systems typically consist of particles with a range of sizes; this range is described by the particle size distribution $n(v,t)$, where $n(v,t)\mathrm{d}v$ is the number of particles per unit gas volume at time t with particle volume between v and $v+\mathrm{d}v$. The size distribution can represent either spherical particles or aggregates [2]. The evolution of this size distribution with time is described by the general dynamic equation [2, 3, 45]. This equation accounts for changes in the distribution due to coagulation, condensation/evaporation, and particle formation and removal. Many of the terms in the general dynamic equation depend on the transport properties of the system. Thus, one must be able to accurately describe the transport properties (e.g. drag and torque on the particles as a function of the gas properties and the particle size, shape, and orientation) in order to predict the dynamic behavior of the aerosol. Again, this is the primary motivation for the research described in this dissertation.

1.2 Creeping Flow

The statistical behavior of a dilute gas is described by the Boltzmann transport equation,

$$\frac{\partial f}{\partial t} + \boldsymbol{c}\cdot\nabla f + \frac{\boldsymbol{F}_E}{m}\cdot\frac{\partial f}{\partial \boldsymbol{c}} = \left.\frac{\delta f}{\delta t}\right|_{\mathrm{coll}} \tag{1.2}$$

where $f(\boldsymbol{r},\boldsymbol{c},t)\mathrm{d}\boldsymbol{r}\mathrm{d}\boldsymbol{c}$ is the number of gas molecules in differential volume $\mathrm{d}\boldsymbol{r}$ with velocity $\boldsymbol{c}+\mathrm{d}\boldsymbol{c}$ at time t, ∇f is the spatial gradient of $f(\boldsymbol{r},\boldsymbol{c},t)$, $\partial f/\partial \boldsymbol{c}$ is its gradient with respect to the molecular velocity, and $\boldsymbol{F}_E/m$ is the external force (e.g. electrical, magnetic) per unit mass on the molecules [40, 46]. The right-hand

side of the above equation is the collision integral. Thus, the Boltzmann equation tracks the probability distribution of molecular velocities as a function of position and time, accounting for convection (the second term on the left-hand side), external forces on the molecules (the third term on the left-hand side), and collisions between gas molecules that alter their velocities (the term on the right-hand side) [40]. It is a complicated integro-differential equation that can only be solved for a very small number of cases [46]. (See Chapter 2 for more details about the Boltzmann equation.)

For near-equilibrium situations where the smallest length scale of the problem is much greater than the mean free path of the gas (i.e. Kn $\ll 1$), one can use Chapman-Enskog theory to derive the mass, momentum, and energy balance equations that govern continuum transport [47]. Conservation of momentum for near-equilibrium, continuum flow in an incompressible, Newtownian fluid is given by the Navier-Stokes equation,

$$\rho\left(\frac{\partial \boldsymbol{u}}{\partial t} + \boldsymbol{u}\cdot\nabla\boldsymbol{u}\right) = -\nabla p + \mu\nabla^2\boldsymbol{u} + \rho\boldsymbol{g} \tag{1.3}$$

where $\boldsymbol{u}(\boldsymbol{x},t)$ is the bulk gas velocity at position $\boldsymbol{x}$ at time t, $\boldsymbol{g}$ is gravitational acceleration, and ρ, p, and μ are the gas density, pressure, and viscosity. The coefficients of viscosity, diffusion, and heat conduction that appear in the continuum transport equations can be related to the molecular velocity distribution function through the Chapman-Enskog expansion. (See Refs. [40, 46] for further discussion on this topic.)

The Navier-Stokes equation is less complicated than the Boltzmann equation, but it is still a non-linear differential equation, making it difficult to solve analytically except in special cases. However, we can significantly simplify the equation for cases where the inertial terms (i.e. the left-hand side of the Navier-Stokes equation) are negligible, leading to the Stokes equation governing creeping flow in the continuum:

$$\mathbf{0} = -\nabla \mathcal{P} + \mu \nabla^2 \boldsymbol{u} \tag{1.4}$$

Here, $\nabla \mathcal{P} \equiv \nabla p + \rho \boldsymbol{g}$ combines the pressure term with the gravitational term, which can be done because gravity is a conservative vector field [48].

The Stokes equation is valid for $\mathrm{Re} \ll 1$, where the Reynolds number represents the ratio of inertial to viscous forces and is defined as $\mathrm{Re} \equiv \rho U L / \mu$. Here, U and L are the characteristic speed and length scale in the problem. (For a sphere with radius a moving with velocity $\boldsymbol{U}_0$, $U = |\boldsymbol{U}_0|$ and $L = a$.) The Mach number ($\mathrm{Ma} \equiv U/c_s$, where c_s is the speed of sound in the gas) must also be very small for the creeping flow approximation to be valid, though in the continuum the Reynolds number condition is typically more restrictive. (Note that the Mach number must be small in order for a gas flow to be considered incompressible.) Unlike the Boltzmann and Navier-Stokes equations, the Stokes equation is linear, which gives it a number of interesting mathematical properties, some of which I will discuss later. From a practical standpoint, it makes the equation much easier to solve.

For non-continuum flow, Eq. (1.4) no longer applies; however, one can still be in the creeping flow regime, provided the usual conditions of very low Reynolds and

Mach numbers are satisfied. This allows us to simplify the Boltzmann equation to determine the flow field around and drag on an aerosol particle, as I will explain in more detail in this dissertation. (See, especially, Chapters 2 and 3.)

Before describing the methods one might use to calculate the drag on a particle, I must first introduce two important features resulting from the linearity of the creeping flow equations (whether the Stokes equation for continuum flow or the BGK equation – the subject of Chapter 2 – for non-continuum flow).

First, there is a linear relationship between the translational and rotational velocities $\boldsymbol{U}_O$ and $\boldsymbol{\omega}$ of a particle and the drag and torque $\boldsymbol{F}$ and $\boldsymbol{T}_O$ exerted by the fluid on the particle [49]:

$$\boldsymbol{F} = -\boldsymbol{\Xi}_t \cdot \boldsymbol{U}_O - \boldsymbol{\Xi}_{O,c}^{\dagger} \cdot \boldsymbol{\omega} \tag{1.5a}$$

$$\boldsymbol{T} = -\boldsymbol{\Xi}_{O,c} \cdot \boldsymbol{U}_O - \boldsymbol{\Xi}_{O,r}^{\dagger} \cdot \boldsymbol{\omega} \tag{1.5b}$$

Here, the translational, rotational, and translation-rotation coupling friction tensors $\boldsymbol{\Xi}_t$, $\boldsymbol{\Xi}_{O,r}$, and $\boldsymbol{\Xi}_{O,c}$ are functions of the particle size, shape, and orientation. The coupling tensor reflects the fact that in general, a translating particle can experience a net torque, which can induce particle rotation. Likewise, a rotating particle can experience a net force that induces particle translation. The dagger symbol represents the transpose of the tensor, while the subscript O signifies that the variable is defined with respect to the center of mass of the particle (i.e. $\boldsymbol{U}_O$ is the translational velocity of particle center of mass). Note that $\boldsymbol{\Xi}_t$ and $\boldsymbol{\Xi}_{O,r}$ are symmetric. For

isotropic particles such as spheres, the coupling tensor is zero, while the translational and rotational tensors are $\boldsymbol{\Xi}_t = \zeta_t \mathbf{I}$ and $\boldsymbol{\Xi}_{O,r} = \zeta_{O,r}\mathbf{I}$. Here, $\mathbf{I}$ is the identity tensor and ζ_t and $\zeta_{O,r}$ are the (scalar) translational and rotational friction coefficients for the sphere, which are given in the following section. Thus, for an isotropic particle one need only determine two coefficients to describe the force and torque on a particle with specified velocity. For an arbitrary particle, one must determine 21 parameters: the 6 independent components of $\boldsymbol{\Xi}_t$, the 6 independent components of $\boldsymbol{\Xi}_{O,r}$, and all 9 components of $\boldsymbol{\Xi}_{O,c}$.

The second important consequence of the linearity of the creeping flow equations is that one may solve the equations using superposition. This means that we may add up the velocity results for problems where the solution is known (e.g. Stokes flow around a sphere moving through an infinite fluid) to get results for a different problem where the solution is more difficult to determine (e.g. two spheres in Stokes flow), provided the superposed solution satisfies the equation and boundary conditions of the more difficult problem [48]. This property of linear equations forms the basis for the Kirkwood-Riseman approach that I will discuss shortly.

1.3 Aerosol Transport

While the work described in this dissertation primarily concerns transport of particles in the transition regime, it is necessary to first review the theoretical development of the drag on a particle in the continuum and free molecule regimes. There are two main reasons for doing so: first, the extended Kirkwood-Riseman (EKR)

method introduced in this dissertation incorporates elements from the continuum and free molecule regimes; second, the drag computed using the EKR method should approach the continuum and free molecule expressions in the limits of very small and very large Knudsen numbers. Thus, the review of aerosol particle transport is divided into sections relevant to the continuum, free molecule, and transition regimes.

1.3.1 Continuum Regime

The creeping (or Stokes) flow equation forms the basis for any study of the behavior of particles in low-Reynolds-number flow in the continuum. Stokes [50] was the first to solve the creeping motion equation [Eq. (1.4)] for a sphere with radius a, resulting in the expression now know as Stokes' law,

$$\boldsymbol{F} = -6\pi\mu a\boldsymbol{U} \equiv -\zeta_{t,0}^{c}\boldsymbol{U} \tag{1.6}$$

where $\zeta_{t,0}^{c}$ is the translational friction coefficient for a sphere in continuum flow. One can also solve Eq. (1.4) for a sphere rotating with angular velocity $\boldsymbol{\omega}$; the torque on the rotating sphere is given by

$$\boldsymbol{T} = -8\pi\mu a^{3}\boldsymbol{\omega} \equiv -\zeta_{r,0}^{c}\boldsymbol{\omega} \tag{1.7}$$

where $\zeta_{r,0}^{c}$ is the rotational friction coefficient for a sphere in continuum flow about its center of mass.

In principal, one can solve the Stokes equation for the velocity and pressure fields around a particle of arbitrary shape moving with translational velocity $\boldsymbol{U}$ and angular velocity $\boldsymbol{\omega}$, then integrate the resulting stress profile at the particle surface to determine the lift and drag forces and the torque on the particle. In this way, one can obtain the friction tensors relating the translational and angular velocities of the particle to the drag and torque exerted on the particle by the fluid [Eq. (1.5)]. Brenner [29] describes this process in detail, as well as the relationship between the force and torque on a particle of arbitrary shape and its diffusive properties. In practice, the Stokes equation can only be solved analytically for simple shapes, so that alternative methods are need to determine the forces on an aggregate of spheres.

Kirkwood and Riseman [28] proposed that the force on each spherical element of an N-sphere aggregate can be obtained by considering the effects of all of the elements on the fluid flow pattern. The strength of those effects is given by an appropriate hydrodynamic interaction tensor, $\mathbf{T}_{ij}$, so that the force on the ith spherical element becomes

$$\boldsymbol{F}_i = -\zeta^c_{t,0}\boldsymbol{U}_i - \zeta^c_{t,0}\sum_{i\neq j}^{N}\mathbf{T}_{ij}\cdot\boldsymbol{F}_j \tag{1.8}$$

where $\boldsymbol{U}_i$ is the velocity of the ith sphere. For a rigid, non-rotating particle, all spheres move with the same velocity, so $\boldsymbol{U}_i = \boldsymbol{U}$. The total force on the particle is simply the sum of the forces on the N spherical elements. By repeating the calculation for flow in three mutually-orthogonal directions, one can obtain the translational friction tensor $\boldsymbol{\Xi}_t$. Ignoring the effects of coupling between transla-

tional and rotational motion, the scalar translational friction coefficient ζ_t is the harmonic mean of the eigenvalues of $\boldsymbol{\Xi}_t$ [29, 49].

The Kirkwood-Riseman (KR) framework can also be used to calculate the torque on a rotating particle and the coupling between translational and rotational motions, as described in the works of Garcia de la Torre and colleagues (e.g. Refs. [51–53]). This procedure accounts for rotational and coupling hydrodynamic interactions and yields the rotational and coupling friction tensors, $\boldsymbol{\Xi}_r$ and $\boldsymbol{\Xi}_c$. From the three friction tensors, one obtains the translation, rotation, and coupling diffusion tensors through a generalization of the Stokes-Einstein law derived by Brenner [29].

Kirkwood and Riseman originally applied their theory to flexible macromolecules; Bernal et al. [51] and Chen et al. [30] later applied the theory to rigid macromolecules and fractal aggregates, respectively. KR theory has been used extensively to compute the transport properties of macromolecules, colloids, and fractal aggregates [30, 51–56].

In its original form, KR theory used the Oseen tensor for $\mathbf{T}_{ij}$. Subsequent applications of the theory for pure translational motion have used the Rotne-Prager-Yamakawa (RPY) tensor [57, 58]. More complicated translational, rotational, and coupling hydrodynamic interaction tensors are also available in the literature [59–61]. Carrasco and Garcıa de la Torre [53] have shown that KR theory with the RPY tensor yields translational friction coefficients within a few percent of the friction coefficients calculated with more sophisticated methods for the simple particles they studied.

Hubbard and Douglas [31] developed a different approach for calculating the translational friction coefficient of an arbitrarily-shaped Brownian particle by noting the approximate relationship between the friction coefficient and the electrostatic capacitance C,

$$\zeta_t^c \approx 6\pi\mu C \tag{1.9}$$

The Zeno algorithm [62] uses a random walk approach to calculate the electrostatic capacitance – and thus the translational friction coefficient. The accuracy of the Hubbard-Douglas approximation is within 1% for shapes where ζ_t^c is known and within a few percent for an arbitarily-shaped particle [63]. These results suggest that the Hubbard-Douglas method is more accurate than KR for relatively simple shapes. For larger fractal aggregates, the differences between the two methods is less significant. (See Chapter 4.)

For fractal aggregates, research suggests that the friction coefficient in the continuum regime follows a power-law relationship,

$$\zeta_t^c = AN^\eta \tag{1.10}$$

Sorensen [4] analyzed the results of various experimental and computational studies and found that $\eta \approx 0.46$ for $N < 100$ and $\eta \approx 0.56$ for $N > 100$ for clusters formed by diffusion-limited cluster aggregation ($k_0 \approx 1.3$, $d_f \approx 1.78$).

1.3.2 Free Molecule Regime

The drag on a particle in the free molecule regime can be calculated using kinetic theory. However, because the particle is much smaller than the gas mean free path, it has very little impact on the distribution of molecular velocities in the gas. As a result, the aerodynamic force on the particle can be calculating by assuming that the gas molecules impinging on the surface have a Maxwell-Boltzmann distribution of velocities. This assumption obviates the need to solve the Boltzmann equation to obtain the drag on a particle in free molecule flow.

Epstein [32] first calculated the drag on a sphere in creeping flow in the free molecule regime as

$$\boldsymbol{F} = -\frac{\sqrt{2\pi}}{3}\left(1+\frac{\pi\alpha}{8}\right)\left(\frac{k_B T}{m}\right)^{1/2}\rho a^2 \boldsymbol{U} \equiv -\zeta_{t,0}^{FM}\boldsymbol{U} \tag{1.11}$$

where k_B is the Boltzmann constant, T and ρ are the gas temperature and density, m is the mass of a gas molecule, and α is the fraction of gas molecules that are in thermal equilibrium after reflecting from the particle surface (i.e. the fraction of molecules reflected diffusely). Thus, the drag on a sphere in free molecule flow is proportional to a^2, whereas the drag is proportional to a in the continuum. Epstein also calculated the torque on a rotating sphere,

$$\boldsymbol{T} = -\frac{\sqrt{32\pi}}{3}\alpha\left(\frac{k_B T}{m}\right)^{1/2}\rho a^4 \boldsymbol{\omega} \equiv -\zeta_{r,0}^{FM}\boldsymbol{\omega} \tag{1.12}$$

showing that the torque is proportional to a^4 for free molecule flow, compared to a^3 in the continuum regime [32].

Dahneke [33] extended Epstein's analysis to develop analytic expressions for the drag on various convex bodies. The analysis is more complicated for concave bodies – such as fractal aggregates – due to shielding of incoming molecules by parts of the surface and the possibility of multiple collisions between a molecule and the particle. Thus, numerical techniques are required for concave bodies. These techniques track the trajectories of gas molecules near the particle to determine whether or not the molecules hit the particles. For those molecules that hit the surface, the momentum transfer is computed using an appropriate reflection law. Chan and Dahneke [34] used this ballistic approach to compute the drag on straight chain aggregates for flow parallel and perpendicular to the long axis of the chain. Meakin and Deutch [55] applied the approach to determine the drag on fractal aggregates and found that the drag is proportional to the projected area of the aggregate. Mackowski [36] performed a similar analysis and developed an empirical correlation for the translational friction coefficient as a function of the fractal dimension and prefactor and the number of spheres for the range of parameters studied.

One could also apply the ballistic approach to compute the torque on a rotating particle, though it does not appear anyone has done so based on the dearth of information in the literature. Instead, researchers have used simplified techniques to estimate the rotational friction or diffusion coefficient of aggregates in the free molecule regime [6].

For fractal aggregates, results suggest that there is a power-law relationship

between the free molecule translational friction coefficient and the number of spheres in the aggregate; this is similar to the observed behavior in the continuum. Summarizing the available experimental and computational results in the literature, Sorensen [4] recommended a power-law exponent of $\eta \approx 0.92$ for DLCA clusters of all sizes in the free molecule regime.

1.3.3 Transition Regime

As the particle size increases, the assumption that the particle has no impact on the molecular velocity distribution around the particle no longer holds, and a more rigorous application of kinetic theory is required. In the transition regime, the drag can be obtained by solving the Boltzmann equation and integrating the stress on the surface of the profile. However, the Boltzmann equation is exceeding difficult to solve even for the simple case of a sphere, so significant simplifications are needed to make the problem tractable. These simplifications will be described shortly, but first I will focus on empirical models based on experimental data.

Millikan [64] laid the groundwork for determining the drag on a sphere in the transition regime. Data from his famous oil drop experiments demonstrates the transition between the continuum and free molecule regimes, where the drag is proportional to a and a^2, respectively. To cover the entire Knudsen number range, one can apply a slip correction factor $C_c(\mathrm{Kn})$ to Stokes' law,

$$\zeta_{t,0} = \frac{6\pi\mu a}{C_c(\mathrm{Kn})} \tag{1.13}$$

where the slip correction factor has the form

$$C_c(\mathrm{Kn}) = 1 + \mathrm{Kn}[A + B\exp(-C/\mathrm{Kn})] \tag{1.14}$$

The coefficients A, B, and C are selected to fit the experimental data; the coefficients of Davies [65] and Allen and Raabe [66] are commonly used in aerosol applications. Eq. (1.13) approaches the continuum and free molecule friction coefficients defined in Eqs. (1.6) and (1.11) for $\mathrm{Kn} \ll 1$ and $\mathrm{Kn} \gg 1$, respectively.

Other researchers have developed empirical models for the drag on fractal aggregates in the transition regime. Rogak et al. [37] proposed substituting the projected area radius ($a_{\mathrm{PA}} = \sqrt{\mathrm{PA}/\pi}$) for a in Eq. (1.13). Lall and Friedlander [38] suggested that the drag on an aggregate with fractal dimension less than 2 can be approximated as a straight chain. Their correlation applies Chan and Dahneke's results for chain elements in the free molecule regime [34]. Finally, Eggersdorfer et al. [39] relate the mobility radius (i.e. the radius of a sphere with the same drag as the particles) to the number of primary spheres and the fractal dimension and prefactor of the aggregate. The resulting model is similar to Rogak's model for particles formed by DLCA. These three models provide simple relationships for the drag on fractal aggregates, though they are only valid near the free molecule regime. (See Chapter 4.)

Dahneke [67] proposed an adjusted sphere method (ASM) for particles of arbitrary shape, where the drag on the particle is given by an expression analogous to Eq. (1.13). The difference is that a and Kn should be replaced by an appropri-

ate characteristic length and aggregate Knudsen number. Through scaling analysis, Zhang et al. [41] demonstrated that the appropriate characteristic length is the hydrodynamic radius R_H (i.e. the radius of a sphere that has the same drag as the particle in continuum flow), and the aggregate Knudsen number is

$$\mathrm{Kn}_{\mathrm{agg}} = \pi\lambda R_H/\mathrm{PA} \tag{1.15}$$

where PA is the projected area of the particle. R_H can be computed using the KR or Hubbard-Douglas methods, and PA can be computed using ballistic methods. Thus, the aggregate Knudsen number is proportional to the ratio of continuum and free molecule measures of the drag. The drag calculated using the ASM is in good agreement with experimental and computational results [41, 68, 69].

A number of researchers have managed to solve simplified forms of the Boltzmann equation for spheres and other axisymmetric bodies. Cercignani and Pagani [70] described the general approach for solving the Boltzmann equation with the Bhatnagar-Gross-Krook (BGK) model [71] in place of the Boltzmann collision operator using a variational technique. The BGK model assumes that the non-equilibrium distribution of molecular velocities in the gas relaxes to an equilibrium distribution after one collision. Kogan [72] has shown that this approximation is valid for most physical situations. The variational approach of Cercignani and Pagani is valid for any axisymmetric body.

Cercignani et al. [73] applied that technique to determine the drag on a sphere as a function of Knudsen number. Their results are within a few percent of a fit

to Millikan's data over a wide range of Knudsen numbers. Loyalka and colleagues [74–76] obtained the velocity profile around the sphere as well as the drag using methods similar to Cercignani et al. [73]. Later, Loyalka [77] and Takata et al. [78] solved the problem using a linearized form of the Boltzmann collision operator. The velocity and drag results from these studies are similar to the previous BGK model results, which were obtained at a significantly lower computational cost than the linearized Boltzmann results. Loyalka [77] also solved the linearized Boltzmann equation to determine the velocity around and torque on a rotating sphere in the transition flow regime.

In principal, one could solve the Boltzmann or BGK equation numerically to obtain the drag on and flow field around a particle with arbitrary shape, but this is exceedingly difficult in practice, especially for concave particles. One approach for doing so is the direct simulation Monte Carlo method [40], which tracks a number of test molecules and reconstructs the velocity distribution in the gas from the behavior of these test molecules. This method is computationally expensive and is less accurate near the continuum regime due to the finite size of the test domain [41].

Melas et al. [79] determined the friction coefficient for aggregates in the near-continuum regime by solving the Laplace equation with a slip boundary condition. This approach is an extension of the Hubbard-Douglas approach (which uses the stick boundary condition at the particle surface). Melas et al. [80] estimated that this approach is valid for $\mathrm{Kn} < 2$, meaning some other approach is needed for particles closer to the free molecule regime.

Tandon and Rosner [81] developed a method for calculating the friction coefficient for fractal aggregates using a porous sphere approach. The porosity is a function of radial position in the sphere and is obtained from the pair distribution function for the orientation-averaged coordinates of monomers in the aggregate. The velocity around the porous sphere is governed by the Stokes equations, while the flow within the sphere is obtained by solving the Brinkman equation [4, 81]. Rosner and Tandon [82] have shown that the porous sphere method gives friction coefficient results in good agreement with the Adjusted Sphere Method of Dahneke [67] and Zhang et al. [41] for any primary sphere size, provided the aggregate is large enough that one can accurately treat the outer flow using the Stokes equation. In other words, the aggregate size (e.g. the radius of gyration) must be very large compared to the gas mean free path. Again, this means that a different approach is needed for aggregates closer to the free molecule regime.

1.4 Experimental Techniques for Obtaining Particle Size

The work contained in this dissertation focuses on the theory of aerosol physics; that is, I have not performed an experiments to support this work. Fortunately, there is some data in the published literature to validate – or at least qualitatively support – my theoretical results. To aid the reader in understanding comparisons between the results in this dissertation and available experimental data, I will provide an overview of the experimental techniques used to size aerosol particles that are pertinent to my own work.

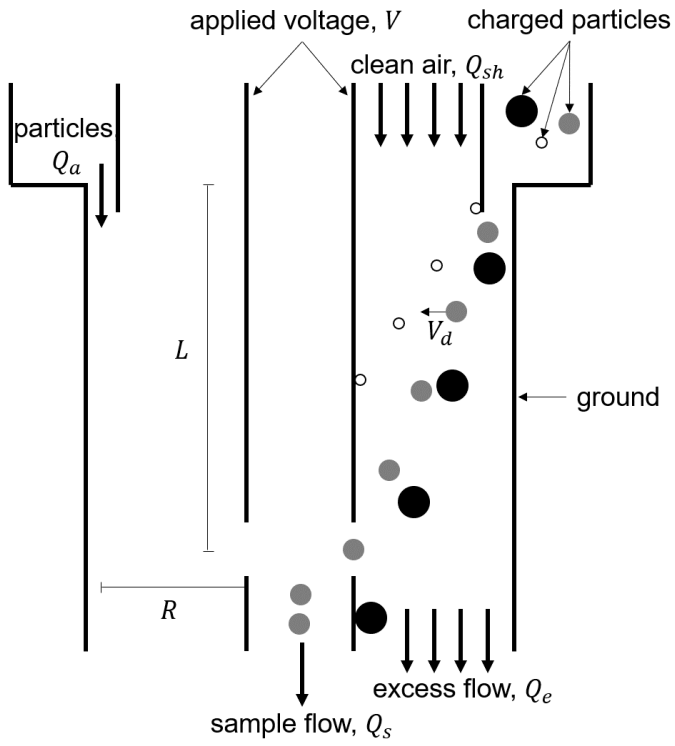

Figure 1.1: Differential mobility analyzer (DMA) for selecting charged particles with a specified mobility. The mobility size is selected by controlling the DMA voltage and air flow rate.

Broadly speaking, we can divide the relevant experimental techniques into two categories: those techniques that measure the mobility of a particle, and those that measure its light scattering behavior. I will address each of these categories separately in the following subsections.

1.4.1 Mobility Measurements

The first class of instruments that I will review measure how a particle moves in an applied force field. Perhaps the most widely-used such instrument for aerosol studies is the cylindrical differential mobility analyzer (DMA), shown in Fig. 1.1.

A DMA system works as follows. First, an aerosol stream passes through a

neutralizer to obtain a known equilibrium charge distribution [2, 83]. The aerosol stream enters the the cylindrical DMA at flow rate Q_a along with a stream of clean air (i.e. the sheath flow, Q_{sh}). Particles are advected with the sheath flow; at the same time, positively charged particles drift from the outer cylinder wall to the inner wall, which has a negative potential. This drift velocity is the velocity required to balance the electrical and aerodynamic drag forces on the particle:

$$\zeta_t V_d = qE \tag{1.16}$$

Here, ζ_t is the particle translational friction coefficient, V_d is the drift velocity, q is the charge on the particle, and E is the electric field strength. The field and drift velocity are in the same direction. Particles that travel a radial distance R in the time they travel an axial distance L pass through the slit in the DMA. The remaining particles either deposit on the outer (negatively charged particles) or inner (positively charged particles with higher mobility than the sampled particles) wall of the DMA or pass out of the DMA with the excess flow. One selects the voltage (and thus the field strength) and the sheath flow rate to obtain particles with a desired electrical mobility Z, where

$$Z = \frac{V_d}{E} = \frac{q}{\zeta} \tag{1.17}$$

By scanning through a series of voltages and counting the number of particles in the sample flow at each voltage (e.g. with a condensation particle counter, as explained

in Chapter 6 of Friedlander [2]), one can determine the particle size distribution for the aerosol that enters the DMA [2].

Often, researchers present the mobility as an equivalent sphere size by solving Eq. (1.13) implicitly to find the mobility diameter d_m [37–39, 43, 44, 68, 84]. Of course, for a sphere the mobility diameter is equivalent to its geometric diameter. The situation is much more complicated for fractal aggregates, so it is difficult to obtain information about particle mass from a DMA. Furthermore, the DMA selects some particles that have multiple charges in addition to those with a single charge, which results in some error in the size distribution (since the larger, multiply-charged particles have the same electrical mobility as the smaller, singly-charged particles).

To address these difficulty, systems for characterizing non-spherical particles often involve both mobility measurements in a DMA and mass measurements in an aerosol particle mass (APM) analyzer [43, 44, 85, 86]. Just as a DMA relies on a balance between the electric force and the aerodynamic drag on a particle, an APM sizes particles by balancing the electric force with the centrifugal force. When the two forces are equal, the particle passes through the APM; otherwise, the particle deposits on the inner or outer wall of the APM. In this way, one can size-select particles based on their mass-to-charge ratio.

Researchers have developed other systems using combined mass and/or mobility measurements to obtain additional size and shape information about aerosol particles [44, 87, 88]. In many cases, mass and mobility measurements are supplemented by information about primary particle size from transmission electron microscopy (TEM) images; this information can be used with basic assumptions

about the fractal dimension of the aggregate to estimate the number of primary spheres it contains [6, 44].

1.4.2 Optical Measurements

The second class of aerosol instruments that are relevant to my research involve measuring the intensity of light scattered by the particles. (See Bohren and Huffman [89] for the detailed discussion on the theory of light scattering by small particles.) These optical instruments are used for a variety of purposes, from determining the number density of particles in a gas stream (e.g. in a condensation particle counter), to obtaining information about particle shape, to determining the rotational diffusion coefficient of a particle. I will focus my attention on the latter application.

In general, the angular distribution of the light scattered by a particle is a function of that particle's orientation. In the absence of a strong external force field, the light scattered by a nano-scale aerosol particle is an average over all orientations, where all orientations are equally probable due to the randomizing effects of Brownian motion. However, particles can become aligned in a strong electric field if the interaction energy between the induced dipole in the particle and the field is much larger in magnitude than the Brownian energy $k_B T$, where k_B is the Boltzmann constant and T is the temperature. By measuring the change in scattered light intensity when the field is on and off, one can obtain some information about the shape of particles. One can also obtain the rotational diffusion coefficient of a particle by turning off the field and measuring the time required for the scattered

light intensity to relax to a value corresponding to the random particle orientation. Such measurements have been reported in the literature for soot particles from various sources [90, 91]; I will later compare my results for the rotational diffusion coefficients of soot-like aggregates to the experimental data of Colbeck et al. [91]. This experimental technique also offers an alternative approach to the method I describe in Chapter 7 for obtaining particle shape information.

1.5 Scope of the Dissertation

This dissertation describes a method [92] for calculating the drag on an aggregate of spheres in point contact in the transition flow regime, based on Kirkwood-Riseman theory originally developed for the continuum regime [28]. Generally speaking, Chapters 2, 3, and 5 introduce the method, while Chapters 4 and 6-8 focus on applications of the method.

In Chapter 2, I discuss the Bhatnagar-Gross-Krook model equation and its solution for flow around a sphere as a function of the Knudsen number. This chapter follows the earlier work of Loyalka and colleagues [74–76]. I include this discussion because my EKR method uses the flow around an isolated sphere to determine the drag and torque on an N-sphere aggregate.

In Chapter 3, I develop a new approach for computing the hydrodynamic friction tensor and scalar friction coefficient for an aerosol fractal aggregate in the transition regime [92]. My approach involves solving the BGK equation for the velocity field around a sphere and using the velocity field to calculate the force on

each primary sphere in the aggregate due to the presence of the other spheres. It is essentially an extension of Kirkwood-Riseman theory from the continuum flow regime to the entire Knudsen range (Knudsen number from 0.01 to 100 based on the primary sphere radius). Results compare well to published Direct Simulation Monte Carlo results and converge to the correct continuum and free molecule limits. My calculations for clusters with up to 100 spheres support the theory that aggregate slip correction factors collapse to a single curve when plotted as a function of an appropriate aggregate Knudsen number. This self-consistent field approach calculates the friction coefficient very quickly, so the approach is well-suited for testing existing scaling laws in the field of aerosol science and technology, as I demonstrate for the adjusted sphere scaling method.

In Chapter 4, I use the self-consistent field method described in Chapter 3 to calculate the translational friction coefficient of fractal aerosol particles formed by diffusion-limited cluster aggregation (DLCA) [93]. The method involves solving the Bhatnagar-Gross-Krook model for the velocity around a sphere in the transition flow regime. The velocity and drag results are then used in an extension of Kirkwood-Riseman theory to obtain the drag on the aggregrate. Results span a range of primary sphere Knudsen numbers from 0.01 to 100 for clusters with up to $N = 2000$ primary spheres. Calculated friction coefficients are in good agreement with experimental data and approach the correct continuum and free molecule limits for small and large Knudsen numbers, respectively. Results show that particles exhibit more continuum-like behavior as the number of primary spheres increase, even when the primary particle is in the free molecule regime; as an illustrative

example, the friction coefficient for aggregates with primary sphere Kn = 1 are approximately equal to the continuum friction coefficient for $N > 500$. I estimate that the calculations are within 10% of the true values of the friction coefficients for the range of Kn and N presented here. Finally, I use my results to develop an analytical expression (Equation 4.38) for the friction coefficient over a wide range of aggregate and primary particle sizes.

In Chapter 5, I apply extended Kirkwood-Riseman theory to compute the translation, rotation, and coupling friction tensors and the scalar rotational friction coefficient for an aerosol fractal aggregate in the transition flow regime [94]. The method can be used for particles consisting of spheres in contact. The approach considers only the linear velocity of the primary spheres in a rotating aggregate and ignores rotational and coupling interactions between spheres. I show that this simplified approach is within approximately 40% of the true value for any particle for Knudsen numbers between 0.01 and 100. The method is especially accurate (i.e. within about 5%) near the free molecule regime, where there is little interaction between the particle and the flow field, and for particles with low fractal dimension (less than ≈ 2) consisting of many spheres, where the average distance between spheres is large and translational interaction effects dominate. Results suggest that there is a universal relationship between the rotational friction coefficient and an aggregate Knudsen number, defined as the ratio of continuum to free molecule rotational friction coefficients.

In Chapter 6, I apply the EKR method to calculate the rotational friction coefficient for fractal aerosol particles in the transition flow regime [95]. The method

considers hydrodynamic interactions between spheres in a rotating aggregate due to the linear velocities of the spheres. Results are consistent with electro-optical measurements of soot alignment. Calculated rotational friction coefficients are also in good agreement with continuum and free molecule results in the limits of small (Kn = 0.01) and large (Kn = 100) primary sphere Knudsen numbers. As demonstrated for the translational friction coefficient (Chapter 4), the rotational friction coefficient approaches the continuum limit as either the primary sphere size or the number of primary spheres increases. I apply my results to develop an analytical expression (Equation 6.26) for the rotational friction coefficient as a function of the primary sphere size and number of primary spheres. One important finding is that the ratio of the translation to rotational diffusion times is nearly independent of cluster size. I include an extension of previous scaling analysis for aerosol aggregates to include rotational motion.

In Chapter 7, I study the effects of electric field strength on the mobility of soot-like fractal aggregates (fractal dimension of 1.78) [96]. The probability distribution for the particle orientation is governed by the ratio of the interaction energy between the electric field and the induced dipole in the particle to the energy associated with Brownian forces in the surrounding medium. I use the extended Kirkwood-Riseman method to calculate the friction tensor for aggregates of up to 2000 spheres, with primary sphere sizes in the transition and near-free-molecule regimes. My results for electrical mobility versus field strength are in good agreement with published experimental data for soot, which show an increase in mobility on the order of 8% from random to aligned orientations. My calculations show

that particles become aligned at decreasing field strength as particle size increases because particle polarizability increases with volume. Large aggregates are at least partially aligned at field strengths below 1000 V/cm, though the small change in mobility means that alignment is not an issue in many practical applications. However, improved DMAs would be required to take advantage of small changes in mobility to provide shape characterization.

In Chapter 8, I present a method for calculating the hydrodynamic interactions between particles in the kinetic (or transition) regime, characterized by non-negligible particle Knudsen numbers. Such particles are often present in aerosol systems. The method is based on my extended Kirkwood-Riseman theory [92], which accounts for interactions between spheres using the velocity field around a translating sphere as a function of Knudsen number. Results for the two-sphere problem at small Knudsen numbers are in good agreement with those obtained using Felderhof's interaction tensors for mixed slip-stick boundary conditions, which are accurate to order r^{-7} [97]. The strength of interactions decreases with increasing Knudsen number. Results for two fractal aggregates demonstrate that one can apply a point force approach for interactions between particles in the transition regime; the interaction tensor is similar to the Oseen tensor for continuum flow. Using this point force approach, I present an analysis for the settling of an unbounded cloud of particles. The analysis shows that for sufficiently high volume fractions and cloud radii, the cloud behaves as a gas droplet in continuum flow even when the individual particles are small relative to the mean free path of the gas. The method presented here can be applied in a Brownian dynamics simulation analogous to Stokesian

dynamics to study the behavior of a dense aerosol system.

Chapter 9 is the Reference Manual for the NGDE code. The NGDE code uses a nodal method to solve the general dynamic equation for an aerosol undergoing coagulation, nucleation, and surface growth. This method is similar to widely-used sectional methods for solving the general dynamic equation, but by dividing the particle size distribution into discrete volume nodes, it eliminates many of the mathematical complexities of sectional methods. I have converted the original C version of NGDE to the MATLAB language, added a dynamic time step algorithm that reduces the code execution time by orders of magnitude, and created a new post-processing tool for viewing the evolution of the particle size distribution and the light scattering, extinction, and absorption coefficients. Results of sample problems compare well to results obtained from other methods. Because of NGDE's simplicity and accuracy, it is well-suited for use as part of courses in aerosol dynamics.

The main body of the dissertation closes with a summary of the important conclusions of my research in Chapter 10.

Chapter 2: The BGK Model Equation

2.1 Introduction

Solution of the density, velocity, and temperature fields around a sphere in the transition regime ($0.01 < \mathrm{Kn} < 100$) requires consideration of the Boltzmann equation or its derivatives. For steady flow, the Boltzmann equation can be written in dimensional form as

$$\tilde{\boldsymbol{c}} \cdot \widetilde{\nabla} f = \left.\frac{\delta f}{\delta t}\right|_{\mathrm{coll}} \tag{2.1}$$

where $\tilde{\boldsymbol{c}}$ is the molecular velocity, $f = f(\tilde{\boldsymbol{r}}, \tilde{\boldsymbol{c}})$ is the molecular velocity distribution function, and the term on the right-hand side of the equation is the collision operator.[1] The distribution function is defined such that $f(\tilde{\boldsymbol{r}}, \tilde{\boldsymbol{c}})\mathrm{d}\tilde{\boldsymbol{r}}\mathrm{d}\tilde{\boldsymbol{c}}$ represents the number of gas molecules in differential volume $\mathrm{d}\tilde{\boldsymbol{r}}$ centered at location $\tilde{\boldsymbol{r}}$ that have a velocity between $\tilde{\boldsymbol{c}}$ and $\tilde{\boldsymbol{c}} + \mathrm{d}\tilde{\boldsymbol{c}}$.

The collision operator can be written as the difference between two terms. The

[1] Throughout this chapter, I am using bold symbols to denote vectors, bold symbols with hats to denote unit vectors, the subscript ∞ to denote properties far from the perturbation, and a tilde over dimensional quantities that also appear in non-dimensional form without the tilde. To expand on the latter point, I do not add a tilde to all dimensional quantities; I only add it to explicitly differentiate between dimensional and non-dimensional variants of the same quantity. For example, temperature always appears as T because I only use it as a dimensional quantity, whereas the molecular velocity $\boldsymbol{c}$ appears with and without the tilde to signify dimensional and non-dimensional variants.

first (positive) term represents the rate at which molecules are scattered into the interval $[\tilde{\boldsymbol{c}}, \tilde{\boldsymbol{c}}+\mathrm{d}\tilde{\boldsymbol{c}}]$ as a result of collisions, while the second (negative) term represents the molecules in this velocity interval that are scattered out of the interval due to collisions with other molecules. The collision operator is the chief source of difficulty in the Boltzmann equation; it makes solving the equation analytically impossible for all but the simplest cases.

To address this difficulty, Bhatnagar, Gross, and Krook [71] proposed a simplified form of the collision operator,

$$\left.\frac{\delta f}{\delta t}\right|_{\text{coll}} = \frac{f_0(\tilde{\boldsymbol{r}}, \tilde{\boldsymbol{c}}) - f(\tilde{\boldsymbol{r}}, \tilde{\boldsymbol{c}})}{\tau(\tilde{c})} \tag{2.2}$$

where $\tau(\tilde{c})$ is the (velocity-dependent) mean collision time in the gas and

$$f_0 = n\left(\frac{m}{2\pi k_B T}\right)^{3/2} \exp\left[-\frac{m|\tilde{\boldsymbol{c}} - \tilde{\boldsymbol{U}}|^2}{2k_B T}\right] \tag{2.3}$$

is the Maxwell-Boltzmann distribution at the local number density n, bulk velocity $\tilde{\boldsymbol{U}}$, and temperature T. The BGK model for the collision operator expresses the fact that any distribution f decays to the Maxwellian distribution, where the relaxation time can be approximated as the time between collisions [71, 72]. The second term on the right-hand side of Eqn. (2.2) has the same general form as the depletion term in the Boltzmann collision operator: in both cases, depletion is directly proportional to $f(\tilde{\boldsymbol{r}}, \tilde{\boldsymbol{c}})$ and to the frequency of collisions between molecules with velocity $\tilde{\boldsymbol{c}}$ and all other molecules. Strictly speaking, the collision frequency is a function of the

molecular velocity, though it is possible to use an average collision time [46] (hence the appearance of the mean collision time $\bar{\tau}$ in later equations). The f_0 term in Eq. (2.2) does not have a direct mathematical relationship to the replenishing term in the Boltzmann equation. Instead, this term in the BGK model assumes that the distribution relaxes to the local Maxwellian distribution after one collision. Kogan [72] has demonstrated that in most physical situations, the velocity distribution after one collision is fairly close to the equilibrium distribution. Thus, the BGK model is a reasonable approximation to the Boltzmann collision operator, especially for near-equilibrium situations like creeping flow of a sphere at the same temperature as the surrounding gas.

Based on the preceding discussion, we can simplify our equation for the distribution function by substituting the BGK model for the collision operator in the Boltzmann equation. The resulting equation is known as the Krook equation. For steady flow, we have

$$\tilde{\boldsymbol{c}} \cdot \widetilde{\nabla} f = \frac{f_0(\tilde{\boldsymbol{r}}, \tilde{\boldsymbol{c}}) - f(\tilde{\boldsymbol{r}}, \tilde{\boldsymbol{c}})}{\tau(\tilde{c})} \tag{2.4}$$

We can non-dimensionalize the above equation by defining the variables

$$\boldsymbol{c} = \frac{\tilde{\boldsymbol{c}}}{(2k_B T_\infty/m)^{1/2}} \tag{2.5a}$$

$$\boldsymbol{U} = \frac{\tilde{\boldsymbol{U}}}{(2k_B T_\infty/m)^{1/2}} \tag{2.5b}$$

$$\boldsymbol{r} = \frac{\tilde{\boldsymbol{r}}}{\bar{\tau}(2k_B T_\infty/m)^{1/2}} \tag{2.5c}$$

where $\bar{\tau}$ is the collision time averaged over all molecular velocities. Setting the mean collision time as $\bar{\tau} = \mu/p$ (where p is pressure) and the viscosity as $\mu = 0.499\lambda\rho\bar{c}$, the non-dimensional sphere radius is related to the Knudsen number by the following expression:[2]

$$r_0 = \frac{\tilde{r}_0}{\bar{\tau}(2k_B T_\infty/m)^{1/2}} = \frac{\sqrt{\pi}}{1.996}\mathrm{Kn}^{-1} \tag{2.5d}$$

Applying the length and velocities scales in Eq. (2.5), the non-dimensional Krook equation for steady flow becomes

$$\boldsymbol{c}\cdot\nabla f = f_0(\boldsymbol{r},\boldsymbol{c}) - f(\boldsymbol{r},\boldsymbol{c}) \tag{2.6}$$

While the Krook equation is much simpler than the Boltzmann equation, the Krook equation is still difficult to solve because the number density, bulk velocity, and temperature that appear in f_0 are all functions of the local conditions in the gas. In other words, these variables each depend on f.

To simplify the equation further, we can treat any disturbance in the distribution function as a small perturbation to the linearized far-away distribution function $f_\infty(1 + 2\boldsymbol{c}\cdot\boldsymbol{U}_\infty)$,[3]

$$f \approx f_\infty(1 + 2\boldsymbol{c}\cdot\boldsymbol{U}_\infty + h) \tag{2.7}$$

[2]The definition of the mean collision time comes from the Chapman-Enskog solution of the Krook equation, which shows that μ from the Chapman-Enskog solution is identical to μ for continuum flow if we set $\mu = p\bar{\tau}$ [46]. The expression relating the viscosity to the mean free path applies to monatomic gases [46], but it is a reasonable approximation for air and is used in many aerosol studies in the literature (e.g. [41, 73])

[3]Here, we have linearized the Maxwellian distribution defined in Eq. (2.3) by expanding the distribution in powers of $\boldsymbol{U}_\infty$. This approach assumes that the stream velocity is very small compared to the thermal speed, which is certainly true for creeping flow.

where

$$f_\infty = n_\infty \left(\frac{m}{2\pi k_B T_\infty}\right)^{3/2} \exp\left(-\frac{m\tilde{\boldsymbol{c}}^2}{2k_B T_\infty}\right) \tag{2.8}$$

We can also linearize the Maxwellian distribution to get

$$\begin{aligned} f_0 \approx & f_\infty(1 + 2\boldsymbol{c}\cdot\boldsymbol{U}_\infty) + \left.\frac{\partial[f(1+2\boldsymbol{c}\cdot\boldsymbol{U})]}{\partial n}\right|_\infty (n - n_\infty) \\ & + \left.\frac{\partial[f(1+2\boldsymbol{c}\cdot\boldsymbol{U})]}{\partial \boldsymbol{U}}\right|_\infty \cdot(\boldsymbol{U} - \boldsymbol{U}_\infty) + \left.\frac{\partial[f(1+2\boldsymbol{c}\cdot\boldsymbol{U})]}{\partial T}\right|_\infty (T - T_\infty) \\ = & f_\infty\left[1 + 2\boldsymbol{c}\cdot\boldsymbol{U}_\infty + \left(\frac{n}{n_\infty} - 1\right) + 2\boldsymbol{c}\cdot(\boldsymbol{U} - \boldsymbol{U}_\infty) + \left(c^2 - \frac{3}{2}\right)\left(\frac{T}{T_\infty} - 1\right)\right] \end{aligned}$$

$$f_0 \approx f_\infty\left[1 + 2\boldsymbol{c}\cdot\boldsymbol{U}_\infty + \varepsilon_1 + \boldsymbol{c}\cdot\boldsymbol{\varepsilon}_2 + \left(c^2 - \frac{3}{2}\right)\varepsilon_3\right] \tag{2.9}$$

where

$$n(\boldsymbol{r}) = n_\infty(1 + \varepsilon_1) \tag{2.10a}$$

$$\boldsymbol{U}(\boldsymbol{r}) = \boldsymbol{U}_\infty + \frac{1}{2}\boldsymbol{\varepsilon}_2 \tag{2.10b}$$

$$T(\boldsymbol{r}) = T_\infty(1 + \varepsilon_3) \tag{2.10c}$$

and ε_1, $\boldsymbol{\varepsilon}_2$, and ε_3 are perturbations to the far-field number density, velocity, and temperature, respectively. These perturbations will be defined shortly.

From kinetic theory, the number density, bulk velocity, and temperature are defined in terms of moments of the distribution function f:

$$n = \int f \mathrm{d}\boldsymbol{c} \tag{2.11a}$$

$$\boldsymbol{U} = \frac{1}{n}\int \boldsymbol{c} f \mathrm{d}\boldsymbol{c} \tag{2.11b}$$

$$\frac{3}{2}T = \frac{1}{n}\int c^2 f \mathrm{d}\boldsymbol{c} \tag{2.11c}$$

We define the pertrubation ε_1 and $\boldsymbol{\varepsilon}_2$ by substituting Eq. (2.7) into Eqns. (2.11a) and (2.11b), respectively:

$$n = \int f_\infty(1 + 2\boldsymbol{c}\cdot\boldsymbol{U}_\infty + h)\mathrm{d}\boldsymbol{c} = n_\infty + n_\infty \pi^{-3/2}\int h\exp(-c^2)\mathrm{d}\boldsymbol{c} = n_\infty(1+\varepsilon_1)$$
$$\boldsymbol{U} = \frac{1}{n_\infty}\int f_\infty(1 + 2\boldsymbol{c}\cdot\boldsymbol{U}_\infty + h)\boldsymbol{c}\mathrm{d}\boldsymbol{c} = \boldsymbol{U}_\infty + \pi^{-3/2}\int h\boldsymbol{c}\exp(-c^2)\mathrm{d}\boldsymbol{c} = \boldsymbol{U}_\infty + \frac{1}{2}\boldsymbol{\varepsilon}_2$$

Similarly, we define the temperature perturbation by substituting Eq. (2.7) into Eq. (2.11c):

$$\frac{3}{2}T = \frac{1}{n}\int f_\infty(1 + 2\boldsymbol{c}\cdot\boldsymbol{U}_\infty + h)c^2\mathrm{d}\boldsymbol{c}$$
$$\frac{3}{2}T_\infty(1+\varepsilon_3) = \frac{1}{n_\infty(1+\varepsilon_1)}\int f_\infty(1 + 2\boldsymbol{c}\cdot\boldsymbol{U}_\infty + h)c^2\mathrm{d}\boldsymbol{c}$$
$$\frac{3}{2}T_\infty(1+\varepsilon_1+\varepsilon_3+\varepsilon_1\varepsilon_3) = \frac{3}{2}T_\infty + \pi^{-3/2}\int c^2 h\exp(-c^2)\mathrm{d}\boldsymbol{c}$$
$$\varepsilon_3 = \frac{2}{3}\left[\pi^{-3/2}\int c^2 h\exp(-c^2)\mathrm{d}\boldsymbol{c} - \frac{3}{2}\varepsilon_1\right] = \frac{2}{3\pi^{3/2}}\int h\exp(-c^2)\left(c^2 - \frac{3}{2}\right)\mathrm{d}\boldsymbol{c}$$

Note that we have ignored the $\varepsilon_1\varepsilon_3$ term because it is of order ε^2 (and thus very small compared to the other terms in the equation). To summarize, the number density, bulk velocity, and temperature perturbations are moments of the perturbation to the distribution function h and are defined as

$$\varepsilon_1(\boldsymbol{r}) = (h, 1) \tag{2.12a}$$

$$\boldsymbol{\varepsilon}_2(\boldsymbol{r}) = 2(h, \boldsymbol{c}) \tag{2.12b}$$

$$\varepsilon_3(\boldsymbol{r}) = \frac{2}{3}\left(h, c^2 - \frac{3}{2}\right) \tag{2.12c}$$

where the inner product $(h(\boldsymbol{r}, \boldsymbol{c}), g(\boldsymbol{c}))$ is defined as

$$(h, g) = \pi^{-3/2} \int_{-\infty}^{\infty} hg \exp(-c^2) \mathrm{d}\boldsymbol{c} \tag{2.13}$$

We can apply the linearized forms of f and f_0 given by Eqns. (2.7) and (2.9) to Eq. (2.6):

$$\begin{aligned}
\boldsymbol{c} \cdot \nabla f =& f_0 - f \\
\boldsymbol{c} \cdot \nabla [f_\infty (1 + 2\boldsymbol{c} \cdot \boldsymbol{U}_\infty + h)] =& f_\infty \left[1 + 2\boldsymbol{c} \cdot \boldsymbol{U}_\infty + \varepsilon_1 + \boldsymbol{c} \cdot \boldsymbol{\varepsilon}_2 + \left(c^2 - \frac{3}{2}\right)\varepsilon_3\right] \\
& - f_\infty (1 + 2\boldsymbol{c} \cdot \boldsymbol{U}_\infty + h) \\
\boldsymbol{c} \cdot \nabla h =& \varepsilon_1 + \boldsymbol{c} \cdot \boldsymbol{\varepsilon}_2 + \left(c^2 - \frac{3}{2}\right)\varepsilon_3 - h
\end{aligned}$$

This equation can be written as

$$\boldsymbol{c} \cdot \nabla h = \mathcal{L} h \tag{2.14}$$

where the operator $\mathcal{L}$ is defined as

$$\mathcal{L} h = \varepsilon_1 + \boldsymbol{c} \cdot \boldsymbol{\varepsilon}_2 + \frac{2}{3}\left(c^2 - \frac{3}{2}\right)\varepsilon_3 - h \tag{2.15}$$

It is in this form [i.e. Eqns. (2.14) and (2.15)] that the Krook equation appears in

papers by Cercignani and Pagani [70] and Lea and Loyalka [75].

Now that I have completed the derivation of the BGK model and Krook equation, I can apply the equation to practical problems of mass transfer to and flow around a sphere. I will first discuss briefly the isothermal mass transfer problem because it is simpler mathematically than the flow problem, and thus it provides a good introduction for solving the Krook equation. Once I have discussed solving the condensation problem, I will turn my attention to the problem most relevant to this dissertation, that of uniform flow around a sphere. Note that in solving these problems, I am following the derivation of Lea [74].

2.2 Solution of the Krook Equation for Isothermal Mass Transfer to a Sphere

Let us start by considering mass transfer of a dilute vapor to a sphere. There is no bulk flow, so $\boldsymbol{\varepsilon}_2 = 0$. We will also assume that the region of interest is isothermal, so $\varepsilon_3 = 0$. This leaves us with the following equation for the perturbation to the distribution function:

$$\boldsymbol{c} \cdot \nabla h = (h, 1) - h \tag{2.16}$$

We can write this equation in terms of the characteristic path, s:

$$\frac{\mathrm{d}h}{\mathrm{d}s} + \frac{h}{c} = \frac{(h, 1)}{c} \tag{2.17}$$

Here, the derivative along the characteristic path is related to the diffusion term on the left-hand side of Eq. (2.14) by

$$\begin{aligned}\hat{\boldsymbol{\Omega}} \cdot \nabla h =& \Omega_x \frac{\partial h}{\partial x} + \Omega_y \frac{\partial h}{\partial y} + \Omega_z \frac{\partial h}{\partial z} \\ =& \frac{\partial x}{\partial s}\frac{\partial h}{\partial x} + \frac{\partial y}{\partial s}\frac{\partial h}{\partial y} + \frac{\partial z}{\partial s}\frac{\partial h}{\partial z} \\ =& \frac{\mathrm{d}h}{\mathrm{d}s}\end{aligned}$$

where $\hat{\boldsymbol{\Omega}} = \boldsymbol{c}/c$ is the direction vector of the molecular velocity. The geometry of this problem is shown in Fig. 2.1.

We can solve Eq. (2.17) using an integration factor, giving

$$h(\boldsymbol{r}, \boldsymbol{c}) = \exp\left(-\frac{s}{c}\right) \int_{-\infty}^{s} \exp\left(\frac{s''}{c}\right) \frac{h''}{c} \mathrm{d}s'' \tag{2.18}$$

where $h = h(\boldsymbol{r}_p + s\,\hat{\boldsymbol{\Omega}}, c\,\hat{\boldsymbol{\Omega}})$ and $h'' = h(\boldsymbol{r}_p + s''\hat{\boldsymbol{\Omega}}, c\,\hat{\boldsymbol{\Omega}})$. Substituting $s' = s - s'' = |\boldsymbol{r} - \boldsymbol{r}'|$ (see Fig. 2.1), our integral equation becomes

$$h(\boldsymbol{r}, \boldsymbol{c}) = \int_{0}^{\infty} \exp\left(-\frac{s'}{c}\right) \frac{(h')}{c} \mathrm{d}s' \tag{2.19}$$

where $h' = h(\boldsymbol{r} - s'\hat{\boldsymbol{\Omega}}, c\,\hat{\boldsymbol{\Omega}})$. The above equation applies to all paths that are outside of the solid angle ω. Within the solid angle, we must account for the boundary condition at the surface, which in this case is

$$h(\boldsymbol{r}, \boldsymbol{c}) = 0, \quad \boldsymbol{c} \cdot \hat{\boldsymbol{n}} > 0, \, \boldsymbol{r} = r_0 \hat{\mathbf{e}}_{\mathbf{r}} \tag{2.20}$$

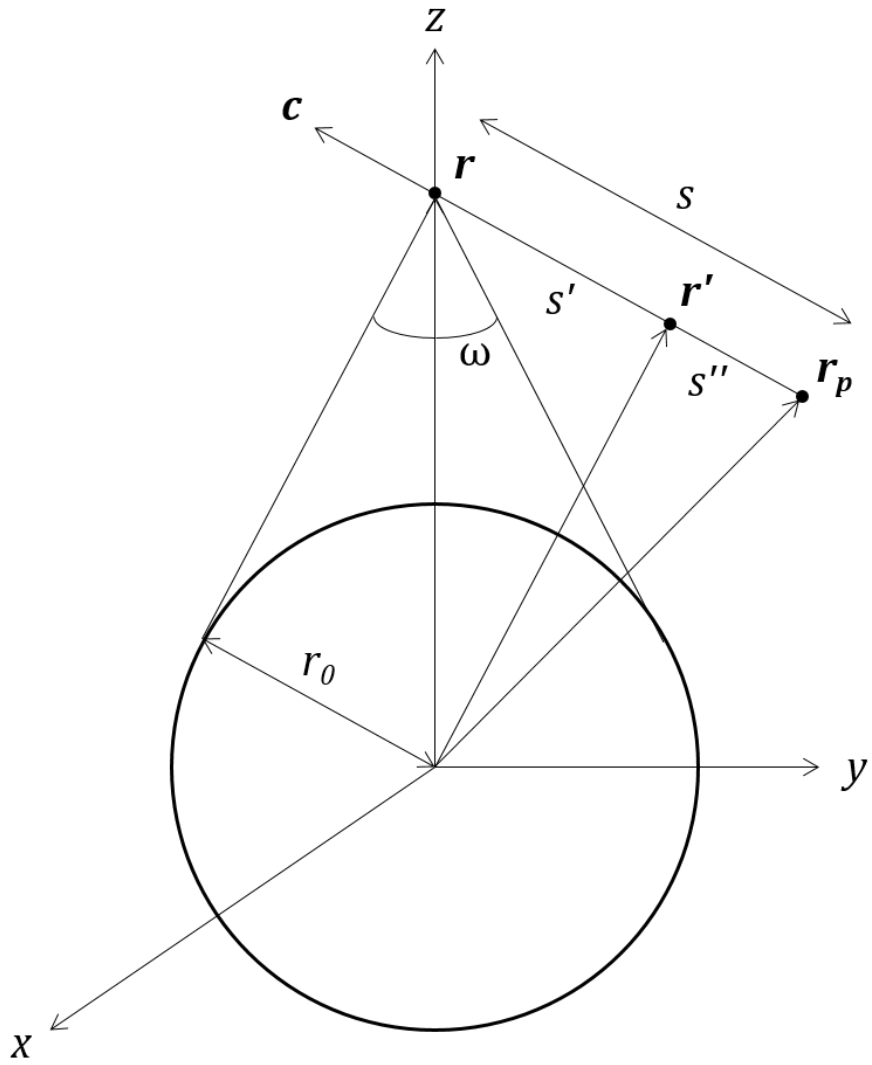

Figure 2.1: Geometry for the mass transfer problem (adapted from Fig. 1 of Lea [74])

This BC represents the fact that all vapor molecules that reach the sphere are absorbed and none are reflected. With this condition, the contribution to h from points within solid angle ω are

$$h(\boldsymbol{r},\boldsymbol{c}) = \int_0^{|\boldsymbol{r}-\boldsymbol{r}_0|} \exp\left(-\frac{s'}{c}\right) \frac{(h',1)}{c} \mathrm{d}s' \tag{2.21}$$

where the upper limit of integration is the distance between point $\boldsymbol{r}$ and the surface of the sphere.

For this problem, we are most interested in the number density moment $\varepsilon_1 = (h,1)$. Taking the moment of Eq. (2.19), we get

$$\begin{aligned}
\varepsilon_1 =& \pi^{-3/2} \int_0^\infty \int_0^\infty \frac{\exp(-c^2)}{c} \exp\left(-\frac{s'}{c}\right) \varepsilon_1(s') \mathrm{d}s' \mathrm{d}\boldsymbol{c} \\
=& \pi^{-3/2} \int_0^\infty \int_0^\infty \int_\theta \int_\phi c \exp\left(-c^2 - \frac{s'}{c}\right) \varepsilon_1(s') \sin\theta \mathrm{d}\phi \mathrm{d}\theta \mathrm{d}s' \mathrm{d}c \\
=& \pi^{-3/2} \int_0^\infty \int_\theta \int_\phi \mathrm{T}_1\left(s'\right) \varepsilon(s') \sin\theta \mathrm{d}\phi \mathrm{d}\theta \mathrm{d}s' \\
=& \pi^{-3/2} \int \frac{\mathrm{T}_1\left(|\boldsymbol{r}-\boldsymbol{r}'|\right)}{|\boldsymbol{r}-\boldsymbol{r}'|^2} \varepsilon_1(r') \mathrm{d}\boldsymbol{r}'
\end{aligned}$$

where

$$\mathrm{T}_n(x) = \int_0^\infty c^n \exp\left(-c^2 - \frac{x}{c}\right) \mathrm{d}c \tag{2.22}$$

and the integration includes the region outside of solid angle ω.[4] More information about $\mathrm{T}_n(x)$ can be found in Section 27.5 of Abramowitz and Stegun [98]. We get

[4] In deriving the equation for ε_1, we first write the integral over molecular velocities in terms of polar coordinates, i.e. $\mathrm{d}\boldsymbol{c} = c^2 \mathrm{d}c \mathrm{d}\hat{\Omega} = c^2 \sin\theta \mathrm{d}\phi \mathrm{d}\theta \mathrm{d}c$. Because the unit vector $\hat{\boldsymbol{\Omega}}$ appears in both the spatial and velocity components of h, and because s' and c are independent variables, we can switch the order of integration over $\mathrm{d}s'$ and $\mathrm{d}c$ and write $\sin\theta \mathrm{d}\phi \mathrm{d}\theta \mathrm{d}s' = \mathrm{d}s \mathrm{d}\hat{\Omega}/s'^2 = \mathrm{d}\boldsymbol{r}'/s'^2$.

the same result if we take the moment of Eq. (2.21), except the integration bounds the region inside solid angle ω between point $\boldsymbol{r}$ and the surface of the sphere. Thus, our equation for the number density moment is

$$\varepsilon_1(r) = \pi^{-3/2} \int_V \frac{\mathrm{T}_1\left(|\boldsymbol{r} - \boldsymbol{r}'|\right)}{|\boldsymbol{r} - \boldsymbol{r}'|^2} \varepsilon_1(r') \mathrm{d}\boldsymbol{r}' \tag{2.23}$$

where V includes all points in space that can be reached from $\boldsymbol{r}$ without first passing through the sphere.

It is possible to solve Eq. (2.23) numerically by providing an initial guess for ε_1 (either as a function or as a set of values are specified values of r), performing the integration for a set of radii, comparing the resulting $\varepsilon_1(r)$ to the initial guess, and iterating (i.e. using Newton's method or some other suitable technique). Note Eq. (2.23) only gives $\varepsilon_1(r)$ up to some constant multiplier, since if we multiply $\varepsilon_1(r')$ by a constant in the integral, we get $\varepsilon_1(r)$ multiplied by that same constant. One obtains the correct numerical values by noting that far from the sphere, the vapor concentration is given by the Chapman-Enskog solution for diffusion [21, 99]. It is possible to simplify Eq. (2.23) further by integrating over the angles θ and ϕ, leaving only the integral over the radius. The procedure is similar to the procedure that I will describe in the next section for flow around a sphere. For further information on solving the mass transfer problem, refer to Lea [74].

2.3 Solution of the Krook Equation for Uniform Flow Around a Sphere

I will now consider the problem that is more pertinent to this dissertation, that of uniform flow around a sphere in the transition regime. I will start with the derivation of the equations, then I will consider the numerical strategies that I will use to solve the problem.

2.3.1 Derivation of the Governing Equations

For this problem, let us consider the situation where the sphere is at the same temperature as the surrounding gas. Note that this does not mean the flow field is isothermal [76, 78], so we must consider all of the terms in the Krook equation.[5]

We start by writing Krook equation with the diffusion term as a derivative along the characteristic path, as we did for the problem of mass transfer to the sphere:

$$\frac{\mathrm{d}h}{\mathrm{d}s} + \frac{h}{c} = \frac{1}{c}\left[(h,1) + 2\boldsymbol{c}\cdot(h,\boldsymbol{c}) + \frac{2}{3}\left(c^2 - \frac{3}{2}\right)\left(h, c^2 - \frac{3}{2}\right)\right] \tag{2.24}$$

Again, we can apply an integrating factor to convert the integro-differential

[5] In continuum flow, the flow field *is* isothermal, but this is not the case outside of the continuum regime. However, Law and Loyalka [76] have shown that accounting for temperature fluctuations has only a minor impact on the calculated velocity profile and drag force. Their published results compare favorably to the earlier results of Lea and Loyalka [75] that assume an isothermal flow field. Nevertheless, I will account for $\varepsilon_3 \neq 0$ in my calculations because it better represents the physics of the problem.

equation to an integral equation, which gives us

$$h(\boldsymbol{r},\boldsymbol{c}) = \int_0^\infty \frac{1}{c}\exp\left[-\frac{s'}{c}\right]\left[(h',1) + 2\boldsymbol{c}\cdot(h',\boldsymbol{c}) + \frac{2}{3}\left(c^2-\frac{3}{2}\right)\left(h',c^2-\frac{3}{2}\right)\right]\mathrm{d}s' \tag{2.25}$$

for the region of space outside of the solid angle ω and

$$h(\boldsymbol{r},\boldsymbol{c}) = h_0\exp\left[-\frac{s}{c}\right] + \int_0^s \frac{1}{c}\exp\left[-\frac{(s-s')}{c}\right]\left[(h',1) + 2\boldsymbol{c}\cdot(h',\boldsymbol{c}) + \frac{2}{3}\left(c^2-\frac{3}{2}\right)\left(h',c^2-\frac{3}{2}\right)\right]\mathrm{d}s' \tag{2.26}$$

for the region of space in the solid angle ω between $\boldsymbol{r}$ and the surface of the sphere. In Eq. (2.25), $s' = |\boldsymbol{r}-\boldsymbol{r}'|$ and $h' = h(\boldsymbol{r}-s'\hat{\boldsymbol{\Omega}},\boldsymbol{c})$. In Eq. (2.26), $s-s' = |\boldsymbol{r}-\boldsymbol{r}'|$, $h' = h(\boldsymbol{r}_0+s'\hat{\boldsymbol{\Omega}},\boldsymbol{c})$, $h_0 = h(\boldsymbol{r}_0,\boldsymbol{c})$ (i.e. the value of h at the surface of the sphere), and $s = |\boldsymbol{r}-\boldsymbol{r}_0|$. (See Fig. 2.2 for the geometry described by Eq. 2.25 and Fig. 2.3 for the geometry described by Eq. 2.26.) The integral terms in these two equations represent the contribution to h from molecules whose last collision was with another gas molecule, while the non-integral term on the right-hand side of Eq. (2.26) describes the contribution to h from molecules whose previous collision was with the sphere.

Next, we must take the moments of $h(\boldsymbol{r},\boldsymbol{c})$ to find $\varepsilon_1(\boldsymbol{r})$, $\boldsymbol{\varepsilon}_2(\boldsymbol{r})$, and ε_3. We

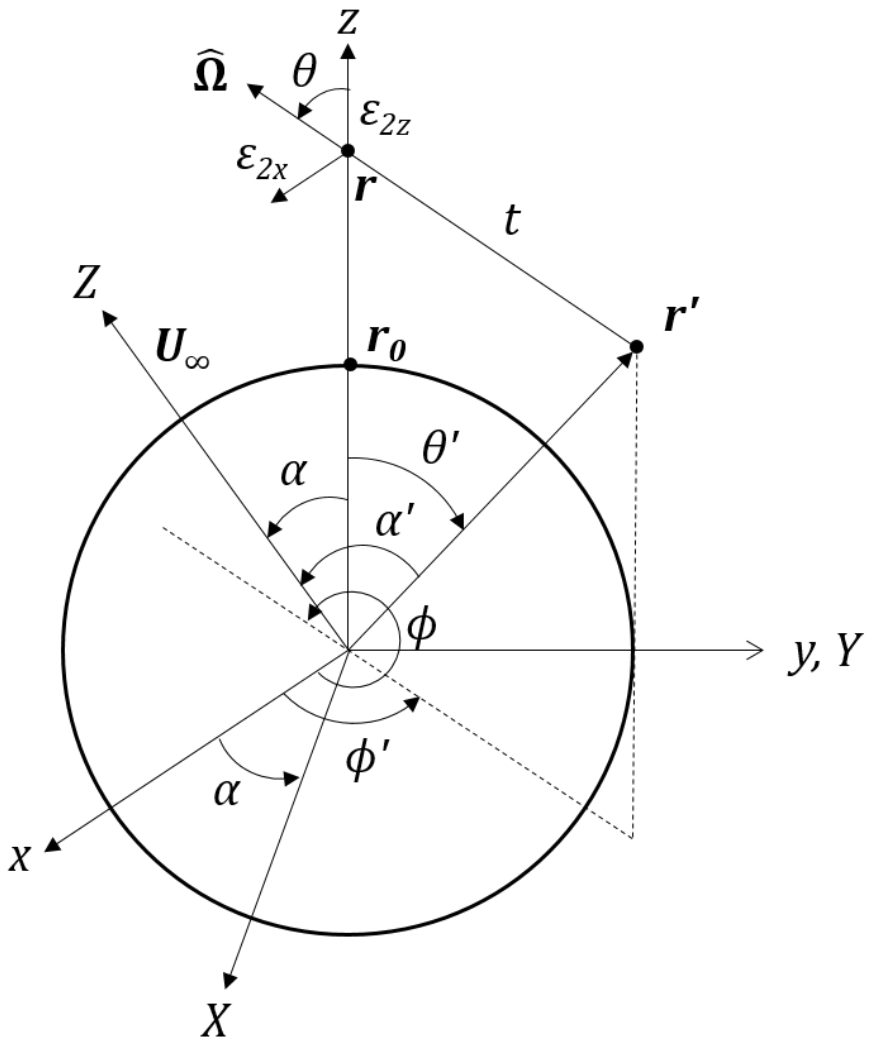

Figure 2.2: Geometry for Eq. 2.25, which describes the contribution to $h(\boldsymbol{r}, \boldsymbol{c})$ from points outside of the solid angle ω

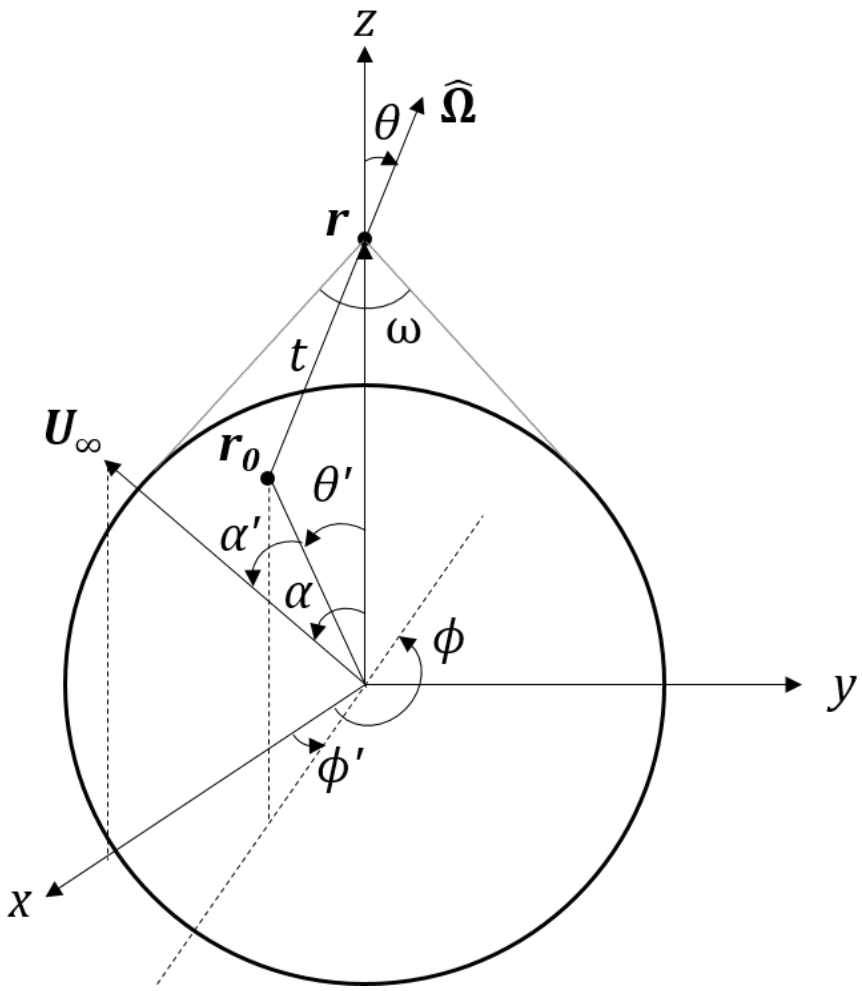

Figure 2.3: Geometry for Eq. 2.26, which describes the contribution to $h(\boldsymbol{r}, \boldsymbol{c})$ from points inside of the solid angle ω, including points on the surface $\boldsymbol{r}_0$

start by taking the moment $(h, 1)$ using Eq. (2.25):

$$\begin{aligned}
\varepsilon_1(\boldsymbol{r}) =& \pi^{-3/2} \int_0^\infty \int_0^\infty \frac{1}{c} \exp\left[-\frac{s'}{c}\right] \left[(h', 1) + 2\boldsymbol{c}\cdot(h', \boldsymbol{c}) \right. \\
& \left. + \frac{2}{3}\left(c^2 - \frac{3}{2}\right)\left(h', c^2 - \frac{3}{2}\right)\right] \mathrm{d}s'\mathrm{d}\boldsymbol{c} \\
=& \pi^{-3/2} \int_0^\infty \int_\theta \int_\phi \int_0^\infty c\sin\theta \exp\left[-\frac{s'}{c}\right] \left[(h', 1) + 2\boldsymbol{c}\cdot(h', \boldsymbol{c}) \right. \\
& \left. + \frac{2}{3}\left(c^2 - \frac{3}{2}\right)\left(h', c^2 - \frac{3}{2}\right)\right] \mathrm{d}c\mathrm{d}\phi\mathrm{d}\theta\mathrm{d}s' \\
=& \pi^{-3/2} \int_0^\infty \int_\theta \int_\phi \sin\theta \left[\mathrm{T}_1(s')(h', 1) + 2\,\mathrm{T}_2(s')\hat{\boldsymbol{\Omega}}\cdot(h', \boldsymbol{c}) \right. \\
& \left. + \frac{2}{3}\left(\mathrm{T}_3(s') - \frac{3}{2}\,\mathrm{T}_1(s')\right)\left(h', c^2 - \frac{3}{2}\right)\right] \mathrm{d}\phi\mathrm{d}\theta\mathrm{d}s' \\
=& \pi^{-3/2} \int \frac{\mathrm{d}\boldsymbol{r}'}{|\boldsymbol{r} - \boldsymbol{r}'|^2} \left[\mathrm{T}_1\,\varepsilon_1(\boldsymbol{r}') + \mathrm{T}_2\,\hat{\boldsymbol{\Omega}}\cdot\boldsymbol{\varepsilon}_2 + \left(\mathrm{T}_3 - \frac{3}{2}\,\mathrm{T}_1\right)\varepsilon_3(\boldsymbol{r}')\right]
\end{aligned}$$

The argument of the T_n functions in the last equality is $|\boldsymbol{r} - \boldsymbol{r}'|$.

Taking the moment $(h, 1)$ using Eq. (2.26) gives the same result for the integral over $\mathrm{d}s'$ (i.e. the second term on the right-hand side of the equation), so now we must determine the contribution from the surface of the sphere. This is simply $\int h_0 \exp(-c^2 - \frac{s}{c})\mathrm{d}\boldsymbol{c}$, where again $s = |\boldsymbol{r} - \boldsymbol{r}_0|$. Thus, the perturbation to the number density is

$$\begin{aligned}
\varepsilon_1(\boldsymbol{r}) = \pi^{-3/2} \left\{ \int_C h(\boldsymbol{r}_0, \boldsymbol{c}) \exp\left(-c^2 - \frac{|\boldsymbol{r} - \boldsymbol{r}_0|}{c}\right) \mathrm{d}\boldsymbol{c} \right. \\
\left. + \int_V \frac{\mathrm{d}\boldsymbol{r}'}{|\boldsymbol{r} - \boldsymbol{r}'|^2} \left[\mathrm{T}_1\,\varepsilon_1(\boldsymbol{r}') + \mathrm{T}_2\,\hat{\boldsymbol{\Omega}}\cdot\boldsymbol{\varepsilon}_2(\boldsymbol{r}') + \left(\mathrm{T}_3 - \frac{3}{2}\,\mathrm{T}_1\right)\varepsilon_3(\boldsymbol{r}')\right] \right\}
\end{aligned} \tag{2.27}$$

The domain C accounts for all molecules reflected from the sphere whose trajectory

passes through $\boldsymbol{r}$, while the domain V includes all points in physical space that can be reached from $\boldsymbol{r}$ without first passing through the sphere (including points within the solid angle ω between r and the surface of the sphere). Note that in the above equations, $\hat{\boldsymbol{\Omega}} = \boldsymbol{c}/c = (\boldsymbol{r} - \boldsymbol{r}')/|\boldsymbol{r} - \boldsymbol{r}'|$.

Taking the moment $2(h, \boldsymbol{c})$ of Eqns. (2.25) and (2.26) gives us the following equation for $\boldsymbol{\varepsilon}_2(\boldsymbol{r})$:

$$\boldsymbol{\varepsilon}_2(\boldsymbol{r}) = 2\pi^{-3/2} \left\{ \int_C \boldsymbol{c}\, h(\boldsymbol{r}_0, \boldsymbol{c}) \exp\left(-c^2 - \frac{|\boldsymbol{r} - \boldsymbol{r}_0|}{c}\right) \mathrm{d}\boldsymbol{c} \right. \\ \left. + \int_V \frac{\mathrm{d}\boldsymbol{r}'}{|\boldsymbol{r} - \boldsymbol{r}'|^2} \left[\mathrm{T}_2\, \varepsilon_1(\boldsymbol{r}') + \mathrm{T}_3\, \hat{\boldsymbol{\Omega}} \cdot \boldsymbol{\varepsilon}_2(\boldsymbol{r}') + \left(\mathrm{T}_4 - \frac{3}{2}\,\mathrm{T}_2\right) \varepsilon_3(\boldsymbol{r}') \right] \hat{\boldsymbol{\Omega}} \right\} \tag{2.28}$$

Likewise, our equation for $\varepsilon_3(\boldsymbol{r})$ is

$$\varepsilon_3(\boldsymbol{r}) = \frac{2}{3}\pi^{-3/2} \left\{ \int_C \left(c^2 - \frac{3}{2}\right) h(\boldsymbol{r}_0, \boldsymbol{c}) \exp\left(-c^2 - \frac{|\boldsymbol{r} - \boldsymbol{r}_0|}{c}\right) \mathrm{d}\boldsymbol{c} \right. \\ + \int_V \frac{\mathrm{d}\boldsymbol{r}'}{|\boldsymbol{r} - \boldsymbol{r}'|^2} \left[\left(\mathrm{T}_3 - \frac{3}{2}\,\mathrm{T}_1\right) \varepsilon_1(\boldsymbol{r}') + \left(\mathrm{T}_4 - \frac{3}{2}\,\mathrm{T}_2\right) \hat{\boldsymbol{\Omega}} \cdot \boldsymbol{\varepsilon}_2(\boldsymbol{r}') \right. \\ \left. \left. + \left(\mathrm{T}_5 - 3\,\mathrm{T}_3 + \frac{9}{4}\,\mathrm{T}_1\right) \varepsilon_3(\boldsymbol{r}') \right] \right\} \tag{2.29}$$

These results are very similar to our result for ε_1, as are the intermediate mathematical steps required to obtain equations for the density, velocity, and temperature perturbations.

Before we can solve for ε_1, $\boldsymbol{\varepsilon}_2$, and ε_3, we must determine the perturbation at the surface of the sphere, $h(\boldsymbol{r}_0, \boldsymbol{c})$. To do so, we must apply the boundary condition

at the surface of the sphere,

$$h(\boldsymbol{r}_0, \boldsymbol{c}) = A(\boldsymbol{r}_0) - 2\boldsymbol{c} \cdot \boldsymbol{U}_\infty, \quad \boldsymbol{c} \cdot \hat{\boldsymbol{n}} > 0 \tag{2.30}$$

Note that our other boundary condition,

$$\lim_{|\boldsymbol{r}| \to \infty} h(\boldsymbol{r}, \boldsymbol{c}) = 0, \tag{2.31}$$

states that the perturbation decays to zero far from the sphere.

The form of Eq. (2.30) assumes diffuse reflection from the surface. ($\hat{\boldsymbol{n}}$ is the normal vector on the surface of the sphere at $\boldsymbol{r}_0$.) Thus, the reflected molecules have a Maxwellian distribution, with $\boldsymbol{U} = 0$ (since the sphere is stationary for this problem), $T = T_\infty$, and unknown number density. If we plug Eq. (2.30) into Eq. (2.7) for f, $\boldsymbol{c} \cdot \hat{\boldsymbol{n}} > 0$, we get

$$f(\boldsymbol{r}_0, \boldsymbol{c}) = f_\infty[1 + A(\boldsymbol{r}_0)], \quad \boldsymbol{c} \cdot \hat{\boldsymbol{n}} > 0$$

This shows that the function $A(\boldsymbol{r}_0)$ is effectively the perturbation to the number density of an equilibrium gas with $n = n_\infty$, $\boldsymbol{U} = 0$, and $T = T_\infty$, so the form of our surface boundary condition for h is correct.

We can determine $A(\boldsymbol{r}_0)$ by applying mass conservation at the surface:

$$\int \boldsymbol{c} \cdot \hat{\boldsymbol{n}} f \, \mathrm{d}\boldsymbol{c} = 0$$

Physically, this integral states that the net mass flux at the surface of the sphere is zero. Breaking our integral into two parts – the molecules moving towards the surface and those moving from the surface – and substituting for f, we get

$$\int_{\boldsymbol{c}\cdot\hat{\boldsymbol{n}}>0} \boldsymbol{c}\cdot\hat{\boldsymbol{n}} f_\infty(1+2\boldsymbol{c}\cdot\boldsymbol{U}_\infty+h)\mathrm{d}\boldsymbol{c} = -\int_{\boldsymbol{c}\cdot\hat{\boldsymbol{n}}<0} \boldsymbol{c}\cdot\hat{\boldsymbol{n}} f_\infty(1+2\boldsymbol{c}\cdot\boldsymbol{U}_\infty+h)\mathrm{d}\boldsymbol{c}$$

The constant terms cancel in the integrals due to the symmetry of the Maxwellian distribution, so our mass balance becomes

$$\int_{\boldsymbol{c}\cdot\hat{\boldsymbol{n}}>0} \boldsymbol{c}\cdot\hat{\boldsymbol{n}} \exp(-c^2)(2\boldsymbol{c}\cdot\boldsymbol{U}_\infty+h_0)\mathrm{d}\boldsymbol{c} = -\int_{\boldsymbol{c}\cdot\hat{\boldsymbol{n}}<0} \boldsymbol{c}\cdot\hat{\boldsymbol{n}} \exp(-c^2)(2\boldsymbol{c}\cdot\boldsymbol{U}_\infty+h_0)\mathrm{d}\boldsymbol{c} \tag{2.32}$$

For the term on the left-hand side, we can substitute Eq. (2.30) for h and perform the integration,

$$\begin{aligned}
\int_{\boldsymbol{c}\cdot\hat{\boldsymbol{n}}>0} \boldsymbol{c}\cdot\hat{\boldsymbol{n}} \exp(-c^2)(2\boldsymbol{c}\cdot\boldsymbol{U}_\infty+h_0)\mathrm{d}\boldsymbol{c} &= \int_{\boldsymbol{c}\cdot\hat{\boldsymbol{n}}>0} \boldsymbol{c}\cdot\hat{\boldsymbol{n}} \exp(-c^2)A(\boldsymbol{r}_0)\mathrm{d}\boldsymbol{c} \\
&= A\int_{\boldsymbol{c}\cdot\hat{\boldsymbol{n}}>0} c\,\hat{\boldsymbol{\Omega}}\cdot\hat{\boldsymbol{n}} \exp(-c^2)\mathrm{d}\boldsymbol{c} \\
&= A\int_0^{\pi/2}\mathrm{d}\theta\int_0^{2\pi}\mathrm{d}\phi\int_0^{\infty}\mathrm{d}c\,c^3\cos\theta\sin\theta\exp(-c^2) \\
&= \frac{\pi}{2}A(\boldsymbol{r}_0)
\end{aligned}$$

We can also integrate the first term on the right-hand side (i.e. the term involving $\boldsymbol{c}\cdot\boldsymbol{U}_\infty$). Before performing the integration, we will define α as the angle between $\hat{\boldsymbol{n}}$ and $\boldsymbol{U}_\infty$, θ as the polar angle between $\hat{\boldsymbol{n}}$ and $\hat{\boldsymbol{\Omega}}$, and ϕ as the angle between $U\sin\alpha$ and $\sin\theta$. (See Fig. 2.4.) These definitions will be used to evaluate

the dot products in the integral. With these conventions established, the integral of the first term on the right-hand side of Eq. (2.32) is

$$
\begin{aligned}
&-2\int_{\boldsymbol{c}\cdot\hat{\boldsymbol{n}}<0} \boldsymbol{c}\cdot\hat{\boldsymbol{n}}\exp(-c^2)\boldsymbol{c}\cdot\boldsymbol{U}_\infty \mathrm{d}\boldsymbol{c} = -2\int_{\boldsymbol{c}\cdot\hat{\boldsymbol{n}}<0} c^2\,\hat{\boldsymbol{\Omega}}\cdot\hat{\boldsymbol{n}}\exp(-c^2)\hat{\boldsymbol{\Omega}}\cdot\boldsymbol{U}_\infty \mathrm{d}\boldsymbol{c} \\
&= -2U\int_0^{\pi/2}\mathrm{d}\theta\int_0^{2\pi}\mathrm{d}\phi\int_0^{\infty}\mathrm{d}c\,c^4\exp(-c^2)\cos\theta\sin\theta(\sin\alpha\sin\theta\cos\phi+\cos\alpha\cos\theta) \\
&= -\frac{\pi^{3/2}}{2}U\cos\alpha
\end{aligned}
$$

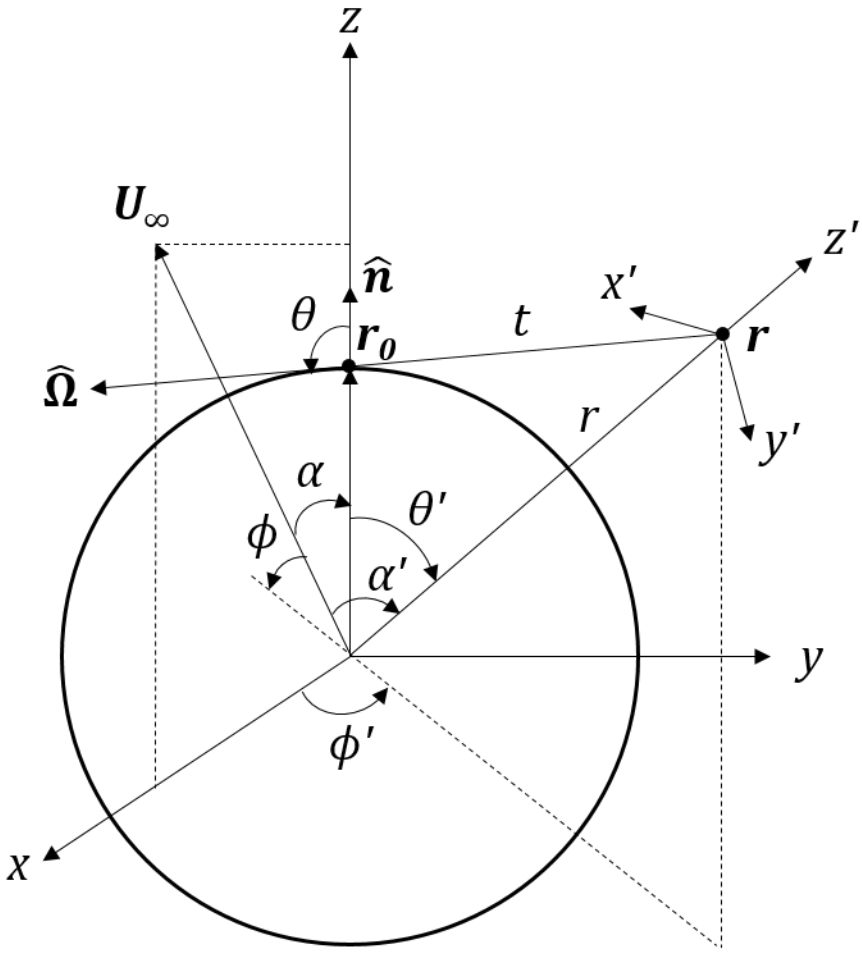

Figure 2.4: Geometry for determining $A(\boldsymbol{r}_0)$

Finally, we can substitute Eq. (2.25) for h_0 in the second term on the right-

hand side of Eq. (2.32) and perform the integration:

$$
\begin{aligned}
&\int_{\boldsymbol{c}\cdot\hat{\boldsymbol{n}}<0} h\boldsymbol{c}\cdot\hat{\boldsymbol{n}}\exp(-c^2)\mathrm{d}\boldsymbol{c} \\
&\qquad = \int_{\boldsymbol{c}\cdot\hat{\boldsymbol{n}}<0} \mathrm{d}\boldsymbol{c} \int_0^\infty \mathrm{d}s'\, \frac{\boldsymbol{c}}{c}\cdot\hat{\boldsymbol{n}} \exp\left[-c^2 - \frac{s'}{c}\right]\left[(h',1) + 2\boldsymbol{c}\cdot(h',\boldsymbol{c})\right. \\
&\qquad\qquad \left. + \frac{2}{3}\left(c^2-\frac{3}{2}\right)\left(h, c^2-\frac{3}{2}\right)\right] \\
&\qquad = \int_0^\infty \mathrm{d}s' \int_{\hat{\boldsymbol{\Omega}}\cdot\hat{\boldsymbol{n}}<0} \mathrm{d}\hat{\Omega} \int_0^\infty \mathrm{d}c\, c^2 \exp\left[-c^2 - \frac{s'}{c}\right]\left[(h',1) + 2\boldsymbol{c}\cdot(h',\boldsymbol{c})\right. \\
&\qquad\qquad \left. + \frac{2}{3}\left(c^2-\frac{3}{2}\right)\left(h, c^2-\frac{3}{2}\right)\right](\hat{\boldsymbol{\Omega}}\cdot\hat{\boldsymbol{n}}) \\
&\qquad = \int_V \frac{\mathrm{d}\boldsymbol{r}}{|\boldsymbol{r}-\boldsymbol{r}_0|^2}\left[\mathrm{T}_2(|\boldsymbol{r}-\boldsymbol{r}_0|)\varepsilon_1(\boldsymbol{r}) + \mathrm{T}_3(|\boldsymbol{r}-\boldsymbol{r}_0|)\hat{\boldsymbol{\Omega}}\cdot\boldsymbol{\varepsilon}_2(\boldsymbol{r})\right. \\
&\qquad\qquad \left. + \left(\mathrm{T}_4(|\boldsymbol{r}-\boldsymbol{r}_0|) - \frac{3}{2}\mathrm{T}_2(|\boldsymbol{r}-\boldsymbol{r}_0|)\right)\right](\hat{\boldsymbol{\Omega}}\cdot\hat{\boldsymbol{n}})
\end{aligned}
$$

Combining these results, we get an equation for $A(\boldsymbol{r}_0)$:

$$
\begin{aligned}
A(\boldsymbol{r}_0) = &-\sqrt{\pi}U\cos\alpha \\
&-\frac{2}{\pi}\int_V \frac{\mathrm{d}\boldsymbol{r}}{|\boldsymbol{r}-\boldsymbol{r}_0|^2}\left[\mathrm{T}_2\,\varepsilon_1(\boldsymbol{r}) + \mathrm{T}_3\,\hat{\boldsymbol{\Omega}}\cdot\boldsymbol{\varepsilon}_2(\boldsymbol{r}) + \left(\mathrm{T}_4 - \frac{3}{2}\mathrm{T}_2\right)\varepsilon_3(\boldsymbol{r})\right](\hat{\boldsymbol{\Omega}}\cdot\hat{\boldsymbol{n}})
\end{aligned}
\tag{2.33}
$$

The argument of the T_n functions in the last equality is $|\boldsymbol{r}-\boldsymbol{r}_0|$. The integral in the equation above sums up the contribution of all molecules that reach the point on the sphere $\boldsymbol{r}_0$ and are reflected from the surface. The integration domain is every point in space with a direct line of sight to the point $\boldsymbol{r}_0$ on the surface of the sphere.

We now substitute our boundary condition Eq. (2.30) for h_0 in Eqns. (2.27–

2.29) to obtain expressions for $\varepsilon_1(\boldsymbol{r})$, $\boldsymbol{\varepsilon}_2(\boldsymbol{r})$, and $\varepsilon_3(\boldsymbol{r})$ that we can solve numerically:

$$\begin{aligned}\varepsilon_1(\boldsymbol{r}) = \pi^{-3/2}\Bigg\{\int_\omega \Big[A(\boldsymbol{r}_0)\,\mathrm{T}_2(|\boldsymbol{r}-\boldsymbol{r}_0|) - 2(\hat{\boldsymbol{\Omega}}\cdot\boldsymbol{U}_\infty)\,\mathrm{T}_3(|\boldsymbol{r}-\boldsymbol{r}_0|)\Big]\,\mathrm{d}\hat{\boldsymbol{\Omega}} \\ + \int_V \frac{\mathrm{d}\boldsymbol{r}'}{|\boldsymbol{r}-\boldsymbol{r}'|^2}\Bigg[\mathrm{T}_1(|\boldsymbol{r}-\boldsymbol{r}'|)\varepsilon_1(\boldsymbol{r}') + \mathrm{T}_2(|\boldsymbol{r}-\boldsymbol{r}'|)\hat{\boldsymbol{\Omega}}\cdot\boldsymbol{\varepsilon}_2(\boldsymbol{r}') \\ + \left(\mathrm{T}_3(|\boldsymbol{r}-\boldsymbol{r}'|) - \frac{3}{2}\,\mathrm{T}_1(|\boldsymbol{r}-\boldsymbol{r}'|)\right)\varepsilon_3(\boldsymbol{r}')\Bigg]\Bigg\}\end{aligned} \tag{2.34}$$

$$\begin{aligned}\boldsymbol{\varepsilon}_2(\boldsymbol{r}) = 2\pi^{-3/2}\Bigg\{\int_\omega \Big[A(\boldsymbol{r}_0)\,\mathrm{T}_3(|\boldsymbol{r}-\boldsymbol{r}_0|) - 2(\hat{\boldsymbol{\Omega}}\cdot\boldsymbol{U}_\infty)\,\mathrm{T}_4(|\boldsymbol{r}-\boldsymbol{r}_0|)\Big]\,\hat{\boldsymbol{\Omega}}\mathrm{d}\hat{\boldsymbol{\Omega}} \\ + \int_V \frac{\mathrm{d}\boldsymbol{r}'}{|\boldsymbol{r}-\boldsymbol{r}'|^2}\Bigg[\mathrm{T}_2(|\boldsymbol{r}-\boldsymbol{r}'|)\varepsilon_1(\boldsymbol{r}') + \mathrm{T}_3(|\boldsymbol{r}-\boldsymbol{r}'|)\hat{\boldsymbol{\Omega}}\cdot\boldsymbol{\varepsilon}_2(\boldsymbol{r}') \\ + \left(\mathrm{T}_4(|\boldsymbol{r}-\boldsymbol{r}'|) - \frac{3}{2}\,\mathrm{T}_2(|\boldsymbol{r}-\boldsymbol{r}'|)\right)\varepsilon_3(\boldsymbol{r}')\Bigg]\hat{\boldsymbol{\Omega}}\Bigg\}\end{aligned} \tag{2.35}$$

$$\begin{aligned}\varepsilon_3(\boldsymbol{r}) = \frac{2}{3}\pi^{-3/2}\Bigg\{\int_\omega \Bigg[A(\boldsymbol{r}_0)\left(\mathrm{T}_4(|\boldsymbol{r}-\boldsymbol{r}_0|) - \frac{3}{2}\,\mathrm{T}_2(|\boldsymbol{r}-\boldsymbol{r}_0|)\right) \\ - 2(\hat{\boldsymbol{\Omega}}\cdot\boldsymbol{U}_\infty)\left(\mathrm{T}_5(|\boldsymbol{r}-\boldsymbol{r}_0|) - \frac{3}{2}\,\mathrm{T}_3(|\boldsymbol{r}-\boldsymbol{r}_0|)\right)\Bigg]\mathrm{d}\hat{\boldsymbol{\Omega}} \\ + \int_V \frac{\mathrm{d}\boldsymbol{r}'}{|\boldsymbol{r}-\boldsymbol{r}'|^2}\Bigg[\left(\mathrm{T}_3(|\boldsymbol{r}-\boldsymbol{r}'|) - \frac{3}{2}\,\mathrm{T}_1(|\boldsymbol{r}-\boldsymbol{r}'|)\right)\varepsilon_1(\boldsymbol{r}') \\ + \left(\mathrm{T}_4(|\boldsymbol{r}-\boldsymbol{r}'|) - \frac{3}{2}\,\mathrm{T}_2(|\boldsymbol{r}-\boldsymbol{r}'|)\right)\hat{\boldsymbol{\Omega}}\cdot\boldsymbol{\varepsilon}_2(\boldsymbol{r}') \\ + \left(\mathrm{T}_5(|\boldsymbol{r}-\boldsymbol{r}'|) - 3\,\mathrm{T}_3(|\boldsymbol{r}-\boldsymbol{r}'|) - \frac{9}{4}\,\mathrm{T}_1(|\boldsymbol{r}-\boldsymbol{r}'|)\right)\varepsilon_3(\boldsymbol{r}')\Bigg]\Bigg\}\end{aligned} \tag{2.36}$$

Note that we have integrated the reflection term over all molecular speeds, leaving an integral over the solid angle ω.

Together, Eqns. (2.33–2.36) fully describe the problem. The equations are lin-

ear, which guarantees a unique solution for $\varepsilon_1(\boldsymbol{r})$, $\boldsymbol{\varepsilon}_2(\boldsymbol{r})$, and $\varepsilon_3(\boldsymbol{r})$. These equations are also valid for any geometry, not just for a sphere, provided the integration bounds are appropriately specified. In theory, we should be able to solve these equations directly; however, such an attempt would be very computationally expensive.

Fortunately, we can simplify the governing equations for ε_1, $\boldsymbol{\varepsilon}_2$, and ε_3 further. Let us define the following vectors:

$$\boldsymbol{\psi}(\boldsymbol{r}) = \begin{bmatrix} \psi_1(\boldsymbol{r}) \\ \psi_2(\boldsymbol{r}) \\ \psi_3(\boldsymbol{r}) \\ \psi_4(\boldsymbol{r}) \end{bmatrix} = \begin{bmatrix} \varepsilon_1(\boldsymbol{r}) \\ \frac{1}{\sqrt{2}}\,\varepsilon_{2r}(\boldsymbol{r}) \\ \frac{1}{\sqrt{2}}\,\varepsilon_{2\theta}(\boldsymbol{r}) \\ \sqrt{\frac{3}{2}}\,\varepsilon_3(\boldsymbol{r}) \end{bmatrix} \tag{2.37}$$

$$\boldsymbol{S}(\boldsymbol{r}) = \pi^{-3/2} \begin{bmatrix} \varepsilon_1^{(0)}(\boldsymbol{r}) \\ \sqrt{2}\,\varepsilon_{2z}^{(0)}(\boldsymbol{r}) \\ \sqrt{2}\,\varepsilon_{2x}^{(0)}(\boldsymbol{r}) \\ \sqrt{\frac{2}{3}}\,\varepsilon_3^{(0)} \end{bmatrix} = \boldsymbol{S}_A(\boldsymbol{r}) + \boldsymbol{S}_U(\boldsymbol{r}) \tag{2.38}$$

$\varepsilon_{2z}(\boldsymbol{r})$ and $-\varepsilon_{2x}(\boldsymbol{r})$ are the perturbations in the r- and θ-velocity, respectively.[6] The source term $\boldsymbol{S}(\boldsymbol{r})$ corresponds to the first term in Eqns. (2.34) and (2.35); $\boldsymbol{S}_U(\boldsymbol{r})$ is the part of the source term containing $\boldsymbol{U}_\infty$ and $\boldsymbol{S}_A(\boldsymbol{r})$ is the other part. These definitions are consistent with the work of Cercignani and Pagani [70] and Law and

[6]The negative sign before ε_{2x} is due to the fact that the positive x-axis used to define ε_{2x} points in the direction of decreasing θ. Thus, $\varepsilon_{2x} = -\varepsilon_{2\theta}$. I recognize that this discrepancy can be confusing, but I am simply retaining the nomenclature used by Lea [74].

Loyalka [76]. We can now write our problem as follows:

$$\boldsymbol{\psi}(\boldsymbol{r}) = \mathcal{L}\boldsymbol{\psi}(\boldsymbol{r}') + \boldsymbol{S}(\boldsymbol{r}) \tag{2.39a}$$

$$\mathcal{L}\boldsymbol{\psi}(\boldsymbol{r}') \equiv \pi^{-3/2} \int_V \Lambda\boldsymbol{\psi}(\boldsymbol{r}') \frac{\mathrm{d}\boldsymbol{r}'}{|\boldsymbol{r}-\boldsymbol{r}'|^2} \tag{2.39b}$$

$$\Lambda\boldsymbol{\psi}(\boldsymbol{r}') \equiv \begin{bmatrix} \mathrm{T}_1\,\varepsilon_1 + \mathrm{T}_2\,\hat{\boldsymbol{\Omega}}\cdot\boldsymbol{\varepsilon}_2 + \left(\mathrm{T}_3 - \frac{3}{2}\,\mathrm{T}_1\right)\varepsilon_3 \\ \sqrt{2}\left[\mathrm{T}_2\,\varepsilon_1 + \mathrm{T}_3\,\hat{\boldsymbol{\Omega}}\cdot\boldsymbol{\varepsilon}_2 + \left(\mathrm{T}_4 - \frac{3}{2}\,\mathrm{T}_2\right)\varepsilon_3\right]\Omega_z \\ \sqrt{2}\left[\mathrm{T}_2\,\varepsilon_1 + \mathrm{T}_3\,\hat{\boldsymbol{\Omega}}\cdot\boldsymbol{\varepsilon}_2 + \left(\mathrm{T}_4 - \frac{3}{2}\,\mathrm{T}_2\right)\varepsilon_3\right]\Omega_x \\ \sqrt{\frac{2}{3}}\left[\left(\mathrm{T}_3 - \frac{3}{2}\,\mathrm{T}_1\right)\varepsilon_1 + \left(\mathrm{T}_4 - \frac{3}{2}\,\mathrm{T}_2\right)\hat{\boldsymbol{\Omega}}\cdot\boldsymbol{\varepsilon}_2 + \left(\mathrm{T}_5 - 3\,\mathrm{T}_3 + \frac{9}{4}\,\mathrm{T}_1\right)\varepsilon_3\right] \end{bmatrix} \tag{2.39c}$$

Here, $\hat{\boldsymbol{\Omega}} = (\boldsymbol{r}-\boldsymbol{r}')/|\boldsymbol{r}-\boldsymbol{r}'|$, $\hat{\Omega}_x$ and $\hat{\Omega}_z$ are the x- and z-components of the molecular trajectory $\hat{\boldsymbol{\Omega}}$, the argument of the T_n functions is $|\boldsymbol{r}-\boldsymbol{r}'|$, and the perturbations ε_n are a function of $\boldsymbol{r}'$.

Let us consider each of the terms in Eq. (2.39). Again, we can break up the source term into the portion that involves $\boldsymbol{U}_\infty$ and the portion that includes $A(\boldsymbol{r}_0)$. For a sphere, the source terms $\boldsymbol{S}_U$ and $\boldsymbol{S}_A$ are

$$\boldsymbol{S}_U(\boldsymbol{r}) = U \begin{bmatrix} W_{U1}(r)\cos\alpha \\ W_{U2}(r)\cos\alpha \\ W_{U3}(r)\sin\alpha \\ W_{U4}(r)\cos\alpha \end{bmatrix} \tag{2.40}$$

$$\boldsymbol{S}_A(\boldsymbol{r}) = gU \begin{bmatrix} W_{A1}(r)\cos\alpha \\ W_{A2}(r)\cos\alpha \\ W_{A3}(r)\sin\alpha \\ W_{A4}(r)\cos\alpha \end{bmatrix} \tag{2.41}$$

where the W functions are defined in Appendix A. Refer to Appendix A for the derivation of Eqns. 2.40 and 2.41.

The constant g in Eq. (2.41) is given by

$$g = \pi^{-1/2} + \frac{2}{U}\int_{r_0}^{\infty} \frac{r}{r_0}(\boldsymbol{\rho}(r)\cdot\boldsymbol{a}(r))\mathrm{d}r \tag{2.42}$$

where $\boldsymbol{a}(r)$ is defined in Appendix A and $\boldsymbol{\rho}(r)$ is defined shortly. Refer to Appendix A for the derivation of g.

As I have mentioned earlier, the problem for $\boldsymbol{\psi}(\boldsymbol{r})$ is linear. Furthermore, the source term is the only non-homogeneous part of the equation. In order for $\boldsymbol{\psi}(\boldsymbol{r})$ to satisfy Eq. (2.39), it must have the same angular dependence as the source terms [73, 74]. In other words, we can write $\boldsymbol{\psi}(\boldsymbol{r})$ as the product of an unknown function of the distance r and a known angular dependence:

$$\boldsymbol{\psi} = \begin{bmatrix} \cos\alpha & 0 & 0 & 0 \\ 0 & \cos\alpha & 0 & 0 \\ 0 & 0 & \sin\alpha & 0 \\ 0 & 0 & 0 & \cos\alpha \end{bmatrix} \cdot \boldsymbol{\rho}(r) = \begin{bmatrix} \rho_1(r)\cos\alpha \\ \rho_2(r)\cos\alpha \\ \rho_3(r)\sin\alpha \\ \rho_4(r)\cos\alpha \end{bmatrix} \tag{2.43}$$

This greatly simplifies the solution, since we need only find the radial dependence of $\boldsymbol{\psi}$.

We can now rewrite the kernel given by Eq. (2.39b) as

$$\mathcal{L}\boldsymbol{\psi}(\boldsymbol{r}') = \pi^{-1/2} \int_{r_0}^{\infty} \frac{r'}{r} \begin{bmatrix} \cos\alpha & 0 & 0 & 0 \\ 0 & \cos\alpha & 0 & 0 \\ 0 & 0 & \sin\alpha & 0 \\ 0 & 0 & 0 & \cos\alpha \end{bmatrix} \cdot \begin{bmatrix} H_{11} & H_{12} & H_{13} & H_{14} \\ H_{21} & H_{22} & H_{23} & H_{24} \\ H_{31} & H_{32} & H_{33} & H_{34} \\ H_{41} & H_{42} & H_{43} & H_{44} \end{bmatrix} \cdot \begin{bmatrix} \rho_1(r') \\ \rho_2(r') \\ \rho_3(r') \\ \rho_4(r') \end{bmatrix} \mathrm{d}r' \quad (2.44)$$

where the matrix $\mathbf{H}(r, r')$ is defined in Appendix A. If we substitute Eq. (2.43) into Eq. (2.39), the angular dependence cancels out, leaving

$$\boldsymbol{\rho}(r) = \pi^{-1/2} \int_{r_0}^{\infty} \frac{r'}{r} \mathbf{H}(r, r') \cdot \boldsymbol{\rho}(r') \mathrm{d}r' + U_\infty \left[\boldsymbol{W}_U(r) + g\boldsymbol{W}_A(r) \right] \quad (2.45)$$

Finally, we can divided this equation by U_∞ to get

$$\boldsymbol{q}(r) = \pi^{-1/2} \int_{r_0}^{\infty} \mathbf{K}(r, r') \cdot \boldsymbol{q}(r') \mathrm{d}r' + \boldsymbol{W}_U(r) + g\boldsymbol{W}_A(r) \quad (2.46)$$

where $\boldsymbol{q} = \boldsymbol{\rho}/U_\infty$ and

$$\mathbf{K}(r, r') = \frac{r'}{r} \mathbf{H}(r, r') \quad (2.47)$$

This is the equation that we will solve to find the density, velocity, and temperature perturbations, which are related to $\boldsymbol{q}$ by

$$\varepsilon_1(\boldsymbol{r}) = U_\infty q_1(r)\cos\alpha \tag{2.48a}$$

$$\varepsilon_{2z}(\boldsymbol{r}) = \sqrt{2}\,U_\infty q_2(r)\cos\alpha \tag{2.48b}$$

$$\varepsilon_{2x}(\boldsymbol{r}) = \sqrt{2}\,U_\infty q_3(r)\sin\alpha \tag{2.48c}$$

$$\varepsilon_3(\boldsymbol{r}) = \sqrt{\frac{2}{3}}\,U_\infty q_4(r)\cos\alpha \tag{2.48d}$$

Again, α is the angle between the free stream velocity and $\boldsymbol{r}$, $\varepsilon_{2z}(\boldsymbol{r})$ is the perturbation in the radial velocity, and $-\varepsilon_{2x}(\boldsymbol{r})$ is the perturbation in the θ-velocity. Thus, the local density and velocity profiles are (in non-dimensional form)

$$n(r,\alpha) = n_\infty\left[1 + q_1(r)U_\infty\cos\alpha\right] \tag{2.49a}$$

$$u_{2r}(r,\alpha) = \left[1 + \frac{1}{\sqrt{2}}\,q_2(r)\right]U_\infty\cos\alpha \tag{2.49b}$$

$$u_{2\theta}(r,\alpha) = -\left[1 + \frac{1}{\sqrt{2}}\,q_3(r)\right]U_\infty\sin\alpha \tag{2.49c}$$

$$T(r,\alpha) = T_\infty\left[1 + \sqrt{\frac{2}{3}}\,q_4(r)U_\infty\cos\alpha\right] \tag{2.49d}$$

Since I am also interested in the drag force on the sphere, I must relate the

drag to $\boldsymbol{q}(r)$. Let us start by writing the expression for the stress tensor,

$$p_{ij}(\boldsymbol{r}) = m \int c_i c_j f(\boldsymbol{r}, \boldsymbol{c}) \mathrm{d}\boldsymbol{c} = \frac{\rho_\infty}{2} \delta_{ij} + \rho_\infty \pi^{-3/2} \int c_i c_j \, \mathrm{e}^{-c^2} \, h(\boldsymbol{r}, \boldsymbol{c}) \mathrm{d}\boldsymbol{c} \tag{2.50}$$

where $\rho_\infty/2$ is the static pressure far from the sphere and δ_{ij} is the Kronecker delta. (Note that p_{ij} must be multiplied by $(2k_b T_\infty/m)$ to get the appropriate dimensions of the stress tensor.) The static pressure is related to the unperturbed distribution f_∞, while the shear stress distribution is related to the perturbation h. Going forward, we can ignore the static pressure contribution to the stress tensor because it will not contribute to the drag force.

To compute the drag force, we must compute the shear stress tensor at the surface of the sphere:

$$\begin{aligned} \tau_{ij}(\boldsymbol{r}_0) = \rho_\infty \pi^{-3/2} \int_{\boldsymbol{c}\cdot\hat{\boldsymbol{n}}<0} c_i c_j \, \mathrm{e}^{-c^2} \, h(\boldsymbol{r}, \boldsymbol{c}) \mathrm{d}\boldsymbol{c} \\ + \rho_\infty \pi^{-3/2} \int_{\boldsymbol{c}\cdot\hat{\boldsymbol{n}}>0} c_i c_j \, \mathrm{e}^{-c^2} \, h(\boldsymbol{r}, \boldsymbol{c}) \mathrm{d}\boldsymbol{c} \end{aligned} \tag{2.51}$$

Here, we have explicitly divided the bounds of the integral in Eq. (2.50) into the set of molecules moving towards the surface and the set of molecules moving away from the surface of the sphere. Substituting Eq. (2.25) into the integral for $\boldsymbol{c}\cdot\hat{\boldsymbol{n}} < 0$ and Eq. (2.26) into the integral for $\boldsymbol{c}\cdot\hat{\boldsymbol{n}} > 0$, we get

$$\tau_{ij}(\boldsymbol{r}_0) = \rho_\infty \pi^{-3/2} \int_V \left[\mathrm{T}_3 \, \varepsilon_1(\boldsymbol{r}) + \mathrm{T}_4 \, \hat{\boldsymbol{\Omega}} \cdot \boldsymbol{\varepsilon}_2(\boldsymbol{r}) + \left(\mathrm{T}_5 - \frac{3}{2} \mathrm{T}_3 \right) \varepsilon_3(\boldsymbol{r}) \right] \Omega_i \Omega_j \frac{\mathrm{d}\boldsymbol{r}}{|\boldsymbol{r} - \boldsymbol{r}_0|}$$

$$+\rho_\infty \pi^{-3/2} A(\boldsymbol{r}_0) \int_{\boldsymbol{c}\cdot\hat{\boldsymbol{n}}>0} c_i c_j \, \mathrm{e}^{-c^2} \, \mathrm{d}\boldsymbol{c} - \rho_\infty \pi^{-3/2} 2\boldsymbol{U}_\infty \cdot \int_{\boldsymbol{c}\cdot\hat{\boldsymbol{n}}>0} \boldsymbol{c}\, c_i c_j \, \mathrm{e}^{-c^2} \, \mathrm{d}\boldsymbol{c} \tag{2.52}$$

where $\hat{\boldsymbol{\Omega}} = (\boldsymbol{r}_0 - \boldsymbol{r})/|\boldsymbol{r}_0 - \boldsymbol{r}|$, the argument of the T_n functions is $|\boldsymbol{r} - \boldsymbol{r}_0|$, and V is the space above the plane tangent to the sphere at $\boldsymbol{r}_0$. This expression gives the shear stress tensor in terms of the coordinate system (x, y, z) in Fig. 2.2, where the z-axis is along the vector normal to the surface at $\boldsymbol{r}_0$ and the velocity $\boldsymbol{U}_\infty$ is in the xz-plane. However, we want to know the drag force in the coordinate system (X, Y, Z) in Fig. 2.2, where $\boldsymbol{U}_\infty$ is along the Z-direction. Thus, we must write the shear stress tensor in terms of (X, Y, Z):

$$\begin{aligned}
\Pi_{XX} =& \tau_{xx}\cos^2\alpha - 2\tau_{xz}\sin\alpha\cos\alpha + \tau_{zz}\sin^2\alpha \\
\Pi_{YY} =& \tau_{yy} \\
\Pi_{ZZ} =& \tau_{xx}\sin^2\alpha + 2\tau_{xz}\sin\alpha\cos\alpha + \tau_{zz}\cos^2\alpha \\
\Pi_{XZ} =& \tau_{xz}\cos^2\alpha + (\tau_{xx} - \tau_{zz})\sin\alpha\cos\alpha - \tau_{xz}\sin^2\alpha = \Pi_{ZX} \\
\Pi_{XY} =& \Pi_{YX} = \Pi_{YZ} = \Pi_{ZY} = 0
\end{aligned} \tag{2.53}$$

Here, α is the angle between $\boldsymbol{U}_\infty$ and $\hat{\boldsymbol{n}}$. (See Fig. 2.4).

The drag is then the integral over the surface of the sphere of the normal component of the shear force,

$$\tilde{\boldsymbol{F}}_D = \left(\frac{2k_B T_\infty}{m}\right) \tilde{r}_0^2 \int_S \boldsymbol{\Pi}\cdot\hat{\boldsymbol{n}}\mathrm{d}S$$

In the (X, Y, Z) coordinate system, the drag is in the negative Z-direction, i.e. in the direction opposite the flow, so we need only consider the Z-component of the drag:

$$\begin{aligned}\tilde{F}_{D,Z} &= \left(\frac{2k_BT_\infty}{m}\right)\tilde{r}_0^2\int_S(\Pi_{ZX},\Pi_{ZY},\Pi_{ZZ})\cdot(-\sin\alpha,0,\cos\alpha)\mathrm{d}S \\ &= \left(\frac{2k_BT_\infty}{m}\right)^{1/2}\tilde{r}_0^2\int_S(-\Pi_{ZX}\sin\alpha+\Pi_{ZZ}\cos\alpha)\mathrm{d}S\end{aligned}$$

Substituting our expressions for Π_{ij} into the above equation for the drag, we get

$$\tilde{F}_{D,Z} = \left(\frac{2k_BT_\infty}{m}\right)\tilde{r}_0^2\int_S(\tau_{xz}\sin\alpha+\tau_{zz}\cos\alpha)\mathrm{d}S$$

Using Eq. (2.52) for the components τ_{zx} and τ_{zz} of the shear stress tensor and performing a lot of algebra, we get the following expression for the drag:

$$\begin{aligned}\tilde{F}_{D,Z} = -\frac{\rho_\infty}{3}\left(\frac{2\pi k_BT_\infty}{m}\right)^{1/2}\tilde{U}\tilde{r}_0^2\Bigg\{\frac{2\pi^{1/2}}{r_0^2}\int_{r_0}^{\infty}r^2[q_1(r)W_{U1}(r)-q_2(r)W_{U2}(r) \\ -2q_3(r)W_{U3}(r)+q_4(r)W_{U4}(r)]\mathrm{d}r+[8-g\pi^{1/2}]\Bigg\} \quad (2.54)\end{aligned}$$

The details of this derivation can be found in Appendix A.

Taking the ratio of the drag we obtain from the BGK model to the free molecular drag,

$$\tilde{F}_{D,fm} = -\frac{\rho_\infty}{3}\left(\frac{2\pi k_BT_\infty}{m}\right)^{1/2}\tilde{U}\tilde{r}_0^2(8+\pi)$$

we get the following drag ratio:

$$F_D = \left\{ \frac{2\pi^{1/2}}{r_0^2} \int_{r_0}^{\infty} r^2 [q_1(r) W_{U1}(r) - q_2(r) W_{U2}(r) - 2q_3(r) W_{U3}(r) + q_4(r) W_{U4}] \mathrm{d}r + [8 - g\pi^{1/2}] \right\} (8+\pi)^{-1} \quad (2.55)$$

2.3.2 Numerical Methods

Eq. (2.46) cannot be solved analytically for $\boldsymbol{q}(r)$, so we must solve the problem numerically at discrete radial locations. One can choose any set of points at which to solve Eq. (2.46), but it makes the most sense to use points corresponding to the Gaussian quadrature nodes.

A brief introduction to the Gaussian quadrature formula is warranted at this point. The integral of any function $f(t)$ in the interval $[-1, 1]$ can be approximated by

$$\int_{-1}^{1} f(t) \mathrm{d}t \approx \sum_{j=1}^{N} A_j f(t_j) \quad (2.56)$$

where $t_1, \ldots, t_N$ are nodes, A_j is the weight of the jth node, and $f(t_j)$ is the value of $f(t)$ at the jth node. The nodes and weights for a given N are available from any number of sources (e.g. Table 25.4 of Abramowitz and Stegun [98]). We can change the interval $[-1, 1]$ to any interval $[a, b]$, such that our approximation of the integral becomes

$$\begin{aligned} \int_a^b f(t) \mathrm{d}t =& \frac{b-a}{2} \int_{-1}^{1} f\left(\frac{b-a}{2} t + \frac{a+b}{2} \right) \mathrm{d}t \\ \approx& \frac{b-a}{2} \sum_{j=1}^{n} A_j f\left(\frac{b-a}{2} t_j + \frac{a+b}{2} \right) \end{aligned} \quad (2.57)$$

The Gaussian quadrature formula works best when the function can be approximated by a polynomial in the interval $[a, b]$; particular care is needed when there are singularities, as is the case for H_{ii} when $r = r'$. Nevertheless, the Gaussian quadrature formula generally provides accurate results using a relatively small number of points, especially when compared to other numerical integration formulas like the trapezoidal rule or Simpson's rule. A good, concise explanation of Gaussian integration may be found in Kreyszig [100].

With this brief introduction concluded, we will return to the discussion of the problem of flow around a sphere. We start by rearranging Eq. (2.46):

$$\begin{aligned} \boldsymbol{q}(r) - \pi^{-1/2} \int_{r_0}^{R'} \mathbf{K}(r, r') \cdot \boldsymbol{q}(r') \mathrm{d}r' \\ = \pi^{-1/2} \int_{R'}^{\infty} \mathbf{K}(r, r') \cdot \tilde{\boldsymbol{q}}(r') \mathrm{d}r' + \boldsymbol{W}_U(r) + g\boldsymbol{W}_A(r) \equiv \boldsymbol{S}'(r) \end{aligned} \quad (2.58)$$

Here, we have broken the kernel integral into two separate integrals: one over our region of interest from r_0 to R', and another over the region farther away from the sphere. The right-hand side of Eq. (2.58) can be thought of as an effective source term $\boldsymbol{S}'(r)$ that includes both the contribution to $\boldsymbol{q}(r)$ from molecules reflected from the sphere (i.e. the true source term) and the contribution of molecules that enter the region of interest from farther away.

The function $\tilde{\boldsymbol{q}}(r)$ in Eq. (2.58) is a trial function for the perturbation far from the sphere. Using the asymptotic solution of Takata et al. [78] for the density, velocity, and temperature far from the sphere, our trial function for $\boldsymbol{q}$ on the right-

hand side of Eq. (2.58) is

$$\tilde{\boldsymbol{q}}(\boldsymbol{r}) = \begin{bmatrix} \left(\frac{\gamma c_1}{r_0} - c_3\right)\left(\frac{r_0}{r}\right)^2 \\ \sqrt{2}\left[c_1\frac{r_0}{r} + c_2\left(\frac{r_0}{r}\right)^3\right] \\ \frac{1}{\sqrt{2}}\left[c_1\frac{r_0}{r} - c_2\left(\frac{r_0}{r}\right)^3\right] \\ c_3\left(\frac{r_0}{r}\right)^2 \end{bmatrix} \tag{2.59}$$

Here, c_1, c_2, and c_3, are constants to be determined for each Kn number, while $\gamma = 1.270$ is a constant appropriate for hard-sphere molecules. For $r_0 \gg 1$ (i.e. for continuum flow), $c_1 = -\frac{3}{2}$, $c_2 = \frac{1}{2}$, and $c_3 = 0$, as we can verify by solving the Stokes equation for flow around a sphere.

We must make one final modification to our governing equation:

$$\boldsymbol{q}(r)\left[1 - \pi^{-1/2}\int_{r_0}^{R'} \mathbf{K}(r,r')\mathrm{d}r'\right] - \pi^{-1/2}\int_{r_0}^{R'} \mathbf{K}(r,r')\cdot\left[\boldsymbol{q}(r') - \boldsymbol{q}(r)\right]\mathrm{d}r' = \boldsymbol{S}'(r) \tag{2.60}$$

Here, we added and subtracted the term $\int \mathbf{K}(r,r')\boldsymbol{q}(r)\mathrm{d}r'$ from the left side. We have done this to deal with the singularities in the kernel at $r = r'$. Because kernel the is infinite at this point, it will cause problems when we use our Gaussian integration formula to calculate the integral. By adding and subtracting a term, we end up multiplying the singular points by zero, which minimizes the problems caused by the singularities in $\mathbf{K}$.

We can now write Eq. (2.46) as a linear algebra problem,

$$\mathbf{B}\boldsymbol{q} = \boldsymbol{S}' \tag{2.61}$$

where $\mathbf{B}$ is a $4N \times 4N$ matrix, $\boldsymbol{q}$ and $\boldsymbol{S}'$ are $4N$-element vectors, and N is the number of nodes in the Gaussian integral formula. The vectors are constructed such that the first N elements correspond to $q_1(r)$ and $S_1'(r)$, the next N elements correspond to $q_2(r)$ and $S_2'(r)$, and so on for $q_3(r)$ and $q_4(r)$.

The nodes r_j for a given sphere radius are

$$r_j = \frac{R' - r_0}{2} t_j + \frac{R' + r_0}{2} \tag{2.62}$$

where t_j are the nodes in the Gaussian quadrature formula (Eq. (2.56)) for the specified N. Lea [74] uses $N = 24$ and $R' = 10$ for all calculations, but we are free to choose the number of nodes and the size of our region of interest on a case-by-case basis. With that said, I am generally using $R' = 10$ because this choice yields drag results that compare well with Millikan's experiments and with the computational results of Cercignani et al. [73] and Lea and Loyalka [75].

Lastly, the elements of $\mathbf{B}$ are

$$B_{ij} = \begin{cases} \delta_{pq} - k_{pq}(r_m) + \sum\limits_{\substack{m \neq l \\ l=1}}^{N} \left[\frac{R' - r_0}{2}\right] A_l K_{pq}(r_m, r_l), & m = n \\ -\left[\frac{R' - r_0}{2}\right] A_n K_{pq}(r_m, r_n), & m \neq n \end{cases} \tag{2.63}$$

where δ_{ij} is the Kronecker delta, r_m and r_n are the mth and nth nodes, K_{pq} is an element of the 4×4 matrix $\mathbf{K}$,

$$k_{pq}(r_m) = \int_{r_0}^{R'} K_{pq}(r_m, r')\mathrm{d}r', \tag{2.64}$$

and the various indices are related as follows:

$$i = (p-1)N + m; \quad j = (q-1)N + n;$$

$$1 \leq p, q \leq 4; \quad 1 \leq m, n \leq N; \quad 1 \leq i, j \leq 4N$$

We can think of $\mathbf{B}$ as a 4×4 matrix,

$$\mathbf{B} = \begin{bmatrix} \mathbf{B}'_{11} & \mathbf{B}'_{12} & \mathbf{B}'_{13} & \mathbf{B}'_{14} \\ \mathbf{B}'_{21} & \mathbf{B}'_{22} & \mathbf{B}'_{23} & \mathbf{B}'_{24} \\ \mathbf{B}'_{31} & \mathbf{B}'_{32} & \mathbf{B}'_{33} & \mathbf{B}'_{34} \\ \mathbf{B}'_{41} & \mathbf{B}'_{42} & \mathbf{B}'_{43} & \mathbf{B}'_{44} \end{bmatrix}$$

where each $\mathbf{B}'_{pq}$ is an $N \times N$ matrix. Notice that we must treat the diagonal elements of each $\mathbf{B}'_{pq}$ differently than the off-diagonal elements due to the singularities present in the kernels for the diagonal elements (since the diagonal elements correspond to $r_m = r_n$), as introduced in Eq. (2.60).

I have written a MATLAB function to solve Eq. 2.61. (See Section G.1 for the source code.) The function first populates the matrix $\mathbf{B}$ and the vectors $\boldsymbol{W}_U(r)$

and $\boldsymbol{W}_A(r)$, since the elements of these arrays are independent of the solution $\boldsymbol{q}(r)$. Next, the function calculates $\boldsymbol{S}'(r)$ using the trial function Eq. 2.59 with an initial guess for c_1, c_2, and c_3 to compute g and the kernel integral from R' to infinity in Eq. 2.58. The function then inverts Eq. 2.61 solve for $\boldsymbol{r}$. Since g depends on $\boldsymbol{q}(r)$, we must recompute g and solve for $\boldsymbol{q}(r)$ until the value for g converges.

The continues the above procedure until the solution for $\boldsymbol{q}(r)$ matches the trial function at R', i.e.

$$\begin{bmatrix} q_1(R') \\ q_2(R') \\ q_3(R') \\ q_4(R') \end{bmatrix} = \begin{bmatrix} \left(\frac{\gamma c_1}{r_0} - c_3\right)\left(\frac{r_0}{R'}\right)^2 \\ \sqrt{2}\left[c_1\frac{r_0}{R'} + c_2\left(\frac{r_0}{R'}\right)^3\right] \\ \frac{1}{\sqrt{2}}\left[c_1\frac{r_0}{R'} - c_2\left(\frac{r_0}{R'}\right)^3\right] \\ c_3\left(\frac{r_0}{R'}\right)^2 \end{bmatrix}$$

It uses the MATLAB function `fsolve` to find values for c_1, c_2, and c_3 that minimize the error in the above equation.

2.4 Conclusions

In this chapter, I have presented the derivation of the Krook equation and solved the equation for mass transfer to a sphere (Section 2.2) and uniform flow around a sphere (Section 2.3) for an arbitrary Knudsen number. This work largely mirrors previous work in the literature [73, 74, 76]. In the next few chapters, I will describe how to use these results to determine the drag and torque on aggregates

consisting of N spheres in point contact and apply this method to various aerosol physics problems.

Chapter 3: Friction Coefficient for Translating Particles

3.1 Introduction

Aerosol fractal aggregates formed from the coagulation of smaller, spherical primary particles are found in many natural and industrial settings. Understanding the forces on these aggregates is important in a number of science and engineering disciplines, including combustion, fire safety, atmospheric and environmental sciences, materials engineering [2], and nuclear reactor safety [21]. The translational drag force for a particle moving slowly relative to the surrounding fluid – given by $\boldsymbol{F} = -\zeta \boldsymbol{U}_0$, where $\boldsymbol{U}_0$ is the particle relative velocity and ζ is the orientation-averaged scalar friction factor – is particularly important because it influences the transport properties of the particle, including its diffusion coefficient and electrical mobility.

In many practical applications, the primary sphere radius a is significantly less than the mean free path of the surrounding gas ($\lambda \approx 65$ nm at standard temperature and pressure and an order of magnitude higher near a flame), so that the primary sphere is in or near the free molecule flow regime. At the same time, the radius of gyration R_g for the agglomerate may be comparable to or larger than the mean free path, so that the aggregate is in the transition flow regime. As one example, for

carbonaceous soot $a \approx 5 - 30$ nm and $R_g \approx 30 - 1000$ nm.

There are a number of theories and techniques for computing the translational friction factor of macromolecules and particle aggregates in the continuum regime, including Kirkwood-Riseman (KR) theory [28] and its extensions by Rotne and Prager [57], Yamakawa [58], and Chen et al. [30], as well as algorithms that use the Hubbard and Douglas analogy between the electrostatic capacitance and the friction factor [31, 63, 101]. Likewise, there are established methods for computing ζ in the free molecule regime that simulate the ballistic nature of interactions between gas molecules and aggregates [34–36, 102].

In contrast, there are few approaches for the transition regime. Melas et al. [79] estimated the friction coefficient in the near-continuum regime by solving the Laplace equation with a slip boundary condition at the surface of the particle. In a follow-up paper, the authors determined that their Collision Rate Method is valid for Knudsen numbers less than 2 [80].

Dahneke [67] developed the adjusted sphere method for the transition regime, which applies a slip correction factor to the continuum friction factor. The key to this development is the identification of an aggregate Knudsen number that reduces a problem involving two length scales (primary radius and aggregate radius of gyration) to a single dimensionless length. Dahneke's approach is similar to the approach used to calculate the drag on a sphere in the transition regime, but the adjusted sphere method uses an adjusted Knudsen number based on geometric descriptions of the particle in the continuum (hydrodynamic radius, R_H) and free molecular (projected area, PA) regimes.

Through scaling analysis, Zhang et al. [41] developed an approach analogous to the adjusted sphere method and demonstrated that the approach yields friction factors comparable to Direct Simulation Monte Carlo (DSMC) results for the aggregates they studied (spheres, dimers, and dense and open 20-particle aggregates). However, it requires knowledge of the hydrodynamic radius and the projected area of the particle, which may take tens of minutes to a few hours to obtain computationally for a single particle. Obtaining R_H and PA experimentally is possible, but it requires painstaking TEM measurements [68]. More rigorous computational techniques for calculating the transition regime friction factor – such as DSMC or molecular dynamics – are time consuming: for instance, the reported DSMC calculation times in Ref. [41] were on the order of one CPU week for a given Knudsen number and a given aggregate. Thus, a self-consistent field theory method for quickly estimating the scalar friction factor of an aggregate across the Knudsen range is highly desirable.

In this chapter, I present a new approach for computing the hydrodynamic friction tensor $\mathcal{H}$ and the scalar friction coefficient ζ for fractal aggregates across the entire Knudsen range. This approach involves solving for the velocity field around a sphere in the transition regime and using the velocity field to compute the friction factor for the aggregate. In essence, this approach is an extension of KR theory [28] from the continuum regime to the transition regime. I will first present the solution of the Krook equation for the velocity field around a sphere, which follows the procedure developed by Lea and Loyalka [75] and Law and Loyalka [76]. I then describe the extension of KR theory to the transition regime. Finally, I compare my

results to the DSMC results of Zhang et al. [41] and to the scaling theory in that paper.

3.2 Velocity field

To determine the velocity around a sphere in the transition regime, I use the kinetic theory approach provided by the Boltzmann equation. For this study, I will use the Bhatnagar-Gross-Krook (BGK) model [71] instead of the full Boltzmann collision operator.

Consider a sphere with dimensional radius a^* in a gas moving at constant velocity $\boldsymbol{U}_\infty^*$. I will define the viscosity in terms of the gas mean free path λ as $\mu = 0.499\rho\bar{c}\lambda$, where $\bar{c}$ is the gas mean thermal speed, which is consistent with Ref. [41]. For this study, the non-dimensional sphere radius is related to the Knudsen number $\mathrm{Kn} = \lambda/a^*$ by $a = 0.501\sqrt{\pi}\mathrm{Kn}^{-1}$ [70, 73].

If the flow speed is very small compared to the thermal speed of the gas molecules ($U_\infty \ll 1$), then one can linearize the molecular velocity distribution $f(\boldsymbol{r}, \boldsymbol{c})$,

$$f = \pi^{-3/2}\rho_\infty \, \mathrm{e}^{-c^2} \left[1 + 2\boldsymbol{c}\cdot\boldsymbol{U}_\infty + h\right] \tag{3.1}$$

where ρ_∞ is the density far from the sphere, c is the molecular speed, and h is the perturbation to the distribution function due to the sphere. With this linearization and using the BGK model, one gets the non-dimensional Krook equation,

$$\boldsymbol{c}\cdot\nabla h(\boldsymbol{r}, \boldsymbol{c}) = \varepsilon_1(\boldsymbol{r}) + \boldsymbol{c}\cdot\boldsymbol{\varepsilon}_2(\boldsymbol{r}) + \tfrac{2}{3}(c^2 - \tfrac{3}{2})\varepsilon_3(\boldsymbol{r}) - h \tag{3.2}$$

where ε_1, $\boldsymbol{\varepsilon}_2$, and ε_3 are perturbations to the density, velocity, and temperature fields around the sphere,

$$\rho(\boldsymbol{r}) = \rho_\infty[1 + \varepsilon_1(\boldsymbol{r})] \tag{3.3}$$

$$\boldsymbol{U}(\boldsymbol{r}) = \boldsymbol{U}_\infty + \tfrac{1}{2}\boldsymbol{\varepsilon}_2 \tag{3.4}$$

$$T(\boldsymbol{r}) = T_\infty[1 + \varepsilon_3(\boldsymbol{r})] \tag{3.5}$$

I followed the same general solution procedure for the perturbations as Lea and Loyalka [75] and Law and Loyalka [76], with one exception related to the solution far from the sphere, as discussed below. Notably, I assumed diffuse reflection between the gas molecules and the sphere. This approach gives the r- and θ-components of the velocity perturbation $\boldsymbol{\varepsilon}_2$ as $U_0\sqrt{2}q_2(r)\cos\theta$ and $-U_0\sqrt{2}q_3(r)\sin\theta$, where r is the distance from the origin and θ is the angle between $\boldsymbol{r}$ and $\boldsymbol{U}_\infty$. The full velocity field in spherical coordinates is

$$\boldsymbol{U}(\boldsymbol{r}) = U_\infty \cos\theta \left[1 + \frac{1}{\sqrt{2}} q_2(r)\right] \hat{\mathbf{e}}_{\mathbf{r}} - U_\infty \sin\theta \left[1 + \frac{1}{\sqrt{2}} q_3(r)\right] \hat{\mathbf{e}}_{\boldsymbol{\theta}} \tag{3.6}$$

Far from the sphere (i.e. for $r - a > 10$), I fit $q_2(r)$ and $q_3(r)$ to the asymptotic solution to the Krook equation given by Takata et al. [78],

$$\lim_{r\to\infty} q_2(r) = \sqrt{2}c_1 \frac{a}{r} + \sqrt{2}c_2 \left(\frac{a}{r}\right)^3 \tag{3.7}$$

$$\lim_{r\to\infty} q_2(r) = \frac{c_1}{\sqrt{2}} \frac{a}{r} - \frac{c_2}{\sqrt{2}} \left(\frac{a}{r}\right)^3 \tag{3.8}$$

Lea and Loyalka [75] and Law and Loyalka [76] used a slightly different form of the solution for large distances from the sphere, but otherwise my approach is consistent with the approach in Refs. [75, 76].

I present my solution of the drag as the ratio between drag F for the specified Knudsen number and the free molecule drag F_{FM}. As shown in Figure 3.1, my drag results compare favorably (i.e within 2-3%) with a fit to Millikan's oil drop data [64] reported by Cercignani et al. [73],

$$\frac{F}{F_{FM}} = \frac{A + B}{2\pi^{-1/2}a + A + B\exp[-2\pi^{-1/2}Ca]} \tag{3.9}$$

where $A = 1.234$, $B = 0.414$, and $C = 0.876$. My results are also consistent with previous calculations [73, 75, 76, 78], as shown in Table 3.1. (See Appendix B for more detailed results.)

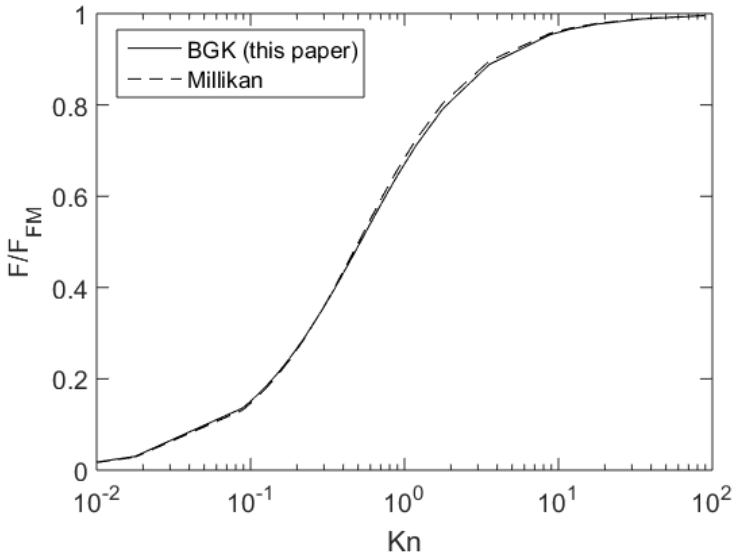

Figure 3.1: Ratio of the calculated drag from the Krook equation to the free molecule drag. Results are compared to a fit to Millikan's data [64]

Table 3.1: Comparison of my results for F/F_{FM} to Millikan's data and to results from previous computational studies

a	Kn	Millikan [64]	Cercignani et al. [73]	Law and Loyalka [76]	This study
0.05	17.8	0.9784	0.9778	0.9771	0.9769
0.075	11.8	0.9677	0.9651	0.9658	0.9654
0.10	8.88	0.9571	0.9529	0.9546	0.9540
0.25	3.55	0.8959	0.8864	0.8912	0.8884
0.50	1.78	0.8036	0.7900	0.8007	0.7916
0.75	1.18	0.7236	0.7088	0.7271	0.7104
1.00	0.888	0.6549	0.6404	0.6513	0.6423
1.25	0.710	0.5961	0.5824	0.5967	0.5850
1.50	0.592	0.5456	0.5332	0.5507	0.5363
1.75	0.507	0.5021	0.4910	0.5115	0.4947
2.00	0.444	0.4645	0.4546	0.4779	0.4588
2.50	0.355	0.4029	0.3951	0.4233	0.4001
3.00	0.296	0.3551	0.3488	0.3521	0.3545
4.00	0.222	0.2863	0.2818	0.2870	0.2884
5.00	0.178	0.2396	0.2360	0.2431	0.2429
6.00	0.148	0.2058	0.2029	0.2120	0.2099
7.00	0.127	0.1804	0.1779	0.1822	0.1848
8.00	0.111	0.1606	0.1583	0.1642	0.1650
9.00	0.0987	0.1447	0.1426	0.1501	0.1492
10.00	0.0888	0.1317	0.1297	0.1388	0.1361

3.3 Kirkwood-Riseman theory

Kirkwood and Riseman [28] demonstrated that the force on the ith element of an N-element polymer chain is given by

$$\boldsymbol{F}_i = -\zeta_0(\boldsymbol{U}_0 - \boldsymbol{u}_i) - \zeta_0 \sum_{i \neq j}^{n} \mathbf{T}_{ij} \cdot \boldsymbol{F}_j \tag{3.10}$$

where $\boldsymbol{U}_0$ is the unperturbed fluid velocity, $\boldsymbol{u}_i$ is the velocity of the ith chain element, ζ_0 is the friction factor given by Stokes' law, and $\mathbf{T}_{ij}$ is the hydrodynamic interaction tensor. The total force on the chain is the vector sum of the forces on the chain elements, $\boldsymbol{F} = \sum_i^N \boldsymbol{F}_i$.

The original derivation used the Oseen tensor for $\mathbf{T}_{ij}$. Rotne and Prager [57] and Yamakawa [58] derived a modified hydrodynamic tensor $\mathbf{T}_{ij}$ that accounts for the curvature of the chain elements and hydrodynamic interactions between two elements,

$$\mathbf{T}_{ij} = \frac{1}{8\pi\mu r_{ij}} \left\{ \left[\mathbf{I} + \frac{\boldsymbol{r}_{ij}\boldsymbol{r}_{ij}}{r_{ij}^2} \right] + \frac{2a^2}{3r_{ij}^2} \left[\mathbf{I} - \frac{3\boldsymbol{r}_{ij}\boldsymbol{r}_{ij}}{r_{ij}^2} \right] \right\} \tag{3.11}$$

where $\boldsymbol{r}_{ij}$ is the vector from the ith element to the jth element and r_{ij} is the distance between the elements. Chen, Deutch, and Meakin later applied this approach to find the translational drag force on a fractal aerosol particle [30, 54, 55].

Rotne and Prager [57] and Yamakawa [58] noted the similarities between their modified interaction tensor and the solution of Stokes flow around a stationary sphere. One can write the perturbation to the velocity caused by the sphere in the

following form:

$$\boldsymbol{v}(\boldsymbol{r}_{ij}) = \mathbf{V}_{ij} \cdot \boldsymbol{U}_0 \tag{3.12}$$

where

$$\mathbf{V}_{ij}(\boldsymbol{r}_{ij}) = \frac{6\pi\mu a}{8\pi\mu r_{ij}} \left[\left(\mathbf{I} + \frac{\boldsymbol{r}_{ij}\boldsymbol{r}_{ij}}{r_{ij}^2} \right) + \frac{a^2}{3r_{ij}^2} \left(\mathbf{I} - \frac{3\boldsymbol{r}_{ij}\boldsymbol{r}_{ij}}{r_{ij}^2} \right) \right] \tag{3.13}$$

Written thus, the velocity perturbation is the dot product of the unperturbed velocity $\boldsymbol{U}_0$ and a tensor $\mathbf{V}_{ij}$ that describes the action of the sphere on the flow. $\mathbf{V}_{ij}$ is the product of the Stokes friction factor (the numerator of the leading coefficient in Eq. (3.13)) and a hydrodynamic tensor that is the same as the modified hydrodynamic interaction tensor in Eq. (3.11), with the exception of the factor of 2 in the r_{ij}^{-3} term in $\mathbf{T}_{ij}$. This suggests that I can replace the product $\zeta_0 \mathbf{T}_{ij}$ in Eq. (3.10) with the tensor $\mathbf{V}_{ij}$ with minimal error, since the term proportional to r_{ij}^{-3} decays quickly as one moves further from the jth particle. The force on the ith particle is now

$$\boldsymbol{F}_i = -\zeta_0 \boldsymbol{U}_0 - \sum_{i \neq j}^{N} \mathbf{V}_{ij} \cdot \boldsymbol{F}_j \tag{3.14}$$

Here, I am assuming that each of the primary particles is translating at the same velocity relative to the background gas, which is appropriate for an aerosol particle. That relative velocity is now specified as $\boldsymbol{U}_0$.

To verify that the error in using the velocity perturbation tensor in place of the product of the modified Oseen tensor and the monomer friction coefficient is small, I calculated the drag on the open and dense 20-particle aggregates described below using both approaches. The error in the drag calculated using $\mathbf{V}_{ij}$ is less

than 2% for the dense aggregate and less than 1% for the open aggregate. This error decreases as the number of primary spheres increases, as expected from the r_{ij}^{-3} dependence.

To extend KR theory from the continuum regime to the transition regime, I set ζ_0 equal to the friction coefficient for a sphere that I calculated using the Krook equation and write the hydrodynamic tensor $\mathbf{V}_{ij}$ in terms of the velocity perturbation $\boldsymbol{\varepsilon}_2$,

$$\mathbf{V}_{ij} = -\frac{q_2(r_{ij})}{\sqrt{2}}\frac{\boldsymbol{r}_{ij}\boldsymbol{r}_{ij}}{r_{ij}^2} - \frac{q_3(r_{ij})}{\sqrt{2}}\left(\mathbf{I} - \frac{\boldsymbol{r}_{ij}\boldsymbol{r}_{ij}}{r_{ij}^2}\right) \tag{3.15}$$

I obtain the orientation-averaged translational friction factor for the particle by following the approach outlined in Happel and Brenner [49]: I calculate $\boldsymbol{F}/U_0$ for three mutually-orthogonal particle orientations, compute the eigenvalues λ_m of the resulting friction tensor, and set the friction coefficient equal to the harmonic average of the eigenvalues,

$$\zeta = \left(\frac{1}{\lambda_1} + \frac{1}{\lambda_2} + \frac{1}{\lambda_3}\right)^{-1} \tag{3.16}$$

Note that the friction tensor is symmetrical (allowing for some numerical uncertainty) in the transition regime, as it is in continuum flow.

Because my drag results from the Krook equation are non-dimensionalized by the free molecule drag force, I obtain the dimensional scalar friction factor by multiplying by the free molecule friction factor for the primary sphere,

$$\zeta^* = \zeta\frac{\pi(8+\pi)}{2.994}\frac{\mu}{\lambda}a^2 \tag{3.17}$$

3.4 Results

Numerous experimental studies have been performed to determine the friction coefficient – or a related quantity, the electrical mobility – for fractal aggregates in the transition regime, as summarized in a review paper by Sorensen [4]. However, most published data lacks the detailed description of particle morphology (i.e. the hydrodynamic radius R_H and the projected area PA) needed for a meaningful comparison with my theoretical calculations. Zhang et al. [41] compared DSMC results to their own data [103], while Thajudeen et al. [68] compared mobility data to the adjusted sphere method scaling law; both studies showed good agreement between theory and experimental data. Thus, I will compare my results to the scaling law and to published DSMC results [41] for well characterized particles over a wide range of Knudsen numbers. Specifically, I have generated aggregates with similar characteristics as the open and dense aggregates in Ref. [41]. These aggregates are shown schematically in Figure 3.2. I generated the particles with a cluster growth algorithm [36] where we specify the fractal prefactor and exponent and the number of primary spheres. I verified that the particles have similar hydrodynamic radii and projected areas as the particles described in Ref. [41] using the Zeno algorithm [62] for R_H and my own algorithm for the projected area. (The Zeno algorithm uses a random walk approach to calculate the electrostatic capacity of an aggregate; Hubbard and Douglas [31] have demonstrated that the hydrodynamic radius is within 1% of the electrostatic capacity for shapes with analytical solutions for both quantities. See Appendix C for a description of my Monte Carlo algorithm.) I

also compared my results for a dimer to the DSMC results.

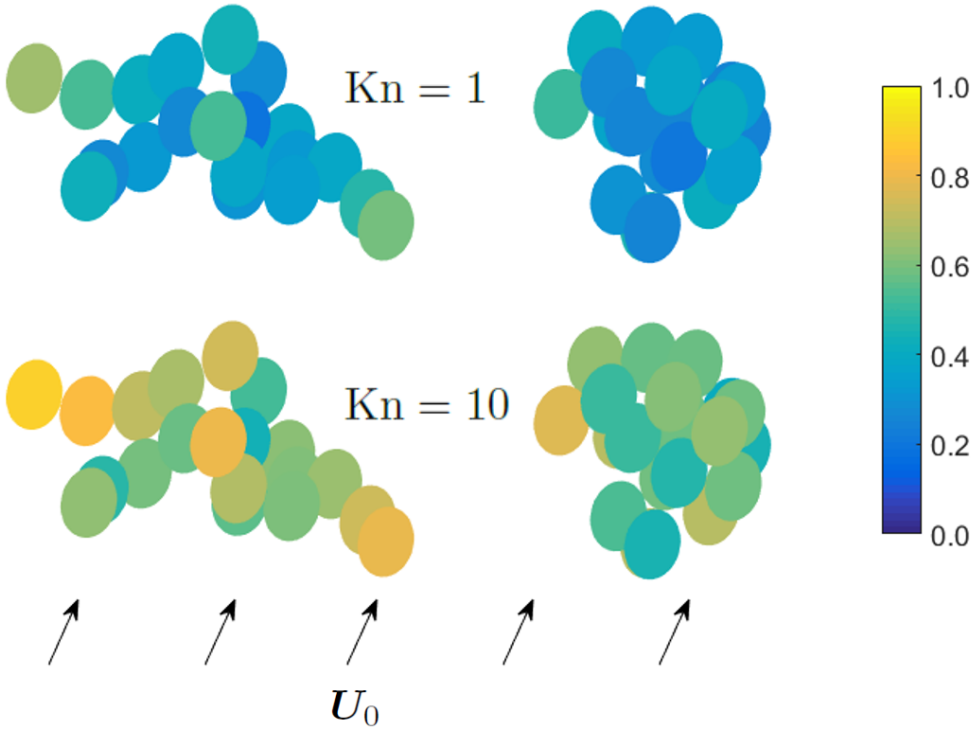

Figure 3.2: Open (left) and dense (right) 20 particle aggregates used in this study. The calculated R_H and PA for these aggregates are very close to the values for the open and dense aggregates in Ref. [41]. The colors represent the calculated ratio of the drag on a primary sphere to the drag on an isolated sphere at the specified Knudsen number. A ratio of unity suggests that a sphere behaves as if it is isolated.

Figure 3.2 illustrates the effects of the Knudsen number on the flow field and drag on each primary sphere. The color of each sphere in the figure is the ratio between the calculated drag F_i on each sphere and the drag $\zeta_0 U_0$ on an isolated sphere at the specified Knudsen number; alternatively, the color represents the fluid velocity at the center of each sphere. The open aggregate at a primary Knudsen number of 10 has relatively little effect on the flow field. Monomers near the periphery of the aggregate behave almost like isolated spheres, while monomers near the interior of the particle experience a lower fluid velocity largely due to direct shielding by the

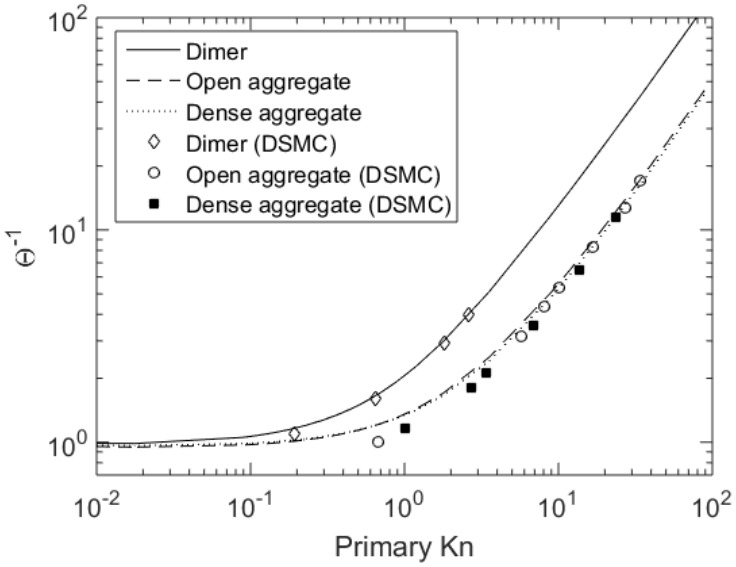

Figure 3.3: Comparison of my results for the slip correction factor to DSMC results from Zhang et al. [41] for a dimer, an open 20 particle aggregate, and a dense 20 particle aggregate. The slip correction factor is the ratio of the continuum friction factor $6\pi\mu R_H$ to the calculated friction factor.

other spheres. This behavior is characteristic of free molecule flow.

For the same particle at a primary Knudsen number of 1, the velocity at each monomer is much lower than in the Kn = 10 case. Clearly, all of the monomers are affected to a larger degree by the presence of the neighboring spheres. The same is true for the dense aggregates with a fractal dimension of 2.5: each monomer has more neighbors, and thus each monomer behaves less like an isolated sphere than in the case of an open aggregate with a fractal dimension of 1.78.

My results for the drag on the dimer and open and dense aggregates are shown in Figure 3.3. Here, I have plotted the aggregate slip correction factor, $\Theta^{-1} = 6\pi\mu R_H/\zeta^*$, versus the primary Knudsen number. Both my results and the DSMC results assume diffuse reflection and full thermal accomodation between the gas molecules and the particle. In general, my KR theory results compare well

with the DSMC results. My calculated slip correction factors are higher than the DSMC slip factors at decreasing Knudsen numbers, though Zhang et al. [41] note that their DSMC results tend to under-predict the slip correction factor due to the finite size of the computational domain. The DSMC results are particularly influenced by domain size at lower Knudsen numbers, which explains the larger deviation between my results and the DSMC results in the near-continuum regime. Note that I discarded one of the near-continuum dense aggregate DSMC points from Ref. [41] because it fell significantly below the continuum limit $\Theta^{-1} = 1$.

I used my extended Kirkwood-Riseman approach to test the observations put forth in Refs. [41, 68, 69] that plots of the slip correction factor versus the aggregate Knudsen number, defined by Zhang et al. [41] as

$$\mathrm{Kn} = \pi\lambda R_H/\mathrm{PA}, \tag{3.18}$$

collapse to a single curve. Figure 3.4 shows my results for aggregates with a range of fractal dimensions and number of primary spheres. I also include the DSMC results from Zhang et al. [41] for comparison. My results and the DSMC results all follow the same general curve, with relatively little deviation among the various calculations. This provides further support to the theory of a universal slip correction factor versus aggregate Knudsen number scaling law.

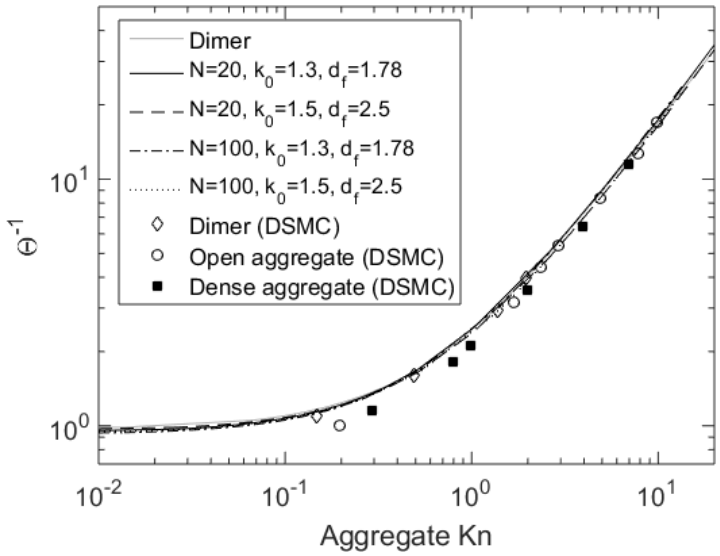

Figure 3.4: Calculated slip correction factors for a range of aggregate morphologies, plotted versus the aggregate Knudsen number. DSMC results from Zhang et al. [41] are included for comparison.

3.5 Discussion

I have introduced a new approach for computing the translational friction coefficient for a fractal aerosol particle across the entire Knudsen range, given the particle's coordinates and primary sphere radius. Coordinates can be generated using a cluster growth algorithm, as I have done for this study, or they can be obtained from TEM images, using methods described in the literature (e.g. Ref. [68]).

The solution method is also very fast: it takes approximately 10 seconds on a single processor to obtain the friction coefficient for approximately 50 Knudsen numbers for a 20-particle aggregate. Furthermore, my Kirkwood-Riseman results converge to the correct continuum and free molecule limits obtained using the Hubbard-Douglas approximation for the continuum and a ballistic approach for

the free molecule aggregate friction factor.

Over the parameter range examined, my results support the validity of the adjusted sphere/scaling method developed by Dahneke [67] and Zhang et al. [41] and promoted by more recent studies [68, 69, 79, 80]. Because the Kirkwood-Riseman approach can provide results quickly across the Knudsen range, this approach may be preferable to DSMC for evaluating scaling laws (such as those developed by Rogak et al. [37], Lall and Friedlander [38], and Eggersdorfer et al. [39]) that relate the friction coefficient to the number of primary spheres in the aggregate.

While I have focused on the friction coefficient in this chapter, my method also determines the friction tensor, which is important when considering particle alignment in an external force field [5]. This is discussed further in Chapter 7.

Finally, I emphasize that my results assume diffuse reflection between the gas molecules and the particle. This is consistent with past computational studies for fractal aerosol particles (e.g. Refs. [36, 41]) and with experimental results, which suggest that most collisions are diffuse [32]. With that said, the Kirkwood-Riseman approach could be applied for alternative reflection models, provided one solves the Krook equation for the velocity using the appropriate boundary condition at the surface of the sphere.

Chapter 4: Analytical Expression for the Friction Coefficient of DLCA Aggregates based on Extended Kirkwood-Riseman Theory

4.1 Introduction

Aerosol particles formed at high temperature are often fractal aggregates described under the assumption of equally-sized spherical primary particles as

$$N = k_0 \left(\frac{R_g}{a} \right)^{d_f} \tag{4.1}$$

where N is the number of primary spheres, R_g is the radius of gyration of the agglomerate, a is the primary sphere radius, and d_f and k_0 are the fractal dimension and prefactor.

The transport properties of these particles (e.g. the diffusion coefficient, settling velocity, and electrical mobility) can be related to the particle scalar friction coefficient ζ_t, which is defined by the relationship between the drag force and the relative velocity between the particle and the fluid,

$$\boldsymbol{F}_d = \zeta_t(\boldsymbol{u}_f - \boldsymbol{u}_p) = \zeta_t \boldsymbol{U} \tag{4.2}$$

where $\boldsymbol{u}_f$ and $\boldsymbol{u}_p$ are the velocities of the fluid and the particle, respectively. Knowledge of the friction coefficient is crucial to predicting particle diffusional, phoretic, and electrostatic behavior in real-world applications.

For the simple case of a sphere with radius a, the friction coefficient is given by Stokes' law,

$$\zeta_t = \frac{6\pi\mu a}{C_c(\mathrm{Kn})} \tag{4.3}$$

where μ is the gas viscosity, $\mathrm{Kn} = \lambda/a$ is the Knudsen number, λ is the gas mean free path, and C_c is the Cunningham slip correction factor,[1]

$$C_c(\mathrm{Kn}) = 1 + \mathrm{Kn}\left[A + B\exp\left(-\frac{C}{\mathrm{Kn}}\right)\right] \tag{4.4}$$

Spheres that are very large compared to the mean free path ($\mathrm{Kn} \to 0$) are in the continuum regime. In this case, the slip correction is unity, and the continuum friction factor is simply

$$\zeta_{t,0}^{c} = 6\pi\mu a \tag{4.5}$$

Spheres that are very small compared to the mean free path are in the free molecule regime, where the friction coefficient is given by Epstein's equation,

$$\zeta_{t,0}^{\mathrm{FM}} = \frac{\pi(8+\alpha\pi)}{2.994}\frac{\mu}{\lambda}a^2 \tag{4.6}$$

The momentum accommodation coefficient α is equal to unity for purely diffuse re-

[1] In this work, I define the viscosity by the relation $\mu = 0.499\rho\bar{c}\lambda$, where ρ is the gas density and $\bar{c}$ is the mean thermal speed. This expression describes a hard sphere gas. Furthermore, I use Davies' coefficients ($A = 1.257$, $B = 0.4$, and $C = 1.1$) [65] in the slip correction factor.

flection and zero for purely specular reflection at the surface of the particle. Epstein [32] determined that most collisions are diffuse.

Determination of the friction coefficient is much more complicated for fractal aggregates. In the continuum regime, the friction coefficient is given by

$$\zeta_t = 6\pi\mu R_H \tag{4.7}$$

where R_H is the particle hydrodynamic radius, which may be obtained by applying either the Kirkwood-Riseman [30, 54–56] or Hubbard-Douglas [31, 101] method. For the free molecule regime, one can obtain the friction coefficient using a ballistic approach [34–36], such that the friction coefficient is related to the orientation-averaged projected area of the particle.

Both computational and experimental results seem to support power-law type relationships between the number of primary spheres in the aggregate and the friction coefficient:

$$\zeta_t = AN^{\eta} \tag{4.8}$$

Sorensen [4] reviewed available experimental data for particles formed by diffusion limited cluster aggregation (DLCA) and proposed exponents of 0.46 for $N < 100$ and 0.56 for $N > 100$ in the continuum regime and 0.92 for all N in the free molecule regime.

In many practical applications, the primary sphere radius is smaller than the gas mean free path, such that the primary spheres may be in the free molecule

flow regime. For situations in which the primary sphere Knudsen number is in the free molecular regime, many researchers (e.g. [34–36]) have used free molecular techniques to compute the scalar friction coefficient for fractal aerosol particles. However, the agglomerate size characterized by the radius of gyration may be comparable to or larger than the mean free path, which leads to some ambiguity about the appropriate flow regime. Therefore, an alternate approach is needed to determine the friction coefficient for particles whose geometric measures (primary sphere radius and radius of gyration) lie in the transition flow regime.

To date, most of the approaches for transition regime drag are based on extrapolation of free molecule or continuum methods to the transition regime or power-law fits to experimental data. One exception is the adjusted sphere method (ASM) developed by Dahneke [67] and [41], which applies a slip correction to the continuum drag based on an aggregate Knudsen number,

$$\zeta_{t,\mathrm{ASM}} = \frac{6\pi\mu R_H}{C_c(\mathrm{Kn}_{\mathrm{agg}})} \tag{4.9}$$

$$\mathrm{Kn}_{\mathrm{agg}} = \frac{\pi\lambda R_H}{\mathrm{PA}} \tag{4.10}$$

where the hydrodynamic radius R_H and the projected area PA are continuum and free molecular measures of particle size, respectively. Zhang et al. [41] found good agreement between the friction coefficient computed using the adjusted sphere method and Direct Simulation Monte Carlo (DSMC) results for a dimer and for open ($d_f = 1.78$, $k_0 = 1.3$) and dense ($d_f = 2.5$, $k_0 = 1.5$) 20-particle aggregates

for a range of aggregate Knudsen numbers. For this approach one must obtain the hydrodynamic radius and projected area, either through TEM analysis or through moderately expensive computational models mentioned previously.

Recently, I developed a self-consistent field method to compute the friction coefficient for a fractal aggregate across the entire Knudsen range (Chapter 3). This method is based on Kirkwood-Riseman theory for the drag on a particle or macromolecule in continuum flow. Initial applications of the self-consistent method show good agreement with DSMC results [41] and with the adjusted sphere method.

Here, I apply my self-consistent field method to compute the scalar friction coefficient for a wide range of primary sphere radii and aggregate sizes. I compare the results to experimental data in the literature [43, 44] and to the predictions of other models that have been developed for the transition regime, including the adjusted sphere method and the correlations developed by Rogak et al. [37], Lall and Friedlander [38], and Eggersdorfer et al. [39].

4.2 Theoretical Methods

4.2.1 Kirkwood-Riseman Theory

Consider an aggregate consisting of N identically-size spherical particles of radius a. Kirkwood and Riseman [28] demonstrated that the force on the ith spherical element can be obtained by considering the effects of all the other elements on the

fluid flow pattern, as described by

$$\boldsymbol{F}_i = \zeta_{t,0}^c \boldsymbol{U}_i - \zeta_{t,0}^c \sum_{i \neq j}^{N} \mathbf{T}_{ij} \cdot \boldsymbol{F}_j \tag{4.11}$$

Here, $\zeta_{t,0}^c = 6\pi\mu a$ is the friction coefficient on the primary spheres as given by Stokes' law, $\boldsymbol{U}_i$ is the velocity of the ith sphere,[2] and $\mathbf{T}_{ij}$ is the hydrodynamic interaction tensor. The original version of the theory uses the Oseen tensor for $\mathbf{T}_{ij}$.

Later researchers extended this approach to fractal aerosol particles [30, 54, 55] and colloids [56]. These later studies used the modified form of the Oseen tensor derived independently by Rotne and Prager [57] and Yamakawa [58]:

$$\mathbf{T}_{ij} = \frac{1}{8\pi\mu r_{ij}} \left[\left(\mathbf{I} + \frac{\boldsymbol{r}_{ij}\boldsymbol{r}_{ij}}{r_{ij}^2} \right) + \frac{2a^2}{3r_{ij}^2} \left(\mathbf{I} - \frac{3\boldsymbol{r}_{ij}\boldsymbol{r}_{ij}}{r_{ij}^2} \right) \right] \tag{4.12}$$

Here, $\boldsymbol{r}_{ij}$ is the vector from the ith particle to the jth particle.

These applications of Kirkwood-Riseman theory involve objects in continuum flow. We now wish to extend this approach to the transition flow regime, using appropriate expressions for the friction coefficient $\zeta_{t,0}$ and the hydrodynamic interaction tensor $\mathbf{T}_{ij}$.

We start by dividing Eq. (4.11) by the friction coefficient to give the fluid velocity at a point $\boldsymbol{r}_i$:

$$\boldsymbol{u}(\boldsymbol{r}_i) = \boldsymbol{U}_i - \sum_{i \neq j}^{N} \mathbf{T}_{ij} \cdot \boldsymbol{F}_j \tag{4.13}$$

In other words, the fluid velocity at a point is the sum of the free stream velocity

[2] If the particle is rigid and if it is not rotating, then $\boldsymbol{U}_i = \boldsymbol{U}$, where $\boldsymbol{U}$ is the particle velocity.

and the velocity perturbations caused by each primary sphere in the particle.

For uniform Stokes flow around an isolated sphere, the velocity obtained by solving the Navier-Stokes equation can be written in the form

$$\boldsymbol{u}(\boldsymbol{r}) = \boldsymbol{U} - \mathbf{V} \cdot \boldsymbol{U} \tag{4.14}$$

where

$$\mathbf{V}(\boldsymbol{r}) = \frac{3a}{4r}\left[\left(\mathbf{I} + \frac{\boldsymbol{r}_{ij}\boldsymbol{r}_{ij}}{r_{ij}^2}\right) + \frac{a^2}{3r_{ij}^2}\left(\mathbf{I} - \frac{3\boldsymbol{r}_{ij}\boldsymbol{r}_{ij}}{r_{ij}^2}\right)\right] \tag{4.15}$$

is the velocity perturbation tensor at the point $\boldsymbol{r}$ and r is the distance of that point from the origin (i.e. the center of the sphere). We can also write the velocity as

$$\boldsymbol{u}(\boldsymbol{r}) = \boldsymbol{U} - \mathbf{T}'(\boldsymbol{r}) \cdot \boldsymbol{F} \tag{4.16}$$

where

$$\mathbf{T}'(\boldsymbol{r}) \equiv \frac{\mathbf{V}(\boldsymbol{r})}{\zeta_{t,0}^c} = \frac{1}{8\pi\mu r}\left[\left(\mathbf{I} + \frac{\boldsymbol{r}_{ij}\boldsymbol{r}_{ij}}{r_{ij}^2}\right) + \frac{a^2}{3r_{ij}^2}\left(\mathbf{I} - \frac{3\boldsymbol{r}_{ij}\boldsymbol{r}_{ij}}{r_{ij}^2}\right)\right] \tag{4.17}$$

and $\boldsymbol{F} = \zeta_{t,0}^c \boldsymbol{U}$ is the drag force on the sphere.

The tensor $\mathbf{T}'$ is the same as the Rotne-Prager-Yamakawa hydrodynamic interaction tensor [Eq. (4.12)], with the exception of the factor of 2 in the r^{-3} term. Since we are primarily concerned with the velocity perturbation at distances greater than $2a$ from the sphere, we can ignore the factor of 2 with minimal error and replace $\mathbf{T}_{ij}$ in Eq. (4.11) with $\mathbf{T}'$. Now, the drag force on the ith sphere of a fractal

particle is

$$\boldsymbol{F}_i = \zeta^c_{t,0}\boldsymbol{U}_i - \sum_{i\neq j}^{N} \mathbf{V}_{ij}\cdot\boldsymbol{F}_j \tag{4.18}$$

where $\mathbf{V}_{ij}$ is the velocity perturbation at the ith sphere caused by the jth sphere.

Of course, there is no reason to make the approximation $\mathbf{T}'(\boldsymbol{r}) \approx \mathbf{T}_{ij}(\boldsymbol{r})$ for continuum flow. However, this approximation allows us to extend Kirkwood-Riseman theory to the transition regime because solving for the velocity profile around an isolated sphere in the transition regime is considerably easier than explicitly considering the hydrodynamic interaction between two spheres in the transition regime. Numerous solutions of the former problem are available in the literature [75, 76, 78, 104], whereas we have not been able to find any reference to the latter problem.

Before we proceed further with our derivation of the force on a fractal aggregate in the transition regime, we will first consider the solution of the kinetic equation for the velocity around a sphere.

4.2.2 Flow around a Sphere

Consider steady flow around a sphere in the transition regime.[3] The gas density, velocity, and temperature far from the sphere are ρ_∞, $\boldsymbol{U}_\infty$, and T_∞, respectively. In the absence of external forces, the Boltzmann equation can be written as

$$\boldsymbol{c}\cdot\nabla f(\boldsymbol{r},\boldsymbol{c}) = \left.\frac{\delta f}{\delta t}\right|_{\text{coll}} \tag{4.19}$$

[3]More information about solving the kinetic equation for flow around a sphere in the transition regime can be found in Chapter 2.

where f is the velocity distribution function and $\boldsymbol{c}$ is the gas molecular velocity. The right-hand side of Eq. (4.19) is the collision operator, which describes the evolution of the distribution function as a result of collisions between gas molecules. The full collision operator is exceedingly complicated, so we will consider the simplified collision operator proposed by Bhatnagar, Gross, and Krook [71]:

$$\left.\frac{\delta f}{\delta t}\right|_{\text{coll, BGK}} = \nu[f_0(\boldsymbol{r}, \boldsymbol{c}) - f(\boldsymbol{r}, \boldsymbol{c})] \tag{4.20}$$

Here, ν is the collision frequency and f_0 is the Maxwellian velocity distribution at point $\boldsymbol{r}$,

$$f_0(\boldsymbol{r}, \boldsymbol{c}) = n\left(\frac{m}{2\pi k_B T}\right)^{3/2} \exp\left(-\frac{m|\boldsymbol{c} - \boldsymbol{U}|^2}{2k_B T}\right) \tag{4.21}$$

where m is the mass of a gas molecule, k_B is the Boltzmann constant, and n, $\boldsymbol{U}$, and T are the local gas number density, bulk velocity, and temperature. Essentially, the BGK model assumes that the non-equilibrium distribution f relaxes to the equilibrium distribution f_0 after one collision, with the collision frequency given by $\nu = p/\mu$, where p is the gas pressure.

If the velocity of the gas around the sphere is small relative to the thermal speed of the gas molecules and the perturbation caused by the sphere is relatively small, then the distribution function can be linearized, giving

$$f(\boldsymbol{r}, \boldsymbol{c}) \approx f_\infty[1 + 2\boldsymbol{c} \cdot \boldsymbol{U}_\infty + h(\boldsymbol{r}, \boldsymbol{c})] \tag{4.22}$$

The Maxwellian distribution f_∞ represents a gas with zero velocity at the far-away

gas density and temperature. The first two terms of the linearization represent the distribution far from the sphere, while the function h represents the perturbation to the distribution caused by the sphere. Likewise, the linearized local Maxwellian distribution can be written

$$f_0(\boldsymbol{r}, \boldsymbol{c}) \approx f_\infty[1 + 2\boldsymbol{c} \cdot \boldsymbol{U}_\infty + \varepsilon_1 + \boldsymbol{c} \cdot \boldsymbol{\varepsilon}_2 + (c^2 + \tfrac{3}{2})\varepsilon_3 \tag{4.23}$$

where ε_1, $\boldsymbol{\varepsilon}_2$, and ε_3 are perturbations to the density, velocity, and temperature of the gas defined below as moments of the distribution function h.

Now define the following non-dimensional variables:

$$\begin{aligned} f^\star &= f\left[n\left(\frac{m}{2k_BT}\right)^{3/2}\right]^{-1} = \pi^{-3/2}\exp\left(-|\boldsymbol{c}^\star - \boldsymbol{U}^\star|^2\right) \\ \boldsymbol{c}^\star &= \boldsymbol{c}\left(\frac{m}{2k_BT}\right)^{1/2} \\ \boldsymbol{r}^\star &= \frac{\boldsymbol{r}}{\nu}\left(\frac{m}{2k_BT}\right)^{1/2} = \boldsymbol{r}\frac{\sqrt{\pi}}{1.996\lambda} \end{aligned} \tag{4.24}$$

The final expression for the non-dimensional radius makes use of the previously defined expressions for the collision frequency and the viscosity of a hard sphere gas. With these definitions, the linearized, non-dimensional BGK equation is

$$\boldsymbol{c}^\star \cdot \nabla h = \varepsilon_1 + \boldsymbol{c}^\star \cdot \boldsymbol{\varepsilon}_2 + (c^{\star 2} - \tfrac{3}{2})\varepsilon_3 - h \tag{4.25}$$

with the moments related to the gas number density, velocity, and temperature by

$$\begin{aligned}
\frac{n}{n_\infty} &= 1 + \varepsilon_1 = 1 + \pi^{3/2} \int h \exp(-c^{\star 2}) \mathrm{d}\boldsymbol{c}^\star \\
\boldsymbol{U}^\star &= \boldsymbol{U}^\star_\infty + \tfrac{1}{2}\boldsymbol{\varepsilon}_2 = \boldsymbol{U}^\star_\infty + \pi^{-3/2} \int h \boldsymbol{c} \exp(-c^{\star 2}) \mathrm{d}2\boldsymbol{c}^\star \\
\frac{T}{T_\infty} &= 1 + \varepsilon_3 = 1 + \tfrac{2}{3}\pi^{-3/2} \int h(c^{\star 2} - \tfrac{3}{2}) \exp(-c^{\star 2}) \mathrm{d}2\boldsymbol{c}^\star
\end{aligned} \tag{4.26}$$

The integrals in the moment equations represent triple integrals over the entire molecular velocity space. The boundary conditions for flow around a sphere are diffuse reflection at the sphere surface and vanishing h far from the sphere.

Lea and Loyalka [75] solved the above problem numerically for the number density and velocity perturbations around the sphere assuming isothermal conditions ($\varepsilon_3 = 0$). Their solution procedure involved solving for the perturbations using a Gaussian quadrature out to a radius of $a^\star + 10$, or about 8.9 mean free paths from the surface, then matching the numerical solution at $a^\star + 10$ to a trial function based on the continuum (Stokes flow) solution. They adjusted the numerical coefficients of the trial function until the inner and outer solutions converged. Law and Loyalka [76] applied this approach for non-isothermal conditions.

We follow the general approach of Loyalka and colleagues, but using the asymptotic solution to the BGK equation for large r [78] as the trial function for $r^\star > a^\star + 10$. Like in continuum flow, the velocity in the transition regime can be written as separable radial and angular components,

$$\varepsilon_{2r} = \sqrt{2} U^\star_\infty q_2(r) \cos\theta$$

$$\varepsilon_{2\theta} = -\sqrt{2}U_{\infty}^{\star} q_3(r) \sin\theta \tag{4.27}$$

where q_2 and q_3 are functions describing the radial dependence of the r- and θ-components of the velocity perturbation obtained by solving the BGK equation. These functions depend on the primary sphere radius, so that the solution procedure applies to a specific Knudsen number. We can also obtain the friction coefficient from the solution of the BGK equation. In general, our velocity results compare well with the velocities reported by Takata et al. [78] based on their solution of the linearized Boltzmann equation, and our drag results compare well with Millikan's data [64]. Note, however, that our calculated friction coefficients for the near continuum regime ($\mathrm{Kn} < 0.1$) are less accurate, likely due to numerical error that is more prominent for lower Knudsen numbers.[4] We will discuss this point further in Section 4.3.2.

4.2.3 Application of BGK Results to Kirkwood-Riseman Theory

I now apply Kirkwood-Riseman theory to particles in the transition regime by explicitly writing the friction coefficient and velocity tensor in Eq. (4.18) as functions of the primary sphere Knudsen number,

$$\boldsymbol{F}_i = \zeta_{t,0}(\mathrm{Kn})\boldsymbol{U}_i - \sum_{i \neq j}^{N} \mathbf{V}_{ij}(\mathrm{Kn}) \cdot \boldsymbol{F}_j$$

[4] This is because the friction coefficient obtained from our solution of the BGK equation is non-dimensionalized by the free molecule friction coefficient (Epstein's equation). As a result, the friction coefficient decays to zero for decreasing Knudsen number, meaning numerical errors are more prominent for the near-continuum regime.

where the velocity perturbation tensor is

$$\mathbf{V}_{ij}(\mathrm{Kn}) = -\frac{q_2(r_{ij},\mathrm{Kn})}{\sqrt{2}}\frac{\boldsymbol{r}_{ij}\boldsymbol{r}_{ij}}{r_{ij}^2} - \frac{q_3(r_{ij},\mathrm{Kn})}{\sqrt{2}}\left(\mathbf{I} - \frac{\boldsymbol{r}_{ij}\boldsymbol{r}_{ij}}{r_{ij}^2}\right) \tag{4.28}$$

For primary spheres separated by distances $r_{ij}^\star < a^\star + 10$, q_2 and q_3 are tables of data; for spheres separated by greater distances, q_2 and q_3 are the asymptotic solutions to the BGK equation for large r with coefficients chosen to match the inner solution for that Knudsen number.

Eq. (4.18) gives the force on each primary sphere for a given flow velocity. (Dividing Eq. (4.18) by the friction coefficient $\zeta_{t,0}$ gives the velocity at each primary sphere.) The total force on the particle is the vector sum of the force on each primary sphere. I obtain the friction tensor $\boldsymbol{\Xi}_t$ by solving Eq. (4.18) for the velocity in three mutually orthogonal directions. The force on the particle for arbitrary fluid velocity is then

$$\boldsymbol{F}_d = \boldsymbol{\Xi}_t \cdot \boldsymbol{U} \tag{4.29}$$

In the slow rotation limit, the scalar friction factor is the harmonic mean of the three eigenvalues of the friction tensor [49]. In the fast rotation limit, the scalar friction factor is the arithmetic mean of the eigenvalues [105].

4.3 Results and Discussion

I have calculated the scalar friction coefficient for a large range of primary sphere sizes and number of primary spheres. All calculations involve particles with

$d_f = 1.78$ and $k_0 = 1.3$, which are representative of aggregates formed by DLCA. The particles have been generated with an algorithm that imitates cluster-cluster aggregation. Due to limitations with our fractal generator, aggregate size is capped at 2000 primary spheres. In this chapter, I am reporting the friction coefficient for the slow rotation limit, meaning I am taking the harmonic average of the friction tensor eigenvalues.

4.3.1 Comparison to Experimental Data and Power-Law Models

Figure 4.1 compares the results of my friction coefficient calculations for a primary sphere Knudsen number of 7 to tandem differential mobility analyzer (TDMA) and combined DMA and aerosol particle mass analyzer (DMA-APM) results [43, 44]. The primary sphere size for the TDMA $80 - 300$ nm and DMA-APM curves was experimentally-determined to be 19.5 nm with a standard deviation of 6.1 nm, while the primary sphere size is assumed to be 19.5 nm for the TDMA $30 - 100$ nm curve [44]. My self-consistent field results compare very well to the experimental data. Furthermore, the self-consistent results support the observation of Shin et al. [43] that deviations from a power-law relationship at high N may be due to hydrodynamic interactions among the primary spheres in the aggregate.

Next, we compare our friction coefficient results to the results from three models for DLCA particle drag in the transition regime.

The Lall and Friedlander [38] model,

$$\zeta_{\mathrm{LF}} = \frac{c^{\star} N \mu a}{\mathrm{Kn}} \tag{4.30}$$

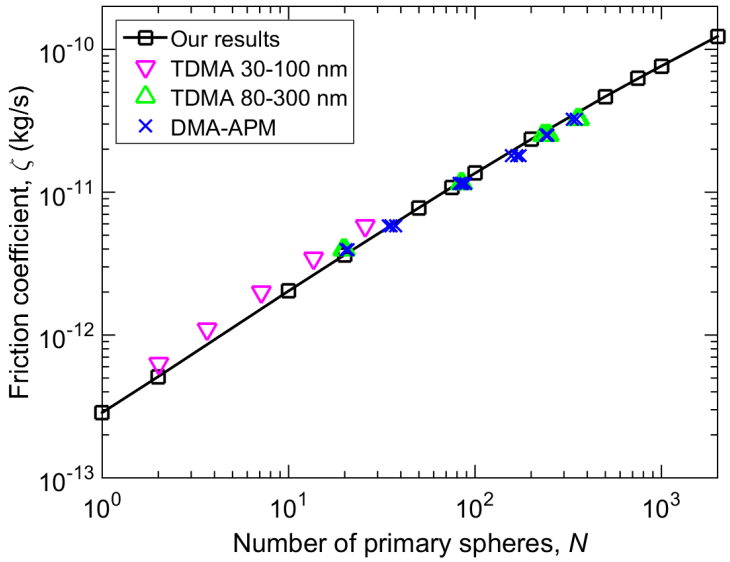

Figure 4.1: Friction factor results for fractal aggregates with primary sphere diameter 19.5 nm in ambient air (Kn = 7). TDMA and DMA-APM results [43, 44] are shown for comparison.

is based on the calculations of Chan and Dahneke [34] for the drag on straight chain aggregates in the free molecular regime. Here, $c^\star = 9.17$ is a dimensionless drag force that assumes 93% diffuse reflection and 7% specular reflection. Chan and Dahneke [34] argued that Eq. (4.30) should be valid for aggregates with $N > 12$ that have occasional kinks and branches. Implicit in Lall & Friedlander's model is that the aggregate behaves as if it is in the free molecule regime as long as the primary spheres are in the free molecule regime. The model of Eggersdorfer et al. [39] model relates the mobility radius – or the radius of a sphere that has the same drag as the particle – to the number of particles through the relationship

$$r_{m,E} = a \left(\frac{N}{k_\alpha} \right)^{1/2D_\alpha} \tag{4.31}$$

where $k_\alpha = 1.1$ and $D_\alpha = 1.08$ are based on DLCA simulations. The friction

coefficient is obtained by substituting the mobility radius into Stokes' law,

$$\zeta_{m,E} = \frac{6\pi\mu r_{m,E}}{C_c(\lambda/r_{m,E})} \tag{4.32}$$

Finally, Rogak et al. [37] noted that the mobility radius is approximately equal to the orientation-averaged projected area radius for particles with mobility radii less than 200 nm. Thus, I compare my results to the friction coefficient calculated using the particle projected area:

$$\zeta_{m,R} = \frac{6\pi\mu\sqrt{\mathrm{PA}/\pi}}{C_c(\lambda/\sqrt{\mathrm{PA}/\pi})} \tag{4.33}$$

I also compare my results to friction coefficients calculated using the adjusted sphere method, Eq. (4.9). I computed the particle hydrodynamic radius using the Zeno code [62], which uses the Hubbard-Douglas approximation, and I computed the projected area using my own algorithm (Appendix C).

Figure 4.2 shows the comparison between my results and the aforementioned models for primary sphere Knudsen numbers of 100, 10, 1, and 0.1, corresponding to sphere radii of 6800 nm, 680 nm, 68 nm, and 6.8 nm, respectively. I also includes free molecule results obtained with my own free molecule code and continuum results obtained with Zeno on select figures. All of the models give results for Kn = 100 for all N that are very similar to the free molecular limit, which is not surprising given the very small primary sphere size. However, for large N all of the models – with the exception of the Lall & Friedlander model – begin to diverge from the free molecular

limit for Kn = 10 primaries, suggesting that hydrodynamic interactions among the primaries are important even at this primary Knudsen number. Interestingly, my results and the ASM results approach the Zeno continuum results as N increases for Kn = 1. Finally, my Kn = 0.1 results compare favorably to the continuum results and to the ASM.

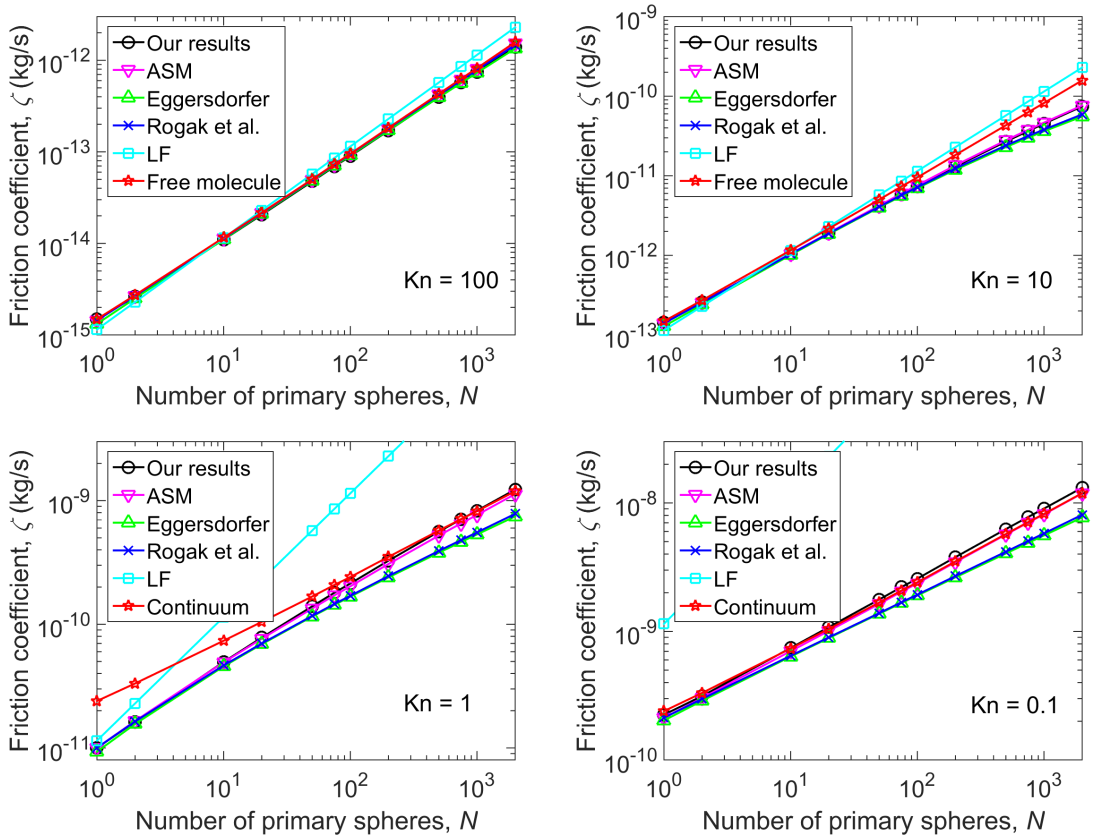

Figure 4.2: Comparison of self-consistent field results to other models for the scalar friction factor for (a) Kn = 100, (b) Kn = 10, (c) Kn = 1, and (d) Kn = 0.1. Results are for particles in ambient air. Where appropriate, free molecular results from a ballistic algorithm and continuum results from the Zeno code are displayed for reference.

Figure 4.3 shows the ratio between the predictions of the aforementioned models and my friction coefficient results for $N = 2000$. Values of unity represent perfect agreement between my results and other models. Once again, there is very good

agreement with the adjusted sphere method across the entire Knudsen range. The Eggersdorfer and Rogak friction coefficients are notably lower than our results at low to moderate primary sphere Knudsen numbers, though it is important to reiterate that this comparison is for large aggregates ($N = 2000$). The agreement between the models is better for smaller aggregates at lower primary sphere Knudsen numbers, as indicated in Figure 4.2.

Additionally, Figure 4.3 illustrates how the aggregate approaches the continuum limit for decreasing Knudsen number: the ratio of the continuum result calculated using the Zeno code to my Kirkwood-Riseman results is near unity for a primary sphere Knudsen number as high as 2. This figure explicitly shows the difference between using the monomer friction coefficient from the BGK model solution and using the monomer friction coefficient from the Cunningham slip correction factor. Differences are largest for small Knudsen numbers, though results are in good agreement with the continuum results at low Knudsen number whether one uses the BGK friction coefficient or the Cunningham slip coefficient for $\zeta_{t,0}$ in Eq. (4.18).

Figure 4.4 clearly illustrates how the friction coefficient diverges from the free molecular limit and exhibits more continuum-like behavior as the particle size (both in terms of N and a) increases. Here, calculated friction coefficients are normalized to the monomer friction coefficient for several primary sphere Knudsen numbers in the transition regime. The power law exponent [i.e. η from Eq. (4.8)] decreases from a value of approximately 0.9 – corresponding to the free molecule regime – as both the number of primary spheres and the primary sphere size increases, until it reaches a limit of approximately 0.54 for the continuum regime. The free molecule

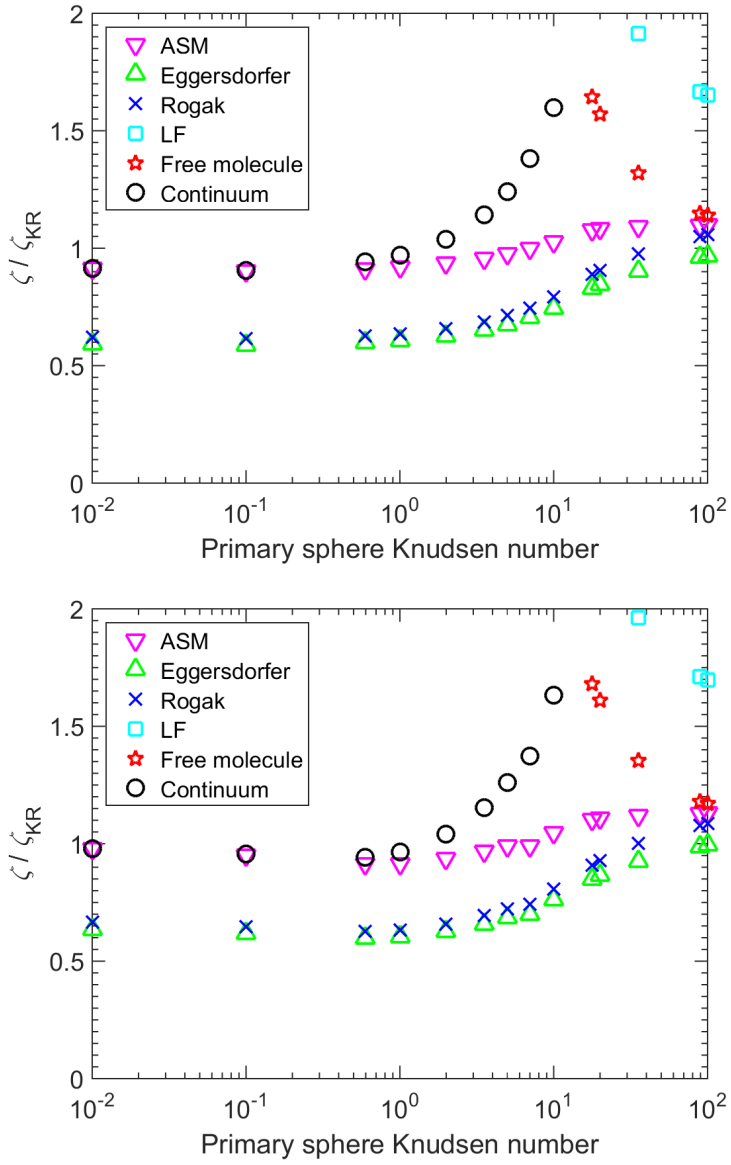

Figure 4.3: Ratio of friction coefficients from other models to my results for $N = 2000$. Free molecule and continuum results are calculated using my own Monte Carlo algorithm and the Zeno algorithm, respectively. For the upper plot, myfriction coefficient results are obtained using the calculated drag from the BGK model. For the lower plot, my friction coefficient results use the Cunningham slip formula for the monomer friction coefficient [$\zeta_{t,0}$ in Eq. (4.18)]. Free molecule results for Kn < 15, LF results for Kn < 35, and continuum results for Kn > 15 are more than twice our self-consistent field results and thus do not appear in the plots above.

and continuum values are in agreement with previous observations [4]. The change in the power law exponent reinforces the importance of accounting for hydrodynamic interactions among primary spheres, even for fairly open aggregates with primary spheres in the near-free molecular regime.

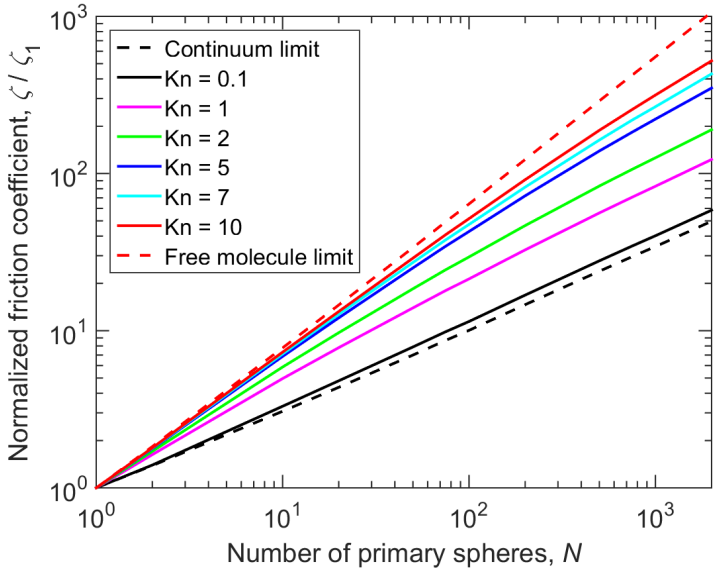

Figure 4.4: Normalized friction coefficient results for a range of aggregate sizes.

Previously researchers have looked at the evolution of the ratio between the mobility radius and the radius of gyration as the number of primary spheres increases. Figure 4.5 compares my self-consistent field results for this ratio ($\beta = R_m/R_g$) to the same calculation in the continuum (where the mobility radius and the hydrodynamic radius are equivalent) and free molecule regimes. Our results agree with previous observations [54–56] that β approaches an asymptotic value in the continuum regime. My results also agree qualitatively with the general observations of Sorensen [4], specifically Figure 2 of that work. However, my asymptotic results for Kn = 0.01 and Kn = 0.1 are approximately 0.85, which is significantly

different (i.e. outside of numerical uncertainty) from the value of 0.75 recommended by Sorensen for the continuum regime. (Note that the Zeno results for the hydrodynamic radius suggest an asymptotic value of $\beta = 0.8$ for large N.) Figure 4.5 also notably shows that the Kn = 1, Kn = 3, and Kn = 10 curves also reach asymptotic limits, again suggesting that aggregates approach the continuum regime behavior as the number of primary spheres increases, even when the primary spheres are in the near-free molecule or transition regime.

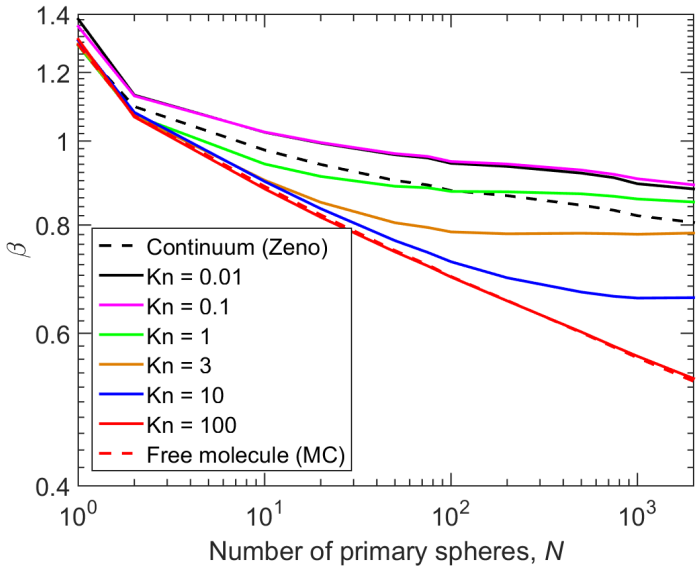

Figure 4.5: Relationship between the mobility radius and the radius of gyration for several Knudsen numbers.

4.3.2 Uncertainty in the Calculated Friction Coefficients

I have demonstrated in this chapter and in the previous chapter that the friction coefficient for DLCA aggregates computed using the extended Kirkwood-Riseman method is in good agreement with experimental data, the continuum and free molecule limits, the adjusted sphere method [41, 67], and Direct Simulation

Monte Carlo results [41]. But the question becomes, how accurate is the extended Kirkwood-Riseman method? To answer this question, I provide a very rough estimate of the error in my results.

There are two primary sources of error in my calculations: the BGK results for the velocity around and drag on a sphere in the transition flow regime, and the Kirkwood-Riseman method itself. There is ample discussion in the literature about the accuracy of the Kirkwood-Riseman method for continuum flow; see Refs. [4, 31, 106, 107] for a small sample. I refer the reader to the literature for a thorough discussion. I simply note that in my experience, the Kirkwood-Riseman results (using either the Stokes flow velocity perturbation or the Rotne-Prager tensor) is within 3% of the Zeno results for DLCA aggregates with 102000 primary spheres. For N = 10, the Kirkwood-Riseman method underpredicts the friction factor by less than 3%. At N = 2000, the Kirkwood-Riseman result is approximately 2% greater than the Zeno result. Thus, I estimate the error in our calculated transition regime friction coefficients due to the Kirkwood-Riseman method itself is on the order of a few percent.

The second source of error is related to the solution of the BGK equation. From this solution, I obtain the velocity around a sphere and the ratio of the drag on the sphere to the free molecule drag. One can easily estimate the error in the drag on a sphere by comparing my results from the BGK equation to the drag from Stokes' law with the Cunningham slip correction factor. Applying Davies' coefficients in the slip correction formula, the calculated error in the BGK drag results is less than 3% for Kn ¿ 0.2. (One obtains similar errors when using the coefficients of Allen

and Raabe [66] in the slip correction factor.) The error is greater at lower Knudsen numbers, as noted in Section 4.2.2; for Kn = 0.01, the BGK drag is approximately 7% greater than the drag from Stokes' law. For most of the Knudsen range, the error in my calculated drag force is comparable to the error in Stokes' law for the slip regime (either due to the model parameters used in the slip correction factor or to experimental uncertainties); the BGK results are only in significant error near the continuum regime.

We can compare our velocity results to the linearized Boltzmann equation results of Takata et al. [78]. The linearized Boltzmann model is more rigorous than the BGK model, but its associated computational cost is much higher than that required to solve the BGK model. Takata et al. present the velocities as a function of the parameter $k_\infty = \sqrt{\pi}\mathrm{Kn}/2$. My velocity results are generally within 1-2% of the linearized Boltzmann results for Kn = 0.11, 1.1, and 11 (k_∞ = 0.1, 1, and 10). From these comparisons of the BGK velocity and drag results to the linearized Boltzmann results and to Stokes' flow in the continuum limit, I estimate that the error in my aggregate friction coefficient results due to the use of the BGK model is less than 5% for Kn > 0.2 and up to 10% for 0.01 < Kn < 0.2.

Combining the two sources of error, I would estimate the overall error in my EKR results to be less than 10% for most of the Knudsen range. This estimate is supported by comparing my friction coefficient results to the ASM results for $N = 2000$ (Figure 4.3): the difference is less than 10% for $0.01 < \mathrm{Kn} < 100$. Also, my calculated friction coefficient results for a primary sphere Knudsen number greater than 5 are within 10% of the direct simulation Monte Carlo results of Zhang

et al. [41] for a 20-particle aggregate with a fractal dimension of 1.78 and a prefactor of 1.3 (Chapter 3).

4.3.3 Analytical Expression for Friction Coefficients of Aggregates

While the Kirkwood-Riseman method is capable of providing the friction coefficient of an aggregate quickly – within seconds for $N \sim 100$ and within minutes for $N \sim 1000$ – it is still not fast enough for use in an aerosol dynamics code. Thus, it would be beneficial to use my friction coefficient results to develop a simple model that provides the friction coefficient given only the number of primary spheres, the primary sphere size, and the gas properties.

Sorensen and Wang [108] proposed computing the friction coefficient in the transition regime as the harmonic sum of the continuum and free molecule expressions,

$$\zeta_t^{-1} = (\zeta_t^c)^{-1} + (\zeta_t^{\mathrm{FM}})^{-1} \tag{4.34}$$

For a sphere, the continuum and free molecule friction coefficients are given by Stokes' law [Eq. (4.5)] and Epstein's equation [Eq. (4.6)], respectively. I adopt this approach for my model of the friction coefficient of DLCA aggregates with fractal dimension and prefactor of 1.78 and 1.3.

I start by writing the continuum and free molecule aggregate friction coefficients as power laws,

$$\zeta_{t,\mathrm{agg}}^m = \zeta^m \left[AN^\eta + (1 - A)\right] \tag{4.35}$$

where ζ^m is the continuum ($m = c$) or free molecule ($m = \mathrm{FM}$) monomer friction

coefficient from Eq. (4.5) or Eq. (4.6), and A and η are model parameters obtained from fits to the continuum (Zeno) or free molecule (Monte Carlo) results for $N = 1$ to 2000. We include the $1 - A$ term in the power law fits to give the correct friction coefficient for a monomer. The free molecule coefficients $A_{\mathrm{FM}} = 0.843$ and $\eta_{\mathrm{FM}} = 0.939$ are in excellent agreement with Mackowski's correlation for the free molecule friction coefficient ($A_{\mathrm{FM}} = 0.847$ and $\eta_{\mathrm{FM}} = 0.94$ for $k_0 = 1.3$ and $d_f = 1.78$) [36]. The continuum coefficients $A_c = 0.852$ and $\eta_c = 0.535$ from my Zeno results are also in good agreement with previous studies, as reported in Sorensen's review article [4].

Taking the harmonic sum of the continuum and free molecule power law fits, I obtain the following expression for the aggregate friction coefficient as a function of the number of primary spheres, the primary sphere radius, and the gas properties:

$$\frac{\zeta_t}{6\pi\mu a} = \left\{\left[A_c N^{\eta_c} + (1 - A_c)\right]^{-1} + B\mathrm{Kn}\left[A_{\mathrm{FM}} N^{\eta_{\mathrm{FM}}} + (1 - A_{\mathrm{FM}})\right]^{-1}\right\}^{-1} \tag{4.36}$$

Here, B = 1.612 for a hard-sphere gas with a momentum accommodation coefficient of unity (i.e. pure diffuse reflection), consistent with my assumptions throughout this chapter. For a monomer in the transition regime, the above relation reduces to

$$\zeta_{t,0} = \frac{6\pi\mu a}{1 + B\mathrm{Kn}} \tag{4.37}$$

Sorensen and Wang [108] point out that the monomer friction coefficient given by the harmonic sum is up to 10% less than the friction coefficient given by Stokes'

law with the slip correction factor. Thus, I apply a correction factor to my model to give the same monomer drag as Stokes' law. The final result is Eq. (4.38), which provides an easily deployed analytic result to compute the friction coefficient over a wide range of aggregate and primary particle sizes.

$$\frac{\zeta_t}{6\pi\mu a} = \frac{1+1.612\mathrm{Kn}}{C_c(\mathrm{Kn})}\left[\left(0.852N^{0.535}+0.148\right)^{-1}\right. \\ \left.+1.612\mathrm{Kn}\left(0.843N^{0.939}+0.157\right)^{-1}\right]^{-1} \quad (4.38)$$

Figure 4.6 plots the friction coefficient calculated from Eq. (4.38) as a function of primary sphere Knudsen number and the number of primary spheres. Results are normalized using Stokes' law evaluated for $a = \lambda/\mathrm{Kn}$. The figure shows a clear transition between continuum behavior, where the friction coefficient is proportional to $1/a$ for a given number of primary spheres, and free molecule behavior characterized by a $1/a^2$ dependence. (The normalized coefficients have no dependence on a in the continuum and a $1/a$ dependence in the free molecule regime.) This figure shows that the transition from the continuum regime to the free molecule regime occurs at larger Knudsen numbers as the number of primary spheres increases, demonstrating once again that particles exhibit more continuum-like behavior as both the Knudsen number and the number of primary spheres increase.

Figure 4.7 shows the error in my fit relative to my self-consistent field results,

$$error = \frac{\zeta_{t,\mathrm{fit}} - \zeta_{t,EKR}}{\zeta_{t,EKR}} \quad (4.39)$$

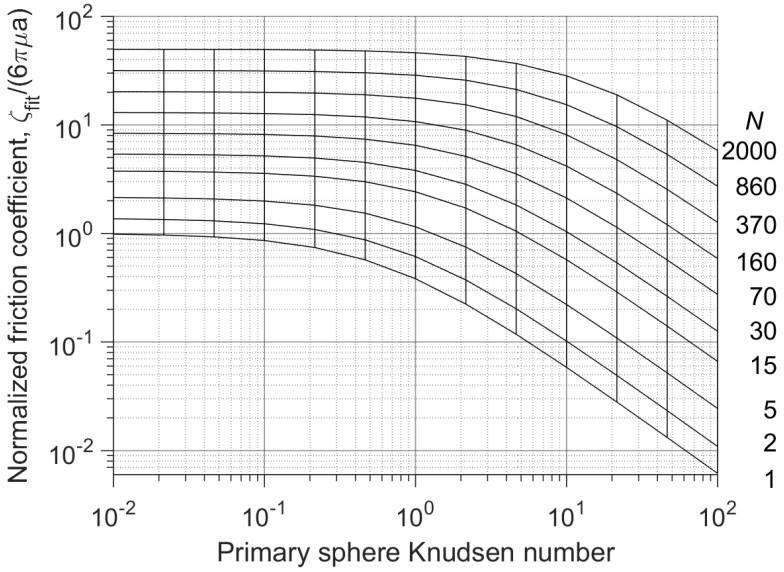

Figure 4.6: Normalized friction coefficient as a function of the primary sphere Knudsen number and the number of primary spheres, N, calculated using Eq. (4.38). Friction coefficients are normalized by Stokes' law evaluated at the specified Knudsen number.

with $\zeta_{t,\text{fit}}$ given by Eq. (4.38). The figure presents the error for a range of aggregate sizes and primary sphere Knudsen numbers. Overall, Eq. (4.38) provides a good fit to my self-consistent field results for all values of N and Kn that we have evaluated. Note that I compare our fit to my EKR results using the semi-empirical slip correction for the monomer drag coefficient, instead of the drag coefficient we obtain by solving the BGK model. As I have stated, this distinction is only significant for monomers near the continuum limit.

4.4 Conclusions

I have presented my self-consistent field results for the translational scalar friction coefficient of DLCA aggregates of 10 to 2000 primary spheres with primary sphere Knudsen numbers between 0.01 and 100. My results compare well to the

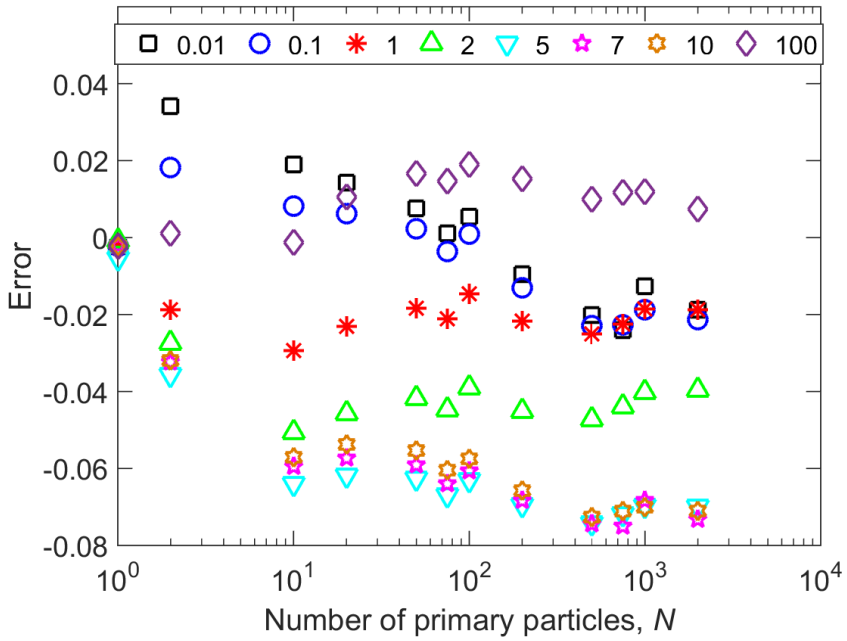

Figure 4.7: Error of my harmonic sum model for the friction coefficient, Eq. (4.38), relative to my extended Kirkwood-Riseman friction coefficient results for a range of Knudsen numbers. Error is calculated with Eq. (4.39); the EKR results in this equation use the monomer friction coefficient from Stokes' law instead of the friction coefficient computed from the BGK model.

experimental data of Shin et al. [43, 44] and to the friction coefficient from the adjusted sphere method [41, 67]. I estimate that my results are within approximately 10% of the true friction coefficient for DLCA aggregates up to 2000 primary spheres for $0.01 < \mathrm{Kn} < 100$, though I would need to compare my results to experimental data over a wide range of primary sphere Knudsen numbers and aggregate sizes to verify this estimate. These results have been obtained by taking the harmonic mean of the eigenvalues of the translational friction tensor. The difference between the harmonic and arithmetic averages of the eigenvalues is generally less than 1%, which is consistent with previous calculations for low-aspect-ratio particles in the free molecule regime [105]. This difference is minor compared to the estimated uncertainty in my results.

One significant finding of this study is that aggregate drag becomes more continuum-like as the number of primary spheres increases, even for primary sphere Knudsen numbers near the free molecule regime. Thus, one should not use free molecule techniques to compute the drag on an aggregate unless the aggregate size is very small with respect to the gas mean free path. This finding supports the theory behind the adjusted sphere method, that one can calculate the drag on an aggregate using an aggregate Knudsen number instead of the primary sphere Knudsen number.

My method is fast, but not fast enough to implement in an aerosol dynamics code. The same is true of the adjusted sphere method, unless one already knows the hydrodynamic radius and projected area of an aggregate. For this reason, I have compared my results to the harmonic sum of power laws for the friction coefficient in the continuum and free molecule regimes. The result presented in Eq. (4.38) provides

an analytical expression for the drag over a range of aggregate and primary particle size. The simple model is within 8% of my self-consistent field results for the entire range of aggregate sizes and primary sphere Knudsen numbers that I have studied. This analysis is for fractal clusters generated using a cluster-cluster aggregation method for a fractal dimension of 1.78 and a prefactor of 1.3.

Chapter 5: Calculating the Rotational Friction Coefficient of Fractal Aerosol Particles in the Transition Regime using Extended Kirkwood-Riseman Theory

5.1 Introduction

Nanoscale aerosol particles consisting of many spheres in point contact are formed in many natural and synthetic processes. The size, shape, and orientation of these particles greatly affect their transport properties [4, 5], optical properties [90, 91, 109], degree of alignment in an external field [6, 90, 91, 109], filtration efficiency [110], and their effects in biological systems, including lung deposition [19, 20].

Much of the theoretical and experimental literature on the transport properties of nano-scale aerosol particles focuses on the translational friction coefficient (or, equivalently, the electrical mobility). There is comparatively little focus on the rotational friction or diffusion coefficients, which affect particle alignment in an external field and relaxation time from an aligned state to a fully random state [6, 90, 91, 109]. Inclusion of rotational dynamics is also important when considering particle coagulation rates in Brownian motion simulations [111].

There are analytical expressions available in the literature for the torque on (or the rotational diffusion coefficient of) simple shapes – such as spheres, rods, and ellipsoids – in both the continuum [29, 49, 112] and free molecule regimes [3, 113, 114]. However, there are no such expressions for complicated shapes such as fractal aggregates. Garcia de la Torre and colleagues have extensively studied the rotational problem for rigid particles consisting of multiple spheres in point contact in the continuum regime [51–53, 107, 115]. More will be said about their work shortly. There are far fewer studies available for the free molecule regime. Li et al. [6] approximate the torque on a fractal aggregate rotating in a quiescent fluid by considering only the linear velocity of each sphere and neglecting the effects of shielding by the other spheres in the cluster, thereby providing an upper bound for the torque. I am unaware of any more detailed methods for calculating the torque on a fractal aggregate in either the free molecule or the transition flow regime. This is significant because in many aerosol applications the primary spheres are much smaller than the mean free path of the gas.

In this chapter, I discuss the application of my extended Kirkwood-Riseman (EKR) theory [92] to the translational and rotational motion of fractal aggregates in the transition flow regime. In Section 5.2 I provide the equations for the drag and torque on a rigid particle, as introduced by Brenner [29]; I describe how one can apply Kirkwood-Riseman theory to the problem; and I employ Monte Carlo to compute the drag and torque on a translating or rotating particle, which I use to validate the EKR method. I present my results for the rotational friction coefficient as a function of Knudsen number and compare my results for $\mathrm{Kn} \ll 1$ and $\mathrm{Kn} \gg 1$

to the continuum and free molecule limits in Section 5.3.

5.2 Drag and torque on a rigid particle

Consider a rigid particle with center of mass moving at velocity $\boldsymbol{U}_O$ and rotating with angular velocity $\boldsymbol{\omega}$, where point O is the origin of the system. For particles in Stokes (i.e. low Reynolds number) flow, the force $\boldsymbol{F}$ and torque $\boldsymbol{T}_O$ on the particle are given by

$$\boldsymbol{F} = -\boldsymbol{\Xi}_t \cdot \boldsymbol{U}_O - \boldsymbol{\Xi}_{O,c}^{\dagger} \cdot \boldsymbol{\omega} \tag{5.1}$$

$$\boldsymbol{T}_O = -\boldsymbol{\Xi}_{O,c} \cdot \boldsymbol{U}_O - \boldsymbol{\Xi}_{O,r} \cdot \boldsymbol{\omega} \tag{5.2}$$

where $\boldsymbol{\Xi}_t$, $\boldsymbol{\Xi}_{O,r}$, and $\boldsymbol{\Xi}_{O,c}$ are the friction tensors for translation, rotation, and translation-rotation coupling, respectively, and $\boldsymbol{\Xi}_{O,c}^{\dagger}$ is the transpose of the coupling tensor. The coupling and rotation tensors are defined with respect to the origin, O, while the translation tensor is independent of the origin.

Brenner [29] proved that these friction tensors are related to the translation, rotation, and coupling diffusion tensors by the generalized Stokes-Einstein relation

$$\mathcal{D}_O = kT\mathcal{M}_O^{-1}, \tag{5.3}$$

where $\mathcal{D}_O$ and $\mathcal{M}_O$ are the 6×6 grand diffusion and friction matrices given by

$$\mathcal{D}_O = \begin{bmatrix} \mathbf{D}_{O,t} & \mathbf{D}_{O,c}^{\dagger} \\ \mathbf{D}_{O,c} & \mathbf{D}_r \end{bmatrix} \tag{5.4}$$

$$\mathcal{M}_O = \begin{bmatrix} \boldsymbol{\Xi}_t & \boldsymbol{\Xi}_{O,c}^{\dagger} \\ \boldsymbol{\Xi}_{O,c} & \boldsymbol{\Xi}_{O,r} \end{bmatrix} \tag{5.5}$$

Rewriting Eq. (5.3) as $\mathcal{M}_O \cdot \mathcal{D}_O = kT\mathbf{I}$, where $\mathbf{I}$ is the identity tensor, one can show that the translation, rotation, and coupling diffusion tensors are related to the friction tensors by [29, 52]

$$\mathbf{D}_{O,t} = kT(\boldsymbol{\Xi}_t - \boldsymbol{\Xi}_{O,c}^{\dagger} \cdot \boldsymbol{\Xi}_{O,r}^{-1} \cdot \boldsymbol{\Xi}_{O,c})^{-1} \tag{5.6}$$

$$\mathbf{D}_r = kT(\boldsymbol{\Xi}_{O,r} - \boldsymbol{\Xi}_{O,c} \cdot \boldsymbol{\Xi}_t^{-1} \cdot \boldsymbol{\Xi}_{O,c}^{\dagger})^{-1} \tag{5.7}$$

$$\mathbf{D}_{O,c} = -kT\, \boldsymbol{\Xi}_{O,r}^{-1} \cdot \boldsymbol{\Xi}_{O,c} \cdot (\boldsymbol{\Xi}_t - \boldsymbol{\Xi}_{O,c}^{\dagger} \cdot \boldsymbol{\Xi}_{O,r}^{-1} \cdot \boldsymbol{\Xi}_{O,c})^{-1} \tag{5.8}$$

According to Brenner [29], the translation and coupling tensors are most meaningful when computed at the center of diffusion. At this point D, the coupling tensor $\boldsymbol{\Xi}_{D,c}$ is symmetrical. The vector from the origin to the center of diffusion $\boldsymbol{r}_{OD}$ can be expressed as [29, 52]

$$\boldsymbol{r}_{OD} = \begin{bmatrix} D_r^{22} + D_r^{33} & -D_r^{12} & -D_r^{13} \\ -D_r^{12} & D_r^{11} + D_r^{33} & -D_r^{23} \\ -D_r^{13} & -D_r^{23} & D_r^{11} + D_r^{22} \end{bmatrix}^{-1} \cdot \begin{bmatrix} D_{O,c}^{23} - D_{O,c}^{32} \\ D_{O,c}^{31} - D_{O,c}^{13} \\ D_{O,c}^{12} - D_{O,c}^{21} \end{bmatrix} \tag{5.9}$$

The translation and coupling tensors at the center of diffusion are given by

$$\mathbf{D}_t = \mathbf{D}_{O,t} - r_{OD} \times \mathbf{D}_r \times \boldsymbol{r}_{OD} + \mathbf{D}_{O,c}^{\dagger} \times \boldsymbol{r}_{OD} - \boldsymbol{r}_{OD} \times \mathbf{D}_{O,c} \tag{5.10}$$

$$\mathbf{D}_c = \mathbf{D}_{O,c} + \mathbf{D}_r \times \boldsymbol{r}_{OD} \tag{5.11}$$

Finally, I can write the scalar translational diffusion coefficient as [52]

$$D_t = kT/\zeta_t = \tfrac{1}{3}\,\mathrm{Tr}\,(\mathbf{D}_t) \tag{5.12}$$

where ζ_t is the translational friction coefficient and $\mathrm{Tr}\,(\mathbf{D}_t)$ is the trace of the translation diffusion tensor. Similarly, I can define scalar rotational diffusion and friction coefficients as

$$D_r = kt/\zeta_r = \tfrac{1}{3}\,\mathrm{Tr}\,(\mathbf{D}_r) \tag{5.13}$$

5.2.1 Kirkwood-Riseman Theory

Based on the preceding discussion, one can fully describe the translational and rotational behavior of a rigid particle, provided one can obtain the translation, rotation, and coupling friction tensors. I will now describe one approach for obtaining those tensors for rigid particles consisting of N spherical elements in the continuum regime. For this discussion, I will consider the case where all N elements have the same radii $a_i = a$, though this need not be the case when applying the general framework described here. I will later discuss how to extend this approach to the transition flow regime.

Kirkwood and Riseman [28] demonstrated that the drag on a particle in continuum flow can be calculated by considering the hydrodynamic interactions between each pair of spheres in the aggregate. Initially, hydrodynamic interactions between spheres were calculated using the Oseen tensor. Later authors introduced more so-

phisticated hydrodynamic interaction tensors to account for the finite size of the spherical elements [57, 58] and for rotational and translation-rotation coupling effects [59–61]. In all of these cases, the relationship between the linear velocity $\boldsymbol{u}_i$ and angular velocity $\boldsymbol{\omega}_i$ of the ith spherical element and the force $\boldsymbol{F}_j$ and torque $\boldsymbol{T}_j$ at the center of each of the N elements is [53]

$$-\boldsymbol{u}_i = \sum_{j=1}^{N} \mathbf{Q}_{ij}^{t} \cdot \boldsymbol{F}_j + \sum_{j=1}^{N} (\mathbf{Q}_{ij}^{c})^{\dagger} \cdot \boldsymbol{T}_j \tag{5.14}$$

$$-\boldsymbol{\omega}_i = \sum_{j=1}^{N} \mathbf{Q}_{ij}^{c} \cdot \boldsymbol{F}_j + \sum_{j=1}^{N} \mathbf{Q}_{ij}^{r} \cdot \boldsymbol{T}_j \tag{5.15}$$

where $\mathbf{Q}_{ij}^{t}$, $\mathbf{Q}_{ij}^{r}$, and $\mathbf{Q}_{ij}^{c}$ are the translation, rotation, and coupling hydrodynamic tensors between the ith and jth spherical elements. These tensors will be defined shortly.

This linear system of equations can be written in matrix form as

$$-\begin{bmatrix} \mathcal{U}_P \\ \mathcal{W} \end{bmatrix} = \begin{bmatrix} \mathbf{Q}^{t} & (\mathbf{Q}^{c})^{\dagger} \\ \mathbf{Q}^{c} & \mathbf{Q}^{r} \end{bmatrix} \begin{bmatrix} \mathcal{F} \\ \mathcal{T}_P \end{bmatrix} \tag{5.16}$$

where $\mathcal{U}_P$, $\mathcal{W}$, $\mathcal{F}$, and $\mathcal{T}_P$ are the $3N$-element vector containing the linear velocities, angular velocities, forces, and torques on the N spherical elements; and $\mathbf{Q}^{t}$, $\mathbf{Q}^{r}$, and $\mathbf{Q}^{c}$ are the $3N \times 3N$ matrices of the translation, rotation, and coupling tensors for all ij-pairs. Note that subscript P indicates that the property is evaluated at the center of each element. For example, the linear velocity of the ith sphere that appears in $\mathcal{U}_P$ is $\boldsymbol{u}_i = \boldsymbol{u}_O + \boldsymbol{\omega} \times \boldsymbol{r}_i$, where $\boldsymbol{r}_i = (x_i, y_i, z_i)$ is the vector from the

origin to the center of the ith element. Inverting Eq. (5.16), I get

$$\begin{bmatrix} \mathcal{F} \\ \mathcal{T}_P \end{bmatrix} = - \begin{bmatrix} \mathbf{S}^t & (\mathbf{S}^c)^\dagger \\ \mathbf{S}^c & \mathbf{S}^r \end{bmatrix} \begin{bmatrix} \mathcal{U}_P \\ \mathcal{W} \end{bmatrix} \tag{5.17}$$

where

$$\begin{bmatrix} \mathbf{S}^t & (\mathbf{S}^c)^\dagger \\ \mathbf{S}^c & \mathbf{S}^r \end{bmatrix} = \begin{bmatrix} \mathbf{Q}^t & (\mathbf{Q}^c)^\dagger \\ \mathbf{Q}^c & \mathbf{Q}^r \end{bmatrix}^{-1} \tag{5.18}$$

Carrasco and Garcıa de la Torre [53] show that the 3×3 submatrices of the $3N \times 3N$ $\mathbf{S}$ matrices are related to the translation, rotation, and coupling friction tensors in Eqs. (5.1) and (5.2) by

$$\mathbf{\Xi}_t = \sum_{i=1}^{N} \sum_{j=1}^{N} \mathbf{S}_{ij}^t \tag{5.19}$$

$$\mathbf{\Xi}_{O,r} = \sum_{i=1}^{N} \sum_{j=1}^{N} \left[\mathbf{S}_{ij}^r - \mathbf{S}_{ij}^c \cdot \mathbf{A}_j + \mathbf{A}_i \cdot (\mathbf{S}_{ij}^c)^\dagger - \mathbf{A}_i \cdot \mathbf{S}_{ij}^t \cdot \mathbf{A}_j \right] \tag{5.20}$$

$$\mathbf{\Xi}_{O,c} = \sum_{i=1}^{N} \sum_{j=1}^{N} \left[\mathbf{S}_{ij}^c + \mathbf{A}_i \cdot \mathbf{S}_{ij}^t \right] \tag{5.21}$$

where

$$\mathbf{A}_i = \begin{bmatrix} 0 & -z_i & y_i \\ z_i & 0 & -x_i \\ -y_i & x_i & 0 \end{bmatrix} \tag{5.22}$$

Carrasco and Garcıa de la Torre [53] summarize the hydrodynamic theories of Reuland et al. [59], Mazur and Van Saarloos [60], and Goldstein [61] and show

that the hydrodynamic interaction tensors $\mathbf{Q}^t_{ij}$, $\mathbf{Q}^r_{ij}$, and $\mathbf{Q}^c_{ij}$ all agree to order r_{ij}^{-3}. These tensors are given by

$$\mathbf{Q}^t_{ij} = \frac{\delta_{ij}}{\zeta_{t,0}}\mathbf{I} + \frac{3(1-\delta_{ij})}{4\zeta_{t,0}}\left[\frac{a}{r_{ij}}\left(\mathbf{I} + \frac{\boldsymbol{r}_{ij}\boldsymbol{r}_{ij}}{r_{ij}^2}\right) + \frac{2a^3}{3r_{ij}^3}\left(\mathbf{I} - \frac{3\boldsymbol{r}_{ij}\boldsymbol{r}_{ij}}{r_{ij}^2}\right)\right] \tag{5.23}$$

$$\mathbf{Q}^r_{ij} = \frac{\delta_{ij}}{\zeta_{r,0}}\mathbf{I} + \frac{(1-\delta_{ij})}{2\zeta_{r,0}}\frac{a^3}{r_{ij}^3}\left[\frac{3\boldsymbol{r}_{ij}\boldsymbol{r}_{ij}}{r_{ij}^2} - \mathbf{I}\right] \tag{5.24}$$

$$\mathbf{Q}^c_{ij} = -\frac{(1-\delta_{ij})}{\zeta_{r,0}}\frac{a^3}{r_{ij}^3}\boldsymbol{\epsilon}\cdot\boldsymbol{r}_{ij} \tag{5.25}$$

where

$$\boldsymbol{\epsilon}\cdot\boldsymbol{r}_{ij} = \begin{bmatrix} 0 & z_{ij} & -y_{ij} \\ -z_{ij} & 0 & x_{ij} \\ y_{ij} & -x_{ij} & 0 \end{bmatrix}, \tag{5.26}$$

δ_{ij} is the Kronecker delta, and $\zeta_{t,0} = 6\pi\mu a$ and $\zeta_{r,0} = 8\pi\mu a^3$ are the continuum friction and torque coefficients. Note that the second term in Eq. (5.23) is the Rotne-Prager-Yamakawa tensor [57, 58] [Eq. (3.11)].

Carrasco and Garcıa de la Torre [53] determined that including terms of order lower than r_{ij}^{-3} in the interaction tensors did not significantly improve results for the simple shapes that they analyzed. Since the effect of these lower order terms drop off rapidly for larger particles, one can safely ignore these terms for the larger particles I will consider in this paper.

5.2.2 *Extension to the Transition Regime*

I now wish to extend this Kirkwood-Riseman framework to the transition flow regime. I start by multiplying Eqs. (5.14) and (5.15) by the monomer friction coefficient $\zeta_{t,0}$ and the monomer torque coefficient $\zeta_{r,0}$, respectively. As Rotne and Prager [57] and Yamakawa [58] have noted, the product of the Rotne-Prager-Yamakawa tensor and the Stokes' law friction coefficient is similar to the flow field $\mathbf{V}_{ij}$ around a translating sphere in Stokes flow,

$$\boldsymbol{v}(\boldsymbol{r}_{ij}) = \mathbf{V}_{ij} \cdot \boldsymbol{U}_0 \tag{5.27}$$

where $\mathbf{V}_{ij}$ is given by Eq. (3.13). The difference between $\mathbf{V}_{ij}$ and $\zeta_{t,0}\mathbf{T}_{ij}$ is a factor of 2 in the r_{ij}^{-3} term in $\zeta_{t,0}\mathbf{T}_{ij}$.

Recently, Corson et al. [92] exploited the similarity between $\mathbf{T}_{ij}$ and the flow around a sphere to extend Kirkwood-Riseman theory to the transition flow regime by solving for the velocity around a sphere as a function of Knudsen number ($\mathrm{Kn} = \lambda/a$, where λ is the mean free path of molecules in the gas) and substituting the resulting $\mathbf{V}_{ij}(\mathrm{Kn})/\zeta_{t,0}(\mathrm{Kn})$ for the second term in Eq. (5.23). This gives the drag on the ith element of a purely-translating N-element particle as

$$\boldsymbol{F}_i = -\zeta_{t,0}(\mathrm{Kn})\boldsymbol{U}_O - \sum_{i \neq j}^{N} \mathbf{V}_{ij}(\mathrm{Kn}) \cdot \boldsymbol{F}_j \tag{5.28}$$

In this case, the translation hydrodynamic interaction tensor is given by

$$\mathbf{Q}^t_{ij}(\mathrm{Kn}) = \frac{1}{\zeta_{t,0}(\mathrm{Kn})}\left[\delta_{ij}\mathbf{I} + (1-\delta_{ij})\mathbf{V}_{ij}(\mathrm{Kn})\right] \tag{5.29}$$

Similarly, I show in Appendix D that the $(1-\delta_{ij})$ terms in the rotation and coupling hydrodynamic interaction tensors are directly related to the flow field around a rotating sphere. Thus, solving for the velocity around and torque on a rotating sphere in the transition flow regime would provide expressions for $\mathbf{Q}^r_{ij}(\mathrm{Kn})$ and $\mathbf{Q}^c_{ij}(\mathrm{Kn})$. This approach should be accurate to order r_{ij}^{-3}, subject to the accuracy of the numerical solution to the kinetic equation in the transition regime and the small error introduced by omitting a factor of 2 in the r_{ij}^{-3} term in the translation hydrodynamic interaction tensor. (These errors are discussed in Chapters 3 and 4). To get the friction tensors for a given particle, one would populate and invert the $6N \times 6N$ $\mathbf{Q}$ matrix and apply Eqs. (5.19)–(5.21).

Alternatively, one can apply a simplified approach to determine the friction and diffusion tensors for a particle in the transition regime. Ignoring rotation and coupling hydrodynamic interactions, the friction tensors are given by [51, 52]

$$\boldsymbol{\Xi}_t = \sum_{i=1}^{N}\sum_{j=1}^{N}\mathbf{S}^t_{ij}(\mathrm{Kn}) \tag{5.30}$$

$$\boldsymbol{\Xi}_{O,c} = \sum_{i=1}^{N}\sum_{j=1}^{N}\boldsymbol{r}_i \times \mathbf{S}^t_{ij}(\mathrm{Kn}) \tag{5.31}$$

$$\boldsymbol{\Xi}_{O,r} = -\sum_{i=1}^{N}\sum_{j=1}^{N}\boldsymbol{r}_i \times \mathbf{S}^t_{ij}(\mathrm{Kn}) \times \boldsymbol{r}_j \tag{5.32}$$

Here, $\mathbf{S}^t$ is the inverse of the $3N \times 3N$ translation matrix $\mathbf{Q}^t$, rather than a $3N \times 3N$ block of the $6N \times 6N$ $\mathbf{Q}$ matrix in Eq. (5.16). This approach is equivalent to considering only the linear velocity $\boldsymbol{\omega} \times \boldsymbol{r}_i$ of each spherical element and ignoring their angular velocities. One obvious flaw of this method is that it predicts zero torque on a rotating sphere and on a chain of spheres rotating around its long axis. García de la Torre and Rodes [107] suggest adding $N\zeta_{r,0}$ to the diagonal elements of $\boldsymbol{\Xi}_{O,r}$ to partially compensate for this error.

For my transition flow regime calculations, I will apply the simplified approach given by Eqs. (5.30)–(5.32). This avoids the need to solve the kinetic equation for a rotating sphere in the transition flow regime and requires inverting a $3N \times 3N$ matrix instead of a $6N \times 6N$ matrix. However, I will apply the volume correction of García de la Torre and Rodes [107] to the rotational friction tensor, using the approximate expression for the ratio of the torque to the free molecule torque given by Loyalka [77] [Eq. (44) in that work]. As I will demonstrate, the simplified approach is sufficiently accurate for larger particles, for which the $\mathcal{O}(r_{ij}^{-3})$ terms in the interaction tensors become less important.

5.2.3 Monte Carlo Calculations for Free Molecule Drag and Torque

In Chapters 3 and 4, I compared my results for the translational friction coefficient to published experimental data and analytical results for the transition flow regime. Unfortunately there is very little information on the rotational diffusion tensor in the transition flow regime. In order to test the extended Kirkwood-Riseman method I must compare to results in the continuum and free molecule limits. Con-

tinuum results will be taken from published results in the literature (where available) or obtained using the hydrodynamic interaction tensors given by Eqs. (5.23)-(5.25). I now describe my approach for calculating the friction tensors in the free molecule limit.

Previous authors [34–36] have used a ballistic approach to calculate the drag on a translating particle in free molecule flow. I use the same approach, but now I consider both translational and rotational motion, and I calculate both the drag and the torque on the particle.

The procedure is as follows. Consider the general case in which the bulk gas velocity is a combination of translational velocity U_O in the positive x-direction and angular velocity ω about the x-axis. (For small translational and angular velocities, this is practically equivalent to a particle moving with translational velocity U_O in the negative x-direction and rotating with angular velocity $-\omega$, but it is easier to consider the case in which the particle is stationary [77].) Surround the particle by a launch sphere with radius R, randomly select starting locations on the surface of the launch sphere, and define local coordinates $(x^\star, y^\star, z^\star)$, where $x^\star$ is the inward normal for the position on the launch sphere. To determine the momentum of gas molecules leaving the launch sphere, sample from the distribution of velocities of gas molecules entering the launch sphere,

$$f(c_{x^\star}, c_{y^\star}, c_{z^\star}) = K c_{x^\star} \, \mathrm{e}^{-[\boldsymbol{c}^\star - (\boldsymbol{U}_O + \boldsymbol{\omega}\times\boldsymbol{R})^\star]^2/2\mathcal{R}T} \tag{5.33}$$

where $\boldsymbol{c}^\star = (c_{x^\star}, c_{y^\star}, c_{z^\star})$ is molecular velocity in the local coordinate system, $\mathcal{R}$ and

T are the gas constant and the gas temperature, the bulk gas velocity $\boldsymbol{U}_O + \boldsymbol{\omega} \times \boldsymbol{R}$ is written in terms of local coordinates, and K is a normalization constant defined such that

$$\int_0^\infty \mathrm{d}c_{x^\star} \int_{-\infty}^\infty \mathrm{d}2c_{y^\star} \int_{-\infty}^\infty \mathrm{d}2c_{z^\star}\, f = 1$$

If the molecule trajectory intersects the particle, calculate the momentum transfer for diffuse reflection from the surface. For diffuse reflection, the molecule direction is sampled from a cosine-squared distribution for the polar angle and an isotropic distribution for the azimuthal angle, while the molecule speed is sampled from the Maxwell-Boltzmann distribution

$$f(c) = 4\pi \sqrt{\left(\frac{1}{2\pi \mathcal{R} T}\right)^3}\, c^2\, \mathrm{e}^{-c^2/2\mathcal{R}T} \tag{5.34}$$

Continue to follow the molecule trajectory until it exits the launch and account for multiple collisions between the gas molecule and the particle. After launching M molecules, calculate the total drag and torque on the particle:

$$\boldsymbol{F} = \frac{A}{M} \sum_{i=1}^{M} \phi_i \boldsymbol{p}_i \tag{5.35}$$

$$\boldsymbol{T} = \frac{A}{M} \sum_{i=1}^{M} \phi_i \boldsymbol{r}_i \times \boldsymbol{p}_i \tag{5.36}$$

Here, A is the launch sphere surface area, $\boldsymbol{p}_i$ is the momentum transferred to the particle by the ith molecule, and $\boldsymbol{r}_i$ is the point at which the molecule collides with the particle. The quantity ϕ_i is the flux of gas molecules entering the launch sphere

at $\boldsymbol{R}_i$ [40],

$$\phi_i = n\sqrt{\frac{\mathcal{R}T}{2\pi}}\left\{ \mathrm{e}^{-s^2\cos^2\theta_i} + \sqrt{\pi}s\cos\theta_i[1+\mathrm{erf}(s\cos\theta_i)] \right\} \tag{5.37}$$

where n is the gas number density, $s = U/\mathcal{R}T$ is the ratio of the bulk velocity to the molecular velocity in the gas, and θ_i is the angle between the bulk velocity and the inward normal to the launch sphere at $\boldsymbol{R}_i$.

Using the above procedure, I determine the translation friction tensor by setting the angular velocity of the flow field equal to zero and calculating the drag $\boldsymbol{F}^x$, $\boldsymbol{F}^y$, and $\boldsymbol{F}^z$ for flow in the x-, y-, and z-directions. For a translation velocity much less than the thermal speed $\sqrt{2\mathcal{R}T}$, the friction tensor is

$$\boldsymbol{\Xi}_t = \frac{1}{U_O}\begin{bmatrix} F_x^x & F_x^y & F_x^z \\ F_y^x & F_y^y & F_y^z \\ F_z^x & F_z^y & F_z^z \end{bmatrix}$$

where F_x^y signifies the x-component of the force on the particle for flow in the y-direction. The pure translation calculation (i.e. $\omega = 0$) also gives the coupling tensor from the torque on the particle per Eq. (5.2). Finally, I calculate the rotation friction tensor by setting the translation velocity to zero and calculating the torque for rotation about the x-, y-, and z-axes.

I have tested my Monte Carlo drag and torque code by comparing my results to published calculation results of Mackowski [36] for the translational friction coefficient (taken as the harmonic average of the eigenvalues of the friction tensor) and

by comparing to simple test cases (e.g. a sphere rotating about its center, a sphere rotating about an axis at a fixed distance from its center) for the torque problem. All of my Monte Carlo results are in excellent agreement with results from alternate calculation methodologies. (See Appendix C.) Furthermore, my calculated translation and rotation friction tensors are symmetrical to within the error in the Monte Carlo calculations. Thus, I can use my Monte Carlo code to evaluate the results of my EKR results in the free molecule limit.

5.3 Results

To verify that the extended Kirkwood-Riseman method produces reasonable results across a wide range of Knudsen numbers, I will compare my calculated rotational friction coefficient ζ_r to its values in the continuum and free molecule limits. I first discuss the continuum and free molecule results.

5.3.1 Continuum regime

Before presenting my results for the rotational friction coefficient in the transition flow regime, it is appropriate to consider the effect of neglecting the rotational and coupling hydrodynamic interaction tensors on ζ_r in the continuum. This issue is discussed in depth in the works of Garcia de la Torre and colleagues (e.g. Refs. [53, 115]). I will be using the EKR method to calculate the translation and rotation friction coefficients of a dimer, a linear hexamer, and an octrahedral hexamer, so I will briefly discuss the results of Carrasco and Garcıa de la Torre [53]

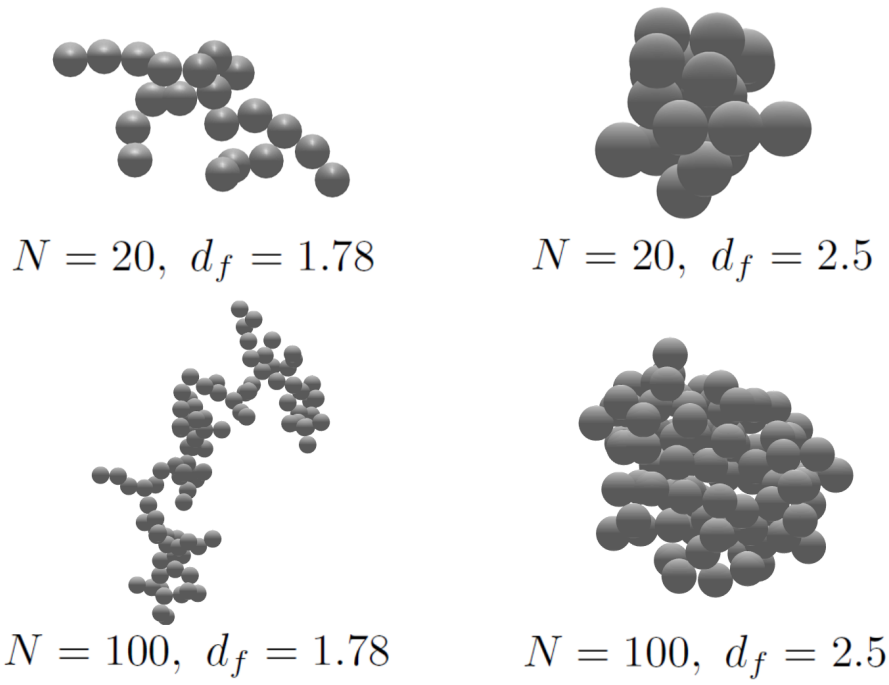

Figure 5.1: Representations of the fractal aggregates used in this study.

for these aggregates. I will also provide continuum results for four different fractal aggregates: $N = 20$, $d_f = 1.78$; $N = 20$, $d_f = 2.5$; $N = 100$, $d_f = 1.78$; and $N = 100$, $d_f = 2.5$. These aggregates are shown in Figure 5.1. Note that these are the same aggregates that I used in Chapter 3. Also note that particles formed by diffusion-limited cluster aggregation processes – such as soot – have a fractal dimension of approximately 1.78.

Carrasco and Garcıa de la Torre [53] provide results of various hydrodynamic interaction models for a dimer, linear hexamer, and octrahedral hexamer. The EKR method in the continuum limit is nearly the same as the KRMV method described in that paper, with the only difference being the factor of 2 in the $\mathcal{O}(r_{ij}^{-3})$ term in $\mathbf{Q}_{ij}^{t}$. Presumably, the most accurate computational results are obtained using the

shell method, where each spherical element in the aggregate is replaced by a large number of frictional units and hydrodynamic interactions are described using the Oseen tensor. I will compare my extended Kirkwood-Riseman results in the continuum limit to the shell method results for the linear and octrahedral hexamers. Exact results are available for a dimer in continuum flow [49], so I will compare my extended Kirkwood-Riseman results to the exact values. Based on Table II of Carrasco and Garcıa de la Torre [53], I would expect the EKR results to underpredict the translational friction coefficient (or overpredict the translational diffusion coefficient) and overpredict the rotational friction coefficient. I would expect better agreement for less compact aggregates, like linear chains or fractals with $d_f = 1.78$, and better agreement for the translational friction coefficient than for the rotational friction coefficient.

Table 5.1 shows translational and rotational friction coefficients for the four fractal aggregates mentioned previously. The Table includes ζ_t and ζ_r computed using terms up to order $\mathcal{O}(r_{ij}^{-3})$ in the interaction tensors (the 3RD method described by Carrasco and Garcıa de la Torre [53]) and using the extended Kirkwood-Riseman method (EKR, where I use the Stokes flow solution around a sphere for the translation interaction tensor and set the coupling and rotation hydrodynamic interaction tensors to zero). Translational friction results are normalized by Stokes' law, $\zeta_{t,0}$; rotational results are normalized to the monomer rotational friction coefficient, $\zeta_{r,0} = 8\pi\mu a^3$.

The difference between $\zeta_t^{\mathrm{c,3RD}}$ and $\zeta_t^{\mathrm{c,EKR}}$ is small ($< 2\%$) for the cases shown here. The difference in the rotational friction coefficient is much larger, with the

Table 5.1: Continuum friction coefficient for fractal aggregates, normalized by the monomer friction results. Friction coefficients are calculated using terms up to order r_{ij}^{-3} in the hydrodynamic interaction tensors (3RD) or my extended Kirkwood-Riseman theory (EKR) in the continuum limit.

Case	$\zeta_t^{\mathrm{c,3RD}}$	$\zeta_t^{\mathrm{c,EKR}}$	$\zeta_r^{\mathrm{c,3RD}}$	$\zeta_r^{\mathrm{c,EKR}}$
$N = 20$, $d_f = 1.78$	4.35	4.31	94.5	110.8
$N = 100$, $d_f = 1.78$	10.3	10.2	1292.0	1376.7
$N = 20$, $d_f = 2.5$	3.41	3.37	42.5	57.5
$N = 100$, $d_f = 2.5$	6.71	6.64	313.6	398.2

greatest difference (35%) occurring for $N = 20$, $d_f = 2.5$. The difference decreases as the average distance between spheres increases due to the reduced importance of the $\mathcal{O}(r_{ij}^{-2})$ and $\mathcal{O}(r_{ij}^{-3})$ terms in the coupling and rotation interaction tensors, respectively. These trends are consistent with the results of Carrasco and Garcıa de la Torre [53] and García de la Torre et al. [115].

It is important to note that the 3RD method tends to underpredict the rotational friction coefficient (or overpredict the rotational diffusion coefficient) compared to more computationally-intensive methods like the shell model [53, 115]. On the other hand, the EKR method appears to overpredict the friction coefficient. In other words, the difference between my EKR results in the continuum and the true value of the rotational friction coefficient may be less than that suggested by the results in Table 5.1. I shall return to this subject in Section 5.4.

5.3.2 Free Molecule Regime

I have computed the free molecule translational and rotational friction coefficients for the seven aggregates described in the previous section. The results are shown in Table 5.2; the values in the table are normalized to the free molecule

Table 5.2: Free molecule results for fractal aggregates, normalized by the monomer friction results

Case	ζ_t^{FM}	ζ_r^{FM}
$N = 2$	1.832	3.829
$N = 6$, $d_f = 1$	5.056	16.46
$N = 6$, octahedron	4.157	21.57
$N = 20$, $d_f = 1.78$	14.48	443.9
$N = 100$, $d_f = 1.78$	64.37	12320
$N = 20$, $d_f = 2.5$	11.64	196.2
$N = 100$, $d_f = 2.5$	43.38	2713

monomer translational and rotational friction coefficients,

$$\zeta_{t,0}^{\mathrm{FM}} = \frac{\pi(8+\pi)}{2.994}\frac{\mu}{\lambda}a^2 \tag{5.38}$$

$$\zeta_{r,0}^{\mathrm{FM}} = \frac{2\pi}{1.497}\frac{\mu}{\lambda}a^4 \tag{5.39}$$

where I have substituted the viscosity for a hard-sphere gas, $\mu = 0.499\rho\bar{c}\lambda$, into the expressions for $\zeta_{t,0}^{\mathrm{FM}}$ and $\zeta_{r,0}^{\mathrm{FM}}$ [3, 32] and assumed diffuse reflection at the surface of the sphere.

My translation friction coefficient results are in excellent agreement with published computational results for linear chains [34] and for fractals with $d_f = 1.78$ [36]. I are unaware of any published results for the denser particles or for the rotational friction coefficients of any of the particles in Table 5.2.

For my free molecule calculations, I sample 10^9 molecular trajectories to ensure good statistical results. Each calculation takes less than three hours on a single processor, and the CPU time increases linearly with the number of trajectories. In general, my results are accurate to three or four significant figures, based on multiple

calculations performed for each case. This level of accuracy is more than sufficient for most practical applications.

5.3.3 Transition Regime

I have performed my extended Kirkwood-Riseman calculations for the seven particles discussed above for Knudsen numbers ranging from 0.01 to 100. In Chapter 3, I reported the translational friction coefficient as a function of Knudsen number for the fractal particles, calculated using the harmonic mean of the eigenvalues of the translational friction tensor Ξ_t. The difference between ζ_t computed using this approach and ζ_t computed using Eq. (5.12) is less than 1%.

Figure 5.2 presents my results for the scalar rotational friction coefficient ζ_r [defined in Eq. (5.13)] of a dimer, linear hexamer, and octahedral hexamer. Results are presented as a slip correction factor,

$$C_r(\mathrm{Kn}) \equiv \frac{\zeta_r^c}{\zeta_r^{\mathrm{EKR}}(\mathrm{Kn})} \tag{5.40}$$

where the continuum rotational friction coefficient ζ_r^c is calculated using the best available method. (C_r is analogous to the Cunningham slip correction factor, which represents the ratio between Stokes' law and the friction coefficient for a sphere in the transition regime. It is also analogous to the parameter Θ^{-1}, defined by Zhang et al. [41] as the ratio of the continuum friction coefficient to the transition regime friction coefficient for an aggregate.) For the dimer, ζ_r^c is given by the exact solution to the Stokes equation [49]; for the hexamers, ζ_r^c is taken as the shell method solution

from Carrasco and Garcıa de la Torre [53]. The free molecule limit for each particle is shown as a dashed line. Note that the curves representing the dimer and the linear hexamer nearly coincide due to the chosen normalization used in the plot.

At small Knudsen numbers, the rotational friction coefficient approaches a constant value that differs from the continuum value for the aggregate ζ_r^c because my calculations neglect rotational and coupling hydrodynamic interactions, as discussed in Section 5.3.1 and illustrated by the results in Table 5.1. At large Knudsen numbers, ζ_r^{EKR} is in excellent agreement with my Monte Carlo calculations for the free molecule rotational friction coefficient (within 5% at Kn=100). The slight discrepancy between the solid and dashed lines in the free molecule limit are due to numerical uncertainty in the Monte Carlo calculations and interpolation error in applying my results for the velocity around a sphere to $\mathbf{V}_{ij}(\mathrm{Kn})$ in Eq. (5.28). (Note that I use a Gaussian quadrature to solve for the velocity within approximately 10 mean free paths of the sphere surface. Thus, interpolation errors are most significant near the free molecule regime, where the sphere radius is comparable to the node spacing.) These results suggest that rotational and coupling interactions between primary spheres are negligible at large Knudsen numbers, as one would expect due to the nature of free molecule flow.

Figure 5.3 presents my results for ζ_r^{EKR} for the fractal particles. Again, the results are plotted as a slip correction factor, but in this case the continuum rotational friction coefficient is calculated using the 3RD method. Note that the two $N = 20$ curves appear to lie on top of each other, as do the two $N = 100$ curves; again, this is due to the chosen normalization.

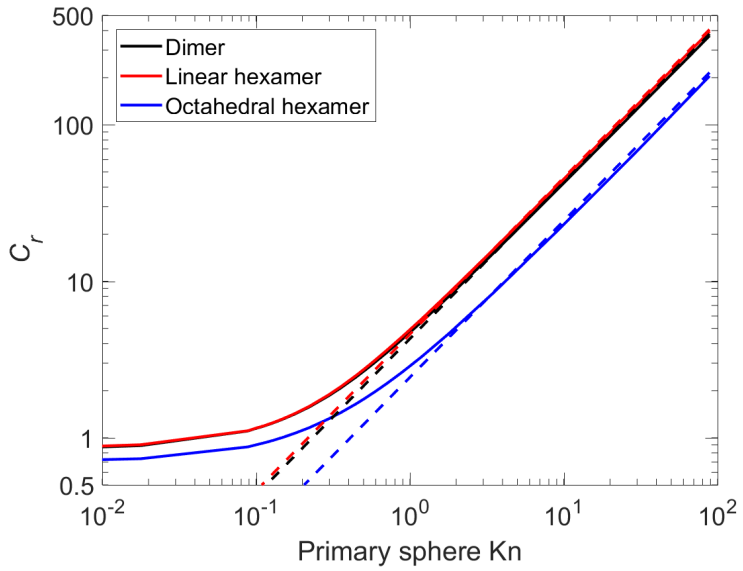

Figure 5.2: Calculated rotational slip correction factor [defined by Eq. (5.40)] for a dimer, linear hexamer, and octahedral hexamer. For the dimer, the continuum value in the slip correction is the exact solution from Happel and Brenner [49]; for the hexamers, the continuum values are the shell method values (SHM) from Table II in Carrasco and Garcıa de la Torre [53]. The free molecule limit for each case (dashed lines) is calculated using my Monte Carlo algorithm.

As with the dimer and hexamers, my results for the fractals are in excellent agreement in the free molecule limit (dashed line), while the errors in the continuum regime are up to 40% because my method neglects rotational and coupling interactions between monomers. This error decreases significantly for larger, less dense particles: for example, the difference between the EKR results and the 3RD results for 100-sphere soot-like fractal is less than 10%. The decrease can be attributed to the reduced importance of the $\mathcal{O}(r_{ij}^{-2})$ and $\mathcal{O}(r_{ij}^{-3})$ terms in the coupling and rotational interaction tensors, respectively, relative to the $\mathcal{O}(r_{ij}^{-1})$ term in the translational interaction tensor. For larger, less dense particles, the monomers are on average spaced further apart than the monomers in a smaller, denser aggregate, such that the translational hydrodynamic interactions dominate.

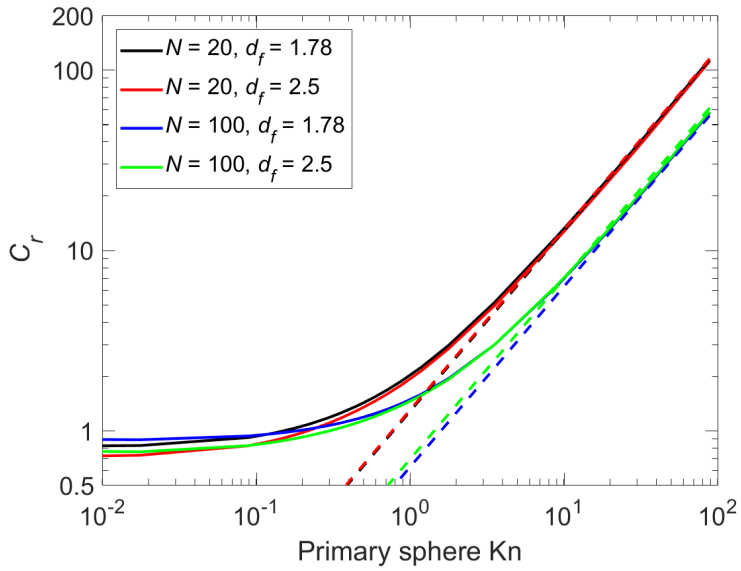

Figure 5.3: Calculated rotational slip correction factor [defined by Eq. (5.40)] for four fractal aggregates. The continuum rotational friction coefficient that appears in the slip correction is calculated using the 3RD method, and the Knudsen-number-dependent friction coefficient is calculated using my EKR method. The free molecular limit for each aggregate (dashed lines) is calculated using my Monte Carlo algorithm.

Dahneke [67] and Zhang et al. [41] posited there exists for the translational friction coefficient a universal relationship between the friction coefficient in the transition flow regime and an aggregate Knudsen number,

$$\frac{\zeta_t^c}{\zeta_t(\mathrm{Kn_{agg}})} = C_c(\mathrm{Kn_{agg}}) \tag{5.41}$$

where C_c is the Cunningham slip correction factor. Zhang et al. [41] showed using dimensional analysis that the appropriate aggregate Knudsen number for translational friction is

$$\mathrm{Kn_{agg}} = \frac{\pi\lambda R_H}{\mathrm{PA}} \tag{5.42}$$

where R_H and PA are the hydrodynamic radius and projected area of the aggregate,

which characterize particle size in the continuum and free molecule regimes, respectively. In other words, the aggregate Knudsen number is proportional to the ratio between the continuum and free molecule friction coefficients for the aggregate.

This Adjusted Sphere Method implies that plots of the aggregate translational slip correction factor [Eq. (5.41)] versus the aggregate Knudsen number [Eq. (5.42)] fall on the same universal curve, regardless of particle shape. Experimental and computational studies [41, 68, 69, 92, 93] suggest that this is indeed the case. Based on this evidence, I propose that the rotational slip correction factor [Eq. (5.40)] should exhibit similar behavior when plotted against an appropriate aggregate Knudsen number. Since the translational aggregate Knudsen number is proportional to the ratio of continuum to free molecule friction coefficients, I posit that the rotational aggregate Knudsen number is

$$\mathrm{Kn}_{r,\mathrm{agg}} = \frac{\zeta_r^c}{\zeta_r^{\mathrm{FM}}} = \frac{23.952}{8+\pi}\frac{\zeta_r^{c\star}}{\zeta_r^{\mathrm{FM}\star}}\mathrm{Kn} \tag{5.43}$$

where Kn is the primary sphere Knudsen number and $\zeta_r^{c\star} \equiv \zeta_r^c/\zeta_{r,0}^c$ and $\zeta_r^{\mathrm{FM}\star} \equiv \zeta_r^{\mathrm{FM}}/\zeta_{r,0}^{\mathrm{FM}}$ are the dimensionless continuum and free molecule rotational friction coefficients for the aggregate.

Figure 5.4 shows my rotational friction coefficient results plotted as the rotational slip correction factor versus the aggregate Knudsen number [Eq. (5.43)]. The dimensionless continuum friction coefficients are calculated with the same reference method used in Figs. 5.2 and 5.3 (i.e. the exact solution for the dimer [49], the shell method for the hexamers [53], and the 3RD method for the 20- and 100-particle ag-

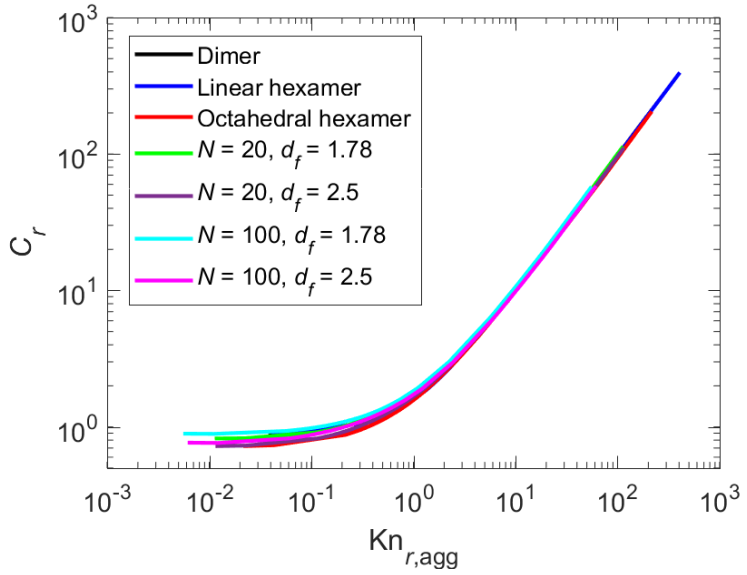

Figure 5.4: Rotational slip correction factor plotted versus an aggregate Knudsen number. The aggregate Knudsen number is the ratio of the friction coefficient calculated as if the aggregate is in continuum flow to the friction coefficient calculated as if the aggregate is in free molecule flow. Continuum friction coefficients are calculated using the same reference method used to calculate the slip correction factor C_r, while the free molecule coefficients are calculated using my Monte Carlo algorithm

gregates). The dimensionless free molecule friction coefficients are calculated using my Monte Carlo algorithm. Roughly speaking, all of the aggregates exhibit the same behavior when plotted in this manner. The differences among the curves near the continuum regime are likely due to neglecting rotational and coupling hydrodynamic interactions when calculating the rotational friction coefficient, as discussed previously. Errors in the calculated continuum friction coefficient may also contribute to the spread among the curves. My results suggest that the aggregate rotational friction coefficient follows some universal function of the rotational aggregate Knudsen number.

5.4 Discussion

I have applied my extended Kirkwood-Riseman theory to calculate the rotational friction coefficient for aerosol particles in the transition flow regime. This approach ignores rotational and translation-rotation coupling interactions between spheres. These effects become less important as the number of primary spheres increase and as the primary sphere size decreases. The former effect is due to the dominance of the $\mathcal{O}(r_{ij}^{-1})$ term in the translational interaction tensor over the lower order terms in the rotational and coupling interaction tensors. The latter effect occurs because smaller particles perturb the flow field less than large particles.

Consistent with this discussion, my EKR results are in excellent agreement with my Monte Carlo results for large Knudsen numbers (i.e. within 5% for Kn = 100). The agreement is not as good in the continuum regime: I have observed errors as high as 40% for dense aggregates relative to the rotational friction coefficient computed considering terms up to order $\mathcal{O}(r_{ij}^{-3})$ in the interaction tensors. The EKR results are in better agreement with the 3RD results for less dense fractal aggregates. It is also worth mentioning that the EKR and 3RD methods respectively under- and over-predict the rotational friction coefficient compared to the computationally-intensive shell method, so the rotational friction coefficient computed using the EKR method is mostly likely in better agreement with the true friction coefficient than my results in Table 5.1 and Figure 5.3 suggest.

My results also suggest that there is a universal relationship between the rotational friction coefficient and an aggregate Knudsen number. This is analogous to

relationship between the translational friction coefficient and the aggregate Knudsen number introduced by Dahneke [67] and Zhang et al. [41], which is supported by experimental data and computational results [41, 68, 69, 92, 93]. For the rotational friction coefficient, the appropriate aggregate Knudsen number is the ratio of the aggregate continuum and free molecule friction coefficients.

I could improve the accuracy of my method – particularly near the continuum regime – if I considered pairwise rotational and coupling interactions between primary spheres in the aggregate. As I have demonstrated (Appendix D), the rotational and coupling interaction tensors are related to the flow field around a rotating sphere; one could solve the kinetic equation for flow around a rotating sphere as a function of Knudsen number to obtain the appropriate interaction tensors in the transition flow regime. With that said, my simplified method is sufficiently accurate for most practical purposes – particularly for larger aggregates with a fractal dimension of 1.78.

Finally, I will note that while I have focused exclusively on the scalar friction coefficient, my method also provides the translation, rotation, and coupling friction tensors. Thus, the extended Kirkwood-Riseman method can be used when considering alignment of aerosol particles in an external field [6, 90, 91, 109, 114] or when simulating Brownian diffusion of small particles.

Chapter 6: Analytical Expression for the Rotational Friction Coefficient of DLCA Aggregates over the Entire Knudsen Regime

6.1 Introduction

The rotational behavior of an aerosol particle can be characterized by the rotational friction and diffusion coefficients ζ_r and D_r, which are related by the Stokes-Einstein relationship $\zeta_r = k_B T / D_r$. The rotational behavior can be important to evaluating the average drift velocity [105, 116] and particle alignment in external electric field and subsequent relaxation [5, 6, 90, 91, 109].

For fractal aggregates that consist of many nano-sized spheres in contact, determining the rotational friction/diffusion coefficient is a difficult problem. This is due to two principal factors: the complicated, fractal-like shape of the aggregates, and the fact that the particle size is often comparable to the mean free path of the molecules in the gas. The latter complication means that the particles are in the transition flow regime, where one must use kinetic theory to solve for the forces and torques exerted by the gas on the aggregates. For these fractal-like particles, the relationship between the number of spheres in the aggregate and its radius of

gyration is

$$N = k_0 \left(\frac{R_g}{a} \right)^{d_f} \tag{6.1}$$

where d_f and k_0 are the fractal dimension and prefactor. For particles formed by diffusion-limited cluster aggregation (DLCA), which is the focus of this work, $k_0 \approx 1.3$ and $d_f \approx 1.78$.

In this chapter, I build on my the work on the rotational friction coefficient of aggregates described in the previous chapter. Here, I apply my extended Kirkwood-Riseman (EKR) theory to determine the rotational friction coefficient of DLCA aggregates over a parameter range of interest to aerosol scientists. I use my results to generate a simple analytical expression for the rotational friction coefficient, as a function of primary sphere size and the number of spheres in the aggregate.

6.2 Theoretical Methods

The force and torque on a rigid particle moving slowly relative to the surrounding fluid can be expressed as

$$\boldsymbol{F} = -\boldsymbol{\Xi}_t \cdot \boldsymbol{U}_O - \boldsymbol{\Xi}_{O,c}^{\dagger} \cdot \boldsymbol{\omega} \tag{6.2}$$

$$\boldsymbol{T}_O = -\boldsymbol{\Xi}_{O,c} \cdot \boldsymbol{U}_O - \boldsymbol{\Xi}_{O,r} \cdot \boldsymbol{\omega} \tag{6.3}$$

where point O is the center of mass of the particle; $\boldsymbol{U}_O$ and $\boldsymbol{\omega}$ are the translational and rotational velocities of the particle; and $\boldsymbol{\Xi}_t$, $\boldsymbol{\Xi}_{O,r}$, and $\boldsymbol{\Xi}_{O,c}$ are the translational, rotational, and translation-rotation coupling friction tensors. The translational,

rotational, and coupling friction tensors relate the particle translational velocity to the force on the particle, the particle angular velocity to the torque on the particle, and the particle translational or angular velocity to the torque or force on the particle, respectively. Note that the subscript O indicates that the property is described relative to the particle's center of mass, while the dagger symbol represents the transpose of a tensor. These equations apply for creeping flow in the continuum, free molecule, and transition regimes, characterized by very small, very large, and intermediate Knudsen numbers, respectively. For spheres, the Knudsen number is defined as $\mathrm{Kn} = \lambda/a$, where λ is the gas mean free path and a is the sphere radius.

Brenner [29] demonstrated that a particles friction and diffusion tensors are connected by a generalized Stokes-Einstein relationship,

$$\boldsymbol{\mathcal{D}}_O = k_B T \boldsymbol{\mathcal{M}}_O^{-1} \tag{6.4}$$

where the grand mobility and diffusion tensors $\boldsymbol{\mathcal{D}}_O$ and $\boldsymbol{\mathcal{M}}_O$ are defined as

$$\boldsymbol{\mathcal{M}}_O = \begin{bmatrix} \boldsymbol{\Xi}_t & \boldsymbol{\Xi}_{O,c}^{\dagger} \\ \boldsymbol{\Xi}_{O,c} & \boldsymbol{\Xi}_{O,r} \end{bmatrix} \tag{6.5}$$

$$\boldsymbol{\mathcal{D}}_O = \begin{bmatrix} \mathbf{D}_t & \mathbf{D}_{O,c}^{\dagger} \\ \mathbf{D}_{O,c} & \mathbf{D}_{O,r} \end{bmatrix} \tag{6.6}$$

The scalar friction and diffusion coefficients are obtained from the trace of the rotational diffusion tensor:

$$D_r = k_B T/\zeta_r = \tfrac{1}{3}\,\mathrm{Tr}(\mathbf{D}_r) \tag{6.7}$$

Analytical expressions are available for the rotational friction/diffusion coefficient of simple shapes in the continuum [29, 49, 112] and free molecule regimes [3, 113, 114], but more approximate methods are needed for fractal-like aggregates of touching spheres. The rotation problem has been studied extensively by Garcia de la Torre and colleagues for rigid particles in continuum flow [51, 53, 115]. Li et al. [6] used a simplified approach in the free molecule regime that ignored shielding by other spheres in the aggregate. In principle, one could use a Monte Carlo approach in the free molecule regime analogous to that used to compute the translational friction coefficient [see e.g. [34, 36, 117, 118]] by replacing the linear velocity field by a rotating velocity field, though no one appears to have published any results using this approach.

Unfortunately, in many practical situations aerosol particles are fractal-like aggregates in the transition flow regime, so a different approach is needed to analyze their rotational behavior. In the previous chapter, I demonstrated that my extended Kirkwood-Riseman (EKR) method can be applied to the rotational problem.

6.2.1 Extended Kirkwood-Riseman Method for the Rotational Friction Coefficient

Kirkwood and Riseman [28] developed a method to determine the force exerted

by a fluid on a particle or m acromolecule consisting of N spherical elements in continuum flow, whereby the force on each element is equal to the force on an isolated sphere minus the perturbations to the flow field caused by the other spheres:

$$\boldsymbol{F}_i = -\zeta^c_{t,0}\boldsymbol{U}_i - \zeta^c_{t,0}\sum_{i\neq j}^{N}\mathbf{T}_{ij}\cdot\boldsymbol{F}_j \tag{6.8}$$

$$\mathbf{T}_{ij} = \frac{1}{8\pi\mu r_{ij}}\left[\left(\mathbf{I}+\frac{\boldsymbol{r}_{ij}\boldsymbol{r}_{ij}}{r^2_{ij}}\right)+\frac{2a^2}{3r^2_{ij}}\left(\mathbf{I}-\frac{3\boldsymbol{r}_{ij}\boldsymbol{r}_{ij}}{r^2_{ij}}\right)\right] \tag{6.9}$$

Here, $\zeta_{r,0} = 6\pi\mu a$ is the monomer translational friction coefficient, $\boldsymbol{U}_i$ is the velocity of the ith sphere in the aggregate, and $\mathbf{T}_{ij}$ is the hydrodynamic interaction tensor that quantifies the effects of the jth sphere on the ith sphere. Applications of KR theory often use the Rotne-Prager-Yamakawa (RPY) tensor [57, 58], Eq. (6.9), for $\mathbf{T}_{ij}$, which is accurate to $\mathcal{O}(r_{ij}^{-3})$, where r_{ij} is the distance between the ith and jth sphere.

The product of the monomer friction coefficient and the RPY tensor is similar to the solution for Stokes flow around a sphere $\mathbf{V}_{ij}$, where $\boldsymbol{u}(r_{ij}) = \mathbf{V}_{ij}\cdot\boldsymbol{U}_j$ is the velocity around a sphere moving with velocity $\boldsymbol{U}_j$. Noting this, I introduced my extended Kirkwood-Riseman (EKR) method by replacing $\zeta_{t,0}\mathbf{T}_{ij}$ in Eq. (6.8) with the velocity tensor for flow around a sphere in the transition regime, $\mathbf{V}_{ij}(\mathrm{Kn})$ (Chapters 3 and 4):

$$\boldsymbol{F}_i = -\zeta_{t,0}(\mathrm{Kn})\boldsymbol{U}_i - \sum_{i\neq j}^{N}\mathbf{V}_{ij}\cdot\boldsymbol{F}_j \tag{6.10}$$

As noted in the above equation, both the velocity tensor and the monomer friction coefficient are functions of the primary sphere Knudsen number. These functions are

obtained by solving the Bhatnagar-Gross-Krook equation [71] using the approach of Loyalka and colleagues [75, 76].

To determine the rotational friction coefficient, I first apply Eq. (6.10) by substituting $\boldsymbol{U}_i = \boldsymbol{\omega} \times \boldsymbol{r}_i$, where $\boldsymbol{\omega}$ is the angular velocity of the aggregate and $\boldsymbol{r}_i$ is the vector from the center of mass to the center of the ith sphere. This gives the force on each sphere in the rotating aggregate. Next, I calculate the torque on each sphere about the center of mass and sum up these torques to determine the total torque on the aggregate:

$$\boldsymbol{T}_O = \sum_{i=1}^{N} \boldsymbol{r}_i \times \boldsymbol{F}_i \tag{6.11}$$

Performing this procedure for angular velocities about three mutually orthogonal axes, I obtain the rotational friction tensor. Finally, I obtain the rotational diffusion tensor and the rotational friction/diffusion coefficient from Eqs. (6.4) and (6.7). Note that the translational and coupling friction tensors that appear in the grand mobility tensor $\boldsymbol{\mathcal{M}}_O$ are obtained by solving Eq. (6.10) for a uniform translational velocity in three orthogonal direction for the force and torque [via Eq. (6.11)] on the particle.

One significant flaw in applying the above method to calculate the torque on a rotating particle is that it yields a value of zero for a sphere or for a straight chain rotating about its long axis. To address this flaw, García de la Torre and Rodes [107] proposed adding the torque of N rotating spheres to the torque computed using KR theory for a rotating aggregate in continuum flow (the so-called volume correction). I take the same approach with the EKR method, except now the monomer rotational

friction coefficient is a function of Knudsen number:

$$\boldsymbol{T}_O = -N\zeta_{r,0}(\mathrm{Kn})\boldsymbol{\omega} + \sum_{i=1}^{N} \boldsymbol{r}_i \times \boldsymbol{F}_i \tag{6.12}$$

There is very little experimental data available for the torque on a rotating sphere as a function of Knudsen number. Tekasakul et al. [119] and Bentz et al. [120] state that their experimental results are in good agreement with the linearized Boltzmann results of Loyalka [77] but do not provide sufficient data for a meaningful comparison. Thus, I use the published computational results of Loyalka and fit those results to an analytical expression for $\zeta_{r,0}(\mathrm{Kn})$. Specifically, I posit that the functional form of the monomer rotational friction coefficient is analogous to the Cunningham slip correction factor that appears in the monomer translational friction coefficient:

$$\zeta_{r,0} = \frac{8\pi\mu a^3}{C_r(\mathrm{Kn})} = \frac{8\pi\mu a^3}{1 + \mathrm{Kn}\left[A_{1r} + A_{2r}\exp\left(-\frac{A_{3r}}{\mathrm{Kn}}\right)\right]} \tag{6.13}$$

The numerator of the above expression represents $\zeta_{r,0}$ in the continuum limit. For very large Knudsen numbers, Eq. (6.13) must reduce to the free molecule expression for $\zeta_{r,0}$ [3, 32],

$$\zeta_{r,0}^{\mathrm{FM}} = \frac{2\pi\alpha}{3}\rho\bar{c}a^4 = \frac{2\pi\alpha}{3(0.499)}\frac{\mu}{\lambda}a^4 \tag{6.14}$$

where α is the fraction of gas molecules that are reflected diffusely from the sphere surface. In the last equality, I use the viscosity of a hard sphere gas, $\mu = 0.499\rho\bar{c}\lambda$, where ρ is the gas density and $\bar{c}$ the mean speed of gas molecules. Using the results from Table IV (Present column) and Eq. (33) from Loyalka [77] and noting that for

diffuse reflection $A_{1r} + A_{2r} = 5.988$, I get the following values for the coefficients in the rotational slip correction factor: $A_{1r} = 3.930$, $A_{2r} = 2.058$, and $A_{3r} = 0.3277$.

A second concern in employing the EKR method is that it ignores rotational and translation-rotation coupling interactions between spheres. Simply put, the linear and rotational motions of a sphere can induce a rotation or torque in another sphere, in accordance with Faxns second law [49]. The rotational and coupling hydrodynamic interaction tensors are (to order r_{ij}^{-3}) equal to vorticity field around a rotating sphere and the vorticity field around a translating sphere, respectively. Thus, one would need to compute these fields as a function of Knudsen number to account for rotational and coupling effects. In addition, one would now need to invert a $6N$-by-$6N$ matrix (instead of a $3N$-by-$3N$ matrix, as in the current method) to obtain the translational, rotational, and coupling friction tensors. (See Chapter 5 for further discussion.) Rotational and coupling hydrodynamic interactions are weaker (i.e. lower order in r_{ij}) than the translational hydrodynamic interactions described by $\mathbf{T}_{ij}$, so I ignore these effects in the EKR method. The resulting error is appreciable (around 30-40%) for very small, dense (i.e. high fractal dimension) aggregates but decreases as the aggregate size (and thus the average distance between spheres) increases (Chapter 5). I will discuss this further later in this chapter.

To apply my method for calculating the rotational friction coefficient, one simply needs the coordinates of the primary spheres in the particle (either from a cluster-cluster aggregation algorithm, as I use for this study, from a detailed Brownian simulation, or from a TEM image) and the velocity field around a sphere. (See Appendix B for velocity results at select Knudsen numbers.) Given this informa-

tion, one forms a 3N-by-3N matrix where each 3-by-3 block is $\mathbf{Q}_{ij} = [\delta_{ij}\mathbf{I} + (1 - \delta_{ij})\mathbf{V}_{ij}(\mathrm{Kn})]/\zeta_{r,0}(\mathrm{Kn})$ and δ_{ij} is the Kronecker delta. The tensor $\mathbf{V}_{ij}$ is a function of primary size and the vector connecting the ith and jth spheres. In other words, one solves Eq. (6.10) as a linear algebra problem to obtain the force on each sphere and uses these results and Eq. (6.12) to determine the torque on the particle. Repeating this procedure for three mutually orthogonal angular velocities, one obtains the rotational friction tensor. See the previous chapter for further discussion.

6.2.2 Adjusted Sphere Method for the Rotational Friction Coefficient

The extended Kirkwood-Riseman method can be applied to determine the friction tensors of an aggregate in the transition flow regime, given the coordinates of the spheres in the aggregate and the velocity around a sphere as a function of the primary sphere Knudsen number. From these friction tensors, one can obtain the rotational friction or diffusion coefficient. Here, I propose a parametric method of determining the rotational friction coefficient that does not rely on the EKR method. This parametric method is based on the adjusted sphere method (ASM) of Dahneke and Zhang et al. for determining the translational friction coefficient. My preliminary results showed that the adjusted sphere approximation can be applied to the rotational friction coefficient (Chapter 5).

Dahneke [67] and Zhang et al. [41] posited that there is a universal relationship between the translational friction coefficient of an aggregate and an aggregate Knudsen number:

$$\zeta_{t,\mathrm{ASM}} = \frac{6\pi\mu R_H}{C_c(\mathrm{Kn}_{t,\mathrm{agg}})} \tag{6.15}$$

$$\mathrm{Kn}_{t,\mathrm{agg}} = \frac{\pi \lambda R_H}{\mathrm{PA}} \tag{6.16}$$

Here, the hydrodynamic radius R_H and orientation-averaged projected area PA are continuum and free molecular measures of the particle size, respectively. The adjusted sphere method allows one to compute the translational friction coefficient of an aggregate given its hydrodynamic radius and projected area.

Melas et al. [80] show that this aggregate Knudsen number is proportional to the ratio of continuum and free molecule expressions for the translational friction coefficient. I propose an analogous approach for the rotational friction coefficient:

$$\zeta_{r,\mathrm{ASM}} = \frac{\zeta_r^c}{C_r(\mathrm{Kn}_{r,\mathrm{agg}})} \tag{6.17}$$

$$\mathrm{Kn}_{r,\mathrm{agg}} = \frac{\zeta_r^c}{(A_{1r} + A_{2r})\zeta_r^{\mathrm{FM}}} \tag{6.18}$$

Here, ζ_r^c and ζ_r^{FM} are the aggregate rotational friction coefficients computed using continuum and free molecular methods, respectively. The rotational slip correction factor formula is the same as C_r defined in Eq. (6.13) and used to compute the monomer rotational friction coefficient; likewise, coefficients $A_{1r} + A_{2r} = 5.988$, just as in the monomer formula.

The adjusted sphere method is useful if one wants to obtain the rotational friction coefficient without worrying about the details of the EKR method. However, ASM incorporates both the continuum and free molecule friction coefficients for an aggregate, and obtaining these expressions typically requires methods at least as complex as the EKR method.

6.2.3 Scaling Laws for the Rotational Friction Coefficient in the Continuum and Free Molecule Regimes

Given the complications involved in determining the rotational friction coefficient of fractal aggregates, it is useful to develop a simple relationship between the aggregate size and structure (i.e. the monomer size, the number of monomers, and the fractal dimensions) and its rotational friction coefficient. Here, I present some theoretical considerations for this relationship in both the continuum and free molecule regimes and use those considerations to develop upper bounds for the rotational friction coefficient. Later, I will use my results for the rotational friction coefficient of DLCA aggregates to improve these simple relationships in the continuum and free molecule regimes and to introduce a new expression for the transition regime.

I begin with the continuum regime, where I will use an analogy with the translational friction coefficient to develop the relationship between the aggregate size and structure and the rotational friction coefficient. As mentioned in the previous section, one can define the hydrodynamic radius as the radius of a sphere with the same translational friction coefficient as the aggregate. Computational studies have shown that this hydrodynamic radius is roughly proportional to the radius of gyration [4, 54, 93], such that the translational friction coefficient can be estimated as $\zeta_t^c \sim 6\pi\mu R_g$. By the same rationale, one can replace the sphere radius in the expression for the rotational friction coefficient with the radius of the gyration of

the aggregate:

$$\zeta_r^c \sim 8\pi\mu R_g^3 \tag{6.19}$$

Using Eq. (6.1), I obtain a scaling relationship between the aggregate size and structure and the rotational friction coefficient:

$$\zeta_r^c \sim k_0^{-3/d_f} \zeta_{r,0}^c N^{3/d_f} \tag{6.20}$$

For DLCA aggregates with $d_f \approx 1.78$, ζ_r^c would scale with $N^{1.685}$ based on this simplified analysis. For the free molecule regime, I use the approach introduced by Li et al. [6] to estimate the rotational relaxation time of an aggregate. In this approach, one assumes that the drag on each sphere in a rotating aggregate is equal to the drag on an isolated sphere moving with linear velocity $\boldsymbol{U}_i = \boldsymbol{\omega} \times \boldsymbol{r}_i$. Computing the torque $\boldsymbol{T}_i = \boldsymbol{r} \times \boldsymbol{F}_i$ on each sphere and summing over all spheres in the aggregate, the torque becomes $\boldsymbol{T} \sim \zeta_{t,0}^{\mathrm{FM}} N R_{g1}^2 \boldsymbol{\omega}$, where R_{g1} is the radius of gyration about the axis of rotation and $\zeta_{t,0}^{\mathrm{FM}}$ is the free molecule translational friction coefficient. Replacing R_{g1} with R_g and using Eq. (6.1), I obtain a scaling relationship between the aggregate size and structure and the rotational friction coefficient in the free molecule regime:

$$\zeta_r^{\mathrm{FM}} \sim k_0^{-2/d_f} \zeta_{r,0}^{\mathrm{FM}} N^{1+(2/d_f)} \tag{6.21}$$

Note that I have also substituted the free molecule rotational friction coefficient for the product $a^2 \zeta_{t,0}^{\mathrm{FM}}$, since the two expressions are related by a constant of order unity. For DLCA aggregates, ζ_r^{FM} would scale with $N^{2.124}$ based on this simplified

analysis.

The above expressions are analogous to the power-law relationship between the translational friction coefficient and the number of spheres in the aggregate observed in numerous experimental and computational studies, as summarized by Sorensen [4]. However, the exponents in Eqs. (6.20) and (6.20) are much higher than the exponents in the translational friction power laws [approximately 0.54 and 0.94 in the continuum and free molecule regimes, respectively [4, 93]], resulting in a much larger variation in the rotational friction coefficient for increasing N.

6.3 Results and Discussion

I have used my EKR method to determine the rotational friction coefficient for DLCA aggregates ($k_0 \approx 1.3$ and $d_f \approx 1.78$) with between 5 and 2000 primary spheres and for primary sphere Knudsen numbers between 0.01 and 100. I have also independently calculated $\zeta_{r,\mathrm{ASM}}$ for these aggregates. The free molecule rotational friction coefficients that appear in the aggregate rotational Knudsen number are calculated using a Monte Carlo algorithm (Appendix C, while the continuum friction coefficients are calculated using a KR-based method that accounts for translational, rotational, and coupling hydrodynamic interactions between spheres in the aggregate. (Specifically, I use the 3RD method described by Carrasco and Garcıa de la Torre [53], which includes terms up to order $\mathcal{O}(r_{ij}^{-3})$ in the hydrodynamic interaction tensors. See Appendix D for more information about rotational and coupling hydrodynamic interactions.) For each aggregate size, I determine the friction coefficients

of 20 different aggregates generated by a cluster-cluster algorithm. Thus, each data point in the following graphs represents the average of 20 realizations of aggregates with the same fractal dimension, prefactor, and number of primary spheres.

6.3.1 Comparison to Experimental Data

There is unfortunately a very limited databased for comparison. Colbeck et al. [91] determined the rotational relaxation time of soot from the combustion of gasoline and other fuels using electro-optic scattering. In this technique, one compares the intensity of scattered light for particles aligned in an electric field to that of randomly-oriented particles. The measured relaxation time is related to the rotational diffusion coefficient by $\tau_r = 1/(6D_r)$. For gasoline combustion generated soot the measured relaxation time was about 4 ms.

Colbeck et al. provide SEM images of soot from the various fuels they used in their study. Based on these images, the maximum aggregate length for the gasoline soot [Figure 2(a) of [91]] is approximately 4000 nm. Since the largest aggregates dominate the light scattering, I base my calculations on the larger clusters. The authors do not specify the primary sphere size or the number of spheres in the aggregate, so I must estimate these properties based on information available in the literature. Köylü and Faeth [42] measured the primary sphere diameter of soot from several gaseous and liquid hydrocarbons, including n-heptane (35 nm), isopropanol (30 nm), benzene (50 nm), and toluene ((51 nm)). Thus, the mean primary sphere diameter for soot from gasoline combustion is likely in the range of $30 - 50$ nm, depending on the fraction of aromatics in the fuel blend.

Table 6.1: Comparison of EKR results to experimental data from Colbeck et al. [91].

Primary Sphere Diameter (nm)	Radius of Gyration (nm)	Number of Primary Spheres	Rotational Relaxation Time (ms)
N/A	N/A	N/A	4[a]
35	1000	508	0.96
40	1000	400	0.96
45	1000	325	0.91
50	1000	269	0.88
35	1500	1045	3.6
40	1500	824	3.5
45	1500	668	3.6
50	1500	554	3.4

[a]Experimental result for gasoline (petrol), from Table 3 of [91]

Using primary sphere sizes of 35, 40, 45, and 50 nm; fractal dimension and prefactor of 1.78 and 1.3; and a radius of gyration equal to 25% or 37.5% of the maximum aggregate length,[1] I can estimate the number of primary spheres in the aggregate. Results for the rotational relaxation times for aggregates generated with the above properties are listed in Table 6.1. It is seen that the results are weakly dependent on the primary sphere size for a fixed radius of gyration. My results based on these simple estimates of the aggregate properties for the larger radius of gyration are in good agreement with the experimental results.

6.3.2 Comparison to Results in the Continuum and Free Molecule Limits

The continuum and free molecule results exhibit the following power-law relationship between the rotational friction coefficient and the number of spheres in the

[1]These are bounding estimates. Note that the algorithm we use to generate our aggregates yields particles whose radii of gyration are $\sim 30-33\%$ of the maximum length.

aggregate:

$$\zeta_r^c = 0.713\zeta_{r,0}^c N^{1.627} \tag{6.22}$$

$$\zeta_r^{\mathrm{FM}} = 1.184\zeta_{r,0}^{\mathrm{FM}} N^{2.019} \tag{6.23}$$

The exponents in these equations are within 5% of the exponents derived from the simple scaling analysis in the previous section. In both the continuum and free molecule regimes, the exponent obtained from my KR and Monte Carlo results are slightly lower than the exponents from my scaling analysis. In the continuum, this may be due to the fact that the hydrodynamic radius of a rotating aggregate increases more slowly than the radius of gyration with increasing aggregate size. Note that this behavior is observed for the translational friction coefficient. In the free molecule regime, the exponent based on the MC calculations is lower than the exponent from my scaling analysis because the scaling analysis does not account for the effects of shielding by other spheres in the aggregate on the drag on each sphere. The effects of shielding increase with aggregate size, which explains the reduced exponent in Eq. (6.23) versus Eq. (6.21).

The large variation in the friction coefficient with N shown in Eqs. (6.22) and (6.23) is evident in Figure 6.1. This figure also shows my EKR and rotational adjusted sphere method results at Knudsen numbers of 0.1, 1, 2, and 10. All results are normalized to the monomer rotational friction coefficient at the primary sphere Knudsen number specified in each plot. At Kn = 0.1, the aggregates behave as if they are in the continuum, as expected. Likewise, at Kn = 10 the aggregates exhibit free molecular behavior, though the EKR and ASM results begin to diverge from

the free molecular limit at large N. At $\mathrm{Kn} = 1$ and $\mathrm{Kn} = 2$, the rotational friction coefficient approaches the continuum limit at large N. These trends are analogous to the trends in the translational friction coefficient as a function of primary sphere Knudsen number and the number of spheres (Chapter 4); the notable difference is that for the translational friction coefficient, the transition to continuum-like behavior occurs at a higher Knudsen number and for aggregates with fewer primary spheres. The reason for this is as follows. First, in the absence of any hydrodynamic interactions or any shielding by other monomers, the torque on each monomer is proportional to $r_i^2 \cos\theta$, where θ is the angle between $\boldsymbol{r}_i$ and the axis of rotation. Second, the spheres furthest from the center of mass are less influenced by the other spheres, and thus behave more as if they are isolated. As a result, the spheres in the extremities of the aggregate experience a higher drag force than spheres in the interior of the particle. Combining these two effects, the spheres furthest from the center of mass have the largest effect on the rotational friction coefficient, and these spheres behave most like they are isolated spheres whose drag force is given by $\zeta_{t,0}(\mathrm{Kn})\boldsymbol{\omega}\boldsymbol{r}_i$. The shielding effect is also evident for the translational friction coefficient, but since all the spheres move at the same translational velocity and are weighted equally (not by the distance from the center of mass), the behavior of the interior spheres dominates the aggregate translational friction coefficient. This explains why the rotational friction coefficient transitions to continuum-like behavior at lower Kn and higher N relative to the translational friction coefficient.

Given the nature of log-log plots in general and the six-order-of-magnitude variation in the rotational friction coefficient between $N = 1$ and $N = 2000$, it is

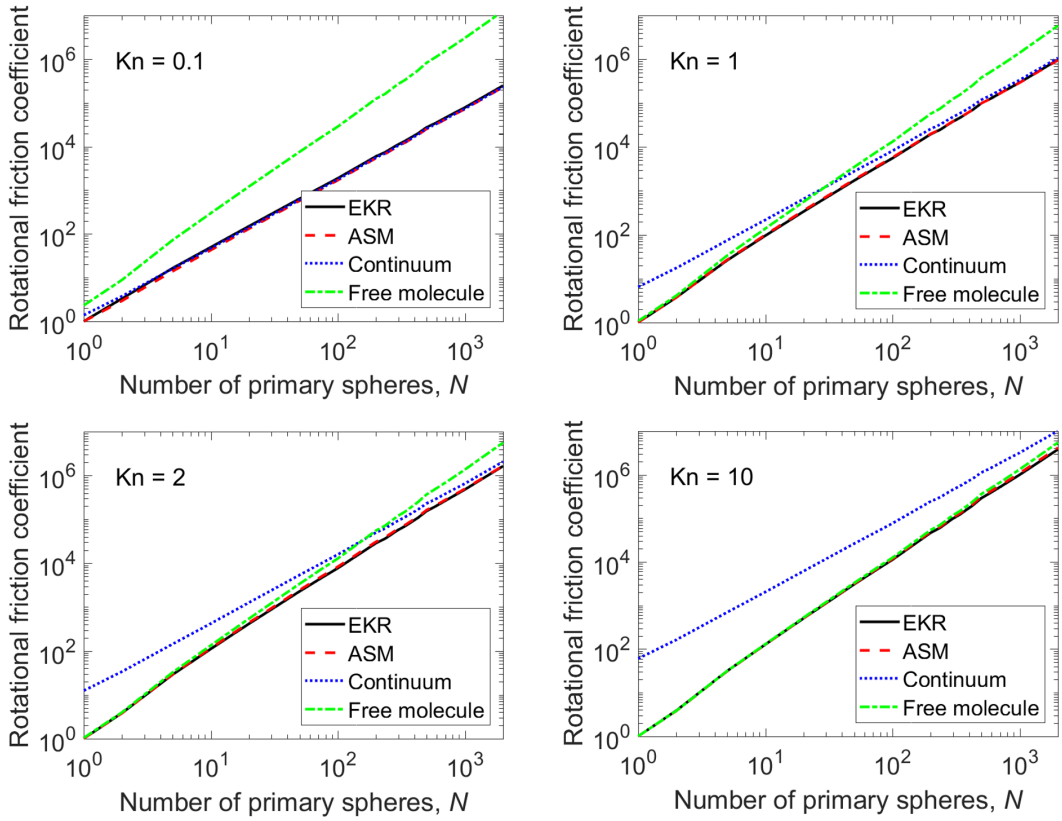

Figure 6.1: Rotational friction coefficient results for Kn = 0.1, 1, 2, and 10. Results are normalized by the monomer rotational friction coefficient for each Knudsen number.

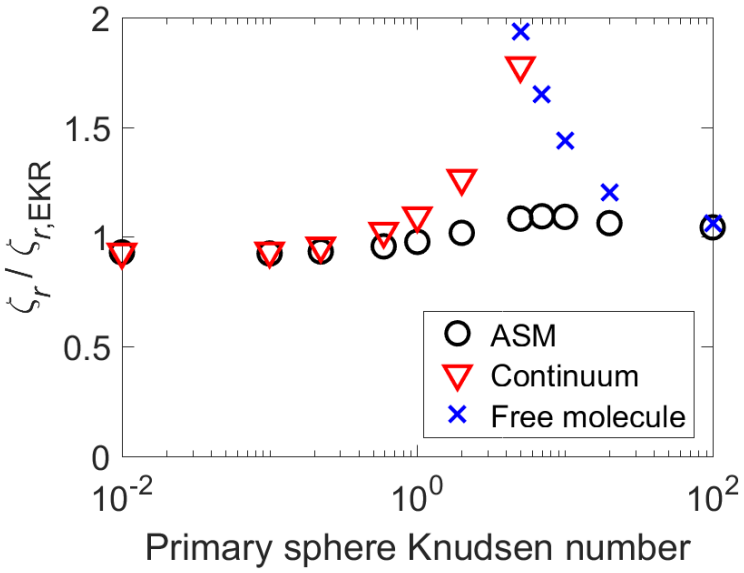

Figure 6.2: Ratio of the rotational friction coefficients for $N = 2000$ calculated using the rotational adjusted sphere method and in the continuum and free molecule limits to the rotational friction coefficient calculated using the EKR method.

difficult to ascertain the differences between the calculation results from the methods shown in Figure 6.1. For this reason, I have plotted the ratio of the adjusted sphere method, continuum, and free molecule rotational friction coefficients to the rotational friction coefficient calculated using the EKR method (Figure 6.2). Results are shown for $N = 2000$. For small Knudsen numbers, my EKR results are in good agreement with the continuum limit, while for very large Knudsen numbers, the EKR results are in good agreement with the free molecule limit. The EKR and ASM results are in good agreement for the entire Knudsen number range, which provides further evidence that there is a universal relationship for the rotational friction coefficient.

6.3.3 Relative Importance of Translational and Rotational Diffusion

One consideration in many aerosol studies is the relative importance of rotational effects on aerosol transport properties. Studies often ignore rotational effects [e.g. on coagulation rates and the resulting shapes of aggregates [121, 122]]. This approach is valid if rotational diffusion is negligible relative to translational diffusion, i.e. if particle orientation changes very little in the time it takes for the particle to diffuse an appreciable distance. The relative importance of rotation on particle transport is captured by the ratio of a characteristic translation time to a characteristic rotation time. Defining the characteristic translation and rotation times as the time required for the particle to diffuse one radius of gyration and rotate one radian, this ratio becomes

$$\frac{\tau_t}{\tau_r} = \frac{R_g^2/6D_t}{1/6D_r} = \frac{R_g^2\zeta_t}{\zeta_r} \tag{6.24}$$

Figure 6.3 shows this ratio as a function of primary sphere Knudsen number and the number of primary spheres, calculated using both my EKR results and analytic expressions for the translational and rotational friction coefficients (introduced in Section 6.3.5 below). Note that the choppy nature of the EKR plot is due to large variations in the rotational friction coefficient for a given set of aggregate parameters, as discussed in the next section. The exact magnitude of the results in this figure is insignificant since I am choosing arbitrary translational and rotational diffusion distances; nevertheless, the results show that in the time it takes an aggregate to diffuse one radius of gyration, it has rotated significantly. Simply put, translational and rotational diffusion are equally important. This is true for all of

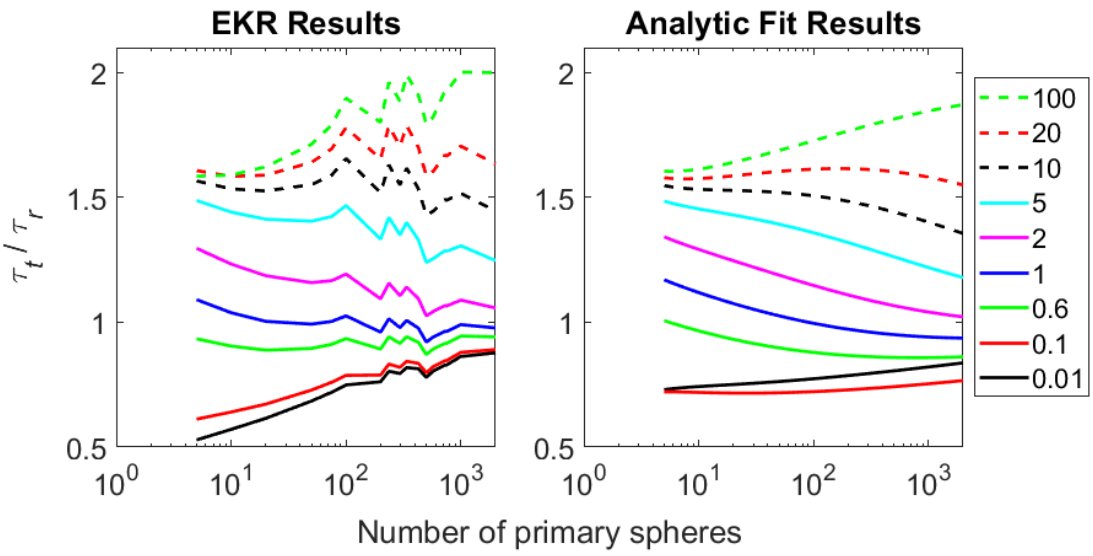

Figure 6.3: Ratio of the characteristic translational diffusion time to the characteristic rotational diffusion time for DLCA aggregates as a function of primary sphere size and the number of primary spheres. Each curve represents the results for the specified primary sphere Knudsen number. The plot on the left shows results of my EKR calculations, while the plot on the right shows results obtained using the analytic fits for the translational and rotational friction coefficients [Eqs. (6.25) and (6.26)].

the primary sphere and aggregate sizes we have included in this study. These results do not imply that ignoring rotational behavior has a significant impact on the results of aerosol transport calculations (e.g. coagulation rates or filtration efficiency); nevertheless, my results suggest that this issue deserves further attention.

It is also interesting to note that the ratio of translational to rotational relaxation times increases as a weak function of N in the continuum (low Kn) and free molecule (large Kn) limits. One can also arrive at this conclusion by substituting the power laws for the continuum and free molecule rotational friction coefficients [Eqs. (6.22) and (6.23)] and the power laws for the translational friction coefficients ($N^{0.54}$ and $N^{0.94}$ in the continuum and free molecule regimes, respectively) into

Eq. (eqn:rsoot:relaxation).[2] In between, the situation is more complicated: the transition to continuum-like behavior happens at lower N and higher Kn for translational transport compared to rotational transport, which explains the decrease in the characteristic diffusion ratio at moderate Knudsen numbers.

6.3.4 Uncertainty in the Calculated Rotational Friction Coefficients

In Chapter 4, I discussed the uncertainty in my calculated translational friction coefficients. There, I identified two main sources of uncertainty: the uncertainty in the calculated velocity tensor and monomer friction coefficient that appear in the EKR method, and KR theory itself. These factors also contribute to the uncertainty in the rotational friction coefficient. However, I must add two additional sources of uncertainty: the effects of neglecting rotational and coupling hydrodynamic interactions and variations in the friction coefficient for aggregates with the same number of primary spheres and the same fractal dimension and prefactor.

As I have mentioned, the linear and rotational velocities of each sphere in the aggregate can induce a torque in the other spheres. In the continuum, the rotational and coupling interactions are order $\mathcal{O}(r_{ij}^{-3})$ and $\mathcal{O}(r_{ij}^{-2})$, respectively, as compared to the translational hydrodynamic interaction tensor, which has leading terms of order $\mathcal{O}(r_{ij}^{-1})$. As a result, I expect that the error in the EKR method would decrease with increasing aggregate size due to the increase in the average distance between monomers. My results confirm this expectation: the difference between the EKR

[2] Note that if one applies the simple scaling arguments from Section 6.2.3 [translational friction coefficient proportional to the radius of gyration in the continuum and to the number of primary spheres in the free molecule regime, and rotational friction coefficients given by Eqs. (6.20) and (6.21)], one predicts that the ratio is independent of N in the continuum and free molecule regimes.

and continuum results at Kn = 0.01 is approximately 25% for $N = 5$ and 8% for $N = 2000$. That 8% difference at $N = 2000$ mirrors the difference between my calculated monomer translational friction coefficient and the friction coefficient given by Stokes law (Chapter 4), suggesting that the effects of coupling and rotational hydrodynamic interactions are negligible for large aggregates. Expressions for the rotational and coupling interaction tensors are unavailable for non-continuum flow, so it is difficult to estimate the effects of neglecting these effects in the transition regime. However, note that the EKR and free molecule results at Kn = 100 are within 5% for the entire aggregate size range we studied. This suggests that rotational and coupling interactions decrease in importance with increasing Knudsen number, as well as for increasing aggregate size. As a result, the uncertainty in the rotational friction coefficients computed using the EKR method is comparable to the uncertainty in my computed translational friction coefficients (i.e. $\sim 10\%$) for all aggregates near the free molecule regime and for large aggregates for any flow regime. This uncertainty is larger (i.e. $\sim 25\%$) for small DLCA aggregates near the continuum regime.

The sources of uncertainty discussed above might better be termed "sources of error," since they represent differences between my results and the true rotational friction coefficient. The final source of uncertainty is just that: variability in the resulting rotational friction coefficient for the same input (namely, the primary sphere Knudsen number, the number of primary spheres, and the fractal dimension and prefactor). My reported results represent averages of results from 20 trials for each set of inputs; here, the variability is due to differences in the coordinates of the spheres that comprise the aggregate. For the translational friction coefficient, this

uncertainty is present, but it is very small: the standard deviation in the calculated friction coefficient is less than 2% of the mean for all primary sphere and aggregate sizes. However, for the rotational friction coefficient the standard deviation is as high as 20% of the mean, and the standard deviation varies with Kn: it is lowest near the continuum regime and largest near the free molecule regime. These variations can be understood in the context of my earlier discussion on the influence of peripheral spheres on the rotational friction coefficient: spheres far from the center of mass have a much larger impact on the rotational friction coefficient than spheres near the center of mass. Thus, variations in the coordinates of the spheres in the aggregate that have little impact on the translational friction coefficient are amplified when determining the rotational friction coefficient. Figure 6.4 illustrates this point. In the figure, I show the torque on each sphere in two rotating 20-sphere aggregates for rotation about the three principal axes (i.e. the axes for which the rotational friction tensor is diagonal). The calculations are performed at Kn = 10. The scale is the same for all six cases shown: the values indicate the torque on the sphere, divided by the largest torque among the six cases. These two aggregates have the same (i.e. within 0.5%) translational friction coefficient, but the rotational friction coefficient – essentially the harmonic average of the friction coefficient for each principal axis – of aggregate 2 is only 75% of the rotational friction coefficient of aggregate 1. Thus, even though the torque is highest for aggregate 2 rotating about the y- and z-axes, the torque about the x-axis is so low that the harmonic average is less than the harmonic average of the torque coefficients for aggregate 1. Again, these effects are dominated by spheres near the periphery of the aggregate,

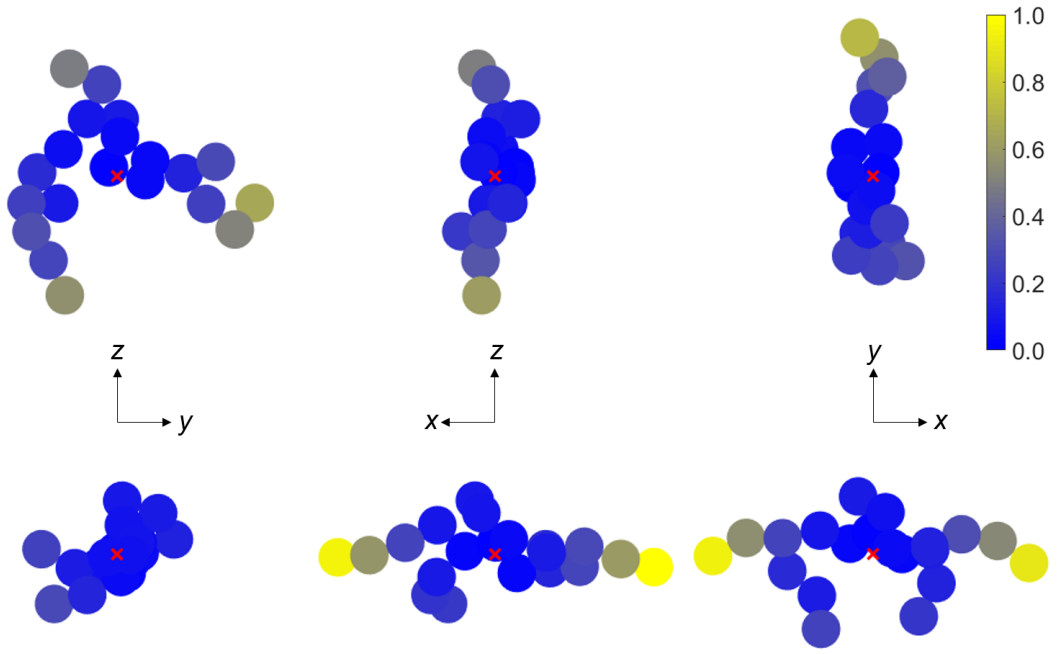

Figure 6.4: Torque on each sphere of two 20-particle aggregates rotating about the x-, y-, and z-axes (left, middle, and right, respectively) for Kn = 10. The rotation axis is out of the page. The torque is normalized by the maximum torque among the six cases. The rotational friction coefficient for aggregate 2 (bottom) is approximately 75% of the rotational friction coefficient for aggregate 1 (top).

as indicated by figure.

The effect of the peripheral spheres on the rotational friction coefficient is more significant near the free molecule regime because these spheres behave almost as if they are isolated, whereas in the continuum even the peripheral spheres are somewhat affected by the particles overall effect on the flow field. This behavior is illustrated in Figure 6.5, which shows the ratio of the drag on each sphere in a 20-sphere aggregate to the drag on an isolated sphere (i.e. $F_i/[\zeta_{t,0}(\mathrm{Kn})U_i]$) for three different Knudsen numbers. Note that the uncertainty due to variations in particle shape (as illustrated in Figure 6.4) does not affect the EKR results for

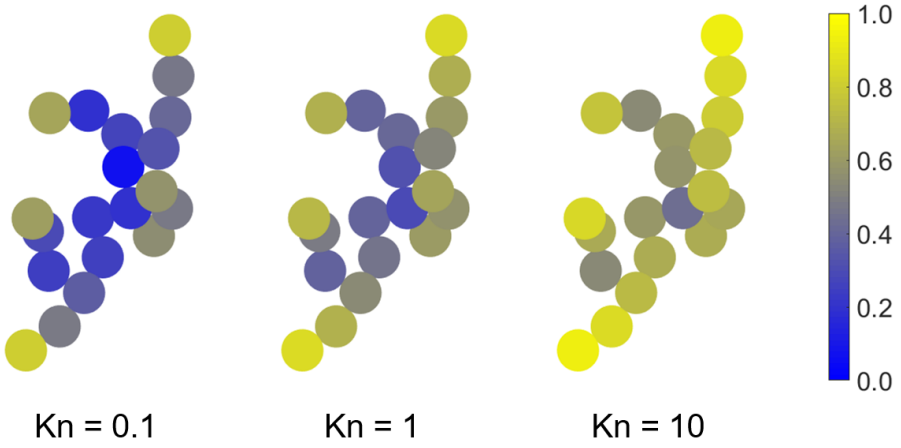

Figure 6.5: Ratio of the drag on each sphere in a 20-particle aggregate to the drag on an isolated sphere (i.e. the monomer momentum shielding factor). Here, the particle is rotating about the z-axis (out of the page). A value of unity indicates that the sphere behaves as if it is isolated, while a value near zero indicates that the perturbations caused by the other spheres have a significant impact on the drag.

individual particle realizations; rather it represents the variation in the rotational friction coefficient for the same set of inputs.

6.3.5 Analytical Expression for Rotational Friction Coefficients of DLCA Aggregates

Previously, I developed an analytical expression for the translational friction coefficient of DLCA aggregates [Eq. (4.38) in Chapter 4] that I verified with my EKR results:

$$\frac{\zeta_t}{6\pi\mu a} = \frac{1+1.612\mathrm{Kn}}{C_c(\mathrm{Kn})}\left[\left(0.852N^{0.535}+0.148\right)^{-1}\right.$$
$$\left.+1.612\mathrm{Kn}\left(0.843N^{0.939}+0.157\right)^{-1}\right]^{-1} \quad (6.25)$$

I will use the same approach to develop an analytical expression for the rotational friction coefficient, which may be used to quickly estimate the characteristic rotational relaxation time for a Brownian particle.

My expression is based on the harmonic sum of the continuum and free molecule power-law expressions for the rotational friction coefficient [Eqs. (6.22) and (6.23)]. In addition, I have added a term to each power law to give the correct value for the monomer friction coefficient, and I have corrected for the fact that the harmonic sum of the continuum and free molecule monomer friction coefficients differs from the monomer friction coefficient given by Eq. (6.13). The resulting expression is

$$\frac{\zeta_r}{8\pi\mu a^3} = \frac{1+5.988\mathrm{Kn}}{C_r(\mathrm{Kn})}\left[\left(0.713N^{1.63}+0.287\right)^{-1}\right. \\ \left.+5.988\mathrm{Kn}\left(1.184N^{2}.02-0.184\right)^{-1}\right]^{-1} \quad (6.26)$$

Figure 6.6 shows the error in the fit relative to my EKR results:

$$error = \frac{\zeta_{r,\mathrm{fit}}-\zeta_{r,\mathrm{EKR}}}{\zeta_{r,\mathrm{EKR}}} \quad (6.27)$$

The error is within approximately 15% for much of the primary sphere Knudsen number and aggregate size range studied here, though the error for smaller aggregates near the continuum regime is higher. Again, this is because the continuum power-law expression is based on results from a more rigorous method of calculating the rotational friction coefficient, where I account for rotational and coupling hydro-

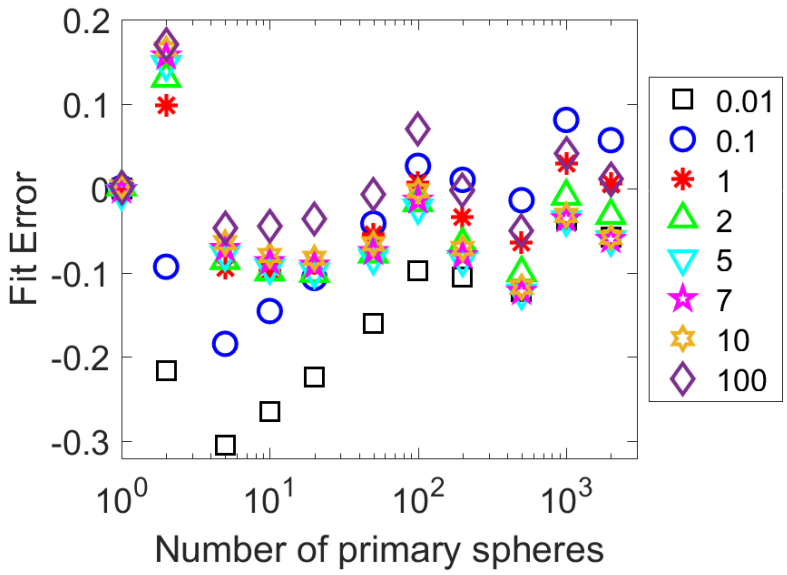

Figure 6.6: Error in the analytical expression for the rotational friction coefficient [Eq. (6.26)] relative to my EKR results. This error is defined by Eq. (6.27).

dynamic interactions. Thus, the error in Eq. (6.26) relative to the true rotational friction coefficient near the continuum regime is likely much lower than indicated by Figure 6.6, which shows the error relative to the EKR results that overestimate the rotational friction coefficient for small aggregates near the continuum regime. However, my fit does not account for uncertainties in the rotational friction coefficient due to variations in the aggregate shape. Thus, the true error in the fit may be as high as 30% for a given aggregate. This is still acceptable given the lack of alternative methods for estimating the rotational friction coefficient in the transition regime.

6.4 Conclusions

I have presented my self-consistent field results for the rotational friction coefficient of DLCA aggregates consisting of 5 to 2000 primary spheres with primary sphere Knudsen numbers between 0.01 and 100. My results are in good agreement with the continuum and free molecule limits for small and large Knudsen numbers, respectively. The computed relaxation times from an aligned to randomly oriented agglomerate are consistent with the measurements by Colbeck et al. [91] for soot produced from gasoline. I estimate that my calculated rotational friction coefficients are within 30% of the true value for the range of parameters I have studied, with the greatest errors occurring for small aggregates near the continuum regime and significantly better agreement for all aggregates near the free molecule regime and for large aggregates in any flow regime.

I have used the EKR method to calculate the ratio of translational to rotational characteristic diffusion times. A potentially important finding is that this ratio is nearly independent of cluster size. My results show that aggregates rotate significantly in the time it takes to diffuse one radius of gyration. This finding suggests that further study is needed to assess the importance of rotation on aerosol coagulation and deposition behavior.

I have introduced an analytic expression for the rotational friction coefficient of DLCA aggregates ($d_f = 1.78$ and $k_0 = 1.3$). This simple model can be applied to quickly estimate the characteristic rotational relaxation time for studies involving particle alignment in an external field. I have extended scaling analyses for the con-

tinuum and free molecule friction coefficients to the rotational problem, which can also be used to estimate the rotational friction/diffusion coefficient of an aggregate in these limits.

I have also provided an expression for the monomer rotational friction coefficient as a function of Knudsen number, based on the computational results of Loyalka [77]. This expression includes a slip correction factor with the same general form as the Cunningham slip correction factor used for the translational friction coefficient of a sphere.

Chapter 7: The Effect of Electric Field Induced Alignment on the Electrical Mobility of Fractal Aggregates

7.1 Introduction

The transport behavior of nano-scale particles depends on particle size, shape, and orientation. In the absence of an external field, Brownian motion randomizes the particle orientation, such that the measured transport property (e.g. intensity of scattered light, particle mobility) represents an average over all equally-likely particle orientations. In a strong field, particles become aligned in an orientation that minimizes their energy in the field [1, 105]. This effect has been demonstrated experimentally by placing particles in an external electric field and measuring changes in scattered light intensity [90, 91] or electrical mobility [5, 6, 87, 123] as the field strength changes.

One common experimental technique for sizing nanoparticles involves using a differential mobility analyzer (DMA) to determine the mobility of particles in an electric field. The particle transport behavior is often expressed in terms of the mobility diameter, which is the diameter of a sphere that has the same mobility as the particle. For spherical particles, the measured mobility diameter is equal to the

geometric diameter and is independent of field strength. However, for non-spherical particles, the mobility is a function of field strength. Plots of mobility versus field strength are typically S-shaped, with the lower plateau at low fields representing fully random particle orientation and the upper plateau at high fields representing fully aligned orientation [5, 6, 87, 123]. The increase in mobility (decrease in drag and mobility diameter) with increasing field strength is due to the electrical polarizability of the particles. This means that particles tend to align such that the longest particle dimension is parallel to the electric field. For example, a long, thin rod orients its long axis parallel to the electric field direction at high field strengths.

Researchers have proposed experimental methods for obtaining shape information or separating particles with different shapes by exploiting the dependence of particle mobility on orientation in a DMA [6, 87, 88]. Such procedures involve size-selecting particles in consecutive DMAs operated at different field strengths (or, equivalently, at different sheath flow rates). The observed change in mobility may give some clues about the shape of particles in the tandem DMAs.

The present study applies the theory of Li et al. [105] for the average particle mobility as a function of field strength to calculate the mobility of aggregates with a fractal dimension of 1.78, which is characteristic of soot and other particles formed by diffusion-limited cluster aggregation. In the present study, I apply my extended Kirkwood-Riseman (EKR) method (see Chapter 3) to obtain the translational friction tensor that appears in the theory of Li et al. [5, 105]. I compare my results to experimental data [6], and I show how the particle mobility changes with electric field strength for a wide range of primary sphere diameters and aggregate sizes. I

also use the EKR method to estimate the particle rotational relaxation time (see Chapter 6) to evaluate the range of particle sizes for which it is appropriate to apply the orientationally-averaged drift velocity method of Li et al. [105] to compute to particle mobility. Finally, I discuss the implications of my results for obtaining shape information by measuring the effect of electric field strength on particle mobility.

7.2 Theoretical Methods

Before discussing my theoretical methods in detail, I will provide an overview of its various components. First, I compute the velocity field and the monomer friction coefficient as a function of Knudsen number by solving the Bhatnagar-Gross-Krook model equation [71] using the method of Loyalka and colleagues [75, 76]. The BGK equation is a simplified, linearized version of the Boltzmann transport equation, valid for near-equilibrium situations such as creeping flow of a sphere. This is done once for each Knudsen number, with the velocity results saved for future use. (See Appendix B.)

The second component involves computing the friction tensor for a cluster of monomers by self consistently computing the flow field at each monomer resulting from the flow field arising from all the other monomers (Chapter 3). The low density of the aggregates is key to carrying out the calculations of large clusters in a short time. This approach was initially used by Kirkwood and Riseman [28] for computing the friction tensor for macromolecules in continuum flow. By using the BGK results for the flow field in the transition regime, I can compute the friction

tensor of clusters composed of equally-sized monomer units. I have also applied the theory to determine the rotational friction tensor (Chapter 5), which is necessary for assessing the possible effect of rotation on the mobility.

Another element of the analysis is the calculation of the cluster polarizability tensor, which is needed for computing the potential energy associated with alignment. I have obtained the polarizability tensor for the aggregates in this study from ZENO (Mansfield et al., 2001), which uses a random walk algorithm [63] to compute (among other things) the polarizability tensor for a perfectly conducting particle of arbitrary shape. I assume that aggregate particles (e.g. soot) are perfectly conducting.

The final element involves the matrix manipulations and the ensemble averaging [49, 105] to obtain the drift velocity (mobility) in the direction of the electric field.

I now discuss the theory in more detail in the following sections.

7.2.1 Particle Orientation in an Electric Field

The probability distribution of a particle's orientation in an electric field is given by the Boltzmann distribution [1],

$$f(\phi,\theta,\psi) = \frac{\mathrm{e}^{-U/k_BT}}{\int_0^{2\pi}\int_0^{2\pi}\int_0^{2\pi}\mathrm{e}^{-U/k_BT}\sin\theta \mathrm{d}\phi \mathrm{d}2\theta \mathrm{d}2\psi} \tag{7.1}$$

where U is the energy of the particle in the electric field for the particle orientation given by the Euler angles (ϕ,θ,ψ). This equation shows that the probability

distribution is affected by the competition between randomizing Brownian forces from collisions of gas molecules with the particle and electrical forces that tend to align the particle in a particular direction. For non-polar materials, the interaction energy includes contributions from free charges on the particle and from an induced dipole due to polarization in the electric field [124]. The interaction energy from a fixed charge is

$$U_e = -q\boldsymbol{r}_e \cdot \boldsymbol{E} \tag{7.2}$$

where $\boldsymbol{r}_e$ is the vector from the center of mass to the point charge and $\boldsymbol{E}$ is the electric field. For a conducting particle, the interaction energy from an induced dipole is given by [124]

$$U_p = -\tfrac{1}{2}\boldsymbol{E} \cdot \boldsymbol{\alpha} \cdot \boldsymbol{E} \tag{7.3}$$

where $\boldsymbol{\alpha}$ is the electrical polarizability tensor. According to Fuchs [1], aerosol particles can be assumed to be conductors, even when comprised of non-conducting materials, due to the ever presence of surface contaminants.

From Eqs. (7.2) and (7.3, the free charge and induced dipole interaction energies increase linearly and quadratically, respectively, with electric field strength. Furthermore, the charge interaction energy increases linearly with particle characteristic length, while the induced dipole interaction energy increases linearly with particle volume. Because the polarization energy increases with a3 while the charge energy increases with a, and because the particle orientation depends on the Boltzmann factor $\mathrm{e}^{-U/k_B T}$, one can often ignore the effects of point charges when computing the probability distribution for the particles orientation. For example, Li

et al. [5] determined that the ratio of polarization energy to fixed charge energy is greater than 10 for carbon nanotubes with mobility diameters greater than 100 nm, while Zelenyuk and Imre [87] observed no effects of particle charge on the mobility of aligned doublets with primary sphere diameters of 240 nm. Also, for a conducting particle the charge can move rapidly, so that one can consider the charge to be distributed evenly throughout the particle [124]. Based on these considerations, I will consider only the polarization energy when computing the particle mobility.

To evaluate the probability distribution [Eq. (7.1)], it helps to define two coordinate systems: a body-fixed coordinate system (x', y', z') that rotates with the particle, and a space-fixed (or laboratory) coordinate system (x, y, z). (See Figure E.1 in Appendix E.) For convenience, I will choose the body-fixed axes to coincide with the principal axes of the polarizability tensor. In this representation, the minimum polarization energy occurs when the electric field is along the z'-direction. I will set the space-fixed axes so that the z-axis is parallel to the electric field.

The relationship between a vector in laboratory coordinates and a vector in body-fixed coordinates is given by the following relationship:

$$\boldsymbol{b} = \mathbf{A} \cdot \boldsymbol{b}' \tag{7.4}$$

The rotation matrix $\mathbf{A}$ represents three successive rotations from the body-fixed system to the space-fixed system. For the ZXZ sequence of rotations, the rotation

matrix is given by

$$\mathbf{A} = \begin{bmatrix} \cos\phi\cos\psi - \cos\theta\sin\phi\sin\psi & -\cos\phi\sin\psi - \cos\theta\sin\phi\cos\psi & \sin\phi\sin\theta \\ \sin\phi\cos\psi + \cos\theta\cos\phi\sin\psi & -\sin\phi\sin\psi + \cos\theta\cos\phi\cos\psi & -\cos\phi\sin\theta \\ \sin\psi\sin\theta & \cos\psi\sin\theta & \cos\theta \end{bmatrix} \tag{7.5}$$

where ϕ, θ, and ψ are the angles of the first, second, and third rotations, respectively. One useful property of the rotation matrix is that its inverse is equal to its transpose (Gel'fand, et al., 1963). Because of this property and my choice of laboratory coordinates, the electric field in body-fixed coordinates is given by

$$\boldsymbol{E}' = \begin{bmatrix} \sin\psi\sin\theta \\ \cos\psi\sin\theta \\ \cos\theta \end{bmatrix} E \tag{7.6}$$

where E is the field strength. This shows that the probability distribution is a function of only two of the three Euler angles. Using the above expression for the electric field and noting that the polarizability tensor in body-fixed coordinates is diagonal, I can explicitly write the interaction energy as

$$U = -\tfrac{1}{2}(\alpha_1 \sin^2\psi \sin^2\theta + \alpha_2 \cos^2\psi \sin^2\theta + \alpha_3 \cos^2\theta)E^2 \tag{7.7}$$

where $\alpha_3 > \alpha_2 > \alpha_1$ are the eigenvalues of the polarizability tensor.

7.2.2 Average Drift Velocity of a Particle in an Electric Field

We use the probability distribution in Eq. (7.1) to calculate the average drift velocity – and thus the mobility – of a particle in an electric field [105]. The drift velocity is obtained by balancing the electric force on the particle with the aerodynamic force for a given particle orientation:[1]

$$\boldsymbol{V}_d = q\boldsymbol{\Xi}_t^{-1} \cdot \boldsymbol{E} \tag{7.8}$$

Here, $\boldsymbol{\Xi}_t$ is the translational friction tensor and q is the charge on the particle. Combining Eqs. (7.1) and (7.8), we get the following expression for the particle orientation-averaged drift velocity for a given electric field strength:

$$\langle \boldsymbol{V}_d \rangle = \frac{q \int_0^{2\pi} \int_0^{2\pi} \int_0^{2\pi} \left(\boldsymbol{\Xi}_t^{-1} \cdot \boldsymbol{E}\right) \mathrm{e}^{-U/k_B T} \sin\theta \mathrm{d}2\phi \mathrm{d}2\theta \mathrm{d}2\psi}{\int_0^{2\pi} \int_0^{2\pi} \int_0^{2\pi} \mathrm{e}^{-U/k_B T} \sin\theta \mathrm{d}2\phi \mathrm{d}2\theta \mathrm{d}2\psi} \tag{7.9}$$

In general, the orientation-averaged drift velocity is not parallel to the electric field. However, the component of the drift velocity parallel to the electric field is typically much larger than the components of the velocity perpendicular to the field. For example, the perpendicular components of the drift velocity for soot-like fractal aggregates are typically less than 5% of the parallel component. Thus, we can define the particle mobility in terms of the parallel component of the orientation-averaged drift velocity,

$$Z = \langle V_{d,z} \rangle / E \tag{7.10}$$

[1] The linear relationship between the velocity and the drag force is valid in the creeping flow regime, which applies for all of the conditions considered in this study.

Again, I have positioned the laboratory-fixed coordinate system so that the electric field is in the z-direction. The z-component of the drift velocity can be written in terms of the Euler angles and the components of the friction tensor in body-fixed coordinates:

$$\langle V_{d,z}\rangle = qE\big(M_{33}\langle\cos^2\theta\rangle + M_{22}\langle\cos^2\psi\sin^2\theta\rangle + M_{11}\langle\sin^2\psi\sin^2\theta\rangle + M_{12}\langle\sin 2\psi\sin^2\theta\rangle + M_{13}\langle\sin\psi\sin 2\theta\rangle + M_{23}\rangle\cos\psi\sin 2\theta\rangle\big) \quad (7.11)$$

Here, the angle brackets indicate orientation averages based on the distribution given by Eq. (7.1) and the M_{ij}s are components of the mobility tensor (i.e. the inverse of the friction tensor) in body-fixed coordinates, i.e.

$$\mathbf{M} \equiv \begin{bmatrix} M_{11} & M_{12} & M_{13} \\ M_{12} & M_{22} & M_{23} \\ M_{13} & M_{23} & M_{33} \end{bmatrix} = \left(\boldsymbol{\Xi}_t'\right)^{-1} \quad (7.12)$$

In going from Eq. (7.9) to Eq. (7.11), I use the relation between the body-fixed ($\boldsymbol{\Xi}_t'$) and space-fixed ($\boldsymbol{\Xi}_t$) friction tensors, $\boldsymbol{\Xi}_t^{-1} = \mathbf{A}\cdot\left(\boldsymbol{\Xi}_t'\right)^{-1}\cdot\mathbf{A}^\dagger$, where the dagger symbol denotes the transpose of the rotation matrix. Note that Eq. (7.11) reduces to the expressions given by Li et al. [5] for the special case of an axisymmetric body, where $M_{12} = M_{13} = M_{23} = 0$, $M_{11} = M_{22} = M_\perp$, and $M_{33} = M_\parallel$.

For a randomly-oriented particle, the averaged mobility is

$$Z_{rand} = \frac{q}{3}\left(\frac{1}{\zeta_1} + \frac{1}{\zeta_2} + \frac{1}{\zeta_3}\right) \quad (7.13)$$

where $\zeta_1 > \zeta_2 > \zeta_3$ are the eigenvalues of the translational friction tensor. At very high field strengths, the particle will be oriented in the direction that minimizes the electric field interaction energy. Thus, the high-field mobility is

$$Z_{align} = q\hat{\boldsymbol{k}} \cdot \left(\boldsymbol{\Xi}_t'\right)^{-1} \cdot \hat{\boldsymbol{k}} = qM_{33} \tag{7.14}$$

where $\hat{\boldsymbol{k}}$ is the unit vector in the z-direction.

7.2.3 Friction Tensor for an Aggregate

To calculate the orientation-averaged mobility of soot-like particles, one must be able to determine the translational friction tensor for fractal aggregates consisting of N primary spheres with radius a, where the Knudsen number of the primaries ($\mathrm{Kn} = \lambda/a$) is in the transition regime between continuum ($\mathrm{Kn} \ll 1$) and free molecule ($\mathrm{Kn} \gg 1$) limits. To do so, I will use my extension (Chapter 3) of Kirkwood-Riseman theory [28] from the continuum regime to the transition regime.

Kirkwood and Riseman proposed a method for calculating the translational friction coefficient for a macromolecule or particle consisting of spherical subunits. The drag on each sphere in the aggregate is obtained by considering the effects of the other spheres in the particle on the flow field. The resulting force is the sum of the drag on an isolated particle and the perturbations due to the other spheres:

$$\boldsymbol{F} = -\zeta_0 \boldsymbol{U}_i - \zeta_0 \sum_{i \neq j}^{N} \mathbf{T}_{ij} \cdot \boldsymbol{F}_j \tag{7.15}$$

Here, $\zeta_0 = 6\pi\mu a$ is the friction coefficient for a sphere, given by Stokes law; $\boldsymbol{U}_i$ is the velocity of the ith sphere; and $\mathbf{T}_{ij}$ is the hydrodynamic interaction tensor. Carrasco and Garcıa de la Torre [53] discuss some of the hydrodynamic interaction tensors that have been proposed in the past and the relative accuracy of the various forms of $\mathbf{T}_{ij}$. They conclude that the Rotne-Prager-Yamakawa (RPY) tensor [57, 58] – which is accurate to order r_{ij}^{-3}, where r_{ij} is the distance between spheres – is sufficiently accurate for practical purposes.

Noting that the product of the RPY tensor and the monomer friction coefficient is similar to the tensor $\mathbf{V}_{ij}$ describing the flow field around a sphere moving with velocity $\boldsymbol{U}_i$ (i.e. $\boldsymbol{u}(r_{ij}) = \mathbf{V}_{ij} \cdot \boldsymbol{U}_i$), I proposed replacing $\zeta_0 \mathbf{T}_{ij}$ with $\mathbf{V}_{ij}$, the velocity field around a moving sphere in the transition flow regime:

$$\boldsymbol{F} = -\zeta_0(\mathrm{Kn})\boldsymbol{U}_i - \sum_{i \neq j}^{N} \mathbf{V}_{ij}(\mathrm{Kn}) \cdot \boldsymbol{F}_j \tag{7.16}$$

This extended Kirkwood-Riseman (EKR) approach is valid for creeping flow for any Knudsen number, provided one can accurately solve for the velocity field around a sphere as a function of Kn.

I obtain the velocity field and the monomer friction coefficientthat appear in Eq.(7.16) by solving the Bhatnagar-Gross-Krook model equation [71] using the method of Loyalka and colleagues [75, 76]. The BGK equation is a simplified, linearized version of the Boltzmann transport equation, valid for near-equilibrium situations such as creeping flow of a sphere. (See Chapter 2.) I solve Eq. (7.16) for unit particle velocity in the x-, y-, and z-directions to determine the translational

friction tensor. My EKR results for the translational friction coefficient of fractal aggregates compare well to published experimental data and calculational results (Chapters 3 and 4).

7.3 Results

To determine the orientation-averaged mobility of fractal aggregates, I solve Eq. (7.11) with the translational friction tensor calculated using the EKR method and the polarizability tensor [which appears in the potential energy term, Eq. (7.7), that affects particle orientation] obtained from ZENO [62]. ZENO uses a random walk algorithm [63] to compute (among other things) the polarizability tensor for a perfectly conducting particle of arbitrary shape. Again, I assume that soot particles are perfectly conducting. The polarizability and friction tensors are specified in terms of the body-fixed axes, which correspond to the principal axes of the polarizability tensor, as discussed previously. I obtain the orientation averages in Eq. (7.11) by integrating numerically using a 2D quadrature method (MATLAB function `integral2`). I generate the aggregates using a cluster-cluster algorithm [36]. For each N, I generate 20 clusters and present the average results of the 20 cases.

7.3.1 Comparison to Experimental Data

Li et al. [6] used a pulsed-field differential mobility analyzer (PFDMA) to determine the electrical mobility of soot aggregates composed of 5-nm-radius primaries

(Kn = 13.5 for $\lambda = 67.3$ nm). They size-selected aggregates with mobility diameters of approximately 129 nm, 154 nm, and 200 nm in a DMA operated at high field ($\sim 7000 - 8000$ V/cm), then used the PFDMA to measure the mobility of these aggregates as a function of electric field strength.

For my calculations, I must first estimate the aggregate size and structure from the reported mobilities. Like Li et al., I assume that the aggregates have a fractal morphology,

$$N = k_0 \left(\frac{R_g}{a} \right)^{d_f} \tag{7.17}$$

with fractal dimension $d_f = 1.78$ and prefactor $k_0 = 1.3$. I determine the number of primaries iteratively until I obtain a set of particles whose average random mobility (as calculated using my EKR method) is in good agreement with the experimental mobility at low field. I repeat this procedure for the three data sets, corresponding to mobility diameters of 129 nm, 154 nm, and 200 nm. As an initial guess for N, I solve for N in my expression for the friction coefficient of DLCA aggregates [Eq. (4.38) of Chapter 4]:

$$\frac{\zeta_t}{6\pi\mu a} = \frac{1 + 1.612\text{Kn}}{C_c(\text{Kn})} \left[\left(0.852 N^{0.535} + 0.148 \right)^{-1} + 1.612\text{Kn} \left(0.843 N^{0.939} + 0.157 \right)^{-1} \right]^{-1} \tag{7.18}$$

The friction coefficient is related to the mobility by $\zeta_t = q/Z$.

Figure 7.1 compares the results of my calculations to data from Li et al. [6]. Overall, the results are in good agreement with the data enabling me to consider a

parametric study outside the bounds of available experimental data.

7.3.2 Effects of Aggregate Size and Field Strength on Mobility

Now that I have shown that the theory of Li et al. used in concert with my EKR method can be used to calculate the orientation-averaged mobility of soot as a function of electric field strength, I will use this approach to calculate the mobility of DLCA aggregates over a wider range of primary sphere and aggregate sizes. Again, my mobility results represent the average of 20 realizations from the fractal generator. My calculations assume that Brownian rotation is slow compared to the translational relaxation time of the particles. This means that the drag force and the electric force are immediately balanced at each particle orientation. Mulholland et al. [116] show the slow rotation limit applies for reduced rotational velocity $\alpha_{nr} = 2D_{r,\min}\tau_t < 0.05$. Here, $\tau_t = m/\zeta_h$ is the translational relaxation time, ζ_h is the translational friction coefficient computed as the harmonic mean of the eigenvalues of the translational friction tensor, m is the particle mass, and $D_{r,\min}$ is the rotational diffusion coefficient of the particle about the axis that yields the minimum D_r. I will examine the validity of this assumption in the Discussion section below.

Figure 7.2 shows the effect of electric field strength on the normalized mobility Z/Z_{rand} of $N = 100$ and $N = 1000$ aggregates at Knudsen numbers corresponding to primary sphere radii of 25 nm (Kn = 2.7), 13.5 nm (Kn = 5), 9.6 nm (Kn = 7), 6.7 nm (Kn = 10), and 5 nm (Kn = 13.5). Particles become aligned at lower electric fields as the primary size and the number of primaries increase. For $N = 1000$,

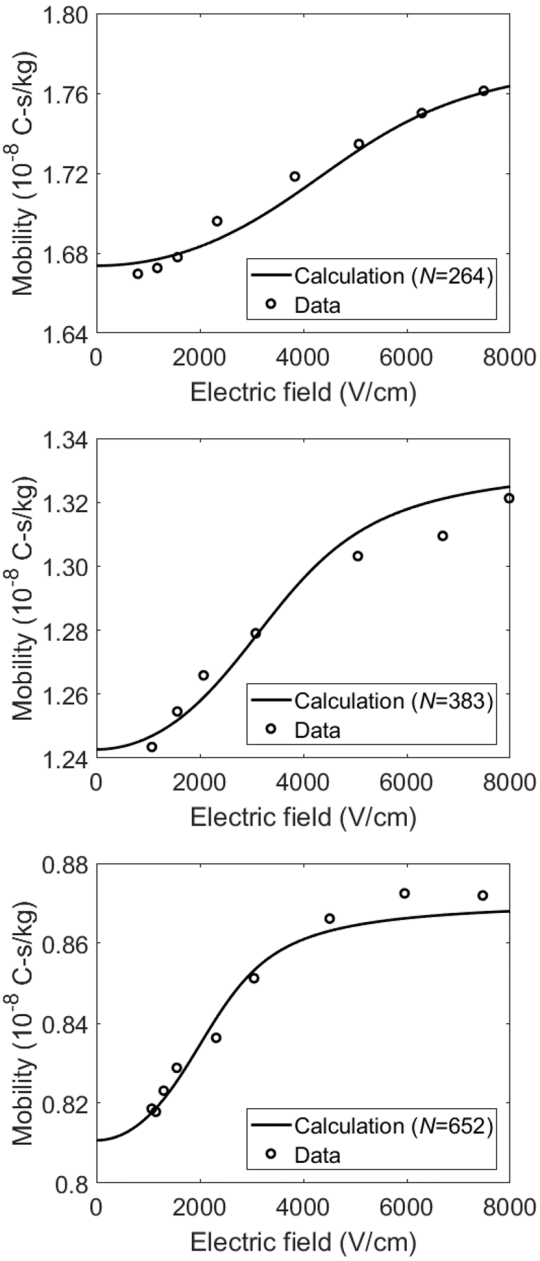

Figure 7.1: Comparison of my calculated orientation-averaged mobilities to experimental data from Li et al. [6] for mobility diameters of $\sim$ 129 nm, $\sim$ 154 nm, and $\sim$ 200 nm (based on the high-field mobilities). The number of primaries used for the calculations represent the best fits to the data.

particles are fully aligned at fields as low as approximately 500 V/cm for the 25 nm primaries versus approximately 5000 V/cm for the 5 nm primaries. The physical basis of this result will be discussed later in this chapter. The normalized fully-aligned mobility for the 1000-sphere aggregates increases slightly with decreasing Knudsen number (increasing primary radius). The maximum increase in mobility from random orientation to fully-aligned is approximately 8%.[2]

Figure 7.3 shows normalized mobility versus electric field strength for Kn = 2.7 and Kn = 13.5 at various aggregate sizes. All but the smallest aggregates with Kn25nm radius primaries (Kn = 2.7) are fully aligned at 8000 V/cm, while only the larger aggregates with 5 nm radius primaries (Kn = 13.5) are fully-aligned at this field strength. The latter point is consistent with the data of Li et al. [6] and my results shown in Figure 7.1. Note that several of the lines in the Kn = 2.7 plot cross each other. This is due to statistical variations in the fully-aligned mobility, caused by the finite number of particles I use to generate the results for each N. I will return to this issue in the final paragraph of this section.

From Figures 7.2 and 7.3, it is clear that particle orientation may not be fully random even at low field strengths. It is useful to determine the maximum field at which the particle orientation is random; I show this maximum field as a function of N and Kn in Figure 7.4. Here, I consider the particle orientation to no longer be random when the mobility increases by 0.5% from the mobility in the limit of zero field. Again, particles begin to partially align at lower field strengths as particle size

[2]For comparison, the change in the intensity of scattered light between aligned and random states has been demonstrated to be as large as $\sim 50\%$ for soot [90, 91].

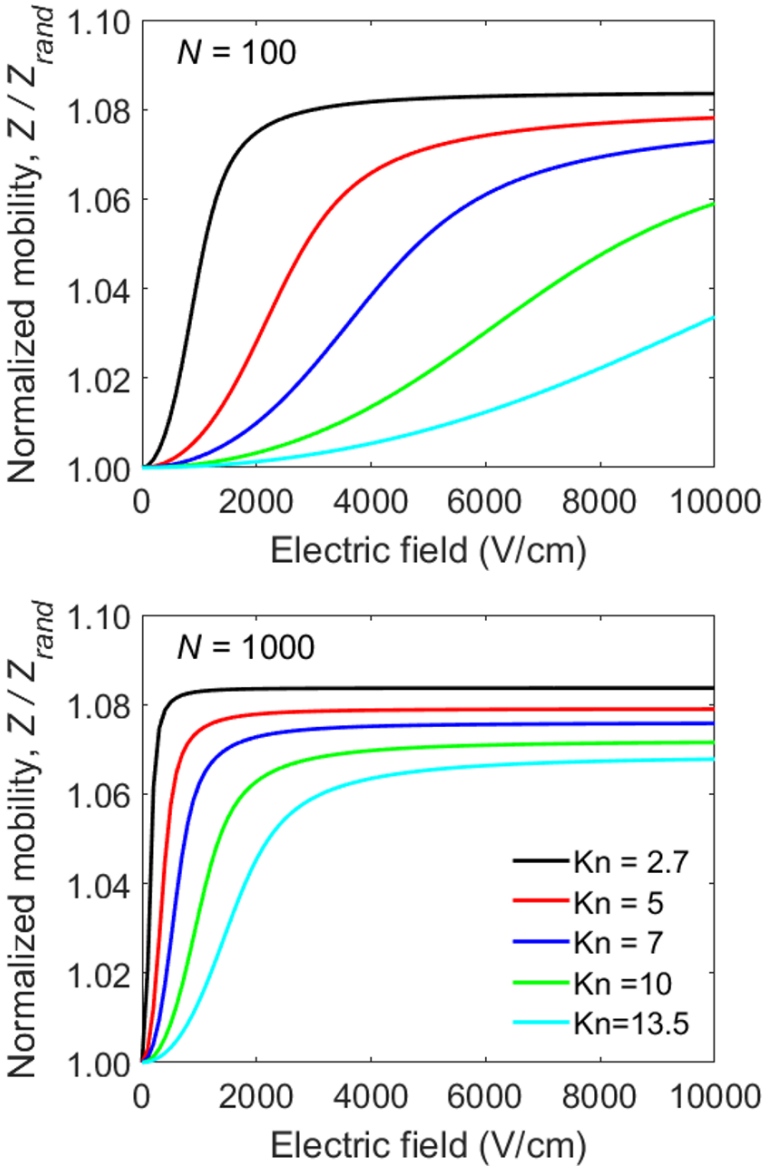

Figure 7.2: Normalized mobility as a function of electric field strength for 100-sphere (top) and 1000-sphere (bottom) aggregates.

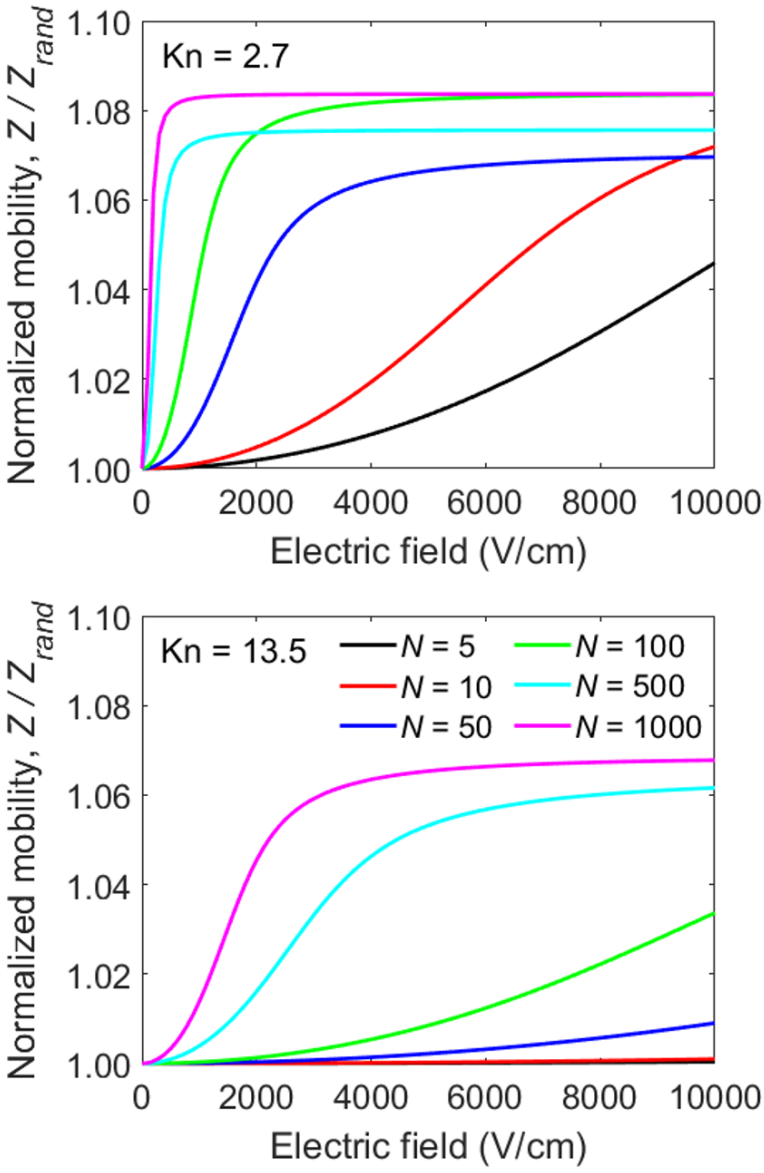

Figure 7.3: Normalized mobility as a function of electric field strength for aggregates with primary sphere radii of 25 nm (Kn = 2.7, top) and 5 nm (Kn = 13.5, bottom). Note that the $N = 100$ and $N = 1000$ curves in this figure correspond to the Kn = 2.7 and Kn = 13.5 curves in Figure 7.2.

(both N and a) increase.

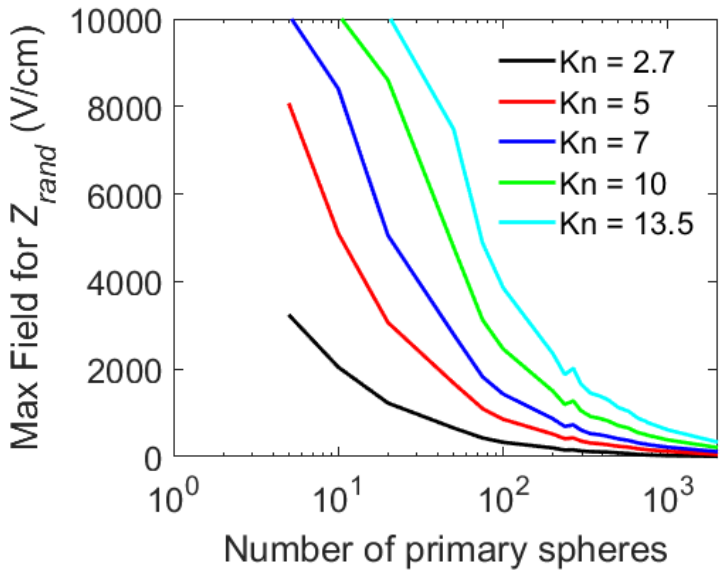

Figure 7.4: Maximum electric field strength at which particles are randomly oriented, defined as having a mobility within 0.5% of the mobility in the limit of zero field strength. Note that results are capped at an upper limit of $E = 10,000$ V/cm.

Finally, Figure 7.5 shows the mobility ratio, Z_{align}/Z_{rand}, as a function of N for several Knudsen numbers. The random and fully-aligned mobilities are calculated using Eqs. (13) and (14), respectively. Generally speaking, the mobility ratio is constant with increasing N near the continuum regime and decreases with N in the free molecule regime. At intermediate Knudsen numbers, the aligned-versus-random behavior becomes more continuum-like at large N; this is analogous to the behavior I have observed for the translational friction coefficient of soot-like aggregates (Chapter 4). I will explain this behavior in the Discussion section below. Note that each point in the figure represents an average over 20 particle realizations. To give an idea of the uncertainty in the mean values shown in the figure, we show bounds of one standard deviation of the mean for several N in the continuum and

free molecule limits. See Appendix E for further discussion about the variability in the mobility ratio results.

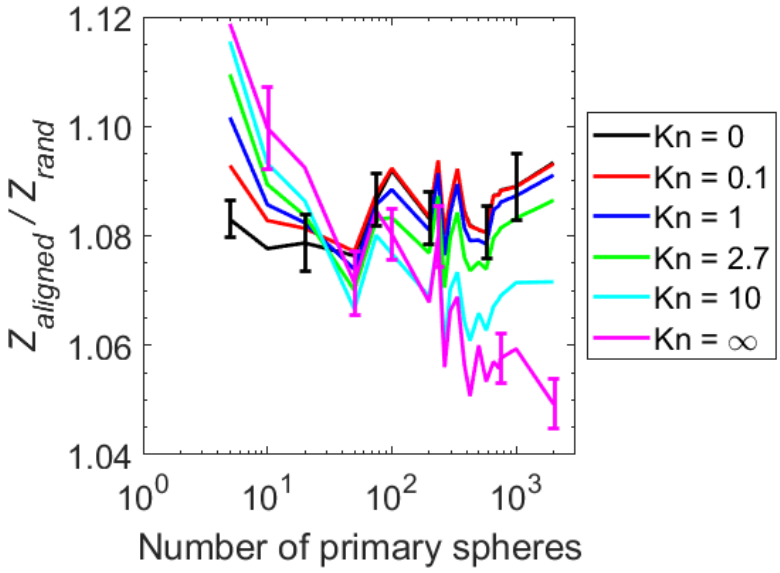

Figure 7.5: Ratio of fully-aligned to random electric mobilities for wide range of primary sphere Knudsen numbers and the number of primaries. The Kn = 0 and Kn = ∞ curves represent the continuum and free molecular limits, as calculated using the standard KR theory with the RPY tensor [see e.g. Chen et al. [30]] and using a Monte Carlo code (Chapter 6), respectively. Uncertainties of one standard deviation of the mean (based on 20 samples with the same fractal dimension but different morphologies) are shown for the continuum and free molecule results for several N.

The choppiness in the plots in Figure 7.5 can be explained by the statistics of my results: the standard deviation of Z_{align}/Z_{rand} is approximately 0.03 for all cases, and thus the standard deviation of the mean[3] is approximately 0.007. Assuming the samples are normally distributed about the population mean, we would expect 68% of the samples to be within one standard deviation of the population mean. Indeed, most of the mean mobility ratios for Kn = 0, 0.1, and 1 are within 0.007 of an estimated population mean of 1.085, so it is reasonable to conclude that the spread

[3]For a sample of n trials having a sample standard deviation s, the standard deviation of the mean is $\sigma_{\bar{x}} = s/\sqrt{n}$.

in Z_{align}/Z_{rand} is partially due to my finite sample size.

7.4 Discussion

7.4.1 General Observations

My results show that particle alignment occurs at decreasing electric field strengths as the primary sphere Knudsen number decreases (primary sphere radius increases) and as the number of primaries increases. This occurs because polarizability is proportional to volume, so that interaction energy between the electric field and the induced dipole increases with volume. The particle becomes fully aligned when the magnitude of the interaction energy is significantly greater than the Brownian energy $k_B T$.

I also show that the ratio of fully-aligned to random mobility is a function of the number of primary spheres and the primary sphere size. Near the continuum regime, the mobility ratio is approximately constant with N; near the free molecule regime, the mobility ratio decreases with N. I discuss this topic in some detail in Appendix E, but the brief explanation is as follows: the mobility of an aggregate in the continuum and free molecule regimes is roughly inversely proportional to the radius of gyration [4, 54, 93] and the orientation-averaged projected area [41], respectively. Similarly, the continuum and free molecule aligned mobilities are correlated to the inverses of the radius of gyration about the major axis of the polarizability tensor (i.e. the z'-axis), $R_{gz'}$, and the projected area in the plane normal to the z'-axis, $\mathrm{PA}_{z'}$. (See Appendix E.) Averaged over 20 cases, the ratio $R_g/R_{gz'}$ is approximately

constant (after accounting for the statistical fluctuations described above) with N, while $PA/PA_{z'}$ decreases with N, mirroring the trends in the mobility ratios in the continuum and free molecule limits.

7.4.2 Validity of the Slow Rotation Assumption

My calculations assume that Brownian rotation is slow compared to translational relaxation, i.e. the aggregates are in the slow rotation limit. To assess the validity of this assumption, I use the EKR method to determine the translational friction coefficient (ζ_h, the harmonic average of the eigenvalues of the friction tensor) and the minimum rotational diffusion coefficient. Using these calculated friction and diffusion coefficients, I compute the reduced rotation velocity α_{nr}, as shown in Figure 7.6.

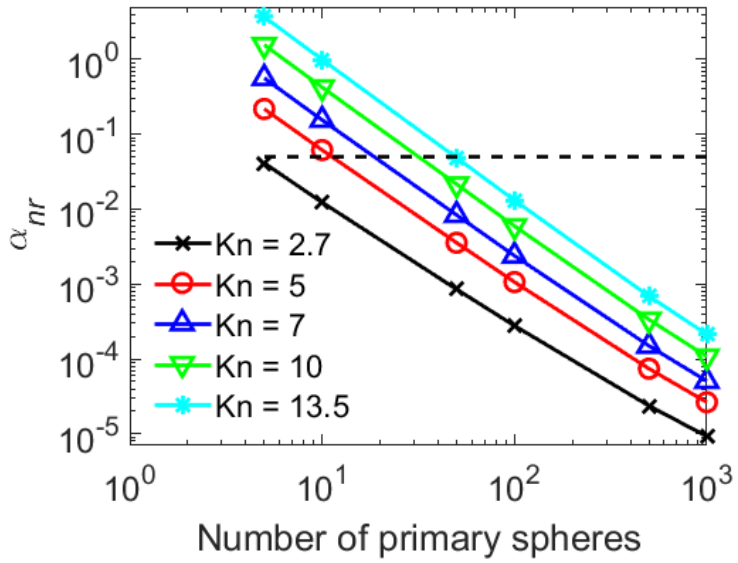

Figure 7.6: Reduced rotation velocity for a range of primary sphere sizes and Knudsen numbers. Soot density is taken as 2 g/mL [125, 126]. Particles with a reduced rotation velocity less than 0.05 (the dotted line) are in the slow rotation limit.

The figure shows that particles with Knudsen numbers less than 13.5 and more than approximately 50 primary spheres are in the slow rotation limit ($\alpha_{nr} < 0.05$ [116]); none of the particles in this study are in the fast rotation limit ($\alpha_{nr} > 10$). Note that for fast rotation, one should use an orientation-averaged drag approach to calculate the mobility, as opposed to the orientation-averaged drift velocity approach in the slow rotation limit. At low field strength, the fast rotation limit yields a scalar friction coefficient equal to the arithmetic average of the eigenvalues, instead of the harmonic average in the slow rotation limit [105]. (The two approaches yield the same result for the fully aligned case.) Thus, some of the particles included in this study are not in the slow rotation limit. However, the maximum difference between the mobility calculated using the averaged drift velocity is at most 1% less than the mobility calculated using the averaged drag force for the particles in this study (i.e. those with fractal dimensions of 1.78). In other words, it makes little difference which approach one uses to calculate the mobility of DLCA aggregates. The distinction becomes more significant for particles with a large aspect ratio, such as long, thin rods, where there is a large difference between the largest and smallest eigenvalues of the friction tensor.

7.4.3 Polarizability Versus Friction

A conducting particle in an electric field will orient itself to minimize its interaction energy with the field, in the absence of any Brownian thermal forces. The minimum energy occurs when the charge separation in the particle is greatest. This means that a rod or a chain of spheres will orient itself such that its long axis is

parallel to the electric field, while the fractal particles in this study are oriented such that the axis through the most widely separated two spheres is parallel to the field. One would expect that the minimum drag force also occurs when it moves along its most elongated direction. This is exactly the case for axisymmetric particles like rods and cylinders, so that the most likely orientation of the particle in an electric field is the orientation with the minimum drag. For fractals, the situation is more complicated: there is a finite angle between the eigenvector of the friction tensor corresponding to the minimum drag and the principal axis of the polarizability tensor (the most favorable orientation). In most cases, this angle is small ($< 10°$), though I have observed angles as large as $25°$ between these two eigenvectors. This means that the most favorable orientation does not necessarily minimize the drag for fractals.

A somewhat related issue is that translating particles with arbitrary shape experience a torque, where the relationship between the particle velocity and the torque exerted by the fluid on the particle is governed by the coupling tensor [49]. For non-skew particles (such as rods and cylinders), there is no translational-rotational coupling, but for skew particles like fractals the coupling tensor is non-zero. The question is whether or not the hydrodynamic torque is sufficient to overcome the interaction energy between the induced dipole and the field and reorient the particle.

To answer this question, I calculated the coupling torque on 1000-sphere aggregates with a primary sphere Knudsen number of 13.5, using the EKR method to determine the coupling tensor and the orientation-averaged drift velocity at a field strength of 4000 V/cm (roughly corresponding to the minimum field strength

at which the particle is fully aligned). The resulting torque is more than two orders of magnitude lower than the interaction energy. I repeated this calculation for $N = 100$, Kn $= 2.7$, and $E = 200$ V/cm; again, the coupling torque is significantly lower than the interaction energy. This shows that the coupling torque has no effect on the particle orientation at high field strength.[4]

7.4.4 Using Field-dependent Mobility to Evaluate Particle Shape

My results clearly show that particle mobility increases with electric field from a fully random state at low fields to a fully oriented state at higher fields. The transition occurs at decreasing fields for increasing particle size (both in terms of primary sphere size and the number of primaries), as expected since polarizability is proportional to particle volume.

This behavior has prompted some researchers to propose methods to separate particles with different shapes by exploiting the changes in mobility at different electric fields, such as by size-selecting particles in a DMA followed by separation with second DMA operated at a different field strength [87, 88]. Using this method, one can distinguish between spheres (or aggregates with fractal dimension near 3) and more elongated particles like rods, chains, prolate ellipsoids, or soot-like aggregates, since the mobility of a sphere does not change with field strength. In practice, this technique may not be feasible for some particle sizes due to limitations

[4] At low field strength, translational-rotational coupling has a small but noticeable effect on the orientation-averaged drag force. For this reason, one must account for rotational and translation-rotation coupling effects when determining the translational diffusion of skew particles [29]. To fully account for rotational and coupling effects at intermediate fields – where both hydrodynamic torques and induced-dipole energies affect particle orientation – one could use a Brownian approach similar to that of Fernandes and García de la Torre [127].

of current commercially available DMA operating conditions and configurations. For example, Li et al. [6] estimate that they cannot operate their experimental system at fields below 1000 V/cm. At this field strength, larger particles are fully-aligned (see Figures 7.2 and 7.3), so measuring the mobility at fields of 1000 V/cm and e.g. 8000 V/cm would yield the same result and lead to the erroneous conclusion that the particle is spherical. At the other end of the size spectrum, small fractals experience minimal changes in mobility over the range of electric fields studied here. It may also be difficult to operate a DMA at a low enough field to ensure that the particle orientation is fully random. One can consult Figure 7.4 to determine if it is possible to select randomly oriented particles for the operating conditions of ones DMA setup.

There are also issues distinguishing between two non-spherical particles with different shapes. For example, the fully-aligned mobility of a doublet in continuum flow is 8% greater than the mobility of a randomly oriented doublet [49, 53]. This is comparable to the increase in mobility from random to fully-aligned orientations for the soot particles included in this study. Thus, a doublet with primary size near the continuum regime and a soot-like particle with the same low-field mobility will behave similarly at higher voltages, making it difficult to distinguish between these particles. As another example, I looked at the effect of the prefactor [k_0 in Eq. (7.17)] on the mobility of DLCA aggregates. While the prefactor does affect the mobility (with lower prefactors resulting in decreased mobility for the same number of primary spheres), it has little effect on the ratio of the fully-aligned to fully random mobilities.

Beyond the experimental issues mentioned above, it is also difficult to accurately calculate the mobility of a fractal aggregate in the transition regime. I have estimated that the EKR method yields orientation-averaged translational friction coefficients within 10% of the true value (Chapter 4), which translates to uncertainties in any estimate of the primary sphere size or the number of primary spheres. An obvious example is my attempt to fit my results to the data of Li et al. (2016), as illustrated by Figure 7.1: my estimated aggregate sizes (in terms of N) are likely within about 10% of the true value (though the actual error estimate depends on the relationship between N and the friction coefficient). This situation is simplified by the fact that we know the primary sphere size from TEM measurements, and we have a good estimate of the fractal dimension and prefactor from numerous studies of soot. (See Sorensen [4] for a review of these studies.)

In total, the above factors mean that while it may be theoretically possible to extract shape information from DMA measurements made at different field strengths, it is difficult, and probably further consideration should be given to development of DMA configurations optimized for this purpose.

7.5 Conclusions

I have applied the EKR method for calculating the translational friction tensor of fractal aggregates to verify the theory of Li et al. [105] for the average mobility of a particle in an electric field. My results compare well to published experimental data for soot [6]. Furthermore, I use the EKR method to calculate the average

mobility of aggregates over a range of primary sphere sizes in the transition and near free molecule regimes with up to 2000 primary spheres. The maximum increase in mobility from random to fully-aligned orientations is approximately 8% for the soot-like aggregates ($d_f = 1.78$, $k_0 = 1.3$) included in this study. While my calculations cover the Knudsen number range of 2.7 to 13.5 – which represents a representative range of primary sphere sizes in soot particles (see, e.g. [6, 42]) – this approach is valid for any primary sphere size and number of primaries, provided the particle is in the slow rotation limit. See Chapters 4 and 6 for translational and rotational friction coefficient results at larger and smaller Knudsen numbers.

While it is theoretically possible to use the relationship between mobility and field strength to obtain size and shape information about particles or to separate particles with similar mobility but different shapes, my results suggest there are several practical issues related to the experimental setup and to the accuracy of the methods used to relate the data to size and shape information. It is especially difficult to obtain shape information for either very large or very small soot-like aggregates because large aggregates are fully aligned at even very low field strengths and small aggregates require very high field strengths to align. In these limits, the measured mobility at low ($\sim$ 1000 V/cm) and high ($\sim$ 8000 V/cm) field strengths would be nearly equal, which would suggest – incorrectly – that these fractal aggregates are actually spherical.

Chapter 8: Hydrodynamic Interactions between Particles

8.1 Introduction

The vast majority of the literature on aerosol particle transport treats the particles as if they are isolated when calculating the drag. This approach is valid for very dilute aerosols, where the average separation between particles is large, and thus hydrodynamic interactions between particles are negligible. For example, the mean settling velocity of a system of spheres in continuum flow is $U_0(1 - 6.55\phi)$, where ϕ is the particle volume fraction and U_0 is the velocity each sphere would have if it was alone in an infinite fluid [128]. As another example, the viscosity of a suspension of spheres in continuum flow is $\mu(1 + 2.5\phi)$, where μ is the fluid viscosity [2]. Clearly, the interaction effects on the settling velocity and suspension viscosity are negligible for aerosol systems consisting of spheres at typical volume fractions.

However, there are situations where one might expect interactions between particles to be more significant. Sorensen et al. [129] has demonstrated that aerogels can form under certain conditions in sooting flames. In this process, fractal aggregates formed by diffusion limited cluster aggregation (DLCA) reach a critical size and begin to fill the entire physical volume because the aggregate fractal dimension ($d_f \approx 1.78$) is less than the spatial dimension. One would expect hydrodynamic in-

teractions between the soot aggregates to be more significant than between spheres at the same volume fraction, due to the stringy nature of the DLCA aggregates. More generally, for coagulating systems aerosol particles must approach each other, so that interparticle hydrodynamic interactions may affect the coagulation rate.

Much of the literature on hydrodynamic interactions between particles focuses on spheres in the continuum regime [1, 128, 130–136]. Little attention has been paid to interactions between particles in the transition (or kinetic) flow regime, when the particle size is comparable to the gas mean free path, as is often the case in aerosol systems [2, 4]. Such an investigation is now possible using my theory for hydrodynamic interactions in the kinetic regime [92].

The present study examines the forces exerted by aerosol particles on their neighbors due to hydrodynamic interactions between the particles and the surrounding fluid. I consider both spheres and soot-like fractal aggregates moving parallel, anti-parallel and perpendicular to their line of centers. (See Figure 8.1.) I employ the extended Kirkwood-Riseman (EKR) method [92] to solve for the hydrodynamic forces on the particles in the transition flow regime as a function of the separation distance between particles, the Knudsen number ($\mathrm{Kn} \equiv \lambda/a$), where λ is the gas mean free path and a is the sphere radius) of the primary sphere(s) that comprise the particles, and the number of primary spheres in the particle. As an example of a situation where hydrodynamic interactions may be significant, I present calculations for the settling velocity of a cloud in an unbounded medium. Throughout this study, I assume the particles are in the creeping flow regime ($\mathrm{Re} \ll 1$, Ma

1).

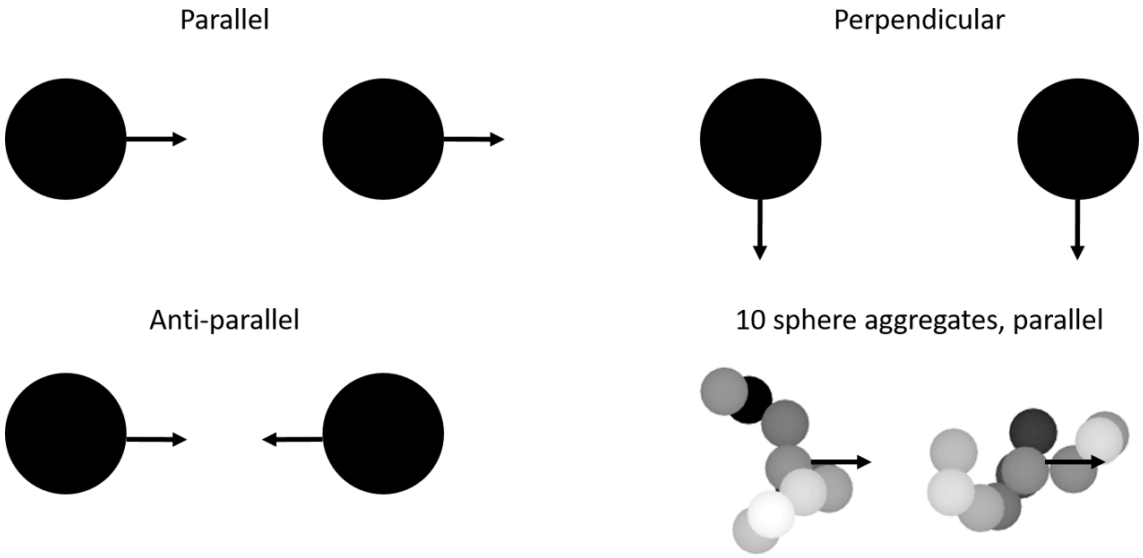

Figure 8.1: Two spheres in the parallel, anti-parallel, and perpendicular flow configurations, and two 10-sphere aggregates with random orientations in parallel flow. The descriptor refers to the direction of movement relative to the line connecting the center of mass of each particle.

8.2 Theoretical methods

Let us consider two arbitrarily-shaped particles immersed in a viscous fluid. Particles 1 and 2 are subjected to external forces $\boldsymbol{F}_1$ and $\boldsymbol{F}_2$, respectively; the centers of mass of the particles are connected by vector $\boldsymbol{r}$. (The forces may result from the presence of the particles in a gravitational or electromagnetic field.) I shall assume that we are in the creeping flow regime, such that inertial forces on both the fluid and the particles are negligible compared to viscous forces. In this regime, there is a linear relationship between the forces on the particles and their velocities,

$$\begin{bmatrix} \boldsymbol{U}_1 \\ \boldsymbol{U}_2 \end{bmatrix} = \begin{bmatrix} \mathbf{M}_{11} & \mathbf{M}_{12} \\ \mathbf{M}_{21} & \mathbf{M}_{22} \end{bmatrix} \cdot \begin{bmatrix} \boldsymbol{F}_1 \\ \boldsymbol{F}_2 \end{bmatrix} \tag{8.1}$$

where $\mathbf{M}_{ij}$ is the mobility tensor that relates the force on particle j to the velocity of particle i. The mobility tensors are functions of the size and shape of both particles and the distance between them. As $r \to \infty$, hydrodynamic interactions between particles become negligible. In this case, $\mathbf{M}_{12} = \mathbf{M}_{21} \approx \mathbf{0}$, and the mobility tensors $\mathbf{M}_{11}$ and $\mathbf{M}_{22}$ are simply the inverses of the translational friction tensors $\boldsymbol{\Xi}_t$ for particles 1 and 2, defined by the relation

$$\boldsymbol{F} = -\boldsymbol{\Xi}_t \cdot \boldsymbol{U} = -\mathbf{M}_{ii}^{-1} \cdot \boldsymbol{U} \tag{8.2}$$

My goal is to determine the mobility tensors for particles in the transition flow regime as a function of particle size, shape, and separation distance. Before tackling this problem, it is worth considering the simpler case of two spheres in continuum flow. From there, I will describe how one can approach the problem for fractal aggregates in the continuum, before discussing how to apply the extended Kirkwood-Riseman method for particles in the transition regime.

8.2.1 Two spheres in continuum flow

The instantaneous velocity of two spheres subjected to external forces $\boldsymbol{F}_1$ and $\boldsymbol{F}_2$ has been studied by a number of authors [49, 97, 130, 131, 134, 137]. Exact solutions are available for two spheres moving parallel and perpendicular to their line of centers. For arbitrary $\boldsymbol{r}$, the problem can be solved using the method of reflections, whereby the mobility tensors are determined as expansions in powers of the inverse of interparticle separation distance r. (See Happel and Brenner [49]

for more information about the method of reflections, including its application to the two-sphere problem and to the problem of a particle in a tube.) Since the mobility tensors are symmetric about the line of centers connecting the spheres, we can formally write

$$\mathbf{M}_{ij} = A_{ij}\frac{\boldsymbol{rr}}{r^2} + B_{ij}\left(\mathbf{I} - \frac{\boldsymbol{rr}}{r^2}\right) \tag{8.3}$$

where the non-dimensional coefficients A_{ij} and B_{ij} can be written as expansions in powers of r^{-n},

$$A_{ij} = \sum_{n=0}^{\infty} a_{ij,n} r^{-n} \tag{8.4a}$$

$$B_{ij} = \sum_{n=0}^{\infty} b_{ij,n} r^{-n} \tag{8.4b}$$

One obtains the coefficients $a_{ij,n}$ and $b_{ij,n}$ from the method of reflections.

One can include successive terms in the expansions for A_{ij} and B_{ij} to obtain increasingly accurate results for the mobility tensors. The simplest approach is the point force approximation, where $\mathbf{M}_{ii} = \zeta_i^{-1}\mathbf{I}$, $\mathbf{M}_{ij}$ is given by the Oseen tensor (the r^{-1} term in Eq. (8.5) below), and $\zeta_i = 6\pi\mu a_i$ is the monomer friction coefficient for a sphere with radius a_i. The next level of approximation yields $\mathbf{M}_{ii} = \zeta_i^{-1}\mathbf{I}$ and

$$\begin{aligned}
\mathbf{M}_{ij} &= \frac{1}{8\pi\mu r}\left[\left(\mathbf{I} + \frac{\boldsymbol{rr}}{r^2}\right) + \left(\frac{a_i^2 + a_j^2}{3r^2}\right)\left(\mathbf{I} - \frac{3\boldsymbol{rr}}{r^2}\right)\right] \\
&= \frac{1}{8\pi\mu r}\left[\left(1 - \frac{a_i^2 + a_j^2}{3r^2}\right)\frac{2\boldsymbol{rr}}{r^2} + \left(1 + \frac{a_i^2 + a_j^2}{3r^2}\right)\left(\mathbf{I} - \frac{\boldsymbol{rr}}{r^2}\right)\right]
\end{aligned} \tag{8.5}$$

for $i \neq j$. For $a_i = a_j$, Eq. (8.5) reduces to the Rotne-Prager-Yamakawa tensor [57, 58]. Batchelor [134] provides expressions for the mobility tensors accurate to

order r^{-5}, while Felderhof [97] uses the method of reflections to derive expressions valid to order r^{-7} for mixed slip-stick boundary conditions. Results from Felderhof's interaction tensor are equal to available exact solutions to the two-sphere problem except for very small separation distances (i.e. nearly touching spheres), where higher order terms become important [97].

Note that if sphere 2 is much smaller than sphere 1 (i.e. $a_2 \ll a_1$) and if r is large enough that terms higher than order r^{-3} are negligible, sphere 2 will simply be advected by the Stokes velocity field generated by sphere 1. This becomes clear solving Eq. (8.1) for $\boldsymbol{U}_2$ with $\boldsymbol{F}_2 = \boldsymbol{0}$, $\boldsymbol{F}_1 = 6\pi\mu a_1 \boldsymbol{U}_1$, and using Eq. (8.5) for $\mathbf{M}_{21}$ with $a_2 \ll a_1$:

$$\boldsymbol{U}_2 = \left[\frac{3a_1}{4r}\left(\mathbf{I} + \frac{\boldsymbol{r}\boldsymbol{r}}{r^2}\right) + \frac{a_1^3}{4r^3}\left(\mathbf{I} - \frac{3\boldsymbol{r}\boldsymbol{r}}{r^2}\right)\right] \equiv \mathbf{V}(\boldsymbol{r}) \cdot \boldsymbol{U}_1 \tag{8.6}$$

Here, $\mathbf{V}(\boldsymbol{r}) \cdot \boldsymbol{U}_1$ is the Stokes velocity field around a sphere moving with velocity $\boldsymbol{U}_1$. I will refer to $\mathbf{V}(\boldsymbol{r})$ as the Stokes tensor.

Any of the above expressions for the mobility tensors can be used to solve the two sphere problem for arbitrary sphere sizes a_1 and a_2 (provided the continuum approximation is still valid), center-to-center distance and orientation $\boldsymbol{r}$, and external forces $\boldsymbol{F}_1$ and $\boldsymbol{F}_2$. Tables 8.1-8.3 show results for the speed of each sphere as a function of separation distance for equal-sized spheres and equal force magnitude. (For $a_1 = a_2$, the speeds of the spheres are equal.) The tables include results for the exact solutions to the two-sphere problem [130, 132, 133], the mobility expression of Felderhof for stick boundary conditions [97], and my EKR method (i.e. using

r/a	Exact	Felderhof	EKR
2	1.550	1.623	1.688
2.01	1.549	1.618	1.685
2.1	1.536	1.582	1.660
2.5	1.486	1.493	1.568
3	1.432	1.433	1.481
3.5	1.386	1.386	1.417
4	1.347	1.347	1.367
5	1.287	1.287	1.296
7	1.210	1.210	1.213
10	1.149	1.149	1.150
15	1.100	1.100	1.100

Table 8.1: Speed of two spheres moving parallel to their line of centers, relative to the speed of isolated spheres subjected to the same external force. The EKR or Stokes tensor solution refers to $\mathbf{M}_{ii} = \zeta_i^{-1}$ and $\mathbf{M}_{ij} = \zeta_i^{-1}\mathbf{V}(\boldsymbol{r})$, where $\mathbf{V}(\boldsymbol{r})$ is defined in Eq. (8.6). The Felderhof tensors [97] are accurate to order r^{-7}. The exact solution is given by Stimson and Jeffery [130].

the Stokes tensor) for the three cases shown in Figure 8.1. In all cases, the Stokes tensor results are in very good agreement (less than 1% difference) with the exact results for > 5. As expected, the error is more significant for smaller separation distances because the Stokes tensor does not include terms of order r^{-4} and higher and because there is a missing factor of 2 in the r^{-3} term.

8.2.2 Aggregates in continuum flow

Experiments and simulations have shown that particles formed by diffusion-limited cluster aggregation have a fractal morphology with fractal dimension $d_f \approx 1.78$ and prefactor $k_0 \approx 1.3$ [4]. These parameters relate the radius of gyration to the number of spheres in the aggregate,

$$N = k_0 \left(\frac{R_g}{a} \right)^{d_f} \tag{8.7}$$

r/a	Exact	Felderhof	EKR
2	0.000	0.080	0.313
2.01	0.019	0.089	0.315
2.1	0.135	0.161	0.340
2.5	0.361	0.360	0.432
3	0.491	0.490	0.519
3.5	0.570	0.570	0.583
4	0.626	0.626	0.633
5	0.702	0.702	0.704
7	0.787	0.787	0.787
10	0.851	0.851	0.851
15	0.900	0.900	0.900

Table 8.2: Speed of two spheres moving anti-parallel to their line of centers, relative to the speed of isolated spheres subjected to the same external force. The exact solution is given by Brenner [132].

r/a	Exact	Felderhof	EKR
2	1.380	1.421	1.406
2.01	1.403	1.419	1.404
2.1	1.392	1.399	1.384
2.5	1.326	1.328	1.316
3	1.267	1.267	1.259
3.5	1.225	1.225	1.220
4	1.195	1.195	1.191
5	1.154	1.154	1.152
7	1.109	1.109	1.108
10	1.075	1.075	1.075
15	1.050	1.050	1.050

Table 8.3: Speed of two spheres moving perpendicular to their line of centers, relative to the speed of isolated spheres subjected to the same external force. The exact solution is given by Goldman et al. [133].

Notable examples of DLCA aggregates include soot, as well as titania and other ceramic powders synthesized in aerosol flame reactors [7].

In the previous section, I reviewed how one can solve the two sphere problem to various levels of approximation. I now describe how to use a similar approach for aggregates.

In approaches based on Kirkwood-Riseman theory [28], one uses any of the above expressions for the interactions between pairs of spheres to determine the force on a macromolecule or particle consisting of N spherical subunits. The resulting system of equations is analogous to Eq. (8.1):

$$-\boldsymbol{U}_i = \sum_{j=1} \mathbf{M}_{ij} \cdot \boldsymbol{F}_j \tag{8.8}$$

Here, $\boldsymbol{F}_j$ is the force exerted by the fluid on the jth primary sphere in an aggregate, which is unknown, whereas in Eq. (8.1) $\boldsymbol{F}_j$ represents the known external force on the jth particle in a two-particle system. (The negative sign appearing in Eq. (8.8) is a consequence of the shift from the force exerted by the particle – as in Eq. (8.1) – to the force exerted on the ith primary sphere by the fluid.) To determine the force on a macromolecule or particle whose subunits have velocities $\boldsymbol{U}_i$, one solves the above linear system for the force on each sphere, then sums over all spheres to get the total force. Alternatively, if the total external force on the particle is given (e.g. gravity or the force on charged particle in an electric field), one can solve Eq. (8.8) iteratively to get the particle velocity such that the calculated force distribution is consistent with the total force.

KR-based treatments rely on the underlying linearity of the Stokes flow equations. In their original formulation, Kirkwood and Riseman [28] set $\mathbf{M}_{ij} = \delta_{ij}\zeta_i^{-1} + (1 - \delta_{ij})\mathbf{T}_{ij}$, where δ_{ij} is the Kronecker delta and $\mathbf{T}_{ij}$ is the Oseen tensor. Later applications of KR theory [30, 56, 107] replace the Oseen tensor with the Rotne-Prager-Yamakawa tensor. One can use higher order approximations for the mobility tensors (e.g. the Felderhof expressions); one can also account for multi-body effects using mobility tensors derived by Mazur and Van Saarloos [60]. However, Carrasco and Garcıa de la Torre [53] have shown that using these more rigorous methods to calculate a particles friction and diffusion tensors offer little improvement over using KR-theory with the Rotne-Prager-Yamakawa tensor.

One can use the same KR-based methods to determine the forces between two aggregates: one again solves the system of equations given by Eq. (8.8), but now one sums over the spheres in each aggregate to determine the total hydrodynamic force. Again, one can perform this calculation for aggregates with specified velocities or specified external forces. By comparing this result to the force on an isolated aggregate, one can determine the effect of the second aggregate on the mobility of the first.

8.2.3 Extended Kirkwood-Riseman theory

The previous subsections have focused on situations where the continuum approach is valid. For particles consisting of spheres with diameters on the order of tens of nanometers moving through air at standard temperature and pressure ($\lambda \approx 67$ nm), one cannot use the expressions for interactions between particles in

the continuum, but one can use the same general Eq. (8.8) relating the velocity of particles in the transition regime to the drag forces exerted on the particles by the fluid. One only needs to determine the mobility tensors as a function of the primary sphere Knudsen numbers.

Noting that the Stokes velocity tensor provides a reasonable approximation for the mobility tensor between two spheres in the continuum (see Tables 8.1-8.3), I [92] proposed replacing the Stokes velocity tensor with a Knudsen-number-dependent velocity tensor obtained by solving the Bhatnagar-Gross-Krook (BGK) equation [71] for flow around a sphere. (The BGK equation is a simplified, linearized version of the Boltzmann transport equation that is valid for near-equilibrium situations [72]). Velocities calculated using the BGK equation compare well to solutions of the linearized Boltzmann equation [77, 78].) The resulting set of equations relating the sphere velocities to the drag is

$$\boldsymbol{F}_i = -\zeta_i(\mathrm{Kn}_i)\boldsymbol{U}_i - \zeta_i(\mathrm{Kn}_i)\sum_{i\neq j}^{N}\zeta_j^{-1}(\mathrm{Kn}_j)\mathbf{V}_{ij}(\mathrm{Kn}_j)\cdot\boldsymbol{F}_j \tag{8.9}$$

Note that the force on sphere i depends on the friction coefficient for sphere i and the velocities around the other j spheres.

My previous work [92, 93] has demonstrated that using the velocity and drag results from the BGK equation and solving Eq. (8.9) yields accurate results for the translational friction coefficient of fractal aggregates across the entire Knudsen regime. This suggests that the EKR method can be used to determine the hydrodynamic forces between particles in the kinetic regime.

8.2.4 Point force approach

If one is only concerned about interactions between widely separated particles, the analysis can be greatly simplified by treating the particles as point forces. In the continuum, the flow field generated by the point force is often called the Stokeslet and can be written as

$$\boldsymbol{u}(\boldsymbol{r}) = \frac{1}{8\pi\mu r}\left(\mathbf{I} + \frac{\boldsymbol{r}\boldsymbol{r}}{r^2}\right) \cdot \boldsymbol{F} \tag{8.10}$$

where the term multiplying the point force is the Oseen tensor. If the object is a sphere, $\boldsymbol{F}$ is given by Stokes law, and Eq. (8.10) gives the flow field for large r. Interestingly, this flow field is valid regardless of the shape of the object exerting the force on the fluid. This means that the flow field far from an object looks like the flow around a sphere exerting the same force on the fluid as the object, even when the object is highly non-spherical. This behavior is due to viscous effects in the fluid.

Based on the preceding discussion, we can determine the interactions between the aggregates using a point force approach, such that the total hydrodynamic force on each aggregate can be obtained by simultaneously solving the following equations:

$$\boldsymbol{F}_i = -\boldsymbol{\Xi}_{i,0} \cdot \boldsymbol{U}_i - \boldsymbol{\Xi}_{i,0} \cdot \sum_{i \neq j}^{N} \left[\frac{1}{8\pi\mu r_{ij}}\left(\mathbf{I} + \frac{\boldsymbol{r}\boldsymbol{r}}{r^2}\right)\right] \cdot \boldsymbol{F}_j \tag{8.11}$$

Here, N is the number of `aggregates` in the system, $\boldsymbol{r}_{ij}$ is the vector between the center of mass of ith and jth aggregates and $\boldsymbol{\Xi}_{i,0}$ is the translational friction tensor for aggregate i when it is alone in an infinite fluid. Mackaplow and Shaqfeh [138]

demonstrated that the point force approach applied to the problem of sedimentation of fibers in a semi-dilute homogeneous suspension, yields results similar to those of a more sophisticated Monte Carlo simulation of the problem.

The point force approach should also be valid in the transition regime, albeit with a Knudsen-number-dependent hydrodynamic interaction tensor in place of the Oseen tensor. In fact, the transition regime interaction tensor should have the same form as the Oseen tensor but with a different coefficient in place of 1/8. This is because the fluid velocity far from a sphere has the general form

$$\boldsymbol{u}(\boldsymbol{r}) = -\frac{c_1(\mathrm{Kn})}{2}\frac{a}{r}\left(\mathbf{I}+\frac{\boldsymbol{r}\boldsymbol{r}}{r^2}\right)\cdot\boldsymbol{U} = -\frac{c_1(\mathrm{Kn})}{2\zeta_{i,0}(\mathrm{Kn})}\frac{a}{r}\left(\mathbf{I}+\frac{\boldsymbol{r}\boldsymbol{r}}{r^2}\right)\cdot\boldsymbol{F} \tag{8.12}$$

where $\boldsymbol{U}$ is the sphere velocity, $\boldsymbol{F}$ is the force exerted by the sphere on the fluid, and $c_1(\mathrm{Kn})$ is a coefficient that can be obtained by solving the BGK or linearized Boltzmann equation for flow around a sphere [78, 92]. In the continuum, $c_1 = -3/2$, and Eq. (8.12) reduces to Eq. (8.10).

Substituting Eq. (8.12) for the Oseen tensor in Eq. (8.11), we get the following result for a system of N aerosol aggregates:

$$\boldsymbol{F}_i = -\boldsymbol{\Xi}_{i,0}(\mathrm{Kn}_i)\cdot\boldsymbol{U}_i - \boldsymbol{\Xi}_{i,0}(\mathrm{Kn}_i)\cdot\sum_{i\neq j}^{N}\left[-\frac{c_1(\mathrm{Kn}_{j,\mathrm{eff}})}{2\zeta_{j,0}}\left(\mathbf{I}+\frac{\boldsymbol{r}\boldsymbol{r}}{r^2}\right)\right]\cdot\boldsymbol{F}_j \tag{8.13}$$

Here, $a_{j,\mathrm{eff}}$ is the radius and $\mathrm{Kn}_{j,\mathrm{eff}} = \lambda/a_{j,\mathrm{eff}}$ the Knudsen number of a sphere with friction coefficient $\zeta_{j,0} = |\boldsymbol{\Xi}_{j,0}(\mathrm{Kn}_j)\cdot\boldsymbol{U}_j/\boldsymbol{U}_j|$, where $\boldsymbol{\Xi}_{j,0}(\mathrm{Kn}_j)$ is the friction tensor for aggregate j alone in an infinite fluid and $\boldsymbol{U}_j$ is the velocity of aggregate j. One

solves implicitly for the effective radius of the cluster,

$$\zeta_{j,0}(\mathrm{Kn}_{j,\mathrm{eff}}) = \frac{6\pi\mu a_{j,\mathrm{eff}}}{C_c(\lambda/a_{j,\mathrm{eff}})} \tag{8.14}$$

where C_c is the Cunningham slip correction factor. I have explicitly stated the dependence of the aggregate friction tensors on the Knudsen number of the primary spheres in the aggregate; of course, the friction tensor also depends on the number of spheres in the aggregate and the configuration of those spheres. Note that Eq. (8.14) accounts for the orientation of each cluster through the use of the friction tensors, and by determining the effective radius based on the drag force for a particular aggregate orientation relative to the flow. However, one can further simplify Eq. (8.13) by replacing the friction tensors with the scalar friction coefficients based on orientation averages for the particles. This simplification is justified for aerosol particles due to the randomizing effects of Brownian forces.

To apply the point force approximation for a system of aggregates in the transition regime, one must first determine the friction tensor for each aggregate [e.g. by solving Eq. (8.9)]. Next, one must determine the effective sphere radius for each aggregate. One obtains the coefficient $c_1(\mathrm{Kn}_{j,\mathrm{eff}})$ for each aggregate from a table of BGK or linearized Boltzmann results. With this information, one can solve Eq. (8.13) for the hydrodynamic forces on the system of aggregates. Again, one can replace the friction tensors with the scalar friction coefficient for each aggregate. One can use the adjusted sphere method [41, 67] or my EKR method [92] to quickly determine the friction coefficient for each aggregate, which significantly reduces the

complexity of the problem.

Using the point force approach is beneficial because one can significantly reduce the number of simultaneous equations that one must solve compared to considering the pairwise interactions among all of the spheres in all of the aggregates. This is especially useful if one is considering a system consisting of identical aggregates (such that one need only determine the friction tensor once) or if one is considering interactions between coagulating aerosols (such that the friction tensors for the aggregates remain constant until two particles coagulate, at which point one need only calculate the friction tensor for the new particle). While the point force approach is strictly valid only for widely separated particles, I will show in the following section that this approach provides reasonable results even when the aggregates are fairly close together.

8.3 Two particle results

I have used my extended Kirkwood-Riseman method [Eq. (8.9)] to determine the hydrodynamic forces between two aggregates moving parallel, anti-parallel, and perpendicular to their line of centers in the transition flow regime. I start by considering two spheres, then move to the case of two fractal aggregates. For simplicity, I will focus on cases where the two particles are identical, though I do consider the effects of orientation for the aggregate calculations.

8.3.1 Sphere results

Figure 8.2 shows the results for two spheres moving parallel, anti-parallel, and perpendicular to their line of centers. Results are plotted as a function of separation distance for three different Knudsen numbers. Here, I show the ratio of the velocity of each sphere subjected to the same external force (albeit in opposite directions for the anti-parallel case) to the velocity it would have if was alone in an infinite medium subjected to the same force. Note that one can obtain the effect on the hydrodynamic force for specified velocity by taking the inverse of the results in Figure 2. I also present the velocities calculated using Felderhofs mobility tensors [97] for mixed slip-stick boundary conditions for Kn = 0.1. These tensors are accurate to order r^{-7} and are expected to yield nearly exact results except for very small separation distances for this near-continuum situation.

The figure shows that my EKR results are in good agreement with the Felderhof mobility tensor results for near-continuum conditions (or near-stick boundary conditions, in the case of the Felderhof results). For $r/a > 3$, the two methods yield results within about 2% of each other; this is not surprising, since the higher order terms in the expansions representing the mobility tensors decay quickly with increasing separation. The error is still fairly low ($< 8\%$) for touching spheres moving parallel and perpendicular to their line of centers but is much more significant for the anti-parallel configuration. This is because my EKR method ignores lubrication forces between the particles, whereas Felderhofs mobility tensors partially account for these forces through the higher order terms in the expansion.

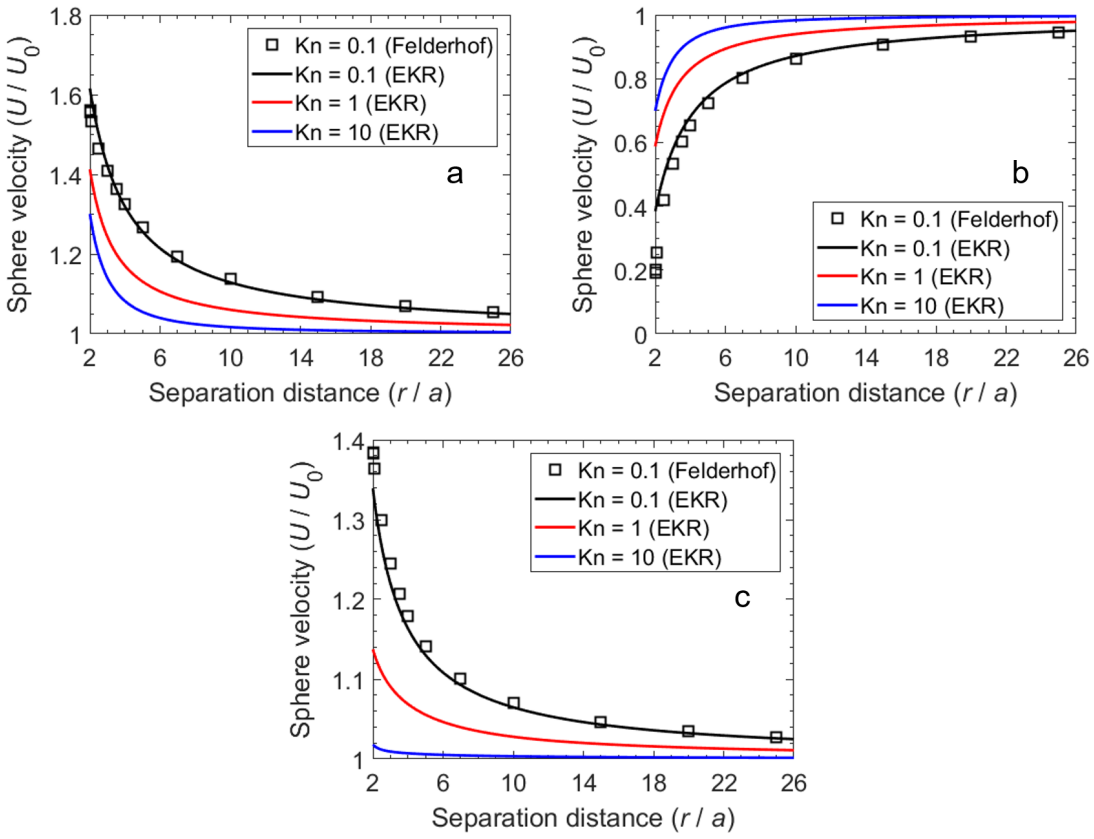

Figure 8.2: Speed of two spheres moving (a) parallel, (b) anti-parallel, and (c) perpendicular to their line of centers, relative to the speed of isolated spheres subjected to the same external force. Results using the mobility tensors of Felderhof [97] for mixed slip-stick boundary conditions are shown for comparison to the Kn = 0.1 results. Note that for the Felderhof calculations I use a slip length of 0.9875 times the gas mean free path based on the best-estimate results of Loyalka [139].

As expected, the strength of the hydrodynamic interactions between spheres decreases with increasing Knudsen number. For the perpendicular configuration, the two spheres behave almost as if they are isolated even when they are in contact at high Knudsen number; the effect is more important in the parallel and anti-parallel configurations, likely due to direct shielding of incoming gas molecules by the other sphere and molecules that collide with both spheres before colliding with other gas molecules.

As we saw in the previous section, the long-range hydrodynamic interactions have a r^{-1} dependence in the continuum, as given by the Oseen tensor. The r^{-1} dependence is also evident in my transition regime results in Figure 8.2. The coefficient of the r^{-1} term is a function of the Knudsen number. This result is directly related to the asymptotic behavior of the velocity field at large distances from a sphere, as I have discussed in Section 8.2.4 above.

8.3.2 Aggregate results

Figure 8.3 shows the results for two aggregates moving parallel to their line of centers. Results are shown for two aggregates with 10 spheres each and for two aggregates with 1000 spheres. The results are presented as the ratio of the drag on one of the aggregates to the drag on that aggregate when it is alone in an infinite fluid. Solid lines represent the full EKR solution [Eq. (8.9)], while the dotted lines represent the point force results [Eq. (8.13)]. From the figures, the point force solution is sufficiently accurate for all but the closest separations, which greatly simplifies any analysis of the effects of hydrodynamic interactions between aggregates. Also,

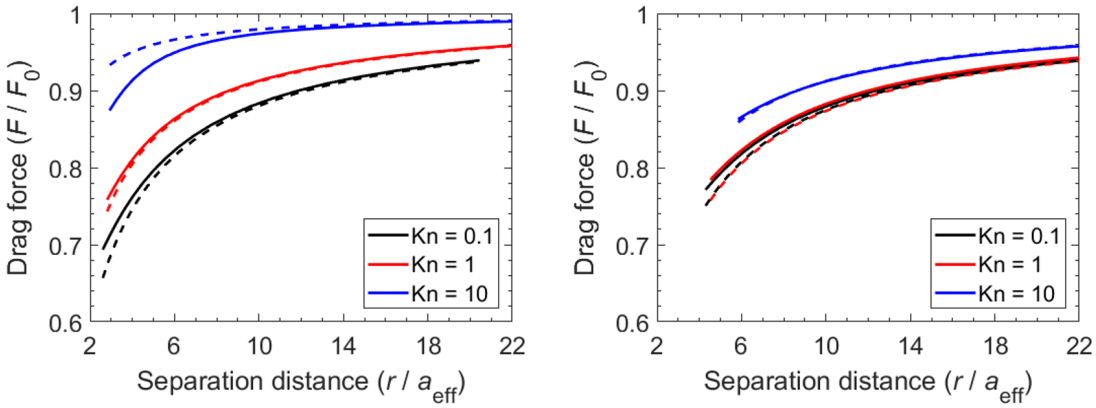

Figure 8.3: Hydrodynamic force on an aggregate as a function of the distance between its center of mass and the center of mass of an identical aggregate. The left plot shows results for $N = 10$, while the right plot shows results for $N = 1000$. The solid lines represent the full EKR results [Eq. (8.9)], while the dotted lines represent the point force results [Eq. (8.13)]. The drag force is normalized by the drag on one of the aggregates in an infinite fluid, while the separation distance is presented as the number of effective sphere radii (i.e. the radius of a sphere experiencing drag force F_0) between the centers of mass of the particles.

the aggregates exhibit more continuum-like behavior as the number of spheres in the aggregate increases, which is analogous to the behavior I have observed for the translational and rotational friction coefficients of DLCA aggregates (Chapters 4 and 6).

Figure 8.3 presents the results for aggregates with a fixed orientation. Figure 8.4 explores the effect of orientation on the reduction in the drag force for $N = 500$ and a primary sphere Knudsen number of 2.7. Results are shown for two aggregates with a shape anisotropy $A_{31} = 2.0$ and for two aggregates with $A_{31} = 6.5$, where A_{31} is the ratio of the largest to smallest eigenvalues of the inertia tensor of the particle. Since each cluster in the first pair is fairly isotropic (A_{31} near unity), there is little change in the hydrodynamic force on each cluster as the particles rotate. In contrast, there is a noticeable difference in hydrodynamic force as the more

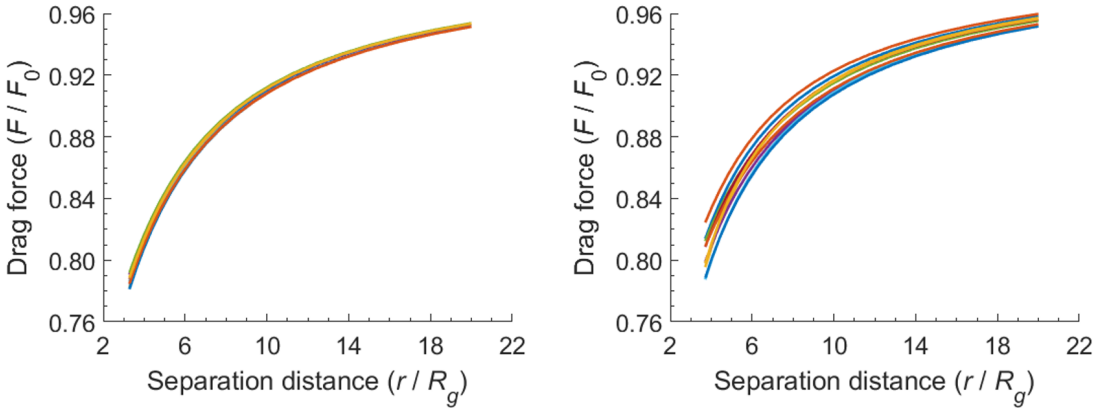

Figure 8.4: Effects of orientation on the hydrodynamic force on one of two 500-sphere aggregates with primary sphere Kn = 2.7 (sphere radius of 25 nm at room temperature). Results are presented as the ratio of the force on an aggregate for the specified separation distance to the force on the aggregate alone in an infinite fluid at a particular orientation. Each line represents a randomly chosen orientation for each aggregate in the two-aggregate system. The left figure is for an aggregate with anisotropy $A_{31} = 2.0$, while the right figure is for an aggregate with $A_{31} = 6.5$.

anisotropic particles rotate. This is especially true for small separation distances. Note that in each case I normalize by the force on the particle for that particular orientation.

8.4 Discussion

My results show that hydrodynamic interactions between particles in the transition flow regime are significant for small separation distances and still noticeable at separations of more than 10 sphere diameters or 20 times the radius of gyration of an aggregate. The effect is stronger near the continuum than near the free molecule regime and stronger for parallel and anti-parallel configurations than for perpendicular configurations for all particle sizes.

With that said, hydrodynamic interactions likely have little effect on mea-

surable quantities of interest (e.g. deposition and coagulation rates) except in very dense aerosol systems, due to the large average particle separations in most practical systems. As an example, consider an aerosol consisting of spherical particles with volume fraction ϕ. The average spacing between the particles is $\bar{L}/a = (4\pi/3\phi)^{1/3}$, so at a relatively high volume fraction of 10^{-4}, the average spacing approximately 35 sphere radii. Near the continuum, the hydrodynamic force between spheres is less than 5% of the external force generating the sphere motion; this ratio decreases with increasing Knudsen number.

Of course, aerosol particles are not arranged in a grid, with equal spacing between particles. Still, the expressions for the settling velocity and suspension viscosity in the introduction account for the probability distribution of sphere locations in a suspension. Thus, interparticle hydrodynamic interactions have very little impact on these parameters for an aerosol consisting of spherical particles at typical volume fractions.

The situation is more complicated for fractal aggregates due to the difference between the fractal dimension and the spatial dimension. To understand why, let us consider an aerosol consisting of a large number of identical N-sphere aggregates. The average distance between the centers of mass of the aggregates is simply $\bar{L}/a = (4\pi N/3\pi)^{1/3}$, regardless of the fractal dimension of the aggregates. Now let us rewrite the average spacing in terms of the radius of gyration:

$$\frac{\bar{L}}{R_g} = \frac{(4\pi N/3\phi)^{1/3}}{(N/k_0)^{1/d_f}} = \left(\frac{4\pi k_0^{3/d_f}}{3\phi}\right)^{1/3} N^{\frac{d_f-3}{3d_f}} \tag{8.15}$$

Here, k_0 and d_f are the prefactor and fractal dimension of the aggregates. For DLCA aggregates ($k_0 \approx 1.3$, $d_f \approx 1.78$), and for a volume fraction of 10^{-4}, the average spacing between aggregates is 24 radii of gyration for $N = 10$ and 8.3 radii of gyration for $N = 1000$. Since the radius of gyration is approximately equal to the effective hydrodynamic radius of a particle in continuum flow, we can consult the near-continuum results in Figure 8.3 to estimate the hydrodynamic force between the aggregates in the parallel flow configuration at these average separation distances. For $N = 1000$, the drag force for the parallel configuration is approximately 85% of the drag at infinite separation distance for Kn = 0.1. Compare this to the result for a system of spheres in continuum flow, where the average separation is 34 radii, and the force at this separation is 96% of the force at infinite separation for Kn = 0.1.

8.4.1 Aerosol clouds

One interesting problem involving hydrodynamic interactions among particles is the settling of an unbounded aerosol cloud in a gravitational field. This problem has been studied extensively for spherical particles in the continuum. (For a small sample, refer to the works of Burgers [131] or to Fuchs [1].) The behavior of the particle cloud depends on the volume fraction of particles in the cloud. For sufficiently low volume fractions, the particles behave as if they are isolated, as one would expect. In this case, the velocity of each particle is obtained by balancing the gravitational force F_g with the drag force,

$$v_{s1} = \frac{F_g}{\zeta_0} \tag{8.16}$$

For high volume fractions, the particles entrain the surrounding fluid, and the cloud behaves as a gas bubble with the same viscosity as the fluid surrounding the cloud [1, 131]. In this case, the velocity of the cloud is given by

$$v_{s2} = \frac{\frac{4}{3}\pi R^3 n F_g}{5\pi\mu R} = \frac{4R^2 n F_g}{15\mu} \tag{8.17}$$

where R is the radius of the cloud and n is the number concentration of particles. In the first equality, I explicitly write the velocity as the ratio between the total gravitational force on the cloud and the drag on a spherical bubble with equal viscosity in the inner and outer fluids. The particles behave as if they are isolated when $v_{s2}/v_{s1} \ll 1$ and as a cloud with velocity given by Eq. (8.17) when $v_{s2}/v_{s1} \gg 1$ [1].

The above analysis is applicable for aggregates in continuum flow, with a few important caveats. First, one must use appropriate values for the gravitational and drag forces on the aggregate. Second, the effects of the aggregates on the effective viscosity of the cloud must be negligible; of course, this restriction also applies to the aforementioned case of spherical particles. Additionally, I will ignore the effects of hydrodynamic interactions on the orientation of the aggregates. I will address this restriction in more detail in the following section. With the above caveats, we can write the ratio v_{s2}/v_{s1} for a cloud consisting of identical N-sphere aggregates as

$$\frac{v_{s2}}{v_{s1}} = \frac{6\phi\zeta_0^\star R^2}{5Na^2} \tag{8.18}$$

where $\zeta_0^\star \equiv 6\pi\mu a\zeta_0$ is the non-dimensional friction coefficient for the aggregate when it is alone in an infinite fluid. Note that the volume fraction is simply the number density times the volume of one aggregate, i.e. $\phi = \frac{4}{3}\pi a^3 Nn$.

Now, I will consider whether or not the above analysis applies to particles – whether spheres or aggregates – in the transition regime. (Again, if one wishes to consider aggregates, the analysis is subject to the caveats mentioned above for particles in continuum flow.) To do so, I will consider an idealized situation: a cloud of radius R that consists of identical particles in a cubic lattice. For this problem, each particle experiences the same external force, so we can directly solve Eq. (8.13) for the velocity of each particle in the cloud, $\boldsymbol{U}_i$. If Fuchs analysis is applicable for particles in the transition regime, then the calculated velocity should approach that given by Eq. (8.17) when the ratio v_{s2}/v_{s1} [Eq. (8.18)] is much greater than unity and should approach F_g/ζ_0 when the result of Eq. (8.18) is much less than unity.

Figure 8.5 shows the average particle velocity in the aerosol cloud as a function of the aerosol volume fraction. The calculations are performed for 25-nm-radius spheres (Kn = 2.7) and a 25-m-radius cloud. Average velocities are normalized by the settling velocity of an isolated sphere (i.e. by v_{s1}). The figure shows that for $v_{s2}/v_{s1} \gg 1$, the average velocity of particles in the cloud approaches v_{s2}, and for $v_{s2}/v_{s1} \ll 1$, the particles behave as if they are isolated.

These results show that a cloud of aerosol particles can behave as a gas droplet in continuum flow even when the individual particles are small relative to the mean free path of the gas. This occurs for sufficiently large cloud sizes and particle volume fractions.

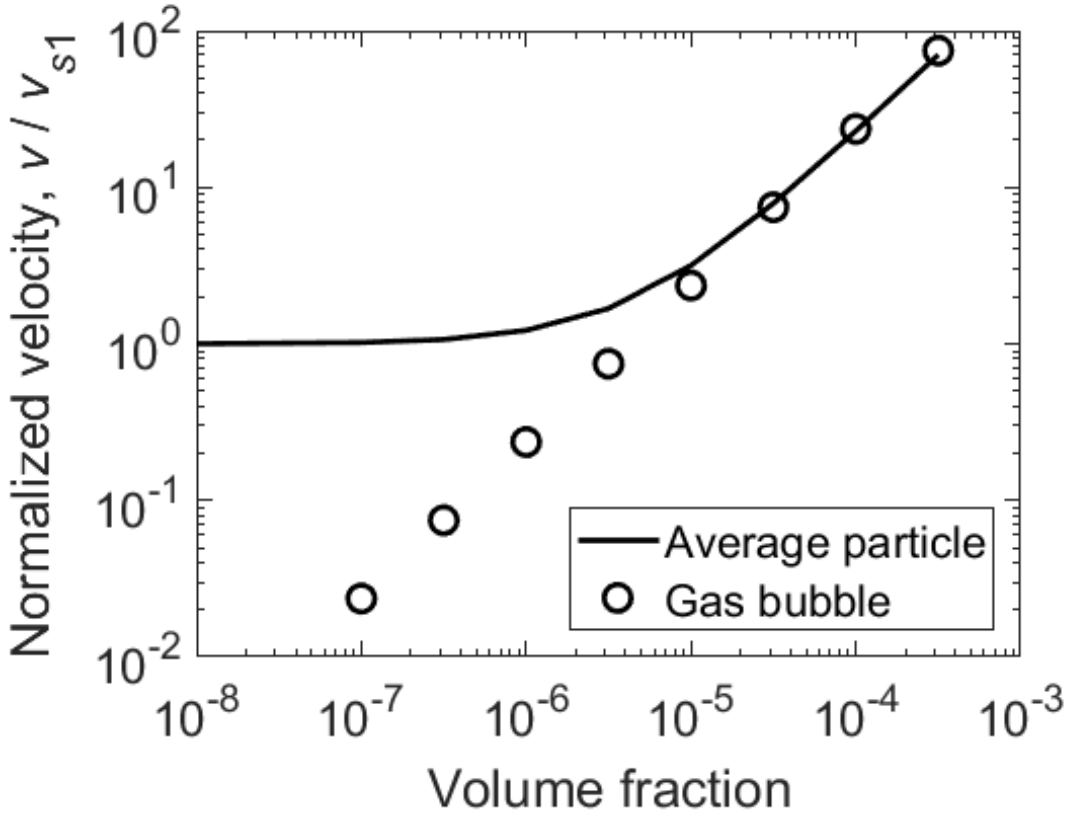

Figure 8.5: Average velocity for a cloud of spheres, normalized by the settling velocity of a single particle, v_{s1}. The velocity of a gas bubble having the same volume fraction and cloud radius is also shown. For $v_{s2}/v_{s1} \gg 1$, the average velocity approaches the gas bubble velocity, and the two curves coincide. For $v_{s2}/v_{s1} \ll 1$, the particles behave as if they are isolated.

Of course, in real-world situations the cloud will not be perfectly spherical, nor will it be composed of monodisperse particles arranged in a regular grid. Nevertheless, we can reach some qualitative conclusions about the behavior of a real-world cloud of aerosol particles from the results of the ideal case. First, the deposition velocity of the particles in the cloud may be significantly greater than the deposition velocity of an isolated particle. This enhanced settling velocity is due to the fact that the particles entrain the surrounding fluid. Second, a collection of particles that behave as if they are in the transition flow regime when they are isolated (or when the volume fraction is very small) can behave like a cloud of continuum particles when the particle volume fraction increases. This is because the long-range hydrodynamic interactions between particles decay as $1/r$, regardless of the size of the particle relative to the gas mean free path.

8.4.2 Additional considerations

Before concluding, I will address a number of assumptions that I have made for my analysis. First, I have ignored rotational effects when considering interactions between particles. The complete description of two particles has the same general form as Eq. (8.1), but one replaces the 3-element velocity and force vectors with 6-element vectors that include the angular velocity of and torque exerted by the particle, respectively. Likewise, one would need to incorporate rotational effects in the generalized mobility tensors $\mathbf{M}_{ij}$, which now have size 6-by-6. See Brenner [29] or Carrasco and Garcıa de la Torre [53] for the effects of rotation on a single particle in the continuum and my previous work [94] for how one might consider rotational

effects in the kinetic regime. The two-particle principles follow from the application of KR-based theories to single-particle systems.

Second, I have mostly ignored Brownian effects in my calculations, except to note that Brownian forces would likely randomize the orientations of aggregates in an aerosol. Strictly speaking, one must account for hydrodynamic interactions when determining the probability distribution for the particle orientation. For example, Mackaplow and Shaqfeh [138] have performed dynamic simulations showing non-Brownian fibers aligning with gravity due to hydrodynamic effects. Therefore, the orientation of aerosol aggregates will depend on the competition between hydrodynamic effects that tend to align particles and Brownian effects that tend to randomize their orientation. This is analogous to the behavior of a perfectly-conducting aerosol particle in an external electric field [96, 105].

Additionally, Brownian forces affect the spatial distribution of particles in a cloud or suspension. Diffusion is partially responsible (along with shear) for breakup of clouds [1], so the analysis in the previous section applies only for some initial period while the cloud remains intact. For statistically homogeneous systems, one must account for the particle probability distribution when determining suspension behavior. In principle, one can apply the methods used in Stokesian dynamics simulations (see, e.g., Ermak and McCammon [135] and Brady and Bossis [136]) for non-continuum flows, provided one modifies the hydrodynamic interaction terms in the algorithms. I have provided here the translational hydrodynamic interaction tensors, while I describe how to account for rotational and translation-rotation coupling effects elsewhere (Chapter 5).

Third, my calculations have been performed for isothermal conditions. As Fuchs notes, cloud behavior is often driven by temperature differences between the cloud interior and the surrounding gas [1]. Because aerosols are often generated in non-isothermal systems (e.g. flames), one must take care in applying my analysis to real-world systems.

Finally, my calculations assume the particles are in an unbounded, non-periodic system. Note that in periodic, statistically homogeneous suspensions, the sedimentation velocity decreases with increasing particle volume fraction [128]. In contrast, unbounded clouds of particles settle at a faster rate as volume fraction increases, as is clear from Eq. (8.18). The difference is due to the gas behavior: for an unbounded cloud, the gas can flow around the cloud to occupy the space vacated by the settling cloud, whereas the gas must flow between the particles in the opposite direction of the sedimentation velocity. This counter flow serves to reduce the sedimentation velocity of the periodic suspension.

8.5 Conclusions

I have described how one would apply my extended Kirkwood-Riseman theory to interactions between spheres and aggregate particles as a function of the distance between particles and the particle size and shape (number of spheres, primary sphere Knudsen number, fractal dimension). I have provided sample results for the effects of hydrodynamic interactions between two spheres and two aggregates. In both cases, the interactions are weaker than for particles in continuum flow, and the

interaction strength decreases with increasing Knudsen number. Note that in many aerosols of engineering interest, the particle volume fraction is very small, and on average one can rightly neglect these interactions. However, for aerosols near the gel point, such interactions may be important.

I have applied my method to an unbounded cloud of spheres with non-negligible Knudsen numbers and shown that it behaves similarly to a cloud of larger particles. This analysis applies to an isothermal, spherical cloud of particles arranged in a regular grid, but the conclusion that hydrodynamic interactions among a large group of particles can significantly affect settling behavior also applies in less restrictive conditions.

The above work provides some of the hydrodynamic interaction terms necessary to perform a Brownian dynamics simulation of an aerosol consisting of particles with non-negligible Knudsen numbers. One could either apply the point force method described here or my more complicated EKR method to account for Brownian (through the generalized Stokes-Einstein relation; see Ermak and McCammon [135]) and hydrodynamic effects on the aerosol behavior. One can also account for rotational effects using the EKR method, as discussed elsewhere [94]. Taken together, this work can form the basis for a dynamic simulation of a dense aerosol system.

Chapter 9: NGDE: A MATLAB-based Code for Solving the Aerosol General Dynamic Equation

The previous chapters in this dissertation have largely concentrated on single-particle behavior (the exception being the study of interparticle hydrodynamic interactions in Chapter 8). For the present chapter, I will shift my focus to the dynamic behavior of an aerosol system undergoing nucleation, surface growth, and coagulation. Note that this chapter provides the technical background for the NGDE code. The User Manual for the code is included as Appendix F. One can obtain the NGDE code on the Zachariah Group website.

9.1 Introduction

The behavior of an aerosol system is governed by the general dynamic equation [2, 3, 45], which can be written as

$$\frac{\partial n}{\partial t} = \frac{1}{2}\int_0^v \beta(v-v',v')n(v',t)n(v-v',t)\mathrm{d}v' - \int_0^\infty \beta(v,v')n(v,t)n(v',t)\mathrm{d}v' - \frac{\partial}{\partial v}[n(v,t)G(v,t)] + S(v,t) - R(v,t) \quad (9.1)$$

Here, $n(v,t)$ is the particle size distribution (PSD) as a function of time t and particle volume v, where $n(v,t)\mathrm{d}v$ is the number of aerosol particles per unit volume of gas with particle volume between v and $v+\mathrm{d}v$; $\beta(v,v')$ is the collision kernel for particles with volumes v and v'; $G(v,t)$ is the growth rate of particles with volume v due to condensation/evaporation; $S(v,t)$ is the rate at which particles are added to the system (e.g. by homogeneous nucleation); and $R(v,t)$ is the rate at which particles are removed from the system (e.g. by deposition on surfaces). The integrals represent how the size distribution changes due to coagulation.[1]

Eq. (9.1) is non-linear integro-differential equation that can be solved analytically only for a small number of cases. (See, for example, Refs. [140, 141]). Thus, one must typically resort to numerical methods to solve for the evolution of the PSD with time. However, solving the GDE numerically is complicated by the orders-of-magnitude difference in volume between the smallest and largest particles in an aerosol. As suggested by the bounds of the integrals in Eq. (9.1), one must determine the size distribution for an infinite range of particle sizes. Fortunately, the physical characteristics of the system allow one to establish upper and lower bounds for the size distribution. For example, large particles may deposit quickly due to gravitational forces, so one can assume particles greater than some upper bound have an infinite removal rate. On the other hand, no particle can be smaller than a single molecule (ignoring of course the subatomic domain), thus establishing a natural lower bound for the size distribution. In addition, thermodynamic con-

[1]The integrals in Eq. (9.1) only account for growth due to particle-particle collisions. Of course, it is possible that two particles could collide with sufficient energy to break them into smaller particles, but such high-energy collisions are rare in situations of interest to the aerosol scientist and are therefore ignored in Eq. (9.1).

siderations limit the smallest stable size of molecular clusters, such that one can ignore particles consisting of fewer molecules than some critical size. Even with these simplifications, solving the GDE numerically is hardly a trivial endeavor.

This chapter describes a fairly simple method for solving the general dynamic equation: a MATLAB-based code using a nodal method that is similar in principle to the sectional method pioneered by Gelbard and colleagues [26, 142, 143]. The MATLAB version of the NGDE code is based on an earlier version of the code [27] written in C. A number of new features have added to the MATLAB version of the code. The most significant additions are the implementation of a dynamic time-step algorithm that significantly speeds up the calculation run-time and the introduction of a post-processing tool for visualizing the code results.

Before the NGDE code is described in detail, a brief overview of various techniques used to solve the GDE numerically is provided. Next, the constituent models for nucleation, coagulation, and surface growth used in NGDE; the dynamic time-step algorithm; and the available calculation types and general solution procedure are described. Results are presented for a few sample problems. These results are compared to the results of other numerical solutions of the problems published in the literature. The chapter closes with a discussion about the limitations of NGDE and the ways in which one may improve the code, as well as a brief introduction to the post-processing tool NGDEplot. More details about running NGDE, code input and output, and code structure can be found in the NGDE User Manual (Appendix F).

9.2 Overview of Numerical Methods for Solving the GDE

Numerical methods for solving the GDE can be divided into three broad classes: J-space methods, moment methods, and sectional methods [45]. J-space methods [144] involve transforming the continuous PSD to J-space, integrating the J-space distribution function with respect to time, and taking the inverse transform to obtain the PSD as a function of time. Moment methods [145] start by assuming some form for the size distribution and its moments (i.e. the product of the distribution and powers of the particle volume, integrated over all volumes) and involve solving for the evolution of the moments of the size distribution. In addition to the integration schemes needed to solve for the time-dependent evolution of the PSD (e.g. the Euler method or Kunge-Kutta method), both J-space and moment methods require the use of quadrature formulas to integrate the distribution or moment equations with respect to volume. For this reason, these methods are somewhat mathematically complex and can prove a hindrance for the novice aerosol scientist.

On the other hand, sectional methods [26, 142, 143] are more intuitive ways of solving the general dynamic equation that make fewer assumptions about the shape of the size distribution. These methods divide the size distribution into discrete size bins and solve the GDE for each size bin as a system of coupled equations. The number concentration of particles in bin k at time t is defined as

$$N_k(t) = \int_{v_{k-1}}^{v_k} n(v,t)\mathrm{d}v \tag{9.2}$$

where v_{k-1} and v_k are the lower and upper bounds (in terms of volume) of bin k. The evolution of the number concentration of particles in bin k can be written as

$$\frac{\mathrm{d}N_k}{\mathrm{d}t} = \left.\frac{\mathrm{d}N_k}{\mathrm{d}t}\right|_{coag} + \left.\frac{\mathrm{d}N_k}{\mathrm{d}t}\right|_{nucl} + \left.\frac{\mathrm{d}N_k}{\mathrm{d}t}\right|_{growth} + \left.\frac{\mathrm{d}N_k}{\mathrm{d}t}\right|_{dep} \tag{9.3}$$

where the first, second, and third terms on the right-hand-side represent the changes in the number concentration in bin k due to coagulation, nucleation, and surface growth. These terms will be discussed later in this chapter. The final term in the equation represents losses due to deposition. Deposition is not considered in NGDE; nevertheless, this term is included in the above equation for completeness, in case one wishes to include deposition in NGDE in the future. (See Section 9.5.) For the sectional method, one must also track the total volume (or mass) of particles within each size bin,

$$V_k(t) = \int_{v_{k-1}}^{v_k} v n(v,t) \mathrm{d}v \tag{9.4}$$

using an equation similar to the equation above for the number concentration.

One complication inherent in sectional methods is that one must use average properties within each bin to calculate the coagulation and growth rates. For example, consider the increase in the number concentration of particles in bin k due to coagulation of particles in bins i and j, $\bar{\beta}_{ijk} N_i N_j$. Here, $\bar{\beta}_{ijk}$ must represent the collision kernel for all particles with volumes within bins i and j that combine to

form particles with volumes within bin k. This collision kernel is defined as

$$\bar{\beta}_{ijk} \equiv \frac{\int_{v_{i-1}}^{v_i} \int_{v_{j-1}}^{v_j} \theta(v_i', v_j', v_k) \beta(v_i', v_j') n(v_i', t) n(v_j', t) \mathrm{d}v_j' \mathrm{d}v_i'}{N_i(t) N_j(t)} \tag{9.5}$$

where $\theta(v_i', v_j', v_k)$ is a function such that $\theta = 1$ when $v_{k-1} < v_i' + v_j' < v_k$ and $\theta = 0$ otherwise [142]. In other words, θ ensures that only collisions between particles whose combined volume is within bin k are included in the average collision kernel. To evaluate $\bar{\beta}_{ijk}$, one must properly define the function θ, which is difficult to do in practice. Furthermore, one must make some assumption about the form of the particle size distribution *within* each bin, i.e. $n(v, t)$ for $v_{i-1} < v < v_i$ and $v_{j-1} < v < v_j$. Similar considerations apply when determining the rates of condensation and evaporation from particles in bin k.

These issues can be avoided by replacing the finite bins with discrete particle size nodes, such that particles can only exist at the nodes. Thus, there is no need to determine average properties within each size bin; instead, one need only determine the collision kernel for discrete particle sizes. This nodal method is markedly simpler than standard sectional methods, making it an ideal solution technique for anyone first learning about the general dynamic equation (or for anyone who wants to avoid the mathematical complexities of more rigorous techniques). While it has its limitations – which will be discussed later in this chapter – the nodal method yields results that are sufficiently accurate for many applications.

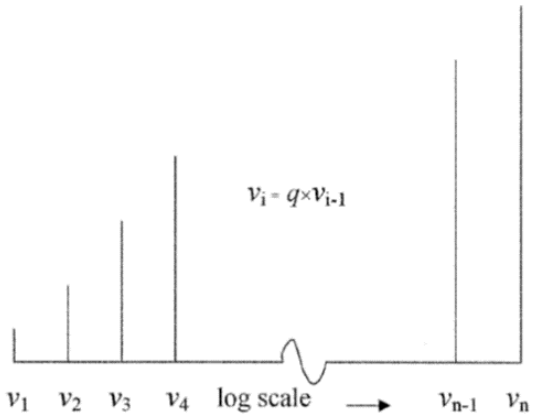

Figure 9.1: NGDE volume nodes are equally spaced on a logarithmic scale covering 12 orders of magnitude. (This figure original appears as Figure 1 in Prakash et al. [27].)

9.3 NGDE Code Description

NGDE solves the general dynamic equation – specifically, the form given by Eq. (9.3) – for the particle size distribution. The PSD is divided into discrete size nodes; by default, the size nodes cover 12 orders of magnitude in particle volume, from the size of a monomer ($\sim 10^{-29}$ m^3) to particles with diameters of a few microns ($\sim 10^{-17}$ m^3). The user chooses the number of volume nodes for determining the PSD; the default is 41. The nodes are equally-spaced on a logarithmic scale in terms of particle volume, as shown in Figure 9.1.

NGDE can perform four different calculations: (1) coagulation only; (2) coagulation plus nucleation; (3) coagulation, nucleation, and surface growth (i.e. the full GDE); and (4) pure surface growth. The user input – including specification of the calculation type and the number of nodes for the PSD – takes the form of a MATLAB data structure. For details about the input options, please see the

NGDE User Manual (Appendix F). The pure coagulation calculation begins with a monodisperse aerosol and continues until some fixed end-time. Currently, this end time is 1000 times the estimated time to reach the self-preserving PSD. (See Section 9.4.1 for information about the self-preserving size distribution.) The other three calculation types begin with a slightly supersaturated ($S = 1.001$, where S is the saturation ratio) vapor at some user-specified temperature. The calculation proceeds as the system cools from the initial temperature to some end temperature (300 K by default) at the specified cooldown rate. In all cases, NGDE determines the coagulation, nucleation, and/or surface growth rates at each time step based on the current conditions in the system. The details of how the code calculates these rates and about the integration scheme are given below.

9.3.1 Coagulation

Coagulation – which occurs when two particles collide and combine to form a larger particle – is governed by the Smoluchowski equation,

$$\left.\frac{\mathrm{d}N_k}{\mathrm{d}t}\right|_{coag} = \frac{1}{2}\sum_{i=2}^{M}\sum_{j=2}^{M}\chi_{ijk}\beta_{i,j}N_iN_j - N_k\sum_{i=2}^{M}\beta_{i,k}N_i \tag{9.6}$$

where M is the number of volume nodes; χ_{ijk} is a size-splitting operator for nodes i, j, and k; and $\beta_{i,j} \equiv \beta(v_i, v_j)$ is the collision kernel between nodes i and j. The summations begin at node 2 because node 1 represents monomers (i.e. the vapor form of the particulate species).[2] Here, particles with volumes v_i and v_j collide to

[2]Note that for pure coagulation, node 1 represents particles, so the summations in Eq. (9.6) begin at $i = 1$, $j = 1$.

form a larger particle with volume $v_i + v_j$.

The size-splitting operator is defined as follows [27]:

$$\chi_{ijk} = \begin{cases} \frac{v_{k+1}-(v_i+v_j)}{v_{k+1}-v_k} & \text{if } v_k \leq v_i + v_j \leq v_{k+1} \\ \frac{(v_i+v_j)-v_{k-1}}{v_k-v_{k-1}} & \text{if } v_{k-1} \leq v_i + v_j \leq v_k \\ 0 & \text{otherwise} \end{cases} \tag{9.7}$$

Since newly-formed particles with volume $v_i + v_j$ likely fall between two volume nodes, χ_{ijk} divides the number of coagulated particles into nodes with volumes just larger and just smaller than $v_i + v_j$. To do so, χ_{ijk} simply uses linear interpolation based on particle volume. The operator also ensures that collisions between particles with volumes v_i and v_j only contribute to the growth of particles with volume v_k if $v_{k-1} \leq v_i + v_j < v_{k+1}$. The NGDE code assumes perfect coalescence upon collision, which means that all particles are spherical.

Currently, users have two choices for calculating the collision kernel $\beta_{i,j}$: a form based on kinetic theory in the free molecule regime (i.e. Kn $\gg 1$) and Fuchs' form of the collision kernel for the transition regime (i.e. Kn ~ 1), where Kn $\equiv \lambda/a$ is the Knudsen number for particles with radius a in a background gas with mean free path λ. The free molecule form of the collision kernel is [2]

$$\beta_{i,j} \equiv \beta(v_i, v_j) = \left(\frac{3}{4\pi}\right)^{1/6} \left(\frac{6k_B T}{\rho_p}\right)^{1/2} \left(\frac{1}{v_i} + \frac{1}{v_j}\right)^{1/2} (v_i^{1/3} + v_j^{1/3})^2 \tag{9.8}$$

where k_B is the Boltzmann constant, T is the gas temperature, and ρ_p is the particle

density. Fuchs' form [1] is given by [146]

$$\beta_{i,j} = 2\pi D_i D_j (d_{pi} + d_{pj}) \left[\frac{d_{pi} + d_{pj}}{d_{pi} + d_{pj} + 2(g_i^2 + g_j^2)^{1/2}} + \frac{8(D_i + D_j)}{(\bar{c}_i^2 + \bar{c}_j^2)^{1/2}(d_{pi} + d_{pj})} \right]^{-1} \tag{9.9}$$

where

$$\mathrm{Kn}_i = \frac{2\lambda}{d_{pi}} \tag{9.10a}$$

$$\bar{c}_i = \left(\frac{8 k_B T}{\pi m_i} \right)^{1/2} \tag{9.10b}$$

$$\ell_i = \frac{8 D_i}{\pi \bar{c}_i} \tag{9.10c}$$

$$g_i = \frac{1}{3 d_{pi} \ell_i} [(d_{pi} + \ell_i)^3 - (d_{pi}^2 + \ell_i^2)^{3/2}] - d_{pi} \tag{9.10d}$$

$$D_i = \frac{k_B T}{3\pi \mu d_{pi}} \left(\frac{5 + 4\mathrm{Kn}_i + 6\mathrm{Kn}_i^2 + 18\mathrm{Kn}_i^3}{5 - \mathrm{Kn}_i + (8 + \pi)\mathrm{Kn}_i^2} \right) \tag{9.10e}$$

and d_{pi}, is the diameter, m_i the mass, $\bar{c}_i$ the mean thermal speed, and D_i the diffusion coefficient of particles with volume v_i.

9.3.2 Nucleation

Nucleation occurs when a non-equilibrium, supersaturated vapor condenses to return to equilibrium; condensation on existing particles is known as heterogeneous nucleation, while condensation to form new particles is called homogeneous nucleation [2]. In the context of the NGDE code, nucleation strictly refers to homogeneous nucleation; condensation on existing particles falls under the purview of surface growth, as discussed in the next subsection.

New particles form when monomers collide to form stable molecular clusters. Clusters with fewer monomers than the critical cluster size $k^\star$ are unstable and quickly dissociate, while clusters consisting of $k^\star$ monomers are stable and tend to grow rapidly. The critical cluster size is a function of the vapor properties and the thermodynamic conditions (e.g. saturation ratio, temperature, pressure) of the system. There are a number of models for calculating the critical cluster size and the nucleation rate; NGDE uses classical nucleation theory with the self-consistent correction (SCC) proposed by Girshick and Chiu [147]. For this model, the nucleation rate J_k and critical cluster size $k^\star$ are

$$J_k = n_s^2 S v_1 \left(\frac{2\sigma}{\pi m_1}\right)^{0.5} \exp\left(\theta - \frac{4\theta^3}{27 \ln^2 S}\right) \tag{9.11}$$

$$k^\star = \left(\frac{2}{3}\frac{\theta}{\ln S}\right)^3 \tag{9.12}$$

This corresponds to a critical particle volume of

$$v^\star = k^\star v_1 = \frac{\pi}{6}\left(\frac{4\sigma v_1}{k_B T \ln S}\right)^3 \tag{9.13}$$

In these equations, n_s is the monomer concentration at saturation; σ is the surface tension of the condensed species; $\theta = s_1\sigma/k_B T$ is the non-dimensional surface tension; and s_1, v_1, and m_1 are the surface area, volume. and mass of a monomer.

Since the critical volume $v^\star$ is unlikely to be exactly equal to any of the volume nodes, NGDE places nucleated particles in the node just larger than $v^\star$ and adjusts

the nucleation rate using the parameter ξ_k, where

$$\xi_k = \begin{cases} \frac{v^\star}{v_k} & \text{if } v_{k-1} < v^\star \leq v_k \\ \frac{v^\star}{v_2} & \text{if } v^\star \leq v_1 \\ 0 & \text{otherwise} \end{cases} \tag{9.14}$$

Thus, the nucleation rate for node k is given by [27]

$$\left.\frac{\mathrm{d}N_k}{\mathrm{d}t}\right|_{nucl} = \xi_k J_k \tag{9.15}$$

and the rate of change in the monomer concentration is

$$\left.\frac{\mathrm{d}N_1}{\mathrm{d}t}\right|_{nucl} = -k^\star J_k \tag{9.16}$$

9.3.3 Surface Growth

Condensation on or evaporation from the surface of a spherical particle with volume v_k is driven by the difference between the actual monomer concentration, N_1, and the monomer concentration over the particle at saturation, $N^s_{1,k}$, which is given by

$$N^s_{1,k} = n_s \exp\left(\frac{d^\star_p \ln S}{d_{pk}}\right) = n_s \exp\left(\frac{4\sigma v_1}{k_B T d_{pk}}\right) \tag{9.17}$$

The increase in the saturation monomer concentration over a curved surface versus the saturation concentration over a flat surface (n_s in the above equation) is known as the Kelvin effect. Note that this effect is usually negligible for the larger volume

nodes used in NGDE, but it plays a major role in the behavior of smaller particles. Condensation and evaporation rates also depend upon the collision frequency between monomers and particles.

Incorporating the above effects, the condensation/evaporation rate for node k is

$$\left.\frac{\mathrm{d}N_k}{\mathrm{d}t}\right|_{growth} = \alpha_1 + \alpha_2 - \alpha_3 - \alpha_4 \tag{9.18}$$

where

$$\alpha_1 = \begin{cases} \frac{v_1}{v_k - v_{k-1}} \beta_{1,k-1} (N_1 - N^s_{1,k-1}) N_{k-1} & \text{if } N_1 > N^s_{1,k-1} \\ 0 & \text{otherwise} \end{cases} \tag{9.19a}$$

$$\alpha_2 = \begin{cases} -\frac{v_1}{v_{k+1} - v_k} \beta_{1,k+1} (N_1 - N^s_{1,k+1}) N_{k+1} & \text{if } N_1 < N^s_{1,k+1} \\ 0 & \text{otherwise} \end{cases} \tag{9.19b}$$

$$\alpha_3 = \begin{cases} \frac{v_1}{v_{k+1} - v_k} \beta_{1,k} (N_1 - N^s_{1,k}) N_k & \text{if } N_1 > N^s_{1,k} \\ 0 & \text{otherwise} \end{cases} \tag{9.19c}$$

$$\alpha_4 = \begin{cases} -\frac{v_1}{v_k - v_{k-1}} \beta_{1,k} (N_1 - N^s_{1,k}) N_k & \text{if } N_1 < N^s_{1,k} \\ 0 & \text{otherwise} \end{cases} \tag{9.19d}$$

Here, α_1 and α_2 represent an increase in N_k due to condensation on particles with volume v_{k-1} and evaporation from particles with volume v_{k+1}, respectively, while α_3 and α_4 represent a decrease in N_k due to condensation on and evaporation from

particles with volume v_k, respectively. The leading factor in the above α's represents size-splitting to deal with the fact that particles with volume v_k do not grow or shrink into particles with volumes v_{k+1} or v_{k-1} within a single time step.

Eq. (9.18) applies for $k \geq 2$; the monomer balance ($k = 1$) is given by

$$\left.\frac{\mathrm{d}N_1}{\mathrm{d}t}\right|_{growth} = \sum_{k=2}^{M}(\gamma_{2k} - \gamma_{1k}) \tag{9.20}$$

where

$$\gamma_{1k} = \begin{cases} \beta_{1,k}(N_1 - N_{1,k}^s)N_k & \text{if } N_1 > N_{1,k}^s \\ 0 & \text{otherwise} \end{cases} \tag{9.21a}$$

$$\gamma_{2k} = \begin{cases} -\beta_{1,k}(N_1 - N_{1,k}^s)N_k & \text{if } N_1 < N_{1,k}^s \\ 0 & \text{otherwise} \end{cases} \tag{9.21b}$$

Here, γ_{1k} represents the loss of monomers due to condensation on particles in node k, and γ_{2k} represents the gain of monomers due to evaporation from particles in node k.

9.3.4 Solution Strategy

NGDE uses an explicit Eulerian method to integrate Eq. (9.3) with respect to time. Specifically, the particle size distribution at time $t + \Delta t$ is given by

$$N_k(t + \Delta t) = N_k(t) + \Delta t \left[\left.\frac{\mathrm{d}N_k(t)}{\mathrm{d}t}\right|_{coag} + \left.\frac{\mathrm{d}N_k(t)}{\mathrm{d}t}\right|_{nucl} + \left.\frac{\mathrm{d}N_k(t)}{\mathrm{d}t}\right|_{growth} \right] \tag{9.22}$$

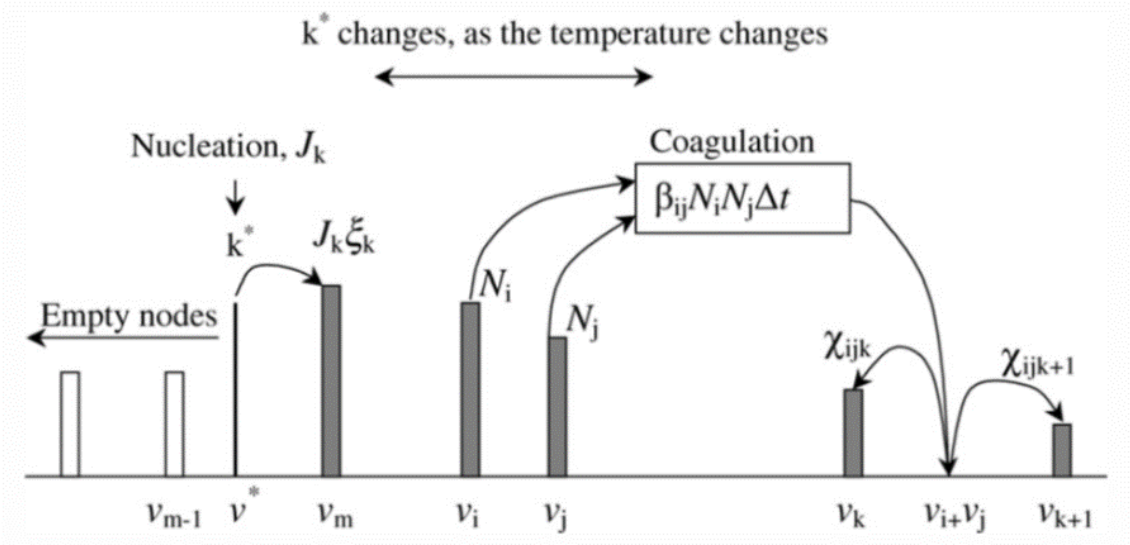

Figure 9.2: NGDE solves the general dynamic equation according to the illustration above. (This figure original appears as Figure 2 in Prakash et al. [27].)

where the coagulation, nucleation, and growth rates are given by Eqs. (9.6), (9.15), and (9.18) for $k \geq 2$, and the nucleation and growth rates are given by Eqs. (9.16) and (9.20) for monomers ($k = 1$). These rates are based on the conditions at time t. Figure 9.2 summarizes the calculations performed by NGDE.

Because the code uses an explicit solver, the time step must be small enough to ensure that the calculated coagulation, nucleation, and surface growth rates do not change significantly by the end of the time step. At the same time, the time step must be large enough for the code to complete its simulation in a reasonable CPU time. For these reasons, the MATLAB version of the code uses a dynamic time-step algorithm to choose Δt based on the conditions at time t:

$$\Delta t = \min(\Delta t_{coag},\, 0.5\Delta t_{neg},\, \Delta t_{mon},\, \Delta t_{sat},\, \Delta t_{user}) \tag{9.23}$$

The Δt's are defined as follows:

$$\Delta t_{coag} = \frac{0.001}{\beta_{min} N_{tot}} \tag{9.24a}$$

is 0.1% of the characteristic coagulation time, where $\beta_{min} = \min(\beta_{i,j})$ for $i, j \geq 2$ and N_{tot} is the total number concentration of particles (excluding monomers);

$$\Delta t_{neg} = \min_k \left(\left| \frac{N_k}{\mathrm{d}N_k/\mathrm{d}t} \right| \right) \tag{9.24b}$$

is the minimum time at which the number concentration in any node would become negative based on current coagulation, nucleation, and growth rates;

$$\Delta t_{mon} = \frac{0.001 N_1}{|\mathrm{d}N_1/\mathrm{d}t|} \tag{9.24c}$$

is the time in which the monomer concentration changes by 0.1%;

$$\Delta t_{sat} = \left| \frac{0.01 S P_s}{\frac{\mathrm{d}T}{\mathrm{d}t} N_1 k_B \left(1 - \frac{D}{T}\right)} \right| \tag{9.24d}$$

is the time in which the saturation ratio changes by 1%, where P_s is the saturation vapor pressure, $\mathrm{d}T/\mathrm{d}t$ is the cooldown rate and D is a constant used to determine the saturation vapor pressure; and

$$\Delta t_{user} = 10^{-4} \tag{9.24e}$$

is a user-specified maximum time step. The time-step algorithm has a number of hard-wired coefficients, including those used to specify the allowable fraction of the characteristic coagulation time and the allowable changes in the number concentration of particles, the number concentration of monomers, and the saturation ratio. The chosen values of these parameters reflect the desire to minimize the required calculation time while ensuring the calculation results are reasonable.

9.4 Sample Results

Sample problems have been developed to test the NGDE code. Test problems for pure coagulation and pure surface growth are used to validate the relevant models in the code. Additional sample problems representing combined nucleation and coagulation and the full GDE are presented to show that the code is producing reasonable results. All of the sample problems are for aluminum in argon gas.

The sample problems are described in the following subsections.

9.4.1 Pure Coagulation

An interesting feature of coagulating systems is that after a sufficiently long time, the non-dimensional aerosol size distribution $\psi = \phi n(v,t)/N_{tot}^2$ becomes independent of time and of the initial conditions of the system [2, 148, 149]. This time-independent PSD is known as the self-preserving distribution (SPD). Here, the non-dimensional particle volume is $\eta = N_{tot}v/\phi$, N_{tot} and ϕ are the total number concentration and volume fraction of particles in the system, and $n(v,t)\mathrm{d}v$ is the

number concentration of particles with volume between v and $v + \mathrm{d}v$ at time t.

The first test problem for NGDE involves coagulation of an initially monodisperse aerosol with a particle diameter of 1 nm and number concentration of 10^{24} m^{-3}. The calculation is performed at $T = 1773$ K for aluminum particles with density $\rho_p = 2700\text{kg/m}^3$. The calculated PSD should collapse to the self-preserving distribution after time [149]

$$t_{SPD} = \frac{\tau_f}{\beta_f N_0} \tag{9.25}$$

where

$$\beta_f = \left(\frac{3}{4\pi}\right)^{1/6} \left(\frac{6k_B T}{\rho_p}\right)^{1/2} v_0^{1/6} \tag{9.26}$$

is the free molecule coagulation coefficient for particles with volume v_0, N_0 and v_0 are the initial number concentration and volume of particles in the aerosol, and τ_f is a time constant for coagulation in the free molecule regime. Vemury et al. [149] found $\tau_f \approx 5$ when the bins in their sectional code are spaced such that $v_k = 2v_{k-1}$. Thus, the self-preserving distribution should be reached after $t_{SPD} = 30$ ns for the initial conditions of this problem.

To test the effects of NGDE node spacing on the results, the pure coagulation calculation has been performed with 21, 41, and 101 nodes, corresponding to node spacings of $v_k = 4.0v_{k-1}$, $v_k = 2.0v_{k-1}$, and $v_k = 1.3v_{k-1}$. For all cases, the non-dimensional size distribution ψ becomes independent of time and is approximately equal to the self-preserving distribution ψ_f as calculated by Vemury et al. [149]. The results are shown in Figure 9.3. For all three cases, the calculated size distribution reaches a constant distribution by approximately 30 ns, which is in good

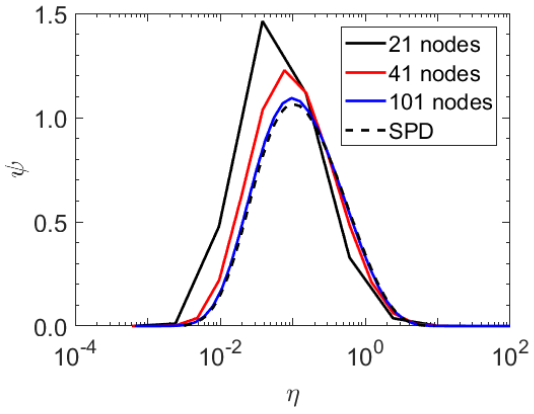

Figure 9.3: Non-dimensional size distribution for the pure coagulation problem after 1 μs, compared to the SPD for the free molecule regime, as determined by Vemury et al. [149] using an accurate sectional method. The calculated size distribution reaches a self-preserving distribution by 30 ns and remains constant until the end of the calculation at 30 μs (i.e. 1000 times the estimated t_{SPD}). Note that the difference between the PSD calculated by NGDE and the self-preserving distribution calculated by Vemury et al. [149] is due in part to ambiguities in defining a "bin width" for a size distribution with "zero-width" nodes.

agreement with t_{SPD} found by Vemury et al. [149].[3] For the case with 101 nodes, the distribution from NGDE is in excellent agreement with the SPD, but there are noticeable differences between the distribution from NDGE with 21 and 41 nodes and the SPD. These differences are due in part to ambiguity in defining a bin width for calculating n: for a sectional code, the bin width is simply the difference between the largest and smallest particle volume in each bin, but for a nodal code, the "bins" are zero-width nodes. In Figure 9.3 and in the NGDEplot post-processing tool, the bin widths are set to $\Delta v_k = (v_{k+1} - v_{k-1})/2$, i.e. "bin" k has upper bound at the midpoint between nodes k and $k+1$ and lower bound at the midpoint between nodes $k-1$ and k.

An additional way to evaluate the NGDE results is to compare the moments of

[3]This is based on the time at which the moments of the particle size distribution are approximately equal to the steady-state values of the moments given in Table 9.1.

the calculated distribution to the moments of the self-preserving distribution. The ith moment of the non-dimensional particle size distribution is defined as

$$M_i = \int_0^\infty \eta^i \phi \mathrm{d}\eta \tag{9.27}$$

where i is any real number. Many of these moments are related to important properties of the aerosol size distribution: $i = 0$ represents the total number concentration of particles; $i = 1/3$, $2/3$, and 1 are proportional to the mean diameter, surface area, and volume of particles in the system; and $i = 2$ is proportional to the intensity of light scattered by the particles when they are much smaller than the wavelength of incident light.

As shown in Table 9.1, the NGDE results with 101 nodes are in excellent agreement with the SPD results, with differences of approximately 7% for the second moment and less than 2% for all other moments. The NGDE results for 41 nodes are in good agreement (less than 9% difference from the SPD) for all but the second moment of the distribution (42% difference). These results suggest that using 41 nodes to represent 12 orders of magnitude in volume yields sufficiently accurate results for pure coagulation.

9.4.2 Pure Surface Growth

The second test problem involves condensation of aluminum vapor on a monodisperse aerosol as the system cools from 1773 K to 300 K at 1000 K/s. Particles are placed in node 25 out of 41, corresponding to a particle diameter of 79 nm. The

Table 9.1: Moments, M_i, of the particle size distribution for the pure coagulation calculation. Results are shown for NGDE calculations with 21, 41, and 101 nodes. The SPD results are from Vemury et al. [149].

i	21 Nodes	41 Nodes	101 Nodes	SPD
-1/2	2.0303	1.7047	1.5877	1.5641
-1/3	1.5233	1.3649	1.3056	1.2937
-1/6	1.2025	1.1431	1.1201	1.1155
0	1.0000	1.0000	1.0000	1.0001
1/6	0.8766	0.9122	0.9266	0.9296
1/3	0.8103	0.8657	0.8884	0.8929
1/2	0.7896	0.8530	0.8789	0.8836
2/3	0.8111	0.8707	0.8947	0.8984
5/6	0.8777	0.9186	0.9347	0.9360
1	1.0000	1.0000	1.0000	0.9998
2	6.2769	2.9543	2.2399	2.0873

initial number concentration is 10^{10} m^{-3}.

For pure surface growth, the aerosol should remain monodisperse with constant number concentration. Only the volume of each particle (and thus the total mass or volume of particles) changes. Thus, one can easily solve the following system of first-order, ordinary differential equations for pure surface growth with changing temperature:

$$\frac{\mathrm{d}T}{\mathrm{d}t} = -dTdt \tag{9.28a}$$

$$\frac{\mathrm{d}N_1}{\mathrm{d}t} = -\beta_{1,p}(N_1 - N_{1,p}^s)N_p \tag{9.28b}$$

$$\frac{\mathrm{d}v_p}{\mathrm{d}t} = -\frac{m_1}{\rho_p N_p}\frac{\mathrm{d}N_1}{\mathrm{d}t} = \frac{m_1}{\rho_p}\beta_{1,p}(N_1 - N_{1,p}^s) \tag{9.28c}$$

Here, $dTdt$ is the cooldown rate, $\beta_{1,p}$ is the collision kernel between monomers and particles with volume v_p given by Eq. (9.8), $N_{1,p}^s$ is the saturation monomer concentration over particles with volume v_p (or diameter d_p) given by Eq. (9.17),

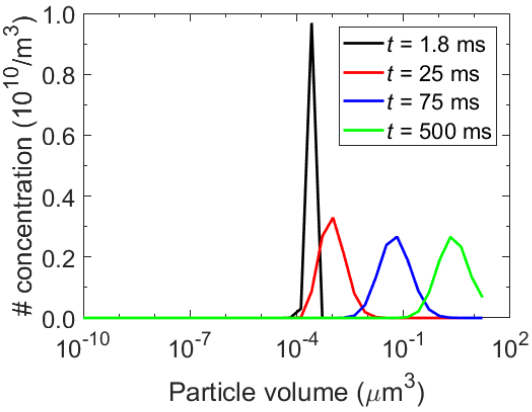

Figure 9.4: Size distribution calculated by NGDE for the pure surface growth sample problem. The distribution should remain monodisperse, but it spreads out over time because of numerical diffusion introduced by the size-splitting algorithm.

m_1 is the mass of a monomer, and ρ_p is the particle density. One can solve for the system temperature T, monomer concentration N_1, and particle volume v_p using any ODE solver, such as the MATLAB function `ode45`.

Figure 9.4 shows the size distribution calculated by NGDE for the pure surface growth problem. The PSD is shown at several different times. While the size distribution should remain monodisperse, the PSD calculated by NGDE spreads out with time due to numerical diffusion. Note that sectional methods also suffer from the same issue for pure surface growth. Fortunately, NGDE correctly determines the volume mean particle size (Figure 9.5) and the (constant) total number concentration. This shows that NGDE can provide correct results for the zeroth (number concentration) and first (average volume) moments of the distribution for surface growth problems, even though the distribution is much broader than expected.

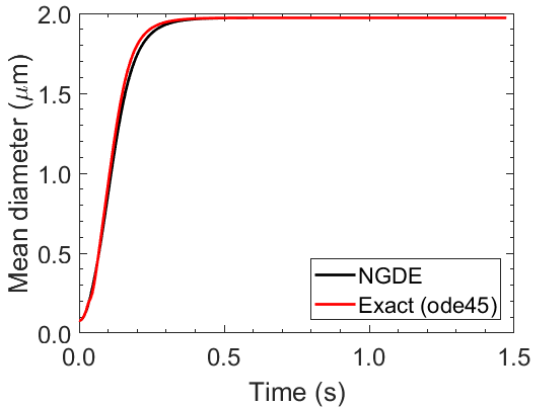

Figure 9.5: Volume-mean particle diameter calculated by NGDE for the pure surface growth problem. NGDE results are in excellent agreement with the mean diameter from the "exact" solution of the problem [i.e. Eq. (9.28) solved using the MATLAB function `ode45`, which integrates the system of ODEs using a 4th/5th order Runge-Kutta method].

9.4.3 Nucleation and Coagulation

The third sample problem tests nucleation and coagulation of aluminum as the system cools from 1773 K to 300 K at 1000 K/s. Initially, there are no particles in the system, and aluminum vapor is very slightly super-saturated ($S = 1.001$). This calculation is performed with 41 volume nodes.

Figure 9.6 shows the evolution of the size distribution with time, and Figure 9.7 shows the critical particle volume (i.e. the volume of newly-formed particles) and the nucleation rate. Particles begin to form between $t = 0.1$ s and $t = 0.18$ s. At this point, coagulation is negligible, so the particle distribution is very narrow, with most particles existing at nodes near the critical volume for nucleation ($v^\star \sim 1$ nm^3 at this point in the calculation). As the particles begin to coagulate, the size distribution broadens while the average volume increases. At longer times, the distribution is bimodal, with the mode at lower volumes representing newly formed particles and

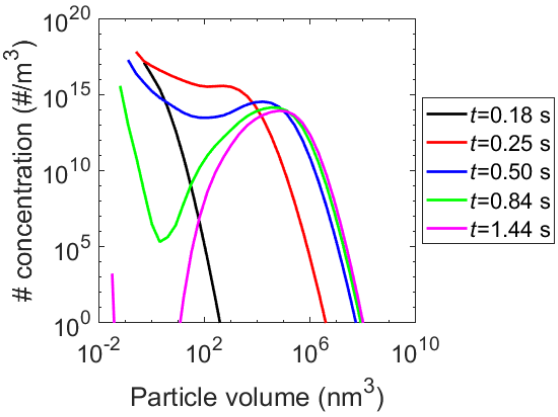

Figure 9.6: Particle size distribution at select times for nucleation and coagulation of aluminum. The distribution becomes bimodal due to the combined influence of new particle formation at lower volume nodes and coagulation to populate the larger volume nodes.

the mode at higher volumes representing particles formed earlier in the calculation that have since coagulated. This behavior is common in atmospheric systems, where sources continuously produce small particles that coagulate to form larger particles [2]. The nucleation rate decreases from $t = 0.2$ s until the end of the calculation, resulting in the decay of the lower mode of the bimodal PSD.

9.4.4 Full GDE for Condensation of Aluminum

The final sample problem involves solving the full GDE as a system of slightly super-saturated aluminum vapor cools from 1773 K to 300 K at a rate of 1000 K/s. Once again, the calculation is performed using 41 nodes.

Figure 9.8 shows the particle size distribution at select times. The particle number concentration remains near zero for the first 0.1 seconds of the calculation. At this point, the saturation ratio has reached a large enough value to allow for significant nucleation rates. Nucleation rates are very large between approximately 0.1 s

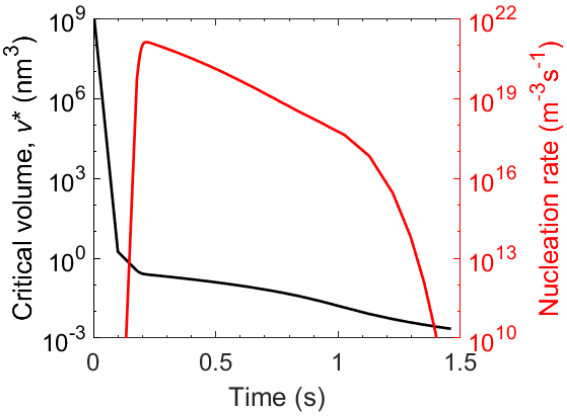

Figure 9.7: Critical volume and nucleation rate for nucleation and coagulation of aluminum. Initially, the critical volume is very large (near one micron) due to the low saturation ratio, but the critical volume quickly decreases as the temperature drops and the saturation ratio increases. [Refer to Eq. (9.13) for the relationship between critical volume and saturation ratio.]

and 0.15 s (Figure 9.9); after this brief burst of particle formation, nucleation rates are negligible for the remainder of the calculation. These nucleated particles grow quickly and form a nearly-lognormal peak centered near 10^6 nm^3 by approximately 0.15 s. The smaller peak at this time is due to nucleation. After the saturation ratio drops to nearly unity, larger particles grow slowly, while smaller particles evaporate due to the Kelvin effect. These processes continue for the remainder of the calculation, resulting in a final lognormal distribution with a single peak at 6.1×10^6 nm^3. The number concentration remains nearly constant after nucleation ceases, which shows that coagulation is negligible for these number concentrations.

This sample problem shows the important role of surface growth in the aerosol dynamics. For the same conditions as the nucleation plus coagulation problem, the calculated number concentration is orders of magnitude lower because monomers that condensed on existing particles are unavailable to nucleate to form new parti-

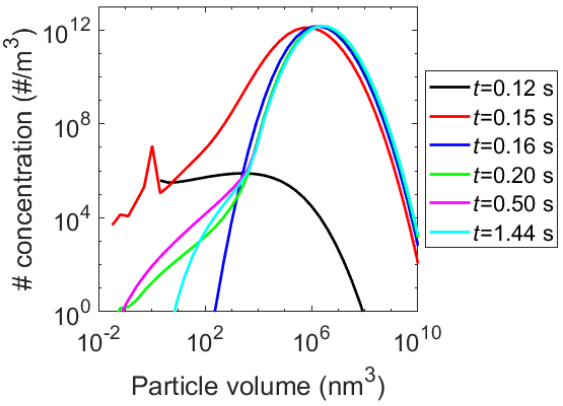

Figure 9.8: Particle size distribution at select times for nucleation, coagulation, and surface growth of aluminum. Particle formation begins around $t = 0.1$ s and effectly ends by $t = 0.16$ s. After this time, the size distribution changes due primarily to surface growth. Coagulation plays a minor role due to the low number density and short time frame of the problem.

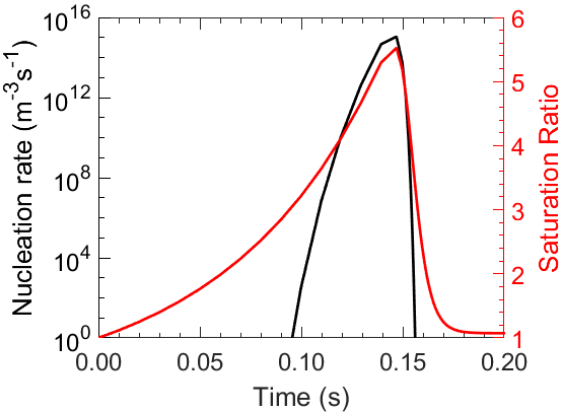

Figure 9.9: Nucleation rate and saturation ratio early in the simulation for nucleation, coagulation, and surface growth of aluminum by NGDE. Nucleation rates are significant for the short period of time when the saturation ratio is greater than ~ 3. After this period, very few new particles form as condensation on existing particles dominates the behavior of the system.

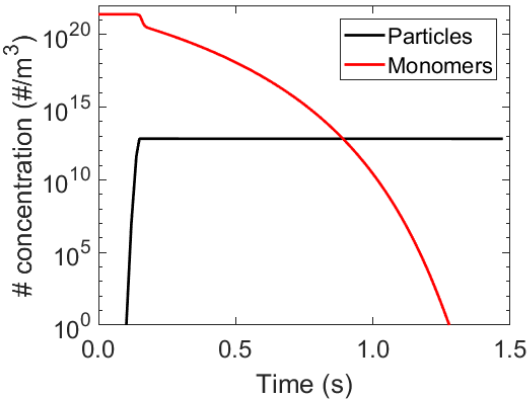

Figure 9.10: Monomer and total particle concentration for nucleation, coagulation, and surface growth of aluminum. The particle concentration is nearly constant (decrease of less than 2%) after particle nucleation stops around $t = 0.16$ s. Particles grow primarily by surface growth, as evidenced by the steady decline in the monomer concentration.

cles. At the same time, the volume-mean particle diameter is larger at the end of the full GDE calculation than the mean diameter when surface growth is neglected (230 nm versus 59 nm). Note that the total particle volume is nearly the same in both calculations.

9.5 Limitations of NGDE

The sample problems discussed in the previous section demonstrate that NGDE yields results in good agreement with other available numeric solutions of the general dynamic equation. However, there are a number of limitations of the code. Some of these limitations – particularly the numerical diffusion observed in the pure surface growth problem – are intrinsic to the nodal method specifically and sectional methods in general. Other limitations can be addressed by modifying the code. Some of these limitations, and suggestions for improvement, are discussed in this section.

One limitation is that NGDE does not include an energy balance. This means that the code ignores the latent heat involved in nucleation, condensation, and evaporation. Ignoring the latent heat is reasonable because NGDE requires a user-specified cooldown rate for calculation types involving nucleation and growth; one can assume that temperature changes due to particle formation and growth are included implicitly in this cooldown rate. However, if one is concerned with a system where the latent heat plays a significant role in the dynamics, then one would need to add the energy balance to the code. This would also require the user to specify data about the latent heat as a function of thermodynamic conditions. Such changes could be made with only a modest effort.

A second limitation is that NGDE does not account for particle sources and sinks. In aerosol systems, deposition often plays an important role in affecting the particle size distribution. Some deposition mechanisms could be included fairly easily in NGDE. For example, the settling velocity of a particle with diameter d_k in a gravitational field is given by

$$u_{g,k} = \frac{(\rho_p - \rho_f) g d_k^2 C_c(\mathrm{Kn}_k)}{18\mu} \tag{9.29}$$

where $\rho_p - \rho_f$ is the difference between the particle and fluid densities, μ is the fluid viscosity, and C_c is the Cunningham slip correction factor for spheres with Knudsen number $\mathrm{Kn}_k = 2\lambda/d_k$. Assuming a well-mixed aerosol, the decrease in number concentration of particles in node k due to settling in time Δt in a box with height L is $N_k u_{g,k} \Delta t / L$; one could simply add a subroutine to perform this calculation and

include it as a loss term in the particle mass balance. Similarly, one could add a subroutine to add particles to a given volume node to represent an aerosol source term.

Another limitation is that NGDE is written with specific situations in mind: coagulation of an initially monodisperse aerosol; nucleation, coagulation, and surface growth for an initially saturated system experiencing a constant decrease in temperature; and surface growth on a monodisperse aerosol for a constant change in temperature. It may be desirable to allow for some flexibility in the calculation types, such as allowing the user to specify a polydisperse size distribution or non-constant cooldown rate. Fortunately, many such changes would require only minor changes to the code and code input. Even less effort is required to modify some of the hard-wired parameters (e.g. initial saturation ratio, maximum allowable change in saturation ratio in the dynamic time-step algorithm) in the code. For guidance in changing the code, please refer to the NGDE User Manual (Appendix F).

9.6 NGDEplot

As part of the conversion of NGDE to MATLAB, a new post-processing tool has been developed to display how certain parameters evolve with time. Currently, NGDEplot can create movies showing the evolution of the particle size distribution (in various forms) and/or the scattering, absorption, and extinction coefficients for the distribution. The user can save the frames for later playback using MATLAB's `movie` command. In addition, NGDEplot can display static plots showing

the nucleation rate, saturation ratio, and mean particle diameter.

NGDEplot works as follows. First, the code unpacks the simulation results contained in the NGDE output parameter `results2` and reads user-specified input. The remainder of NGDEplot is fairly straightforward: other than simple manipulation of the NGDE results, the code mostly consists of commands that control the appearance of the plots. With that said, the light scattering calculations warrant a brief explanation.

Before showing the light-scattering movie, NGDEplot determines the scattering, absorption, and extinction efficiencies for each volume node by calling a Mie scattering code [89]. The Bohren Mie code was converted from a Fortran code provided by Professors Eugene Clothiaux and Craig Bohren from the Pennsylvania State University; the conversion was performed using the automated MATLAB function `f2matlab` available through MATLAB File Exchange on the MathWorks website. Extensive testing was performed to ensure that the converted code returns correct values for the optical efficiencies.

Using the efficiencies for each volume node obtained from the Bohren Mie code, NGDEplot calculates the scattering, absorption, and extinction coefficients for the distribution, where the scattering coefficient is given by

$$K_{sca}(\lambda, t) = \sum_{k=2}^{M} \frac{\pi}{4} d_{pk}^2 Q_{sca,k}(\lambda) N_k(t) \tag{9.30}$$

Here, d_{pk} is the diameter of particles in node k, M is the total number of nodes, and $Q_{sca,k}$ is the scattering efficiency for particles in node k for incident light with

wavelength λ. The extinction coefficient is calculated by replacing Q_{sca} in the above equation with Q_{ext}, while the absorption coefficient is simply $K_{abs} = K_{ext} - K_{sca}$. (Note that the optical cross sections are also functions of the refractive index of the particles.) The optical coefficients are calculated at each time t for a range wavelengths that includes the visible spectrum, as well as portions of the ultraviolet and infrared spectra. Note that the summation begins at $k = 2$ unless the NGDE results are from a pure coagulation calculation, in which case the summation begins at $k = 1$.

More information about running NGDEplot can be found in the NGDE User Manual (Appendix F). Sample screenshots of the size distribution and light scattering movies are shown in Figures 9.11 and 9.12.

9.7 Conclusions

The NGDE code uses a nodal method to solve the general dynamic equation for the evolution of an aerosol particle size distribution with time. The method is similar to sectional methods, but the discrete nature of the nodes makes the resulting code much simpler than sectional codes. Even with this simplified approach, the NGDE code gives results in good agreement with available results obtained using other methods. Because of its simplicity and accuracy, NGDE is well-suited to serve as a teaching tool in college courses on aerosol physics and dynamics.

The MATLAB version of the code includes a new dynamic time-step algorithm that decreases the code execution time by orders of magnitude. For example, the

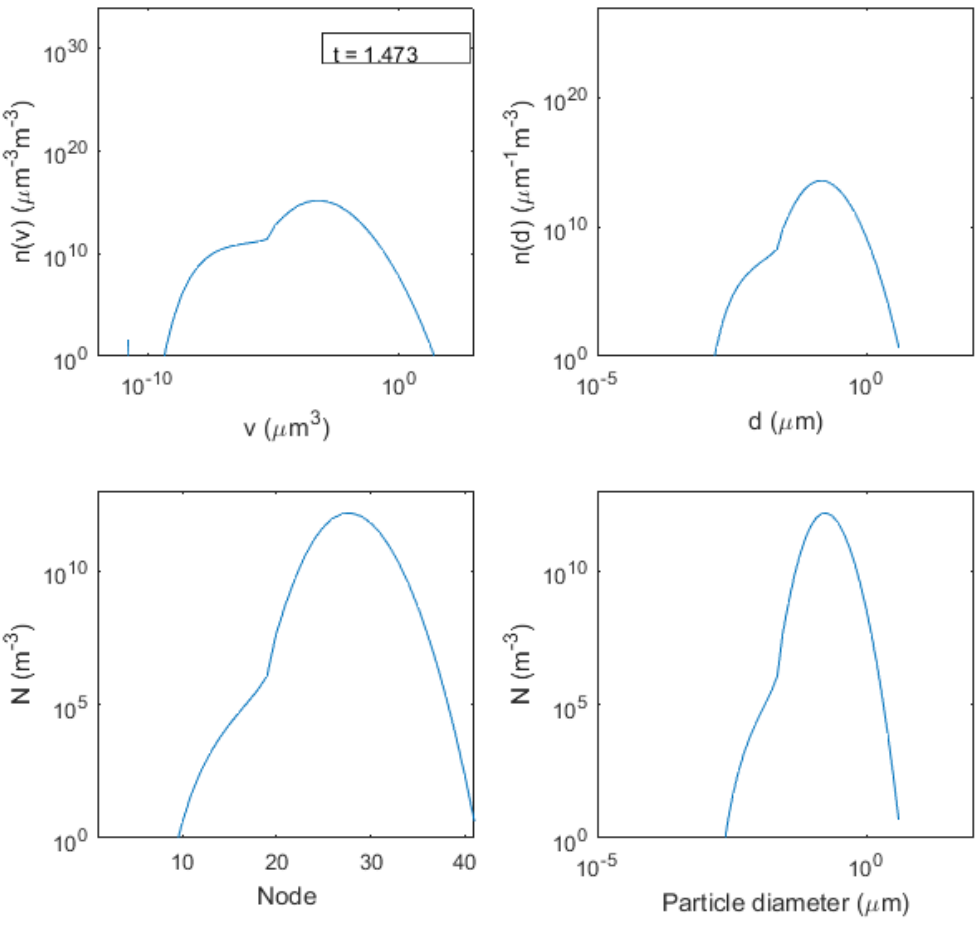

Figure 9.11: Screenshot of the particle size distribution movie from NGDEplot. This still is from the end of full GDE sample problem described in Section 9.4.4.

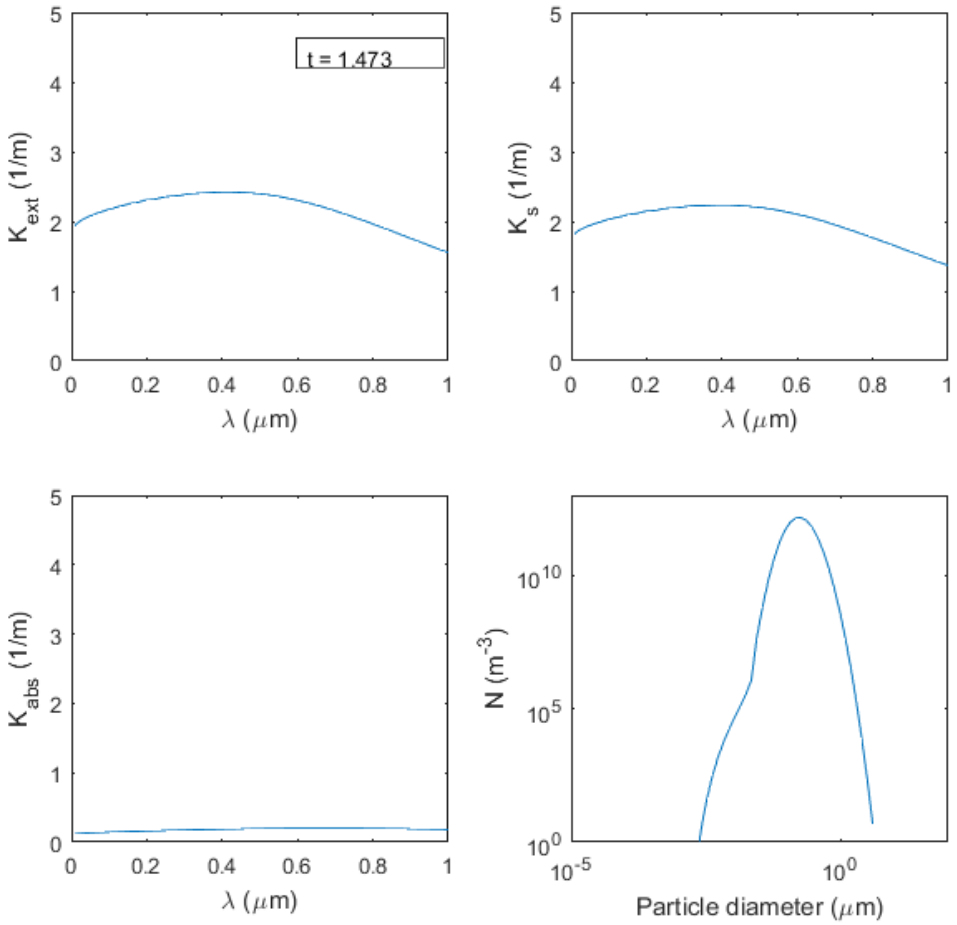

Figure 9.12: Screenshot of the light scattering movie from NGDEplot. This still is from the end of full GDE sample problem described in Section 9.4.4. The Mie calculations are performed for a refractive index of $n = 1 + 6.4\text{i}$, which is an average value for aluminum in the visible spectrum [150].

full GDE sample problem described in Section 9.4.4 takes approximately 10 minutes to run with the dynamic time-step algorithm in MATLAB but more than a day to run in the original C version of the code. Furthermore, the MATLAB version of NGDE comes with post-processing tool NGDEplot that utilizes MATLAB's built-in plotting features to display results for the particle size distribution and the light scattering, absorption, and extinction coefficients.

Chapter 10: Conclusions and Recommendations for Future Work

In this dissertation, I have described my method for determining the force and torque on aggregates in the transition regime and discussed its use to study various problems related to aerosol particle physics. Now, I will summarize the important conclusions of my work and suggest areas for further study.

10.1 Conclusions

I have developed a method for calculating the translational, rotational, and coupling friction tensors for aggregates consisting of spheres in point contact when the primary sphere Knudsen number is in the transition regime (i.e. $0.01 < \mathrm{Kn} < 100$). My method addresses an important practical problem because a significant fraction of terrestrial aerosols is generated as aggregates of very small primary spheres [4, 7]. It synthesizes two previous approaches for computing the transport properties of particles: the Kirkwood-Riseman method originally developed in the late 1940s to determine the intrinsic viscosity and translational diffusion of polymers [28], and the efforts of Loyalka and others to determine the velocity around a sphere in rarefied flow [75–78]. Since that time, researchers have made significant improvements to KR theory for describing hydrodynamic interactions between spheres in

the continuum [30, 51, 57, 58, 97]; however, no effort had been made to extend this approach to the transition regime using the results of Loyalka. This gap in the literature is likely due to the analytical and numerical complexities involved in solving the Boltzmann transport equation for each primary sphere Knudsen number of interest, even when the equation is posed in a simplified form like the Bhatnagar-Gross-Krook equation [71]. My method plugs this gap and extends KR theory to the transition regime in order to improve predictions of the transport behavior of aerosol aggregates consisting of nano-scale primary spheres.

From the friction tensors determined using my method, one can obtain the translational and rotational friction coefficients by averaging over all particle orientations; one can also obtain the diffusion tensors and coefficients through a generalized Stokes-Einstein relation. Results for the translational friction coefficient compare well to Direct Simulation Monte Carlo results and experimental data published in the literature. The calculated translational friction coefficients also approach the continuum and free molecule results from the Zeno algorithm and a Monte Carlo algorithm in the limit of very small and very large primary sphere Knudsen numbers, respectively. This suggests that the friction and diffusion coefficients obtained using my method can be used in various relations describing aerosol transport (e.g. to determine gravitational settling rates, electrical mobilities, or coagulation rates for non-spherical particles), while the friction and diffusion tensors can be used in aerosol dynamics simulations (e.g. for coagulation or Brownian motion).

Based on this success in calculating the friction tensors and coefficients, I have applied the method to study a number of problems related to aerosol physics.

First, I looked at the effects of primary sphere size (characterized by the Knudsen number) and the number of spheres (N) on the translational and rotational friction coefficients of particles formed by diffusion-limited cluster aggregation. In both cases, I found that the friction coefficients approach the continuum limit as the Knudsen number decreases or as the number of spheres increases. For example, DLCA aggregates consisting of 1000 spheres are in the continuum limit even when the primary sphere Knudsen number is unity. This supports the general premise of the Adjusted Sphere Method [41, 67], that one can determine the translational friction coefficient of an aggregate using an aggregate Knudsen number based on its hydrodynamic radius (i.e. a continuum measure of particle size) and its orientation-averaged projected area (i.e. a free molecular measure of particle size). In response to this finding, I showed that one can determine the rotational friction coefficient using an aggregate Knudsen number for rotational motion that is proportional to the ratio of continuum and free molecule rotational friction coefficients.

As part of this effort to determine the translational and rotational friction coefficients, I showed that the ratio of translational to rotational characteristic diffusion times is near unity for DLCA aggregates, regardless of primary sphere or aggregate size. In other words, these particles rotate significantly during the average time required to diffuse one radius of gyration. This finding is significant because most aerosol studies ignore the effects of rotation on the particle dynamics. My results suggest the effect of rotation on particle dynamics requires further study.

One major advantage of my method compared to the DSMC method is that it is very fast: one can determine the friction tensors for aggregates with 100 pri-

mary spheres within seconds, while aggregates with 2000 spheres take minutes on a single processor. (Compare this to DSMC, which takes days on a single processor to determine the friction coefficient for a 20-sphere aggregate [41]). However, the required computational time is still too excessive to incorporate this method in an aerosol dynamics code. Therefore, I have used my results for the translational and rotational friction coefficients of DLCA aggregates to develop an analytical expression that returns these coefficients as a function of the primary sphere radius, the number of spheres in the aggregate, and the gas properties. My analytical expression for the translational friction coefficient is more accurate than previous correlations for DLCA aggregates [37–39] when compared to my EKR results. The rotational friction coefficient expression appears to be the first of its kind published in the literature. Researchers can use these expressions to quickly estimate the friction coefficients for soot-like aggregates.

Next, I applied my EKR method to determine the orientation-averaged mobility of a particle in an electric field. The mobility is a function of particle size and field strength due to the interaction of the induced dipole in the particle with the electric field. My orientation-averaged mobility results as a function of field strength are in good agreement with experimental data published in the literature. In general, for DLCA aggregates the mobility is less than 10% greater when the particle is aligned with the field than when all orientations are equally probable (i.e. at very low field strengths). Thus, one could in theory use the relationship between mobility and field strength to obtain size information or to separate particles with similar mobility at one field strength but different shapes (and hence different mobilities

from each other at a different field strength). However, my results suggest there are several practical issues related to the experimental setup and to the accuracy of the methods used to relate the data to size and shape information (such as my EKR method). It is especially difficult to obtain shape information for either very large or very small soot-like aggregates because it is difficult to operate a DMA at low enough voltages to ensure that large aggregates have a fully random orientation, and small aggregates require very high field strengths to align. In these limits, the measured mobility at low and high field strengths would be nearly equal, which would suggest – incorrectly – that these fractal aggregates are actually spherical.

Finally, I showed that one can use my method to determine the hydrodynamic forces between spheres or aggregates in the transition regime, where the centers of mass of the particles are separated by a distance r. This effort is a natural extension of the single-particle work discussed in the earlier chapters of my work: it includes the interactions among the primary spheres in multiple aggregates as well as within one aggregate. I have demonstrated that while the strength of interactions between particles weakens as the primary sphere Knudsen number decreases, such interactions follow the characteristic $1/r$ behavior observed for continuum particles. From this result, I described how one can adopt the point force method for widely separated particles in the continuum to particles in the transition regime; the only difference is the leading coefficient that appears in the Oseen hydrodynamic interaction tensor. I have used this point force approach to show that a spherical cloud of particles with non-negligible Knudsen numbers behaves just like a cloud in the continuum, provided certain conditions (e.g. cloud radius, particle volume fraction)

are satisfied.

In addition to my work in calculating the transport behavior of aggregates, I have made significant improvements to the NGDE code, which solves the general dynamic equation for the change in the aerosol size distribution due to nucleation, coagulation, and surface growth. In particular, I converted the code from C to MATLAB to make use of MATLAB's built-in plotting features, I added a dynamic time-step algorithm to significantly reduce code execution time and improve code stability, and I developed a post-processing tool to generate movies showing the evolution of the size distribution and the optical properties of the aerosol. These improvements will enhance the code's intended use in teaching students about the effects of nucleation, coagulation, and surface growth on aerosol dynamics.

10.2 Recommendations for Future Work

10.2.1 Friction Coefficient Expressions for non-DLCA Aggregates

Much of my work has focused on DLCA aggregates because such particles are found in many areas of interest to the aerosol science. However, it is possible to form particles with other fractal dimensions. (See, for example, Figure 8.3 of Friedlander [2].) One could use my EKR method to determine the functional relationship between the primary sphere size and number of spheres in the aggregate and its translational and rotational friction coefficients in order to develop analytic expressions similar to my expressions for DLCA aggregates [Eqs. (4.38) and (6.26)]. One could include these expressions in an aerosol dynamics code to account for the

transport behavior of aggregates as a function of the primary sphere size, number of primary spheres, and fractal dimension.

Similarly, one could compare the properties of aggregates generated with the Mackowski algorithm – which I have used to create the particles used in this study – with those generated by direct numerical simulation of the aggregate trajectories. This is of interest to determine how well the properties of particles generated by a simplified algorithm match the properties of particles from a more realistic, Langevin-style simulation (as described below).

10.2.2 Aggregates with Polydisperse Primary Spheres

All of my calculations involve aggregates that consist of equally-sized primary spheres. This is an idealized situation; in reality, aggregates typically consist of primary spheres with some distribution of radii. Bernal et al. [51] have demonstrated how one can account for polydispersity in the continuum, and Spyrogianni et al. [151] have applied the method to determine the effect of polydispersity on aggregate settling rates. Now, I will describe how to address this issue in the transition regime.

To account for polydispersity, we must make a slight change to my extended Kirkwood-Riseman method. In the continuum, the force on the ith sphere with radius a_i moving with velocity u_i is given by

$$\boldsymbol{F}_i = -\zeta^c_{t,0}(a_i)\boldsymbol{u}_i - \zeta^c_{t,0}(a_i)\sum_{i\neq j}^{N}\mathbf{T}_{ij}(a_i, a_j, \boldsymbol{r}_{ij})\cdot\boldsymbol{F}_j \tag{10.1}$$

where a_j is the radius of the jth sphere and the hydrodynamic interaction tensor is a

function of a_i, a_j, and the distance between the spheres. My EKR method replaces the hydrodynamic interaction tensor with the quotient of the velocity tensor and the monomer friction coefficient *for sphere j*. Thus, to account for polydisperse primaries, my EKR method becomes

$$\boldsymbol{F}_i = -\zeta_{t,0}(\mathrm{Kn}_i)\boldsymbol{u}_i - \zeta_{t,0}(\mathrm{Kn}_i)\sum_{i\neq j}^{N}\zeta_{t,0}^{-1}(\mathrm{Kn}_j)\mathbf{V}_{ij}(\mathrm{Kn}_j, \boldsymbol{r}_{ij})\cdot\boldsymbol{F}_j \tag{10.2}$$

The only difference between this expression and the expression for monodisperse primaries is the appearance of the friction coefficient ratio $\zeta_{t,0}(\mathrm{Kn}_i)/\zeta_{t,0}(\mathrm{Kn}_j)$ for primary spheres with Knudsen numbers of $\mathrm{Kn}_i \equiv \lambda/a_i$ and $\mathrm{Kn}_j \equiv \lambda/a_j$. For monodisperse primaries ($\mathrm{Kn}_i = \mathrm{Kn}_j \equiv \mathrm{Kn}$), the ratio cancels, leaving the expression that has appeared throughout the earlier chapters of this disseration,

$$\boldsymbol{F}_i = -\zeta_{t,0}(\mathrm{Kn})\boldsymbol{u}_i - \sum_{i\neq j}^{N}\mathbf{V}_{ij}(\mathrm{Kn})\cdot\boldsymbol{F}_j$$

There are a number of practical challenges that must be addressed in order to determine the friction coefficient of aggregates with polydisperse primaries. The first challenge is to generate the coordinates for the spheres in the aggregates. The Mackowski algorithm I have been using creates aggregates with unit primary sphere size. One would need to modify the algorithm to account for polydisperse primaries. One could do so by sampling the primary sphere sizes from a specified distribution (such as a lognormal distribution a geometric standard deviation $\sigma_g = 1.2$, in agreement with experiments of soot formation in premixed diffusion flames Köylü and

Faeth [42]). Alternatively, one could obtain particles from a dynamic simulation of particle aggregation [151].

Also, one would need to make significant modifications to my MATLAB program for calculating the friction tensors (`bgk_tensors`; see Appendix G) to account for polydispersity. Currently, my program loads the velocity and monomer friction coefficient results obtained by solving the BGK equation. These results are stored in individual MATLAB data files indexed by the non-dimensional monomer radius r_0 [defined by Eq. (2.5d)]. To account for polydisperse primaries, one would need to access multiple data files, each one associated with the Knudsen number of one of the monomers in the aggregate. This would require there to be a file of BGK results for each primary sphere Knudsen number. Alternatively, one could compile all of the BGK results in a table and interpolate based on the primary sphere Knudsen number and the distance between spheres. Likewise, one would need to interpolate to determine the coefficients c_1 and c_2 [see Eq. (2.59)] for the velocity far from the sphere. Such changes would not be difficult to implement.

With that said, it is unlikely that accounting for polydispersity would have a significant impact on aggregate transport properties. For example, Spyrogianni et al. [151] found that aggregates in the continuum with polydisperse primaries settle faster than aggregates with monodisperse aggregates with equal mean primary diameters, but only because the polydisperse aggregates have greater mass than the monodisperse aggregates. In other words, the settling velocity of aggregates in the continuum is unaffected by monomer polydispersity, once one corrects for differences in particle mass. Nevertheless, this does not guarantee that the same behavior would

be observed in the transition regime, especially if there is a broad distribution of primary sizes. (See, for example, the particles described in Ref. [152].) One could test whether or not this is the case using my EKR method, with Eq. (10.2) to account for polydispersity.

10.2.3 Rotational and Coupling Interactions

My EKR method ignores rotational and coupling hydrodynamic interactions between spheres in an aggregate. Such interactions are weaker than the translational interactions included in my method, so one can safely neglect these effects when the average distance between spheres in the aggregate increases. However, when the average distance between spheres is small, rotational and coupling interactions become significant, and the error in the rotational friction coefficient calculated using the EKR method can be large (up to 40% for the cases I have studied).

Expressions for the rotational and coupling hydrodynamic interaction tensors in the continuum are available in the literature, as summarized by Carrasco and Garcıa de la Torre [53]. I have shown that to order r_{ij}^{-3}, the rotational and coupling hydrodynamic interaction tensors are related to the vorticity and velocity fields around a rotating sphere. (See Appendix D.) This suggests that one could obtain the rotational and coupling interaction tensors as a function of Knudsen number by solving the BGK equation for the flow field around a rotating sphere. Loyalka [77] has already performed this calculation; unfortunately, the paper does not provide detailed results for the velocity around the rotating sphere, nor does it go into much detail about the solution procedure. Still, the problem is not significantly different

from the translating sphere problem; the main difference is in the far-field velocity distribution function, where instead of a uniform translational velocity $\boldsymbol{U}$ there is a position-specific velocity $\boldsymbol{\omega} \times \boldsymbol{r}$. The rotational problem is slightly more complicated due to this difference, but in principal one can use the same approach developed by Lea [74] that I have described in Chapter 2.

After obtaining the velocity and vorticity fields around a rotating sphere – and thus the coupling and rotational hydrodynamic interaction tensors as a function of Knudsen number – the next step would be to incorporate these tensors in the EKR method. The approach is analogous to the method described by Carrasco and García de la Torre [53] for calculating the force and torque on a particle in the continuum; the only difference is that one replaces the continuum translational, rotational, and coupling interaction tensors with the velocity field around a translating sphere, the vorticity field around a rotating sphere, and the velocity field around a rotating sphere obtained by solving the BGK equation as a function of Knudsen number. This effort should significantly improve the accuracy of the calculated rotational friction coefficient, especially for small aggregates near the continuum regime.

10.2.4 Brownian Dynamics

The final suggested extension of my research is to incorporate my EKR method into Brownian dynamics simulations to study the effects of particle rotation and hydrodynamic interactions on various parameters of interest to the aerosol scientist (e.g. coagulation rates, sedimentation rates, the size and shape of coagulated aerosols). This would involve solving the Langevin equations for each particle in an

N-particle system. The Langevin equations for particle i describe its translational and rotational velocities ($\boldsymbol{u}_i$ and $\boldsymbol{\omega}_i$) and position in space-fixed coordinates and orientation in particle-fixed coordinates ($\boldsymbol{x}_i$ and $(\phi_i, \omega_i, \psi_i)$):

$$\frac{\mathrm{d}m_i\boldsymbol{u}_i}{\mathrm{d}t} = -\boldsymbol{\Xi}_{t,i}\cdot\boldsymbol{u}_i - \boldsymbol{\Xi}^{\dagger}_{c,i}\cdot\boldsymbol{\omega}_i + \sum_{j=1}^{N}\boldsymbol{F}_{H,ij} + \boldsymbol{F}_{E,i} + \boldsymbol{F}_{B,i} \tag{10.3}$$

$$\mathbf{I}_i\cdot\frac{\mathrm{d}\boldsymbol{\omega}_i}{\mathrm{d}t} + \boldsymbol{\omega}_i\times(\mathbf{I}_i\cdot\boldsymbol{\omega}_i) = -\boldsymbol{\Xi}_{c,i}\cdot\boldsymbol{u}_i - \boldsymbol{\Xi}_{r,i}\cdot\boldsymbol{\omega}_i + \sum_{j=1}^{N}\boldsymbol{T}_{H,ij} + \boldsymbol{T}_{E,i} + \boldsymbol{T}_{B,i} \tag{10.4}$$

$$\frac{\mathrm{d}\boldsymbol{x}_i}{\mathrm{d}t} = \boldsymbol{u}_i \tag{10.5}$$

$$\begin{bmatrix} \frac{\mathrm{d}\epsilon_{1i}}{\mathrm{d}t} \\ \frac{\mathrm{d}\epsilon_{2i}}{\mathrm{d}t} \\ \frac{\mathrm{d}\epsilon_{3i}}{\mathrm{d}t} \\ \frac{\mathrm{d}\eta_i}{\mathrm{d}t} \end{bmatrix} = \frac{1}{2}\begin{bmatrix} \eta_i\omega_{x',i} - \epsilon_{3i}\omega_{y',i} + \epsilon_{2i}\omega_{z',i} \\ \epsilon_{3i}\omega_{x',i} + \eta_i\omega_{y',i} - \epsilon_{1i}\omega_{z',i} \\ -\epsilon_{2i}\omega_{x',i} + \epsilon_{1i}\omega_{y',i} + \eta_i\omega_{z',i} \\ -\epsilon_{1i}\omega_{x',i} - \epsilon_{2i}\omega_{y',i} - \epsilon_{3i}\omega_{z',i} \end{bmatrix} \tag{10.6}$$

In these equations, m_i is the mass, $\mathbf{I}_i$ is moment of inertia tensor, $\boldsymbol{F}_{E,i}$ and $\boldsymbol{T}_{E,i}$ are the external forces and torques (e.g. from an electric field), and $\boldsymbol{F}_{B,i}$ and $\boldsymbol{T}_{B,i}$ are fluctuating Brownian forces and torques on particle i, while $\boldsymbol{F}_{H,ij}$ and $\boldsymbol{T}_{H,ij}$ are the hydrodynamic force and torque on particle i due to particle j. Note that the rotational velocity and orientation are written in terms of the particle-fixed axes (x'_i, y'_i, z'_i), which are related to the co-moving axes (i.e. the axes parallel to the space-fixed axes that translate with the particle) by the Euler angles $(\phi_i, \theta_i, \psi_i)$. The friction tensors represent the friction on the particle when it is alone in an infinite fluid (i.e. ignoring the effects of the other particles) and are written in terms of the

co-moving axes. Eq. (10.6) is written in terms of the Euler quaternion $(\epsilon_{1i}, \epsilon_{2i}, \epsilon_{3i}, \eta_i)$, which is related to the Euler angles. (See Ref. [153].) Note that in principal one must consider the effects of all of the particles when determining the fluctuating Brownian force and torque on particle i [136].

Previous studies of Brownian dynamics are restricted to the continuum or free molecule limits [121, 127, 154, 155]. Many of these studies use simplified methods to calculation the aggregate friction coefficient, though Fernandes and García de la Torre [127] apply methods based on Kirkwood-Riseman theory to determine the translational friction tensor $\boldsymbol{\Xi}_t$. Furthermore, the rotational dynamics are often neglected for fractal aggregates [121, 127, 154, 155], though they have been considered in studies of simple shapes shapes such as ellipsoids [153, 156]. Hydrodynamic interactions are included in Stokesian dynamics simulations for particles in the continuum [135, 136] but are typically excluded for non-continuum particles.

Eqs. (10.3)–(10.6) can be solved for a system of particles to determine the effects of the rotation and/or hydrodynamic interactions on the dynamic behavior of the system. To do so, one would have to repeat the simulation multiple times, average the results, and compare various figures of merit (e.g. coagulation rates, sedimentation rates, particle size and fractal dimension) to the same parameters for simulations of the same system that neglect rotational and hydrodynamic effects. During the calculation, one would need to perform the EKR calculation at each time step to determine the friction tensors, hydrodynamic forces and torques, and probability distribution for the Brownian forces and torques for each particle.

One could also perform a Brownian simulation for a single aggregate in an

external field; in this case, one need only perform the EKR calculation for the friction tensors of the particle at the start of the simulation. Calculations could be performed for a range of external field strengths. Results of Brownian trajectories for zero field strength can be used to evaluate the results for the translational and rotational diffusion coefficients computed using rigid body hydrodynamic theory (i.e. the results described in Chapters 3–6). Brownian dynamics results for non-zero field strength could be used to determine the electrical mobility of a particle and can be compared to the results of the particle alignment calculations described in Chapter 7.

Ultimately, these Brownian simulations can be used to evaluate the validity of various assumptions (e.g. treating aggregates as equivalent spheres, ignoring rotation effects, neglecting hydrodynamic interactions) typically made in studies of cluster aggregation kinetics and other dynamic aerosol processes.

Clearly, this suggested project would be a substantial undertaking, both in setting up the problem (i.e. writing the code to solve the Langevin equations above) and in ensemble-averaging and interpreting the results. Additionally, one needs access to powerful computing resources to tackle this problem, given the large number of simulations that would be required to account for the statistical fluctuations inherent in solving the problem and the computational time required to perform a single Brownian trajectory. Given these issues, as well as the likelihood that rotational and hydrodynamic effects may only have minor effects on the dynamic behavior of aerosol systems, it is hardly surprising that this problem has received little attention in the literature. Nevertheless, my method for calculating the friction tensors of

aerosol aggregates in the transition regime provides one of the missing pieces needed to tackle this difficult problem.

Appendix A: Derivation of Expressions in Chapter 2

In this Appendix, I present derivations for several expressions that appear in the solution of the BGK equation for flow around a sphere, as presented in Chapter 2.

A.1 Derivation of the Expression for g [Eq. (2.42)]

In this section, I will present the derivation of the constant g in Eq. (2.42) for flow around a sphere. This derivation follows Appendix D of Lea [74], but I have included more of the intermediate steps for clarity. I have also included information from Law and Loyalka [76] because that study accounts for non-isothermal conditions around the sphere. For this derivation, I will refer to the angles defined in Fig. 2.4.

We start by writing the velocity perturbation vector in terms of coordinates (x', y', z'):

$$\boldsymbol{\varepsilon}_2(r) = \sqrt{2}\,\rho_3 \sin\alpha'\,\hat{\mathbf{e}}_{\mathbf{x}'} + \sqrt{2}\,\rho_2 \cos\alpha'\,\hat{\mathbf{e}}_{\mathbf{z}'} \tag{A.1}$$

Note that the z'-direction is simply $\hat{\mathbf{e}}_{\mathbf{r}}$; the y' direction is chosen to be perpendicular to the plane containing $\boldsymbol{U}_\infty$ and $\hat{\mathbf{e}}_{\mathbf{z}'}$; and the x' direction is of course mutually

orthogonal to the y'- and z'-directions:

$$\hat{\mathbf{e}}_{\mathbf{z'}} = \hat{\mathbf{e}}_{\mathbf{r}}, \quad \hat{\mathbf{e}}_{\mathbf{y'}} = \frac{\hat{\mathbf{e}}_{\mathbf{z'}} \times \hat{\mathbf{e}}_{\mathbf{U}}}{\sin\alpha'}, \quad \hat{\mathbf{e}}_{\mathbf{x'}} = \hat{\mathbf{e}}_{\mathbf{y'}} \times \hat{\mathbf{e}}_{\mathbf{z'}} \tag{A.2}$$

We must now write out the local coordinates (x', y', z'), in terms of coordinates (x, y, z). First, we write $\hat{\mathbf{e}}_{\mathbf{z'}}$ in terms of (x, y, z):

$$\hat{\mathbf{e}}_{\mathbf{z'}} = \sin\theta'\cos\phi'\,\hat{\mathbf{e}}_{\mathbf{x}} + \sin\theta'\sin\phi'\,\hat{\mathbf{e}}_{\mathbf{y}} + \cos\theta'\,\hat{\mathbf{e}}_{\mathbf{z}} \tag{A.3}$$

Next, we write $\hat{\mathbf{e}}_{\mathbf{U}}$ in terms of (x, y, z):

$$\hat{\mathbf{e}}_{\mathbf{U}} = \sin\alpha\,\hat{\mathbf{e}}_{\mathbf{x}} + \cos\alpha\,\hat{\mathbf{e}}_{\mathbf{z}} \tag{A.4}$$

Next, we evaluate the cross product to determine $\hat{\mathbf{e}}_{\mathbf{y'}}$:

$$\begin{aligned}\hat{\mathbf{e}}_{\mathbf{y'}} = \frac{1}{\sin\alpha'}\big[&\sin\theta'\sin\phi'\cos\alpha\,\hat{\mathbf{e}}_{\mathbf{x}} \\ &+ (\sin\alpha'\cos\theta' - \sin\theta'\cos\phi'\cos\alpha)\,\hat{\mathbf{e}}_{\mathbf{y}} - \sin\theta'\sin\phi'\sin\alpha\,\hat{\mathbf{e}}_{\mathbf{z}}\big]\end{aligned} \tag{A.5}$$

Finally, we evaluate the cross product to determine $\hat{\mathbf{e}}_{\mathbf{x'}}$:

$$\begin{aligned}\hat{\mathbf{e}}_{\mathbf{x'}} = \frac{1}{\sin\alpha'}\big[&\left(\sin\alpha\cos^2\theta' - \cos\alpha\sin\theta'\cos\theta'\cos\phi' + \sin\alpha\sin^2\theta'\sin^2\phi'\right)\hat{\mathbf{e}}_{\mathbf{x}} \\ &- \left(\cos\alpha\sin\theta'\cos\theta'\sin\phi' + \sin\alpha\sin^2\theta'\sin\phi'\cos\phi'\right)\hat{\mathbf{e}}_{\mathbf{y}} \\ &+ \left(\cos\alpha\sin^2\theta' - \sin\alpha\sin\theta'\cos\theta'\cos\phi'\right)\hat{\mathbf{e}}_{\mathbf{z}}\big]\end{aligned} \tag{A.6}$$

Now that we have defined the coordinates (x', y', z') in terms of coordinates (x, y, z), we can write our velocity perturbation vector in terms of coordinates (x, y, z):

$$\begin{aligned}\boldsymbol{\varepsilon}_2(r) = \sqrt{2}\big\{\big[&\rho_2 \cos\alpha' \sin\theta' \cos\phi' + \rho_3\big(\sin\alpha\cos^2\theta' - \cos\alpha\sin\theta'\cos\theta'\cos\phi' \\ &+ \sin\alpha\sin^2\theta'\sin^2\phi'\big)\big]\hat{\mathbf{e}}_{\mathbf{x}} + \big[\rho_2\cos\alpha'\sin\theta'\sin\phi' \\ &- \rho_3\big(\cos\alpha\sin\theta'\cos\theta'\sin\phi' + \sin\alpha\sin^2\theta'\sin\phi'\cos\phi'\big)\big]\hat{\mathbf{e}}_{\mathbf{y}} \\ &+ \big[\rho_2\cos\alpha'\cos\theta' + \rho_3\big(\cos\alpha\sin^2\theta' - \sin\alpha\sin\theta'\cos\theta'\cos\phi'\big)\big]\hat{\mathbf{e}}_{\mathbf{z}}\big\}\end{aligned} \tag{A.7}$$

We can now consider our equation for the source term, Eq. (2.33):

$$\begin{aligned}A(\boldsymbol{r}_0) = &-\sqrt{\pi}U\cos\alpha \\ &-\frac{2}{\pi}\int_V \frac{\mathrm{d}\boldsymbol{r}}{|\boldsymbol{r}-\boldsymbol{r}_0|^2}\left[\mathrm{T}_2\,\varepsilon_1(\boldsymbol{r}) + \mathrm{T}_3\,\hat{\boldsymbol{\Omega}}\cdot\boldsymbol{\varepsilon}_2(\boldsymbol{r}) + \left(\mathrm{T}_4 - \frac{3}{2}\,\mathrm{T}_2\right)\varepsilon_3(\boldsymbol{r})\right](\hat{\boldsymbol{\Omega}}\cdot\hat{\boldsymbol{n}})\end{aligned}$$

Here, we have simply written out the triple integral in terms of Cartesian coordinates. Again, the argument of the T_n functions is $|\boldsymbol{r}-\boldsymbol{r}_0|$. Before proceeding further, we will introduce a new coordinate system, (r, t, ϕ'), where r is the distance from the origin to point $\boldsymbol{r}$, $t = |\boldsymbol{r} - \boldsymbol{r}_0|$, and ϕ' is the angle of rotation about the z-axis, with $\phi' = 0$ corresponding to the positive x-axis. These coordinates are related to the (x, y, z) coordinates by the following expressions:

$$x = r\sin\theta'\cos\phi' \tag{A.8a}$$

$$y = r \sin\theta' \sin\phi' \tag{A.8b}$$

$$z = r \cos\theta' \tag{A.8c}$$

where the angles θ and θ' are

$$\cos\theta' = \frac{r^2 + r_0^2 - t^2}{2 r_0 r} \tag{A.9a}$$

$$\cos\theta = \frac{t^2 + r_0^2 - r^2}{2 r_0 t} \tag{A.9b}$$

$$r \sin\theta' = t \sin\theta = \frac{\sqrt{(2 r r_0)^2 - (r^2 + r_0^2 - t^2)^2}}{2 r_0} \tag{A.9c}$$

Note that θ and θ' are independent of ϕ'.

The Jacobian determinant of coordinates (r, t, ϕ') is tr/r_0. In these coordinates, our equation for $A(\boldsymbol{r}_0)$ becomes

$$A(\boldsymbol{r}_0) = -\sqrt{\pi} U \cos\alpha - \frac{2}{\pi} \int_{r_0}^{\infty} \mathrm{d}r \, \frac{r}{r_0} \int_{r-r_0}^{\sqrt{r^2 - r_0^2}} \frac{\mathrm{d}t}{t} \int_0^{2\pi} \mathrm{d}\phi' \left[\mathrm{T}_2(t) \varepsilon_1(\boldsymbol{r}) + \mathrm{T}_3(t) \hat{\boldsymbol{\Omega}} \cdot \boldsymbol{\varepsilon}_2(\boldsymbol{r}) + \left(\mathrm{T}_4(t) - \frac{3}{2} \mathrm{T}_2(r) \right) \varepsilon_3(\boldsymbol{r}) \right] (\cos\theta)$$

Here, θ is the angle between $\hat{\boldsymbol{n}}$ and $\hat{\boldsymbol{\Omega}}$, $\boldsymbol{\varepsilon}_2$ is given by Eq. (A.7), and

$$\hat{\boldsymbol{\Omega}} = \frac{\boldsymbol{r}_0 - \boldsymbol{r}}{|\boldsymbol{r}_0 - \boldsymbol{r}|} = -\sin\theta \cos\phi' \hat{\mathbf{e}}_{\mathbf{x}} - \sin\theta \sin\phi' \hat{\mathbf{e}}_{\mathbf{y}} + \cos\theta \hat{\mathbf{e}}_{\mathbf{z}}$$

We can integrate over ϕ' analytically. We start with the term involving $\varepsilon_1(\boldsymbol{r})$. We use Eq. (2.48a) to write the density perturbation in terms of its radial and

angular components, write $\cos\alpha'$ in terms of the angles (α, θ', ϕ'), and integrate over ϕ':

$$\begin{aligned}\int_0^{2\pi} \mathrm{d}\phi' \ \mathrm{T}_2(t)\varepsilon_1(\boldsymbol{r}) &= \mathrm{T}_2(t)\rho_1(r)\int_0^{2\pi} \mathrm{d}\phi' \ \cos\alpha' \\ &= \mathrm{T}_2(t)\rho_1(r)\int_0^{2\pi} \mathrm{d}\phi' \ [\cos\alpha\cos\theta' + \sin\alpha\sin\theta'\cos\phi'] \\ &= 2\pi \, \mathrm{T}_2(t)\rho_1(r)\cos\alpha\cos\theta'\end{aligned}$$

We get a very similar result for ε_3, with ρ_1 replaced by ρ_4 and the appropriate T_n functions.

For the term involving $\boldsymbol{\varepsilon}_2(\boldsymbol{r})$, we must first evaluate the dot product $\hat{\boldsymbol{\Omega}} \cdot \boldsymbol{\varepsilon}_2(\boldsymbol{r})$:

$$\begin{aligned}\hat{\boldsymbol{\Omega}} \cdot \boldsymbol{\varepsilon}_2(\boldsymbol{r}) = \sqrt{2}\big[&\rho_2 \cos\alpha'(\cos\theta\cos\theta' - \sin\theta\sin\theta'\cos^2\phi' - \sin\theta\sin\theta'\sin^2\phi') \\ &+ \rho_3(\cos\alpha\sin\theta\sin\theta'\cos\theta'\cos^2\phi' - \sin\alpha\sin\theta\cos^2\theta'\cos\phi' \\ &- \sin\alpha\sin\theta\sin^2\theta'\sin^2\phi'\cos\phi' + \cos\alpha\sin\theta\sin\theta'\cos\theta'\sin^2\phi' \\ &+ \sin\alpha\sin\theta\sin^2\theta'\sin^2\phi'\cos\phi' + \cos\alpha\cos\theta\sin^2\theta' \\ &- \sin\alpha\cos\theta\sin\theta'\cos\theta'\cos\phi')\big] \\ = \sqrt{2}\big[&\rho_2(\cos\theta\cos\theta' - \sin\theta\sin\theta')(\cos\alpha\cos\theta' + \sin\alpha\sin\theta'\cos\phi') \\ &+ \rho_3(\cos\alpha\sin\theta\sin\theta'\cos\theta' - \sin\alpha\sin\theta\cos^2\theta'\cos\phi' \\ &+ \cos\alpha\cos\theta\sin^2\theta' - \sin\alpha\cos\theta\sin\theta'\cos\theta'\cos\phi')\big]\end{aligned}$$

When we separate the terms involving $\sin\alpha$ from those involving $\cos\alpha$,

$$\begin{aligned}\hat{\boldsymbol{\Omega}}\cdot\boldsymbol{\varepsilon}_2(\boldsymbol{r}) =&\sqrt{2}\cos\alpha\big[\rho_2(\cos\theta\cos^2\theta' - \sin\theta\sin\theta'\cos\theta')\\ &+ \rho_3(\sin\theta\sin\theta'\cos\theta' + \cos\theta\sin^2\theta')\big]\\ &+ \sqrt{2}\sin\alpha\big[\rho_2(\cos\theta\sin\theta'\cos\theta'\cos\phi' - \sin\theta\sin^2\theta'\cos\phi')\\ &- \rho_3(\sin\theta\cos^2\theta'\cos\phi' + \cos\theta\sin\theta'\cos\theta'\cos\phi')\big]\end{aligned}$$

we can see that the term involving $\sin\alpha$ are odd functions of ϕ'. This means that these terms will disappear when we integrate over ϕ'. On the other hand, the term involving $\cos\alpha$ does not depend on ϕ', so the integral is simply the $\cos\alpha$ term multiplied by 2π:

$$\begin{aligned}\int_0^{2\pi}\mathrm{d}\phi'\ \mathrm{T}_3(t)\hat{\boldsymbol{\Omega}}\cdot\boldsymbol{\varepsilon}_2(\boldsymbol{r}) = 2\sqrt{2}\pi\,\mathrm{T}_3(t)\big[&\rho_2(\cos\theta\cos^2\theta' - \sin\theta\sin\theta'\cos\theta')\\ &+ \rho_3(\sin\theta\sin\theta'\cos\theta' + \cos\theta\sin^2\theta')\big]\end{aligned}$$

Thus, we can write the function $A(\boldsymbol{r}_0)$ as

$$A(\boldsymbol{r}_0) = gU\cos\alpha \tag{A.10}$$

where the constant g is defined by

$$g = -\pi^{1/2} + 2\int_{r_0}^{\infty}\mathrm{d}r\,\frac{r}{r_0}[\boldsymbol{q}(r)\cdot\boldsymbol{a}(r)]$$

$$a_1(r) = -2\int_{r-r_0}^{\sqrt{r^2-r_0^2}} \frac{\mathrm{d}t}{t}\,\mathrm{T}_2(t)\cos\theta\cos\theta'$$

$$a_2(r) = -2\sqrt{2}\int_{r-r_0}^{\sqrt{r^2-r_0^2}} \frac{\mathrm{d}t}{t}\,\mathrm{T}_3(t)\cos\theta(\cos\theta\cos^2\theta' - \sin\theta\sin\theta'\cos\theta')$$

$$a_3(r) = -2\sqrt{2}\int_{r-r_0}^{\sqrt{r^2-r_0^2}} \frac{\mathrm{d}t}{t}\,\mathrm{T}_3(t)\cos\theta(\sin\theta\sin\theta'\cos\theta' + \cos\theta\sin^2\theta')$$

$$a_4(r) = -2\left(\frac{2}{3}\right)^{1/2}\int_{r-r_0}^{\sqrt{r^2-r_0^2}} \frac{\mathrm{d}t}{t}\left(\mathrm{T}_4(t) - \frac{3}{2}\,\mathrm{T}_2(t)\right)\cos\theta\cos\theta'$$

Finally, we plug in our expressions for $\cos\theta$, $\cos\theta'$, $\sin\theta$, and $\sin\theta'$ to get our expression for g:

$$g = -\pi^{1/2} + 2\int_{r_0}^{\infty} \mathrm{d}r\,\frac{r}{r_0}[\boldsymbol{q}(r)\cdot\boldsymbol{a}(r)] \tag{A.11}$$

$$a_1(r) = \frac{1}{2r_0^2 r}\int_{r-r_0}^{\sqrt{r^2-r_0^2}} \left[t^4 - 2r^2t^2 + (r^4 - r_0^4)\right]\frac{\mathrm{T}_2(t)}{t^2}\mathrm{d}t \tag{A.12}$$

$$a_2(r) = \frac{-1}{2\sqrt{2}r_0^2r^2}\int_{r-r_0}^{\sqrt{r^2-r_0^2}} \Big[t^6 - t^4(r^2+r_0^2) - t^2(r^2-r_0^2)^2 + (r^2-r_0^2)(r^4-r_0^4)\Big]\frac{\mathrm{T}_3(t)}{t^3}\mathrm{d}t \tag{A.13}$$

$$a_3(r) = \frac{1}{2\sqrt{2}r_0^2r^2}\int_{r-r_0}^{\sqrt{r^2-r_0^2}} \Big[t^6 - t^4(3r^2+r_0^2) + t^2(r^2-r_0^2)(3r^2+r_0^2) - (r^2-r_0^2)^2\Big]\frac{\mathrm{T}_3(t)}{t^3}\mathrm{d}t \tag{A.14}$$

$$a_4(r) = \left(\frac{2}{3}\right)^{1/2}\frac{1}{2r_0^2 r}\int_{r-r_0}^{\sqrt{r^2-r_0^2}} \left[t^4 - 2r^2t^2 + (r^4 - r_0^2)\right]\left[\mathrm{T}_4(t) - \frac{3}{2}\,\mathrm{T}_2(t)\right]\frac{\mathrm{d}t}{t^2} \tag{A.15}$$

A.2 Derivation of the Source Term Expressions (Eqns. 2.40–2.41)

In this section, I will present the derivation of the W terms that appear in the source term expressions for flow around a sphere. This derivation follows Appendix

C of Lea [74], but I have included more of the intermediate steps for clarity. I have also included information from Law and Loyalka [76] to account for non-isothermal conditions. For this derivation, I will refer to the angles defined in Fig. 2.3.

We start by writing the source terms $\boldsymbol{S}_A(\boldsymbol{r})$ and $\boldsymbol{S}_U(\boldsymbol{r})$,

$$
\begin{aligned}
S_{A1}(\boldsymbol{r}) =& \pi^{-3/2} \int_\omega A(\boldsymbol{r}_0)\, \mathrm{T}_2(|\boldsymbol{r}-\boldsymbol{r}_0|)\mathrm{d}\hat{\boldsymbol{\Omega}} \\
S_{A2}(\boldsymbol{r}) =& \sqrt{2}\pi^{-3/2} \int_\omega A(\boldsymbol{r}_0)\, \mathrm{T}_3(|\boldsymbol{r}-\boldsymbol{r}_0|)\hat{\Omega}_z \mathrm{d}\hat{\boldsymbol{\Omega}} \\
S_{A3}(\boldsymbol{r}) =& \sqrt{2}\pi^{-3/2} \int_\omega A(\boldsymbol{r}_0)\, \mathrm{T}_3(|\boldsymbol{r}-\boldsymbol{r}_0|)\hat{\Omega}_x \mathrm{d}\hat{\boldsymbol{\Omega}} \\
S_{A4}(\boldsymbol{r}) =& \sqrt{\frac{2}{3}}\pi^{-3/2} \int_\omega A(\boldsymbol{r}_0) \left(\mathrm{T}_4(|\boldsymbol{r}-\boldsymbol{r}_0|) - \frac{3}{2}\mathrm{T}_2(|\boldsymbol{r}-\boldsymbol{r}_0|) \right) \mathrm{d}\hat{\boldsymbol{\Omega}} \\
S_{U1}(\boldsymbol{r}) =& -2\pi^{-3/2} \int_\omega \hat{\boldsymbol{\Omega}}\cdot\boldsymbol{U}_\infty\, \mathrm{T}_3(|\boldsymbol{r}-\boldsymbol{r}_0|)\mathrm{d}\hat{\boldsymbol{\Omega}} \\
S_{U2}(\boldsymbol{r}) =& -2\sqrt{2}\pi^{-3/2} \int_\omega \hat{\boldsymbol{\Omega}}\cdot\boldsymbol{U}_\infty\, \mathrm{T}_4(|\boldsymbol{r}-\boldsymbol{r}_0|)\hat{\Omega}_z \mathrm{d}\hat{\boldsymbol{\Omega}} \\
S_{U3}(\boldsymbol{r}) =& -2\sqrt{2}\pi^{-3/2} \int_\omega \hat{\boldsymbol{\Omega}}\cdot\boldsymbol{U}_\infty\, \mathrm{T}_4(|\boldsymbol{r}-\boldsymbol{r}_0|)\hat{\Omega}_x \mathrm{d}\hat{\boldsymbol{\Omega}} \\
S_{U4}(\boldsymbol{r}) =& -2\sqrt{\frac{2}{3}}\pi^{-3/2} \int_\omega \hat{\boldsymbol{\Omega}}\cdot\boldsymbol{U}_\infty \left(\mathrm{T}_5(|\boldsymbol{r}-\boldsymbol{r}_0|) - \frac{3}{2}\mathrm{T}_3(|\boldsymbol{r}-\boldsymbol{r}_0|) \right) \mathrm{d}\hat{\boldsymbol{\Omega}}
\end{aligned}
$$

where $\mathrm{d}\hat{\boldsymbol{\Omega}} = \sin\theta \mathrm{d}\theta\mathrm{d}\phi$, $\hat{\Omega}_x = \sin\theta\cos\phi$, and $\hat{\Omega}_x = \cos\theta$. Introducing the variable t, where

$$
t = |\boldsymbol{r}-\boldsymbol{r}_0| = \arccos\left(\frac{t^2+r^2-r_0^2}{2rt}\right)
$$

$$
\sin\theta\mathrm{d}\theta = \frac{r^2-r_0^2-t^2}{2rt^2}\mathrm{d}t
$$

the source term equations become

$$
\begin{aligned}
S_{A1}(\boldsymbol{r}) =& \pi^{-3/2} \int_{r-r_0}^{\sqrt{r^2-r_0^2}} \mathrm{d}t \ \mathrm{T}_2(t) \left[\frac{r^2-r_0^2-t^2}{2rt^2}\right] \int_0^{2\pi} \mathrm{d}\phi \, A(\boldsymbol{r}_0) \\
S_{A2}(\boldsymbol{r}) =& \sqrt{2}\pi^{-3/2} \int_{r-r_0}^{\sqrt{r^2-r_0^2}} \mathrm{d}t \ \mathrm{T}_3(t) \cos\theta \left[\frac{r^2-r_0^2-t^2}{2rt^2}\right] \int_0^{2\pi} \mathrm{d}\phi \, A(\boldsymbol{r}_0) \\
S_{A3}(\boldsymbol{r}) =& \sqrt{2}\pi^{-3/2} \int_{r-r_0}^{\sqrt{r^2-r_0^2}} \mathrm{d}t \ \mathrm{T}_3(t) \sin\theta \left[\frac{r^2-r_0^2-t^2}{2rt^2}\right] \int_0^{2\pi} \mathrm{d}\phi \, A(\boldsymbol{r}_0) \cos\phi \\
S_{A4}(\boldsymbol{r}) =& \sqrt{\frac{2}{3}}\pi^{-3/2} \int_{r-r_0}^{\sqrt{r^2-r_0^2}} \mathrm{d}t \ \left(\mathrm{T}_4(t) - \frac{3}{2}\,\mathrm{T}_2(t)\right) \left[\frac{r^2-r_0^2-t^2}{2rt^2}\right] \int_0^{2\pi} \mathrm{d}\phi \, A(\boldsymbol{r}_0) \\
S_{U1}(\boldsymbol{r}) =& -2\pi^{-3/2} \int_{r-r_0}^{\sqrt{r^2-r_0^2}} \mathrm{d}t \ \mathrm{T}_3(t) \left[\frac{r^2-r_0^2-t^2}{2rt^2}\right] \int_0^{2\pi} \mathrm{d}\phi \, (\hat{\boldsymbol{\Omega}} \cdot \boldsymbol{U}_\infty) \\
S_{U2}(\boldsymbol{r}) =& -2\sqrt{2}\pi^{-3/2} \int_{r-r_0}^{\sqrt{r^2-r_0^2}} \mathrm{d}t \ \mathrm{T}_4(t) \cos\theta \left[\frac{r^2-r_0^2-t^2}{2rt^2}\right] \int_0^{2\pi} \mathrm{d}\phi \, (\hat{\boldsymbol{\Omega}} \cdot \boldsymbol{U}_\infty) \\
S_{U3}(\boldsymbol{r}) =& -2\sqrt{2}\pi^{-3/2} \int_{r-r_0}^{\sqrt{r^2-r_0^2}} \mathrm{d}t \ \mathrm{T}_4(t) \sin\theta \left[\frac{r^2-r_0^2-t^2}{2rt^2}\right] \int_0^{2\pi} \mathrm{d}\phi \, (\hat{\boldsymbol{\Omega}} \cdot \boldsymbol{U}_\infty) \cos\phi \\
S_{U4}(\boldsymbol{r}) =& -2\sqrt{\frac{2}{3}}\pi^{-3/2} \int_{r-r_0}^{\sqrt{r^2-r_0^2}} \mathrm{d}t \ \left(\mathrm{T}_5(t) - \frac{3}{2}\,\mathrm{T}_3(t)\right) \left[\frac{r^2-r_0^2-t^2}{2rt^2}\right] \\
& \times \int_0^{2\pi} \mathrm{d}\phi \, (\hat{\boldsymbol{\Omega}} \cdot \boldsymbol{U}_\infty)
\end{aligned}
$$

We can integrate analytically over ϕ, but first we must write $A(\boldsymbol{r}_0)$ and $\hat{\boldsymbol{\Omega}} \cdot \boldsymbol{U}_\infty$ in terms of the angles α, θ, and ϕ. The dot product is

$$
\begin{aligned}
\hat{\boldsymbol{\Omega}} \cdot \boldsymbol{U}_\infty &= \big(\sin\alpha, 0, \cos\alpha\big) \cdot \big(\sin\theta\cos\phi, \sin\theta\sin\phi, \cos\theta\big) \\
&= \sin\alpha\sin\theta\cos\phi + \cos\alpha\cos\theta
\end{aligned}
$$

As we saw in Section A.1,

$$
A(\boldsymbol{r}_0) = gU\cos\alpha' = gU(\cos\alpha\cos\theta' - \sin\alpha\sin\theta'\cos\phi)
$$

We can substitute these expressions into our integrals over ϕ:

$$\begin{aligned}
\int_0^{2\pi} \mathrm{d}\phi\, A(\boldsymbol{r}_0) =& gU \int_0^{2\pi} (\cos\alpha\cos\theta' - \sin\alpha\sin\theta'\cos\phi)\mathrm{d}\phi \\
=& 2\pi gU\cos\alpha\cos\theta' \\
\int_0^{2\pi} \mathrm{d}\phi\, A(\boldsymbol{r}_0)\cos\phi =& gU \int_0^{2\pi} \cos\phi(\cos\alpha\cos\theta' - \sin\alpha\sin\theta'\cos\phi)\mathrm{d}\phi \\
=& -\pi gU\sin\alpha\sin\theta' \\
\int_0^{2\pi} \mathrm{d}\phi\, \hat{\boldsymbol{\Omega}}\cdot\boldsymbol{U}_\infty =& \int_0^{2\pi} (\sin\alpha\sin\theta\cos\phi + \cos\alpha\cos\theta)\mathrm{d}\phi \\
=& 2\pi\cos\alpha\cos\theta \\
\int_0^{2\pi} \mathrm{d}\phi\, \hat{\boldsymbol{\Omega}}\cdot\boldsymbol{U}_\infty\cos\phi =& \int_0^{2\pi} \cos\phi(\sin\alpha\sin\theta\cos\phi + \cos\alpha\cos\theta)\mathrm{d}\phi \\
=& \pi\sin\alpha\sin\theta
\end{aligned}$$

Thus, our source terms are

$$\begin{aligned}
S_{A1}(\boldsymbol{r}) =& 2\pi^{-1/2} gU\cos\alpha \int_{r-r_0}^{\sqrt{r^2-r_0^2}} \mathrm{d}t\ \mathrm{T}_2(t) \left[\frac{r^2-r_0^2-t^2}{2rt^2}\right] \cos\theta' \\
S_{A2}(\boldsymbol{r}) =& 2\sqrt{2}\pi^{-1/2} gU\cos\alpha \int_{r-r_0}^{\sqrt{r^2-r_0^2}} \mathrm{d}t\ \mathrm{T}_3(t) \left[\frac{r^2-r_0^2-t^2}{2rt^2}\right] \cos\theta\cos\theta' \\
S_{A3}(\boldsymbol{r}) =& -\sqrt{2}\pi^{-1/2} gU\sin\alpha \int_{r-r_0}^{\sqrt{r^2-r_0^2}} \mathrm{d}t\ \mathrm{T}_3(t) \left[\frac{r^2-r_0^2-t^2}{2rt^2}\right] \sin\theta\sin\theta' \\
S_{A4}(\boldsymbol{r}) =& 2\left(\frac{2}{3\pi}\right)^{1/2} gU\cos\alpha \int_{r-r_0}^{\sqrt{r^2-r_0^2}} \mathrm{d}t\ \left[\mathrm{T}_4(t) - \frac{3}{2}\mathrm{T}_2(t)\right] \left[\frac{r^2-r_0^2-t^2}{2rt^2}\right] \cos\theta' \\
S_{U1}(\boldsymbol{r}) =& -4\pi^{-1/2}\cos\alpha \int_{r-r_0}^{\sqrt{r^2-r_0^2}} \mathrm{d}t\ \mathrm{T}_3(t) \left[\frac{r^2-r_0^2-t^2}{2rt^2}\right] \cos\theta \\
S_{U2}(\boldsymbol{r}) =& -4\sqrt{2}\pi^{-1/2}\cos\alpha \int_{r-r_0}^{\sqrt{r^2-r_0^2}} \mathrm{d}t\ \mathrm{T}_4(t) \left[\frac{r^2-r_0^2-t^2}{2rt^2}\right] \cos^2\theta \\
S_{U3}(\boldsymbol{r}) =& -2\sqrt{2}\pi^{-1/2}\sin\alpha \int_{r-r_0}^{\sqrt{r^2-r_0^2}} \mathrm{d}t\ \mathrm{T}_4(t) \left[\frac{r^2-r_0^2-t^2}{2rt^2}\right] \sin^2\theta
\end{aligned}$$

$$S_{U4}(\boldsymbol{r}) = -\,4\left(\frac{2}{3\pi}\right)^{1/2}\cos\alpha\int_{r-r_0}^{\sqrt{r^2-r_0^2}}\mathrm{d}t\,\left[\mathrm{T}_5(t)-\frac{3}{2}\,\mathrm{T}_3(t)\right]\left[\frac{r^2-r_0^2-t^2}{2rt^2}\right]\cos\theta$$

Finally, we must write $\cos\theta$, $\cos\theta'$, $\sin\theta$, and $\sin\theta'$ in terms of r, t, and r_0 and substitute these expressions into our source term equations:

$$\cos\theta' = \frac{r^2+r_0^2-t^2}{2r_0 r} \tag{A.16a}$$

$$\cos\theta = \frac{t^2+r^2-r_0^2}{2rt} \tag{A.16b}$$

$$r_0\sin\theta' = t\sin\theta = \frac{\sqrt{(2rr_0)^2-(r^2+r_0^2-t^2)^2}}{2r} \tag{A.16c}$$

This gives us the final expression for the source terms:

$$\boldsymbol{S}_A(\boldsymbol{r}) = gU\begin{bmatrix} W_{A1}(r)\cos\alpha \\ W_{A2}(r)\cos\alpha \\ W_{A3}(r)\sin\alpha \\ W_{A4}(r)\cos\alpha \end{bmatrix} \tag{A.17}$$

$$\boldsymbol{S}_U(\boldsymbol{r}) = U\begin{bmatrix} W_{U1}(r)\cos\alpha \\ W_{U2}(r)\cos\alpha \\ W_{U3}(r)\sin\alpha \\ W_{U4}(r)\cos\alpha \end{bmatrix} \tag{A.18}$$

$$W_{A1}(r) = \frac{1}{2\sqrt{\pi}r^2 r_0} \int \left[t^4 - 2r^2t^2 + (r^4 - r_0^4)\right] \frac{\mathrm{T}_2(t)}{t^2} \mathrm{d}t \tag{A.19}$$

$$W_{A2}(r) = \frac{1}{2\sqrt{2\pi}r^3 r_0} \int \left[t^6 - (r^2 + r_0^2)t^4 - (r^2 - r_0^2)^2 t^2 \right. \tag{A.20}$$

$$\left. + (r^2 + r_0^2)(r^2 - r_0^2)^2\right] \frac{\mathrm{T}_3(t)}{t^3} \mathrm{d}t \tag{A.21}$$

$$W_{A3}(r) = \frac{-1}{4\sqrt{2\pi}r^3 r_0} \int \left[t^6 - (3r^2 + r_0^2)t^4 + (r^2 - r_0^2)(3r^2 + r_0^2)t^2 \right. \tag{A.22}$$

$$\left. - (r^2 - r_0^2)^3\right] \frac{\mathrm{T}_3(t)}{t^3} \mathrm{d}t \tag{A.23}$$

$$W_{A4}(r) = \left(\frac{2}{3}\right)^{1/2} \frac{1}{2\sqrt{\pi}r^2 r_0} \int \left[t^4 - 2r^2t^2 + (r^4 - r_0^4)\right] \left[\mathrm{T}_4(t) - \frac{3}{2}\mathrm{T}_2(t)\right] \frac{\mathrm{d}t}{t^2} \tag{A.24}$$

$$W_{U1}(r) = \frac{1}{\sqrt{\pi}r^2} \int \left[t^4 - (r^2 - r_0^2)^2\right] \frac{\mathrm{T}_3(t)}{t^3} \mathrm{d}t \tag{A.25}$$

$$W_{U2}(r) = \frac{1}{\sqrt{2\pi}r^3} \int \left[t^6 + t^4(r^2 - r_0^2) - t^2(r^2 - r_0^2)^2 - (r^2 - r_0^2)^3\right] \frac{\mathrm{T}_4(t)}{t^4} \mathrm{d}t \tag{A.26}$$

$$W_{U3}(r) = \frac{-1}{2\sqrt{2\pi}r^3} \int \left[t^6 - t^4(3r^2 + r_0^2) + t^2(r^2 - r_0^2)(3r^2 + r_0^2) \right. \tag{A.27}$$

$$\left. - (r^2 - r_0^2)^3\right] \frac{\mathrm{T}_4(t)}{t^4} \mathrm{d}t \tag{A.28}$$

$$W_{U4}(r) = \left(\frac{2}{3}\right)^{1/2} \frac{1}{\sqrt{\pi}r^2} \int \left[t^4 - (r^2 - r_0^2)^2\right] \left[\mathrm{T}_5(t) - \frac{3}{2}\mathrm{T}_3(t)\right] \frac{\mathrm{d}t}{t^3} \tag{A.29}$$

The integration limits are $r - r_0$ and $\sqrt{r^2 - r_0^2}$.

A.3 Derivation of **H**

In this section, I will present the derivation of the H terms that appear in the equations for flow around a sphere. This derivation follows Appendix E of Lea [74], but I have included more of the intermediate steps for clarity. I have also included information from Law and Loyalka [76] to account for non-isothermal conditions. For this derivation, I will refer to the angles defined in Fig. 2.2.

We start by writing $\mathcal{L}\boldsymbol{\psi}(\boldsymbol{r}')$ from Eq. (2.39b):

$$\mathcal{L}\boldsymbol{\psi}(\boldsymbol{r}') = \pi^{-3/2} \int r'^2 \mathrm{d}r' \int \sin\theta' \mathrm{d}\theta' \int \mathrm{d}\phi' \, \Lambda\boldsymbol{\psi}(\boldsymbol{r}') \frac{1}{|\boldsymbol{r} - \boldsymbol{r}'|^2}$$

$$\Lambda\boldsymbol{\psi}(\boldsymbol{r}') \equiv \begin{bmatrix} \mathrm{T}_1 \, \varepsilon_1(\boldsymbol{r}') + \mathrm{T}_2 \, \hat{\boldsymbol{\Omega}} \cdot \boldsymbol{\varepsilon}_2(\boldsymbol{r}') + \left(\mathrm{T}_3 - \frac{3}{2}\mathrm{T}_1\right) \varepsilon_3(\boldsymbol{r}') \\ \sqrt{2}\left[\mathrm{T}_2 \, \varepsilon_1(\boldsymbol{r}') + \mathrm{T}_3 \, \hat{\boldsymbol{\Omega}} \cdot \boldsymbol{\varepsilon}_2(\boldsymbol{r}') + \left(\mathrm{T}_4 - \frac{3}{2}\mathrm{T}_2\right) \varepsilon_3(\boldsymbol{r}')\right] \Omega_z \\ \sqrt{2}\left[\mathrm{T}_2 \, \varepsilon_1(\boldsymbol{r}') + \mathrm{T}_3 \, \hat{\boldsymbol{\Omega}} \cdot \boldsymbol{\varepsilon}_2(\boldsymbol{r}') + \left(\mathrm{T}_4 - \frac{3}{2}\mathrm{T}_2\right) \varepsilon_3(\boldsymbol{r}')\right] \Omega_x \\ \sqrt{\frac{2}{3}}\left[\left(\mathrm{T}_3 - \frac{3}{2}\mathrm{T}_1\right) \varepsilon_1(\boldsymbol{r}') + \left(\mathrm{T}_4 - \frac{3}{2}\mathrm{T}_2\right) \hat{\boldsymbol{\Omega}} \cdot \boldsymbol{\varepsilon}_2(\boldsymbol{r}') + \left(\mathrm{T}_5 - 3\,\mathrm{T}_3 + \frac{9}{4}\mathrm{T}_1\right) \varepsilon_3(\boldsymbol{r}')\right] \end{bmatrix}$$

Note that the argument of ε_1, $\boldsymbol{\varepsilon}_2$, and ε_3 is $\boldsymbol{r}'$. Here, we have explicitly written the volume integral in polar coordinates, though we have not written the integration bounds because the bounds are difficult to formulate in these coordinates. Instead, it makes sense to transform the integral over θ' to an integral over $t \equiv |\boldsymbol{r} - \boldsymbol{r}'|$. We relate t to θ' by

$$t = \sqrt{r^2 + r'^2 - 2rr'\cos\theta'}$$

Taking the derivative of both sides, we get

$$\mathrm{d}t = \frac{rr'\sin\theta'}{\sqrt{r^2 + r'^2 - 2rr'\cos\theta}} \mathrm{d}\theta' = \frac{rr'\sin\theta'}{t} \mathrm{d}\theta'$$

Thus, our differential volume is now

$$\mathrm{d}\boldsymbol{r}' = r'^2 \sin\theta' \mathrm{d}r' \mathrm{d}\theta' \mathrm{d}\phi' = \frac{r'}{r} t \mathrm{d}r' \mathrm{d}t \mathrm{d}\phi' \tag{A.30}$$

and Eq. (2.39b) becomes

$$\mathcal{L}\boldsymbol{\psi}(\boldsymbol{r}') = \pi^{-3/2}\int_{r_0}^{\infty}\frac{r'}{r}\mathrm{d}r'\int_{|r-r'|}^{\sqrt{r^2-r_0^2}+\sqrt{r'^2-r_0^2}}\frac{\mathrm{d}t}{t}\int_0^{2\pi}\mathrm{d}\phi'\,\Lambda\boldsymbol{\psi}(\boldsymbol{r}')$$

Next, we must write the expression $\Lambda\boldsymbol{\psi}(\boldsymbol{r}')$ in terms of the angles defined in Fig. 2.2. The density and temperature perturbations are simply

$$\varepsilon_1(\boldsymbol{r}') = \rho_1(r')\cos\alpha' = \rho_1(r)[\cos\alpha\cos\theta' + \sin\alpha\sin\theta'\cos\phi']$$

$$\varepsilon_3(\boldsymbol{r}') = \left(\frac{2}{3}\right)^{1/2}\rho_4(r')\cos\alpha' = \left(\frac{2}{3}\right)^{1/2}\rho_4(r)[\cos\alpha\cos\theta' + \sin\alpha\sin\theta'\cos\phi']$$

This is the same expression that we used in Section A.1. Similarly, we have

$$\hat{\boldsymbol{\Omega}} = \frac{\boldsymbol{r}-\boldsymbol{r}'}{|\boldsymbol{r}-\boldsymbol{r}'|} = -\sin\theta\cos\phi'\hat{\mathbf{e}}_{\mathbf{x}} - \sin\theta\sin\phi'\hat{\mathbf{e}}_{\mathbf{y}} + \cos\theta\hat{\mathbf{e}}_{\mathbf{z}}$$

and

$$\begin{aligned}\hat{\boldsymbol{\Omega}}\cdot\boldsymbol{\varepsilon}_2(\boldsymbol{r}') =& \sqrt{2}\cos\alpha\big[\rho_2(\cos\theta\cos^2\theta' - \sin\theta\sin\theta'\cos\theta')\\ &+ \rho_3(\sin\theta\sin\theta'\cos\theta' + \cos\theta\sin^2\theta')\big]\\ &+ \sqrt{2}\sin\alpha\big[\rho_2(\cos\theta\sin\theta'\cos\theta'\cos\phi' - \sin\theta\sin^2\theta'\cos\phi')\\ &- \rho_3(\sin\theta\cos^2\theta'\cos\phi' + \cos\theta\sin\theta'\cos\theta'\cos\phi')\big]\end{aligned}$$

Integrating over ϕ', we have

$$\begin{aligned}
\int_0^{2\pi} \varepsilon_1(\boldsymbol{r}')\mathrm{d}\phi' =& 2\pi\rho_1(r')\cos\theta'\cos\alpha \\
\int_0^{2\pi} \hat{\boldsymbol{\Omega}}\cdot\boldsymbol{\varepsilon}_2(\boldsymbol{r}')\mathrm{d}\phi' =& 2\sqrt{2}\pi\big[\rho_2(\cos\theta\cos^2\theta' - \sin\theta\sin\theta'\cos\theta') \\
&+ \rho_3(\sin\theta\sin\theta'\cos\theta' + \cos\theta\sin^2\theta')\big]\cos\alpha \\
\int_0^{2\pi} \varepsilon_1(\boldsymbol{r}')\hat{\Omega}_z\mathrm{d}\phi' =& 2\pi\rho_1(r')\cos\theta\cos\theta'\cos\alpha \\
\int_0^{2\pi} \hat{\boldsymbol{\Omega}}\cdot\boldsymbol{\varepsilon}_2(\boldsymbol{r}')\hat{\Omega}_z\mathrm{d}\phi' =& 2\sqrt{2}\pi\big[\rho_2(\cos^2\theta\cos^2\theta' - \sin\theta\cos\theta\sin\theta'\cos\theta') \\
&+ \rho_3(\sin\theta\cos\theta\sin\theta'\cos\theta' + \cos^2\theta\sin^2\theta')\big]\cos\alpha \\
\int_0^{2\pi} \varepsilon_1(\boldsymbol{r}')\hat{\Omega}_x\mathrm{d}\phi' =& -\pi\rho_1(r')\sin\theta\sin\theta'\sin\alpha \\
\int_0^{2\pi} \hat{\boldsymbol{\Omega}}\cdot\boldsymbol{\varepsilon}_2(\boldsymbol{r}')\hat{\Omega}_x\mathrm{d}\phi' =& \sqrt{2}\pi\big[\rho_2(\sin^2\theta\sin^2\theta' - \sin\theta\cos\theta\sin\theta'\cos\theta') \\
&+ \rho_3(\sin^2\theta\cos^2\theta' + \sin\theta\cos\theta\sin\theta'\cos\theta')\big]\sin\alpha
\end{aligned}$$

We can now write $\mathcal{L}\boldsymbol{\psi}(\boldsymbol{r}')$ as

$$\mathcal{L}\boldsymbol{\psi}(\boldsymbol{r}') = \pi^{-1/2} \int_{r_0}^{\infty} \frac{r'}{r} \begin{bmatrix} \cos\alpha & 0 & 0 & 0 \\ 0 & \cos\alpha & 0 & 0 \\ 0 & 0 & \sin\alpha & 0 \\ 0 & 0 & 0 & \cos\alpha \end{bmatrix} \cdot \begin{bmatrix} H_{11} & H_{12} & H_{13} & H_{14} \\ H_{21} & H_{22} & H_{23} & H_{24} \\ H_{31} & H_{32} & H_{33} & H_{34} \\ H_{41} & H_{42} & H_{43} & H_{44} \end{bmatrix} \cdot \begin{bmatrix} \rho_1(r') \\ \rho_2(r') \\ \rho_3(r') \\ \rho_4(r') \end{bmatrix} \mathrm{d}r'$$

where

$$\begin{aligned}
H_{11}(r,r') =& 2 \int \cos\theta' \frac{\mathrm{T}_1(t)}{t} \mathrm{d}t \\
H_{12}(r,r') =& 2\sqrt{2} \int \left[\cos\theta\cos^2\theta' - \sin\theta\sin\theta'\cos\theta'\right] \frac{\mathrm{T}_2(t)}{t} \mathrm{d}t \\
H_{13}(r,r') =& 2\sqrt{2} \int \left[\sin\theta\sin\theta'\cos\theta' + \cos\theta\sin^2\theta'\right] \frac{\mathrm{T}_2(t)}{t} \mathrm{d}t \\
H_{14}(r,r') =& 2\left(\frac{2}{3}\right)^{1/2} \int \cos\theta' \left[\mathrm{T}_3(t) - \frac{3}{2}\mathrm{T}_1(t)\right] \frac{\mathrm{d}t}{t} \\
H_{21}(r,r') =& 2\sqrt{2} \int \cos\theta\cos\theta' \frac{\mathrm{T}_2(t)}{t} \mathrm{d}t \\
H_{22}(r,r') =& 4 \int \left[\cos^2\theta\cos^2\theta' - \sin\theta\cos\theta\sin\theta'\cos\theta'\right] \frac{\mathrm{T}_3(t)}{t} \mathrm{d}t \\
H_{23}(r,r') =& 4 \int \left[\sin\theta\cos\theta\sin\theta'\cos\theta' + \cos^2\theta\sin^2\theta'\right] \frac{\mathrm{T}_3(t)}{t} \mathrm{d}t \\
H_{24}(r,r') =& 2\sqrt{2}\left(\frac{2}{3}\right)^{1/2} \int \cos\theta\cos\theta' \left[\mathrm{T}_4(t) - \frac{3}{2}\mathrm{T}_2(t)\right] \frac{\mathrm{d}t}{t} \\
H_{31}(r,r') =& -\sqrt{2} \int \sin\theta\sin\theta' \frac{\mathrm{T}_2(t)}{t} \mathrm{d}t
\end{aligned}$$

$$
\begin{aligned}
H_{32}(r,r') =& 2\int \left[\sin^2\theta\sin^2\theta' - \sin\theta\cos\theta\sin\theta'\cos\theta'\right]\frac{\mathrm{T}_3(t)}{t}\mathrm{d}t \\
H_{33}(r,r') =& 2\int \left[\sin^2\theta\cos^2\theta' + \sin\theta\cos\theta\sin\theta'\cos\theta'\right]\frac{\mathrm{T}_3(t)}{t}\mathrm{d}t \\
H_{34}(r,r') =& -\sqrt{2}\left(\frac{2}{3}\right)^{1/2}\int \sin\theta\sin\theta'\left[\mathrm{T}_4(t) - \frac{3}{2}\mathrm{T}_2(t)\right]\frac{\mathrm{d}t}{t} \\
H_{41}(r,r') =& 2\left(\frac{2}{3}\right)^{1/2}\int \cos\theta'\left[\mathrm{T}_3(t) - \frac{3}{2}\mathrm{T}_1(t)\right]\frac{\mathrm{d}t}{t} \\
H_{42}(r,r') =& 2\sqrt{2}\left(\frac{2}{3}\right)^{1/2}\int \left[\cos\theta\cos^2\theta' - \sin\theta\sin\theta'\cos\theta'\right]\left[\mathrm{T}_4(t) - \frac{3}{2}\mathrm{T}_2(t)\right]\frac{\mathrm{d}t}{t} \\
H_{43}(r,r') =& 2\sqrt{2}\left(\frac{2}{3}\right)^{1/2}\int \left[\sin\theta\sin\theta'\cos\theta' + \cos\theta\sin^2\theta'\right]\left[\mathrm{T}_4(t) - \frac{3}{2}\mathrm{T}_2(t)\right]\frac{\mathrm{d}t}{t} \\
H_{44}(r,r') =& 2\left(\frac{2}{3}\right)\int \cos\theta'\left[\mathrm{T}_5(t) - 3\,\mathrm{T}_3(t) + \frac{9}{4}\mathrm{T}_1(t)\right]\frac{\mathrm{d}t}{t}
\end{aligned}
$$

Finally, we will write $\cos\theta$, $\cos\theta'$, $\sin\theta$, and $\sin\theta'$ in terms of r', r, and t:

$$\cos\theta' = \frac{r^2 + r'^2 - t^2}{2rr'} \tag{A.31a}$$

$$\cos\theta = \frac{t^2 + r^2 - r'^2}{2rt} \tag{A.31b}$$

$$r'\sin\theta' = t\sin\theta = \frac{\sqrt{(2rr')^2 - (r^2 + r'^2 - t^2)^2}}{2r} \tag{A.31c}$$

Substituting these expressions into the above equations for $\mathbf{H}(r,r')$, we get

$$H_{11}(r,r') = \frac{-1}{rr'}\int \left[t^2 - (r^2 + r'^2)\right]\frac{\mathrm{T}_1(t)}{t}\mathrm{d}t \tag{A.32}$$

$$H_{12}(r,r') = \frac{1}{\sqrt{2}rr'^2}\int \left[t^4 - 2r^2t^2 - (r'^4 - r^4)\right]\frac{\mathrm{T}_2(t)}{t^2}\mathrm{d}t \tag{A.33}$$

$$H_{13}(r,r') = \frac{-1}{\sqrt{2}rr'^2}\int \left[t^4 - 2(r'^2 + r^2)t^2 + (r'^2 - r^2)^2\right]\frac{\mathrm{T}_2(t)}{t^2}\mathrm{d}t \tag{A.34}$$

$$H_{14}(r,r') = \frac{-\sqrt{2}}{\sqrt{3}rr'}\int \left[t^2 - (r^2 + r'^2)\right]\left[\mathrm{T}_3(t) - \frac{3}{2}\mathrm{T}_1(t)\right]\frac{\mathrm{d}t}{t} \tag{A.35}$$

$$H_{21}(r,r') = \frac{-1}{\sqrt{2}r^2r'} \int \left[t^4 - 2r'^2t^2 - (r^4 - r'^4)\right] \frac{\mathrm{T}_2(t)}{t^2}\mathrm{d}t \tag{A.36}$$

$$H_{22}(r,r') = \frac{1}{2r^2r'^2} \int \left[t^6 - t^4(r'^2 + r^2) - t^2(r^2 - r'^2)^2 + (r'^2 - r^2)(r'^4 - r^4)\right] \frac{\mathrm{T}_3(t)}{t^3}\mathrm{d}t \tag{A.37}$$

$$H_{23}(r,r') = \frac{-1}{2r^2r'^2} \int \left[t^6 - t^4(3r'^2 + r^2) + t^2(r'^2 - r^2)(3r'^2 + r^2) - (r'^2 - r^2)^3\right] \frac{\mathrm{T}_3(t)}{t^3}\mathrm{d}t \tag{A.38}$$

$$H_{24}(r,r') = \frac{-1}{\sqrt{3}r^2r'} \int \left[t^4 - 2r'^2t^2 - (r^4 - r'^4)\right] \left[\mathrm{T}_4(t) - \frac{3}{2}\,\mathrm{T}_2(t)\right] \frac{\mathrm{d}t}{t} \tag{A.39}$$

$$H_{31}(r,r') = \frac{1}{2\sqrt{2}r^2r} \int \left[t^4 - 2(r'^2 + r^2)t^2 + (r^2 - r'^2)^2\right] \frac{\mathrm{T}_2(t)}{t^2}\mathrm{d}t \tag{A.40}$$

$$H_{32}(r,r') = \frac{-1}{4r^2r'^2} \int \left[t^6 - t^4(3r^2 + r'^2) + t^2(r^2 - r'^2)(3r^2 + r'^2) - (r^2 - r'^2)^3\right] \frac{\mathrm{T}_3(t)}{t^3}\mathrm{d}t \tag{A.41}$$

$$H_{33}(r,r') = \frac{1}{4r^2r'^2} \int \left[t^6 - t^4(3r^2 + 3r'^2) + t^2(3r^4 + 2r^2r'^2 + 3r'^4) - (r^4 - r'^4)(r^2 - r'^2)\right] \frac{\mathrm{T}_3(t)}{t^3}\mathrm{d}t \tag{A.42}$$

$$H_{34}(r,r') = \frac{1}{2\sqrt{3}r^2r} \int \left[t^4 - 2(r'^2 + r^2)t^2 + (r^2 - r'^2)^2\right] \left[\mathrm{T}_4(t) - \frac{3}{2}\,\mathrm{T}_2(t)\right] \frac{\mathrm{d}t}{t} \tag{A.43}$$

$$H_{41}(r,r') = \frac{-\sqrt{2}}{\sqrt{3}rr'} \int \left[t^2 - (r^2 + r'^2)\right] \left[\mathrm{T}_3(t) - \frac{3}{2}\,\mathrm{T}_1(t)\right] \frac{\mathrm{d}t}{t} \tag{A.44}$$

$$H_{42}(r,r') = \frac{1}{\sqrt{3}rr'^2} \int \left[t^4 - 2r^2t^2 - (r'^4 - r^4)\right] \left[\mathrm{T}_4(t) - \frac{3}{2}\,\mathrm{T}_2(t)\right] \frac{\mathrm{d}t}{t} \tag{A.45}$$

$$H_{43}(r,r') = \frac{-1}{\sqrt{3}rr'^2} \int \left[t^4 - 2(r'^2 + r^2)t^2 + (r'^2 - r^2)^2\right] \left[\mathrm{T}_4(t) - \frac{3}{2}\,\mathrm{T}_2(t)\right] \frac{\mathrm{d}t}{t} \tag{A.46}$$

$$H_{44}(r,r') = \frac{-2}{3rr'} \int \left[t^2 - (r^2 + r'^2)\right] \left[\mathrm{T}_5(t) - 3\,\mathrm{T}_3(t) + \frac{9}{4}\,\mathrm{T}_1(t)\right] \frac{\mathrm{d}t}{t} \tag{A.47}$$

where the integration extends from $|r - r'|$ to $\sqrt{r^2 + r_0^2} + \sqrt{r'^2 - r_0^2}$.

A.4 Derivation of the Drag Expression (Eq. (2.54))

In this section, I will present the derivation of the expression for the drag, Eq. (2.54). For this section, I will be using the same coordinates that I used in Section A.1.

We will start by writing our expression for the shear stress [Eq. (2.52)] in compressed form:

$$\tau_{ij}(\boldsymbol{r}_0) = \rho_\infty \left[B_{ij} + C_{ij} - D_{ij}\right] \tag{A.48}$$

$$B_{ij} \equiv \pi^{-3/2} \int_V \Bigg[\mathrm{T}_3(|\boldsymbol{r} - \boldsymbol{r}_0|)\varepsilon_1(\boldsymbol{r}) + \mathrm{T}_4(|\boldsymbol{r} - \boldsymbol{r}_0|)\hat{\boldsymbol{\Omega}} \cdot \boldsymbol{\varepsilon}_2(\boldsymbol{r}) + \left(\mathrm{T}_5(|\boldsymbol{r} - \boldsymbol{r}_0|) - \frac{3}{2}\,\mathrm{T}_3(|\boldsymbol{r} - \boldsymbol{r}_0|) \right) \varepsilon_3(\boldsymbol{r}) \Bigg] \Omega_i \Omega_j \frac{\mathrm{d}\boldsymbol{r}}{|\boldsymbol{r} - \boldsymbol{r}_0|} \tag{A.49a}$$

where

$$C_{ij} \equiv \pi^{-3/2} A(\boldsymbol{r}_0) \int_{\boldsymbol{c}\cdot\hat{\boldsymbol{n}}>0} c_i c_j \, \mathrm{e}^{-c^2} \, \mathrm{d}\boldsymbol{c} \tag{A.49b}$$

$$D_{ij} \equiv \pi^{-3/2} 2\boldsymbol{U}_\infty \cdot \int_{\boldsymbol{c}\cdot\hat{\boldsymbol{n}}>0} \boldsymbol{c}\, c_i c_j \, \mathrm{e}^{-c^2} \, \mathrm{d}\boldsymbol{c} \tag{A.49c}$$

In terms of this new notation, the drag force is

$$\tilde{F}_{D,Z} = \rho_\infty \left(\frac{2k_B T_\infty}{m} \right) \tilde{r}_0^2 \int_0^{2\pi} \mathrm{d}\phi \int_0^{\pi} \mathrm{d}\alpha \, \sin\alpha \big[(B_{zx} + C_{zx} - D_{zx}) \sin\alpha + (B_{zz} + C_{zz} - D_{zz}) \cos\alpha \big] \tag{A.50}$$

where α is the angle between $\boldsymbol{U}_\infty$ and $\hat{\boldsymbol{n}}$.

We will first focus on the expression B_{ij}. In terms of the coordinates (r, t, ϕ') from Section A.1, we have

$$B_{ij} = \pi^{-3/2} \int_{r_0}^{\infty} \mathrm{d}r \frac{r}{r_0} \int_{r-r_0}^{\sqrt{r^2-r_0^2}} \frac{\mathrm{d}t}{t} \int_0^{2\pi} \mathrm{d}\phi' \left[\mathrm{T}_3(t)\varepsilon_1(\boldsymbol{r}) - \mathrm{T}_4(t)\hat{\boldsymbol{\Omega}} \cdot \boldsymbol{\varepsilon}_2(\boldsymbol{r}) \right] \Omega_i \Omega_j$$

Next, we substitute the expressions for $\varepsilon_1(\boldsymbol{r})$ and $\boldsymbol{U}_\infty \cdot \boldsymbol{\varepsilon}_2(\boldsymbol{r})$ from Section A.1 into the integral:

$$\begin{aligned} B_{ij} =& \pi^{-3/2} \int \mathrm{d}r \, \frac{r}{r_0} \int \frac{\mathrm{d}t}{t} \int \mathrm{d}\phi' \Bigg[\mathrm{T}_3(t)\rho_1(r)\big(\cos\alpha \cos\theta' + \sin\alpha \sin\theta' \cos\phi' \big) \\ &+ \sqrt{2}\, \mathrm{T}_4(t) \cos\alpha \big\{ \rho_2(r)\big(\cos\theta \cos^2\theta' - \sin\theta \sin\theta' \cos\theta' \big) + \rho_3\big(\sin\theta \sin\theta' \cos\theta' \\ &+ \cos\theta \sin^2\theta' \big) \big\} + \sqrt{2}\, \mathrm{T}_4(t) \sin\alpha \big\{ \rho_2(r)\big(\cos\theta \sin\theta' \cos\theta' \cos\phi' \\ &- \sin\theta \sin^2\theta' \cos\phi' \big) - \rho_3(r)\big(\sin\theta \cos^2\theta' \cos\phi' + \cos\theta \sin\theta' \cos\theta' \cos\phi' \big) \big\} \\ &+ \sqrt{\frac{2}{3}} \left(\mathrm{T}_5(t) - \frac{3}{2}\, \mathrm{T}_3(t) \right) \rho_4(r)\big(\cos\alpha \cos\theta' + \sin\alpha \sin\theta' \cos\phi' \big) \Bigg] \Omega_i \Omega_j \end{aligned}$$

We can integrate analytically over ϕ' for each i, j. As we saw in the derivation of the drag force, we need only consider two components of the shear stress tensor, τ_{zx} and τ_{zz}. Thus, we will only perform the integration for B_{zx} and B_{zz}. In these coordinates, $\Omega_x = -\sin\theta \cos\phi'$ and $\Omega_z = \cos\theta$. The integral will be non-zero only for even functions of ϕ', meaning terms containing $\cos\phi'$ will be zero while terms containing $\cos^2\phi'$ are multiplied by π and terms independent of ϕ' are multiplied by

2π. Thus, the terms B_{zx} and B_{zz} are

$$\begin{aligned} B_{zx} =& \pi^{-1/2} U \sin\alpha \int \mathrm{d}r\, \frac{r}{r_0} \int \frac{\mathrm{d}t}{t} \Bigg[-\mathrm{T}_3(t) q_1(r) \sin\theta \cos\theta \sin\theta' \\ &+ \sqrt{2}\, \mathrm{T}_4(t) q_2(r) \big(\sin^2\theta \cos\theta \sin^2\theta' - \sin\theta \cos^2\theta \sin\theta' \cos\theta' \big) \\ &+ \sqrt{2}\, \mathrm{T}_4(t) q_3(r) \big(\sin^2\theta \cos\theta \cos^2\theta' + \sin\theta \cos^2\theta \sin\theta' \cos\theta' \big) \\ &- \sqrt{\frac{2}{3}} \left(\mathrm{T}_5(t) - \frac{3}{2}\, \mathrm{T}_3(t) \right) \rho_4(r) \sin\theta \cos\theta \sin\theta' \Bigg] \end{aligned} \tag{A.51}$$

$$\begin{aligned} B_{zz} =& 2\pi^{-1/2} U \cos\alpha \int \mathrm{d}r\, \frac{r}{r_0} \int \frac{\mathrm{d}t}{t} \Bigg[\mathrm{T}_3(t) q_1(r) \cos^2\theta \cos\theta' \\ &+ \sqrt{2}\, \mathrm{T}_4(t) q_2(r) \big(\cos^3\theta \cos^2\theta' - \sin\theta \cos^2\theta \sin\theta' \cos\theta' \big) \\ &+ \sqrt{2}\, \mathrm{T}_4(t) q_3(r) \big(\cos^3\theta \sin^2\theta' + \sin\theta \cos^2\theta \sin\theta' \cos\theta' \big) \\ &+ \sqrt{\frac{2}{3}} \left(\mathrm{T}_5(t) - \frac{3}{2}\, \mathrm{T}_3(t) \right) \rho_4(r) \cos^2\theta \cos\theta' \Bigg] \end{aligned} \tag{A.52}$$

We will eventually substitute Eq. (A.9) for $\cos\theta$, $\cos\theta'$, $\sin\theta$, and $\sin\theta'$, but we will defer that substitution until later in this section.

Let us now turn our attention to C_{ij} and D_{ij}. In terms of the (x, y, z) coordinates, with z normal to the sphere at $\boldsymbol{r}_0$, these expressions are

$$C_{ij} = \pi^{-3/2} g U \cos\alpha \int_0^\infty \mathrm{d}c_z \int_{-\infty}^\infty \mathrm{d}c_y \int_{-\infty}^\infty \mathrm{d}c_x\, c_i c_j\, \mathrm{e}^{-c_x^2 - c_y^2 - c_z^2}$$

$$D_{ij} = 2\pi^{-3/2} U \int_0^\infty \mathrm{d}c_z \int_{-\infty}^\infty \mathrm{d}c_y \int_{-\infty}^\infty \mathrm{d}c_x\, (c_x \sin\alpha + c_z \cos\alpha) c_i c_j\, \mathrm{e}^{-c_x^2 - c_y^2 - c_z^2}$$

Here, we have substituted $A(\boldsymbol{r}_0) = gU\cos\alpha$ and $\boldsymbol{U}_\infty \cdot \boldsymbol{c} = U c_z \cos\alpha$ into our expressions for C_{ij} and D_{ij}, respectively. The above integrals are straightforward to

compute for any ij, giving

$$C_{zx} = 0 \qquad C_{zz} = \frac{1}{4} g U \cos\alpha$$
$$D_{zx} = \frac{U}{2\pi^{1/2}} \sin\alpha \qquad D_{zz} = \pi^{-1/2} U \cos\alpha$$

We can now consider the drag force given by Eq. (A.50). Since θ and θ' are independent of α and ϕ, the integration in the drag expression is straightforward, giving the following expression for the drag:

$$\begin{aligned}
\tilde{F}_{D,Z} =& \rho_\infty \left(\frac{2k_B T_\infty}{m}\right) \tilde{r}_0^2 \int_0^{2\pi} \mathrm{d}\phi \int_0^{\pi} \mathrm{d}\alpha \, \sin\alpha \big[(B_{zx} - D_{zx}) \sin\alpha \\
&+ (B_{zz} + C_{zz} - D_{zz}) \cos\alpha \big] \\
=& \rho_\infty U \left(\frac{2k_B T_\infty}{m}\right) \tilde{r}_0^2 \int_0^{2\pi} \mathrm{d}\phi \int_0^{\pi} \mathrm{d}\alpha \, \left[\left(\frac{B_{zx}}{U \sin\alpha} - \frac{1}{2\pi^{1/2}} \right) \sin^3\alpha \right. \\
&\left. + \left(\frac{B_{zz}}{U\cos\alpha} + \frac{g}{4} - \pi^{-1/2} \right) \sin\alpha \cos^2\alpha \right] \\
=& \rho_\infty \tilde{U} \left(\frac{2k_B T_\infty}{m}\right)^{1/2} \tilde{r}_0^2 \frac{4\pi}{3} \left[\frac{2B_{zx}}{U\sin\alpha} + \frac{B_{zz}}{U\cos\alpha} + \frac{g}{4} - 2\pi^{-1/2} \right] \\
=& \frac{\rho_\infty \tilde{U}}{3} \left(\frac{2\pi k_B T_\infty}{m}\right)^{1/2} \tilde{r}_0^2 \left[4\pi^{1/2} \left(\frac{2B_{zx}}{U\sin\alpha} + \frac{B_{zz}}{U\cos\alpha} \right) + g\pi^{1/2} - 8 \right] \\
=& -\frac{\rho_\infty \tilde{U}}{3} \left(\frac{2\pi k_B T_\infty}{m}\right)^{1/2} \tilde{r}_0^2 \Bigg[8 - g\pi^{1/2} + 8 \int \mathrm{d}r \, \frac{r}{r_0} \int \frac{\mathrm{d}t}{t} \\
&\times \Big\{ \mathrm{T}_3(t) q_1(r) \big(\sin\theta\cos\theta\sin\theta' - \cos^2\theta\cos\theta' \big) \\
&- \sqrt{2}\, \mathrm{T}_4(t) q_2(r) \big(\cos^3\theta\cos^2\theta' - 2\sin\theta\cos^2\theta\sin\theta'\cos\theta' \\
&+ \sin^2\theta\cos\theta\sin^2\theta' \big) - \sqrt{2}\, \mathrm{T}_4(t) q_3(r) \big(\cos^3\theta\sin^2\theta' \\
&+ 2\sin\theta\cos^2\theta\sin\theta'\cos\theta' + \sin^2\theta\cos\theta\cos^2\theta' \big) \\
&+ \sqrt{\frac{2}{3}} \left(\mathrm{T}_5(t) - \frac{3}{2}\mathrm{T}_3(t) \right) q_4(r) \big(\sin\theta\cos\theta\sin\theta' - \cos^2\theta\cos\theta' \big) \Big\} \Bigg]
\end{aligned}$$

We next substitute Eq. (A.9) for $\cos\theta$, $\cos\theta'$, $\sin\theta$, and $\sin\theta'$:

$$\begin{aligned}\tilde{F}_{D,Z} = &-\frac{\rho_\infty \tilde{U}}{3}\left(\frac{2\pi k_B T_\infty}{m}\right)^{1/2} \tilde{r}_0^2\Bigg[8 - g\pi^{1/2} + \int \mathrm{d}r\, \frac{2\pi^{1/2} r^2}{r_0^2} \\ &\times \Bigg\{ \frac{q_1(r)}{\sqrt{\pi} r^2} \int \mathrm{d}t \frac{\mathrm{T}_3(t)}{t^3}\left[t^4 - (r^2 - r_0^2)^2\right] \\ &- \frac{q_2(r)}{\sqrt{2\pi} r^3} \int \mathrm{d}t \frac{\mathrm{T}_4(t)}{t^4}\left[t^6 + t^4(r^2 - r_0^2) - t^2(r^2 - r_0^2)^2 - (r^2 - r_0^2)^3\right] \\ &+ \frac{q_3(r)}{\sqrt{2\pi} r^3} \int \mathrm{d}t \frac{\mathrm{T}_4(t)}{t^4}\left[t^6 - t^4(3r^2 + r_0^2) + t^2(3r^2 + r_0^2)(r^2 - r_0^2) - (r^2 - r_0^2)^3\right] \\ &+ \frac{\sqrt{2} q_4(r)}{\sqrt{3\pi} r^2} \int \frac{\mathrm{d}t}{t^3}\left[\mathrm{T}_5(t) - \frac{3}{2}\mathrm{T}_3(t)\right]\left[t^4 - (r^2 - r_0^2)^2\right] \Bigg\}\Bigg]\end{aligned}$$

The integrals over t in the above expressions are the W_U expressions from Section A.2. After replacing the integrals over t with Eqns. (A.25–A.28), we arrive at our final expression for the drag in terms of $\boldsymbol{q}(r)$ (Eq. (2.54)):

$$\begin{aligned}\tilde{F}_{D,Z} = -\frac{\rho_\infty \tilde{U}}{3}\left(\frac{2\pi k_B T_\infty}{m}\right)^{1/2} \tilde{r}_0^2\Bigg[8 - g\pi^{1/2} + \int \mathrm{d}r\, \frac{2\pi^{1/2} r^2}{r_0^2}\Bigg\{ q_1(r) W_{U1}(r) \\ - q_2(r) W_{U2}(r) - 2q_3(r) W_{U3}(r) + q_4(r) W_{U4}(r)\Bigg\}\Bigg]\end{aligned}$$

Appendix B: BGK Results

My method for calculating the drag on an aerosol fractal aggregate in the transition regime requires knowledge of the velocity field around a sphere. I determined the velocity field using the Bhatnagar-Gross-Krook model [71] in the linearized Boltzmann equation, following the procedure of Lea and Loyalka [75] and Law and Loyalka [76]. I am providing results here in case anyone wishes to apply my method for calculating the drag force on an aggregate.

I have listed the calculated values of $q_2(r)$ and $q_3(r)$ for a range of Knudsen numbers in Tables B.1–B.24. I have included the values for c_1 and c_2 in Table B.25. These variables have been defined Chapter 3. Note that when I compute the drag force on an aggregate, I use the asymptotic solutions for q_2 and q_3 when the distance r_{ij} between primary spheres is greater than the maximum r in the tables below.

Table B.1: Results for $a = 0.01$ (Kn = 88.8)

r	$q_2(r)$	$q_3(r)$	r	$q_2(r)$	$q_3(r)$
0.0135	-8.6764E-01	-6.9165E-02	5.1318	-5.3060E-05	-3.4932E-05
0.0283	-2.0298E-01	9.3393E-05	5.3750	-5.1404E-05	-3.4073E-05
0.0549	-5.3819E-02	-2.6852E-04	5.6173	-4.9893E-05	-3.3251E-05
0.0933	-1.8869E-02	-3.8681E-04	5.8582	-4.8509E-05	-3.2461E-05
0.1434	-8.1915E-03	-3.2227E-04	6.0971	-4.7236E-05	-3.1700E-05
0.2050	-4.1498E-03	-2.5401E-04	6.3334	-4.6062E-05	-3.0965E-05
0.2779	-2.3575E-03	-2.0311E-04	6.5666	-4.4975E-05	-3.0253E-05
0.3622	-1.4627E-03	-1.6673E-04	6.7961	-4.3967E-05	-2.9565E-05
0.4574	-9.7309E-04	-1.4044E-04	7.0214	-4.3029E-05	-2.8899E-05
0.5634	-6.8506E-04	-1.2099E-04	7.2418	-4.2157E-05	-2.8250E-05
0.6800	-5.0536E-04	-1.0622E-04	7.4570	-4.1342E-05	-2.7623E-05
0.8069	-3.8766E-04	-9.4762E-05	7.6664	-4.0582E-05	-2.7016E-05
0.9437	-3.0736E-04	-8.5675E-05	7.8695	-3.9871E-05	-2.6429E-05
1.0901	-2.5064E-04	-7.8335E-05	8.0658	-3.9208E-05	-2.5861E-05
1.2459	-2.0936E-04	-7.2310E-05	8.2548	-3.8588E-05	-2.5314E-05
1.4106	-1.7853E-04	-6.7291E-05	8.4362	-3.8009E-05	-2.4788E-05
1.5838	-1.5496E-04	-6.3055E-05	8.6094	-3.7470E-05	-2.4283E-05
1.7652	-1.3660E-04	-5.9438E-05	8.7741	-3.6969E-05	-2.3800E-05
1.9542	-1.2202E-04	-5.6316E-05	8.9299	-3.6504E-05	-2.3340E-05
2.1505	-1.1026E-04	-5.3594E-05	9.0763	-3.6075E-05	-2.2904E-05
2.3536	-1.0064E-04	-5.1200E-05	9.2131	-3.5679E-05	-2.2492E-05
2.5630	-9.2671E-05	-4.9076E-05	9.3400	-3.5317E-05	-2.2105E-05
2.7782	-8.5989E-05	-4.7176E-05	9.4566	-3.4989E-05	-2.1745E-05
2.9986	-8.0328E-05	-4.5462E-05	9.5626	-3.4693E-05	-2.1413E-05
3.2239	-7.5484E-05	-4.3907E-05	9.6578	-3.4429E-05	-2.1108E-05
3.4534	-7.1301E-05	-4.2485E-05	9.7421	-3.4197E-05	-2.0832E-05
3.6866	-6.7661E-05	-4.1175E-05	9.8150	-3.3997E-05	-2.0587E-05
3.9229	-6.4468E-05	-3.9963E-05	9.8766	-3.3829E-05	-2.0374E-05
4.1618	-6.1649E-05	-3.8832E-05	9.9267	-3.3693E-05	-2.0192E-05
4.4027	-5.9142E-05	-3.7773E-05	9.9651	-3.3588E-05	-2.0046E-05
4.6450	-5.6900E-05	-3.6775E-05	9.9917	-3.3516E-05	-1.9936E-05
4.8882	-5.4883E-05	-3.5830E-05	10.0065	-3.3475E-05	-1.9868E-05

Table B.2: Results for $a = 0.025$ (Kn = 35.5)

r	$q_2(r)$	$q_3(r)$	r	$q_2(r)$	$q_3(r)$
0.0285	-1.1687E+00	-2.0677E-01	5.1468	-2.2857E-04	-1.2281E-04
0.0433	-5.4136E-01	-1.8587E-02	5.3900	-2.1898E-04	-1.1877E-04
0.0699	-2.1113E-01	-2.5890E-03	5.6323	-2.1031E-04	-1.1500E-04
0.1083	-8.9083E-02	-1.7876E-03	5.8732	-2.0244E-04	-1.1148E-04
0.1584	-4.2528E-02	-1.5542E-03	6.1121	-1.9528E-04	-1.0819E-04
0.2200	-2.2709E-02	-1.2898E-03	6.3484	-1.8875E-04	-1.0510E-04
0.2929	-1.3300E-02	-1.0571E-03	6.5816	-1.8278E-04	-1.0219E-04
0.3772	-8.3971E-03	-8.7321E-04	6.8111	-1.7731E-04	-9.9451E-05
0.4724	-5.6372E-03	-7.3198E-04	7.0364	-1.7228E-04	-9.6876E-05
0.5784	-3.9811E-03	-6.2338E-04	7.2568	-1.6767E-04	-9.4437E-05
0.6950	-2.9330E-03	-5.3888E-04	7.4720	-1.6342E-04	-9.2138E-05
0.8219	-2.2391E-03	-4.7214E-04	7.6814	-1.5950E-04	-8.9968E-05
0.9587	-1.7619E-03	-4.1859E-04	7.8845	-1.5589E-04	-8.7920E-05
1.1051	-1.4227E-03	-3.7500E-04	8.0808	-1.5256E-04	-8.5987E-05
1.2609	-1.1745E-03	-3.3902E-04	8.2698	-1.4950E-04	-8.4166E-05
1.4256	-9.8848E-04	-3.0896E-04	8.4512	-1.4667E-04	-8.2450E-05
1.5988	-8.4587E-04	-2.8355E-04	8.6244	-1.4407E-04	-8.0837E-05
1.7802	-7.3443E-04	-2.6186E-04	8.7891	-1.4169E-04	-7.9325E-05
1.9692	-6.4582E-04	-2.4317E-04	8.9449	-1.3951E-04	-7.7911E-05
2.1655	-5.7428E-04	-2.2694E-04	9.0913	-1.3751E-04	-7.6594E-05
2.3686	-5.1573E-04	-2.1274E-04	9.2281	-1.3569E-04	-7.5372E-05
2.5780	-4.6720E-04	-2.0022E-04	9.3550	-1.3405E-04	-7.4243E-05
2.7932	-4.2653E-04	-1.8912E-04	9.4716	-1.3257E-04	-7.3209E-05
3.0136	-3.9211E-04	-1.7922E-04	9.5776	-1.3125E-04	-7.2268E-05
3.2389	-3.6271E-04	-1.7034E-04	9.6728	-1.3009E-04	-7.1419E-05
3.4684	-3.3738E-04	-1.6233E-04	9.7571	-1.2907E-04	-7.0664E-05
3.7016	-3.1540E-04	-1.5508E-04	9.8300	-1.2820E-04	-7.0003E-05
3.9379	-2.9619E-04	-1.4849E-04	9.8916	-1.2748E-04	-6.9438E-05
4.1768	-2.7930E-04	-1.4247E-04	9.9417	-1.2689E-04	-6.8966E-05
4.4177	-2.6436E-04	-1.3694E-04	9.9801	-1.2644E-04	-6.8594E-05
4.6600	-2.5108E-04	-1.3186E-04	10.0067	-1.2614E-04	-6.8324E-05
4.9032	-2.3921E-04	-1.2716E-04	10.0215	-1.2596E-04	-6.8163E-05

Table B.3: Results for $a = 0.05$ (Kn = 17.8)

r	$q_2(r)$	$q_3(r)$	r	$q_2(r)$	$q_3(r)$
0.0535	-1.2925E+00	-3.3188E-01	5.1718	-7.7134E-04	-3.6368E-04
0.0683	-8.5319E-01	-7.8173E-02	5.4150	-7.3460E-04	-3.4943E-04
0.0949	-4.5889E-01	-1.8149E-02	5.6573	-7.0147E-04	-3.3632E-04
0.1333	-2.3791E-01	-7.6369E-03	5.8982	-6.7151E-04	-3.2423E-04
0.1834	-1.2860E-01	-5.3797E-03	6.1371	-6.4435E-04	-3.1309E-04
0.2450	-7.4124E-02	-4.3695E-03	6.3734	-6.1966E-04	-3.0279E-04
0.3179	-4.5581E-02	-3.6359E-03	6.6066	-5.9718E-04	-2.9326E-04
0.4022	-2.9714E-02	-3.0511E-03	6.8361	-5.7667E-04	-2.8443E-04
0.4974	-2.0380E-02	-2.5840E-03	7.0614	-5.5792E-04	-2.7626E-04
0.6034	-1.4601E-02	-2.2116E-03	7.2818	-5.4078E-04	-2.6867E-04
0.7200	-1.0858E-02	-1.9135E-03	7.4970	-5.2508E-04	-2.6164E-04
0.8469	-8.3375E-03	-1.6730E-03	7.7064	-5.1069E-04	-2.5512E-04
0.9837	-6.5807E-03	-1.4768E-03	7.9095	-4.9750E-04	-2.4908E-04
1.1301	-5.3188E-03	-1.3151E-03	8.1058	-4.8541E-04	-2.4347E-04
1.2859	-4.3882E-03	-1.1805E-03	8.2948	-4.7434E-04	-2.3829E-04
1.4506	-3.6857E-03	-1.0671E-03	8.4762	-4.6419E-04	-2.3349E-04
1.6238	-3.1443E-03	-9.7086E-04	8.6494	-4.5491E-04	-2.2906E-04
1.8052	-2.7194E-03	-8.8836E-04	8.8141	-4.4644E-04	-2.2497E-04
1.9942	-2.3803E-03	-8.1711E-04	8.9699	-4.3873E-04	-2.2122E-04
2.1905	-2.1057E-03	-7.5513E-04	9.1163	-4.3172E-04	-2.1779E-04
2.3936	-1.8803E-03	-7.0086E-04	9.2531	-4.2538E-04	-2.1465E-04
2.6030	-1.6932E-03	-6.5307E-04	9.3800	-4.1966E-04	-2.1181E-04
2.8182	-1.5362E-03	-6.1074E-04	9.4966	-4.1455E-04	-2.0924E-04
3.0386	-1.4032E-03	-5.7307E-04	9.6026	-4.1001E-04	-2.0695E-04
3.2639	-1.2894E-03	-5.3939E-04	9.6978	-4.0602E-04	-2.0492E-04
3.4934	-1.1914E-03	-5.0916E-04	9.7821	-4.0255E-04	-2.0314E-04
3.7266	-1.1064E-03	-4.8193E-04	9.8550	-3.9960E-04	-2.0162E-04
3.9629	-1.0321E-03	-4.5731E-04	9.9166	-3.9714E-04	-2.0035E-04
4.2018	-9.6678E-04	-4.3497E-04	9.9667	-3.9516E-04	-1.9931E-04
4.4427	-9.0910E-04	-4.1466E-04	10.0051	-3.9366E-04	-1.9852E-04
4.6850	-8.5790E-04	-3.9614E-04	10.0317	-3.9262E-04	-1.9797E-04
4.9282	-8.1222E-04	-3.7920E-04	10.0465	-3.9204E-04	-1.9766E-04

Table B.4: Results for $a = 0.075$ (Kn = 11.8)

r	$q_2(r)$	$q_3(r)$	r	$q_2(r)$	$q_3(r)$
0.0785	-1.3351E+00	-4.0357E-01	5.1968	-1.6182E-03	-7.2215E-04
0.0933	-1.0118E+00	-1.3874E-01	5.4400	-1.5378E-03	-6.9182E-04
0.1199	-6.4227E-01	-4.4412E-02	5.6823	-1.4654E-03	-6.6404E-04
0.1583	-3.8015E-01	-1.8857E-02	5.9232	-1.4000E-03	-6.3856E-04
0.2084	-2.2541E-01	-1.1779E-02	6.1621	-1.3407E-03	-6.1516E-04
0.2700	-1.3832E-01	-9.0517E-03	6.3984	-1.2869E-03	-5.9366E-04
0.3429	-8.8756E-02	-7.4545E-03	6.6316	-1.2379E-03	-5.7390E-04
0.4272	-5.9595E-02	-6.2821E-03	6.8611	-1.1933E-03	-5.5570E-04
0.5224	-4.1735E-02	-5.3573E-03	7.0864	-1.1526E-03	-5.3896E-04
0.6284	-3.0351E-02	-4.6129E-03	7.3068	-1.1154E-03	-5.2354E-04
0.7450	-2.2817E-02	-4.0085E-03	7.5220	-1.0814E-03	-5.0934E-04
0.8719	-1.7659E-02	-3.5140E-03	7.7314	-1.0503E-03	-4.9628E-04
1.0087	-1.4017E-02	-3.1061E-03	7.9345	-1.0218E-03	-4.8426E-04
1.1551	-1.1375E-02	-2.7666E-03	8.1308	-9.9574E-04	-4.7321E-04
1.3109	-9.4102E-03	-2.4816E-03	8.3198	-9.7191E-04	-4.6307E-04
1.4756	-7.9174E-03	-2.2402E-03	8.5012	-9.5013E-04	-4.5376E-04
1.6488	-6.7607E-03	-2.0341E-03	8.6744	-9.3024E-04	-4.4524E-04
1.8302	-5.8488E-03	-1.8568E-03	8.8391	-9.1212E-04	-4.3746E-04
2.0192	-5.1183E-03	-1.7032E-03	8.9949	-8.9565E-04	-4.3037E-04
2.2155	-4.5249E-03	-1.5693E-03	9.1413	-8.8071E-04	-4.2394E-04
2.4186	-4.0368E-03	-1.4517E-03	9.2781	-8.6721E-04	-4.1812E-04
2.6280	-3.6306E-03	-1.3481E-03	9.4050	-8.5508E-04	-4.1289E-04
2.8432	-3.2890E-03	-1.2563E-03	9.5216	-8.4424E-04	-4.0822E-04
3.0636	-2.9991E-03	-1.1745E-03	9.6276	-8.3463E-04	-4.0409E-04
3.2889	-2.7510E-03	-1.1014E-03	9.7228	-8.2620E-04	-4.0046E-04
3.5184	-2.5370E-03	-1.0358E-03	9.8071	-8.1888E-04	-3.9733E-04
3.7516	-2.3511E-03	-9.7680E-04	9.8800	-8.1266E-04	-3.9467E-04
3.9879	-2.1886E-03	-9.2350E-04	9.9416	-8.0748E-04	-3.9248E-04
4.2268	-2.0458E-03	-8.7525E-04	9.9917	-8.0332E-04	-3.9073E-04
4.4677	-1.9196E-03	-8.3146E-04	10.0301	-8.0016E-04	-3.8941E-04
4.7100	-1.8075E-03	-7.9162E-04	10.0567	-7.9799E-04	-3.8853E-04
4.9532	-1.7076E-03	-7.5531E-04	10.0715	-7.9678E-04	-3.8805E-04

Table B.5: Results for $a = 0.1$ (Kn = 8.88)

r	$q_2(r)$	$q_3(r)$	r	$q_2(r)$	$q_3(r)$
0.1035	-1.3563E+00	-4.5258E-01	5.2218	-2.7589E-03	-1.1976E-03
0.1183	-1.1049E+00	-1.9204E-01	5.4650	-2.6195E-03	-1.1456E-03
0.1449	-7.7518E-01	-7.5273E-02	5.7073	-2.4940E-03	-1.0980E-03
0.1833	-5.0281E-01	-3.4494E-02	5.9482	-2.3805E-03	-1.0545E-03
0.2334	-3.2005E-01	-2.0792E-02	6.1871	-2.2777E-03	-1.0146E-03
0.2950	-2.0679E-01	-1.5336E-02	6.4234	-2.1844E-03	-9.7808E-04
0.3679	-1.3770E-01	-1.2420E-02	6.6566	-2.0995E-03	-9.4456E-04
0.4522	-9.4958E-02	-1.0442E-02	6.8861	-2.0222E-03	-9.1380E-04
0.5474	-6.7806E-02	-8.9315E-03	7.1114	-1.9517E-03	-8.8557E-04
0.6534	-5.0023E-02	-7.7233E-03	7.3318	-1.8873E-03	-8.5966E-04
0.7700	-3.8012E-02	-6.7380E-03	7.5470	-1.8285E-03	-8.3589E-04
0.8969	-2.9657E-02	-5.9256E-03	7.7564	-1.7747E-03	-8.1409E-04
1.0337	-2.3685E-02	-5.2501E-03	7.9595	-1.7255E-03	-7.9411E-04
1.1801	-1.9310E-02	-4.6837E-03	8.1558	-1.6805E-03	-7.7581E-04
1.3359	-1.6031E-02	-4.2052E-03	8.3448	-1.6394E-03	-7.5909E-04
1.5006	-1.3524E-02	-3.7977E-03	8.5262	-1.6019E-03	-7.4381E-04
1.6738	-1.1571E-02	-3.4483E-03	8.6994	-1.5676E-03	-7.2988E-04
1.8552	-1.0024E-02	-3.1465E-03	8.8641	-1.5364E-03	-7.1721E-04
2.0442	-8.7802E-03	-2.8842E-03	9.0199	-1.5081E-03	-7.0576E-04
2.2405	-7.7669E-03	-2.6549E-03	9.1663	-1.4824E-03	-6.9536E-04
2.4436	-6.9310E-03	-2.4534E-03	9.3031	-1.4592E-03	-6.8602E-04
2.6530	-6.2339E-03	-2.2754E-03	9.4300	-1.4384E-03	-6.7767E-04
2.8682	-5.6466E-03	-2.1174E-03	9.5466	-1.4198E-03	-6.7025E-04
3.0886	-5.1473E-03	-1.9766E-03	9.6526	-1.4033E-03	-6.6372E-04
3.3139	-4.7193E-03	-1.8506E-03	9.7478	-1.3889E-03	-6.5802E-04
3.5434	-4.3498E-03	-1.7376E-03	9.8321	-1.3763E-03	-6.5313E-04
3.7766	-4.0285E-03	-1.6359E-03	9.9050	-1.3657E-03	-6.4901E-04
4.0129	-3.7474E-03	-1.5440E-03	9.9666	-1.3568E-03	-6.4565E-04
4.2518	-3.5001E-03	-1.4609E-03	10.0167	-1.3497E-03	-6.4297E-04
4.4927	-3.2814E-03	-1.3854E-03	10.0551	-1.3443E-03	-6.4099E-04
4.7350	-3.0872E-03	-1.3169E-03	10.0817	-1.3406E-03	-6.3968E-04
4.9782	-2.9140E-03	-1.2545E-03	10.0965	-1.3386E-03	-6.3899E-04

Table B.6: Results for $a = 0.25$ (Kn = 3.55)

r	$q_2(r)$	$q_3(r)$	r	$q_2(r)$	$q_3(r)$
0.2535	-1.3934E+00	-6.0267E-01	5.3718	-1.5604E-02	-6.7970E-03
0.2683	-1.2953E+00	-3.9984E-01	5.6150	-1.4839E-02	-6.5073E-03
0.2949	-1.1258E+00	-2.5248E-01	5.8573	-1.4147E-02	-6.2415E-03
0.3333	-9.2440E-01	-1.6101E-01	6.0982	-1.3520E-02	-5.9971E-03
0.3834	-7.3047E-01	-1.0879E-01	6.3371	-1.2951E-02	-5.7725E-03
0.4450	-5.6573E-01	-7.9479E-02	6.5734	-1.2432E-02	-5.5658E-03
0.5179	-4.3563E-01	-6.2340E-02	6.8066	-1.1960E-02	-5.3755E-03
0.6022	-3.3681E-01	-5.1482E-02	7.0361	-1.1528E-02	-5.2003E-03
0.6974	-2.6303E-01	-4.3952E-02	7.2614	-1.1134E-02	-5.0389E-03
0.8034	-2.0816E-01	-3.8309E-02	7.4818	-1.0773E-02	-4.8903E-03
0.9200	-1.6719E-01	-3.3840E-02	7.6970	-1.0443E-02	-4.7533E-03
1.0469	-1.3631E-01	-3.0173E-02	7.9064	-1.0140E-02	-4.6273E-03
1.1837	-1.1277E-01	-2.7095E-02	8.1095	-9.8629E-03	-4.5113E-03
1.3301	-9.4596E-02	-2.4474E-02	8.3058	-9.6090E-03	-4.4047E-03
1.4859	-8.0380E-02	-2.2218E-02	8.4948	-9.3765E-03	-4.3068E-03
1.6506	-6.9114E-02	-2.0262E-02	8.6762	-9.1640E-03	-4.2171E-03
1.8238	-6.0075E-02	-1.8555E-02	8.8494	-8.9697E-03	-4.1349E-03
2.0052	-5.2735E-02	-1.7058E-02	9.0141	-8.7926E-03	-4.0599E-03
2.1942	-4.6708E-02	-1.5738E-02	9.1699	-8.6315E-03	-3.9917E-03
2.3905	-4.1708E-02	-1.4569E-02	9.3163	-8.4853E-03	-3.9295E-03
2.5936	-3.7519E-02	-1.3531E-02	9.4531	-8.3532E-03	-3.8733E-03
2.8030	-3.3979E-02	-1.2604E-02	9.5800	-8.2344E-03	-3.8229E-03
3.0182	-3.0961E-02	-1.1774E-02	9.6966	-8.1282E-03	-3.7777E-03
3.2386	-2.8369E-02	-1.1028E-02	9.8026	-8.0340E-03	-3.7377E-03
3.4639	-2.6128E-02	-1.0357E-02	9.8978	-7.9514E-03	-3.7026E-03
3.6934	-2.4177E-02	-9.7503E-03	9.9821	-7.8797E-03	-3.6722E-03
3.9266	-2.2469E-02	-9.2009E-03	10.0550	-7.8186E-03	-3.6462E-03
4.1629	-2.0965E-02	-8.7023E-03	10.1166	-7.7678E-03	-3.6247E-03
4.4018	-1.9635E-02	-8.2487E-03	10.1667	-7.7270E-03	-3.6074E-03
4.6427	-1.8453E-02	-7.8354E-03	10.2051	-7.6960E-03	-3.5943E-03
4.8850	-1.7398E-02	-7.4580E-03	10.2317	-7.6746E-03	-3.5853E-03
5.1282	-1.6453E-02	-7.1130E-03	10.2465	-7.6628E-03	-3.5802E-03

Table B.7: Results for $a = 0.5$ (Kn = 1.78)

r	$q_2(r)$	$q_3(r)$	r	$q_2(r)$	$q_3(r)$
0.5035	-1.4050E+00	-7.2269E-01	5.6218	-5.2901E-02	-2.3187E-02
0.5183	-1.3617E+00	-5.7935E-01	5.8650	-5.0428E-02	-2.2238E-02
0.5449	-1.2801E+00	-4.5249E-01	6.1073	-4.8182E-02	-2.1364E-02
0.5833	-1.1674E+00	-3.5102E-01	6.3482	-4.6138E-02	-2.0559E-02
0.6334	-1.0369E+00	-2.7496E-01	6.5871	-4.4274E-02	-1.9816E-02
0.6950	-9.0248E-01	-2.2000E-01	6.8234	-4.2572E-02	-1.9131E-02
0.7679	-7.7481E-01	-1.8073E-01	7.0566	-4.1016E-02	-1.8499E-02
0.8522	-6.6010E-01	-1.5238E-01	7.2861	-3.9591E-02	-1.7916E-02
0.9474	-5.6080E-01	-1.3140E-01	7.5114	-3.8285E-02	-1.7378E-02
1.0534	-4.7688E-01	-1.1534E-01	7.7318	-3.7087E-02	-1.6881E-02
1.1700	-4.0698E-01	-1.0264E-01	7.9470	-3.5988E-02	-1.6422E-02
1.2969	-3.4918E-01	-9.2270E-02	8.1564	-3.4979E-02	-1.6000E-02
1.4337	-3.0151E-01	-8.3598E-02	8.3595	-3.4053E-02	-1.5610E-02
1.5801	-2.6217E-01	-7.6204E-02	8.5558	-3.3203E-02	-1.5252E-02
1.7359	-2.2960E-01	-6.9808E-02	8.7448	-3.2424E-02	-1.4922E-02
1.9006	-2.0252E-01	-6.4215E-02	8.9262	-3.1711E-02	-1.4620E-02
2.0738	-1.7987E-01	-5.9286E-02	9.0994	-3.1058E-02	-1.4343E-02
2.2552	-1.6081E-01	-5.4914E-02	9.2641	-3.0462E-02	-1.4089E-02
2.4442	-1.4468E-01	-5.1015E-02	9.4199	-2.9920E-02	-1.3858E-02
2.6405	-1.3094E-01	-4.7525E-02	9.5663	-2.9427E-02	-1.3648E-02
2.8436	-1.1916E-01	-4.4390E-02	9.7031	-2.8981E-02	-1.3458E-02
3.0530	-1.0900E-01	-4.1564E-02	9.8300	-2.8580E-02	-1.3287E-02
3.2682	-1.0018E-01	-3.9010E-02	9.9466	-2.8221E-02	-1.3134E-02
3.4886	-9.2497E-02	-3.6697E-02	10.0526	-2.7903E-02	-1.2999E-02
3.7139	-8.5759E-02	-3.4596E-02	10.1478	-2.7623E-02	-1.2879E-02
3.9434	-7.9821E-02	-3.2685E-02	10.2321	-2.7380E-02	-1.2776E-02
4.1766	-7.4569E-02	-3.0943E-02	10.3050	-2.7173E-02	-1.2688E-02
4.4129	-6.9899E-02	-2.9352E-02	10.3666	-2.7001E-02	-1.2615E-02
4.6518	-6.5733E-02	-2.7896E-02	10.4167	-2.6863E-02	-1.2556E-02
4.8927	-6.2003E-02	-2.6564E-02	10.4551	-2.6758E-02	-1.2512E-02
5.1350	-5.8652E-02	-2.5342E-02	10.4817	-2.6685E-02	-1.2481E-02
5.3782	-5.5631E-02	-2.4219E-02	10.4965	-2.6645E-02	-1.2464E-02

Table B.8: Results for $a = 0.75$ (Kn = 1.18)

r	$q_2(r)$	$q_3(r)$	r	$q_2(r)$	$q_3(r)$
0.7535	-1.4087E+00	-8.0092E-01	5.8718	-1.0172E-01	-4.4921E-02
0.7683	-1.3830E+00	-6.9036E-01	6.1150	-9.7188E-02	-4.3148E-02
0.7949	-1.3334E+00	-5.8475E-01	6.3573	-9.3051E-02	-4.1510E-02
0.8333	-1.2613E+00	-4.9151E-01	6.5982	-8.9269E-02	-3.9998E-02
0.8834	-1.1717E+00	-4.1337E-01	6.8371	-8.5810E-02	-3.8600E-02
0.9450	-1.0716E+00	-3.5010E-01	7.0734	-8.2640E-02	-3.7309E-02
1.0179	-9.6787E-01	-2.9982E-01	7.3066	-7.9732E-02	-3.6114E-02
1.1022	-8.6636E-01	-2.6012E-01	7.5361	-7.7062E-02	-3.5012E-02
1.1974	-7.7099E-01	-2.2859E-01	7.7614	-7.4609E-02	-3.3989E-02
1.3034	-6.8404E-01	-2.0327E-01	7.9818	-7.2354E-02	-3.3045E-02
1.4200	-6.0642E-01	-1.8257E-01	8.1970	-7.0281E-02	-3.2173E-02
1.5469	-5.3814E-01	-1.6536E-01	8.4064	-6.8374E-02	-3.1368E-02
1.6837	-4.7864E-01	-1.5080E-01	8.6095	-6.6621E-02	-3.0626E-02
1.8301	-4.2709E-01	-1.3830E-01	8.8058	-6.5010E-02	-2.9941E-02
1.9859	-3.8254E-01	-1.2741E-01	8.9948	-6.3530E-02	-2.9311E-02
2.1506	-3.4407E-01	-1.1785E-01	9.1762	-6.2160E-02	-2.8733E-02
2.3238	-3.1082E-01	-1.0937E-01	9.3494	-6.0931E-02	-2.8202E-02
2.5052	-2.8202E-01	-1.0180E-01	9.5141	-5.9794E-02	-2.7716E-02
2.6942	-2.5701E-01	-9.5018E-02	9.6699	-5.8758E-02	-2.7272E-02
2.8905	-2.3522E-01	-8.8905E-02	9.8163	-5.7817E-02	-2.6869E-02
3.0936	-2.1617E-01	-8.3378E-02	9.9531	-5.6965E-02	-2.6504E-02
3.3030	-1.9944E-01	-7.8367E-02	10.0800	-5.6197E-02	-2.6176E-02
3.5182	-1.8471E-01	-7.3811E-02	10.1966	-5.5510E-02	-2.5881E-02
3.7386	-1.7168E-01	-6.9660E-02	10.3026	-5.4899E-02	-2.5620E-02
3.9639	-1.6012E-01	-6.5871E-02	10.3978	-5.4363E-02	-2.5391E-02
4.1934	-1.4982E-01	-6.2406E-02	10.4821	-5.3897E-02	-2.5192E-02
4.4266	-1.4061E-01	-5.9232E-02	10.5550	-5.3500E-02	-2.5022E-02
4.6629	-1.3236E-01	-5.6321E-02	10.6166	-5.3170E-02	-2.4881E-02
4.9018	-1.2494E-01	-5.3648E-02	10.6667	-5.2904E-02	-2.4768E-02
5.1427	-1.1825E-01	-5.1190E-02	10.7051	-5.2702E-02	-2.4682E-02
5.3850	-1.1220E-01	-4.8927E-02	10.7317	-5.2563E-02	-2.4622E-02
5.6282	-1.0671E-01	-4.6843E-02	10.7465	-5.2486E-02	-2.4590E-02

Table B.9: Results for $a = 1.0$ (Kn = 0.888)

r	$q_2(r)$	$q_3(r)$	r	$q_2(r)$	$q_3(r)$
1.0035	-1.4105E+00	-8.6031E-01	6.1218	-1.5598E-01	-6.9474E-02
1.0183	-1.3930E+00	-7.7068E-01	6.3650	-1.4934E-01	-6.6822E-02
1.0449	-1.3591E+00	-6.8131E-01	6.6073	-1.4325E-01	-6.4366E-02
1.0833	-1.3087E+00	-5.9800E-01	6.8482	-1.3767E-01	-6.2094E-02
1.1334	-1.2437E+00	-5.2370E-01	7.0871	-1.3255E-01	-5.9989E-02
1.1950	-1.1678E+00	-4.5947E-01	7.3234	-1.2784E-01	-5.8041E-02
1.2679	-1.0852E+00	-4.0506E-01	7.5566	-1.2351E-01	-5.6236E-02
1.3522	-1.0000E+00	-3.5946E-01	7.7861	-1.1953E-01	-5.4565E-02
1.4474	-9.1578E-01	-3.2139E-01	8.0114	-1.1585E-01	-5.3018E-02
1.5534	-8.3500E-01	-2.8949E-01	8.2318	-1.1247E-01	-5.1586E-02
1.6700	-7.5939E-01	-2.6259E-01	8.4470	-1.0935E-01	-5.0260E-02
1.7969	-6.8989E-01	-2.3968E-01	8.6564	-1.0648E-01	-4.9036E-02
1.9337	-6.2683E-01	-2.1996E-01	8.8595	-1.0384E-01	-4.7905E-02
2.0801	-5.7014E-01	-2.0281E-01	9.0558	-1.0140E-01	-4.6861E-02
2.2359	-5.1949E-01	-1.8776E-01	9.2448	-9.9164E-02	-4.5899E-02
2.4006	-4.7443E-01	-1.7443E-01	9.4262	-9.7108E-02	-4.5015E-02
2.5738	-4.3443E-01	-1.6254E-01	9.5994	-9.5222E-02	-4.4203E-02
2.7552	-3.9894E-01	-1.5188E-01	9.7641	-9.3496E-02	-4.3459E-02
2.9442	-3.6745E-01	-1.4227E-01	9.9199	-9.1920E-02	-4.2780E-02
3.1405	-3.3948E-01	-1.3357E-01	10.0663	-9.0488E-02	-4.2162E-02
3.3436	-3.1460E-01	-1.2567E-01	10.2031	-8.9189E-02	-4.1602E-02
3.5530	-2.9242E-01	-1.1848E-01	10.3300	-8.8018E-02	-4.1098E-02
3.7682	-2.7262E-01	-1.1190E-01	10.4466	-8.6970E-02	-4.0646E-02
3.9886	-2.5488E-01	-1.0589E-01	10.5526	-8.6039E-02	-4.0245E-02
4.2139	-2.3897E-01	-1.0038E-01	10.6478	-8.5219E-02	-3.9892E-02
4.4434	-2.2466E-01	-9.5319E-02	10.7321	-8.4507E-02	-3.9586E-02
4.6766	-2.1175E-01	-9.0668E-02	10.8050	-8.3900E-02	-3.9325E-02
4.9129	-2.0008E-01	-8.6386E-02	10.8666	-8.3395E-02	-3.9108E-02
5.1518	-1.8952E-01	-8.2442E-02	10.9167	-8.2989E-02	-3.8934E-02
5.3927	-1.7992E-01	-7.8803E-02	10.9551	-8.2681E-02	-3.8802E-02
5.6350	-1.7119E-01	-7.5445E-02	10.9817	-8.2468E-02	-3.8711E-02
5.8782	-1.6324E-01	-7.2342E-02	10.9965	-8.2350E-02	-3.8660E-02

Table B.10: Results for $a = 1.25$ (Kn = 0.710)

r	$q_2(r)$	$q_3(r)$	r	$q_2(r)$	$q_3(r)$
1.2535	-1.4115E+00	-9.0799E-01	6.3718	-2.1200E-01	-9.5307E-02
1.2683	-1.3987E+00	-8.3292E-01	6.6150	-2.0338E-01	-9.1777E-02
1.2949	-1.3739E+00	-7.5591E-01	6.8573	-1.9545E-01	-8.8505E-02
1.3333	-1.3365E+00	-6.8152E-01	7.0982	-1.8815E-01	-8.5469E-02
1.3834	-1.2872E+00	-6.1247E-01	7.3371	-1.8142E-01	-8.2654E-02
1.4450	-1.2281E+00	-5.5016E-01	7.5734	-1.7523E-01	-8.0043E-02
1.5179	-1.1616E+00	-4.9505E-01	7.8066	-1.6951E-01	-7.7621E-02
1.6022	-1.0906E+00	-4.4694E-01	8.0361	-1.6423E-01	-7.5375E-02
1.6974	-1.0178E+00	-4.0524E-01	8.2614	-1.5936E-01	-7.3293E-02
1.8034	-9.4558E-01	-3.6915E-01	8.4818	-1.5486E-01	-7.1363E-02
1.9200	-8.7559E-01	-3.3787E-01	8.6970	-1.5071E-01	-6.9576E-02
2.0469	-8.0911E-01	-3.1064E-01	8.9064	-1.4688E-01	-6.7922E-02
2.1837	-7.4689E-01	-2.8679E-01	9.1095	-1.4334E-01	-6.6393E-02
2.3301	-6.8934E-01	-2.6578E-01	9.3058	-1.4008E-01	-6.4981E-02
2.4859	-6.3654E-01	-2.4714E-01	9.4948	-1.3708E-01	-6.3679E-02
2.6506	-5.8841E-01	-2.3050E-01	9.6762	-1.3432E-01	-6.2480E-02
2.8238	-5.4473E-01	-2.1556E-01	9.8494	-1.3178E-01	-6.1378E-02
3.0052	-5.0519E-01	-2.0208E-01	10.0141	-1.2946E-01	-6.0369E-02
3.1942	-4.6946E-01	-1.8987E-01	10.1699	-1.2733E-01	-5.9447E-02
3.3905	-4.3720E-01	-1.7877E-01	10.3163	-1.2540E-01	-5.8607E-02
3.5936	-4.0806E-01	-1.6865E-01	10.4531	-1.2365E-01	-5.7845E-02
3.8030	-3.8175E-01	-1.5939E-01	10.5800	-1.2207E-01	-5.7159E-02
4.0182	-3.5796E-01	-1.5091E-01	10.6966	-1.2065E-01	-5.6544E-02
4.2386	-3.3642E-01	-1.4312E-01	10.8026	-1.1939E-01	-5.5997E-02
4.4639	-3.1690E-01	-1.3595E-01	10.8978	-1.1828E-01	-5.5517E-02
4.6934	-2.9919E-01	-1.2935E-01	10.9821	-1.1732E-01	-5.5100E-02
4.9266	-2.8308E-01	-1.2327E-01	11.0550	-1.1650E-01	-5.4745E-02
5.1629	-2.6841E-01	-1.1765E-01	11.1166	-1.1582E-01	-5.4449E-02
5.4018	-2.5503E-01	-1.1247E-01	11.1667	-1.1527E-01	-5.4211E-02
5.6427	-2.4281E-01	-1.0767E-01	11.2051	-1.1485E-01	-5.4031E-02
5.8850	-2.3163E-01	-1.0323E-01	11.2317	-1.1456E-01	-5.3906E-02
6.1282	-2.2140E-01	-9.9116E-02	11.2465	-1.1440E-01	-5.3838E-02

Table B.11: Results for $a = 1.5$ (Kn $= 0.592$)

r	$q_2(r)$	$q_3(r)$	r	$q_2(r)$	$q_3(r)$
1.5035	-1.4121E+00	-9.4744E-01	6.6218	-2.6772E-01	-1.2157E-01
1.5183	-1.4022E+00	-8.8310E-01	6.8650	-2.5731E-01	-1.1719E-01
1.5449	-1.3832E+00	-8.1567E-01	7.1073	-2.4770E-01	-1.1313E-01
1.5833	-1.3542E+00	-7.4889E-01	7.3482	-2.3882E-01	-1.0935E-01
1.6334	-1.3156E+00	-6.8510E-01	7.5871	-2.3062E-01	-1.0585E-01
1.6950	-1.2683E+00	-6.2576E-01	7.8234	-2.2304E-01	-1.0259E-01
1.7679	-1.2139E+00	-5.7164E-01	8.0566	-2.1602E-01	-9.9564E-02
1.8522	-1.1544E+00	-5.2293E-01	8.2861	-2.0953E-01	-9.6754E-02
1.9474	-1.0919E+00	-4.7950E-01	8.5114	-2.0353E-01	-9.4147E-02
2.0534	-1.0281E+00	-4.4094E-01	8.7318	-1.9798E-01	-9.1728E-02
2.1700	-9.6463E-01	-4.0677E-01	8.9470	-1.9284E-01	-8.9485E-02
2.2969	-9.0283E-01	-3.7644E-01	9.1564	-1.8809E-01	-8.7407E-02
2.4337	-8.4358E-01	-3.4947E-01	9.3595	-1.8370E-01	-8.5484E-02
2.5801	-7.8750E-01	-3.2539E-01	9.5558	-1.7965E-01	-8.3707E-02
2.7359	-7.3494E-01	-3.0381E-01	9.7448	-1.7591E-01	-8.2066E-02
2.9006	-6.8605E-01	-2.8437E-01	9.9262	-1.7247E-01	-8.0555E-02
3.0738	-6.4085E-01	-2.6680E-01	10.0994	-1.6930E-01	-7.9166E-02
3.2552	-5.9924E-01	-2.5086E-01	10.2641	-1.6640E-01	-7.7892E-02
3.4442	-5.6104E-01	-2.3635E-01	10.4199	-1.6375E-01	-7.6726E-02
3.6405	-5.2605E-01	-2.2309E-01	10.5663	-1.6133E-01	-7.5665E-02
3.8436	-4.9405E-01	-2.1095E-01	10.7031	-1.5913E-01	-7.4702E-02
4.0530	-4.6479E-01	-1.9981E-01	10.8300	-1.5716E-01	-7.3834E-02
4.2682	-4.3805E-01	-1.8957E-01	10.9466	-1.5538E-01	-7.3055E-02
4.4886	-4.1361E-01	-1.8014E-01	11.0526	-1.5380E-01	-7.2363E-02
4.7139	-3.9125E-01	-1.7144E-01	11.1478	-1.5241E-01	-7.1755E-02
4.9434	-3.7078E-01	-1.6340E-01	11.2321	-1.5120E-01	-7.1226E-02
5.1766	-3.5204E-01	-1.5597E-01	11.3050	-1.5016E-01	-7.0776E-02
5.4129	-3.3486E-01	-1.4910E-01	11.3666	-1.4930E-01	-7.0402E-02
5.6518	-3.1909E-01	-1.4273E-01	11.4167	-1.4861E-01	-7.0100E-02
5.8927	-3.0460E-01	-1.3683E-01	11.4551	-1.4809E-01	-6.9871E-02
6.1350	-2.9128E-01	-1.3136E-01	11.4817	-1.4772E-01	-6.9714E-02
6.3782	-2.7902E-01	-1.2628E-01	11.4965	-1.4752E-01	-6.9626E-02

Table B.12: Results for $a = 1.75$ (Kn = 0.5074)

r	$q_2(r)$	$q_3(r)$	r	$q_2(r)$	$q_3(r)$
1.7535	-1.4125E+00	-9.8074E-01	6.8718	-3.2190E-01	-1.4768E-01
1.7683	-1.4047E+00	-9.2461E-01	7.1150	-3.0991E-01	-1.4250E-01
1.7949	-1.3896E+00	-8.6480E-01	7.3573	-2.9882E-01	-1.3769E-01
1.8333	-1.3664E+00	-8.0441E-01	7.5982	-2.8854E-01	-1.3321E-01
1.8834	-1.3352E+00	-7.4547E-01	7.8371	-2.7901E-01	-1.2904E-01
1.9450	-1.2966E+00	-6.8939E-01	8.0734	-2.7018E-01	-1.2517E-01
2.0179	-1.2514E+00	-6.3702E-01	8.3066	-2.6199E-01	-1.2157E-01
2.1022	-1.2011E+00	-5.8879E-01	8.5361	-2.5439E-01	-1.1822E-01
2.1974	-1.1471E+00	-5.4482E-01	8.7614	-2.4735E-01	-1.1511E-01
2.3034	-1.0909E+00	-5.0498E-01	8.9818	-2.4082E-01	-1.1222E-01
2.4200	-1.0339E+00	-4.6901E-01	9.1970	-2.3477E-01	-1.0954E-01
2.5469	-9.7720E-01	-4.3658E-01	9.4064	-2.2916E-01	-1.0705E-01
2.6837	-9.2179E-01	-4.0731E-01	9.6095	-2.2398E-01	-1.0475E-01
2.8301	-8.6835E-01	-3.8089E-01	9.8058	-2.1918E-01	-1.0262E-01
2.9859	-8.1736E-01	-3.5696E-01	9.9948	-2.1475E-01	-1.0065E-01
3.1506	-7.6913E-01	-3.3523E-01	10.1762	-2.1067E-01	-9.8834E-02
3.3238	-7.2384E-01	-3.1546E-01	10.3494	-2.0691E-01	-9.7164E-02
3.5052	-6.8152E-01	-2.9741E-01	10.5141	-2.0346E-01	-9.5637E-02
3.6942	-6.4216E-01	-2.8089E-01	10.6699	-2.0031E-01	-9.4231E-02
3.8905	-6.0565E-01	-2.6574E-01	10.8163	-1.9743E-01	-9.2953E-02
4.0936	-5.7186E-01	-2.5182E-01	10.9531	-1.9481E-01	-9.1794E-02
4.3030	-5.4065E-01	-2.3899E-01	11.0800	-1.9245E-01	-9.0746E-02
4.5182	-5.1184E-01	-2.2716E-01	11.1966	-1.9033E-01	-8.9808E-02
4.7386	-4.8527E-01	-2.1623E-01	11.3026	-1.8844E-01	-8.8974E-02
4.9639	-4.6077E-01	-2.0613E-01	11.3978	-1.8678E-01	-8.8239E-02
5.1934	-4.3817E-01	-1.9677E-01	11.4821	-1.8533E-01	-8.7602E-02
5.4266	-4.1734E-01	-1.8810E-01	11.5550	-1.8410E-01	-8.7058E-02
5.6629	-3.9812E-01	-1.8006E-01	11.6166	-1.8307E-01	-8.6605E-02
5.9018	-3.8037E-01	-1.7260E-01	11.6667	-1.8224E-01	-8.6242E-02
6.1427	-3.6399E-01	-1.6567E-01	11.7051	-1.8161E-01	-8.5966E-02
6.3850	-3.4885E-01	-1.5923E-01	11.7317	-1.8118E-01	-8.5775E-02
6.6282	-3.3485E-01	-1.5324E-01	11.7465	-1.8094E-01	-8.5669E-02

Table B.13: Results for $a = 2.0$ (Kn $= 0.444$)

r	$q_2(r)$	$q_3(r)$	r	$q_2(r)$	$q_3(r)$
2.0035	-1.4128E+00	-1.0093E+00	7.1218	-3.7389E-01	-1.7335E-01
2.0183	-1.4064E+00	-9.5964E-01	7.3650	-3.6055E-01	-1.6742E-01
2.0449	-1.3941E+00	-9.0600E-01	7.6073	-3.4816E-01	-1.6191E-01
2.0833	-1.3751E+00	-8.5099E-01	7.8482	-3.3665E-01	-1.5677E-01
2.1334	-1.3494E+00	-7.9641E-01	8.0871	-3.2595E-01	-1.5198E-01
2.1950	-1.3172E+00	-7.4353E-01	8.3234	-3.1601E-01	-1.4752E-01
2.2679	-1.2792E+00	-6.9324E-01	8.5566	-3.0677E-01	-1.4338E-01
2.3522	-1.2361E+00	-6.4607E-01	8.7861	-2.9817E-01	-1.3952E-01
2.4474	-1.1893E+00	-6.0229E-01	9.0114	-2.9019E-01	-1.3592E-01
2.5534	-1.1397E+00	-5.6196E-01	9.2318	-2.8278E-01	-1.3259E-01
2.6700	-1.0886E+00	-5.2498E-01	9.4470	-2.7590E-01	-1.2949E-01
2.7969	-1.0369E+00	-4.9118E-01	9.6564	-2.6952E-01	-1.2661E-01
2.9337	-9.8554E-01	-4.6031E-01	9.8595	-2.6360E-01	-1.2394E-01
3.0801	-9.3524E-01	-4.3213E-01	10.0558	-2.5812E-01	-1.2147E-01
3.2359	-8.8653E-01	-4.0638E-01	10.2448	-2.5305E-01	-1.1919E-01
3.4006	-8.3980E-01	-3.8282E-01	10.4262	-2.4838E-01	-1.1708E-01
3.5738	-7.9531E-01	-3.6123E-01	10.5994	-2.4408E-01	-1.1514E-01
3.7552	-7.5322E-01	-3.4142E-01	10.7641	-2.4012E-01	-1.1336E-01
3.9442	-7.1360E-01	-3.2319E-01	10.9199	-2.3649E-01	-1.1174E-01
4.1405	-6.7645E-01	-3.0640E-01	11.0663	-2.3318E-01	-1.1025E-01
4.3436	-6.4172E-01	-2.9090E-01	11.2031	-2.3017E-01	-1.0890E-01
4.5530	-6.0932E-01	-2.7659E-01	11.3300	-2.2745E-01	-1.0768E-01
4.7682	-5.7917E-01	-2.6334E-01	11.4466	-2.2501E-01	-1.0659E-01
4.9886	-5.5113E-01	-2.5108E-01	11.5526	-2.2283E-01	-1.0562E-01
5.2139	-5.2508E-01	-2.3970E-01	11.6478	-2.2091E-01	-1.0476E-01
5.4434	-5.0089E-01	-2.2914E-01	11.7321	-2.1925E-01	-1.0402E-01
5.6766	-4.7845E-01	-2.1934E-01	11.8050	-2.1782E-01	-1.0338E-01
5.9129	-4.5762E-01	-2.1023E-01	11.8666	-2.1663E-01	-1.0286E-01
6.1518	-4.3829E-01	-2.0176E-01	11.9167	-2.1568E-01	-1.0243E-01
6.3927	-4.2035E-01	-1.9387E-01	11.9551	-2.1495E-01	-1.0211E-01
6.6350	-4.0370E-01	-1.8654E-01	11.9817	-2.1445E-01	-1.0189E-01
6.8782	-3.8824E-01	-1.7971E-01	11.9965	-2.1417E-01	-1.0177E-01

Table B.14: Results for $a = 2.5$ (Kn = 0.355)

r	$q_2(r)$	$q_3(r)$	r	$q_2(r)$	$q_3(r)$
2.5035	-1.4132E+00	-1.0558E+00	7.6218	-4.7018E-01	-2.2274E-01
2.5183	-1.4087E+00	-1.0157E+00	7.8650	-4.5476E-01	-2.1548E-01
2.5449	-1.4000E+00	-9.7139E-01	8.1073	-4.4034E-01	-2.0870E-01
2.5833	-1.3866E+00	-9.2488E-01	8.3482	-4.2687E-01	-2.0237E-01
2.6334	-1.3682E+00	-8.7757E-01	8.5871	-4.1429E-01	-1.9646E-01
2.6950	-1.3449E+00	-8.3051E-01	8.8234	-4.0253E-01	-1.9095E-01
2.7679	-1.3168E+00	-7.8453E-01	9.0566	-3.9156E-01	-1.8581E-01
2.8522	-1.2844E+00	-7.4021E-01	9.2861	-3.8132E-01	-1.8101E-01
2.9474	-1.2483E+00	-6.9798E-01	9.5114	-3.7177E-01	-1.7654E-01
3.0534	-1.2093E+00	-6.5806E-01	9.7318	-3.6286E-01	-1.7237E-01
3.1700	-1.1680E+00	-6.2057E-01	9.9470	-3.5457E-01	-1.6850E-01
3.2969	-1.1251E+00	-5.8554E-01	10.1564	-3.4686E-01	-1.6490E-01
3.4337	-1.0815E+00	-5.5290E-01	10.3595	-3.3968E-01	-1.6156E-01
3.5801	-1.0378E+00	-5.2256E-01	10.5558	-3.3303E-01	-1.5846E-01
3.7359	-9.9433E-01	-4.9440E-01	10.7448	-3.2686E-01	-1.5560E-01
3.9006	-9.5171E-01	-4.6828E-01	10.9262	-3.2114E-01	-1.5295E-01
4.0738	-9.1024E-01	-4.4404E-01	11.0994	-3.1587E-01	-1.5051E-01
4.2552	-8.7018E-01	-4.2156E-01	11.2641	-3.1102E-01	-1.4827E-01
4.4442	-8.3172E-01	-4.0069E-01	11.4199	-3.0657E-01	-1.4622E-01
4.6405	-7.9499E-01	-3.8130E-01	11.5663	-3.0250E-01	-1.4434E-01
4.8436	-7.6005E-01	-3.6328E-01	11.7031	-2.9879E-01	-1.4264E-01
5.0530	-7.2694E-01	-3.4653E-01	11.8300	-2.9544E-01	-1.4110E-01
5.2682	-6.9564E-01	-3.3094E-01	11.9466	-2.9242E-01	-1.3972E-01
5.4886	-6.6614E-01	-3.1641E-01	12.0526	-2.8973E-01	-1.3849E-01
5.7139	-6.3837E-01	-3.0289E-01	12.1478	-2.8736E-01	-1.3740E-01
5.9434	-6.1228E-01	-2.9028E-01	12.2321	-2.8529E-01	-1.3646E-01
6.1766	-5.8779E-01	-2.7853E-01	12.3050	-2.8353E-01	-1.3566E-01
6.4129	-5.6482E-01	-2.6755E-01	12.3666	-2.8205E-01	-1.3499E-01
6.6518	-5.4331E-01	-2.5732E-01	12.4167	-2.8087E-01	-1.3445E-01
6.8927	-5.2317E-01	-2.4777E-01	12.4551	-2.7996E-01	-1.3404E-01
7.1350	-5.0431E-01	-2.3885E-01	12.4817	-2.7934E-01	-1.3376E-01
7.3782	-4.8667E-01	-2.3052E-01	12.4965	-2.7900E-01	-1.3360E-01

Table B.15: Results for $a = 3.0$ (Kn = 0.296)

r	$q_2(r)$	$q_3(r)$	r	$q_2(r)$	$q_3(r)$
3.0035	-1.4134E+00	-1.0922E+00	8.1218	-5.5593E-01	-2.6910E-01
3.0183	-1.4101E+00	-1.0587E+00	8.3650	-5.3910E-01	-2.6070E-01
3.0449	-1.4036E+00	-1.0211E+00	8.6073	-5.2329E-01	-2.5283E-01
3.0833	-1.3935E+00	-9.8093E-01	8.8482	-5.0844E-01	-2.4547E-01
3.1334	-1.3797E+00	-9.3932E-01	9.0871	-4.9450E-01	-2.3859E-01
3.1950	-1.3621E+00	-8.9716E-01	9.3234	-4.8142E-01	-2.3216E-01
3.2679	-1.3405E+00	-8.5518E-01	9.5566	-4.6916E-01	-2.2615E-01
3.3522	-1.3153E+00	-8.1393E-01	9.7861	-4.5768E-01	-2.2053E-01
3.4474	-1.2868E+00	-7.7386E-01	10.0114	-4.4693E-01	-2.1530E-01
3.5534	-1.2554E+00	-7.3528E-01	10.2318	-4.3688E-01	-2.1041E-01
3.6700	-1.2216E+00	-6.9841E-01	10.4470	-4.2749E-01	-2.0586E-01
3.7969	-1.1859E+00	-6.6336E-01	10.6564	-4.1873E-01	-2.0162E-01
3.9337	-1.1489E+00	-6.3020E-01	10.8595	-4.1056E-01	-1.9768E-01
4.0801	-1.1111E+00	-5.9893E-01	11.0558	-4.0296E-01	-1.9402E-01
4.2359	-1.0728E+00	-5.6954E-01	11.2448	-3.9590E-01	-1.9064E-01
4.4006	-1.0347E+00	-5.4193E-01	11.4262	-3.8936E-01	-1.8751E-01
4.5738	-9.9688E-01	-5.1606E-01	11.5994	-3.8330E-01	-1.8462E-01
4.7552	-9.5978E-01	-4.9183E-01	11.7641	-3.7772E-01	-1.8196E-01
4.9442	-9.2361E-01	-4.6915E-01	11.9199	-3.7259E-01	-1.7952E-01
5.1405	-8.8855E-01	-4.4793E-01	12.0663	-3.6789E-01	-1.7730E-01
5.3436	-8.5472E-01	-4.2807E-01	12.2031	-3.6360E-01	-1.7527E-01
5.5530	-8.2224E-01	-4.0949E-01	12.3300	-3.5972E-01	-1.7344E-01
5.7682	-7.9115E-01	-3.9210E-01	12.4466	-3.5622E-01	-1.7180E-01
5.9886	-7.6150E-01	-3.7584E-01	12.5526	-3.5310E-01	-1.7033E-01
6.2139	-7.3329E-01	-3.6062E-01	12.6478	-3.5035E-01	-1.6904E-01
6.4434	-7.0650E-01	-3.4637E-01	12.7321	-3.4795E-01	-1.6792E-01
6.6766	-6.8112E-01	-3.3303E-01	12.8050	-3.4590E-01	-1.6696E-01
6.9129	-6.5710E-01	-3.2055E-01	12.8666	-3.4418E-01	-1.6616E-01
7.1518	-6.3442E-01	-3.0886E-01	12.9167	-3.4280E-01	-1.6552E-01
7.3927	-6.1301E-01	-2.9792E-01	12.9551	-3.4175E-01	-1.6503E-01
7.6350	-5.9283E-01	-2.8767E-01	12.9817	-3.4103E-01	-1.6469E-01
7.8782	-5.7382E-01	-2.7808E-01	12.9965	-3.4062E-01	-1.6451E-01

Table B.16: Results for $a = 4.0$ (Kn = 0.222)

r	$q_2(r)$	$q_3(r)$	r	$q_2(r)$	$q_3(r)$
4.0035	-1.4138E+00	-1.1457E+00	9.1218	-6.9885E-01	-3.5284E-01
4.0183	-1.4117E+00	-1.1208E+00	9.3650	-6.8069E-01	-3.4266E-01
4.0449	-1.4076E+00	-1.0921E+00	9.6073	-6.6347E-01	-3.3309E-01
4.0833	-1.4014E+00	-1.0606E+00	9.8482	-6.4714E-01	-3.2411E-01
4.1334	-1.3928E+00	-1.0272E+00	10.0871	-6.3170E-01	-3.1567E-01
4.1950	-1.3816E+00	-9.9255E-01	10.3234	-6.1709E-01	-3.0777E-01
4.2679	-1.3677E+00	-9.5714E-01	10.5566	-6.0329E-01	-3.0035E-01
4.3522	-1.3512E+00	-9.2145E-01	10.7861	-5.9031E-01	-2.9341E-01
4.4474	-1.3322E+00	-8.8588E-01	11.0114	-5.7806E-01	-2.8691E-01
4.5534	-1.3108E+00	-8.5077E-01	11.2318	-5.6654E-01	-2.8084E-01
4.6700	-1.2871E+00	-8.1638E-01	11.4470	-5.5572E-01	-2.7516E-01
4.7969	-1.2616E+00	-7.8292E-01	11.6564	-5.4557E-01	-2.6987E-01
4.9337	-1.2344E+00	-7.5055E-01	11.8595	-5.3607E-01	-2.6493E-01
5.0801	-1.2059E+00	-7.1938E-01	12.0558	-5.2719E-01	-2.6034E-01
5.2359	-1.1764E+00	-6.8949E-01	12.2448	-5.1890E-01	-2.5608E-01
5.4006	-1.1461E+00	-6.6091E-01	12.4262	-5.1119E-01	-2.5214E-01
5.5738	-1.1154E+00	-6.3368E-01	12.5994	-5.0404E-01	-2.4849E-01
5.7552	-1.0846E+00	-6.0780E-01	12.7641	-4.9742E-01	-2.4513E-01
5.9442	-1.0538E+00	-5.8320E-01	12.9199	-4.9132E-01	-2.4205E-01
6.1405	-1.0232E+00	-5.5989E-01	13.0663	-4.8572E-01	-2.3922E-01
6.3436	-9.9314E-01	-5.3783E-01	13.2031	-4.8059E-01	-2.3665E-01
6.5530	-9.6364E-01	-5.1698E-01	13.3300	-4.7594E-01	-2.3433E-01
6.7682	-9.3486E-01	-4.9727E-01	13.4466	-4.7174E-01	-2.3224E-01
6.9886	-9.0690E-01	-4.7867E-01	13.5526	-4.6799E-01	-2.3037E-01
7.2139	-8.7982E-01	-4.6113E-01	13.6478	-4.6467E-01	-2.2872E-01
7.4434	-8.5369E-01	-4.4458E-01	13.7321	-4.6177E-01	-2.2729E-01
7.6766	-8.2854E-01	-4.2899E-01	13.8050	-4.5929E-01	-2.2607E-01
7.9129	-8.0438E-01	-4.1430E-01	13.8666	-4.5722E-01	-2.2505E-01
8.1518	-7.8126E-01	-4.0047E-01	13.9167	-4.5555E-01	-2.2423E-01
8.3927	-7.5916E-01	-3.8745E-01	13.9551	-4.5428E-01	-2.2360E-01
8.6350	-7.3806E-01	-3.7520E-01	13.9817	-4.5340E-01	-2.2317E-01
8.8782	-7.1796E-01	-3.6368E-01	13.9965	-4.5291E-01	-2.2293E-01

Table B.17: Results for $a = 5.0$ (Kn = 0.178)

r	$q_2(r)$	$q_3(r)$	r	$q_2(r)$	$q_3(r)$
5.0035	-1.4139E+00	-1.1835E+00	10.1218	-8.1081E-01	-4.2599E-01
5.0183	-1.4125E+00	-1.1638E+00	10.3650	-7.9254E-01	-4.1455E-01
5.0449	-1.4097E+00	-1.1407E+00	10.6073	-7.7507E-01	-4.0376E-01
5.0833	-1.4054E+00	-1.1149E+00	10.8482	-7.5839E-01	-3.9363E-01
5.1334	-1.3995E+00	-1.0871E+00	11.0871	-7.4248E-01	-3.8403E-01
5.1950	-1.3918E+00	-1.0577E+00	11.3234	-7.2735E-01	-3.7502E-01
5.2679	-1.3821E+00	-1.0272E+00	11.5566	-7.1299E-01	-3.6656E-01
5.3522	-1.3705E+00	-9.9603E-01	11.7861	-6.9938E-01	-3.5861E-01
5.4474	-1.3569E+00	-9.6443E-01	12.0114	-6.8648E-01	-3.5116E-01
5.5534	-1.3414E+00	-9.3271E-01	12.2318	-6.7429E-01	-3.4417E-01
5.6700	-1.3241E+00	-9.0116E-01	12.4470	-6.6278E-01	-3.3763E-01
5.7969	-1.3050E+00	-8.6997E-01	12.6564	-6.5194E-01	-3.3151E-01
5.9337	-1.2844E+00	-8.3934E-01	12.8595	-6.4174E-01	-3.2580E-01
6.0801	-1.2624E+00	-8.0941E-01	13.0558	-6.3218E-01	-3.2048E-01
6.2359	-1.2392E+00	-7.8032E-01	13.2448	-6.2323E-01	-3.1553E-01
6.4006	-1.2151E+00	-7.5213E-01	13.4262	-6.1487E-01	-3.1094E-01
6.5738	-1.1902E+00	-7.2493E-01	13.5994	-6.0709E-01	-3.0669E-01
6.7552	-1.1647E+00	-6.9876E-01	13.7641	-5.9987E-01	-3.0277E-01
6.9442	-1.1388E+00	-6.7365E-01	13.9199	-5.9320E-01	-2.9916E-01
7.1405	-1.1128E+00	-6.4960E-01	14.0663	-5.8705E-01	-2.9586E-01
7.3436	-1.0867E+00	-6.2663E-01	14.2031	-5.8142E-01	-2.9285E-01
7.5530	-1.0608E+00	-6.0471E-01	14.3300	-5.7630E-01	-2.9011E-01
7.7682	-1.0351E+00	-5.8383E-01	14.4466	-5.7167E-01	-2.8766E-01
7.9886	-1.0098E+00	-5.6398E-01	14.5526	-5.6752E-01	-2.8546E-01
8.2139	-9.8498E-01	-5.4512E-01	14.6478	-5.6385E-01	-2.8353E-01
8.4434	-9.6072E-01	-5.2723E-01	14.7321	-5.6064E-01	-2.8184E-01
8.6766	-9.3707E-01	-5.1026E-01	14.8050	-5.5789E-01	-2.8040E-01
8.9129	-9.1414E-01	-4.9418E-01	14.8666	-5.5559E-01	-2.7920E-01
9.1518	-8.9191E-01	-4.7897E-01	14.9167	-5.5374E-01	-2.7823E-01
9.3927	-8.7045E-01	-4.6457E-01	14.9551	-5.5232E-01	-2.7749E-01
9.6350	-8.4977E-01	-4.5097E-01	14.9817	-5.5135E-01	-2.7699E-01
9.8782	-8.2989E-01	-4.3812E-01	14.9965	-5.5080E-01	-2.7670E-01

Table B.18: Results for $a = 6.0$ (Kn $= 0.148$)

r	$q_2(r)$	$q_3(r)$	r	$q_2(r)$	$q_3(r)$
6.0035	-1.4140E+00	-1.2117E+00	11.1218	-8.9929E-01	-4.9006E-01
6.0183	-1.4129E+00	-1.1956E+00	11.3650	-8.8154E-01	-4.7774E-01
6.0449	-1.4109E+00	-1.1762E+00	11.6073	-8.6447E-01	-4.6609E-01
6.0833	-1.4078E+00	-1.1544E+00	11.8482	-8.4807E-01	-4.5508E-01
6.1334	-1.4035E+00	-1.1306E+00	12.0871	-8.3235E-01	-4.4468E-01
6.1950	-1.3978E+00	-1.1051E+00	12.3234	-8.1732E-01	-4.3488E-01
6.2679	-1.3907E+00	-1.0784E+00	12.5566	-8.0296E-01	-4.2564E-01
6.3522	-1.3821E+00	-1.0508E+00	12.7861	-7.8927E-01	-4.1695E-01
6.4474	-1.3719E+00	-1.0225E+00	13.0114	-7.7625E-01	-4.0877E-01
6.5534	-1.3602E+00	-9.9376E-01	13.2318	-7.6389E-01	-4.0109E-01
6.6700	-1.3469E+00	-9.6485E-01	13.4470	-7.5218E-01	-3.9389E-01
6.7969	-1.3322E+00	-9.3596E-01	13.6564	-7.4110E-01	-3.8714E-01
6.9337	-1.3161E+00	-9.0728E-01	13.8595	-7.3065E-01	-3.8083E-01
7.0801	-1.2987E+00	-8.7895E-01	14.0558	-7.2081E-01	-3.7494E-01
7.2359	-1.2802E+00	-8.5112E-01	14.2448	-7.1157E-01	-3.6946E-01
7.4006	-1.2606E+00	-8.2390E-01	14.4262	-7.0292E-01	-3.6438E-01
7.5738	-1.2401E+00	-7.9739E-01	14.5994	-6.9484E-01	-3.5964E-01
7.7552	-1.2189E+00	-7.7164E-01	14.7641	-6.8732E-01	-3.5527E-01
7.9442	-1.1972E+00	-7.4671E-01	14.9199	-6.8036E-01	-3.5125E-01
8.1405	-1.1750E+00	-7.2265E-01	15.0663	-6.7394E-01	-3.4756E-01
8.3436	-1.1525E+00	-6.9949E-01	15.2031	-6.6804E-01	-3.4419E-01
8.5530	-1.1299E+00	-6.7723E-01	15.3300	-6.6267E-01	-3.4115E-01
8.7682	-1.1073E+00	-6.5589E-01	15.4466	-6.5779E-01	-3.3838E-01
8.9886	-1.0848E+00	-6.3546E-01	15.5526	-6.5344E-01	-3.3593E-01
9.2139	-1.0624E+00	-6.1594E-01	15.6478	-6.4957E-01	-3.3376E-01
9.4434	-1.0403E+00	-5.9730E-01	15.7321	-6.4618E-01	-3.3186E-01
9.6766	-1.0187E+00	-5.7955E-01	15.8050	-6.4328E-01	-3.3024E-01
9.9129	-9.9739E-01	-5.6265E-01	15.8666	-6.4084E-01	-3.2889E-01
10.1518	-9.7661E-01	-5.4657E-01	15.9167	-6.3888E-01	-3.2780E-01
10.3927	-9.5638E-01	-5.3130E-01	15.9551	-6.3739E-01	-3.2697E-01
10.6350	-9.3673E-01	-5.1681E-01	15.9817	-6.3635E-01	-3.2640E-01
10.8782	-9.1769E-01	-5.0307E-01	15.9965	-6.3578E-01	-3.2609E-01

Table B.19: Results for $a = 7.0$ (Kn = 0.1269)

r	$q_2(r)$	$q_3(r)$	r	$q_2(r)$	$q_3(r)$
7.0035	-1.4140E+00	-1.2337E+00	12.1218	-9.7017E-01	-5.4667E-01
7.0183	-1.4132E+00	-1.2200E+00	12.3650	-9.5328E-01	-5.3376E-01
7.0449	-1.4117E+00	-1.2035E+00	12.6073	-9.3693E-01	-5.2151E-01
7.0833	-1.4094E+00	-1.1845E+00	12.8482	-9.2114E-01	-5.0990E-01
7.1334	-1.4060E+00	-1.1637E+00	13.0871	-9.0592E-01	-4.9892E-01
7.1950	-1.4017E+00	-1.1413E+00	13.3234	-8.9132E-01	-4.8853E-01
7.2679	-1.3962E+00	-1.1176E+00	13.5566	-8.7731E-01	-4.7872E-01
7.3522	-1.3896E+00	-1.0928E+00	13.7861	-8.6389E-01	-4.6947E-01
7.4474	-1.3817E+00	-1.0672E+00	14.0114	-8.5107E-01	-4.6075E-01
7.5534	-1.3725E+00	-1.0410E+00	14.2318	-8.3886E-01	-4.5255E-01
7.6700	-1.3621E+00	-1.0145E+00	14.4470	-8.2725E-01	-4.4484E-01
7.7969	-1.3504E+00	-9.8772E-01	14.6564	-8.1622E-01	-4.3760E-01
7.9337	-1.3375E+00	-9.6093E-01	14.8595	-8.0579E-01	-4.3083E-01
8.0801	-1.3234E+00	-9.3426E-01	15.0558	-7.9593E-01	-4.2449E-01
8.2359	-1.3083E+00	-9.0785E-01	15.2448	-7.8665E-01	-4.1858E-01
8.4006	-1.2921E+00	-8.8182E-01	15.4262	-7.7794E-01	-4.1308E-01
8.5738	-1.2751E+00	-8.5627E-01	15.5994	-7.6979E-01	-4.0798E-01
8.7552	-1.2573E+00	-8.3128E-01	15.7641	-7.6218E-01	-4.0326E-01
8.9442	-1.2389E+00	-8.0692E-01	15.9199	-7.5514E-01	-3.9890E-01
9.1405	-1.2199E+00	-7.8325E-01	16.0663	-7.4861E-01	-3.9491E-01
9.3436	-1.2005E+00	-7.6031E-01	16.2031	-7.4262E-01	-3.9126E-01
9.5530	-1.1808E+00	-7.3814E-01	16.3300	-7.3714E-01	-3.8794E-01
9.7682	-1.1609E+00	-7.1676E-01	16.4466	-7.3218E-01	-3.8495E-01
9.9886	-1.1409E+00	-6.9620E-01	16.5526	-7.2772E-01	-3.8229E-01
10.2139	-1.1209E+00	-6.7643E-01	16.6478	-7.2376E-01	-3.7993E-01
10.4434	-1.1010E+00	-6.5748E-01	16.7321	-7.2029E-01	-3.7785E-01
10.6766	-1.0813E+00	-6.3933E-01	16.8050	-7.1732E-01	-3.7609E-01
10.9129	-1.0618E+00	-6.2199E-01	16.8666	-7.1482E-01	-3.7463E-01
11.1518	-1.0427E+00	-6.0542E-01	16.9167	-7.1281E-01	-3.7343E-01
11.3927	-1.0239E+00	-5.8963E-01	16.9551	-7.1127E-01	-3.7253E-01
11.6350	-1.0055E+00	-5.7459E-01	16.9817	-7.1021E-01	-3.7190E-01
11.8782	-9.8759E-01	-5.6027E-01	16.9965	-7.0962E-01	-3.7156E-01

Table B.20: Results for $a = 8.0$ (Kn = 0.111)

r	$q_2(r)$	$q_3(r)$	r	$q_2(r)$	$q_3(r)$
8.0035	-1.4141E+00	-1.2514E+00	13.1218	-1.0278E+00	-5.9716E-01
8.0183	-1.4135E+00	-1.2396E+00	13.3650	-1.0119E+00	-5.8386E-01
8.0449	-1.4122E+00	-1.2251E+00	13.6073	-9.9639E-01	-5.7121E-01
8.0833	-1.4104E+00	-1.2084E+00	13.8482	-9.8139E-01	-5.5920E-01
8.1334	-1.4078E+00	-1.1899E+00	14.0871	-9.6688E-01	-5.4780E-01
8.1950	-1.4044E+00	-1.1699E+00	14.3234	-9.5287E-01	-5.3700E-01
8.2679	-1.4000E+00	-1.1486E+00	14.5566	-9.3938E-01	-5.2678E-01
8.3522	-1.3947E+00	-1.1262E+00	14.7861	-9.2642E-01	-5.1712E-01
8.4474	-1.3884E+00	-1.1029E+00	15.0114	-9.1400E-01	-5.0800E-01
8.5534	-1.3811E+00	-1.0789E+00	15.2318	-9.0212E-01	-4.9940E-01
8.6700	-1.3726E+00	-1.0544E+00	15.4470	-8.9079E-01	-4.9130E-01
8.7969	-1.3631E+00	-1.0295E+00	15.6564	-8.8000E-01	-4.8370E-01
8.9337	-1.3526E+00	-1.0045E+00	15.8595	-8.6977E-01	-4.7656E-01
9.0801	-1.3410E+00	-9.7939E-01	16.0558	-8.6008E-01	-4.6988E-01
9.2359	-1.3284E+00	-9.5441E-01	16.2448	-8.5093E-01	-4.6364E-01
9.4006	-1.3149E+00	-9.2962E-01	16.4262	-8.4231E-01	-4.5782E-01
9.5738	-1.3006E+00	-9.0515E-01	16.5994	-8.3424E-01	-4.5242E-01
9.7552	-1.2855E+00	-8.8107E-01	16.7641	-8.2669E-01	-4.4741E-01
9.9442	-1.2697E+00	-8.5747E-01	16.9199	-8.1968E-01	-4.4279E-01
10.1405	-1.2534E+00	-8.3441E-01	17.0663	-8.1317E-01	-4.3855E-01
10.3436	-1.2365E+00	-8.1194E-01	17.2031	-8.0719E-01	-4.3466E-01
10.5530	-1.2193E+00	-7.9012E-01	17.3300	-8.0171E-01	-4.3114E-01
10.7682	-1.2018E+00	-7.6897E-01	17.4466	-7.9675E-01	-4.2795E-01
10.9886	-1.1840E+00	-7.4853E-01	17.5526	-7.9228E-01	-4.2510E-01
11.2139	-1.1662E+00	-7.2881E-01	17.6478	-7.8831E-01	-4.2258E-01
11.4434	-1.1483E+00	-7.0981E-01	17.7321	-7.8482E-01	-4.2039E-01
11.6766	-1.1304E+00	-6.9156E-01	17.8050	-7.8182E-01	-4.1850E-01
11.9129	-1.1127E+00	-6.7401E-01	17.8666	-7.7931E-01	-4.1693E-01
12.1518	-1.0951E+00	-6.5722E-01	17.9167	-7.7729E-01	-4.1566E-01
12.3927	-1.0778E+00	-6.4114E-01	17.9551	-7.7574E-01	-4.1470E-01
12.6350	-1.0608E+00	-6.2578E-01	17.9817	-7.7467E-01	-4.1403E-01
12.8782	-1.0441E+00	-6.1113E-01	17.9965	-7.7408E-01	-4.1367E-01

Table B.21: Results for $a = 9.0$ (Kn = 0.0987)

r	$q_2(r)$	$q_3(r)$	r	$q_2(r)$	$q_3(r)$
9.0035	-1.4141E+00	-1.2659E+00	14.1218	-1.0750E+00	-6.4219E-01
9.0183	-1.4136E+00	-1.2555E+00	14.3650	-1.0601E+00	-6.2867E-01
9.0449	-1.4126E+00	-1.2427E+00	14.6073	-1.0456E+00	-6.1577E-01
9.0833	-1.4111E+00	-1.2278E+00	14.8482	-1.0314E+00	-6.0349E-01
9.1334	-1.4090E+00	-1.2112E+00	15.0871	-1.0177E+00	-5.9182E-01
9.1950	-1.4062E+00	-1.1931E+00	15.3234	-1.0043E+00	-5.8074E-01
9.2679	-1.4027E+00	-1.1737E+00	15.5566	-9.9149E-01	-5.7023E-01
9.3522	-1.3984E+00	-1.1532E+00	15.7861	-9.7909E-01	-5.6028E-01
9.4474	-1.3932E+00	-1.1318E+00	16.0114	-9.6716E-01	-5.5087E-01
9.5534	-1.3872E+00	-1.1097E+00	16.2318	-9.5573E-01	-5.4198E-01
9.6700	-1.3803E+00	-1.0870E+00	16.4470	-9.4479E-01	-5.3361E-01
9.7969	-1.3724E+00	-1.0638E+00	16.6564	-9.3434E-01	-5.2572E-01
9.9337	-1.3636E+00	-1.0404E+00	16.8595	-9.2441E-01	-5.1831E-01
10.0801	-1.3539E+00	-1.0168E+00	17.0558	-9.1499E-01	-5.1136E-01
10.2359	-1.3433E+00	-9.9314E-01	17.2448	-9.0607E-01	-5.0490E-01
10.4006	-1.3319E+00	-9.6958E-01	17.4262	-8.9766E-01	-4.9881E-01
10.5738	-1.3196E+00	-9.4620E-01	17.5994	-8.8976E-01	-4.9316E-01
10.7552	-1.3067E+00	-9.2307E-01	17.7641	-8.8236E-01	-4.8794E-01
10.9442	-1.2931E+00	-9.0031E-01	17.9199	-8.7547E-01	-4.8310E-01
11.1405	-1.2789E+00	-8.7796E-01	18.0663	-8.6908E-01	-4.7866E-01
11.3436	-1.2642E+00	-8.5610E-01	18.2031	-8.6318E-01	-4.7459E-01
11.5530	-1.2490E+00	-8.3475E-01	18.3300	-8.5778E-01	-4.7089E-01
11.7682	-1.2335E+00	-8.1399E-01	18.4466	-8.5288E-01	-4.6756E-01
11.9886	-1.2177E+00	-7.9383E-01	18.5526	-8.4846E-01	-4.6457E-01
12.2139	-1.2018E+00	-7.7431E-01	18.6478	-8.4453E-01	-4.6192E-01
12.4434	-1.1857E+00	-7.5545E-01	18.7321	-8.4109E-01	-4.5961E-01
12.6766	-1.1695E+00	-7.3725E-01	18.8050	-8.3812E-01	-4.5764E-01
12.9129	-1.1534E+00	-7.1973E-01	18.8666	-8.3563E-01	-4.5597E-01
13.1518	-1.1373E+00	-7.0287E-01	18.9167	-8.3362E-01	-4.5464E-01
13.3927	-1.1214E+00	-6.8670E-01	18.9551	-8.3208E-01	-4.5363E-01
13.6350	-1.1057E+00	-6.7120E-01	18.9817	-8.3101E-01	-4.5292E-01
13.8782	-1.0902E+00	-6.5637E-01	18.9965	-8.3043E-01	-4.5254E-01

Table B.22: Results for $a = 10.0$ (Kn = 0.0888)

r	$q_2(r)$	$q_3(r)$	r	$q_2(r)$	$q_3(r)$
10.0035	-1.4141E+00	-1.2781E+00	15.1218	-1.1142E+00	-6.8287E-01
10.0183	-1.4137E+00	-1.2689E+00	15.3650	-1.1004E+00	-6.6917E-01
10.0449	-1.4129E+00	-1.2573E+00	15.6073	-1.0868E+00	-6.5613E-01
10.0833	-1.4116E+00	-1.2439E+00	15.8482	-1.0735E+00	-6.4370E-01
10.1334	-1.4099E+00	-1.2288E+00	16.0871	-1.0605E+00	-6.3185E-01
10.1950	-1.4076E+00	-1.2123E+00	16.3234	-1.0479E+00	-6.2058E-01
10.2679	-1.4047E+00	-1.1945E+00	16.5566	-1.0357E+00	-6.0987E-01
10.3522	-1.4011E+00	-1.1757E+00	16.7861	-1.0239E+00	-5.9972E-01
10.4474	-1.3969E+00	-1.1559E+00	17.0114	-1.0126E+00	-5.9011E-01
10.5534	-1.3918E+00	-1.1354E+00	17.2318	-1.0016E+00	-5.8100E-01
10.6700	-1.3860E+00	-1.1143E+00	17.4470	-9.9113E-01	-5.7241E-01
10.7969	-1.3794E+00	-1.0926E+00	17.6564	-9.8110E-01	-5.6432E-01
10.9337	-1.3719E+00	-1.0706E+00	17.8595	-9.7153E-01	-5.5670E-01
11.0801	-1.3637E+00	-1.0484E+00	18.0558	-9.6243E-01	-5.4955E-01
11.2359	-1.3546E+00	-1.0260E+00	18.2448	-9.5380E-01	-5.4286E-01
11.4006	-1.3449E+00	-1.0036E+00	18.4262	-9.4563E-01	-5.3661E-01
11.5738	-1.3343E+00	-9.8128E-01	18.5994	-9.3798E-01	-5.3079E-01
11.7552	-1.3231E+00	-9.5912E-01	18.7641	-9.3079E-01	-5.2539E-01
11.9442	-1.3113E+00	-9.3721E-01	18.9199	-9.2407E-01	-5.2039E-01
12.1405	-1.2988E+00	-9.1562E-01	19.0663	-9.1784E-01	-5.1579E-01
12.3436	-1.2859E+00	-8.9441E-01	19.2031	-9.1208E-01	-5.1158E-01
12.5530	-1.2725E+00	-8.7365E-01	19.3300	-9.0680E-01	-5.0774E-01
12.7682	-1.2587E+00	-8.5336E-01	19.4466	-9.0200E-01	-5.0428E-01
12.9886	-1.2446E+00	-8.3360E-01	19.5526	-8.9768E-01	-5.0118E-01
13.2139	-1.2303E+00	-8.1441E-01	19.6478	-8.9383E-01	-4.9843E-01
13.4434	-1.2158E+00	-7.9579E-01	19.7321	-8.9045E-01	-4.9603E-01
13.6766	-1.2012E+00	-7.7778E-01	19.8050	-8.8754E-01	-4.9397E-01
13.9129	-1.1865E+00	-7.6038E-01	19.8666	-8.8509E-01	-4.9225E-01
14.1518	-1.1718E+00	-7.4361E-01	19.9167	-8.8312E-01	-4.9086E-01
14.3927	-1.1572E+00	-7.2747E-01	19.9551	-8.8160E-01	-4.8981E-01
14.6350	-1.1427E+00	-7.1196E-01	19.9817	-8.8056E-01	-4.8907E-01
14.8782	-1.1284E+00	-6.9708E-01	19.9965	-8.7998E-01	-4.8867E-01

Table B.23: Results for $a = 50$ (Kn = 0.0178)

r	$q_2(r)$	$q_3(r)$	r	$q_2(r)$	$q_3(r)$
50.0035	-1.4142E+00	-1.3838E+00	55.1218	-1.3893E+00	-1.1870E+00
50.0183	-1.4142E+00	-1.3823E+00	55.3650	-1.3875E+00	-1.1795E+00
50.0449	-1.4142E+00	-1.3801E+00	55.6073	-1.3856E+00	-1.1722E+00
50.0833	-1.4141E+00	-1.3775E+00	55.8482	-1.3837E+00	-1.1649E+00
50.1334	-1.4140E+00	-1.3743E+00	56.0871	-1.3818E+00	-1.1579E+00
50.1950	-1.4139E+00	-1.3708E+00	56.3234	-1.3799E+00	-1.1510E+00
50.2679	-1.4138E+00	-1.3668E+00	56.5566	-1.3780E+00	-1.1443E+00
50.3522	-1.4136E+00	-1.3625E+00	56.7861	-1.3760E+00	-1.1379E+00
50.4474	-1.4134E+00	-1.3579E+00	57.0114	-1.3741E+00	-1.1314E+00
50.5534	-1.4132E+00	-1.3529E+00	57.2318	-1.3722E+00	-1.1253E+00
50.6700	-1.4129E+00	-1.3476E+00	57.4470	-1.3703E+00	-1.1193E+00
50.7969	-1.4125E+00	-1.3420E+00	57.6564	-1.3685E+00	-1.1136E+00
50.9337	-1.4121E+00	-1.3361E+00	57.8595	-1.3667E+00	-1.1082E+00
51.0801	-1.4117E+00	-1.3299E+00	58.0558	-1.3649E+00	-1.1029E+00
51.2359	-1.4112E+00	-1.3235E+00	58.2448	-1.3632E+00	-1.0979E+00
51.4006	-1.4106E+00	-1.3168E+00	58.4262	-1.3615E+00	-1.0932E+00
51.5738	-1.4099E+00	-1.3099E+00	58.5994	-1.3599E+00	-1.0887E+00
51.7552	-1.4092E+00	-1.3029E+00	58.7641	-1.3584E+00	-1.0845E+00
51.9442	-1.4084E+00	-1.2956E+00	58.9199	-1.3569E+00	-1.0805E+00
52.1405	-1.4075E+00	-1.2882E+00	59.0663	-1.3555E+00	-1.0768E+00
52.3436	-1.4066E+00	-1.2807E+00	59.2031	-1.3542E+00	-1.0734E+00
52.5530	-1.4055E+00	-1.2730E+00	59.3300	-1.3530E+00	-1.0702E+00
52.7682	-1.4044E+00	-1.2654E+00	59.4466	-1.3519E+00	-1.0674E+00
52.9886	-1.4032E+00	-1.2575E+00	59.5526	-1.3509E+00	-1.0648E+00
53.2139	-1.4019E+00	-1.2496E+00	59.6478	-1.3499E+00	-1.0624E+00
53.4434	-1.4006E+00	-1.2417E+00	59.7321	-1.3491E+00	-1.0603E+00
53.6766	-1.3992E+00	-1.2338E+00	59.8050	-1.3484E+00	-1.0586E+00
53.9129	-1.3977E+00	-1.2258E+00	59.8666	-1.3478E+00	-1.0571E+00
54.1518	-1.3961E+00	-1.2179E+00	59.9167	-1.3473E+00	-1.0559E+00
54.3927	-1.3945E+00	-1.2101E+00	59.9551	-1.3465E+00	-1.0549E+00
54.6350	-1.3928E+00	-1.2023E+00	59.9817	-1.3467E+00	-1.0543E+00
54.8782	-1.3911E+00	-1.1946E+00	59.9965	-1.3466E+00	-1.0540E+00

Table B.24: Results for $a = 100$ (Kn = 0.00888)

r	$q_2(r)$	$q_3(r)$	r	$q_2(r)$	$q_3(r)$
100.0035	-1.4141E+00	-1.3993E+00	105.1218	-1.4074E+00	-1.2950E+00
100.0183	-1.4142E+00	-1.3986E+00	105.3650	-1.4069E+00	-1.2906E+00
100.0449	-1.4142E+00	-1.3975E+00	105.6073	-1.4063E+00	-1.2864E+00
100.0833	-1.4142E+00	-1.3962E+00	105.8482	-1.4058E+00	-1.2823E+00
100.1334	-1.4142E+00	-1.3947E+00	106.0871	-1.4052E+00	-1.2780E+00
100.1950	-1.4141E+00	-1.3930E+00	106.3234	-1.4046E+00	-1.2738E+00
100.2679	-1.4141E+00	-1.3910E+00	106.5566	-1.4040E+00	-1.2698E+00
100.3522	-1.4141E+00	-1.3889E+00	106.7861	-1.4035E+00	-1.2658E+00
100.4474	-1.4140E+00	-1.3866E+00	107.0114	-1.4029E+00	-1.2620E+00
100.5534	-1.4140E+00	-1.3841E+00	107.2318	-1.4023E+00	-1.2583E+00
100.6700	-1.4139E+00	-1.3814E+00	107.4470	-1.4017E+00	-1.2546E+00
100.7969	-1.4138E+00	-1.3786E+00	107.6564	-1.4011E+00	-1.2511E+00
100.9337	-1.4137E+00	-1.3756E+00	107.8595	-1.4005E+00	-1.2477E+00
101.0801	-1.4136E+00	-1.3724E+00	108.0558	-1.3999E+00	-1.2445E+00
101.2359	-1.4135E+00	-1.3692E+00	108.2448	-1.3994E+00	-1.2413E+00
101.4006	-1.4133E+00	-1.3657E+00	108.4262	-1.3989E+00	-1.2383E+00
101.5738	-1.4131E+00	-1.3623E+00	108.5994	-1.3984E+00	-1.2355E+00
101.7552	-1.4129E+00	-1.3585E+00	108.7641	-1.3979E+00	-1.2328E+00
101.9442	-1.4127E+00	-1.3547E+00	108.9199	-1.3974E+00	-1.2303E+00
102.1405	-1.4125E+00	-1.3508E+00	109.0663	-1.3969E+00	-1.2280E+00
102.3436	-1.4122E+00	-1.3469E+00	109.2031	-1.3965E+00	-1.2258E+00
102.5530	-1.4120E+00	-1.3427E+00	109.3300	-1.3961E+00	-1.2237E+00
102.7682	-1.4117E+00	-1.3386E+00	109.4466	-1.3957E+00	-1.2219E+00
102.9886	-1.4113E+00	-1.3343E+00	109.5526	-1.3954E+00	-1.2202E+00
103.2139	-1.4110E+00	-1.3301E+00	109.6478	-1.3951E+00	-1.2187E+00
103.4434	-1.4106E+00	-1.3257E+00	109.7321	-1.3948E+00	-1.2173E+00
103.6766	-1.4102E+00	-1.3213E+00	109.8050	-1.3946E+00	-1.2162E+00
103.9129	-1.4098E+00	-1.3170E+00	109.8666	-1.3944E+00	-1.2152E+00
104.1518	-1.4094E+00	-1.3125E+00	109.9167	-1.3942E+00	-1.2145E+00
104.3927	-1.4089E+00	-1.3082E+00	109.9551	-1.3941E+00	-1.2138E+00
104.6350	-1.4084E+00	-1.3037E+00	109.9817	-1.3940E+00	-1.2134E+00
104.8782	-1.4079E+00	-1.2993E+00	109.9965	-1.3940E+00	-1.2132E+00

Table B.25: Results for c_1 and c_2

r_0	Kn	c_1	c_2
0.01	88.8	-0.0269	-14.7212
0.025	35.5	-0.0379	-14.3333
0.05	17.8	-0.0564	-13.6869
0.075	11.8	-0.0748	-13.0404
0.1	8.88	-0.0932	-12.3940
0.25	3.55	-0.2147	-12.1216
0.5	1.78	-0.3826	-5.5702
0.75	1.18	-0.5148	-3.4101
1.0	0.888	-0.6205	-2.3438
1.25	0.710	-0.7061	-1.7167
1.5	0.592	-0.7767	-1.3043
1.75	0.5074	-0.8356	-1.0166
2.0	0.444	-0.8854	-0.8038
2.5	0.355	-0.9649	-0.5150
3.0	0.296	-1.0253	-0.3295
4.0	0.222	-1.1115	-0.1039
5.0	0.178	-1.1706	0.0268
6.0	0.148	-1.2137	0.1113
7.0	0.1269	-1.2468	0.1707
8.0	0.111	-1.2734	0.2153
9.0	0.0987	-1.2949	0.2489
10.0	0.0888	-1.3129	0.2758
50.0	0.0178	-1.4655	0.4651
100	0.00888	-1.4857	0.4858

Appendix C: Monte Carlo Drag and Torque Results

I have developed a Monte Carlo algorithm to compute the drag and torque on an N-sphere aggregate in the free molecule regime. The algorithm is described in Section 5.2.3. Here, I compare the results of my Monte Carlo algorithm to exact results (where available) and to the drag results of Mackowski [36].

C.1 Drag on a Translating Sphere

The drag on a sphere in creeping flow in the free molecule regime $\boldsymbol{F}_0$ is given by Epstein's equation [32]. For purely diffuse reflection, my Monte Carlo algorithm gives the drag as $\boldsymbol{F}_{\mathrm{MC}} = 1.001\boldsymbol{F}_0$, and thus my MC results are in very good agreement with the exact solution.

C.2 Drag on an Aggregate

Mackowski [36] developed a correlation for the drag on a fractal aggregate as a function of the number of monomers N, the fractal dimension d_f, and the fractal prefactor k_0. The correlation is based on the results of his own Monte Carlo calculations. Using Mackowski's correlation [Eq. (68) of Ref. [36]], the translational friction coefficients, normalized by Epstein's equation, for 20- and 100-sphere aggre-

gates with $d_f = 1.78$ and $k_0 = 1.3$ are 14.15 and 64.23, respectively. In comparison, my Monte Carlo results for the 20- and 100-sphere aggregates with these fractal dimensions are 14.51 and 64.58, respectively. Thus, my MC results are in very good agreement with Mackowski's correlation.

C.3 Torque on a Rotating Sphere

Epstein [32] calculates the torque on a sphere rotating about an axis through its center. Using my Monte Carlo algorithm, I get $\boldsymbol{T}_{MC} = 0.995\boldsymbol{T}_0$, which is in very good agreement with the exact value.

For a sphere rotating slowly around an axis located a distance R from its center, the magnitude of the torque is given by

$$T = \zeta_{t,0}\omega R^2 + \zeta_{r,0}\omega \tag{C.1}$$

In other words, the torque is the sum of the torque on a sphere rotating about its center with angular velocity ω and the torque due to the linear velocity of the sphere center ωR moving at a distance R from the origin. My Monte Carlo results for the torque for $R = a$ and $R = 2a$ are $3.763\zeta_{r,0}\omega$ and $12.15\zeta_{r,0}\omega$, respectively, where a is the sphere radius. These results are in very good agreement with the exact results $T = 3.785\zeta_{r,0}\omega$ and $T = 12.14\zeta_{r,0}\omega$ for a sphere rotating around an axis $R = a$ and $R = 2a$ from its center.

Appendix D: Relationship between the Rotation and Coupling Interaction Tensors and the Flow around a Sphere

As mentioned in Section 5.2.2, the $(1-\delta_{ij})r_{ij}^{-3}$ and $(1-\delta_{ij})r_{ij}^{-2}$ terms in the rotation and coupling hydrodynamic interaction tensors are related to the flow around a sphere. We provide the derivation in this appendix. Note that this derivation is similar to the derivation of the lower order terms in the method of reflections [59, 60].

We will start with the rotation hydrodynamic tensor $\mathbf{Q}_{ij}^{r}$. Consider a sphere rotating in a quiescent fluid with angular velocity $\boldsymbol{\omega}_j$. This angular motion is sustained by applying a torque $\boldsymbol{T}_j = \zeta_{r,0}\boldsymbol{\omega}_j$ to the sphere. The velocity induced in the fluid at a location $\boldsymbol{r}_{ij}$ from the rotating sphere can be written in spherical coordinates as

$$\boldsymbol{v}(\boldsymbol{r}_{ij}) = \frac{\omega a^3}{r_{ij}^2}\sin\theta\hat{\mathbf{e}}_{\boldsymbol{\phi}} \tag{D.1}$$

where $\hat{\mathbf{e}}_{\boldsymbol{\phi}}$ is the unit vector in the ϕ-direction. The vorticity in the fluid is

$$\boldsymbol{w}(\boldsymbol{r}_{ij}) = \nabla \times \boldsymbol{v} = \frac{\omega a^3}{r_{ij}^3}(2\cos\theta\hat{\mathbf{e}}_{\mathbf{r}} + \sin\theta\hat{\mathbf{e}}_{\boldsymbol{\theta}}) \tag{D.2}$$

Converting to Cartesian coordinates and performing some simple manipulations, we

find that the vorticity can be written

$$\boldsymbol{w}(\boldsymbol{r}_{ij}) = \frac{a^3}{r_{ij}^3}\left(\frac{3\boldsymbol{r}_{ij}\boldsymbol{r}_{ij}}{r_{ij}^2} - \mathbf{I}\right)\cdot\boldsymbol{\omega}_j \tag{D.3}$$

A sphere placed in the fluid at $\boldsymbol{r}_{ij}$ would rotate with angular velocity $\boldsymbol{\omega}_i = \frac{1}{2}\boldsymbol{w}(\boldsymbol{r}_{ij})$ [49], which can be written

$$\boldsymbol{\omega}_i = \left[\frac{1}{2\zeta_{r,0}}\frac{a^3}{r_{ij}^3}\left(\frac{3\boldsymbol{r}_{ij}\boldsymbol{r}_{ij}}{r_{ij}^2} - \mathbf{I}\right)\right]\cdot\boldsymbol{T}_j \tag{D.4}$$

The term in square brackets is the $(1-\delta_{ij})$ term in the rotation hydrodynamic interaction tensor [Eq. (5.24)], proving that the rotational interaction between two spheres is related to the vorticity of the flow field around a rotating sphere.

We now turn our attention to the coupling tensor $\mathbf{Q}_{ij}^c$. Consider a sphere translating through a quiescent fluid with velocity $\boldsymbol{u}_j$ due to some external force $\boldsymbol{F}_j = \zeta_{t,0}\boldsymbol{u}_j$. The vorticity at point $\boldsymbol{r}_{ij}$ in spherical coordinates is

$$\boldsymbol{w}_j = -\frac{3}{2}\frac{a}{r_{ij}^2}u_j\sin\theta\hat{\mathbf{e}}_{\boldsymbol{\phi}} \tag{D.5}$$

We can write this more generally as

$$\boldsymbol{w}_j = -\frac{3}{2}\frac{a}{r_{ij}^3}\boldsymbol{u}_j\times\boldsymbol{r}_{ij} = \frac{3}{2}\frac{a}{r_{ij}^3}\boldsymbol{r}_{ij}\times\boldsymbol{u}_j \tag{D.6}$$

We can write the cross product $\boldsymbol{r}_{ij}\times\boldsymbol{u}_j$ as $\mathbf{A}_{ij}\cdot\boldsymbol{u}_j$, where $\mathbf{A}_{ij} = -\boldsymbol{\epsilon}\cdot\boldsymbol{r}_{ij}$, such that

the vorticity becomes

$$\boldsymbol{w}_j = -\left(\frac{3}{2}\frac{a}{r_{ij}^3}\boldsymbol{\epsilon}\cdot\boldsymbol{r}_{ij}\right)\cdot\boldsymbol{u}_j \tag{D.7}$$

Again, a sphere placed in the fluid at $\boldsymbol{r}_{ij}$ would rotate with angular velocity equal to half the vorticity,

$$\boldsymbol{\omega}_j = -\left(\frac{3}{4}\frac{a}{r_{ij}^3}\boldsymbol{\epsilon}\cdot\boldsymbol{r}_{ij}\right)\cdot\frac{\boldsymbol{F}_j}{6\pi\mu a} \tag{D.8}$$

Rearranging and introducing $\zeta_{r,0} = 8\pi\mu a^3$, we get

$$\boldsymbol{\omega}_j = \left(-\frac{\boldsymbol{\epsilon}\cdot\boldsymbol{r}_{ij}}{\zeta_{r,0}}\frac{a^3}{r_{ij}^3}\right)\cdot\boldsymbol{F}_j \tag{D.9}$$

The term in parentheses is the coupling interaction tensor $\mathbf{Q}_{ij}^c$ given by Eq. (5.25). This shows that the $\mathcal{O}(r_{ij}^{-2})$ term in the translation-rotation coupling interaction tensor is given by the vorticity in the flow field for a translating sphere.

Alternatively, we can derive the coupling tensor by considering the velocity field around a rotating sphere given by Eq. (D.1). Writing the velocity using the cross product $\boldsymbol{r}_{ij}\times\boldsymbol{\omega}_j$ and converting the cross product to $-(\boldsymbol{\epsilon}\cdot\boldsymbol{r}_{ij})\cdot\boldsymbol{\omega}_j$, the velocity becomes

$$\boldsymbol{v}(\boldsymbol{r}_{ij}) = \frac{a^3}{r_{ij}^3}(\boldsymbol{\epsilon}\cdot\boldsymbol{r}_{ij})\cdot\boldsymbol{\omega}_j \tag{D.10}$$

Writing this equation using the torque applied on sphere j to maintain the angular velocity $\boldsymbol{\omega}_j$, we see that the fluid velocity at $\boldsymbol{r}_{ij}$ is

$$\boldsymbol{v}(\boldsymbol{r}_{ij}) = \left(\frac{\boldsymbol{\epsilon}\cdot\boldsymbol{r}_{ij}}{\zeta_{r,0}}\frac{a^3}{r_{ij}^3}\right)\cdot\boldsymbol{T}_j \tag{D.11}$$

The term in parentheses is the transpose of $\mathbf{Q}_{ij}^{c}$ as written in Eq. (5.25), which shows that the $\mathcal{O}(r_{ij}^{-2})$ term in $(\mathbf{Q}_{ij}^{c})^{\dagger}$ is given by the velocity field around a rotating sphere.

Appendix E: Supplemental Material for Chapter 7

In this appendix, I provide a diagram of the body-fixed and space-fixed coordinate systems used for my aggregate alignment calculations (Chapter 7), I show probability distributions for one particle at different field strengths, I provide an example calculation for one aggregate, and I expand upon my discussion of the effects of Knudsen number and the number of primary spheres on fully-aligned particle electrical mobility.

E.1 Euler Angles

The Euler angles (ϕ, θ, ψ) relate the body-fixed coordinates (x', y', z') to the space-fixed coordinates (x, y, z), as shown in Figure E.1. For our calculations, the electric field is in the z-direction, and the principal axis of the polarizability tensor is in the z'-direction. When the particle is aligned with the electric field, the z- and z'-axes coincide.

E.2 Probability Distributions

Eq. (eqn:align:potential) gives the potential of a conducting particle in an electric field as a function of the polarizability tensor of the particle, the field strength,

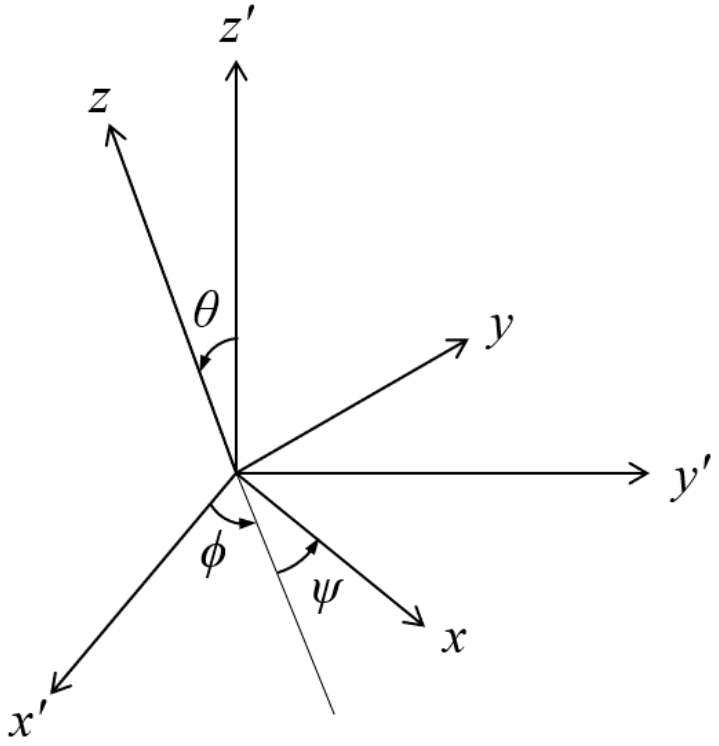

Figure E.1: Representation of the Euler angles (ϕ, θ, ψ) that relate the body-fixed coordinates (x', y', z') to the space-fixed coordinates (x, y, z).

and the orientation of the particle relative to the field. When the electric field is in the z-direction in space-fixed coordinates, the potential is a function of only two of the three Euler angles shown in Figure E.1. In Figure E.2 below, I show the probability distribution for a particle with 652 primary spheres with radius 5 nm at three electric field strengths. The probability distribution is defined by Eq. (7.1). At $E = 1000$ V/cm, the particle orientation is nearly random, while at $E = 8000$ V/cm, the particle is aligned with the field. Note that the aligned particle can still rotate around the principal axis of the polarizability tensor. Mobility results for this particle are shown in Figure 7.1.

E.3 Sample Calculation

The theory described in Chapter 7 requires one to determine the translational friction tensor and the polarizability tensor for an aggregate in order to determine the mobility of the particle at a given field strength. Here, I provide an example problem for an aggregate with 10 primary spheres each having a radius $a = 37.9$ nm (Kn $= 1.78$ for $\lambda = 67.3$ nm). The aggregate has a fractal dimension of 1.78 and a prefactor of 1.3. The coordinates for the center of each sphere in the aggregate are given in Table E.1. Coordinates are given relative to the center of mass of the aggregate for an arbitrary Cartesian system. Velocity results for this Knudsen number are available in Appendix B.

Using EKR theory (Chapters 4 and 6), one can determine the translational, rotational, and coupling friction tensors in terms of the Cartesian coordinate system

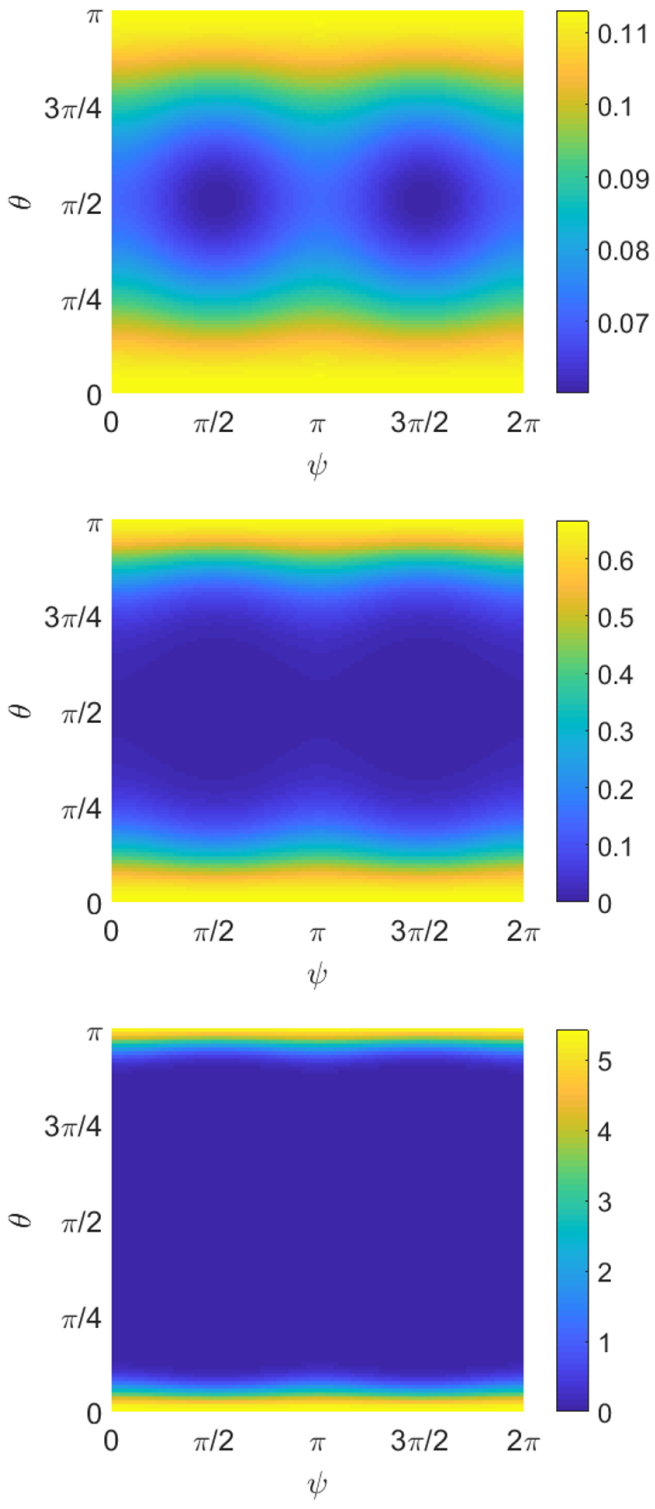

Figure E.2: Probability distributions for particles with 652 primary spheres with 5 nm radii. Probability distributions are given for 3 field strengths: 1000 V/cm (top), 3000 V/cm(middle), and 8000 V/cm (bottom). Note the different scales in the figure: the bottom figure has a much broader scale than the top figure.

Table E.1: Coordinates of the center of each sphere in my sample aggregate. Coordinates have been non-dimensionalized by the primary sphere radius. Since the center of mass is at (0,0,0), simply multiply by the sphere radius to get the coordinates in dimensional form.

Sphere	x	y	z
1	-0.1717	-0.2663	-2.2887
2	2.0578	-0.0414	-0.2788
3	0.0587	-0.0934	-0.3096
4	0.3888	1.4840	-3.0774
5	-3.0183	-0.9897	2.3343
6	-1.7995	-1.6475	0.8915
7	-1.0953	-1.5832	-0.9794
8	-2.9090	0.6522	1.1976
9	3.1193	1.1203	2.2399
10	3.3692	1.3651	0.2707

in which the particle coordinates are given:

$$\boldsymbol{\Xi}_t = \begin{bmatrix} 4.490 & -0.2919 & 0.1575 \\ -0.2919 & 4.710 & 0.1075 \\ 0.1575 & 0.1075 & 4.304 \end{bmatrix} \zeta_{t,0}^{\mathrm{FM}} \tag{E.1}$$

$$\boldsymbol{\Xi}_{O,r} = \begin{bmatrix} 29.66 & -7.276 & 1.057 \\ -7.276 & 51.56 & 1.238 \\ 1.057 & 1.238 & 42.77 \end{bmatrix} a^2 \zeta_{t,0}^{\mathrm{FM}} \tag{E.2}$$

$$\boldsymbol{\Xi}_{O,c} = \begin{bmatrix} -0.6409 & -0.3110 & 0.5337 \\ 0.9522 & 0.5417 & 0.2755 \\ -0.7883 & 0.6892 & 0.0884 \end{bmatrix} a \zeta_{t,0}^{\mathrm{FM}} \tag{E.3}$$

Here, $\zeta_{t,0}^{\mathrm{FM}}$ is the free molecule friction coefficient based on the primary sphere radius.

For consistency with my velocity results, one should assume full thermal accommodation when calculating the friction coefficient. The rotational and coupling tensors are written with respect to the center of mass of the particle.

I obtain the polarizability tensor from ZENO [62]:

$$\boldsymbol{\alpha} = \begin{bmatrix} 513.0 & 114.1 & -39.24 \\ 114.1 & 226.7 & -31.19 \\ -39.24 & -31.19 & 394.1 \end{bmatrix} \epsilon_0 a^3 \tag{E.4}$$

Here, ϵ_0 is the permittivity of free space. Note that ZENO uses stochastic methods to obtain the polarizability tensor, so the code results can change slightly depending on the number of trials used in the calculation and on the initial seed to the random number generator. Also note that the polarizability, translational friction, and rotational friction tensors are symmetric, as expected.

For my calculations of the mobility as a function of electric field strength, I choose the body-fixed coordinate system based on the eigenvectors of the polarizability tensor: the z'-axis is the eigenvector associated with the largest eigenvalue of the tensor, while the x'-axis coincides with the eigenvector of the smallest eigenvalue of the tensor. In this coordinate system, the polarizability and translational friction tensors become

$$\boldsymbol{\alpha}' = \boldsymbol{V}^\dagger \cdot \boldsymbol{\alpha} \cdot \boldsymbol{V} = \begin{bmatrix} 185.4 & 0 & 0 \\ 0 & 382.3 & 0 \\ 0 & 0 & 566.0 \end{bmatrix} \epsilon_0 a^3 \tag{E.5}$$

$$\boldsymbol{\Xi}'_t = \boldsymbol{V}^\dagger \cdot \boldsymbol{\Xi}_t \cdot \boldsymbol{V} = \begin{bmatrix} 4.869 & 0.0349 & -0.1459 \\ 0.0349 & 4.404 & -0.1777 \\ -0.1459 & -0.1777 & 4.232 \end{bmatrix} \zeta_{t,0}^{\mathrm{FM}} \tag{E.6}$$

where

$$\boldsymbol{V} = \begin{bmatrix} 0.3193 & 0.2783 & -0.9059 \\ -0.9442 & 0.0116 & -0.3293 \\ -0.0811 & 0.9604 & 0.2664 \end{bmatrix} \tag{E.7}$$

is the tensor whose columns are the eigenvectors of $\boldsymbol{\alpha}$ and $\boldsymbol{V}^\dagger$ is the transpose of that tensor. I take the inverse of the translational friction tensor to obtain the mobility tensor in body-fixed coordinates:

$$\boldsymbol{M} = \boldsymbol{\Xi}'_t = \begin{bmatrix} 0.2056 & -0.0013 & 0.0070 \\ -0.0013 & 0.2275 & 0.0095 \\ 0.0070 & 0.0095 & 0.2369 \end{bmatrix} \left(\zeta_{t,0}^{\mathrm{FM}}\right)^{-1} \tag{E.8}$$

Note that the mobility tensor in the body-fixed coordinate system is nearly, but not quite, diagonal. For non-skew particles like spheres or prolate spheroids, the eigenvectors for the polarizability a nd translational friction/mobility tensors would be the same, and thus the mobility tensor would be diagonal in the body-fixed system corresponding to the eigenvectors of the polarizability tensor.

From Eqs. (7.6) and (7.7) and the polarizability tensor above, the potential of

this particle in an electric field due to the induced dipole effects is

$$U = -\tfrac{1}{2}(185.4\sin^2\psi\sin^2\theta + 382.3\cos^2\psi\sin^2\theta + 566.0\cos^2\theta)\epsilon_0 a^3 E^2 \tag{E.9}$$

where the angles are defined in Figure E.1. From Eqs. (7.8) and (7.9) and the mobility tensor above, the mobility of the particle as a function of field strength is

$$\begin{aligned} Z = \frac{\langle V_{d,z}\rangle}{E} = \frac{q}{\zeta_{t,0}^{\mathrm{FM}}}\Big(&0.2369\langle\cos^2\theta\rangle + 0.2275\langle\cos^2\psi\sin^2\theta\rangle + 0.2056\langle\sin^2\psi\sin^2\theta\rangle \\ &- 0.0013\langle\sin 2\psi\sin^2\theta\rangle + 0.0070\langle\sin\psi\sin 2\theta\rangle + 0.0095\rangle\cos\psi\sin 2\theta\rangle\Big) \end{aligned} \tag{E.10}$$

At very low field strengths, we get the mobility of the randomly oriented particle, $Z_{rand} = 0.2233q/\zeta_{t,0}^{\mathrm{FM}}$. At very high field strengths, we get the mobility of the aligned particle, $Z_{rand} = 0.2369q/\zeta_{t,0}^{\mathrm{FM}} = 1.061Z_{rand}$. At a field strength of 5000 V/cm, we get $Z_{rand} = 0.2317q/\zeta_{t,0}^{\mathrm{FM}} = 1.038Z_{rand}$.

Note that we can also use my analytic expression for the translational friction coefficient [Eq. (4.38) of Chapter 4] to obtain Z_{rand}. From this expression, we get $Z_{rand}^{\star} = 0.2289q/\zeta_{t,0}^{\mathrm{FM}} = 1.025Z_{rand}$, where Z_{rand} is the mobility we get from the EKR method. This shows that my analytic expression gives a good estimate of the friction coefficient or mobility of a randomly oriented DLCA particle, without having to deal with the complexities of the EKR method. Note that my analytic expression does not account for different morphologies (i.e. different sphere coordinates) for the same primary sphere diameter, same N, and same fractal dimension.

E.4 Effects of Knudsen Number and the Number of Primary Spheres on Fully-Aligned Particle Mobility

To evaluate the impact of particle size and flow regime on the aligned mobility of soot-like particles, I calculated the random (electric field strength $E \to 0$) and fully-aligned ($E \to \infty$) mobilities for a wide range of N and Kn. I also calculated the random and fully-aligned mobilities using the standard Kirkwood-Riseman approach with the Rotne-Prager-Yamakawa hydrodynamic interaction tensor [see, for example, [30]] and using a Monte Carlo code (Chapter 5 and Appendix C) for the continuum ($\mathrm{Kn} = 0$) and free molecular ($\mathrm{Kn} = \infty$) limits, respectively.

Figure 7.5 in the main body of this Disseration (repeated here as Figure E.3) shows the calculated ratio of aligned to random mobility. The choppiness of the graphs is due to the finite sample size of the aggregates I am using for these calculations. The standard deviation of the mean of each data set (i.e. the mobility ratio of 20 cases at a given Kn and N) is on the order of 0.007, which is significant compared to the scale of the graph and the fluctuations in the mobility ratio with N for a given Knudsen number. Accounting for these fluctuations due to the finite sample size, we notice a few clear trends: while the mobility ratio is approximately constant with N in the continuum regime, there is a clear decrease in mobility ratio with increasing N near the free molecule regime. At intermediate Knudsen numbers, the particles exhibit more continuum-like behavior with increasing N, which is consistent with my earlier results for the translational friction coefficient (Chapter 4).

I will consider the physical reasons for these trends in the following paragraphs.

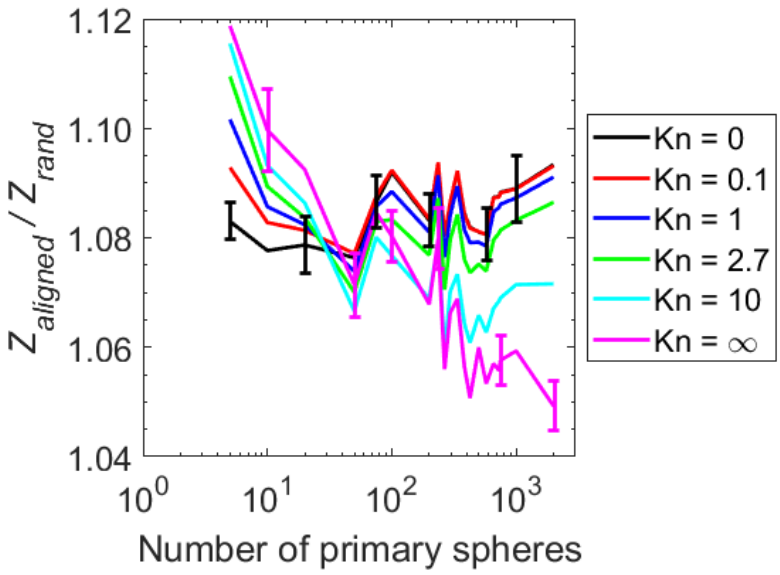

Figure E.3: Ratio of fully-aligned to random electric mobilities for wide range of primary sphere Knudsen numbers and the number of primaries. The Kn = 0 and Kn = ∞ curves represent the continuum and free molecular limits, as calculated using the standard KR theory with the RPY tensor [see e.g. Chen et al. [30]] and using a Monte Carlo code (Chapter 6), respectively. Uncertainties of one standard deviation of the mean (based on 20 samples with the same fractal dimension but different morphologies) are shown for the continuum and free molecule results for several N.

The continuum-like behavior of particles with many primary spheres at intermediate Knudsen numbers has a straightforward explanation: as the particle size increases, it has a larger effect on the velocity field of the surrounding fluid. In other words, the particle behaves less like a collection of spheres in the transition regime and more like an object that is large compared to the mean free path of molecules in the fluid.

The behavior in the continuum and free molecular limits is more difficult to explain. I will start by focusing on the continuum regime.

The continuum (randomly-oriented) friction coefficient can be written

$$\zeta = 6\pi\mu R_H \tag{E.11}$$

where the hydrodynamic radius R_H is the radius of a sphere that experiences the same drag as the particle. Studies have shown that the hydrodynamic radius is approximately equal to the radius of gyration for soot-like particles [4, 54, 93]. This relationship between the hydrodynamic radius and the radius of gyration is only valid for a randomly-oriented particle. Nevertheless, let us suppose that the drag force on a particle in a fixed orientation moving in the z-direction is related to the particles radius of gyration about the z-axis, which is defined as

$$R_{gz} = \sqrt{\frac{\sum_i^N (x_i^2 + y_i^2)}{N}} \tag{E.12}$$

for an aggregate of N spheres. Here, the center of the ith sphere is located at (x_i, y_i, z_i), while the center of mass of the particle is at the origin. Clearly, the drag is not directly proportional to R_{gz}. As an example, the drag on a chain of spheres or a rod moving parallel to its long axis increases with chain or rod length, even though R_{gz} is independent of the chain or rod length. However, the drag on a rod does increase as its radius increases (with length held constant), so a larger R_{gz} corresponds to increased drag. I will look at the ratio of the radius of gyration to the radius of gyration about the principal axis of the polarizability tensor (i.e. the axis parallel to the particle velocity when the particle is fully-aligned with

the electric field) to evaluate whether trends in R_g/R_{gz} are correlated to trends in the continuum mobility ratio Z_{align}/Z_{rand}.[1] If this is the case, we can use trends in R_g/R_{gz} to qualitatively predict the effects of alignment on mobility.

To evaluate whether R_g/R_{gz} and Z_{align}/Z_{rand} are correlated, I calculated these ratios for all 20 cases for each N and plotted the results in Figure E.4. I have included results for $N = 5$, 10, 50, 100, 500, and 1000; results for other N are similar. In general, aggregates with a low radius of gyration ratio also have a low mobility ratio. Thus, we can conclude that there is a correlation between these two ratios.

As further verification of the correlation between R_g/R_{gz} and Z_{align}/Z_{rand}, I have computed the average ratios for a given N, then plotted the results in Figure E.5. Once again, we see that the ratios appear to be correlated.

Given that the radius of gyration ratio and the mobility ratio appear to be correlated, we can look at the trends in R_g/R_{gz} to help explain the behavior of the continuum curve in Figure E.3. Notably, there is less spread in the mean values of R_g/R_{gz} versus N than there is in Z_{align}/Z_{rand} for a given N, as evidenced by the scale of the y-axis in Figure E.4 compared to the scale in Figure E.5. For example, the ratio of the maximum to the minimum values of the mean R_g/R_{gz} vs. N is 1.14, while for a typical set of 20 particles for a given N the ratio of maximum to minimum values of R_g/R_{gz} is 1.65. Likewise, the continuum mobility ratio varies from 1.076 (at $N = 50$) to 1.094 (at $N = 236$ and $N = 2000$), while the minimum and maximum mobility ratios for $N = 100$ (which represents an average case in terms of the spread

[1] Since the friction coefficient is approximately proportional to the radius of gyration, the mobility is inversely proportional to R_g.

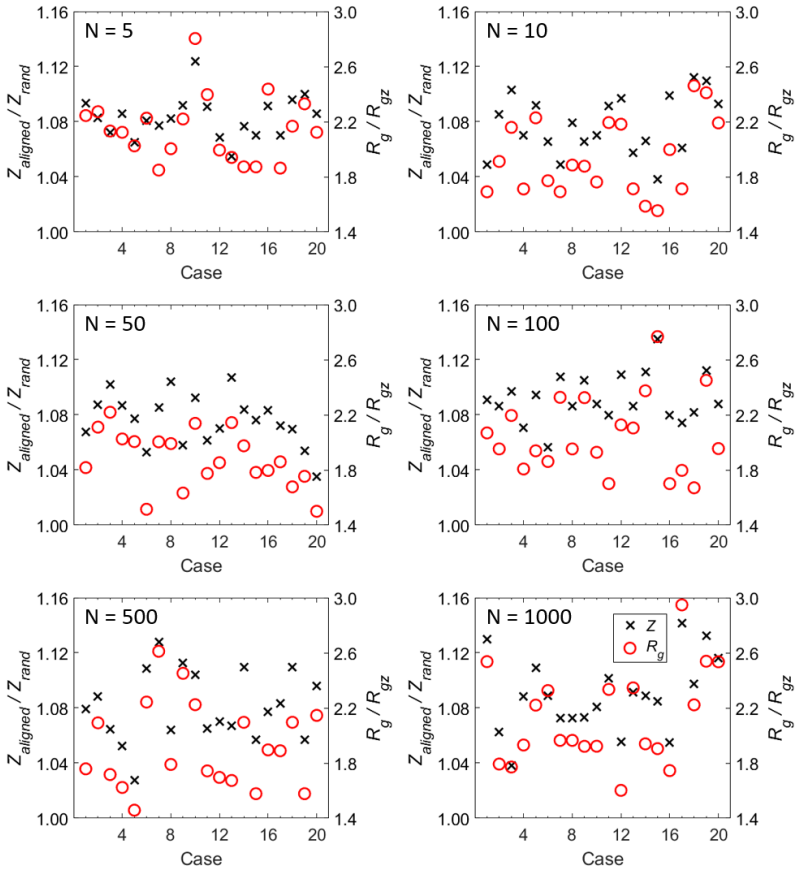

Figure E.4: Comparison of the continuum mobility and radius of gyration ratios for all 20 cases for $N = 5$, 10, 50, 100, 500, and 1000. The xs represent the mobility ratio; the circles represent the radius of gyration ratio.

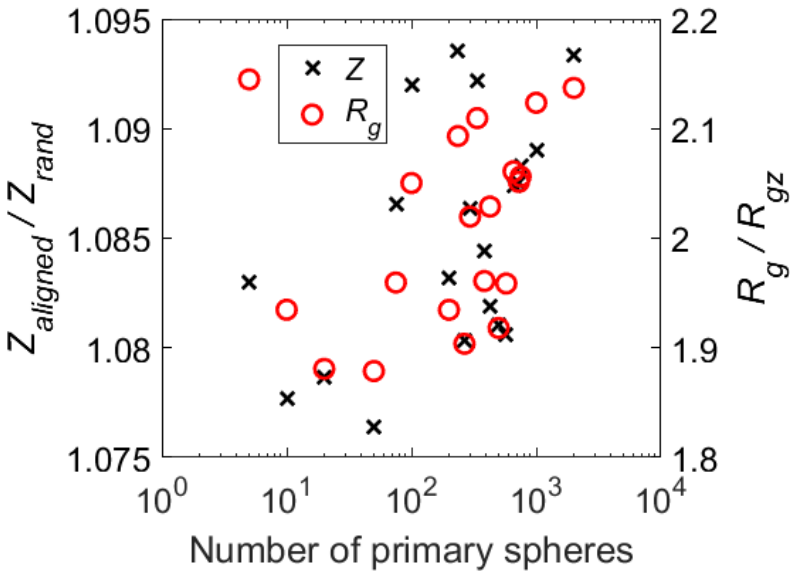

Figure E.5: Comparison between the average continuum mobility ratio and the average radius of gyration ratio as a function of N. In general, a low mobility ratio is correlated with a low radius of gyration ratio; the notable exception is for $N = 5$, which has a large radius of gyration ratio but a modest mobility ratio.

in mobility ratio) range from 1.05 to 1.13. Thus, the mobility ratio in the continuum appears to be more heavily dependent on the specific configuration of spheres in the aggregate than on the number of spheres for a given fractal dimension and prefactor.

Now I will consider the free molecular case. The friction coefficient in the free molecular regime is roughly proportional to the orientation-averaged projected area [41]. As I did for the continuum case, I will suppose that the projected area of the particle in the plane normal to particle velocity when it is fully aligned is correlated to the free molecular drag force for that particle orientation. (Again, I use the example of a rod or chain of spheres to caution that the drag for any particle orientation is not directly proportional to the projected area in the plane perpendicular to the particle velocity.) I have calculated the orientation-averaged projected area using a Monte Carlo approach, while I have calculated PA_z using a

graphical approach (by plotting particle as a collection of spheres and counting the number of black pixels in the projection of the particle on the xy-plane).

To evaluate whether $\mathrm{PA}/\mathrm{PA}_z$ and Z_{align}/Z_{rand} are correlated, I have plotted these ratios to look at how they compare for the aggregates in this study. Figure E.6 compares these ratios for the 20 cases for each of $N = 5$, 10, 50, 100, 500, and 1000. In general, cases with a low mobility ratio also have a low projected area ratio. Figure E.7 shows an even better correlation between the mean values of the projected area and mobility ratios for each N.

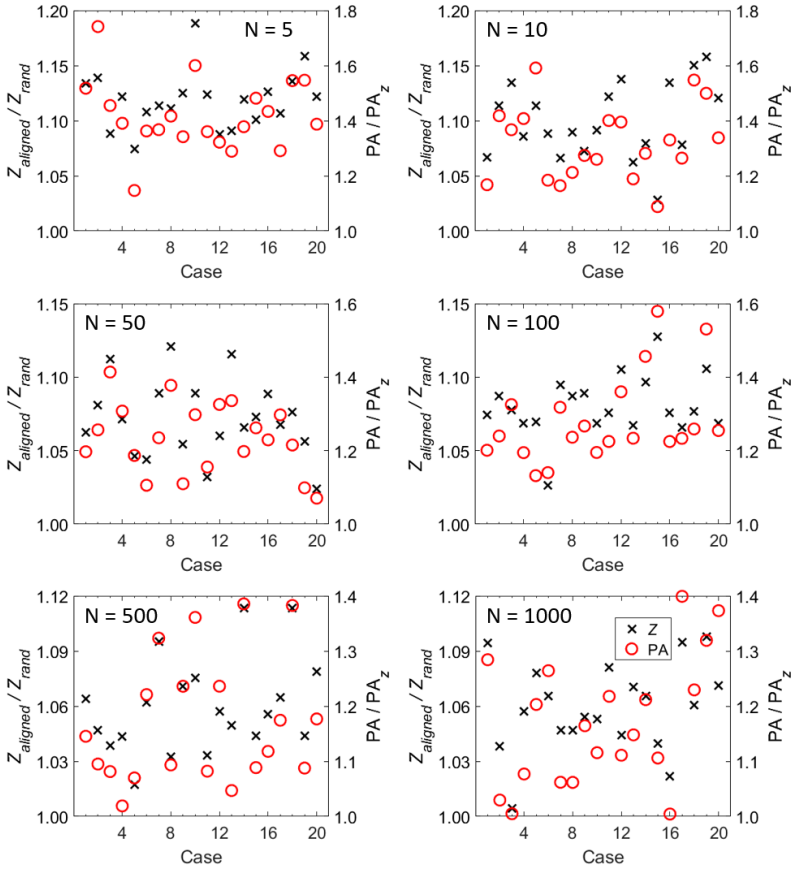

Figure E.6: Comparison of the free molecule mobility and projected area ratios for all 20 cases for $N = 5$, 10, 50, 100, 500, and 1000. The xs represent the mobility ratio; the circles represent the projected area ratio.

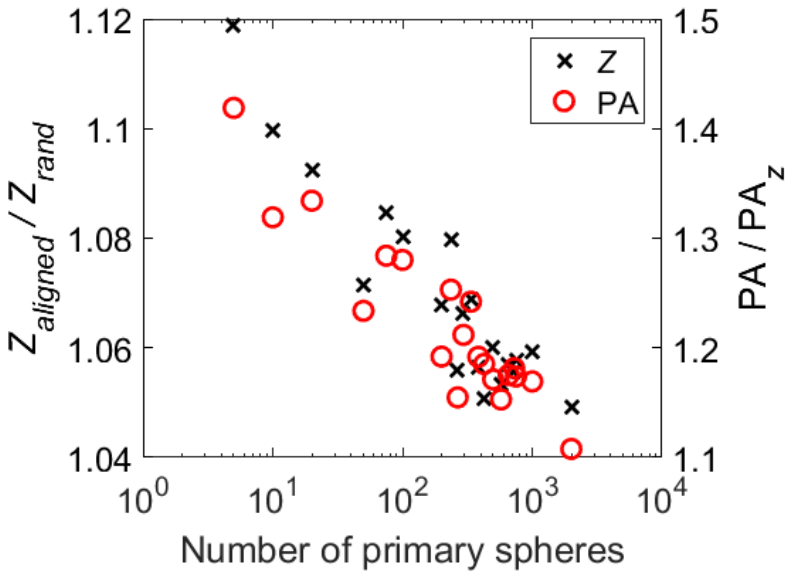

Figure E.7: Comparison between the average free molecule mobility ratio and the average projected area ratio as a function of N. In general, a low mobility ratio is correlated with a low projected area ratio. Both ratios decrease with increasing N.

Since $\mathrm{PA}/\mathrm{PA}_z$ and Z_{align}/Z_{rand} appear to be correlated, we can use trends in the projected area ratio to help explain the alignment behavior in Figure E.3. As the number of primary spheres in the aggregate increases, the projected area on the plane perpendicular to the principal axis of the polarizability tensor decreases relative to the orientation-averaged projected area. In fact, the projected area varies little with orientation at large N. This behavior contrasts with the continuum behavior, where the average radius of gyration ratio is fairly constant with N.

My results demonstrate that the projected area and radius of gyration ratios are correlated with the mobility ratio in the free molecular and continuum regimes, respectively, and thus we can predict the trends in the mobility ratio based on the trends of these surrogate measures. But why is this true?

In the continuum regime, the moving particle has a significant effect on the

velocity of the surrounding fluid. One way to think of this is as follows. The fluid upstream of the particle must move out of the way to avoid the particle; the extent of how far the fluid must move is related to the radius of gyration about the axis parallel to the flow. A larger R_{gz} means the fluid must move further to get out of the way of the particle, which explains the increase in drag (decrease in mobility).

In the free molecular regime, the particle has very little effect on the fluid velocity. In fact, the particle has no effect on the velocity distribution of molecules striking its surface (except for molecules that strike the particle more than once between collisions with other fluid molecules), so we can use a ballistic approach for calculating the drag [36, 54, 117, 118]. Thus, the projected area is related to the free molecular drag: as projected area increases, gas molecules are more likely to strike and transfer their momentum to the particle, thus increasing the drag.

In summary, the ratio of particle mobility in the limit of infinite field strength to mobility in the limit of zero field strength decreases as the number of primary spheres increases in the free molecular regime, while the ratio remains constant in the continuum regime. The trends in the free molecular and continuum regimes can be explained by trends in the projected area ratio and the radius of gyration ratio, respectively. In the continuum regime, the ratio of particle radius of gyration to the radius of gyration about the principal axis of the polarizability tensor (i.e. the axis parallel to the particle velocity when the particle is fully aligned) varies little with N. In the free molecular regime, the ratio of the orientation-averaged projected area to the projected area in the plane perpendicular to the principal axis of the polarizability tensor decreases with increasing N. Note that these trends are for

the average behavior at each N; there are variations in the radius of gyration and projected area ratios for aggregates with the same N, which in turn affect the fully-aligned mobility behavior of the particles. The variations in mobility among aggregates with the same N are large in the continuum regime compared to the variations in the average mobility as a function of N. Finally, at intermediate Knudsen numbers, particles exhibit more continuum-like behavior as the number of primary spheres increases. This is because the aggregate behaves more like a particle with characteristic dimension much larger than the mean free path than a collection of spheres with radii smaller than the mean free path.

Appendix F: NGDE User Manual

This appendix serves as the User Manual for the Nodal General Dynamic Equation (NGDE) solver described in Chapter 9. This manual refers to the MATLAB version of the code; for the C version, see Prakash et al. [27]. Throughout this documentation, text in `this font` represents a variable or expression in the code or a MATLAB command.

The manual is divided into three sections: (1) instructions for running the NGDE code and the post-processing tool; (2) detailed descriptions of input to NGDE (`ngde.m`) and NGDEplot (`ngde_plot.m`) and output from the codes; and (3) discussion about the NGDE code structure. (The code for NGDEplot mostly consists of MATLAB commands for plotting data, so discussion of NGDEplot is limited to its input and output.) For information about the theoretical basis of NGDE and the methods used to solve the general dynamic equation, refer to Chapter 9.

F.1 Running NGDE and NGDEplot

NGDE is distributed as a .zip archive containing the following files:

- `ngde.m`: the NGDE source code
- `ngde_plot.m`: the NGDEplot source code

- `rtpmie_bohren_mie.m`: Mie scattering code used by NGDEplot. The Mie scattering code is based on the Fortran source code in Appendix A of Bohren and Huffman [89]; `rtpmie_bohren_mie.m` has been converted from the Fortran source code provided by Professors Eugene Clothiaux and Craig Bohren from the Pennsylvania State University.

- `ngde_sample_problem.mat`: MATLAB data file containing two MATLAB structure arrays, `ngdein` and `plotoptions`, that provide input to NGDE and NGDEplot, respectively

To run NGDE, perform the following steps:

1. In MATLAB, navigate to the folder containing the files listed above. To do so, click on the "Browse for folder" icon (circled in red in the screenshot below) and open the folder containing the NGDE files. All of the files in the current folder appear in the "Current Folder" panel.

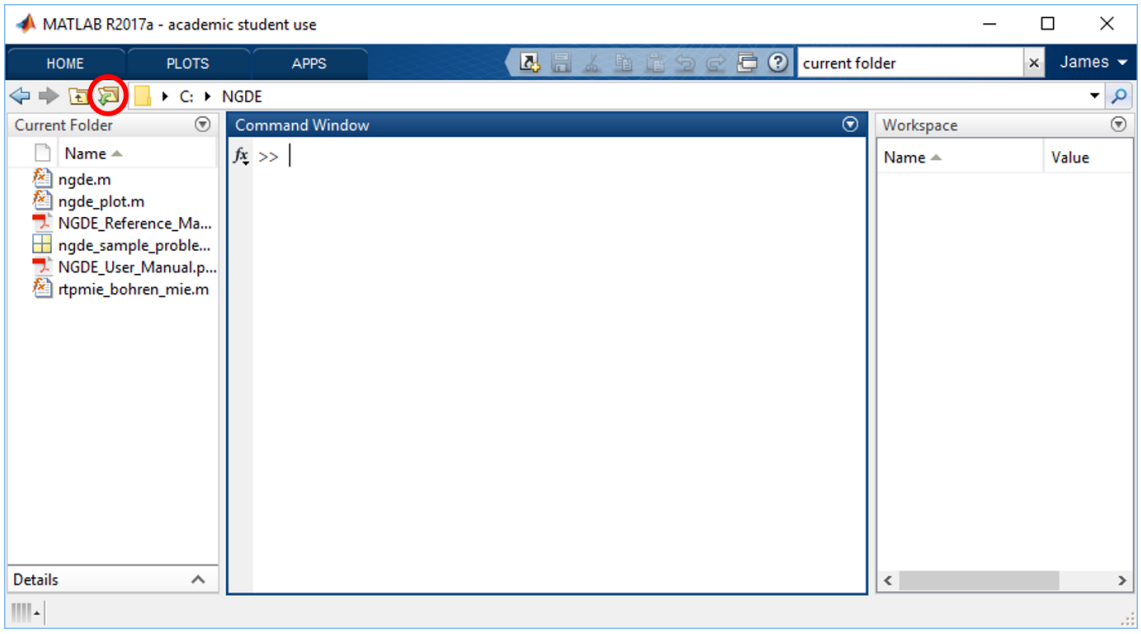

2. Load the NGDE and NGDEplot input structures (`ngdein` and `plotoptions`). This can be done by double-clicking on the `ngde_sample_problem.mat` data file distributed with NGDE, or by double-clicking on any other MATLAB data file that contains NGDE input. After double-clicking on the data file, you should see the `load(...)` statement and the NGDE input structures appear in the Command Window panel and in the Workspace panel, respectively. (See the screenshot below.)

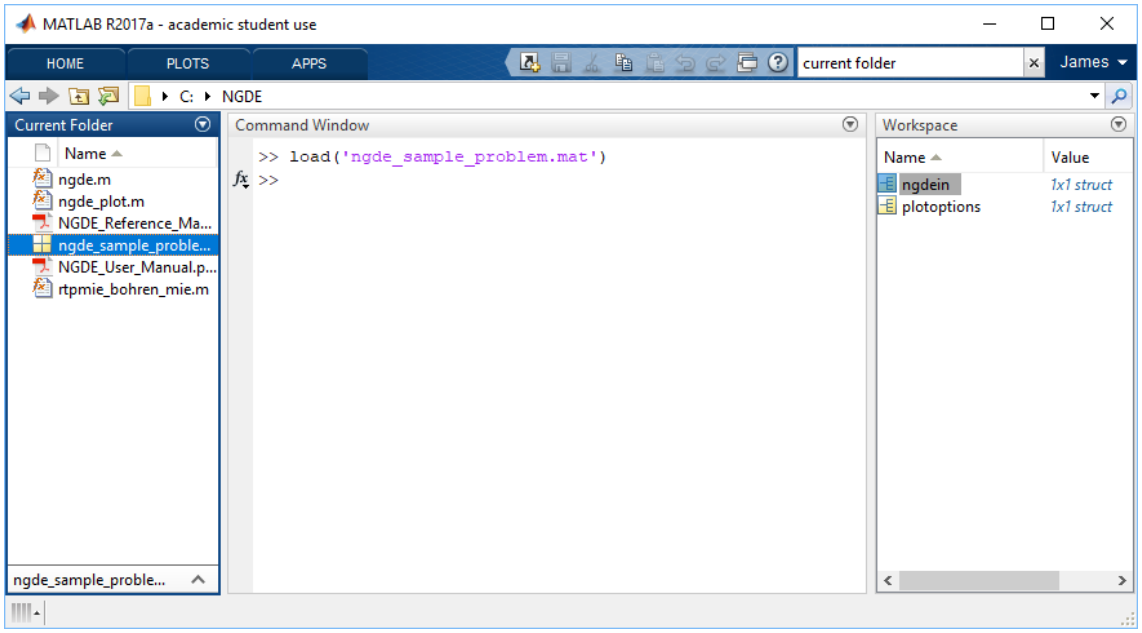

3. If desired, modify the NGDE input. To do so, double-click on the NGDE structure array (named `ngdein` in the code distribution) in the Workspace panel. This will bring up the structure array in the Variables panel. To change any of the input parameters, select the appropriate value (e.g. the value of 300 next to the `Tf` field) and type in the desired value (e.g. type in 400 to end the NGDE simulation when the temperature equals 400 K instead of 300 K).

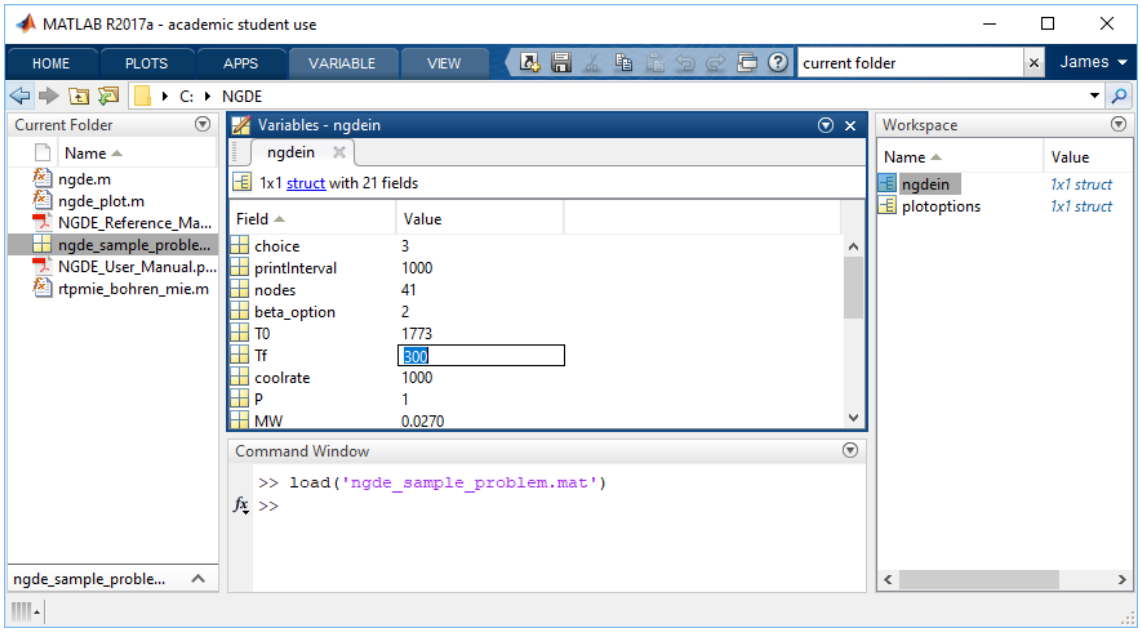

4. Once all of the desired changes have been made to the input structure array, run NGDE by entering the following in the Command Window:

```
[results1,results2]=ngde(ngdein);
```

Here, `results1` and `results2` are the names of the variables where the user will store the size distribution and detailed results from NGDE, respectively, and `ngdein` is the NGDE input structure array. Of course, you can choose any name for these input and output files; these are simply the default names. After hitting enter, the code will begin running, as shown below.

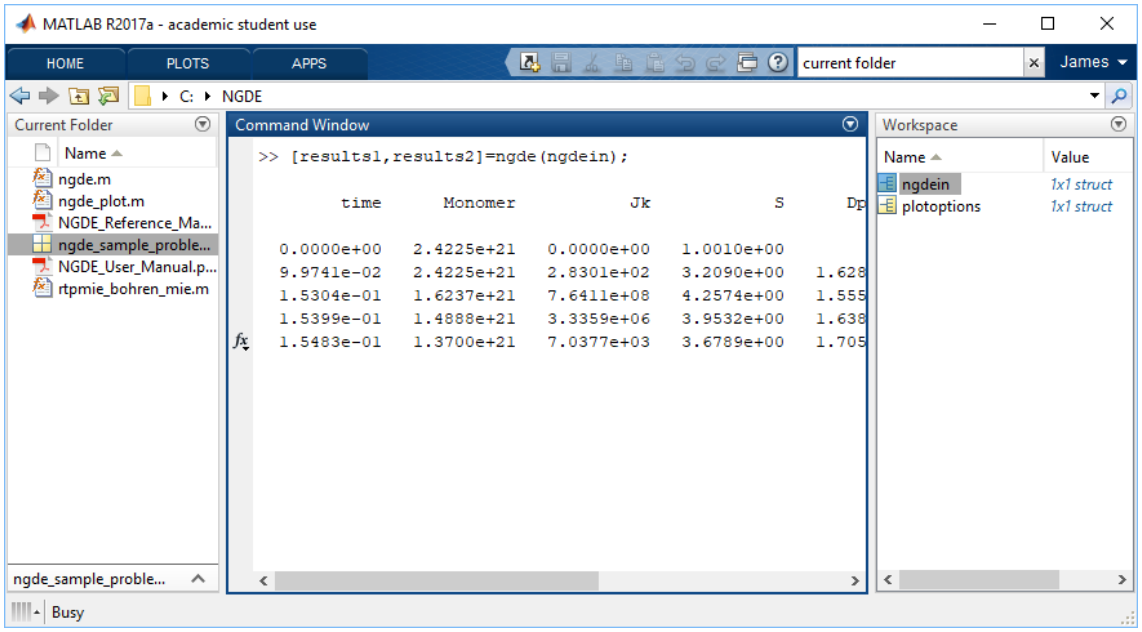

5. If desired, run the NGDEplot post-processing tool entering the following statement in the Command Window:

```
[F1,F2]=ngde_plot(results2,ngdein,plotoptions,saveframes);
```

Here, `F1` and `F2` are the names of the variables where the frames of the size distribution and Mie scattering movies will be stored, respectively; `results2` is the array containing the detailed output results from NGDE; `ngdein` is the NGDE input structure array corresponding to the output array `results2`; `plotoptions` is the NGDEplot input structure array; and `saveframes` is a logical variable, where a non-zero value tells the code to save the frames of the size distribution and Mie scattering movies. Note that you can show a still of a single point in time by specifying `results2(t,:)`, where `t` is the row index of `results2` corresponding to the desired time point. Likewise, you can generate movies of a select portion of the NGDE calculation by passing

the appropriate rows from `results2` to NGDEplot. You may also change the NGDEplot input by double-clicking on the NGDEplot input structure array (`plotoptions` by default) in the Workspace panel and changing the values of the structure array fields.

F.2 Description of Input and Output

F.2.1 NGDE Input (`ngdein`)

The following parameters are included in the NGDE input structure array, `ngdein`. The default values are for the "Full GDE" sample problem described in Chapter 9.

Parameter	**Description**
`choice`	Calculation type. 1 = coagulation only, 2 = nucleation + coagulation, 3 = full GDE, 4 = surface growth only. DEFAULT = 3
`printInterval`	Number of timesteps between plot edits. Too small a value will result in a very large output from the code, which may use up excessive computer memory. DEFAULT = 1000
`nodes`	Number of size nodes to use in the calculation. Note that the code actually creates `nodes+1` volume nodes, but the number concentration in the final node is always zero. This is done to prevent errors in the code. DEFAULT = 41

`beta_option`	Collision frequency function. 1 = free molecule regime, 2 = Fuch's form for FM and transition regime. DEFAULT = 2
`T0`	Initial temperature (K). DEFAULT = 1773
`Tf`	Final temperature (K). Not used if `choice` = 1. DEFAULT = 300
`coolrate`	Cooldown rate for the calculation (K/s). Not used if `choice` = 1. DEFAULT = 1000
`P`	Pressure (atm). DEFAULT = 1
`MW`	Molecular weight of the condensed species (kg/mol). DEFAULT = 0.027
`rho`	Density of the condensed species (kg/m3). DEFAULT = 2700
`A`, `B`	Constants for determining surface tension as a function of temperature, given by `sigma=(A-B*T)*1e-3`, where `sigma` has units of N/m. DEFAULT = 948, 0.202 (for aluminum)
`C`, `D`	Constants for determining saturation vapor pressure as a function of temperature and pressure, given by `Ps=exp(C-D./T).*101325`, where `Ps` has units of Pa. DEFAULT = 13.07, 36373 (for aluminum)
`d`	Initial particle diameter (nm). Only used if `choice` = 1. DEFAULT = 1
`N0`	Initial particle number concentration (#/m^3). Only used if `choice` = 1 or 4. DEFAULT = 1e10

`i0`	Node in which particles are initially placed. Only used if `choice` = 4. DEFAULT = 25
`MWgas`	Molecular weight of the carrier gas (kg/mol). DEFAULT = 0.04 (for argon)
`A_mu`, `B_mu`	Sutherland's constants for viscosity as a function of temperature, given by `mu=A_mu*T^1.5/(B_mu+T)`, where `mu` has units of kg/m-s. DEFAULT = 1.9660e-6, 147.47 (for argon)
`dtUser`	Maximum allowable time step for the calculation. DEFAULT = 1e-4

F.2.2 NGDEplot Input (`plotoptions`)

The following parameters are included in the NGDEplot input structure array, `plotoptions`.

Parameter	**Description**
`npar`	Refractive index of the particles. DEFAULT = 1 + 6.4i (for aluminum in the visible spectrum)
`nmed`	Refractive index of the medium. DEFAULT = 1 (for argon)
`showNmovie`	If non-zero, NGDEplot will show a movie of how the size distribution changes over time. DEFAULT = 1
`showMie`	If non-zero, NGDEplot will show a movie of how the light scattering, extinction, and absorption coefficients change over time. DEFAULT = 1

`showTimePlots` If non-zero, NGDEplot will show plots of several calculated parameters as a function of time. DEFAULT = 0

F.2.3 NGDE and NGDEplot Output

NGDE has two output parameters:

- `results1` is a `nodes`-by-2 array of the particle size distribution; the first column is the volume of a particle at each node, while the second column is the number of particles (per cubic meter) at each node.
- `results2` is an array containing various results as a function of time, where each row of the array represents the results at the time in column 1 of the array. The number of rows will depend on the simulation time and the edit frequency (`printInterval`). The columns are as follows:

Column	Description
1	The time, `t`
2:`nodes`+2	The number concentration at nodes 1 through `nodes`+1, `N` [#/m^3]
`nodes`+3	The nucleation rate, `Jk` [#/m^{3}s]
`nodes`+4	The saturation ratio, `S`
`nodes`+5	The volume mean particle diameter, `dpav` [m]
`nodes`+6	The critical particle size for nucleation, `kstar` [# of monomers]; nucleated particles are placed in the node with particle volume just larger than the volume corresponding to `kstar` monomers
`nodes`+7	The total volume concentration of particles, `Vtot` [m^3]; note that this does not include the volume of monomers
`nodes`+8	The number concentration of particles, `Ntot` [#/m^3]; note that this does not include the number concentration of monomers

For more information about how these parameters are determined, see the technical description of NGDE in Chapter 9.

NGDEplot has two output parameters, `F1` and `F2`, which contain the frames for the size distribution and Mie scattering movies generated by the code. If the user chooses not save the frames (`saveframes`=0) or chooses not to generate one of the movies (`showNmovie`=0 or `showMie`=0), then `F1` and/or `F2` will be zero. To replay

a movie using the saved frames, the user should use MATLAB's `movie` command.

F.3 Code Structure

The goal of this section is to give users a better understanding of how the code works and to identify some hardwired parameters or features that one can modify to improve the code or tailor it to a specific application. The code is divided into three main sections: (1) reading the input structure and initializing variables, (2) subroutines common to more than one of the possible calculation types (see `choice` in Section F.2.1), and (3) the main body of the program. The initialization step is straightforward and will not be discussed here. The following subsections discuss the subroutines and the main body of the code. These subsections largely focus on code structure and logic; for the technical details, refer to Chapter 9 or to the code itself.

F.3.1 NGDE Subroutines

After reading in the input structure and initializing variables, the NGDE code defines a number of separate subroutines or functions, which are listed below. To modify the code, simply find the appropriate subroutine and make the desired changes.

Subroutine	Description
`createNodes`	Establishes the volume of each node, based on the desired number of nodes and a 12 order of magnitude increase in volume between the smallest and largest nodes. The smallest node is either the volume of a monomer (`choice` $\neq 1$) or the volume a particle with diameter `d0` (`choice` $= 1$). Note that the 12 order of magnitude span in volume is hardwired in the code; to change it, modify parameter `vspan`. Note that this subroutine creates an additional node larger than the largest particle size; however, the number concentration for the extra node remains zero throughout the calculation. This node is created to prevent index errors in some of the `for` loops in the code.
`collisionFrequency`	Determines the frequency of collisions between particles in each pair of nodes. The results are used to calculate the rates of coagulation and surface growth for each node. Users have two options for the collision frequency function: the free molecule collision frequency function based on kinetic theory (`beta_option` $= 1$) or Fuchs' form of the collision function for particles in the transition regime (`beta_option` $= 2$).

`sizeSplitting`	Populates the size-splitting array `X` that handles particles that coagulate to a size between two nodes.
`dynamicTimestep`	Chooses a time step based on the behavior of the GDE at each point in time. The overarching goal is to choose the maximum time step that guarantees code stability. The dynamic time-step algorithm selects the time step as the minimum of five options: (1) 0.1% of the characteristic coagulation time; (2) 50% of the maximum time step that results in the number concentration in any node decreasing to zero; (3) the time in which the monomer concentration changes by 0.1%; (4) the time in which the saturation ratio changes by 1%; (5) a user-defined maximum time step, `dtUser`. The percentages are hardwired parameters but can be modified by the user if desired.

`coagulation`	Calculates the coagulation rate for each node, based on the current size distribution, the collision frequency for each pair of nodes (see `collisionFrequency` above), and the size-splitting array `X`.
`surfaceGrowth`	Calculates the condensation and evaporation rates for each node based on the current size distribution, saturation monomer concentration for each node (accounting for the Kelvin effect), and the collision frequency between monomers and particles.
`printResults`	Writes results to the output array `results2`. See Section F.2.3 for the structure of this array.

F.3.2 NGDE Main Program

After the above function definitions, the main body of the NGDE code begins. This portion of the code uses `if-else` statements to branch into four segments, corresponding to the four calculation types as specified with the `choice` input variable. Each branch has the same basic structure: there is an additional initalization step, used to create the volume nodes, populate the size-splitting array `X`, and establish the conditions (e.g. total particle volume `Vtot`, volume mean diameter `dpav`) at time zero; next is a `while` loop, where the code marches forward in time until some condition is met; and finally, the code stores the output in variables `results1` and `results2`.

The exit condition for each `while` loop depends on the calculation type. For `choice` = 1, (pure coagulation), the calculation terminates at 1000 times the estimated time to reach the self-preserving distribution, `t_SPD`. The calculation starts with an initially monodisperse aerosol. As the `while` loop marches the simulation forward in time, the aerosol grows based on the conditions in the `coagulation` subroutine.

For the other choices, the calculation ends when the system reaches `Tf`. Initially, the system is very slightly supersaturated (`S` = 1.001) at some user-specified temperature (`T0`). Within the loop, the code calls the subroutines to determine the time step and nucleation, coagulation, and surface growth rates, as appropriate based on the calculation type. The code updates the size distribution and other associated properties using the results of these subroutines.

F.4 Summary

This user manual has described the input, output, and general structure of the NGDE code, as well as the input and output of the NGDEplot post-processing tool. The user can control many of the parameters in the NGDE code using the `ngdein` input structure; other parameters must be modified directly in the code, such as the initial saturation ratio `S`, the exit conditions for the while loops (`t` $< 1000 *$ `t_SPD` for `choice` = 1 and `T` $<$ `Tf` otherwise), and the span of the size distribution (12 orders of magnitude from the smallest to largest volume nodes, as specified by `vspan`). To make more substantial changes to the code – such as the introduction

of new models for coagulation, nucleation, and growth, or changes to the constant-cooldown conditions of the calculation – one would need to do so in the appropriate subroutines or in the main body of the program.

Appendix G: MATLAB Codes Referenced in this Disseration

G.1 Code for Calculating the Velocity around a Sphere

Below I have included the source code for the MATLAB function used to calculate the velocity around a sphere as a function of Knudsen number, `bgk_sphere_par`. Note that the code takes advantage of MATLAB's parallel computing features. For serial execution (i.e. on one computer core), change the `parfor` loops to `for` loops.

Note that when calculating the density, velocity, and temperature perturbations around and drag on the sphere as a function of $r_0 = \sqrt{\pi}/[4(0.499)\mathrm{Kn}]$, I have used `nodes=64` and `upper_bound=10`. I have experimented with different values of these parameters, but these values seem to work best based on my limited sample size.

`bgk_sphere_par` relies on two other MATLAB functions that I have written: `gaussquad`, which returns the Gaussian quadrature nodes and weights, and `abram`, which returns the $\mathrm{T}_n(x)$ functions that appear when solving the BGK equation. Both of these files consist of long tables of data: `gaussquad(n)` uses a `switch`, `case` structure to return the `n` node points and weights (`tj` and Aj in `bgk_sphere_par`), while `abram(x,n)` interpolates from tables to return $\mathrm{T}_n(x)$ for each value of `x` provided. It would not be helpful to include the file listings here because they would

span over 100 pages. Instead, I will provide the information necessary to recreate these files.

The Gaussian quadrature nodes and weights are available from various sources, including Abramowitz and Stegun [98]. For `gaussquad(n)`, I included nodes and weights for `n=2` to `n=64` nodes; each set of data is its own `case` in the `switch`, `case` structure. `gaussquad(n)` simply returns the nodes and weights for the specified case.

I created the tables in `abram(x,n)` by numerically integrating the function in MATLAB, using the following commands:

```
r=[0,logspace(-2,2,99)]';
for i=1:length(r)
for n=0:9
T(i,j)=integral(@(c) exp(-c.^2-r(i)./c).*(c.^n),0,Inf);
end
end
```

The file `abram(x,n)` consists of the values of `r` and `T`, then the following lines:

```
Tn=x*0;
for i=1:length(x)
Tn(i)=interp1(r,T(:,n+1),x(i),'pchip',0);
end
```

The code returns `T(n)`.

See Chapter 2 and Appendix A for technical details of the BGK equation and its solution for a translating sphere.

G.1.1 Code Listing for bgk_sphere_par

```
% Solve for the density, velocity, and temperature around a sphere
% of non-dimensional radius r0, using a Gaussian quadrature with
% user-specified number of nodes between r0 and r0+upper_bound.
% This function uses the asymptotic solution of the Krook equation
% for large r from (Takata et al., 1993).  Otherwise, the equations
% and overall solution strategy follow (Lea & Loyalka, 1982) and
% (Law & Loyalka, 1986).  See my dissertation (Corson, 2018) for
% more details.
function [rj,eps,coefs,drag]=bgk_sphere_par(r0,nodes,...
    upper_bound,outfile)

tic

if nargin < 4
    outfile=['r0=',num2str(r0),'_results.mat'];
end

%options for integral2
Int2Opts.Method='iterated';
Int2Opts.AbsTol=1e-6;
Int2Opts.RelTol=1e-3;

%Coefficient in (Takata et al., 1993) trial functions
gam=1.270;

%For r between r0 (the surface of the sphere) and
%rp=r0+upper_bound, the BGK equation is solved using a Gaussian
%quadrature.  The nodes and weights tj and Aj are obtained
%from a separate function.
rp=r0+upper_bound;
[tj,Aj]=gaussquad(nodes);

rj=0.5*(r0*(1-tj)+rp*(1+tj));

%Results for c1, c2, and c3 based on earlier calculations;
%these are used to calculate initial guesses for the coefficients
%in the trial functions.
guesses=[0.00888,-0.0261,-14.7502,-0.8594;
    0.010,-0.0269,-14.7212,-0.8591;
    0.025,-0.0379,-14.3333,-0.8545;
```

```
    0.050,-0.0564,-13.6869,-0.8468;
    0.075,-0.0748,-13.0404,-0.8392;
    0.100,-0.0932,-12.3940,-0.8315;
    0.250,-0.2147,-12.1216,-0.2794;
    0.500,-0.3826,-5.5702,-0.2417;
    0.750,-0.5148,-3.4101,-0.2094;
    0.888,-0.5760,-2.7445,-0.1935;
    1.000,-0.6205,-2.3438,-0.1818;
    2.000,-0.8854,-0.8038,-0.1103;
    3.000,-1.0253,-0.3295,-0.0740;
    4.000,-1.1115,-0.1039,-0.0532;
    5.000,-1.1706,0.0268,-0.0418;
    6.000,-1.2137,0.1113,-0.0335;
    7.000,-1.2468,0.1707,-0.0280;
    8.000,-1.2734,0.2153,-0.0246;
    9.000,-1.2949,0.2489,-0.0208;
    10.00,-1.3129,0.2758,-0.0184;
    88.80,-1.4829,0.4830,-6.418e3-4;
    100.0,-1.4857,0.4858,-5.1061e-4;
    1000.,-1.5,   0.5,   0];

% Initialize vectors and matrices
ar1=zeros(nodes,1); ar2=ar1; ar3=ar1;
Wg1=zeros(nodes,1); Wg2=Wg1; Wg3=Wg1; Wu1=Wg1; Wu2=Wg1; Wu3=Wg1;
S1=zeros(nodes,1); S2=S1; S3=S1;
G11=S1; G12=S1; G13=S1; G21=S1; G22=S1; G23=S1; G31=S1;
G32=S1; G33=S1;
K11=zeros(nodes); K12=K11; K13=K11; K21=K11; K22=K11;
K23=K11; K31=K11; K32=K11; K33=K11;
A=zeros(4*nodes);
% Vectors and matrices that account for temperature fluctuation
ar4=ar1; Wg4=Wg1; Wu4=Wu1; K14=K11; K24=K11; K34=K11;
K41=K11; K42=K11; K43=K11; K44=K11;
G14=G11; G24=G11; G34=G11; G41=G11; G42=G11; G43=G11;
G44=G11; S4=S1;

%Loop to calculate a(r), which in turn is used to calculate the
%constant g that appears in the source term
parfor i=1:nodes
%for i=1:nodes
    ar1(i)=1/(2*r0^2*rj(i))*integral(@(t) (t.^4-2*rj(i)^2*t.^2 ...
        +(rj(i)^4-r0^4)).*abram(t,2)./(t.^2),rj(i)-r0, ...
        sqrt(rj(i)^2-r0^2));
    ar2(i)=-1/(2*sqrt(2)*r0^2*rj(i)^2)*integral(@(t) (t.^6-t.^4 ...
        *(rj(i)^2+r0^2)-t.^2*(rj(i)^2-r0^2)^2+(rj(i)^2-r0^2) ...
```

```
        *(rj(i)^4-r0^4)).*abram(t,3)./(t.^3),rj(i)-r0, ...
        sqrt(rj(i)^2-r0^2));
    ar3(i)=1/(2*sqrt(2)*r0^2*rj(i)^2)*integral(@(t) (t.^6-t.^4 ...
        *(3*rj(i)^2+r0^2)+t.^2*(rj(i)^2-r0^2)*(3*rj(i)^2+r0^2) ...
        -(rj(i)^2-r0^2)^3).*abram(t,3)./(t.^3),rj(i)-r0, ...
        sqrt(rj(i)^2-r0^2));
    ar4(i)=sqrt(2/3)/(2*r0^2*rj(i))*integral(@(t) (t.^4 ...
        -2*rj(i)^2*t.^2+(rj(i)^4-r0^4)).*(abram(t,4) ...
        -3/2*abram(t,2))./t.^2,rj(i)-r0,sqrt(rj(i)^2-r0^2));
end

% Loop to calculate the source term W(r)
parfor i=1:nodes
%for i=1:nodes
    LL=rj(i)-r0;
    UL=sqrt(rj(i)^2-r0^2);
    tt=0.5*(LL*(1-tj)+UL*(1+tj));
    C=(UL-LL)/2;
    for j=1:nodes
        Wg1(i)=Wg1(i)+1/(2*sqrt(pi)*rj(i)^2*r0)*(tt(j)^4 ...
            -2*rj(i)^2*tt(j)^2+(rj(i)^4-r0^4)) ...
            .*abram(tt(j),2)/tt(j)^2*Aj(j)*C;
        Wg2(i)=Wg2(i)+1/(2*sqrt(2*pi)*rj(i)^3*r0)*(tt(j)^6 ...
            -(rj(i)^2+r0^2)*tt(j)^4-(rj(i)^2-r0^2)^2*tt(j)^2 ...
            +(rj(i)^2+r0^2)*(rj(i)^2-r0^2)^2).*abram(tt(j),3) ...
            ./tt(j)^3*Aj(j)*C;
        Wg3(i)=Wg3(i)-1/(4*sqrt(2*pi)*rj(i)^3*r0)*(tt(j)^6 ...
            -(3*rj(i)^2+r0^2)*tt(j)^4+(rj(i)^2-r0^2)*(3*rj(i)^2 ...
            +r0^2)*tt(j)^2-(rj(i)^2-r0^2)^3).*abram(tt(j),3) ...
            ./tt(j)^3*Aj(j)*C;
        Wu1(i)=Wu1(i)+1/(sqrt(pi)*rj(i)^2)*(tt(j)^4 ...
            -(rj(i)^2-r0^2)^2).*abram(tt(j),3)./tt(j)^3*Aj(j)*C;
        Wu2(i)=Wu2(i)+1/(sqrt(2*pi)*rj(i)^3)*(tt(j)^6+tt(j)^4 ...
            *(rj(i)^2-r0^2)-tt(j)^2*(rj(i)^2-r0^2)^2 ...
            -(rj(i)^2-r0^2)^3).*abram(tt(j),4)./tt(j)^4*Aj(j)*C;
        Wu3(i)=Wu3(i)-1/(2*sqrt(2*pi)*rj(i)^3)*(tt(j)^6-tt(j)^4 ...
            *(3*rj(i)^2+r0^2)+tt(j)^2*(rj(i)^2-r0^2)*(3*rj(i)^2 ...
            +r0^2)-(rj(i)^2-r0^2)^3).*abram(tt(j),4) ...
            ./tt(j)^4*Aj(j)*C;
        Wg4(i)=Wg4(i)+sqrt(2/3)/(2*sqrt(pi)*rj(i)^2*r0) ...
            *(tt(j)^4-2*rj(i)^2*tt(j)^2+(rj(i)^4-r0^4)) ...
            *(abram(tt(j),4)-3/2*abram(tt(j),2))/tt(j)^2*Aj(j)*C;
        Wu4(i)=Wu4(i)+sqrt(2/3)/(sqrt(pi)*rj(i)^2)*(tt(j)^4 ...
            -(rj(i)^2-r0^2)^2)*(abram(tt(j),5) ...
            -3/2*abram(tt(j),3))/tt(j)^3*Aj(j)*C;
```

```
    end
end

% Loop to evaluate the kernel K(rj(i),r)
parfor i=1:nodes
%for i=1:nodes
    % These are the integrands of the H functions from Lea, 1982
    H11=@(r,t) -1./(rj(i)*r).*abram(t,1).*(t.^2-(rj(i)^2+r.^2))./t;
    H12=@(r,t) 1./(sqrt(2)*rj(i)*r.^2).*abram(t,2) ...
        .*(t.^4-2*rj(i)^2*t.^2-(r.^4-rj(i)^4))./t.^2;
    H13=@(r,t) -1./(sqrt(2)*rj(i)*r.^2).*abram(t,2) ...
        .*(t.^4-2*(r.^2+rj(i)^2).*t.^2+(r.^2-rj(i)^2).^2)./t.^2;
    H21=@(r,t) -1./(sqrt(2)*rj(i)^2*r).*abram(t,2) ...
        .*(t.^4-2*r.^2.*t.^2-(rj(i)^4-r.^4))./t.^2;
    H22=@(r,t) 1./(2*rj(i)^2*r.^2).*abram(t,3).*(t.^6-t.^4 ...
        .*(r.^2+rj(i)^2)-t.^2.*(rj(i)^2-r.^2).^2 ...
        +(r.^2-rj(i)^2).*(r.^4-rj(i)^4))./t.^3;
    H23=@(r,t) -1./(2*rj(i)^2*r.^2).*abram(t,3).*(t.^6-t.^4 ...
        .*(3*r.^2+rj(i)^2)+t.^2.*(r.^2-rj(i)^2) ...
        .*(3*r.^2+rj(i)^2)-(r.^2-rj(i)^2).^3)./t.^3;
    H31=@(r,t) 1./(sqrt(2)*2*rj(i)^2*r).*abram(t,2) ...
        .*(t.^4-2*(rj(i)^2+r.^2).*t.^2+(rj(i)^2-r.^2).^2)./t.^2;
    H32=@(r,t) -1./(4*rj(i)^2*r.^2).*abram(t,3).*(t.^6-t.^4 ...
        .*(3*rj(i)^2+r.^2)+t.^2.*(rj(i)^2-r.^2) ...
        .*(3*rj(i)^2+r.^2)-(rj(i)^2-r.^2).^3)./t.^3;
    H33=@(r,t) 1./(4*rj(i)^2*r.^2).*abram(t,3).*(t.^6-t.^4 ...
        .*(3*rj(i)^2+3*r.^2)+t.^2.*(3*rj(i)^4+2*rj(i)^2*r.^2 ...
        +3*r.^4)-(rj(i)^4-r.^4).*(rj(i)^2-r.^2))./t.^3;
    H14=@(r,t) -sqrt(2/3)./(rj(i)*r) ...
        .*(abram(t,3)-3/2*abram(t,1)).*(t.^2-(rj(i)^2+r.^2))./t;
    H24=@(r,t) -1./(sqrt(3)*rj(i)^2*r).*(abram(t,4) ...
        -3/2*abram(t,2)).*(t.^4-2*r.^2.*t.^2-(rj(i)^4-r.^4))./t.^2;
    H34=@(r,t) 1./(2*sqrt(3)*rj(i)^2*r) ...
        .*(abram(t,4)-3/2*abram(t,2)).*(t.^4-2*(rj(i)^2+r.^2) ...
        .*t.^2+(rj(i)^2-r.^2).^2)./t.^2;
    H41=@(r,t) -sqrt(2/3)./(rj(i)*r).*(abram(t,3) ...
        -3/2*abram(t,1)).*(t.^2-(rj(i)^2+r.^2))./t;
    H42=@(r,t) 1./(sqrt(3)*rj(i)*r.^2) ...
        .*(abram(t,4)-3/2*abram(t,2)) ...
        .*(t.^4-2*rj(i)^2*t.^2-(r.^4-rj(i)^4))./t.^2;
    H43=@(r,t) -1./(sqrt(3)*rj(i)*r.^2) ...
        .*(abram(t,4)-3/2*abram(t,2)).*(t.^4-2*(r.^2+rj(i)^2) ...
        .*t.^2+(r.^2-rj(i)^2).^2)./t.^2;
    H44=@(r,t) -2./(3*rj(i)*r).*(abram(t,5)-3*abram(t,3) ...
        +9/4*abram(t,1)).*(t.^2-(rj(i)^2+r.^2))./t;
```

```
% The G's represent cases when the kernel is singular,
% i.e. when r=rj(i).
G11(i)=pi^(-1/2)*(integral2(@(r,t) r/rj(i).*(H11(r,t)), ...
    r0,rj(i),@(r) abs(rj(i)-r),@(r) sqrt(rj(i)^2-r0^2) ...
    +sqrt(r.^2-r0^2),Int2Opts)+integral2(@(r,t) ...
    r/rj(i).*(H11(r,t)),rj(i),rp,@(r) abs(rj(i)-r), ...
    @(r) sqrt(rj(i)^2-r0^2)+sqrt(r.^2-r0^2),Int2Opts));
G12(i)=pi^(-1/2)*(integral2(@(r,t) r/rj(i).*(H12(r,t)), ...
    r0,rj(i),@(r) abs(rj(i)-r),@(r) sqrt(rj(i)^2-r0^2) ...
    +sqrt(r.^2-r0^2),Int2Opts)+integral2(@(r,t) ...
    r/rj(i).*(H12(r,t)),rj(i),rp,@(r) abs(rj(i)-r), ...
    @(r) sqrt(rj(i)^2-r0^2)+sqrt(r.^2-r0^2),Int2Opts));
G13(i)=pi^(-1/2)*(integral2(@(r,t) r/rj(i).*(H13(r,t)), ...
    r0,rj(i),@(r) abs(rj(i)-r),@(r) sqrt(rj(i)^2-r0^2) ...
    +sqrt(r.^2-r0^2),Int2Opts)+integral2(@(r,t) ...
    r/rj(i).*(H13(r,t)),rj(i),rp,@(r) abs(rj(i)-r), ...
    @(r) sqrt(rj(i)^2-r0^2)+sqrt(r.^2-r0^2),Int2Opts));
G21(i)=pi^(-1/2)*(integral2(@(r,t) r/rj(i).*(H21(r,t)), ...
    r0,rj(i),@(r) abs(rj(i)-r),@(r) sqrt(rj(i)^2-r0^2) ...
    +sqrt(r.^2-r0^2),Int2Opts)+integral2(@(r,t) ...
    r/rj(i).*(H21(r,t)),rj(i),rp,@(r) abs(rj(i)-r), ...
    @(r) sqrt(rj(i)^2-r0^2)+sqrt(r.^2-r0^2),Int2Opts));
G22(i)=pi^(-1/2)*(integral2(@(r,t) r/rj(i).*(H22(r,t)), ...
    r0,rj(i),@(r) abs(rj(i)-r),@(r) sqrt(rj(i)^2-r0^2) ...
    +sqrt(r.^2-r0^2),Int2Opts)+integral2(@(r,t) ...
    r/rj(i).*(H22(r,t)),rj(i),rp,@(r) abs(rj(i)-r), ...
    @(r) sqrt(rj(i)^2-r0^2)+sqrt(r.^2-r0^2),Int2Opts));
G23(i)=pi^(-1/2)*(integral2(@(r,t) r/rj(i).*(H23(r,t)), ...
    r0,rj(i),@(r) abs(rj(i)-r),@(r) sqrt(rj(i)^2-r0^2) ...
    +sqrt(r.^2-r0^2),Int2Opts)+integral2(@(r,t) ...
    r/rj(i).*(H23(r,t)),rj(i),rp,@(r) abs(rj(i)-r), ...
    @(r) sqrt(rj(i)^2-r0^2)+sqrt(r.^2-r0^2),Int2Opts));
G31(i)=pi^(-1/2)*(integral2(@(r,t) r/rj(i).*(H31(r,t)), ...
    r0,rj(i),@(r) abs(rj(i)-r),@(r) sqrt(rj(i)^2-r0^2) ...
    +sqrt(r.^2-r0^2),Int2Opts)+integral2(@(r,t) ...
    r/rj(i).*(H31(r,t)),rj(i),rp,@(r) abs(rj(i)-r),...
    @(r) sqrt(rj(i)^2-r0^2)+sqrt(r.^2-r0^2),Int2Opts));
G32(i)=pi^(-1/2)*(integral2(@(r,t) r/rj(i).*(H32(r,t)), ...
    r0,rj(i),@(r) abs(rj(i)-r),@(r) sqrt(rj(i)^2-r0^2) ...
    +sqrt(r.^2-r0^2),Int2Opts)+integral2(@(r,t) ...
    r/rj(i).*(H32(r,t)),rj(i),rp,@(r) abs(rj(i)-r), ...
    @(r) sqrt(rj(i)^2-r0^2)+sqrt(r.^2-r0^2),Int2Opts));
G33(i)=pi^(-1/2)*(integral2(@(r,t) r/rj(i).*(H33(r,t)), ...
    r0,rj(i),@(r) abs(rj(i)-r),@(r) sqrt(rj(i)^2-r0^2) ...
    +sqrt(r.^2-r0^2),Int2Opts)+integral2(@(r,t) ...
```

```
    r/rj(i).*(H33(r,t)),rj(i),rp,@(r) abs(rj(i)-r), ...
    @(r) sqrt(rj(i)^2-r0^2)+sqrt(r.^2-r0^2),Int2Opts));
G14(i)=pi^(-1/2)*(integral2(@(r,t) r/rj(i).*(H14(r,t)), ...
    r0,rj(i),@(r) abs(rj(i)-r),@(r) sqrt(rj(i)^2-r0^2) ...
    +sqrt(r.^2-r0^2),Int2Opts)+integral2(@(r,t) ...
    r/rj(i).*(H14(r,t)),rj(i),rp,@(r) abs(rj(i)-r), ...
    @(r) sqrt(rj(i)^2-r0^2)+sqrt(r.^2-r0^2),Int2Opts));
G24(i)=pi^(-1/2)*(integral2(@(r,t) r/rj(i).*(H24(r,t)), ...
    r0,rj(i),@(r) abs(rj(i)-r),@(r) sqrt(rj(i)^2-r0^2) ...
    +sqrt(r.^2-r0^2),Int2Opts)+integral2(@(r,t) ...
    r/rj(i).*(H24(r,t)),rj(i),rp,@(r) abs(rj(i)-r), ...
    @(r) sqrt(rj(i)^2-r0^2)+sqrt(r.^2-r0^2),Int2Opts));
G34(i)=pi^(-1/2)*(integral2(@(r,t) r/rj(i).*(H34(r,t)), ...
    r0,rj(i),@(r) abs(rj(i)-r),@(r) sqrt(rj(i)^2-r0^2) ...
    +sqrt(r.^2-r0^2),Int2Opts)+integral2(@(r,t) ...
    r/rj(i).*(H34(r,t)),rj(i),rp,@(r) abs(rj(i)-r), ...
    @(r) sqrt(rj(i)^2-r0^2)+sqrt(r.^2-r0^2),Int2Opts));
G41(i)=pi^(-1/2)*(integral2(@(r,t) r/rj(i).*(H41(r,t)), ...
    r0,rj(i),@(r) abs(rj(i)-r),@(r) sqrt(rj(i)^2-r0^2) ...
    +sqrt(r.^2-r0^2),Int2Opts)+integral2(@(r,t) ...
    r/rj(i).*(H41(r,t)),rj(i),rp,@(r) abs(rj(i)-r), ...
    @(r) sqrt(rj(i)^2-r0^2)+sqrt(r.^2-r0^2),Int2Opts));
G42(i)=pi^(-1/2)*(integral2(@(r,t) r/rj(i).*(H42(r,t)), ...
    r0,rj(i),@(r) abs(rj(i)-r),@(r) sqrt(rj(i)^2-r0^2) ...
    +sqrt(r.^2-r0^2),Int2Opts)+integral2(@(r,t) ...
    r/rj(i).*(H42(r,t)),rj(i),rp,@(r) abs(rj(i)-r), ...
    @(r) sqrt(rj(i)^2-r0^2)+sqrt(r.^2-r0^2),Int2Opts));
G43(i)=pi^(-1/2)*(integral2(@(r,t) r/rj(i).*(H43(r,t)), ...
    r0,rj(i),@(r) abs(rj(i)-r),@(r) sqrt(rj(i)^2-r0^2) ...
    +sqrt(r.^2-r0^2),Int2Opts)+integral2(@(r,t) ...
    r/rj(i).*(H43(r,t)),rj(i),rp,@(r) abs(rj(i)-r), ...
    @(r) sqrt(rj(i)^2-r0^2)+sqrt(r.^2-r0^2),Int2Opts));
G44(i)=pi^(-1/2)*(integral2(@(r,t) r/rj(i).*(H44(r,t)), ...
    r0,rj(i),@(r) abs(rj(i)-r),@(r) sqrt(rj(i)^2-r0^2) ...
    +sqrt(r.^2-r0^2),Int2Opts)+integral2(@(r,t) ...
    r/rj(i).*(H44(r,t)),rj(i),rp,@(r) abs(rj(i)-r), ...
    @(r) sqrt(rj(i)^2-r0^2)+sqrt(r.^2-r0^2),Int2Opts));
for j=1:nodes
    LL=abs(rj(i)-rj(j));
    UL=sqrt(rj(i)^2-r0^2)+sqrt(rj(j)^2-r0^2);
    tt=0.5*(LL*(1-tj)+UL*(1+tj));
    C=(UL-LL)/2;
    K11(i,j)=pi^(-1/2)*sum(rj(j)/rj(i)*H11(rj(j),tt).*Aj*C);
    K12(i,j)=pi^(-1/2)*sum(rj(j)/rj(i)*H12(rj(j),tt).*Aj*C);
    K13(i,j)=pi^(-1/2)*sum(rj(j)/rj(i)*H13(rj(j),tt).*Aj*C);
```

```
        K21(i,j)=pi^(-1/2)*sum(rj(j)/rj(i)*H21(rj(j),tt).*Aj*C);
        K22(i,j)=pi^(-1/2)*sum(rj(j)/rj(i)*H22(rj(j),tt).*Aj*C);
        K23(i,j)=pi^(-1/2)*sum(rj(j)/rj(i)*H23(rj(j),tt).*Aj*C);
        K31(i,j)=pi^(-1/2)*sum(rj(j)/rj(i)*H31(rj(j),tt).*Aj*C);
        K32(i,j)=pi^(-1/2)*sum(rj(j)/rj(i)*H32(rj(j),tt).*Aj*C);
        K33(i,j)=pi^(-1/2)*sum(rj(j)/rj(i)*H33(rj(j),tt).*Aj*C);
        K14(i,j)=pi^(-1/2)*sum(rj(j)/rj(i)*H14(rj(j),tt).*Aj*C);
        K24(i,j)=pi^(-1/2)*sum(rj(j)/rj(i)*H24(rj(j),tt).*Aj*C);
        K34(i,j)=pi^(-1/2)*sum(rj(j)/rj(i)*H34(rj(j),tt).*Aj*C);
        K41(i,j)=pi^(-1/2)*sum(rj(j)/rj(i)*H41(rj(j),tt).*Aj*C);
        K42(i,j)=pi^(-1/2)*sum(rj(j)/rj(i)*H42(rj(j),tt).*Aj*C);
        K43(i,j)=pi^(-1/2)*sum(rj(j)/rj(i)*H43(rj(j),tt).*Aj*C);
        K44(i,j)=pi^(-1/2)*sum(rj(j)/rj(i)*H44(rj(j),tt).*Aj*C);
    end
end

K={K11,K12,K13,K14;
    K21,K22,K23,K24;
    K31,K32,K33,K34;
    K41,K42,K43,K44};
G={G11,G12,G13,G14;
    G21,G22,G23,G24;
    G31,G32,G33,G34;
    G41,G42,G43,G44};

C=(rp-r0)/2;

% Set up coefficient matrix A(i,j)
for p=1:4
    for q=1:4
        for m=1:nodes
            for n=1:nodes
                i=(p-1)*nodes+m;
                j=(q-1)*nodes+n;
                if m==n
                    if p==q
                        A(i,j)=1;
                    end
                    A(i,j)=A(i,j)-G{p,q}(m);
                    for l=1:m-1
                        A(i,j)=A(i,j)+C*Aj(l)*K{p,q}(m,l);
                    end
                    for l=m+1:nodes
                        A(i,j)=A(i,j)+C*Aj(l)*K{p,q}(m,l);
                    end
```

```
                else
                    A(i,j)=-C*Aj(n)*K{p,q}(m,n);
                end
            end
        end
    end
end

% Initial guesses for c1, c2, and c3
guess=interp1(guesses(:,1),guesses(:,2:4),r0,'linear','extrap')';

%Solve for the perturbations to the density, velocity, and
%temperature around the sphere, based on the values of the
%coefficients to the trial functions ("guess") for the solution
%far from the sphere.  The function returns the difference
%between the calculated values of the perturbations from the
%gaussian quadrature solution and the values from the trial
%functions at the boundary between the inner and outer domains
%(r = r0 + upper_bound).
J=0;
    function difference=findQ(guess)
        J=J+1;
        J %Print out the iteration number and the calculation time
        toc
        s1=zeros(nodes,1);s2=s1;s3=s1;s4=s1;
        %Trial functions based on Takata (1993)
        q1t=@(r) (gam*guess(1)/r0-guess(3))./(r/r0).^2;
        q2t=@(r) sqrt(2)*guess(1)./(r/r0) ...
            +sqrt(2)*guess(2)./(r/r0).^3;
        q3t=@(r) 1/sqrt(2)*guess(1)./(r/r0) ...
            -1/sqrt(2)*guess(2)./(r/r0).^3;
        q4t=@(r) sqrt(3/2)*guess(3)./(r/r0).^2;
        %Integrals involving q from r0+upper_bound to infinity
        far1=integral2(@(r,t) r.*q1t(r)./(2*r0^2.*r) ...
            .*(t.^4-2*r.^2.*t.^2+(r.^4-r0^4)).*abram(t,2) ...
            ./(t.^2),rp,Inf,@(r) r-r0,@(r) sqrt(r.^2-r0^2), ...
            Int2Opts);
        far2=-integral2(@(r,t) r.*q2t(r)./(2*sqrt(2)*r0^2*r.^2) ...
            .*(t.^6-t.^4.*(r.^2+r0^2)-t.^2.*(r.^2-r0^2).^2 ...
            +(r.^2-r0^2).*(r.^4-r0^4)).*abram(t,3)./(t.^3), ...
            rp,Inf,@(r) r-r0,@(r) sqrt(r.^2-r0^2),Int2Opts);
        far3=integral2(@(r,t) r.*q3t(r)./(2*sqrt(2)*r0^2*r.^2) ...
            .*(t.^6-t.^4.*(3*r.^2+r0^2)+t.^2.*(r.^2-r0^2) ...
            .*(3*r.^2+r0^2)-(r.^2-r0^2).^3).*abram(t,3)./(t.^3),...
            rp,Inf,@(r) r-r0,@(r) sqrt(r.^2-r0^2),Int2Opts);
```

```
far4=integral2(@(r,t) r.*q4t(r)*sqrt(2/3)./(2*r0^2.*r) ...
    .*(t.^4-2*r.^2.*t.^2+(r.^4-r0^4)).*(abram(t,4) ...
    -1.5*abram(t,2))./(t.^2),rp,Inf,@(r) r-r0, ...
    @(r) sqrt(r.^2-r0^2),Int2Opts);
src=-sqrt(pi)+2/r0*(sum(rj.*(q1t(rj).*ar1+q2t(rj).*ar2 ...
    +q3t(rj).*ar3+q4t(rj).*ar4).*Aj*(rp-r0)/2) ...
    +far1+far2+far3+far4);
W1=Wu1+src*Wg1;
W2=Wu2+src*Wg2;
W3=Wu3+src*Wg3;
W4=Wu4+src*Wg4;
parfor I=1:nodes
%for I=1:nodes
    H11=@(r,t) -1./(rj(I)*r).*abram(t,1) ...
        .*(t.^2-(rj(I)^2+r.^2))./t;
    H12=@(r,t) 1./(sqrt(2)*rj(I)*r.^2).*abram(t,2) ...
        .*(t.^4-2*rj(I)^2*t.^2-(r.^4-rj(I)^4))./t.^2;
    H13=@(r,t) -1./(sqrt(2)*rj(I)*r.^2).*abram(t,2) ...
        .*(t.^4-2*(r.^2+rj(I)^2).*t.^2 ...
        +(r.^2-rj(I)^2).^2)./t.^2;
    H21=@(r,t) -1./(sqrt(2)*rj(I)^2*r).*abram(t,2) ...
        .*(t.^4-2*r.^2.*t.^2-(rj(I)^4-r.^4))./t.^2;
    H22=@(r,t) 1./(2*rj(I)^2*r.^2).*abram(t,3).*(t.^6 ...
        -t.^4.*(r.^2+rj(I)^2)-t.^2.*(rj(I)^2-r.^2).^2 ...
        +(r.^2-rj(I)^2).*(r.^4-rj(I)^4))./t.^3;
    H23=@(r,t) -1./(2*rj(I)^2*r.^2).*abram(t,3).*(t.^6 ...
        -t.^4.*(3*r.^2+rj(I)^2)+t.^2.*(r.^2-rj(I)^2) ...
        .*(3*r.^2+rj(I)^2)-(r.^2-rj(I)^2).^3)./t.^3;
    H31=@(r,t) 1./(sqrt(2)*2*rj(I)^2*r).*abram(t,2) ...
        .*(t.^4-2*(rj(I)^2+r.^2).*t.^2 ...
        +(rj(I)^2-r.^2).^2)./t.^2;
    H32=@(r,t) -1./(4*rj(I)^2*r.^2).*abram(t,3).*(t.^6 ...
        -t.^4.*(3*rj(I)^2+r.^2)+t.^2.*(rj(I)^2-r.^2) ...
        .*(3*rj(I)^2+r.^2)-(rj(I)^2-r.^2).^3)./t.^3;
    H33=@(r,t) 1./(4*rj(I)^2*r.^2).*abram(t,3).*(t.^6 ...
        -t.^4.*(3*rj(I)^2+3*r.^2)+t.^2.*(3*rj(I)^4 ...
        +2*rj(I)^2*r.^2+3*r.^4)-(rj(I)^4-r.^4) ...
        .*(rj(I)^2-r.^2))./t.^3;
    H14=@(r,t) -sqrt(2/3)./(rj(I)*r).*(abram(t,3) ...
        -3/2*abram(t,1)).*(t.^2-(rj(I)^2+r.^2))./t;
    H24=@(r,t) -1./(sqrt(3)*rj(I)^2*r).*(abram(t,4) ...
        -3/2*abram(t,2)).*(t.^4-2*r.^2.*t.^2 ...
        -(rj(I)^4-r.^4))./t.^2;
    H34=@(r,t) 1./(2*sqrt(3)*rj(I)^2*r).*(abram(t,4) ...
        -3/2*abram(t,2)).*(t.^4-2*(rj(I)^2+r.^2) ...
```

```
        .*t.^2+(rj(I)^2-r.^2).^2)./t.^2;
    H41=@(r,t) -sqrt(2/3)./(rj(I)*r).*(abram(t,3) ...
        -3/2*abram(t,1)).*(t.^2-(rj(I)^2+r.^2))./t;
    H42=@(r,t) 1./(sqrt(3)*rj(I)*r.^2).*(abram(t,4) ...
        -3/2*abram(t,2)).*(t.^4-2*rj(I)^2*t.^2 ...
        -(r.^4-rj(I)^4))./t.^2;
    H43=@(r,t) -1./(sqrt(3)*rj(I)*r.^2).*(abram(t,4) ...
        -3/2*abram(t,2)).*(t.^4-2*(r.^2+rj(I)^2).*t.^2 ...
        +(r.^2-rj(I)^2).^2)./t.^2;
    H44=@(r,t) -2./(3*rj(I)*r).*(abram(t,5)-3*abram(t,3)...
        +9/4*abram(t,1)).*(t.^2-(rj(I)^2+r.^2))./t;
    s1(I)=pi^(-1/2)*integral2(@(r,t) r/rj(I).*(q1t(r) ...
        .*H11(r,t)+q2t(r).*H12(r,t)+q3t(r).*H13(r,t) ...
        +q4t(r).*H14(r,t)),rp,Inf,@(r) abs(rj(I)-r), ...
        @(r) sqrt(rj(I)^2-r0^2)+sqrt(r.^2-r0^2),Int2Opts);
    s2(I)=pi^(-1/2)*integral2(@(r,t) r/rj(I).*(q1t(r) ...
        .*H21(r,t)+q2t(r).*H22(r,t)+q3t(r).*H23(r,t) ...
        +q4t(r).*H24(r,t)),rp,Inf,@(r) abs(rj(I)-r), ...
        @(r) sqrt(rj(I)^2-r0^2)+sqrt(r.^2-r0^2),Int2Opts);
    s3(I)=pi^(-1/2)*integral2(@(r,t) r/rj(I).*(q1t(r) ...
        .*H31(r,t)+q2t(r).*H32(r,t)+q3t(r).*H33(r,t) ...
        +q4t(r).*H34(r,t)),rp,Inf,@(r) abs(rj(I)-r), ...
        @(r) sqrt(rj(I)^2-r0^2)+sqrt(r.^2-r0^2),Int2Opts);
    s4(I)=pi^(-1/2)*integral2(@(r,t) r/rj(I).*(q1t(r) ...
        .*H41(r,t)+q2t(r).*H42(r,t)+q3t(r).*H43(r,t) ...
        +q4t(r).*H44(r,t)),rp,Inf,@(r) abs(rj(I)-r), ...
        @(r) sqrt(rj(I)^2-r0^2)+sqrt(r.^2-r0^2),Int2Opts);
end
S=[W1+s1;W2+s2;W3+s3;W4+s4];
Q=A\S;
oldsrc=0;
while abs((oldsrc-src)/src)>1e-6
    oldsrc=src;
    src=-sqrt(pi)+2/r0*(sum(rj.*(Q(1:nodes).*ar1 ...
        +Q(nodes+1:2*nodes).*ar2+Q(2*nodes+1:3*nodes) ...
        .*ar3+Q(3*nodes+1:4*nodes).*ar4).*Aj*(rp-r0)/2) ...
        +far1+far2+far3+far4);
    S=[Wu1+src*Wg1+s1;
        Wu2+src*Wg2+s2;
        Wu3+src*Wg3+s3;
        Wu4+src*Wg4+s4];
    Q=A\S;
end
difference=[Q(nodes)-q1t(rj(end));
    Q(2*nodes)-q2t(rj(end));
```

```
            Q(3*nodes)-q3t(rj(end));
            Q(4*nodes)-q4t(rj(end))];
    end

%Find coefficients in the trial functions for the perturbations
%in the density, velocity, and temperature far from the sphere
coefs=fsolve(@(x) findQ(x),guess);

%Based on the coefficients calculated above, find the drag on the
%sphere.
q1t=@(r) (gam*coefs(1)/r0-coefs(3))./(r/r0).^2;
q2t=@(r) sqrt(2)*coefs(1)./(r/r0)+sqrt(2)*coefs(2)./(r/r0).^3;
q3t=@(r) 1/sqrt(2)*coefs(1)./(r/r0)-1/sqrt(2)*coefs(2)./(r/r0).^3;
q4t=@(r) sqrt(3/2)*coefs(3)./(r/r0).^2;
far1=integral2(@(r,t) r.*q1t(r)./(2*r0^2.*r).*(t.^4-2*r.^2 ...
    .*t.^2+(r.^4-r0^4)).*abram(t,2)./(t.^2),rp,Inf, ...
    @(r) r-r0,@(r) sqrt(r.^2-r0^2),Int2Opts);
far2=-integral2(@(r,t) r.*q2t(r)./(2*sqrt(2)*r0^2*r.^2) ...
    .*(t.^6-t.^4.*(r.^2+r0^2)-t.^2.*(r.^2-r0^2).^2+(r.^2-r0^2) ...
    .*(r.^4-r0^4)).*abram(t,3)./(t.^3),rp,Inf,@(r) r-r0, ...
    @(r) sqrt(r.^2-r0^2),Int2Opts);
far3=integral2(@(r,t) r.*q3t(r)./(2*sqrt(2)*r0^2*r.^2) ...
    .*(t.^6-t.^4.*(3*r.^2+r0^2)+t.^2.*(r.^2-r0^2) ...
    .*(3*r.^2+r0^2)-(r.^2-r0^2).^3).*abram(t,3)./(t.^3), ...
    rp,Inf,@(r) r-r0,@(r) sqrt(r.^2-r0^2),Int2Opts);
far4=integral2(@(r,t) r.*q4t(r)*sqrt(2/3)./(2*r0^2.*r) ...
    .*(t.^4-2*r.^2.*t.^2+(r.^4-r0^4)).*(abram(t,4) ...
    -1.5*abram(t,2))./(t.^2),rp,Inf,@(r) r-r0, ...
    @(r) sqrt(r.^2-r0^2),Int2Opts);
g=-sqrt(pi)+2/r0*(sum(rj.*(q1t(rj).*ar1+q2t(rj).*ar2 ...
    +q3t(rj).*ar3+q4t(rj).*ar4).*Aj*(rp-r0)/2)...
    +far1+far2+far3+far4);
W1=Wu1+g*Wg1;
W2=Wu2+g*Wg2;
W3=Wu3+g*Wg3;
W4=Wu4+g*Wg4;
parfor i=1:nodes
%for i=1:nodes
    H11=@(r,t) -1./(rj(i)*r).*abram(t,1) ...
        .*(t.^2-(rj(i)^2+r.^2))./t;
    H12=@(r,t) 1./(sqrt(2)*rj(i)*r.^2).*abram(t,2) ...
        .*(t.^4-2*rj(i)^2*t.^2-(r.^4-rj(i)^4))./t.^2;
    H13=@(r,t) -1./(sqrt(2)*rj(i)*r.^2).*abram(t,2) ...
        .*(t.^4-2*(r.^2+rj(i)^2).*t.^2+(r.^2-rj(i)^2).^2)./t.^2;
    H21=@(r,t) -1./(sqrt(2)*rj(i)^2*r).*abram(t,2) ...
```

```
    .*(t.^4-2*r.^2.*t.^2-(rj(i)^4-r.^4))./t.^2;
H22=@(r,t) 1./(2*rj(i)^2*r.^2).*abram(t,3) ...
    .*(t.^6-t.^4.*(r.^2+rj(i)^2)-t.^2.*(rj(i)^2-r.^2).^2 ...
    +(r.^2-rj(i)^2).*(r.^4-rj(i)^4))./t.^3;
H23=@(r,t) -1./(2*rj(i)^2*r.^2).*abram(t,3) ...
    .*(t.^6-t.^4.*(3*r.^2+rj(i)^2)+t.^2.*(r.^2-rj(i)^2) ...
    .*(3*r.^2+rj(i)^2)-(r.^2-rj(i)^2).^3)./t.^3;
H31=@(r,t) 1./(sqrt(2)*2*rj(i)^2*r).*abram(t,2) ...
    .*(t.^4-2*(rj(i)^2+r.^2).*t.^2+(rj(i)^2-r.^2).^2)./t.^2;
H32=@(r,t) -1./(4*rj(i)^2*r.^2).*abram(t,3) ...
    .*(t.^6-t.^4.*(3*rj(i)^2+r.^2)+t.^2.*(rj(i)^2-r.^2) ...
    .*(3*rj(i)^2+r.^2)-(rj(i)^2-r.^2).^3)./t.^3;
H33=@(r,t) 1./(4*rj(i)^2*r.^2).*abram(t,3).*(t.^6-t.^4 ...
    .*(3*rj(i)^2+3*r.^2)+t.^2.*(3*rj(i)^4+2*rj(i)^2*r.^2 ...
    +3*r.^4)-(rj(i)^4-r.^4).*(rj(i)^2-r.^2))./t.^3;
H14=@(r,t) -sqrt(2/3)./(rj(i)*r).*(abram(t,3) ...
    -3/2*abram(t,1)).*(t.^2-(rj(i)^2+r.^2))./t;
H24=@(r,t) -1./(sqrt(3)*rj(i)^2*r).*(abram(t,4) ...
    -3/2*abram(t,2)).*(t.^4-2*r.^2.*t.^2-(rj(i)^4-r.^4))./t.^2;
H34=@(r,t) 1./(2*sqrt(3)*rj(i)^2*r).*(abram(t,4) ...
    -3/2*abram(t,2)).*(t.^4-2*(rj(i)^2+r.^2).*t.^2 ...
    +(rj(i)^2-r.^2).^2)./t.^2;
H41=@(r,t) -sqrt(2/3)./(rj(i)*r).*(abram(t,3) ...
    -3/2*abram(t,1)).*(t.^2-(rj(i)^2+r.^2))./t;
H42=@(r,t) 1./(sqrt(3)*rj(i)*r.^2).*(abram(t,4) ...
    -3/2*abram(t,2)).*(t.^4-2*rj(i)^2*t.^2 ...
    -(r.^4-rj(i)^4))./t.^2;
H43=@(r,t) -1./(sqrt(3)*rj(i)*r.^2).*(abram(t,4) ...
    -3/2*abram(t,2)).*(t.^4-2*(r.^2+rj(i)^2).*t.^2 ...
    +(r.^2-rj(i)^2).^2)./t.^2;
H44=@(r,t) -2./(3*rj(i)*r).*(abram(t,5)-3*abram(t,3) ...
    +9/4*abram(t,1)).*(t.^2-(rj(i)^2+r.^2))./t;
S1(i)=pi^(-1/2)*integral2(@(r,t) r/rj(i).*(q1t(r).*H11(r,t) ...
    +q2t(r).*H12(r,t)+q3t(r).*H13(r,t)+q4t(r).*H14(r,t)), ...
    rp,Inf,@(r) abs(rj(i)-r),@(r) sqrt(rj(i)^2-r0^2) ...
    +sqrt(r.^2-r0^2),Int2Opts);
S2(i)=pi^(-1/2)*integral2(@(r,t) r/rj(i).*(q1t(r).*H21(r,t) ...
    +q2t(r).*H22(r,t)+q3t(r).*H23(r,t)+q4t(r).*H24(r,t)), ...
    rp,Inf,@(r) abs(rj(i)-r),@(r) sqrt(rj(i)^2-r0^2) ...
    +sqrt(r.^2-r0^2),Int2Opts);
S3(i)=pi^(-1/2)*integral2(@(r,t) r/rj(i).*(q1t(r).*H31(r,t) ...
    +q2t(r).*H32(r,t)+q3t(r).*H33(r,t)+q4t(r).*H34(r,t)), ...
    rp,Inf,@(r) abs(rj(i)-r),@(r) sqrt(rj(i)^2-r0^2) ...
    +sqrt(r.^2-r0^2),Int2Opts);
S4(i)=pi^(-1/2)*integral2(@(r,t) r/rj(i).*(q1t(r).*H41(r,t) ...
```

```
        +q2t(r).*H42(r,t)+q3t(r).*H43(r,t)+q4t(r).*H44(r,t)), ...
        rp,Inf,@(r) abs(rj(i)-r),@(r) sqrt(rj(i)^2-r0^2) ...
        +sqrt(r.^2-r0^2),Int2Opts);
end
oldg=0;
S=[Wu1+g*Wg1+S1;Wu2+g*Wg2+S2;Wu3+g*Wg3+S3;Wu4+g*Wg4+S4];
eps=A\S;
while (abs(oldg-g)/abs(g))>1e-6
    oldg=g;
    g=-sqrt(pi)+2/r0*(sum(rj.*(eps(1:nodes).*ar1 ...
        +eps(nodes+1:2*nodes).*ar2+eps(2*nodes+1:3*nodes).*ar3 ...
        +eps(3*nodes+1:4*nodes).*ar4).*Aj*(rp-r0)/2) ...
        +far1+far2+far3+far4);
    S=[Wu1+g*Wg1+S1;Wu2+g*Wg2+S2;Wu3+g*Wg3+S3;Wu4+g*Wg4+S4];
    eps=A\S;
end

C=(rp-r0)/2;
fardrag1=2/r0^2*integral2(@(r,t) q1t(r).*(t.^4-(r.^2-r0^2).^2) ...
    .*abram(t,3)./t.^3,rp,Inf,@(r) r-r0,@(r) sqrt(r.^2-r0^2), ...
    Int2Opts);
fardrag2=sqrt(2)/r0^2*integral2(@(r,t) q2t(r)./r.*(t.^6+t.^4 ...
    .*(r.^2-r0^2)-t.^2.*(r.^2-r0^2).^2-(r.^2-r0^2).^3) ...
    .*abram(t,4)./t.^4,rp,Inf,@(r) r-r0,@(r) sqrt(r.^2-r0^2), ...
    Int2Opts);
fardrag3=sqrt(2)/r0^2*integral2(@(r,t) -q3t(r)./r.*(t.^6-t.^4 ...
    .*(3*r.^2+r0^2)+t.^2.*(r.^2-r0^2).*(3*r.^2+r0^2) ...
    -(r.^2-r0^2).^3).*abram(t,4)./t.^4,rp,Inf,@(r) r-r0, ...
    @(r) sqrt(r.^2-r0^2),Int2Opts);
fardrag4=2/r0^2*integral2(@(r,t) sqrt(2/3)*q4t(r).*(t.^4 ...
    -(r.^2-r0^2).^2).*(abram(t,5)-3/2*abram(t,3))./t.^3,rp, ...
    Inf,@(r) r-r0,@(r) sqrt(r.^2-r0^2),Int2Opts);
drag=(fardrag1-fardrag2-fardrag3+fardrag4+2*sqrt(pi)/r0^2*C*Aj' ...
    *(rj.^2.*(eps(1:nodes).*Wu1-eps(nodes+1:2*nodes).*Wu2 ...
    -2*eps(2*nodes+1:3*nodes).*Wu3+eps(3*nodes+1:4*nodes).*Wu4))...
    +8-g*sqrt(pi))/(8+pi);

%Save the results of the calculation
save(outfile,'eps','coefs','drag','rj')

end
```

G.2 Codes for Calculating the Friction and Diffusion Tensors

Below I have included the source code for the MATLAB functions used to calculate the friction and diffusion tensors for an aggregate of N spheres of unit radius in the continuum and transition regimes. `continuum_tensors` uses Kirkwood-Riseman theory with the Rotne-Prager-Yamakawa tensor for translational interactions but ignores rotational and coupling interactions. One can also use the Stokes' velocity tensor in place of the RPY tensor; simply comment in the appropriate lines, as indicated in the source code. `continuum_tensors_3rd` uses Kirkwood-Riseman theory with translational, rotational, and coupling interaction tensors accurate to $\mathcal{O}(r_{ij}^{-3})$; this is referred to as the 3RD approach. `bgk_tensors` uses extended Kirkwood-Riseman theory to solve for the friction and diffusion tensors in the transition regime.

See Chapters 3-6 for technical details of these calculations.

G.2.1 Code Listing for `continuum_tensors`

```
%Solve for the translational, rotational, and coupling friction
%and diffusion tensors of an aggregate in the continuum flow
%regime using the Kirkwood-Riseman method with the
%Rotne-Prager-Yamakawa tensor.  The results are given in
%non-dimensional form.  For dimensional results, multiply the
%translational, coupling, and rotational friction tensors by
%6*pi*mu*a, 6*pi*mu*a^2, and 6*pi*mu*a^3, %respectively, where a
%is the radius of the primary spheres and mu is the gas viscosity.
%
%Input is as follows:
%   bodfile: Text file containing the x,y,z coordinates of the
%       spheres in the aggregate, or an N-by-3 matrix, where N is
%       the number of spheres in the aggregate.  See a sample file
%       for the required format if a text file is to be provided.
```

```
%For details of the KR method, see the following sources:
%   Carrasco, B. & Garcia de la Torre, J.,
%       Journal of Chemical Physics 111 (1999): 4817.
%   Corson, J. et al., Physical Review E 95 (2017): 013103.
%   Corson, J., PhD. Dissertation, University of Maryland (2017).
%
function [Xit,Xic,Xir,DOt,DOc,Dr,rOD,DDt] ...
    = continuum_tensors(bodfile)

%Read in the x,y,z coordinates of the spheres in the aggregate
if ischar(bodfile)
    f=fopen(bodfile);
    coords=textscan(f,'%6c %10.4f %10.4f %10.4f %5d');
    coords=[coords{2},coords{3},coords{4}];
    fclose(f);
else
    coords=bodfile;
end

M=size(coords,1); %Number of spheres

a=1; %Set sphere radius to unity

%Populate lower triangular portion of interaction matrix; because
%T is symmetric, we get complete matrix from T=T+T'.  The factor
%of 0.5 used to create the identity matrix ensures that the values
%on the diagonal of T are all 1.
T=eye(3*M)*0.5;
for i=1:M
    for j=1:i-1
        rij=coords(j,:)-coords(i,:);
        Rij=rij'*rij;
        rij=norm(rij);
        %Use the Rotne-Prager-Yamakawa tensor
        T(3*i-2:3*i,3*j-2:3*j)=3/4*a/rij*(eye(3)+Rij/rij^2)...
            +a^3/(2*rij^3)*(eye(3)-3*Rij/rij^2);
        %Use velocity field for Stokes flow around a sphere
        %T(3*i-2:3*i,3*j-2:3*j)=3/4*a/rij*(eye(3)+Rij/rij^2)...
        %    +a^3/(4*rij^3)*(eye(3)-3*Rij/rij^2);
    end
end
%Form the symmetrical matrix T using the lower-triangular matrix
%populated above, invert it, and determine the friction tensors
%from the inverted matrix.
T=T+T';
```

```
S=inv(T);
clear T
Xit=zeros(3); Xir=zeros(3); Xic=zeros(3);
for i=1:M
    for j=1:M
        Sij=S(3*i-2:3*i,3*j-2:3*j);
        Ai=[0 -coords(i,3) coords(i,2);
            coords(i,3) 0 -coords(i,1);
            -coords(i,2) coords(i,1) 0];
        Aj=[0 -coords(j,3) coords(j,2);
            coords(j,3) 0 -coords(j,1);
            -coords(j,2) coords(j,1) 0];
        Xit=Xit+Sij; % Friction tensor;
        Xic=Xic+Ai*Sij; % Coupling tensor at the origin
        Xir=Xir-Ai*Sij*Aj; % Rotational friction tensor at the origin
    end
end
Xir=Xir+eye(3)*M*4/3;

% Calculate diffusion tensors and vector from the origin
% to the center of diffusion
DOt=inv(Xit-Xic'*(Xir\Xic));
DOc=-inv(Xir)*Xic*inv(Xit-Xic'*(Xir\Xic));
Dr=inv(Xir-Xic*(Xit\Xic'));
rOD=[Dr(2,2)+Dr(3,3), -Dr(1,2), -Dr(1,3);
    -Dr(1,2), Dr(1,1)+Dr(3,3), -Dr(2,3);
    -Dr(1,3), -Dr(2,3), Dr(1,1)+Dr(2,2)]...
    \[DOc(2,3)-DOc(3,2);
    DOc(3,1)-DOc(1,3);
    DOc(1,2)-DOc(2,1)];
A=[0 -rOD(3) rOD(2);rOD(3) 0 -rOD(1);-rOD(2) rOD(1) 0];
DDt=DOt-A*Dr*A+DOc'*A-A*DOc;

end
```

G.2.2 Code Listing for continuum_tensors_3rd

```
%Solve for the translational, rotational, and coupling friction
%and diffusion tensors of an aggregate in the continuum flow
%regime using the Kirkwood-Riseman method with the
%terms up to order r_{ij}^{-3} in the translational, rotational,
%and coupling hydrodynamic interaction tensors (i.e. the 3RD method
```

```
%mentioned by Carrasco & Garcia de la Torre, 1999).  Results are
%given in non-dimensional form.  For dimensional results, multiply
%the translational, coupling, and rotational friction tensors by
%6*pi*mu*a, 6*pi*mu*a^2, and 6*pi*mu*a^3, %respectively, where a
%is the radius of the primary spheres and mu is the gas viscosity.
%
%Input is as follows:
%   bodfile: Text file containing the x,y,z coordinates of the
%       spheres in the aggregate, or an N-by-3 matrix, where N is
%       the number of spheres in the aggregate.  See a sample file
%       for the required format if a text file is to be provided.
%For details of the KR method, see the following sources:
%   Carrasco, B. & Garcia de la Torre, J.,
%       Journal of Chemical Physics 111 (1999): 4817.
%   Corson, J. et al., Physical Review E 95 (2017): 013103.
%   Corson, J., PhD. Dissertation, University of Maryland (2017).
%
function [Xit,Xic,Xir,DOt,DOc,Dr,rOD,DDt] ...
    = continuum_tensors_3rd(bodfile)

%Read in the x,y,z coordinates of the spheres in the aggregate
if ischar(bodfile)
    f=fopen(bodfile);
    coords=textscan(f,'%6c %10.4f %10.4f %10.4f %5d');
    coords=[coords{2},coords{3},coords{4}];
    fclose(f);
else
    coords=bodfile;
end

M=size(coords,1); %Number of spheres

a=1; %Set sphere radius to unity

%Populate the hydrodynamic interaction matrix
T=zeros(6*M);
for i=1:M
    % 3x3 matrices on the diagonal of T
    T(3*i-2:3*i,3*i-2:3*i)=eye(3)/(6*a);
    T(3*i-2+3*M:3*i+3*M,3*i-2+3*M:3*i+3*M)=eye(3)/(8*a^3);
    for j=1:M
        if i==j
            continue
        end
        rij=coords(j,:)-coords(i,:);
```

```
        Rij=rij'*rij;
        epsrij=[0 rij(3) -rij(2);
            -rij(3) 0 rij(1);
            rij(2) -rij(1) 0]/norm(rij);
        rij=norm(rij);
        %Use the RPY tensor for translational interactions
        T(3*i-2:3*i,3*j-2:3*j)=(3/4*a/rij*(eye(3)+Rij/rij^2)...
            +a^3/(2*rij^3)*(eye(3)-3*Rij/rij^2))/(6*a);
        %Rotation portion of the T, mu_rr
        T(3*M+3*i-2:3*M+3*i,3*M+3*j-2:3*M+3*j)=(3*Rij/rij^2 ...
            -eye(3))/(16*rij^3);
        %Rotation-translation coupling, mu_rt
        T(3*M+3*i-2:3*M+3*i,3*j-2:3*j)=-epsrij/(8*rij^2);
        T(3*j-2:3*j,3*M+3*i-2:3*M+3*i)=epsrij/(8*rij^2);
    end
end
%Invert the hydrodynamic interaction matrix T and determine
%the friction tensors from the inverted matrix.
S=inv(T);
clear T
Xit=zeros(3); Xir=zeros(3); Xic=zeros(3);
for i=1:M
    for j=1:M
        lam_tt=S(3*i-2:3*i,3*j-2:3*j);
        lam_rt=S(3*i-2+3*M:3*i+3*M,3*j-2:3*j);
        lam_tr=S(3*i-2:3*i,3*j-2+3*M:3*j+3*M);
        lam_rr=S(3*i-2+3*M:3*i+3*M,3*j-2+3*M:3*j+3*M);
        Ai=[0 -coords(i,3) coords(i,2);
            coords(i,3) 0 -coords(i,1);
            -coords(i,2) coords(i,1) 0];
        Aj=[0 -coords(j,3) coords(j,2);
            coords(j,3) 0 -coords(j,1);
            -coords(j,2) coords(j,1) 0];
        Xit=Xit+lam_tt; %Friction tensor
        Xic=Xic+lam_rt+Ai*lam_tt; %Coupling tensor at the origin
        Xir=Xir+lam_rr-lam_rt*Aj+Ai*lam_tr...
            -Ai*lam_tt*Aj; %Rotational friction tensor at the origin
    end
end
Xit=Xit/(6*a); Xic=Xic/(6*a); Xir=Xir/(6*a);
% Calculate diffusion tensors and vector from the origin
% to the center of diffusion
DOt=inv(Xit-Xic'*(Xir\Xic));
DOc=-inv(Xir)*Xic*inv(Xit-Xic'*(Xir\Xic));
Dr=inv(Xir-Xic*(Xit\Xic'));
```

```
rOD=[Dr(2,2)+Dr(3,3), -Dr(1,2), -Dr(1,3);
    -Dr(1,2), Dr(1,1)+Dr(3,3), -Dr(2,3);
    -Dr(1,3), -Dr(2,3), Dr(1,1)+Dr(2,2)]...
    \[DOc(2,3)-DOc(3,2);DOc(3,1)-DOc(1,3);DOc(1,2)-DOc(2,1)];
A=[0 -rOD(3) rOD(2);rOD(3) 0 -rOD(1);-rOD(2) rOD(1) 0];
DDt=DOt-A*Dr*A+DOc'*A-A*DOc;

end
```

G.2.3 Code Listing for bgk_tensors

```
%Solve for the translational, rotational, and coupling friction
%and diffusion tensors of an aggregate in the transition flow
%regime using the EKR method.  The results are given in
%non-dimensional form.  For dimensional results, multiply the
%translational, coupling, and rotational friction tensors by the
%following factors:
%   Xit = Xit*zeta_{0,epstein}
%   Xic = Xic*zeta_{0,epstein}*a
%   Xir = Xir*zeta_{0,epstein}*a^2
%where
%   zeta_{0,epstein}=pi*(8+pi)/2.994*mu/lambda*a^2
%   a=r0*lambda*1.996/sqrt(pi) is the sphere radius
%   lambda is the gas mean free path
%   mu is the gas viscosity
%
%Input is as follows:
%   bodfile: Text file containing the x,y,z coordinates of the
%       spheres in the aggregate, or an N-by-3 matrix, where N is
%       the number of spheres in the aggregate.  See a sample file
%       for the required format if a text file is to be provided.
%   datafile: Matlab data file containing BGK results.  This file
%       should have four variables: rj, eps, coefs, drag.  rj
%       is a vector containing the radial nodes at which the BGK
%       equation is solved.  eps is a vector containing the BGK
%       results for the density, radial velocity, tangential
%       velocity, and temperature perturbations around the sphere.
%       The first m elements of eps correspond to the density at
%       nodes rj, the next m correspond to the radial velocity, etc.
%       coefs is a vector of coefficients c_1, c_2, and c_3 that
%       appear in the asymptotic solution of the BGK equation far
%       from the sphere.  drag is the drag on the sphere, normalized
```

```
%       by zeta_{0,epstein}, as defined above.
%   r0: Non-dimensional sphere radius, related to the sphere Knudsen
%       number by r0=sqrt(pi)/(4*0.499*Kn).  Note that the BGK
%       results in datafile should correspond to r0.
%For details of the EKR method, see the following sources:
%   Corson, J. et al., Physical Review E 95 (2017): 013103.
%   Corson, J., PhD. Dissertation, University of Maryland (2017).
%
function [Xit,Xic,Xir,DOt,DOc,Dr,rOD,DDt] = bgk_tensors(bodfile,...
    datafile,r0)

%Read in the x,y,z coordinates of the spheres in the aggregate
if ischar(bodfile)
    f=fopen(bodfile);
    coords=textscan(f,'%6c %10.4f %10.4f %10.4f %5d');
    coords=[coords{2},coords{3},coords{4}];
    fclose(f);
else
    coords=bodfile;
end

%Read BGK results from datafile
data=load(datafile);
radii=data.rj;
eps=data.eps;
coefs=data.coefs;
drag=data.drag;

%Results for the torque ratio T/T_fm from Loyalka (1992); results
%for R=0 to R=10 are from Table IV; results for R=25 to R=100 are
%from the slip formula, Eq. (42), with the slip coefficient equal
%to 0.9875.
Loyalka=[0,1;
    0.1, 0.9901;
    0.25,0.9803;
    0.5, 0.9601;
    0.75,0.9427;
    1.0, 0.9206;
    2.0, 0.8362;
    3.0, 0.7514;
    5.0, 0.6080;
    7.0, 0.5044;
    10.0,0.3996;
    25.0,0.1902;
    50.0,0.1004;
```

```
    75.0,0.0682;
    100.,0.0516];

M=size(coords,1); %Number of spheres
%Number of points at which the velocities are given
nodes=length(radii);
%Resize radii relative to the sphere radius
radii=radii/r0;
%Extract q2(r) and q3(r) from eps
q2=eps(nodes+1:2*nodes);
q3=eps(2*nodes+1:3*nodes);
%Define functions for the asymptotic (large r) solution to
%the BGK equation.
q2t=@(r) sqrt(2)*coefs(1)./(r)+sqrt(2)*coefs(2)./(r).^3;
q3t=@(r) 1/sqrt(2)*coefs(1)./(r)-1/sqrt(2)*coefs(2)./(r).^3;

%Populate lower triangular portion of interaction matrix; because
%T is symmetric, we get complete matrix from T=T+T'.  The factor
%of 0.5 used to create the identity matrix ensures that the values
%on the diagonal of T are all 1.
T=eye(3*M)*0.5;
    for i=1:M
        for j=1:i-1
            rij=coords(j,:)-coords(i,:);
            Rij=rij'*rij;
            rij=norm(rij);
            %Interpolate from q2 and q3 rij < radii(end);
            %otherwise, use the functions for the asymptotic
            %solution for large r.
            if rij < radii(end)
                T(3*i-2:3*i,3*j-2:3*j)=-interp1(radii,q2,rij,...
                    'pchip','extrap')/sqrt(2)*(Rij/rij^2)...
                    -interp1(radii,q3,rij,'pchip','extrap')...
                    *(eye(3)-Rij/rij^2)/sqrt(2);
            else
                T(3*i-2:3*i,3*j-2:3*j)=-q2t(rij)/sqrt(2)...
                    *(Rij/rij^2)-q3t(rij)*(eye(3)-Rij/rij^2)...
                    /sqrt(2);
            end
        end
    end
%Form the symmetrical matrix T using the lower-triangular matrix
%populated above, invert it, and determine the friction tensors
%from the inverted matrix.
T=T+T';
```

```
S=drag*inv(T);
clear T
Xit=zeros(3); Xir=zeros(3); Xic=zeros(3);
for i=1:M
    for j=1:M
        Sij=S(3*i-2:3*i,3*j-2:3*j);
        Ai=[0 -coords(i,3) coords(i,2);
            coords(i,3) 0 -coords(i,1);
            -coords(i,2) coords(i,1) 0];
        Aj=[0 -coords(j,3) coords(j,2);
            coords(j,3) 0 -coords(j,1);
            -coords(j,2) coords(j,1) 0];
        Xit=Xit+Sij; %Friction tensor;
        Xic=Xic+Ai*Sij; %Coupling tensor at the origin
        Xir=Xir-Ai*Sij*Aj; %Rotational friction tensor at the origin
    end
end
Xir=Xir+eye(3)*M*4/(8+pi)...
    *interp1(Loyalka(:,1),Loyalka(:,2),r0,'pchip','extrap');

%Calculate diffusion tensors and vector from the origin to
%the center of diffusion
DOt=inv(Xit-Xic'*(Xir\Xic));
DOc=-inv(Xir)*Xic*inv(Xit-Xic'*(Xir\Xic));
Dr=inv(Xir-Xic*(Xit\Xic'));
rOD=[Dr(2,2)+Dr(3,3), -Dr(1,2), -Dr(1,3);
    -Dr(1,2), Dr(1,1)+Dr(3,3), -Dr(2,3);
    -Dr(1,3), -Dr(2,3), Dr(1,1)+Dr(2,2)]...
    \[DOc(2,3)-DOc(3,2);DOc(3,1)-DOc(1,3);DOc(1,2)-DOc(2,1)];
A=[0 -rOD(3) rOD(2);rOD(3) 0 -rOD(1);-rOD(2) rOD(1) 0];
DDt=DOt-A*Dr*A+DOc'*A-A*DOc;

end
```

G.3 Codes for Calculating the Average Friction Coefficient of a Particle in an Electric Field

Below I have included the source code for the MATLAB functions used to calculate the orientation-averaged translational friction coefficient for an aggregate of N spheres of unit radius in an external electric field. The first function (`avg_bgk_velocity`) uses the average-drift-velocity approach of Li et al. [105]; the second function (`avg_bgk_drag`) uses Li et al.'s averaged-drag-force approach. The user must provide the electric field strength; the polarizability tensor, or a Zeno output file containing the tensor; and either the translational friction tensor normalized by the free molecule friction coefficient of a primary sphere in the aggregate, or the necessary information to perform the EKR calculation for the friction tensor. (See the listing for `bgk_tensors` above.)

See Chapter 7 for technical details of the orientation-averaged friction coefficient calculations.

G.3.1 Code Listing for `avg_bgk_velocity`

```
%This function calculates the scalar friction coefficient of an
%aggregate using the averaged-drift velocity approach of
%Li et al, 2014.
%
%Input parameters are as follows:
%   ee: Electric field strength [W/cm**2].
%   r0: Non-dimensional sphere radius, related to the sphere Knudsen
%       number by r0=sqrt(pi)/(4*0.499*Kn).  Note that the BGK
%       results in datafile should correspond to r0.
```

```
%   zenofile: File containing Zeno results (for the polarizability
%       tensor), or a 3-by-3 matrix containing the polarizability
%       tensor.  If the polarizability tensor is provided, it
%       must be provided in non-dimensional form, such that the
%       dimensional polarizability tensor alpha is related to
%       the non-dimensional zenofile by
%       alpha=zenofile*a^3*epsilon_0, where epsilon_0 is the
%       permittivity of free space and a is the primary sphere
%       radius.
%   bodfile: Text file containing the x,y,z coordinates of the
%       spheres in the aggregate, or a 3-by-3 matrix containing
%       the translational friction tensor.  See a sample file
%       for the required format if a text file is to be provided.
%       If the translational friction tensor is provided, it must
%       be in non-dimensional form, Xit=Xit/zeta_FM, where
%       zeta_FM is the free molecule monomer friction coefficient
%       from Epstein's equation.
%   datafile: Matlab data file containing BGK results.  This file
%       should have four variables: rj, eps, coefs, drag.  rj
%       is a vector containing the radial nodes at which the BGK
%       equation is solved.  eps is a vector containing the BGK
%       results for the density, radial velocity, tangential
%       velocity, and temperature perturbations around the sphere.
%       The first m elements of eps correspond to the density at
%       nodes rj, the next m correspond to the radial velocity, etc.
%       coefs is a vector of coefficients c_1, c_2, and c_3 that
%       appear in the asymptotic solution of the BGK equation far
%       from the sphere.  drag is the drag on the sphere, normalized
%       by zeta_{0,epstein}, as defined above.  If the
%       translational friction tensor is provided (see entry for
%       bodfile above), datafile is not used.
%
function [favg,F] = avg_bgk_velocity(ee,r0,zenofile,...
    bodfile,datafile)

%Check to see whether or not the polarizability tensor
%has been provided
if size(zenofile) == [3,3]
    alpha=zenofile;
else %If not, get polarizability tensor from specified file
    f=fopen(zenofile);
    C=textscan(f,'%s');
    if C{1,1}{61}(1) == 'P'
        alpha(:,1)=[str2double(C{1,1}{63}(2:end-1));
            str2double(C{1,1}{64}(1:end-1));
```

```
            str2double(C{1,1}{65}(1:end-1))];
        alpha(:,2)=[str2double(C{1,1}{66}(1:end-1));
            str2double(C{1,1}{67}(1:end-1));
            str2double(C{1,1}{68}(1:end-1))];
        alpha(:,3)=[str2double(C{1,1}{69}(1:end-1));
            str2double(C{1,1}{70}(1:end-1));
            str2double(C{1,1}{71}(1:end-1))];
    elseif C{1,1}{66}(1) == 'P'
        alpha(:,1)=[str2double(C{1,1}{68}(2:end-1));
            str2double(C{1,1}{69}(1:end-1));
            str2double(C{1,1}{70}(1:end-1))];
        alpha(:,2)=[str2double(C{1,1}{71}(1:end-1));
            str2double(C{1,1}{72}(1:end-1));
            str2double(C{1,1}{73}(1:end-1))];
        alpha(:,3)=[str2double(C{1,1}{74}(1:end-1));
            str2double(C{1,1}{75}(1:end-1));
            str2double(C{1,1}{76}(1:end-1))];
    else
        alpha(:,1)=[str2double(C{1,1}{80}(2:end-1));
            str2double(C{1,1}{81}(1:end-1));
            str2double(C{1,1}{82}(1:end-1))];
        alpha(:,2)=[str2double(C{1,1}{83}(1:end-1));
            str2double(C{1,1}{84}(1:end-1));
            str2double(C{1,1}{85}(1:end-1))];
        alpha(:,3)=[str2double(C{1,1}{86}(1:end-1));
            str2double(C{1,1}{87}(1:end-1));
            str2double(C{1,1}{88}(1:end-1))];
    end
    fclose(f);
end
%Diagonalize the polarizability tensor
[V,alpha]=eig(alpha);
if alpha(3,3)==max(alpha*[1;1;1])
    P=eye(3);
elseif alpha(2,2)==max(alpha*[1;1;1])
    P=[1,0,0;0,0,-1;0,1,0];
else
    P=[0,0,-1;0,1,0;1,0,0];
end
alpha=P'*alpha*P;
%Convert to appropriate units
lambda=67.3e-9; %MFP [nm]
mu=1.85e-5; %viscosity [kg/m-s]
a=4*0.499*r0*lambda/sqrt(pi); %Primary sphere radius [m]
alpha=alpha*a^3*8.854e-12; %Polarizability tensor [C-m^2/V]
```

```
E=[0;0;1]; %Electric field is in the positive z-direction
ee=ee*100; %Convert electric field strength to W/m
kT=298*1.38e-23; %Brownian energy [J]; assume T = 298 K
pmax=0.5*ee^2*alpha(3,3)/kT; %Max potential energy between
    %the aggregate and the field; normalized by the
    %Brownian energy
zetafm=pi*(8+pi)/(6*0.499)*mu/lambda*a^2; %Monomer friction
    %coefficient in the FM regime; used to dimensionalize the
    %results of this Matlab function [kg/s]

%Check to see whether or not the friction tensor has been provided
if size(bodfile) == [3,3]
    F=P'*V'*bodfile*V*P;
%If not, perform BGK calculation and rotate to the body-fixed axes
%defined by the polarizability tensor
else
    F=bgk_tensors(bodfile,datafile,r0);
    F=P'*V'*F*V*P;
end
K=inv(F); %K is the mobility matrix
    %(i.e. the inverse of the friction matrix)

%Define functions for the probability and the z-component of
%the drift velocity as a function of orientation
p=@(ps,th) exp(0.5*(sin(ps).^2.*sin(th).^2*alpha(1,1)...
    +cos(ps).^2.*sin(th).^2*alpha(2,2)...
    +(cos(th).^2-1)*alpha(3,3))*ee^2/kT);
vz=@(ps,th) K(3,3)*cos(th).^2+K(2,2)*cos(ps).^2.*sin(th).^2 ...
    +K(1,1)*sin(th).^2.*sin(ps).^2+K(1,2)*sin(th).^2.*sin(2*ps)...
    +K(1,3)*sin(2*th).*sin(ps)+K(2,3)*cos(ps).*sin(2*th);
%Calculate the average friction coefficient
Q=integral2(@(ps,th) p(ps,th).*sin(th),0,2*pi,0,pi); %
    %Q == partition function, used to normalize probability p
vd=integral2(@(ps,th) p(ps,th).*vz(ps,th).*sin(th),0,2*pi,0,pi)/Q;
favg=1/vd*zetafm; %Orientation-averaged friction coef [kg/s]

end
```

G.3.2 Code Listing for avg_bgk_drag

```
%This function calculates the scalar friction coefficient of an
%aggregate using the averaged-drag force approach of
```

```
%Li et al, 2014.
%
%Input parameters are as follows:
%   ee: Electric field strength [W/cm**2].
%   r0: Non-dimensional sphere radius, related to the sphere Knudsen
%       number by r0=sqrt(pi)/(4*0.499*Kn).  Note that the BGK
%       results in datafile should correspond to r0.
%   zenofile: File containing Zeno results (for the polarizability
%       tensor), or a 3-by-3 matrix containing the polarizability
%       tensor.  If the polarizability tensor is provided, it
%       must be provided in non-dimensional form, such that the
%       dimensional polarizability tensor alpha is related to
%       the non-dimensional zenofile by
%       alpha=zenofile*a^3*epsilon_0, where epsilon_0 is the
%       permittivity of free space and a is the primary sphere
%       radius.
%   bodfile: Text file containing the x,y,z coordinates of the
%       spheres in the aggregate, or a 3-by-3 matrix containing
%       the translational friction tensor.  See a sample file
%       for the required format if a text file is to be provided.
%       If the translational friction tensor is provided, it must
%       be in non-dimensional form, Xit=Xit/zeta_FM, where
%       zeta_FM is the free molecule monomer friction coefficient
%       from Epstein's equation.
%   datafile: Matlab data file containing BGK results.  This file
%       should have four variables: rj, eps, coefs, drag.  rj
%       is a vector containing the radial nodes at which the BGK
%       equation is solved.  eps is a vector containing the BGK
%       results for the density, radial velocity, tangential
%       velocity, and temperature perturbations around the sphere.
%       The first m elements of eps correspond to the density at
%       nodes rj, the next m correspond to the radial velocity, etc.
%       coefs is a vector of coefficients c_1, c_2, and c_3 that
%       appear in the asymptotic solution of the BGK equation far
%       from the sphere.  drag is the drag on the sphere, normalized
%       by zeta_{0,epstein}, as defined above.  If the
%       translational friction tensor is provided (see entry for
%       bodfile above), datafile is not used.
%
function [favg,F] = avg_bgk_drag(ee,r0,zenofile,bodfile,datafile)

%Check to see whether or not the polarizability tensor
%has been provided
if size(zenofile) == [3,3]
    alpha=zenofile;
```

```
else %If not, get polarizability tensor from specified file
    f=fopen(zenofile);
    C=textscan(f,'%s');
    if C{1,1}{61}(1) == 'P'
        alpha(:,1)=[str2double(C{1,1}{63}(2:end-1));
            str2double(C{1,1}{64}(1:end-1));
            str2double(C{1,1}{65}(1:end-1))];
        alpha(:,2)=[str2double(C{1,1}{66}(1:end-1));
            str2double(C{1,1}{67}(1:end-1));
            str2double(C{1,1}{68}(1:end-1))];
        alpha(:,3)=[str2double(C{1,1}{69}(1:end-1));
            str2double(C{1,1}{70}(1:end-1));
            str2double(C{1,1}{71}(1:end-1))];
    elseif C{1,1}{66}(1) == 'P'
        alpha(:,1)=[str2double(C{1,1}{68}(2:end-1));
            str2double(C{1,1}{69}(1:end-1));
            str2double(C{1,1}{70}(1:end-1))];
        alpha(:,2)=[str2double(C{1,1}{71}(1:end-1));
            str2double(C{1,1}{72}(1:end-1));
            str2double(C{1,1}{73}(1:end-1))];
        alpha(:,3)=[str2double(C{1,1}{74}(1:end-1));
            str2double(C{1,1}{75}(1:end-1));
            str2double(C{1,1}{76}(1:end-1))];
    else
        alpha(:,1)=[str2double(C{1,1}{80}(2:end-1));
            str2double(C{1,1}{81}(1:end-1));
            str2double(C{1,1}{82}(1:end-1))];
        alpha(:,2)=[str2double(C{1,1}{83}(1:end-1));
            str2double(C{1,1}{84}(1:end-1));
            str2double(C{1,1}{85}(1:end-1))];
        alpha(:,3)=[str2double(C{1,1}{86}(1:end-1));
            str2double(C{1,1}{87}(1:end-1));
            str2double(C{1,1}{88}(1:end-1))];
    end
    fclose(f);
end
%Diagonalize the polarizability tensor
[V,alpha]=eig(alpha);
if alpha(3,3)==max(alpha*[1;1;1])
    P=eye(3);
elseif alpha(2,2)==max(alpha*[1;1;1])
    P=[1,0,0;0,0,-1;0,1,0];
else
    P=[0,0,-1;0,1,0;1,0,0];
end
```

```
alpha=P'*alpha*P;
%Convert to appropriate units
lambda=67.3e-9; %MFP [nm]
mu=1.85e-5; %viscosity [kg/m-s]
a=4*0.499*r0*lambda/sqrt(pi); %Primary sphere radius [m]
alpha=alpha*a^3*8.854e-12; %Polarizability tensor [C-m^2/V]
E=[0;0;1]; %Electric field is in the positive z-direction
ee=ee*100; %Convert electric field strength to W/m
kT=298*1.38e-23; %Brownian energy [J]; assume T = 298 K
pmax=0.5*ee^2*alpha(3,3)/kT; %Max potential energy between
    %the aggregate and the field; normalized by the
    %Brownian energy
zetafm=pi*(8+pi)/(6*0.499)*mu/lambda*a^2; %Monomer friction
    %coefficient in the FM regime; used to dimensionalize the
    %results of this Matlab function [kg/s]

%Check to see whether or not the friction tensor has been provided
if size(bodfile) == [3,3]
    F=P'*V'*bodfile*V*P;
%If not, perform BGK calculation and rotate to the body-fixed axes
%defined by the polarizability tensor
else
    F=bgk_tensors(bodfile,datafile,r0);
    F=P'*V'*F*V*P;
end

%Define functions for the probability and the z-component of
%the drag force as a function of orientation
p=@(ps,th) exp(0.5*(sin(ps).^2.*sin(th).^2*alpha(1,1)...
    +cos(ps).^2.*sin(th).^2*alpha(2,2)...
    +(cos(th).^2-1)*alpha(3,3))*ee^2/kT);
Fz=@(ps,th) F(3,3)*cos(th).^2+F(2,2)*cos(ps).^2.*sin(th).^2 ...
    +F(1,1)*sin(th).^2.*sin(ps).^2+F(1,2)*sin(th).^2.*sin(2*ps)...
    +F(1,3)*sin(2*th).*sin(ps)+F(2,3)*cos(ps).*sin(2*th);
%Calculate the average friction coefficient
Q=integral2(@(ps,th) p(ps,th).*sin(th),0,2*pi,0,pi); %
    %Q == partition function, used to normalize probability p
Favg=integral2(@(ps,th) p(ps,th).*Fz(ps,th).*sin(th),0,2*pi,0,pi)/Q;
favg=Favg*zetafm; %Orientation-averaged friction coef [kg/s]

end
```

G.4 Codes for Hydrodynamic Interactions between Particles

Below I have included the source code for the MATLAB functions used to determine the hydrodynamic interactions between particles (Chapter 8). The first function (`bgk_two_particles`) determines the drag on each particle in a two particle system for the specified coordinates of the spheres in each particle, the primary sphere Knudsen number, the distance between the center of mass of each particle, and the particle velocities. The second function (`bgk_cloud`) calculates the velocity of each particle in a spherical cloud based on the radius of the cloud and on the particle volume fraction, friction coefficient, and Knudsen number.

See Chapter 8 for technical details of the hydrodynamic interaction calculations.

G.4.1 Code Listing for `bgk_two_particles`

```
%This function calculates the hydrodynamic force on each particle
%in a two-particle system.  The interactions between primary spheres
%in the particles are determined using the extended
%Kirkwood-Riseman method (Corson et al., Phys. Rev. E. 95(1), 2017).
%Results are also given for the drag each particle would experience
%if it was isolated in an infinite fluid (i.e. when the separation
%distance between particles goes to infinity).  The results are
%given in non-dimensional form.  For dimensional
%results, multiply the forces following factor:
%   F = F*zeta_{0,epstein}*U
%where
%   zeta_{0,epstein}=pi*(8+pi)/2.994*mu/lambda*a^2
%   a=r0*lambda*1.996/sqrt(pi) is the sphere radius
%   lambda is the gas mean free path
%   mu is the gas viscosity
%   U is the unit used to specify particle velocities U1 and U2
```

```
%
%Input parameters are as follows:
%   bodfile1: Text file containing the x,y,z coordinates of the
%       spheres in aggregate 1, or an N-by-3 matrix, where N is
%       the number of spheres in the aggregate.  See a sample file
%       for the required format if a text file is to be provided.
%   bodfile2: Text file containing the x,y,z coordinates of the
%       spheres in aggregate 2, or an N-by-3 matrix, where N is
%       the number of spheres in the aggregate.  See a sample file
%       for the required format if a text file is to be provided.
%   datafile: Matlab data file containing BGK results.  This file
%       should have four variables: rj, eps, coefs, drag.  rj
%       is a vector containing the radial nodes at which the BGK
%       equation is solved.  eps is a vector containing the BGK
%       results for the density, radial velocity, tangential
%       velocity, and temperature perturbations around the sphere.
%       The first m elements of eps correspond to the density at
%       nodes rj, the next m correspond to the radial velocity, etc.
%       coefs is a vector of coefficients c_1, c_2, and c_3 that
%       appear in the asymptotic solution of the BGK equation far
%       from the sphere.  drag is the drag on the sphere, normalized
%       by zeta_{0,epstein}, as defined above.
%   r0: Non-dimensional sphere radius, related to the sphere Knudsen
%       number by r0=sqrt(pi)/(4*0.499*Kn).  Note that the BGK
%       results in datafile should correspond to r0.
%   separation: Vector connecting the center of mass of particle 1
%       to the center of mass of particle 2.  The distance
%       is in units of primary sphere radius.
%   U1: Velocity of particle 1 in arbitrary units
%   U2: Velocity of particle 2 in arbitrary units
%
function [F1,F2,F01,F02]=bgk_two_particles(bodfile1,bodfile2,...
    datafile,r0,separation,U1,U2)

%Make sure separation is a row vector to prevent errors
separation=reshape(separation,[1 3]);

%Get coordinates for particles 1 and 2
if ischar(bodfile1)
    f=fopen(bodfile1);
    coords1=textscan(f,'%6c %10.4f %10.4f %10.4f %5d');
    coords1=[coords1{2},coords1{3},coords1{4}];
    fclose(f);
else
    coords1=bodfile1;
```

```
end
if ischar(bodfile2)
    f=fopen(bodfile2);
    coords2=textscan(f,'%6c %10.4f %10.4f %10.4f %5d');
    coords2=[coords2{2},coords2{3},coords2{4}];
    fclose(f);
else
    coords2=bodfile2;
end
%Add and subtract separation vectors from the coordinates
coords1=coords1+repmat(separation,length(coords1(:,1)),1)/2;
coords2=coords2-repmat(separation,length(coords2(:,1)),1)/2;
%Combine coordinates from particles 1 and 2 into one data structure
coords=[coords1;coords2];

data=load(datafile);
radii=data.rj;
eps=data.eps;
coefs=data.coefs;
drag=data.drag;

M=size(coords,1); %Total number of spheres in both particles
M1=size(coords1,1); %Number of spheres in particle 1
M2=size(coords2,1); %Number of spheres in particle 2
%Number of points at which the velocities are given
nodes=length(radii);
%Resize radii relative to the sphere radius
radii=radii/r0;
%Extract q2(r) and q3(r) from eps
q2=eps(nodes+1:2*nodes);
q3=eps(2*nodes+1:3*nodes);
q2t=@(r) sqrt(2)*coefs(1)./(r)+sqrt(2)*coefs(2)./(r).^3;
q3t=@(r) 1/sqrt(2)*coefs(1)./(r)-1/sqrt(2)*coefs(2)./(r).^3;

%Make matrix to store velocity of each sphere
U=zeros(3,M);
U(1,1:M1)=drag*U1(1);
U(2,1:M1)=drag*U1(2);
U(3,1:M1)=drag*U1(3);
U(1,M1+1:M)=drag*U2(1);
U(2,M1+1:M)=drag*U2(2);
U(3,M1+1:M)=drag*U2(3);
%Convert matrix to vectors to facilitate linear algebra solution
U=reshape(U,[3*M,1]);
```

```
%Populate lower triangular portion of interaction matrix;
%because T is symmetric, we get complete matrix from T=T+T'.
%The factor of 0.5 used to create the identity matrix ensures
%that the values on the diagonal of T are all 1.
T=eye(3*M)*0.5;
    for i=1:M
        for j=1:i-1
            rij=coords(j,:)-coords(i,:);
            Rij=rij'*rij;
            rij=norm(rij);
            %Use data from Lea and Loyalka, 1982, along with derived
            %formula
            if rij < radii(end)
                T(3*i-2:3*i,3*j-2:3*j)=-interp1(radii,q2,rij,...
                    'pchip','extrap')/sqrt(2)*(Rij/rij^2)...
                    -interp1(radii,q3,rij,'pchip','extrap')...
                    *(eye(3)-Rij/rij^2)/sqrt(2);
            else
                T(3*i-2:3*i,3*j-2:3*j)=-q2t(rij)/sqrt(2)...
                    *(Rij/rij^2)-q3t(rij)*(eye(3)-Rij/rij^2)...
                    /sqrt(2);
            end
        end
    end
%Form the symmetrical matrix T using the lower-triangular matrix
%we populated above
T=T+T';
F=T\U;
F=reshape(F,[3,M])';
%Determine the force on each particle
F1=sum(F(1:M1,:),1);
F2=sum(F(M1+1:M,:),1);
%Determine the force on each particle if it is isolated
S1=inv(T(1:3*M1,1:3*M1))*drag;
F01=zeros(3);
for i=1:M1
    for j=1:M1
        Sij=S1(3*i-2:3*i,3*j-2:3*j);
        F01=F01+Sij; % Friction tensor for isolated particle 1
    end
end
S2=inv(T(3*M1+1:3*M,3*M1+1:3*M))*drag;
F02=zeros(3);
for i=1:M2
    for j=1:M2
```

```
        Sij=S2(3*i-2:3*i,3*j-2:3*j);
        F02=F02+Sij; % Friction tensor for isolated particle 2
    end
end

end
```

G.4.2 Code Listing for bgk_cloud

```
%This function calculates the velocity of each particle in
%a spherical cloud.  The particles are arranged in a regular
%rectangular grid.  Each particle is the same size and experiences
%the same external force (e.g. the force of gravity).  The code
%uses a point force method for non-continuum particles.
%The results are given in non-dimensional form by dividing the
%velocity by the velocity each particle would have if it was
%alone in an infinite fluid experiencing the same external force.
%
%Input parameters are as follows:
%   phi: Particle volume fraction in the cloud
%       for the required format if a text file is to be provided.
%   zeta: Friction coefficient for each particle, normalized by
%       Epstein's equation,
%       zeta_{0,epstein}=pi*(8+pi)/2.994*mu/lambda*a^2
%   N: Number of spheres in each particle; if N>1, each particle
%       is an aggregate
%   Kn: Primary sphere Knudsen number
%   cloudrad: Radius of the circular cloud of particles
%
function [U,coords] = bgk_cloud(phi,zeta,N,Kn,cloudrad)

%Node spacing for aggregates with N spheres
L=(4*pi*N/(3*phi))^(1/3);

%Node points
nodes=0:L:L+cloudrad;
nodes=[-nodes(end:-1:2),nodes];
%Number of nodes.  The cloud consists of a 3D, n-by-n-by-n grid of
%equally-spaced particles.
n=length(nodes);

%Set the grid coordinates
```

```
%coords=zeros(M,3);
M=0;
for i=1:n
    for j=1:n
        for k=1:n
            if norm([nodes(i),nodes(j),nodes(k)])<=cloudrad
                M=M+1;
                coords(M,:)=[nodes(i),nodes(j),nodes(k)];
            end
        end
    end
end

%Determine the effective sphere size and the coefficient c1
%in the hydrodynamic interaction term
Cc=@(Kn) 1+Kn.*(1.257+0.4*exp(-1.1./Kn));
aeff=fsolve(@(a) 1-(8+pi)*Cc(Kn./a)*zeta./(36*.499*Kn*a),1);
Kneff=Kn/aeff;
c1=get_c1(Kneff);

U=0*coords;

%Determine the velocities; the velocity of sphere i is
%   u_i=[0;0;1]+sum_{i\neq j}T_{ij}*[0;0;1]
%where [0;0;1] is the normalized velocity the sphere
%would have if it was alone in an infinite fluid and T_{ij}
%is the velocity tensor around sphere j
for i=1:M
    U(i,:)=[0,0,1];
    for j=1:i-1
        rij=coords(j,:)-coords(i,:);
        Rij=rij'*rij;
        rij=norm(rij);
        T=-c1/2*aeff/rij*(eye(3)+Rij/rij^2)*[0;0;1];
        U(i,:)=U(i,:)+T';
    end
    for j=i+1:M
        rij=coords(j,:)-coords(i,:);
        Rij=rij'*rij;
        rij=norm(rij);
        T=-c1/2*aeff/rij*(eye(3)+Rij/rij^2)*[0;0;1];
        U(i,:)=U(i,:)+T';
    end
 end
```

```
end

function c1=get_c1(Kneff)

results=[0.00100000330103084,-1.50000000000000;
    0.00888002931315389,-1.48570344760713;
    0.0100000330103084,-1.48289594184936;
    0.0177600586263078,-1.46549558211423;
    0.0307267450282141,-1.43445528240899;
    0.0319425514861651,-1.43196708006806;
    0.0321740192505576,-1.43143453851274;
    0.0439605411542272,-1.40531002377626;
    0.0457733469750200,-1.40107279504826;
    0.0462501526726765,-1.40004970203708;
    0.0498878051300780,-1.39260388823354;
    0.0710402345052311,-1.34737220217562;
    0.0733886720095363,-1.34271424782340;
    0.0746220950685201,-1.34015845200810;
    0.0752544857046940,-1.33883481743332;
    0.0888002931315389,-1.31287863666467;
    0.0914524131117805,-1.30796980781124;
    0.0934739927700409,-1.30416195054598;
    0.0986669923683765,-1.29489226387913;
    0.100000330103084,-1.29259732469631;
    0.103256154804115,-1.28681575294805;
    0.106347656444957,-1.28147952131604;
    0.108293040404316,-1.27800956474164;
    0.111000366414424,-1.27340641424302;
    0.112833917575018,-1.27028453245384;
    0.148000488552565,-1.21371512310943;
    0.153368381919756,-1.20564257152255;
    0.158571952020605,-1.19790999542810;
    0.177600586263078,-1.17058108398838;
    0.222000732828847,-1.11152705469468;
    0.224810868687440,-1.10796421368653;
    0.248740316895067,-1.07877454770160;
    0.259649979916780,-1.06602375573901;
    0.296000977105130,-1.02526711131977;
    0.309408686869473,-1.01090376654656;
    0.312677088491334,-1.00749077881340;
    0.319425514861651,-1.00054637096953;
    0.330112613871892,-0.989656069389966;
    0.337643700119920,-0.982110085768983;
    0.355201172526155,-0.964899381185821;
```

0.360976801347719,-0.959351241563024;
0.370001221381412,-0.950650149617769;
0.444001465657694,-0.885439122815643;
0.450762909297152,-0.879881745753469;
0.462501526726765,-0.870274716693120;
0.480001584494805,-0.856574960658491;
0.507430246465936,-0.835629618679835;
0.522354665479641,-0.824727150242144;
0.541465202021579,-0.811001567718485;
0.592001954210259,-0.776725108676454;
0.608221185832458,-0.766318500586142;
0.672729493420749,-0.727041807705684;
0.710402345052311,-0.706087358715459;
0.853848972418643,-0.635349895187173;
0.862138768267368,-0.631686617740032;
0.870591109132734,-0.627973793024235;
0.888002931315389,-0.620465383723801;
1.00000330103084,-0.575967854009263;
1.04348170542349,-0.560310261228538;
1.18400390842052,-0.514765064439723;
1.34545898684150,-0.470715703993602;
1.43226279244418,-0.449900766293788;
1.64141022424286,-0.406436008989048;
1.77600586263078,-0.382577551475560;
1.89339644203708,-0.363913509990032;
2.00000660206169,-0.348442640233600;
2.22000732828847,-0.320287048255757;
2.29458121786922,-0.311735817784993;
2.68278831213108,-0.273641427999317;
2.80127107670470,-0.263783862704728;
3.00000990309253,-0.248735495332713;
3.22910156841960,-0.231501041361636;
3.26471665924775,-0.231161177027969;
3.36364746710375,-0.224408494612492;
3.55201172526156,-0.214680751106139;
3.84416853383285,-0.200153427272282;
4.24881785318368,-0.182982441031353;
4.62501526726765,-0.169458890693224;
4.80001584494805,-0.163823640031794;
4.82610288758364,-0.163015430672425;
4.98878051300780,-0.158149023776157;
5.16280774020575,-0.153254881401797;
5.95975121688180,-0.134209619067310;
6.72729493420749,-0.117429350671894;
6.99214906547550,-0.115605358650687;

```
    8.88002931315389,-0.0932081818613417;
    10.0000330103084,-0.0849534017314433;
    10.1139286026810,-0.0842245513328470;
    11.2833917575018,-0.0775245651729286;
    11.8400390842052,-0.0747839505227221;
    13.4545898684150,-0.0681752177326948;
    13.5988197751208,-0.0676599360292581;
    16.8501504993432,-0.0583854353709664;
    17.7600586263078,-0.0563648468965600;
    20.0000660206169,-0.0522394912334894;
    26.9909705566987,-0.0437872519905655;
    34.0231008166816,-0.0387726176692985;
    35.5201172526156,-0.0379489334389416;
    88.8002931315389,-0.0268922634420460;
    100.000330103084,-0.0260747426475103];

c1=interp1(results(:,1),results(:,2),Kneff);

end
```

Bibliography

[1] Fuchs, N. A. *The Mechanics of Aerosols*. Pergamon Press, Oxford, England, 1964.

[2] Friedlander, S. K. *Smoke, Dust, and Haze: Fundamentals of Aerosol Dynamics*. Topics in chemical engineering. Oxford University Press, New York, 2 edition, 2000.

[3] Williams, M. M. R. and Loyalka, S. K. *Aerosol Science: Theory and Practice: With Special Applications to the Nuclear Industry*. Pergamon Press, Oxford, 1991.

[4] Sorensen, C. M. The mobility of fractal aggregates: A review. *Aerosol Science and Technology*, 45(7):765–779, 2011.

[5] Li, M., Mulholland, G. W., and Zachariah, M. R. The effect of orientation on the mobility and dynamic shape factor of charged axially symmetric particles in an electric field. *Aerosol Science and Technology*, 46(9):1035–1044, 2012.

[6] Li, M., Mulholland, G. W., and Zachariah, M. R. The effect of alignment on the electric mobility of soot. *Aerosol Science and Technology*, 50(10):1003–1016, 2016.

[7] Pratsinis, S. E. Flame aerosol synthesis of ceramic powders. *Progress in Energy and Combustion Science*, 24(3):197–219, 1998.

[8] Mädler, L., Kammler, H. K., Mueller, R., and Pratsinis, S. E. Controlled synthesis of nanostructured particles by flame spray pyrolysis. *Journal of Aerosol Science*, 33(2):369–389, 2002.

[9] Johannessen, T., Jensen, J. R., Mosleh, M., Johansen, J., Quaade, U., and Livbjerg, H. Flame synthesis of nanoparticles: Applications in catalysis and product/process engineering. *Chemical Engineering Research and Design*, 82 (11):1444–1452, 2004.

[10] Strobel, R., Baiker, A., and Pratsinis, S. E. Aerosol flame synthesis of catalysts. *Advanced Powder Technology*, 17(5):457–480, 2006.

[11] Bluth, G. J. S., Doiron, S. D., Schnetzler, C. C., Krueger, A. J., and Walter, L. S. Global tracking of the SO2 clouds from the June, 1991 Mount Pinatubo eruptions. *Geophysical Research Letters*, 19(2):151–154, 1992.

[12] Minnis, P., Harrison, E. F., Stowe, L. L., Gibson, G. G., Denn, F. M., Doelling, D. R., and Smith, W. L. Radiative climate forcing by the Mount Pinatubo eruption. *Science*, 259(5100):1411–1415, 1993.

[13] Jacobson, M. Z. Strong radiative heating due to the mixing state of black carbon in atmospheric aerosols. *Nature*, 409(6821):695–697, 2001.

[14] Menon, S., Hansen, J., Nazarenko, L., and Luo, Y. Climate effects of black carbon aerosols in China and India. *Science*, 297(5590):2250–2253, 2002.

[15] Novakov, T., Ramanathan, V., Hansen, J. E., Kirchstetter, T. W., Sato, M., Sinton, J. E., and Sathaye, J. A. Large historical changes of fossil-fuel black carbon aerosols. *Geophysical Research Letters*, 30(6), 2003.

[16] IPCC. *Climate Change 2013: the physical science basis: Working Group I contribution to the Fifth assessment report of the Intergovernmental Panel on Climate Change*. Cambridge University Press, Cambridge, United Kingdom and New York, NY, USA, 2013. [Stocker, T.F., D. Qin, G.-K. Plattner, M. Tignor, S.K. Allen, J. Boschung, A. Nauels, Y. Xia, V. Bex and P.M. Midgley (eds.)].

[17] Brunner, T. J., Wick, P., Manser, P., Spohn, P., Grass, R. N., Limbach, L. K., Bruinink, A., and Stark, W. J. In vitro cytotoxicity of oxide nanoparticles: Comparison to asbestos, silica, and the effect of particle solubility. *Environmental science & technology*, 40(14):4374–4381, 2006.

[18] Rojas-Martinez, R., Perez-Padilla, R., Olaiz-Fernandez, G., Mendoza-Alvarado, L., Moreno-Macias, H., Fortoul, T., McDonnell, W., Loomis, D., and Romieu, I. Lung function growth in children with long-term exposure to air pollutants in Mexico City. *American Journal of Respiratory and Critical Care Medicine*, 176(4):377–384, 2007.

[19] Branche, C. M., Schulte, P., and Geraci, C. Approaches to safe nanotechnology – managing the health and safety concerns associated with engineered nanomaterials, 2009.

[20] Albanese, A., Tang, P. S., and Chan, W. C. W. The effect of nanoparticle size, shape, and surface chemistry on biological systems. *Annual review of biomedical engineering*, 14:1–16, 2012.

[21] Loyalka, S. K. Mechanics of aerosols in nuclear reactor safety: A review. *Progress in Nuclear Energy*, 12(1):1–56, 1983.

[22] Devell, L., Tovedal, H., Bergström, U., Appelgren, A., Chyssler, J., and Andersson, L. Initial observations of fallout from the reactor accident at Chernobyl. *Nature*, 321(6067):192–193, 1986.

[23] Dubrova, Y. E., Nesterov, V. N., Krouchinsky, N. G., Ostapenko, V. A., et al. Human minisatellite mutation rate after the Chernobyl accident. *Nature*, 380 (6576):683, 1996.

[24] Chino, M., Nakayama, H., Nagai, H., Terada, H., Katata, G., and Yamazawa, H. Preliminary estimation of release amounts of 131I and 137Cs accidentally discharged from the Fukushima Daiichi nuclear power plant into the atmosphere. *Journal of nuclear science and technology*, 48(7):1129–1134, 2011.

[25] Morino, Y., Ohara, T., and Nishizawa, M. Atmospheric behavior, deposition, and budget of radioactive materials from the Fukushima Daiichi nuclear power plant in March 2011. *Geophysical Research Letters*, 38(7), 2011.

[26] Gelbard, F. MAEROS User Manual. Technical Report NUREG/CR-1391, Sandia National Laboratories, December 1982.

[27] Prakash, A., Bapat, A. P., and Zachariah, M. R. A simple numerical algorithm and software for solution of nucleation, surface growth, and coagulation problems. *Aerosol Science and Technology*, 37(11):892–898, 2003.

[28] Kirkwood, J. G. and Riseman, J. The intrinsic viscosities and diffusion constants of flexible macromolecules in solution. *The Journal of Chemical Physics*, 16(6):565–573, 1948.

[29] Brenner, H. Coupling between the translational and rotational Brownian motions of rigid particles of arbitrary shape: II. General theory. *Journal of colloid and interface science*, 23(3):407–436, 1967.

[30] Chen, Z.-Y., Deutch, J. M., and Meakin, P. Translational friction coefficient of diffusion limited aggregates. *The Journal of chemical physics*, 80(6):2982–2983, 1984.

[31] Hubbard, J. B. and Douglas, J. F. Hydrodynamic friction of arbitrarily shaped Brownian particles. *Physical Review E*, 47(5):R2983, 1993.

[32] Epstein, P. S. On the resistance experienced by spheres in their motion through gases. *Physical Review*, 23(6):710, 1924.

[33] Dahneke, B. E. Slip correction factors for nonspherical bodies – II Free molecule flow. *Journal of Aerosol Science*, 4(2):147–161, 1973.

[34] Chan, P. and Dahneke, B. Free-molecule drag on straight chains of uniform spheres. *Journal of Applied Physics*, 52(5):3106–3110, 1981.

[35] Meakin, P., Donn, B., and Mulholland, G. W. Collisions between point masses and fractal aggregates. *Langmuir*, 5(2):510–518, 1989.

[36] Mackowski, D. W. Monte Carlo simulation of hydrodynamic drag and thermophoresis of fractal aggregates of spheres in the free-molecule flow regime. *Journal of aerosol science*, 37(3):242–259, 2006.

[37] Rogak, S. N., Flagan, R. C., and Nguyen, H. V. The mobility and structure of aerosol agglomerates. *Aerosol Science and Technology*, 18(1):25–47, 1993.

[38] Lall, A. A. and Friedlander, S. K. On-line measurement of ultrafine aggregate surface area and volume distributions by electrical mobility analysis: I. Theoretical analysis. *Journal of Aerosol Science*, 37(3):260–271, 2006.

[39] Eggersdorfer, M. L., Gröhn, A. J., Sorensen, C. M., McMurry, P. H., and Pratsinis, S. E. Mass-mobility characterization of flame-made ZrO2 aerosols: Primary particle diameter and extent of aggregation. *Journal of colloid and interface science*, 387(1):12–23, 2012.

[40] Bird, G. A. *Molecular gas dynamics, Clarendon*. Oxford, 1976.

[41] Zhang, C., Thajudeen, T., Larriba, C., Schwartzentruber, T. E., and Hogan Jr, C. J. Determination of the scalar friction factor for nonspherical particles and aggregates across the entire Knudsen number range by direct simulation monte carlo (DSMC). *Aerosol Science and Technology*, 46(10):1065–1078, 2012.

[42] Köylü, Ü. Ö. and Faeth, G. M. Structure of overfire soot in buoyant turbulent diffusion flames at long residence times. *Combustion and Flame*, 89(2):140–156, 1992.

[43] Shin, W. G., Mulholland, G. W., Kim, S., Wang, J., Emery, M. S., and Pui, D. Y. H. Friction coefficient and mass of silver agglomerates in the transition regime. *Journal of Aerosol Science*, 40(7):573–587, 2009.

[44] Shin, W. G., Mulholland, G. W., and Pui, D. Y. H. Determination of volume, scaling exponents, and particle alignment of nanoparticle agglomerates using tandem differential mobility analyzers. *Journal of Aerosol Science*, 41(7):665–681, 2010.

[45] Seigneur, C., Hudischewskyj, A. B., Seinfeld, J. H., Whitby, K. T., Whitby, E. R., Brock, J. R., and Barnes, H. M. Simulation of aerosol dynamics: A comparative review of mathematical models. *Aerosol Science and Technology*, 5(2):205–222, 1986.

[46] Vincenti, W. G. and Kruger, C. H. *Introduction to Physical Gas Dynamics*, volume 1. Wiley, 1965.

[47] Chapman, S. and Cowling, T. *The Mathematical Theory of Non-Uniform Gases*. Cambridge University Press, 2 edition, 1952.

[48] Deen, W. M. *Analysis of Transport Phenomena*. Topics in chemical engineering. Oxford University Press, 2012. ISBN 9780199740284. URL https://books.google.com/books?id=60YsAwEACAAJ.

[49] Happel, J. and Brenner, H. *Low Reynolds Number Hydrodynamics: With Special Applications to Particulate Media*. Prentice-Hall international series in the physical and chemical engineering sciences. Prentice-Hall, Eaglewood Cliffs, NJ, 1965.

[50] Stokes, G. G. On the effect of the internal friction of fluids on the motion of pendulums. *Transactions of the Cambridge Philosophical Society*, 9, 1851.

[51] Bernal, J. M. G., La Torre, D., and García, J. Transport properties and hydrodynamic centers of rigid macromolecules with arbitrary shapes. *Biopolymers*, 19(4):751–766, 1980.

[52] García de La Torre, J., Jimenez, A., and Freire, J. J. Monte Carlo calculation of hydrodynamic properties of freely jointed, freely rotating, and real polymethylene chains. *Macromolecules*, 15(1):148–154, 1982.

[53] Carrasco, B. and Garcıa de la Torre, J. Improved hydrodynamic interaction in macromolecular bead models. *The Journal of chemical physics*, 111(10): 4817–4826, 1999.

[54] Meakin, P., Chen, Z.-Y., and Deutch, J. M. The translational friction coefficient and time dependent cluster size distribution of three dimensional cluster–cluster aggregation. *The Journal of Chemical Physics*, 82(8):3786–3789, 1985.

[55] Meakin, P. and Deutch, J. M. Properties of the fractal measure describing the hydrodynamic force distributions for fractal aggregates moving in a quiescent fluid. *The Journal of chemical physics*, 86(8):4648–4656, 1987.

[56] Lattuada, M., Wu, H., and Morbidelli, M. Hydrodynamic radius of fractal clusters. *Journal of colloid and interface science*, 268(1):96–105, 2003.

[57] Rotne, J. and Prager, S. Variational treatment of hydrodynamic interaction in polymers. *The Journal of Chemical Physics*, 50(11):4831–4837, 1969.

[58] Yamakawa, H. Transport properties of polymer chains in dilute solution: Hydrodynamic interaction. *The Journal of Chemical Physics*, 53(1):436–443, 1970.

[59] Reuland, P., Felderhof, B. U., and Jones, R. B. Hydrodynamic interaction of two spherically symmetric polymers. *Physica A: Statistical Mechanics and its Applications*, 93(3-4):465–475, 1978.

[60] Mazur, P. and Van Saarloos, W. Many-sphere hydrodynamic interactions and mobilities in a suspension. *Physica A: Statistical Mechanics and its Applications*, 115(1-2):21–57, 1982.

[61] Goldstein, R. F. Macromolecular diffusion constants: a calculational strategy. *The Journal of chemical physics*, 83(5):2390–2397, 1985.

[62] Mansfield, M. L., Douglas, J. F., and Garboczi, E. J. Intrinsic viscosity and the electrical polarizability of arbitrarily shaped objects. *Phys. Rev. E*, 64: 061401, Nov 2001. doi: 10.1103/PhysRevE.64.061401. URL http://link.aps.org/doi/10.1103/PhysRevE.64.061401.

[63] Douglas, J. F., Zhou, H.-X., and Hubbard, J. B. Hydrodynamic friction and the capacitance of arbitrarily shaped objects. *Phys. Rev. E*, 49:5319–5331, 1994.

[64] Millikan, R. A. The general law of fall of a small spherical body through a gas, and its bearing upon the nature of molecular reflection from surfaces. *Physical Review*, 22(1):1, 1923.

[65] Davies, C. N. Definitive equations for the fluid resistance of spheres. *Proceedings of the Physical Society*, 57(4):259, 1945.

[66] Allen, M. D. and Raabe, O. G. Slip correction measurements of spherical solid aerosol particles in an improved Millikan apparatus. *Aerosol Science and Technology*, 4(3):269–286, 1985.

[67] Dahneke, B. E. Slip correction factors for nonspherical bodies – III The form of the general law. *Journal of Aerosol Science*, 4(2):163–170, 1973.

[68] Thajudeen, T., Jeon, S., and Hogan, C. J. The mobilities of flame synthesized aggregates/agglomerates in the transition regime. *Journal of Aerosol Science*, 80:45–57, 2015.

[69] Gopalakrishnan, R., McMurry, P. H., and Hogan, C. J. The electrical mobilities and scalar friction factors of modest-to-high aspect ratio particles in the transition regime. *Journal of Aerosol Science*, 82:24–39, 2015.

[70] Cercignani, C. and Pagani, C. D. Flow of a rarefied gas past an axisymmetric body. I. General remarks. *Physics of Fluids (1958-1988)*, 11(7):1395–1399, 1968.

[71] Bhatnagar, P. L., Gross, E. P., and Krook, M. A model for collision processes in gases. I. Small amplitude processes in charged and neutral one-component systems. *Physical Review*, 94(3):511–525, 1954.

[72] Kogan, M. N. On the equations of motion of a rarefied gas. *Journal of Applied Mathematics and Mechanics*, 22(4):597–607, 1958.

[73] Cercignani, C., Pagani, C. D., and Bassanini, P. Flow of a rarefied gas past an axisymmetric body. II. Case of a sphere. *Physics of Fluids (1958-1988)*, 11 (7):1399–1403, 1968.

[74] Lea, K.-C. *Mass, Heat and Momentum Transfer to a Sphere in a Rarefied Gas*. PhD thesis, University of Missouri-Columbia, August 1980.

[75] Lea, K. C. and Loyalka, S. K. Motion of a sphere in a rarefied gas. *Physics of Fluids (1958-1988)*, 25(9):1550–1557, 1982.

[76] Law, W. S. and Loyalka, S. K. Motion of a sphere in a rarefied gas. II. Role of temperature variation in the knudsen layer. *Physics of Fluids (1958-1988)*, 29(11):3886–3888, 1986.

[77] Loyalka, S. K. Motion of a sphere in a gas: Numerical solution of the linearized Boltzmann equation. *Physics of Fluids A: Fluid Dynamics*, 4(5):1049–1056, 1992.

[78] Takata, S., Sone, Y., and Aoki, K. Numerical analysis of a uniform flow of a rarefied gas past a sphere on the basis of the Boltzmann equation for hard-sphere molecules. *Physics of Fluids A: Fluid Dynamics (1989-1993)*, 5(3): 716–737, 1993.

[79] Melas, A. D., Isella, L., Konstandopoulos, A. G., and Drossinos, Y. Friction coefficient and mobility radius of fractal-like aggregates in the transition regime. *Aerosol Science and Technology*, 48(12):1320–1331, 2014.

[80] Melas, A. D., Isella, L., Konstandopoulos, A. G., and Drossinos, Y. A methodology to calculate the friction coefficient in the transition regime: Application to straight chains. *Journal of Aerosol Science*, 82:40–50, 2015.

[81] Tandon, P. and Rosner, D. E. Translation Brownian diffusion coefficient of large (multiparticle) suspended aggregates. *Industrial & engineering chemistry research*, 34(10):3265–3277, 1995.

[82] Rosner, D. E. and Tandon, P. Aggregation-and rarefaction-effects on particle mass deposition rates by convective-diffusion, thermophoresis or inertial impaction: Consequences of multi-spherule 'momentum shielding'. *Aerosol Science and Technology*, pages 1–17, 2017.

[83] Flagan, R. C. History of electrical aerosol measurements. *Aerosol Science and Technology*, 28(4):301–380, 1998.

[84] Cheng, Y.-S., Allen, M. D., Gallegos, D. P., Yeh, H.-C., and Peterson, K. Drag force and slip correction of aggregate aerosols. *Aerosol Science and Technology*, 8(3):199–214, 1988.

[85] Ehara, K., Hagwood, C., and Coakley, K. J. Novel method to classify aerosol particles according to their mass-to-charge ratioaerosol particle mass analyser. *Journal of Aerosol Science*, 27(2):217–234, 1996.

[86] Radney, J. G., Ma, X., Gillis, K. A., Zachariah, M. R., Hodges, J. T., and Zangmeister, C. D. Direct measurements of mass-specific optical cross sections of single-component aerosol mixtures. *Analytical chemistry*, 85(17):8319–8325, 2013.

[87] Zelenyuk, A. and Imre, D. On the effect of particle alignment in the DMA. *Aerosol science and technology*, 41(2):112–124, 2007.

[88] Li, M., You, R., Mulholland, G. W., and Zachariah, M. R. Development of a pulsed-field differential mobility analyzer: A method for measuring shape parameters for nonspherical particles. *Aerosol Science and Technology*, 48(1): 22–30, 2014.

[89] Bohren, C. F. and Huffman, D. R. *Absorption and Scattering of Light by Small Particles*. John Wiley & Sons, 1983.

[90] Weiss, R. E., Kapustin, V. N., and Hobbs, P. V. Chain-aggregate aerosols in smoke from the Kuwait oil fires. *Journal of Geophysical Research: Atmospheres*, 97(D13):14527–14531, 1992.

[91] Colbeck, I., Atkinson, B., and Johar, Y. The morphology and optical properties of soot produced by different fuels. *Journal of aerosol science*, 28(5): 715–723, 1997.

[92] Corson, J., Mulholland, G. W., and Zachariah, M. R. Friction factor for aerosol fractal aggregates over the entire Knudsen range. *Physical Review E*, 95(1):013103, 2017.

[93] Corson, J., Mulholland, G. W., and Zachariah, M. R. Analytical expression for the friction coefficient of DLCA aggregates based on extended Kirkwood-Riseman theory. *Aerosol Science and Technology*, 51(6):766–777, 2017.

[94] Corson, J., Mulholland, G. W., and Zachariah, M. R. Calculating the rotational friction coefficient of fractal aerosol particles in the transition regime using extended Kirkwood-Riseman theory. *Physical Review E*, 96(1):013110, 2017.

[95] Corson, J., Mulholland, G. W., and Zachariah, M. R. Analytical expression for the rotational friction coefficient of DLCA aggregates over the entire knudsen regime. *Aerosol Science and Technology*, 52(2):209–221, 2018. doi: 10.1080/02786826.2017.1390544.

[96] Corson, J., Mulholland, G. W., and Zachariah, M. R. The effect of electric field induced alignment on the electrical mobility of fractal aggregates. *Aerosol Science and Technology*, page in press, 2018.

[97] Felderhof, B. U. Hydrodynamic interaction between two spheres. *Physica A: Statistical Mechanics and its Applications*, 89(2):373–384, 1977.

[98] Abramowitz, M. and Stegun, I. A. *Handbook of Mathematical Functions: With Formulas, Graphs, and Mathematical Tables*. Applied mathematics series. Dover Publications, 1964. ISBN 9780486612720.

[99] Loyalka, S. K. On the motion of aerosols in nonuniform gases. I. *The Journal of Chemical Physics*, 55(1):1–4, 1971.

[100] Kreyszig, E. *Advanced Engineering Mathematics*. John Wiley & Sons, 2010. ISBN 9780470458365.

[101] Zhou, H.-X., Szabo, A., Douglas, J. F., and Hubbard, J. B. A Brownian dynamics algorithm for calculating the hydrodynamic friction and the electrostatic capacitance of an arbitrarily shaped object. *The Journal of Chemical Physics*, 100(5):3821–3826, 1994.

[102] Shvartsburg, A. A. and Jarrold, M. F. An exact hard-spheres scattering model for the mobilities of polyatomic ions. *Chemical Physics Letters*, 261(1):86–91, 1996.

[103] Cho, K., Hogan Jr, C. J., and Biswas, P. Study of the mobility, surface area, and sintering behavior of agglomerates in the transition regime by tandem differential mobility analysis. *Journal of Nanoparticle Research*, 9(6):1003–1012, 2007.

[104] Sone, Y. and Aoki, K. Forces on a spherical particle in a slightly rarefied gas. *Rarefied Gas Dynamics*, 51(pt 1):417–433, 1977.

[105] Li, M., Mulholland, G. W., and Zachariah, M. R. Understanding the mobility of nonspherical particles in the free molecular regime. *Physical Review E*, 89 (2):022112, 2014.

[106] Swanson, E., Teller, D. C., and de Haën, C. Creeping flow translational resistance of rigid assemblies of spheres. *The Journal of Chemical Physics*, 72 (3):1623–1628, 1980.

[107] García de la Torre, J. and Rodes, V. Effects from bead size and hydrodynamic interactions on the translational and rotational coefficients of macromolecular bead models. *The Journal of chemical physics*, 79(5):2454–2460, 1983.

[108] Sorensen, C. M. and Wang, G. M. Note on the correction for diffusion and drag in the slip regime. *Aerosol Science and Technology*, 33(4):353–356, 2000.

[109] Cheng, M. T., Xie, G. W., Yang, M., and Shaw, D. T. Experimental characterization of chain-aggregate aerosol by electrooptic scattering. *Aerosol Science and Technology*, 14(1):74–81, 1991.

[110] Chen, S.-C., Wang, J., Fissan, H., and Pui, D. Y. H. Exposure assessment of nanosized engineered agglomerates and aggregates using Nuclepore filter. *Journal of nanoparticle research*, 15(10):1955, 2013.

[111] Lattuada, M. Predictive model for diffusion-limited aggregation kinetics of nanocolloids under high concentration. *The Journal of Physical Chemistry B*, 116(1):120–129, 2011.

[112] Ortega, A. and Garcıa de la Torre, J. Hydrodynamic properties of rodlike and disklike particles in dilute solution. *The Journal of Chemical Physics*, 119(18): 9914–9919, 2003.

[113] Halbritter, J. Torque on a rotating ellipsoid in a rarefied gas. *Zeitschrift für Naturforschung A*, 29(12):1717–1722, 1974.

[114] Li, M., Mulholland, G. W., and Zachariah, M. R. Rotational diffusion coefficient (or rotational mobility) of a nanorod in the free-molecular regime. *Aerosol Science and Technology*, 48(2):139–141, 2014.

[115] García de la Torre, J., del Rio Echenique, G., and Ortega, A. Improved calculation of rotational diffusion and intrinsic viscosity of bead models for macromolecules and nanoparticles. *The Journal of Physical Chemistry B*, 111 (5):955–961, 2007.

[116] Mulholland, G. W., Hagwood, C. R., Li, M., and Zachariah, M. R. Effect of particle rotation on the drift velocity for nonspherical aerosol particles. *Journal of Aerosol Science*, 101:65–76, 2016.

[117] Larriba, C. and Hogan Jr, C. J. Ion mobilities in diatomic gases: Measurement versus prediction with non-specular scattering models. *The Journal of Physical Chemistry A*, 117(19):3887–3901, 2013.

[118] Shrivastav, V., Nahin, M., Hogan, C. J., and Larriba-Andaluz, C. Benchmark comparison for a multi-processing ion mobility calculator in the free molecular regime. *Journal of The American Society for Mass Spectrometry*, 28:1540–1551, 2017.

[119] Tekasakul, P., Bentz, J. A., Tompson, R. V., and Loyalka, S. K. The spinning rotor gauge: Measurements of viscosity, velocity slip coefficients, and tangential momentum accommodation coefficients. *Journal of Vacuum Science & Technology A: Vacuum, Surfaces, and Films*, 14(5):2946–2952, 1996.

[120] Bentz, J. A., Tompson, R. V., and Loyalka, S. K. Measurements of viscosity, velocity slip coefficients, and tangential momentum accommodation coefficients using a modified spinning rotor gauge. *Journal of Vacuum Science & Technology A: Vacuum, Surfaces, and Films*, 19(1):317–324, 2001.

[121] Mountain, R. D., Mulholland, G. W., and Baum, H. Simulation of aerosol agglomeration in the free molecular and continuum flow regimes. *Journal of Colloid and Interface Science*, 114(1):67–81, 1986.

[122] Heinson, W. R., Pierce, F., Sorensen, C. M., and Chakrabarti, A. Crossover from ballistic to Epstein diffusion in the free-molecular regime. *Aerosol Science and Technology*, 48(7):738–746, 2014.

[123] Kousaka, Y., Endo, Y., Ichitsubo, H., and Alonso, M. Orientation-specific dynamic shape factors for doublets and triplets of spheres in the transition regime. *Aerosol science and technology*, 24(1):36–44, 1996.

[124] Bottcher, C. J. F. and Belle, O. C. V. *Theory of Electric Polarization, Vol. 1: Dielectrics in Static Fields*. Elsevier Scientific Publishing Company, Amsterdam, 1973.

[125] Dobbins, R. A. Soot inception temperature and the carbonization rate of precursor particles. *Combustion and Flame*, 130(3):204–214, 2002.

[126] Park, K., Kittelson, D. B., Zachariah, M. R., and McMurry, P. H. Measurement of inherent material density of nanoparticle agglomerates. *Journal of Nanoparticle Research*, 6(2):267–272, 2004.

[127] Fernandes, M. X. and García de la Torre, J. Brownian dynamics simulation of rigid particles of arbitrary shape in external fields. *Biophysical journal*, 83 (6):3039–3048, 2002.

[128] Batchelor, G. K. Sedimentation in a dilute dispersion of spheres. *Journal of fluid mechanics*, 52(2):245–268, 1972.

[129] Sorensen, C. M., Hageman, W. B., Rush, T. J., Huang, H., and Oh, C. Aerogelation in a flame soot aerosol. *Physical Review Letters*, 80(8):1782–1785, 1998.

[130] Stimson, M. and Jeffery, G. B. The motion of two spheres in a viscous fluid. *Proceedings of the Royal Society of London. Series A, Containing Papers of a Mathematical and Physical Character*, 111(757):110–116, 1926.

[131] Burgers, J. M. Hydrodynamics. – On the influence of the concentration of a suspension upon the sedimentation velocity (in particular for a suspension of spherical particles). In *Selected Papers of JM Burgers*, pages 452–477. Springer, 1995.

[132] Brenner, H. The slow motion of a sphere through a viscous fluid towards a plane surface. *Chemical engineering science*, 16(3-4):242–251, 1961.

[133] Goldman, A., Cox, R., and Brenner, H. The slow motion of two identical arbitrarily oriented spheres through a viscous fluid. *Chemical Engineering Science*, 21(12):1151–1170, 1966.

[134] Batchelor, G. K. Brownian diffusion of particles with hydrodynamic interaction. *Journal of Fluid Mechanics*, 74(1):1–29, 1976.

[135] Ermak, D. L. and McCammon, J. A. Brownian dynamics with hydrodynamic interactions. *The Journal of chemical physics*, 69(4):1352–1360, 1978.

[136] Brady, J. F. and Bossis, G. Stokesian dynamics. *Annual review of fluid mechanics*, 20(1):111–157, 1988.

[137] Smoluchowski, M. *On the practical applicability of Stokes' law of resistance, and the modifications of it required in certain cases*. University Press, 1912.

[138] Mackaplow, M. B. and Shaqfeh, E. S. G. A numerical study of the sedimentation of fibre suspensions. *Journal of Fluid Mechanics*, 376:149–182, 1998.

[139] Loyalka, S. K. Slip and jump coefficients for rarefied gas flows: Variational results for Lennard-Jones and n (r)-6 potentials. *Physica A: Statistical Mechanics and its Applications*, 163(3):813–821, 1990.

[140] Peterson, T. W., Gelbard, F., and Seinfeld, J. H. Dynamics of source-reinforced, coagulating, and condensing aerosols. *Journal of colloid and interface science*, 63(3):426–445, 1978.

[141] Gelbard, F. and Seinfeld, J. H. Exact solution of the general dynamic equation for aerosol growth by condensation. *Journal of Colloid and Interface Science*, 68(1):173–183, 1979.

[142] Gelbard, F., Tambour, Y., and Seinfeld, J. H. Sectional representations for simulating aerosol dynamics. *Journal of Colloid and Interface Science*, 76(2): 541–556, 1980.

[143] Gelbard, F. and Seinfeld, J. H. Simulation of multicomponent aerosol dynamics. *Journal of colloid and Interface Science*, 78(2):485–501, 1980.

[144] Suck, S. and Brock, J. Evolution of atmospheric aerosol particle size distributions via Brownian coagulation numerical simulation. *Journal of Aerosol Science*, 10(6):581–590, 1979.

[145] Whitby, K. T. Determination of aerosol growth rates in the atmosphere using lumped mode aerosol dynamics. *Journal of Aerosol Science*, 12(3):173–178, 1981.

[146] Seinfeld, J. H. and Pandis, S. N. *Atmospheric Chemistry and Physics: From Air Pollution to Climate Change*. John Wiley & Sons, New York, NY, 1998.

[147] Girshick, S. L. and Chiu, C.-P. Kinetic nucleation theory: A new expression for the rate of homogeneous nucleation from an ideal supersaturated vapor. *The journal of chemical physics*, 93(2):1273–1277, 1990.

[148] Friedlander, S. K. and Wang, C. S. The self-preserving particle size distribution for coagulation by Brownian motion. *Journal of Colloid and Interface Science*, 22(2):126–132, 1966.

[149] Vemury, S., Kusters, K. A., and Pratsinis, S. E. Time-lag for attainment of the self-preserving particle size distribution by coagulation. *Journal of Colloid and Interface Science*, 165(1):53–59, 1994.

[150] Brewster, M. Q. *Thermal Radiative Transfer and Properties*. John Wiley & Sons, 1992.

[151] Spyrogianni, A., Karadima, K. S., Goudeli, E., Mavrantzas, V. G., and Pratsinis, S. E. Mobility and settling rate of agglomerates of polydisperse nanoparticles. *The Journal of chemical physics*, 148(6):064703, 2018.

[152] Kelesidis, G. A., Goudeli, E., and Pratsinis, S. E. Morphology and mobility diameter of carbonaceous aerosols during agglomeration and surface growth. *Carbon*, 121:527–535, 2017.

[153] Feng, Y. and Kleinstreuer, C. Analysis of non-spherical particle transport in complex internal shear flows. *Physics of Fluids*, 25(9):091904, 2013.

[154] Kolb, M., Botet, R., and Jullien, R. Scaling of kinetically growing clusters. *Physical Review Letters*, 51(13):1123, 1983.

[155] Meakin, P. The effects of rotational diffusion on the fractal dimensionality of structures formed by cluster–cluster aggregation. *The Journal of Chemical Physics*, 81(10):4637–4639, 1984.

[156] Tian, L., Ahmadi, G., and Tu, J. Brownian diffusion of fibers. *Aerosol Science and Technology*, 50(5):474–486, 2016.

Publications and Presentations

Accepted publications

1. **Corson, J.**, Mulholland, G. W., and Zachariah, M. R. Friction factor for aerosol fractal aggregates over the entire Knudsen range. *Physical Review E*, 95(1):013103, 2017. DOI: 10.1103/PhysRevE.95.013103.

2. **Corson, J.**, Mulholland, G. W., and Zachariah, M. R. Analytical expression for the friction coefficient of DLCA aggregates based on extended Kirkwood-Riseman theory. *Aerosol Science and Technology*, 51(6):766–777, 2017. DOI: 10.1080/02786826.2017.1300635.

3. **Corson, J.**, Mulholland, G. W., and Zachariah, M. R. Calculating the rotational friction coefficient of fractal aerosol particles in the transition regime using extended Kirkwood-Riseman theory. *Physical Review E*, 96(1):013110, 2017. DOI: 10.1103/PhysRevE.96.013110.

4. **Corson, J.**, Mulholland, G. W., and Zachariah, M. R. Analytical expression for the rotational friction coefficient of DLCA aggregates over the entire knudsen regime. *Aerosol Science and Technology*, 52(2):209–221, 2018. DOI: 10.1080/02786826.2017.1390544.

5. **Corson, J.**, Mulholland, G. W., and Zachariah, M. R. The effect of electric field induced alignment on the electrical mobility of fractal aggregates. *Aerosol*

Science and Technology, 2018. DOI: 10.1080/02786826.2018.1427210.

Submitted publications

1. **Corson, J.**, Mulholland, G. W., and Zachariah, M. R. Hydrodynamic Interactions between Aerosol Particles in the Transition Regime. *Journal of Fluid Mechanics*.

Delivered presentations (presenting author underlined)

1. **Corson, J.**, Zachariah, M. R., Mulholland, G. W., and Baum, H. Extension of Kirkwood-Riseman Theory across the Entire Range of Knudsen Numbers. Annual Meeting of the American Physical Society Division of Fluid Dynamics. Portland, OR. November 2016. (Platform presentation)

2. **Corson, J.**, Mulholland, G. W., and Zachariah, M. R. Calculating the Translational Friction Coefficient of DLCA Aggregates in the Transition Regime. American Association for Aerosol Research Annual Meeting. Raleigh, NC. October 2017. (Platform presentation)

3. **Corson, J.**, Mulholland, G. W., and Zachariah, M. R. Drag and Torque on Fractal Aggregates in the Transition Regime. American Association for Aerosol Research Annual Meeting. Raleigh, NC. October 2017. (Poster)

4. **Corson, J.**, Mulholland, G. W., and Zachariah, M. R. Solving the GDE for Nucleation, Surface Growth, and Coagulation using the Nodal Method. American Association for Aerosol Research Annual Meeting. Raleigh, NC. October 2017. (Poster)

5. **Corson, J.**, Mulholland, G. W., and Zachariah, M. R. Drag and Torque on Fractal Aerosol Aggregates Across the Entire Knudsen Regime. Fourteenth Annual Symposium of the Burgers Program for Fluid Dynamics. College Park, MD. November 2017. (Poster)

Planned presentations (abstract submitted)

1. **Corson, J.**, Mulholland, G. W., and Zachariah, M. R. NGDE: A Simple, MATLAB-based Code for Solving the General Dynamic Equation. 10th International Aerosol Conference. St. Louis, MO. September 2018. (Platform presentation)

2. **Corson, J.**, Mulholland, G. W., and Zachariah, M. R. The Effect of Electric Field Induced Alignment on the Electrical Mobility of Fractal Aggregates. 10th International Aerosol Conference. St. Louis, MO. September 2018. (Platform presentation)